STRATEGIC DESIGN OF AMINO ACID BASED LIGANDS AND THEIR SELF-ASSEMBLED HOMOCHIRAL COORDINATION ARCHITECTURES: STRUCTURAL DIVERSITY AND SENSING APPLICATIONS

Navnita Kumar

A thesis submitted for the partial fulfillment of the degree of Doctor of Philosophy

Department of Chemical Sciences
Indian Institute of Science Education and Research Mohali

June 2015

Dedicated to My Parents and My lovely Sister

Declaration

The work presented in this thesis has been carried out by me under the guidance of Prof. Sanjay K. Mandal at the Indian Institute of Science Education and Research Mohali. This work has not been submitted in part or in full for a degree, a diploma, or a fellowship to any other university or institute. Whenever contributions of others are involved, every effort is made to indicate this clearly, with due acknowledgement of collaborative research and discussions. This thesis is a bona fide record of original work done by me and all sources listed within have been detailed in the bibliography.

Navnita Kumar

In my capacity as the supervisor of the candidate's project work, I certify that the above statements by the candidate are true to the best of my knowledge.

Prof. Sanjay K. Mandal

Acknowledgements

I would like to thank all the people who have contributed in their own way for the completion of this fruitful and unforgettable journey. First and foremost, I thank my supervisor, Professor Sanjay K. Mandal, for giving me the intellectual freedom in my work, engaging me in new ideas, and demanding a high quality of work in all my accomplishments. I appreciate all his contributions of time and ideas to make my doctoral work experience productive and stimulating. His critical and logical thinking, never say impossible attitude and disciplined behavior has helped me in growing as a better person both professionally and personally. The joy and enthusiasm he has for his research was a source of constant motivation for me, even during the tough times during this work.

I would also like to thank the doctoral committee members Professor Ramesh Kapoor and Dr. Sanjay Singh for their valuable suggestions.

I gratefully acknowledge Dr. Sadhika Khullar for her understanding, encouragement and personal attention which have helped me throughout my tenure at IISER Mohali. I am also thankful to all my lab members Biswajit Laha, Sandeep Kumar, Vijay Gupta, Datta Markad, Gouri Chakraborty, Prasenjit Das, Shradha Gandhi, Smriti Thakur and Alisha Gogia for creating a fun-filled and cordial environment in the lab which makes research so much enjoyable. I would never forget the beautiful moments I shared with the project students Amita, Karan, Gaurav, Nitish, Sandhya, Uday, Sayan, Geetanjali, Selva, Manpreet and Babita.

I would like to extend my thanks to Prerna, Prithwish and Joydip who are among my most critical and constant supporters and special thanks to my batchmates Vir and Sheena for their constant support. I would also like to thank all the lab assistants, especially Mr. Mangat, Mr. Satwinder and Mr. Bahadur for their help.

I would like to take this opportunity to thank all my teachers who have influenced my life in some way or the other.

I am indebted to MHRD, India, for providing me with a scholarship and IISER Mohali for endowing state-of-the-art infrastructure for my research.

Sincere thanks to my best friends - Pratima, Prasen, Sandy and Anand - for taking all my tantrums and understanding me even when I was on the wrong side of the argument. Finally, I express my gratitude towards my family without whom I would not be the person that I am today. I am indebted to them for the unconditional love and the support they have showered on me throughout my life. And for my little sister 'Sweety' - you were, you are and you will always be my bundle of joy…my reason to smile.

Last but not the least, I thank the Almighty for giving me the courage and dedication to accomplish this journey.

List of Figures

Chapter I

Chapter III

List of Schemes

List of Tables

Chapter III

Appendix

Acronyms and Abbreviations

CPs	Coordination Polymers
SCCs	Supramolecular Coordination Complexes
L-Tyr	L-Tyrosine
L-H_2Tyr4-nitro	L-N-(methyl-4-nitro)-Tyrosine
L-H_2Tyr4-fluoro	L-N-(methyl-4-fluoro)-Tyrosine
L-H_2Tyr4-methoxy	L-N-(methyl-4-methoxy)-Tyrosine
L-H_2Tyrbenz	L-N-(benzyl)-Tyrosine
L-H_2Tyrthio	L-N-(methyl-2-thiophenyl)-Tyrosine
L-H_2Tyr4-pyr	L-N-(methyl-4-pyridyl)-Tyrosine
L-H_3Sersal	L-N-(2-hydroxybenzyl)-Serine
L-H_2Serthio	L-N-(methyl-2-thiophenyl)-Serine
L-H_3ser-5Cl-sal	L-N-(2-hydroxy-5-chlorobenzyl)-Serine
L-H_3ser-3Cl-sal	L-N-(2-hydroxy-3-chlorobenzyl)-Serine
L-H_3ser-3OMe-sal	L-N-(2-hydroxy-3methoxybenzyl)-Serine
L-H_3ser-5NO_2-sal	L-N-(2-hydroxy-5-nitrobenzyl)-Serine
L-H_3ser-5OMe-sal	L-N-(2-hydroxy-5-methoxybenzyl)-Serine
L-H_2Serbenz	L-N-(benzyl)-Serine
L-HPhebenz	L-N-(benzyl)-Phenylalanine
L-HPhe4-OH	L- N-(4-hydoxybenzyl)-phenylalanine
L-HPhethio	L-N-(methyl-2-thiophenyl)-Phenylalanine
L-HPhe4-nitro	L-N-(methyl-4-nitro)-Phenylalanine
L-HGly-4-OH	L- N-(4-hydoxybenzyl)-glycine
L-H_2Hissal	L-N-(2-hydroxybenzyl)-Histidine
L-HTyr-O, N-Didan	L-N,O-didansyl-tyrosine
L-HTyr-N-dan	L-N-dansyl-tyrosine
adi	adipate
succ	succinate
mal	maleate
fum	fumarate

4,4’-bpy	4,4’-bipyridine
DMSO	Dimethyl Sulphoxide
DMF	N, N’-dimethyl Formamide
MeOH	Methanol
RT	Room Temperature
LMCT	Ligand to Metal Charge Transfer

Contents

Synopsis

Since the turn of the new millennium, there is a giant leap in the sphere of strategic design of diverse coordination architectures due to their structural aesthetics and possible roles in various applications such as catalysis, sensing, molecular separation, gas and liquid adsorption, luminescence, ion exchange, magnetism, non-linear optics, etc. The construction of such coordination architectures, which include coordination polymers (CPs) and supramolecular coordination complexes (SCCs), from the metal ions/clusters and organic linkers depends on coordination bonds and supramolecular interactions, such as hydrogen bonds, π-π stacking of aromatic moieties or C-H…O interactions, etc. In CPs coordination bonds provide the major contribution in their constructions while the formation of SCCs of higher dimensionality occurs through the association of discrete precursors, such as monomers and dimers, by strong supramolecular interactions. Modulation of the contribution of coordination bonds and hydrogen bonds has resulted in numerous diverse (structural and functional) coordination architectures in recent years. While these two bonding are orthogonal in nature, the formation of CPs over SCCs and vice versa (and their inter-conversions) could be due to the hierarchical importance of these two forces in the overall structure. Through judicious choice of the components in making such coordination architectures, it is possible to generate materials with tunable structures and properties.

This thesis focuses on (a) the strategic design and synthesis of L-amino acid based ligands in understanding the various factors that influence the self-assembly of homochiral neutral CPs or SCCs of Ni^{2+}, Cu^{2+}, Zn^{2+} and Cd^{2+} under non-hydrothermal conditions in good to high yields, and (b) their applications as selective chromogenic and/or fluorogenic chemosensors for cations (Cu^{2+}), anions (F^-, I^- and OAc^-) and neutral small molecules (nitroaromatics, anilines, etc.). These are characterized by elemental analysis, FT-IR, Raman and UV-Vis spectroscopy, TGA, single crystal and powder X-ray diffraction, and ESI-MS analysis. Their chirality is established in the solution state by polarimetry and CD spectroscopy. There are four chapters in this thesis. A brief summary of each chapter is provided below.

In Chapter I (Introduction), the rationale for the need of the current work is outlined with challenges faced in doing so. To understand the structural and functional aspects of these

coordination architectures, identification of the factors controlling their formation has been the key to global research in this field. On the other hand, induction of chirality in such networks has been sought due to their usefulness in asymmetric catalysis, chiral recognition and enantiomeric separation, non-linear optics, etc. One of the ways to make chiral coordination architectures is the self-assembly of optically pure chiral organic ligands with the metal ions. One such set of ligands that has been utilized to some extent is the reduced Schiff base ligands of various cheap and readily available L-amino acids, which contains multiple hydrogen bond acceptor/donor entities. However, a systematic study to obtain structural diversity due to a variation of these components has not been done.

With a demand for fast and reliable detection of biological and chemical moieties because of their prevalent relevance in global health and environment, in the past few decades numerous molecular sensors (chemosensors and biosensors) have been developed based on the selective or differential binding to various analytes utilizing absorption (chromogenic) and/or fluorescence (fluorogenic) spectroscopy. In the literature, neutral macrocyle based sensors with the first report of octamethylcalix[4]pyrrole by Sessler et al. are the most common, where anion-π interactions are monitored; however, their cumbersome synthesis that increases the cost makes them less favorable. Due to their luminescent property, homochiral coordination architectures of amino acid based ligands are considered an alternate to this challenge.

In Chapter II (Experimental Section), synthesis protocols of all ligands and their homochiral coordination architectures are described. A general methodology was developed to synthesize the ligands at optimized conditions obtained through design of experiments. Except those with neutral and anionic linkers, the coordination architectures were synthesized via a two-component self-assembly reaction of metal salt and the respective monopotassium salt of the ligand in a 1:2 or 1:1 ratio under ambient conditions; the solvent for the reaction was chosen based on the solubility of the product and the by-product, K_2SO_4. With a brief summary of each characterization technique used in this study, procedures for their characterization by various analytical techniques mentioned above are detailed.

In Chapter III (Results and Discussion), there are two major sections: (a) structural diversity in the self-assembled homochiral coordination architectures, and (b) selective chromogenic and/or fluorogenic sensing of cations, anions and neutral small molecules. For showcasing such structural and functional diversity, mostly amino acid based Schiff base ligands are methodically synthesized and structurally characterized. These ligands are temporally engaged in the synthesis of about sixty neutral coordination architectures with unparallel properties, which are detailed below.

A. Structural Diversity in the Self-assembled Homochiral Coordination Architectures

In this subsection, the coordination architectures of the divalent metal ions (Ni^{2+}, Cu^{2+}, Zn^{2+} and Cd^{2+}) are categorized based on the metal to ligand ratios (1:2 and 1:1) where the ligands are found to be either monoanions or dianions in the absence of any other anionic linker; unlike the bifunctional neutral linker, a dicarboxylate linker as the third component in the self-assembly reaction allows the ligand to be monoanionic instead of dianionic. This arises from the overall charge consideration of the coordination architectures as these are neutral in nature.

Coordination architectures with a 1:2 metal to ligand ratio

Through the strategic design of monoanionic ligands, structural diversity in chiral coordination architectures under similar reaction conditions is demonstrated with the formation of either the CPs with a general formula $\{[MX_2]\cdot G\}_n$, where M^{2+} = Ni^{2+}, Cu^{2+}, Zn^{2+} and Cd^{2+}; X = L-HTyrbenz, L-HSerbenz or L-HTyrthio, or SCCs with a general formula $[MY_2(solvent)]\cdot G$, where Y = L-HTyr4-pyr, L-HSerthio, L-Phethio, L-HTyr4-nitro, L-HTyr4-fluoro or HTyr4-methoxy, and solvent = water or methanol; in both the cases, G represents the lattice solvent molecules (water, methanol or DMSO). In addition to the detailed comparison of their spectroscopic data, PXRD patterns and TGA scans, the crystallographic characterization of the Cu^{2+} analogs demonstrates such diversification due to change in metal centers. The coordination architecture in each case is highly influenced by parameters like the substitution on the ligands, the solvent of crystallization, etc. For example, the availability of a donor atom (either from the phenolic OH group or the

carboxylate group of one of the ligands) for bridging between the Cu^{2+} centers provides the CPs while no such availability allows a water/methanol molecule to occupy the fifth site around the Cu^{2+} center for generating hydrogen bonded SCCs. Clearly, the coordination of a water/methanol molecule to the Cu^{2+} center is controlled by the nature of substitution present in the ligand. Even though $\{[Cu(L\text{-}HTyrbenz)_2]\cdot CH_3OH\cdot H_2O\}_n$, and $\{[Cu(L\text{-}HSerbenz)_2]\cdot 3H_2O\}_n$ are CPs with carboxylate bridging, but in the former case it is syn-anti bridging carboxylate whereas in the latter it is anti-anti bridging carboxylate. On the other hand, the essence in the formation of $\{[Cu(L\text{-}HTyrthio)_2]\cdot H_2O\}_n$ lies in the growing of the spiral polymer via the unique phenolic bridging with a distance between two Cu^{2+} centers of 10.806(9)Å.

The formation of SCC, $[Cu(L\text{-}Phethio)_2(H_2O)]\cdot 3H_2O$, illustrates the significance of the phenolic part in generation of a CP. However, the length of the $–CH_2OH$ group in the L-H_2Serthio is much less to bridge between the two Cu^{2+} centers and thus a water molecule is coordinated to occupy the fifth site forming a SCC instead of a CP. In case of L-HTyr4-pyr, strong hydrogen bonding of the pyridyl nitrogen with the phenolic group does not allow the latter to bind to Cu^{2+}.

In order to display the solvent effect on the coordination architectures, two solvates based on the L-HTyr4-nitro ligand $[Cu(L\text{-}HTyr4\text{-}nitro)_2(H_2O)]\cdot 2DMSO$ and $[Cu(L\text{-}HTyr4\text{-}nitro)_2(H_2O)]\cdot 2CH_3OH$ are reported. Due to the variation of the lattice solvent (DMSO vs methanol) hydrogen bonding interactions in these two SCCs are quite different and lead to a great deal of modulation in the conformation of the ligands around the metal center. Furthermore, the DMSO solvate has been found to be preferred over methanol solvate through (a) the conversion of the methanol solvate to the DMSO solvate in dissolving the single crystals of the former in DMSO and (b) exclusive formation of the DMSO solvate from crystallizing $[Cu(L\text{-}HTyr4\text{-}nitro)_2(H_2O)]\cdot 2H_2O$ in a mixture of DMSO/methanol (1:1, v/v). The substitution of the nitro group in L-H_2Tyr4-nitro by a flourine or methoxy group has provided two diverse SCCs, $[Cu(L\text{-}HTyr4\text{-}fluoro)_2(H_2O)]\cdot H_2O$ and $[Cu(L\text{-}HTyr4\text{-}methoxy)_2(CH_3OH)]$.

Coordination architectures with a 1:1 metal to ligand ratio

Unlike the coordination architectures with monoanionic ligands, those with dianionic ligands (such as L-HSersal and its derivatives) not only show a different repeat unit, bis(μ-phenoxo), in the coordination architectures but provide an opportunity to show hierarchical importance of coordination and hydrogen bonds through making derivatives with bifunctional neutral linkers - conversion of CPs to SCCs. With the L-H_3Sersal and its derivatives, a series of isostructural CPs with a general formula $\{[M_2Z_2(H_2O)]\cdot G\}_n$, where M^{2+} = Ni^{2+}, Cu^{2+}, Zn^{2+} and Cd^{2+}; Z = L-HSersal, L-Hser-5OMe-sal, L-Hser-5NO_2-sal, L-Hser-5Cl-sal, L-Hser-3Cl-sal or L- Hser-3OMe-sal and G = Water or DMF, is obtained. It appears that there are no electronic or steric effects on the structures of the coordination architectures due to various substitutions (5-OMe, 5-NO_2, 5-Cl, 3-OMe or 3-Cl) in the ligands. As an example of converting the CPs into SCCs, a bifunctional neutral linker, 4,4'-bpy, is used to make four such derivatives with a general formula $[Cu_2(4,4'\text{-bpy})(Z)_2]\cdot G$, where Z = L-HSersal, L-Hser-5OMe-sal, L-Hser-5NO_2-sal or L-Hser-5Cl-sal and G = water. In doing so, the starting nonporous CPs become porous SCCs as evidenced by the water vapor adsorption studies, which is the first example in the literature.

On the other hand, for the histidine based ligand (L-H_2Hissal), dicarboxylate linkers - adipate, succinate, fumarate and maleate - result in the formation of SCCs with a general formula $[Ni_2(\text{dicarboxylate})(\text{L-HHissal})_2(H_2O)_2]\cdot nH_2O$ (n = 4-8) where the hydroxy group in the ligand is not deprotonated under the conditions tried in this work. All these isostructural SCCs have a unique property for encapsulating water clusters of various sizes. For example, in the adipate analog an octamer of water - the first example of a zig-zag chain structure - is encapsulated within the supramolecular assembly. The strength of hydrogen bonding in the water cluster (the O---O distances: 2.702 Å - 2.760 Å) is similar to that found in ice.

B. Selective Chromogenic and/or Fluorogenic Sensing of Anions, Cations and Neutral Small Molecules

In this subsection, the role of various factors affecting the sensing abilities of the ligands and their selected coordination architectures are discussed intensively. Following the strategy

used to enhance the anion sensing ability of the macrocycles with various electron withdrawing groups, which generates a positive quadruple over their aromatic part for the anion-π interactions, as an example a nitro group is attached at the para position of L-H_2Tyrbenz to obtain L-H_2Tyr4-nitro. Amino acids like L-Tyrosine, L-Phenylalanine and L-Tryptophan act as fluorophores, and thus the ligands derived from these and their coordination architectures show good photoluminescence property that makes these fluorogenic sensors. The mechanism involved for each sensor is also analysed based on the data obtained from various analytical techniques. These are grouped in four categories with details provided below:

(i) Solvent mediated flip-flop fluorogenic sensors for halides (iodide/fluoride)

Utilizing the natural photoluminescence property of L-Tyrosine, the sensing abilities of its derivatives are checked toward various analytes in two solvents with different polarity. For example, L-NaHTyr4-nitro in methanol (**1a**) is found to be an iodide sensor (iodide ion shows a drastic fluorescence quenching) whereas in DMSO (**1b**) it acts as a fluoride sensor (fluoride ion shows enhancement in fluorescence intensity).

The sensing ability of L-NaHTyr4-nitro and L-H_2Tyr4-nitro in DMSO are similar. Furthermore, the ability of L-H_2Tyr-4-nitro in DMSO to act as a reversible pH indicator is also observed. The color of its DMSO solution goes to yellow when pH (below 5) is acidic whereas it turns pink when pH (above 9) is alkaline. Its pH dependent change in color and the UV-Vis absorption are reversible even after several cycles of chronological alternative addition of HCl and NaOH. Thus, L-H_2Tyr4-nitro acts as solvent mediated differential halide sensor and an optical pH indicator**.** In order to further analyze the role of various groups in this kind of differential sensors, a series of other ligands like L-HPhe4-nitro, L-H_2Tyr4-fluoro and L-H_2Tyr4-methoxy are also checked for their ability in anion sensing.

(ii) Solvent assisted chromogenic and/or fluorogenic sensor for anions

Compared to L-NaHTyr4-nitro just discussed above, its Cu^{2+} complex [Cu(L-HTyr4-nitro)$_2$(H_2O)]$\cdot 2H_2O$ in DMSO acts as a colorimetric sensor for F^- and OAc^- (see Figure 7). On addition of F^-, the color of the sensor solution turns green whereas for OAc^- it turns dark

green and for the rest of the halides it remains the same. Furthermore, a solvent effect is observed on its sensing ability where inferior results are observed in methanol compared to DMSO, may be due to the greater extent of interaction between an anion and a protic solvent (methanol) than an aprotic solvent (DMSO) decreasing the intensity of anion-π interactions responsible for such detection. As noted above, a dramatic solvent effect is observed in the coordination architectures of this complex (DMSO vs Methanol solvates). This is also evident from the solvent effect on the intra-ligand electronic transitions. This behavioral change towards F^- and OAc^- is not only observed chromogenically but also verified via a number of spectroscopic techniques including absorption and fluorescence.

In addition to the observation for solvent dependency on the sensing behavior of [Cu(L-HTyr4-nitro)$_2$(H_2O)]·2H_2O, further consideration of other variations of its components, such as the metal center and the substitution of the nitro group by a flourine, hydrogen or methoxy group, provides deeper insight into its function. On replacement Cu^{2+} with Zn^{2+} in it, the sensing ability of the resultant [Zn(L-HTyr4-nitro)$_2$(H_2O)]·2DMSO, which has a similar supramolecular architecture toward F^- is lessened. For the [Cu(L-HTyr4-fluoro)$_2$(H_2O)]·H_2O, a similar sensing behaviour in DMSO is observed compared to the nitro analogue while the {[Cu(L-HTyrbenz)$_2$]·CH_3OH·H_2O}$_n$, which is a CP, shows negligible sensing ability in DMSO. On the other hand, [Cu(L-HTyr4-methoxy)$_2$(CH_3OH)] is found to be a better sensor than the {[Cu(L-HTyrbenz)$_2$]·CH_3OH·H_2O}$_n$ due to the resonance effect of the electron donating methoxy group.

In order to demonstrate the role of two same ligands (homoligands) with electron withdrawing groups, corresponding heteroleptic complexes, [Cu(L-HTyr4-nitro)(L-Tyrosine)] and [Cu(L-HTyr4-fluoro)(L-Tyrosine)]·3H_2O, respectively, are studied and found to be less effective in their sensing abilities for the anions.

(iii) <u>Multi-responsive sensor for cations, anions and neutral molecules</u>

The concept of differential receptor, i.e., a single-molecular multianalyte receptor, is getting very popular in recent times. However, the coalescing of multiple fluorophores into a single receptor to attain the property of differential sensing is not much explored in the literature. In this study, an unprecedented single-molecular multianalyte receptor (ONE-for-THREE), L-

NaHTyrthio, is designed and synthesized based on the amalgamation of two fluorophores (4-hydroxy benzyl group from tyrosine and thiophene) for selective sensing of a cation (Cu^{2+}), neutral small molecules (nitrobenzene and aniline) and an anion (F^-) over other analytes. In this example, similar responses for different kinds of analytes attributes for Cu^{2+} and F^- sensing (using fluorescence quenching) whereas its variable spectral responses accredited towards the sensing of nitrobenzene (fluorescence quenching) and aniline (shift in $\lambda_{emission}$). For all analytes, lifetime measurements with or without analytes to certify the role of static or dynamic quenching are done. In each case, the quenching constant is calculated from the respective Stern-Volmer plot which is found to be non-linear in nature. The role of L-NaHTyrthio as an ON-OFF sensor for Cu^{2+} ions is also studied using Na_4EDTA (where H_4EDTA = ethylene diamine tetraacetic acid).

Through various modulations in the L-NaHTyrthio, the importance of tyrosine and thiophene moieties in the photoluminescence property of the sensor is further established through (a) the replacement of the methylthiophene with a benzyl (L-NaHTyrbenz), methyl-4-pyridyl (L-NaHTyr4-pyr) or 4-nitro-benzyl (L-NaHTyr4-nitro) moiety, (b) the reversal of the position of hydroxy-benzyl and benzyl group (L-NaHTyrbenz vs. L-NaPhe-4-OH) with respect to the chiral center.

(iv) Fluorogenic sensors with four-fold symmetry for nitroanilines

Even though the fluorescence ability of the amino acid based ligands mentioned in the above sections are moderate, the intensity of these ligands are further increased via tagging them with better fluorophores like dansyl chloride in the L-H_2Tyr-N-Dan**.** In doing so, a systematic study of various analytes has indicated selective behaviour of both L-H_2Tyr-N-Dan and its Cu^{2+} paddle-wheel complex [Cu_2(L-HTyr-N-Dan)$_4$(H_2O)$_2$] with four-fold symmetry (based on the crystal structure determination) as sensors for the nitroanilines (particularly p-nitroaniline) through fluorescence quenching due to $\pi-\pi$ interactions between the aromatic moieties of the ligand (dansyl part) and the analyte. Since the dansyl part of the ligand is far from the Cu^{2+} centers in [Cu_2(L-HTyr-N-Dan)$_4$(H_2O)$_2$], there is no marked difference in the quenching ability of various analytes towards [Cu_2(L-HTyr-N-Dan)$_4$(H_2O)$_2$]

compared to the L-H_2Tyr-N-Dan itself with a detection limit of 0.53 ppm for p-nitroaniline. This is further confirmed by its Zn^{2+} analogue, which enhances the fluorescence, with the same detection limit. It should be noted here that in the literature the dansylated amino acids are used as sensors for various metal cations but the use of these for sensing nitro aromatics is done for the first time in this work. Furthermore, a comparative study between the photoluminescence ability of O,N-didansylated L-tyrosine and its coordination architectures is compared to their N-dansylated L-tyrosine analogues.

In Chapter IV (Conclusions and Future Directions), conclusions are drawn from the work in this thesis and future directions of this work are suggested. In this work, the role of various substitutions in the ligands as well as solvent of crystallization has been demonstrated through the formation of diversified coordination architectures. The solid-state structures were determined by single crystal XRD while bulk purity was confirmed by powder XRD. Spectroscopic and thermal properties of these compounds were studied by UV-vis, FTIR, Raman, and TGA, respectively. Polarimetry and CD spectroscopy confirm the homochirality of the ligands and their coordination architectures. Exploration of these coordination architectures in sensing applications has indicated their suitability as selective chromogenic and/or fluorogenic chemosensors for cations, anions and neutral small molecules at the ppb or ppm level. We believe that this study provides a new path for the application of such materials as new sensors for various analytes. In particular, those with Lanthanides will be of great interest in the field.

Chapter I
Introduction

In the last few decades the strategic design of coordination architectures with diverse structural aesthetics and functional tunablity arising from the unlimited combinations of organic (ligands/linkers) and inorganic (metal ions/clusters) building blocks is the main focus in this field. This escalating surge in the research of coordination architectures has been there due to their possible roles in various applications, like catalysis,[1] luminescence,[2,3] molecular separation,[3-6] gas and liquid adsorption,[4-7] magnetism,[3-6,8] etc. These coordination architectures, which include Coordination Polymers (CPs) and Supramolecular Coordination Complexes (SCCs), are formed through self-assembly of various components based on coordination bonds and supramolecular interactions, such as hydrogen bonds, π-π stacking of aromatic moieties or C-H…O interactions, etc.[9-20] Coordination bonds are the major pillars in the building block of coordination polymers whereas the progression of the supramolecular assemblies into higher dimentionality is through strong supramolecular interactions between discrete precursors, such as monomers and dimers.

On the other hand, chiral coordination architectures are envisioned as a versatile tool for various enantioselective applications, including the separation of optical isomers and the promotion of catalytic enantioselective reactions, chiral recognition and enantiomeric separation, non-linear optics, etc.[21-24] The self-assembly of optically pure chiral organic ligands with the metal ions induces chirality in the coordination architecture. Amino acids are the best choice for the preparation of these chiral ligands not only due to their low cost and easy availability but also due to their abilities to act both as hydrogen bond donors and acceptors and to show different binding modes with the metal centers through various functionalities present in these, e.g., carboxylate, amine, hydroxy, etc.[21-24] One such set of ligands that has been utilized to some extent is the reduced Schiff base ligands of various amino acids.[25-52] However, their use in making coordination architectures under hydrothermal conditions is limited due to poor thermal stability.[53]

One of the relevant applications of these coordination architectures is sensing. The demand for fast and reliable detection of biological and chemical moieties is continuously growing because of their prevalent relevance in global health, national security and environment. In recent times, numerous molecular sensors (chemosensors and biosensors) have been developed based on the selective or differential binding to various analytes.[54-58]

Self-assembly of Coordination Architectures

The most prevailing approach to obtaining the coordination architectures is the bottom-up construction of a structural design from the various components by the hierarchical self-assembly process. This self-assembly process is engrossed in a harmonized augmentation of the architectural complexity of the structure.[59] This starts from independent components/precursors and grows in dimensionality through regimented reactivity to obtain the final desirable product(s). Some or all the components like metal ion or cluster, ligands, linkers, solvent and the guest molecules collaborate into the self-assembly to yield diverse coordination architectures as schematically depicted in Figure 1.1.

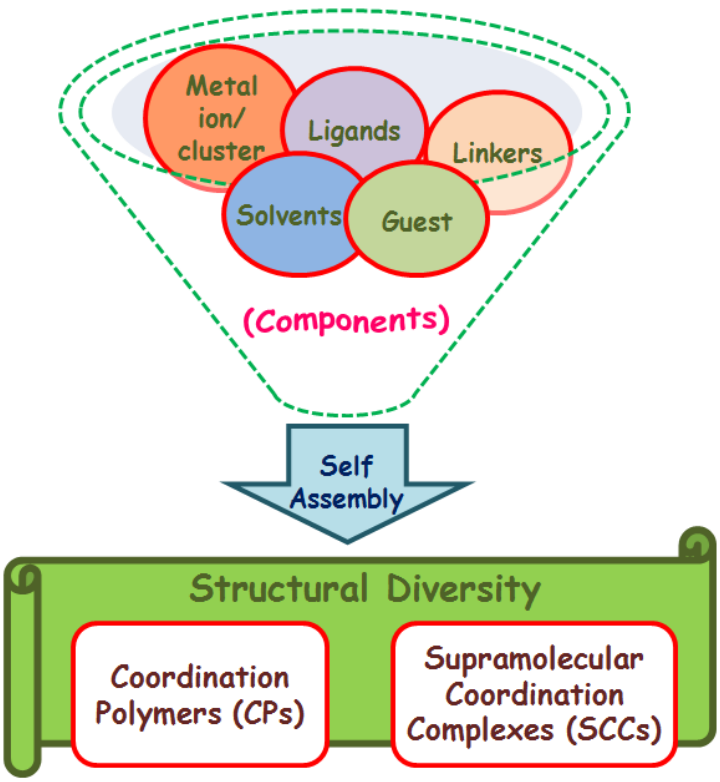

Figure 1.1. General method for the generation and diversification of coordination architectures.

For the reaction between Metal ions/clusters (Lewis acids) and neutral and anionic ligands/linkers (Lewis bases), the former accepts pairs of electrons from the latter. This Lewis acid-base reaction in which ligands/linkers coordinate to a central metal ion by coordinate covalent bonds forms the molecular building units. These molecular building units can either be glued to each other by the interplay of coordination bond by various spanning ligands (linkers) or supramolecular interactions to yield complex coordination architectures.[60-65] Herein, two orthogonal processes are exploited: coordination-driven self-assembly and supramolecular interactions driven self- assembly. The first type of self-assembly yields infinite networks (Coordination Polymers) of metal centers or inorganic clusters bridged by simple organic linkers through metal – ligand coordination bonds. In these network the directionalities of the rigid precursors used determines the structural outcome. In the second type of self-assembly, a higher degree of hierarchical organization of the components is achieved through the use of supramolecular interactions forming diverse networks (Supramolecular Coordination Complexes).

Coordination Polymers (CPs)

In CPs, coordination bonds between the metal ion/clusters and ligands provide the major contribution to their construction.[66-71] The higher dimentionality is also obtained through coordination bonds between the metal ions and the linkers as shown in Figure 1.2.

Supramolecular Coordination Complexes (SCCs)

The formation of supramolecular coordination complexes of higher dimensionality occurs through the association of discrete precursors, such as monomers and dimers, by strong supramolecular interactions like hydrogen bonding, π–π, cation-π, anion-π, hydrophobic or van der Waals interactions as shown in Figure 1.3.[72-76]

The hierarchical formation, in which growing complexity is achieved through well-defined steps that iteratively increase the dimensionality of a material, is particularly attractive in that each unique interaction can be carefully designed. Hence, by striking a perfect balance between coordination bonds and supramolecular interactions in design methodologies desirable coordination architectures with promising functional applications can be achieved.

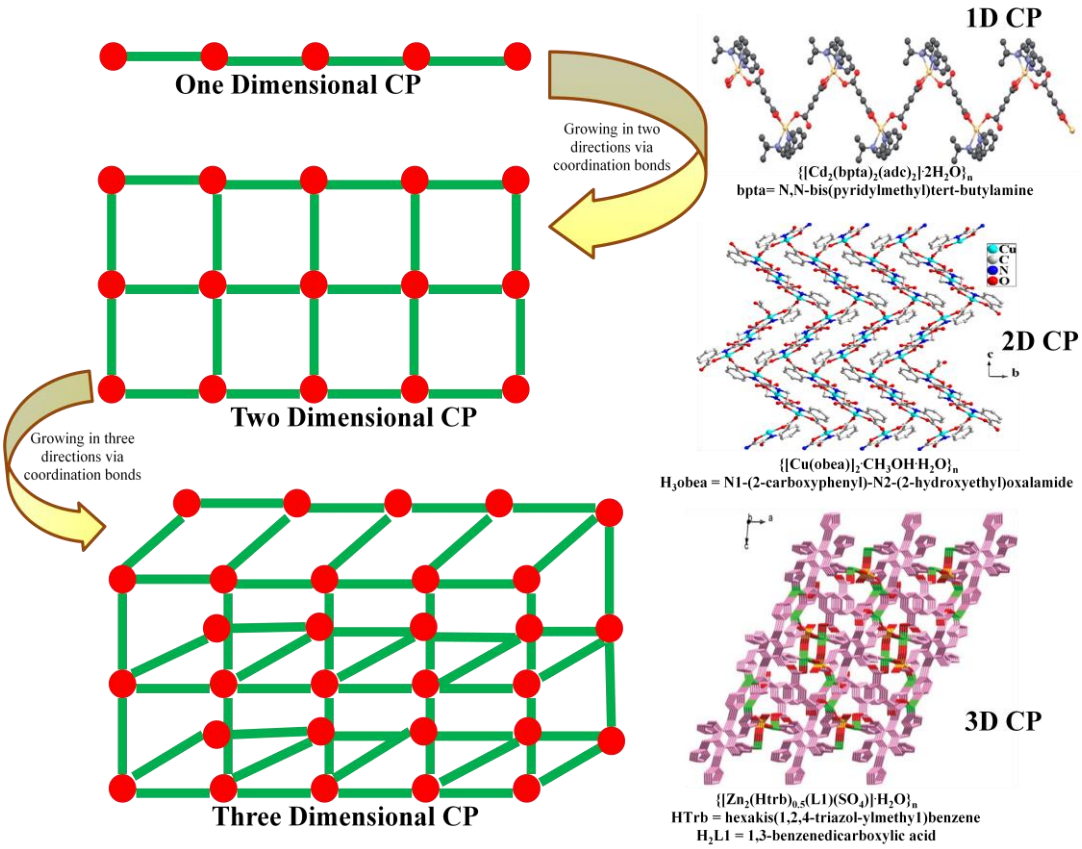

Figure 1.2. Schematic representation for the formation of 1D-, 2D- and 3D coordination polymers with reported compounds as examples.[77-79]

A conventional synthetic method[80] to obtain these coordination architectures is to take metal ion and organic linker in a solution and stir them for few hours at room temperature or elevated temperatures (reflux), allowing self-assembly of the components involved. The simplicity associated with the one pot synthesis has led to its widespread use. However, due to solubility constraints of these coordination architectures, some other methods which exploit the principle of concentration gradient or temperature gradient have also been employed such as layering of solutions, slow diffusion of reactants into each other or solvent evaporation. However, it must be taken into account that temperature can have strong influence on the crystal morphology and stability. MOF-5, MOF-177, HKUST-1, ZIF-8 are some examples synthesized using this strategy.[80-83]

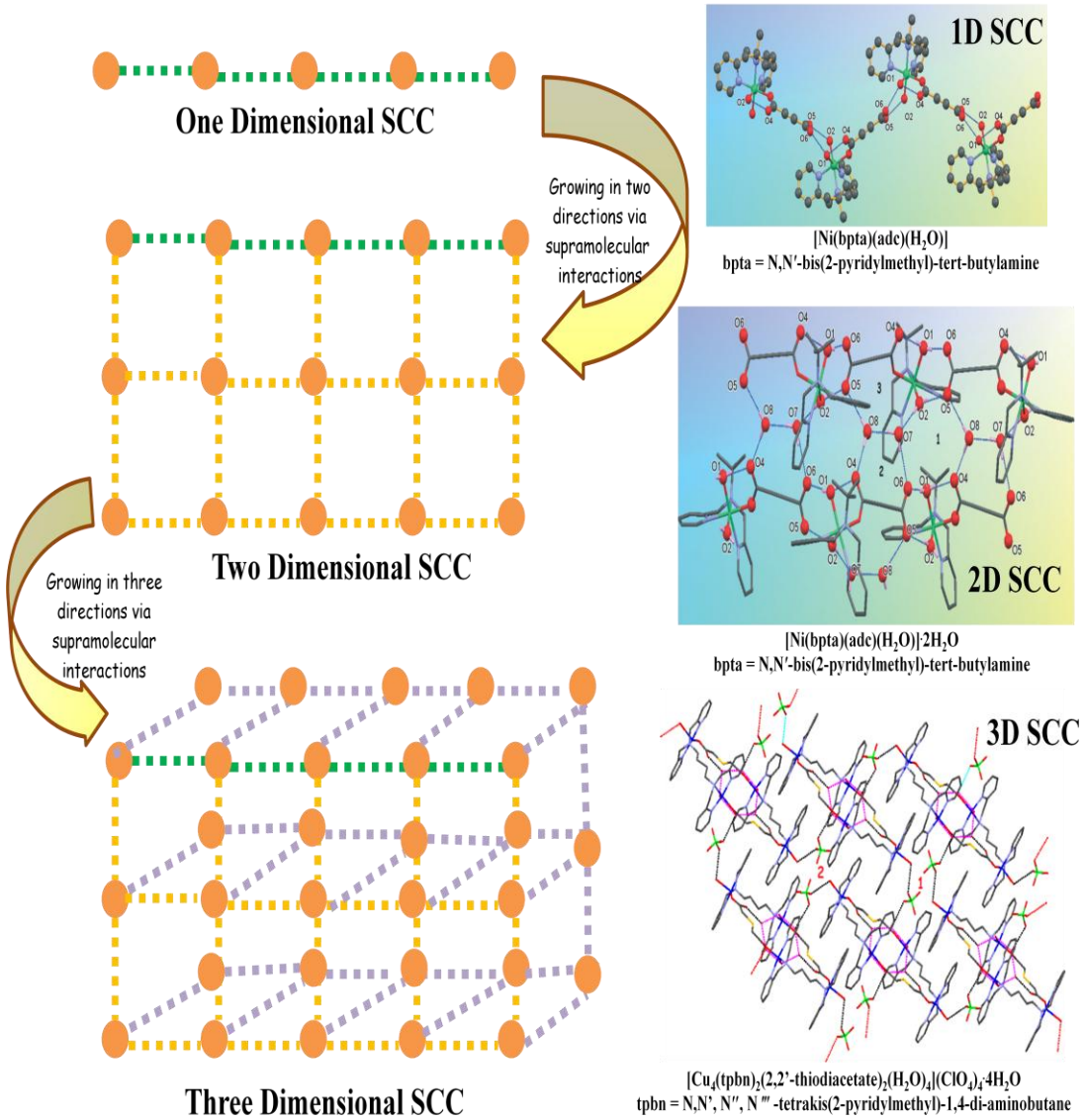

Figure 1.3. Schematic representation for the formation of 1D-, 2D- and 3D supramolecular coordination complexes with reported compounds as examples.[16,20]

Some of the coordination architectures are synthesized using stringent temperature and pressure conditions under hydro-/solvothermal reactions where the reactants are mixed together along with the solvent(s) in a bomb (teflon-coated stainless steel reactor) and placed in a programmable oven under high temperature (120-180 ^{o}C) for few days, followed by the cooling of the bomb to provide a temperature gradient.[84] Other methods like microwave-assisted synthesis, electrochemical synthesis, sonochemical synthesis and mechanochemical synthesis are also extensively explored to increase the efficiency of the reaction by getting

better yield and the ability to scale up, reduce the reaction time and also improve the quality of obtained product.[80] Microwave-assisted synthesis is an energy-efficient method utilizing the phenomenon of interaction of electromagnetic waves with electronic charge carriers and thus focuses on accelerating the rate, obtaining nanoscale product, improving the product quality and generation of selective polymorphs. Ni and Masel[85] were the first to use microwave irradiation to synthesize MOFs. They made IRMOF-1 (also known as MOF-5), IRMOF−2 and IRMOF−3 with reaction times greatly reduced and products being microcrystalline. Starting materials may interact strongly with radiation, therefore choice of solvents and energy input are of great concern. In electrochemical synthesis instead of using the metal salts, a direct introduction of the metal ions through anionic dissolution, into the reaction medium composed of the organic linker and a conducting salt is carried out thus excluding the anions, such as nitrate, perchlorate or chloride, which get incorporated into the framework during the synthesis. The electrochemical route is advantageous as it runs as continuous process and gives a higher solid content. Using this route, researchers from BASF reported several coordination architectures for various combinations of anode materials (Zn, Cu, Mg, Co) and linkers (1,3,5-H_3BTC, 1,2,3-H_3BTC, H_2BDC).[86] The sonochemical synthesis is a fast, energy-efficient, environmentally friendly method that can easily be carried out at room temperature and involves the application of high-energy ultrasound waves to reaction mixtures. There is no direct interaction between these waves and the molecules, as the wavelength of ultrasound is much larger than the molecular dimensions. Very high and very low pressure zones are formed upon sonochemical irradiation, resulting in cavitation, the formation and collapse of bubbles in solution. Crystals of MOF-5 in 1-methyl-2-pyrrolidinone (NMP) has been obtained using this method.[87] The mechanochemical synthesis method, also known as solid-state synthesis, involves grinding of components together to get the product. In 2006, Pichon et al.[88] first reported the synthesis of a copper-isonicotinic acid MOF using this method. In this technique hydrated metal salts are always preferred over non-hydrated ones as the water molecules from these hydrated salts leads to Liquid-assisted grinding (LAG) and thus enhancing the reactivity. Use of very small amount of solvent can also serve the purpose. 1D, 2D and 3D coordination polymers by varying the solvent added to a mixture of fumaric acid and ZnO have been reported.[89]

Sensors as Indispensable Modern Gadgets

Many new molecular sensors are generated due to demands for fast and reliable detection of biological and chemical analytes having prevalent relevance to national security, global health and environment. Sensing explores the molecular recognition and self-assembly of chemical structures using dynamic supramolecular interactions that create ensembles which result in signal modulations upon addition of analytes.[58]

Even though the field of chemosensors are very well delve into, the sensing abilities of these diversified coordination architectures are not yet explored thoroughly. The extensive modular synthesis of these architectures tends to inculcate the exceptional tunability of the structures and chemical as well as morphological properties, thus constituting an important advantage over other conventional classes of chemo-sensory materials. The past decade has seen a tremendous input in the field of designing and developing of various artificial receptors or sensors to sense various analytes like cations, anions and neutral small molecules.[90,91]

In the recent past, a lot of efforts has been put for sensing of numerous heavy- and transition metal ions due to their high toxicity and crucial roles in biological systems.[92-97] In this context, Cu^{2+} plays an important role as copper is an essential trace element (a daily dose suggested by the National Research Council: 1.5 to 3.0 mg for adults, 1.5 to 2.5 mg for children, and 0.4 to 0.6 mg for infants[98]) in various physiological processes, like gene expression and protein functioning.[99] It acts as a critical cofactor for many enzymes utilizing the Cu^{+}/Cu^{2+} transformation.[100,101] A deficiency of Cu^{2+} can even cause myelopathy.[102] However, an excess of Cu^{2+} can drastically affect many living organisms by promoting the generation of reactive oxygen species that can interfere with cellular signalling, and thus damaging the cell structures, leading to apoptosis.[103-107] An increase in the Cu^{2+} level in the body can cause a severe damage to liver and kidney.[108,109] Any disparity in copper homeostasis leads to the damage of central nervous system and can cause various neurodegenerative diseases (e.g., Wilson's diseases, Parkinson's, amyotrophic lateral sclerosis diseases and Alzheimer's disease).[110-115] The normal range for copper ions in ground or surface water is 0.005−30 ppm,[116] however, the widespread use of copper in various other industrial and agricultural processes increases the level of Cu^{2+} in ground water. For the

significant physiological relevance and associated biomedical implications mentioned above, recently there is a lot of effort in developing selective and sensitive Cu^{2+} sensors.[117-128]

Similar to the development of cation sensors, development of selective and efficient signalling units for sensing chemically and biologically important anions has also attained greater heights. [129-134] Among the anions, the fluoride ion is one of the most important anions because it is frequently used as additives in toothpaste and water to prevent dental caries and enamel demineralization.[135-139] However, an excess of fluoride ion can cause fluorosis and nephrotoxic changes in both humans and animals leading to urolithiasis.[140-142] Many vital cell signaling components are affected by fluoride ions for the fact that NaF acts as a potent G-protein activator and Ser/Thr phosphatase inhibitor.[143] Thus, sensing of fluoride ions in low concentration have become progressively more important and highly challenging.[126,144-147] These fluoride ion sensors can also detect UF_6 (uranium enrichment) and chemical warfare agents, e.g., sarin, as the fluoride ion is released upon their hydrolysis.[148]

Neutral small molecules also play very important roles in our daily life. Among the neutral small molecules, nitroaromatics (explosive-like substances), due to their relevance in national security and environmental implications, are of great importance.[149-156] Nitrobenzene is an important constituent in dye, pharmaceuticals and pesticide industry[157,158] but is a highly toxic substance with many detrimental effects.[159-161] Aromatic amines are also very important, with aniline being one of the most common precursor for the synthesis of many essential chemicals like dyes, herbicides, cosmetics, medicines, rubber additives, etc.[162] However, the toxicity of aniline in small doses (a probable oral lethal dose is 50–500 mg/kg for an adult) cause methemoglobinemia; a high concentration of methemoglobin can interfere with the oxygen-carrying capacity of the blood and also affects the upper respiratory tract.[163,164] Aniline is also considered as a splenotoxin[165] and is a potential carcinogenic substance.[166-168] Many sensors are reported for selective sensing of either nitrobenzene[169-174] or aniline.[175-177]

Although various concepts in analyte sensing have been installed to enhance sensitivity, selectivity and the dynamic working range, nevertheless multianalyte sensing still possesses a major challenge. Through the advancement in supramolecular chemistry in recent years, there is a marvellous change in the trend to design differential smart receptors rather than the

selective sensors, which further provide opportunities for the detection of several similar analytes.[178-189] In this regard, multiple chromomeric and/or fluorogenic subunits are intricated into one single molecule so that a single technique with diverse responses[190-193] towards different analytes or multiple techniques[194-196] can be availed to detect these analytes. On the other hand, the use of amino acids, which play a unique role in various biological systems due to their selectivity in substrate binding, is one of the current efforts worldwide for the development of smart receptors.[197-206] These are capable of selective sensing of various chemically and biologically important substrates - anions, cations and neutral molecules. In literature very few the multianalyte sensing is reported that to dealt with sensing of a cation and an anion (e.g. $Zn^{2+/}F^-$, Cu^{2+}/F^-, Cu^{2+}/CN^-, Zn^{2+}/HSO_4^-, Zn^{2+}/S^{2-}, Cu^{2+}/S^{2-}, etc.) by a single sensor, with a few exception where a cation and a neutral molecule (e.g. Cu^{2+}/H_2O_2, Hg^{2+}/nitrobenzene etc.) or two cations (e.g. Ag^+/Mn^{2+}) were detected by a single sensor.[178-182,184,187]

Functioning of a Sensor

For any moiety to function as a sensor, it should successively follow three consecutive steps (as shown in Figure 1.4).[58]

- Generation of a signal is normally dependent on chemical interactions: whenever an analyte approaches a sensor due to various supramolecular interactions or dynamic covalent interactions between them, a signal is generated.

- Detection of a signal is achieved by instrumentation: the signal generated in the previous step is detected by various instruments which are employed with sophisticated detectors like a fluorescence spectrophotometer or an absorption spectrometer.

- Processing of signals can be expedited by chemometric techniques: using various analytical techniques these detected signals are retro-analysed to get the flavor of the nature and type of interactions between the sensor and the analyte. This retroanalysis helps in selective and sensitive detection of an analyte.

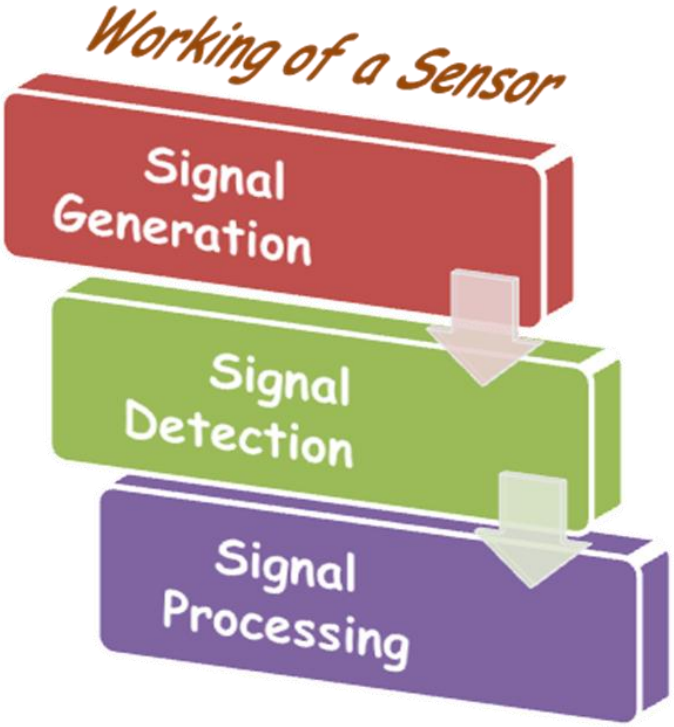

Figure 1.4. Schematic representation of functioning of a sensor.

Use of Fluorescence Spectroscopy in Sensing

Among various detection techniques, fluorescence spectroscopy is most illustrious due to its critical sensitivity, high temporal and spatial resolution and adaptability that allow not only remote detection of various analytes but their imaging within the living cells. The basic mechanism of sensing is the transmission of the signal produced by molecular interaction with the analyte and the fluorescent sensor and furthermore detection by devices based on modern electronics and optics.[207-210]

Fluorescence is much more sensitive than the absorbance spectroscopy because of the diverse ways of measuring absorbance and fluorescence. In absorbance spectroscopy the light intensity is measured as the difference in intensity between light passing through the reference and the sample whereas in fluorescence spectroscopy the intensity is measured directly, without comparison with a reference beam. Even with low fluorophore concentration (10^{-10} M), the measurement of fluorescence intensity is readily accomplished using most fluorometers; no measurement can be done with such low concentration of the molecule in absorbance spectroscopy. The measurement of the fluorescence intensity relative

to a dark background, as compared to the bright reference beam in an absorbance measurement formulates fluorescence spectroscopy as single molecule detection technique. Thus, in fluorescence spectroscopy low levels of light and the electronic impulses can also be detected due to the ability of engrossing of single photons by most photomultiplier tubes (detectors in fluorometers).

A fluorescence process is the result of three consecutive steps, all of which occur on time scales that are separated by several orders of magnitude (as shown in Figure 1.5). Excitation of a molecule (fluorophore) by an incoming photon (absorption of light) takes place in femtosecond regime (10^{-15} seconds), while vibrational relaxation of excited state electrons to the lowest energy level of the excited state (internal conversion) is much slower, i.e., in picoseconds regime (10^{-12} seconds). The final process is radiative emission (fluorescence) of a longer wavelength photon and return of the fluorophore to the ground state, in period of nanoseconds (10^{-9} seconds).

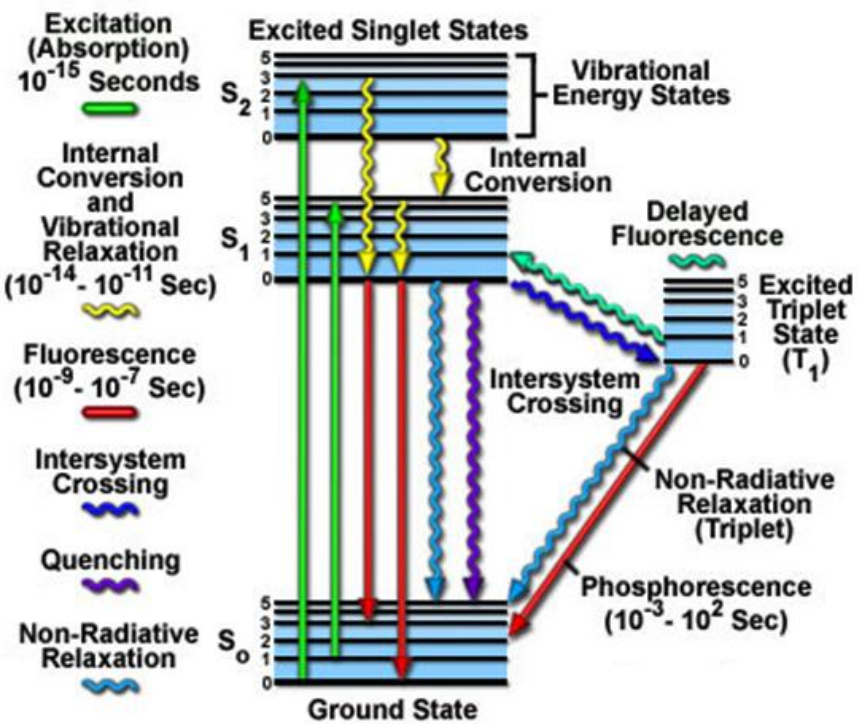

Figure 1.5. Jablonski diagram showing the phenomenon of fluorescence.

Even though the fluorescence phenomenon appears to be almost instantaneous, with highly sophisticated fluorimeters available these days the relatively well separated timeframe

between absorption of a photon and the emission of a second photon by a fluorophore can be well distinguished and then can be further explored for getting many molecular level information. The palette of fluorescence techniques includes observable changes in absorption and emission spectra, quantum yield, lifetimes, quenching, photobleaching, anisotropy, energy transfer, solvent effects, diffusion, complex formation, and a host of environmental variables. For using any technique as a sensing tool, there should be a change in some of the spectral property of the sensor on approach of an analyte e.g. in case of using fluorescence spectroscopy as a sensing tool, change of intensity or intensity ratio are the most common spectral responses seen on interaction between a sensor and an analyte. Hence, any phenomenon that results in a change of intensity, wavelength, anisotropy, or lifetime of a sensor can be used for sensing (see Figure 1.6).

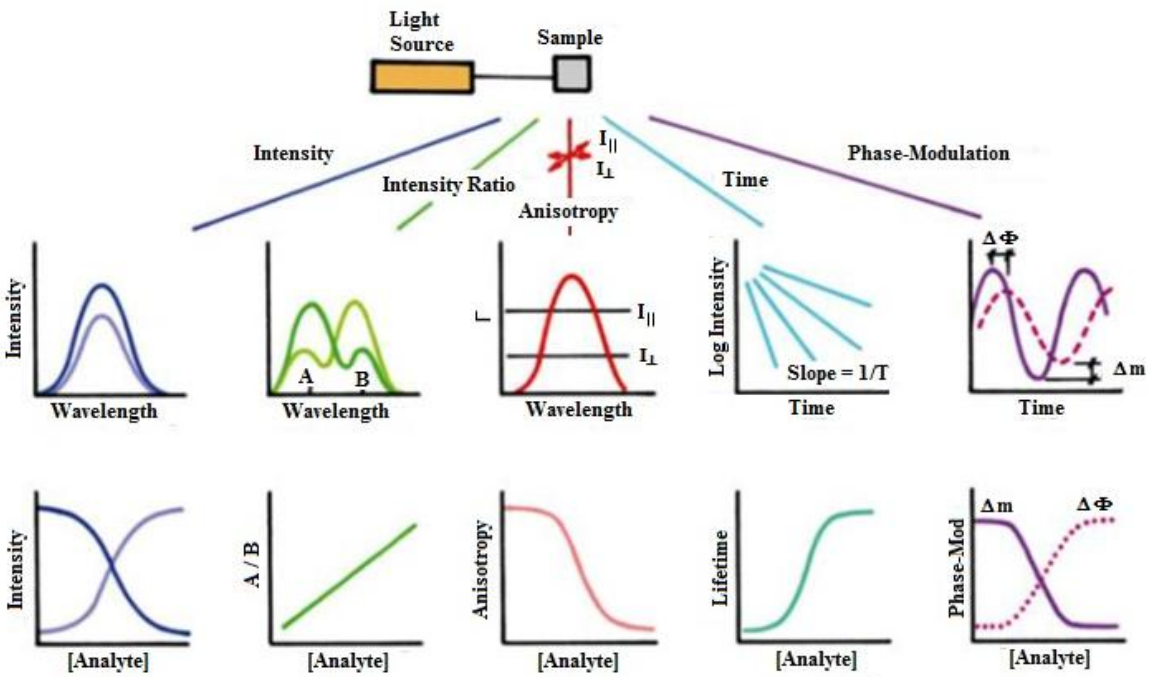

Figure 1.6. Spectral responses of a fluorescent sensor on approach of an analyte.[211]

All of these spectral properties of fluorophores/sensors can be readily evaluated through steady state or time-resolved interpretations of the fluorescence spectroscopy. In steady-state fluorescence spectroscopy, the sample is illuminated with a continuous beam of light, and emission spectrum is recorded. Fluorescence being a nanosecond regime phenomenon even

before detection of emission intensity in steady state measurement, the fluorophore reaches back to the ground state.In lifetime or time-resolved fluorescence spectroscopy, the sample is exposed to a pulse of light, where the pulse width is typically shorter than the decay time of the sample. This intensity decay is recorded with a high-performance detector that permits the intensity or anisotropy to be measured on the nanosecond timescale. Thus, a steady-state observation is simply an average of the time-resolved phenomena over the intensity decay of a sample. A lot of molecular information available from fluorescence is lost during the time averaging process.[211-217]

Fluorescence lifetime of a molecule is very sensitive to its molecular environment. Hence, the measurement of the fluorescence lifetime(s) reveals much about the state of the fluorophore. The simplest mechanism to observe sensing is quenching of the fluorescence intensity of the fluorophore on addition of an analyte which can be very well perceived by the steady state fluorescence measurement; however nature of quenching (dynamic or static) can only be interpreted by the lifetime measurement studies. Time-resolved measurements reveal whether quenching is due to diffusion or to complex formation with the ground-state fluorophores. As dynamic quenching results in change in the lifetime of the fluorophore wherase in static quenching the lifetime would not change. Lifetime-based sensing being independent of the concentration is a means to avoid the difficulties of quantitative intensity measurements which are the biggest hurdle in the steady state fluorescence measurement.

Relevant Prior Examples of Sensors

Schiff Base Ligands as Sensors

Many Schiff base ligands which feature prominently in supramolecular chemistry are mostly used as sensing materials in the construction of potentiometric ion selective electrodes. Till now, more than 200 potentiometric membrane sensors for cations and anions based on Schiff bases have been reported in the literature.[218-223] A large number of different Schiff base ligands have been used as cation carriers in potentiometric sensors as they have shown excellent selectivity, sensitivity, and stability for specific metal ions. However, the use of reduced Schiff bases for sensing application is very limited in the literature. Furthermore, the use of amino acid based reduced Schiff bases as sensors are not known prior to this study.

Hence, the utilization of the cost effective and easily synthesizable amino acid based reduced Schiff bases as sensor has lot of scope in bringing a turning point in the sphere of sensing various analytes.

Coordination Architectures as Sensors

Many CPs and SCCs have shown promising behaviour in sensing and other photophysical-based applications, since the interaction or the binding of an analyte with their coordination architectures can often induces electronic structure changes, which result in emission changes.[173,224-231] Although in most of these cases either the costly and cumbersomely prepared fluorophores are used as ligands or the highly expensive lanthanide architectures are employed for the sensing purpose. Nevertheless, the use of coordination architectures of amino acid based ligands as sensor is unparalleled in literature and opens up a new avenue in sensing.

Motivation and Scope of the Present Research

On analyzing the pre-existing coordination architectures it was found that many prospects were not dealt with properly. Hence, there was a lot of scope in understanding those unexplored facts about the diverse coordination architectures.

- The identification and analysis of various factors/parameters controlling the formation of these architectures can be thoroughly analysed to erase the lack of understanding of the structural and functional aspects of these coordination architectures.
- Utilization of cheap and easily made L-amino acids based ligands with multiple hydrogen bond donor/acceptor entities in generation of higher dimensional homochiral coordination architecture seems the best option to tackle the difficulty faced in obtaining these higher dimension homochiral coordination architectures due to the use of binaphthyl like costly and sterically hindered chiral ligands.
- A methodical and strategical chemical modulation of the components (ligand, linker, metal ion and/or solvents) to obtain a systematic study to obtain structural diversity in the coordination architectures can be a new foot forward in this field.

Similarly, the scope of exploring the sensing application of the ligands and their coordination architectures is also unlimited due to the unavailability of any such prequisitive data in the literature.

- The use of natural fluorescence of cheap L-amino acids (L-Tyrosine, L-Tryptophan and L-phenylalanine) to generate sensors was one of the best alternatives to replace the long existing highly expensive fluorophores/chromophores.
- A proper tuning of amino acid based ligands and their complexes with an attachment of electron withdrawing group to further use them for the anion sensing is the best substitute for the cumbersome and expensive electron deficient macrocycles being used for anion sensing from earlier times.

Based on the above, a plan was formulated for methodical designing of the chiral ligands to bring diversification in their homochiral coordination architectures and then employing these strategically designed ligands and coordination architectures in sensing applications (as shown in Figure 1.7). The execution of the plan properly in the present research resulted in a very fruitful and interesting outcome. The various ligands synthesized for this research are from modulation of naturally occurring amino acid.

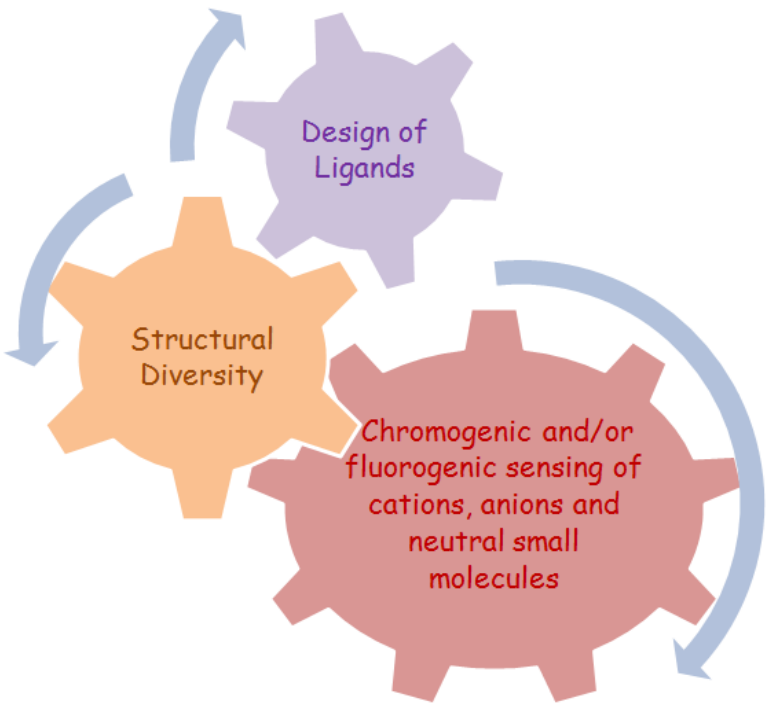

Figure 1.7. Overall plan for the research.

Outcome of the Present Research

A lot of focus was on devising and exploring the various factors responsible for obtaining desirable coordination architectures. Factors involved in the formation of porous (Metal Organic Framework) or non-porous CPs or the SCCs were extensively analyzed. A large number of diversified (structural and functional) coordination architectures was generated by fine-tuning the participation of coordination bonds and hydrogen bonds in their formation. Thus, establishing the parameters that control the formation of CPs or SCCs through chemical modifications in the ligand system allowed us to understand the structure and bonding in these species and to provide further directions in the rational design of improved materials. In this regard, a strategic design of a set of ligands was a way to do so. Furthermore, the incorporation of chirality into these coordination architectures was served by using chiral amino acid based ligands, due to the cost-effectiveness and dual functionalities of amino acids to act as a hydrogen bond donor and acceptor along with the diverse binding modes available within them. A series of well thought amino acid based ligands were synthesized for the present research (as shown in Figure 1.8).

Not only the modulation in the components of the coordination architectures are played with but also the various combinations with varying ratio of the components of the coordination architectures are also considered. A deeper prospect into the role of the solvents in assembling the coordination architectures
and thus influencing the properties are explored to acquire enviable coordination architectures. The role of the polarity and the variable hydrogen bonding capabilities of different solvents to influence the architectures in their own way is also analysed. The idea of renovating one subset of coordination architecture to another (CPs to SCCs or vice versa) is also very fascinating as this conversion can help us to obtain preferred coordination architecture with desirable qualities. Various other factors like insertion of a linker, role of the encapsulated water cluster, etc., to achieve this alteration is also comprehensibly scrutinized.

Furthermore, several of these chiral ligands and their coordination architectures are used as chromogenic as well as fluorogenic sensors for cations, anions and neutral small molecules. In addition to using the natural fluorescence of the amino acids like L-Tyrosine and L-

Phenylalanine, the additional fluorophores (such as a dansyl moiety) tagged to these amino acids are also utilized for the sensing purpose. The compendium of the present work is shown in Figure 1.9.

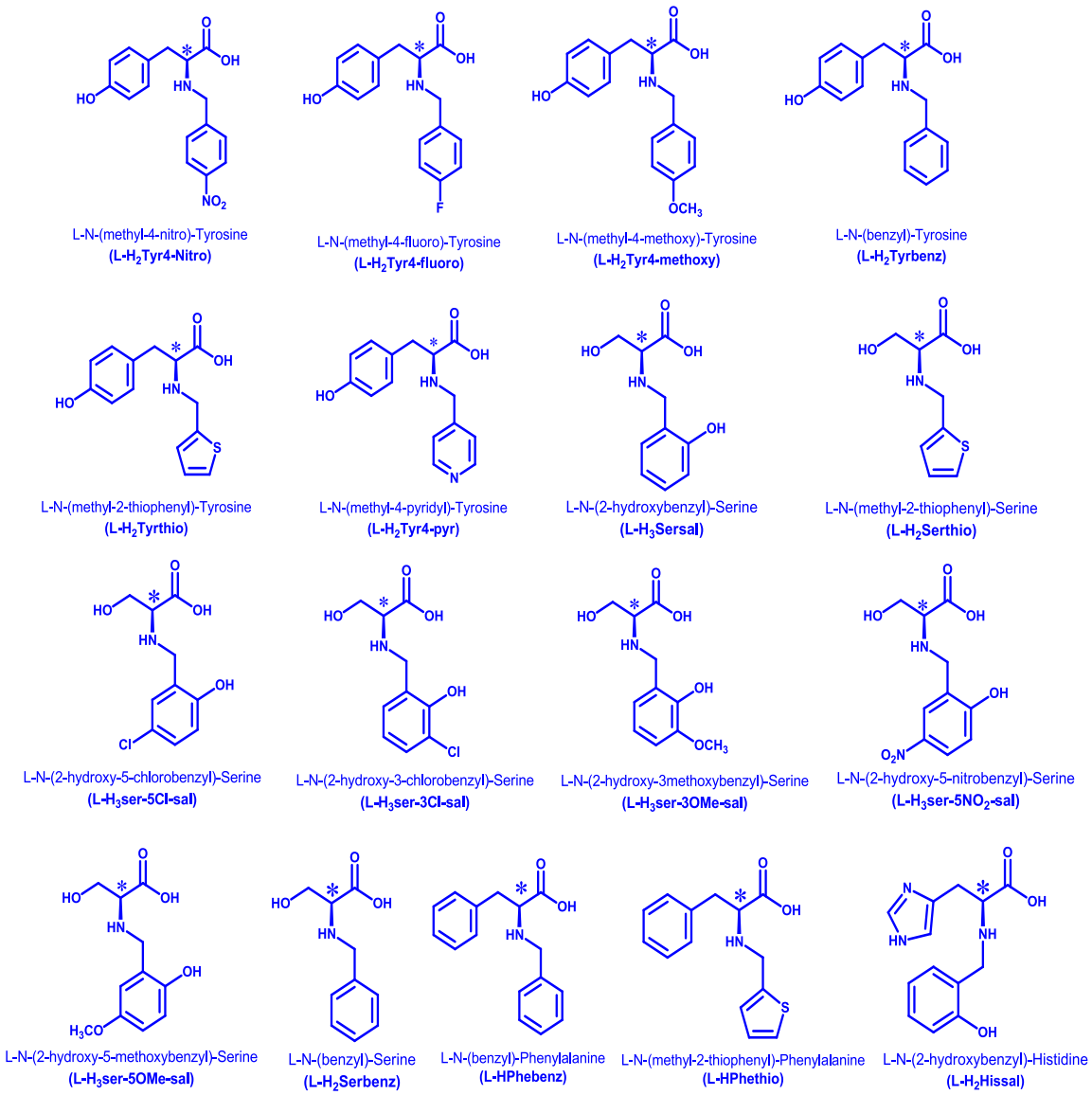

Figure 1.8. List of ligands used in the present work.

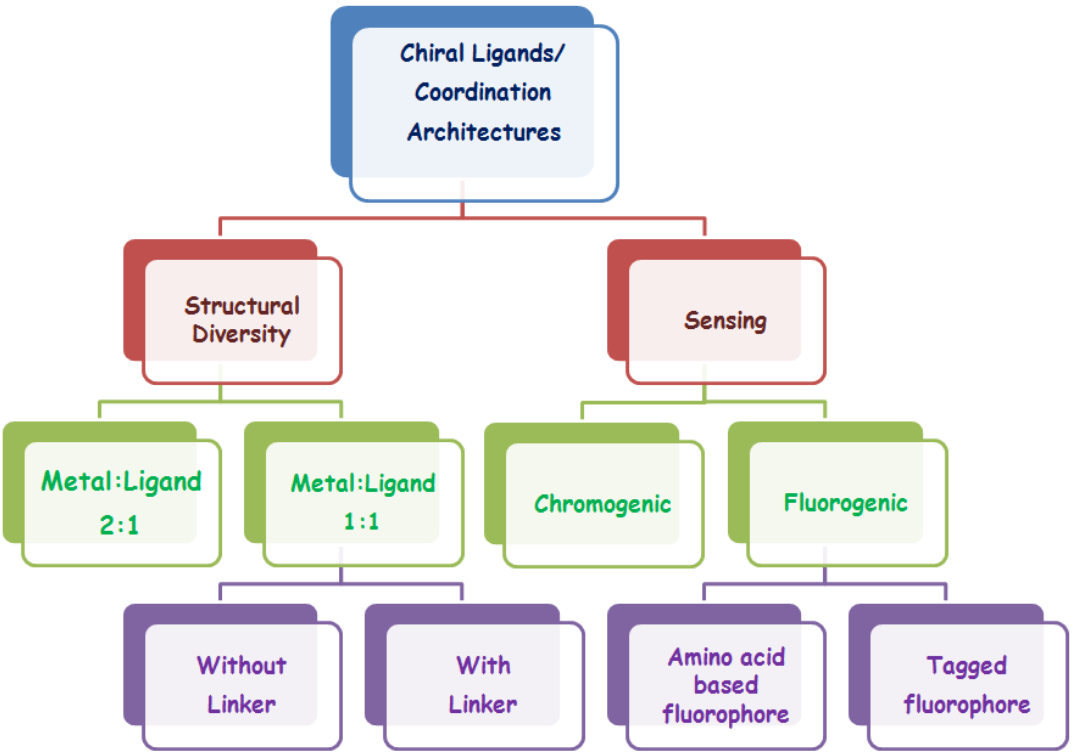

Figure 1.9. Flow diagram of the present research.

Chapter II

Experimental Section

2.1 Materials and Methods

All chemicals and solvents used for synthesis were obtained from commercial sources and were used as received, without further purification. All reactions were carried out under aerobic conditions.

2.2 Physical Measurements

^{1}H NMR spectra of sodium salt of amino acid based reduced Schiff bases ligands were obtained in D_2O solution at 25 $^\circ$C on a Bruker ARX-400 spectrometer; chemical shifts are reported relative to the residual solvent signals.

Elemental analysis (C, H, N) was carried out using either a Mettler CHNS or a Leco-USA Tru Spec CHNS micro version 2.7x analyzer.

Thermogravimetric analysis was carried out from 25 to 500 $^\circ$C (at a heating rate of 10 $^\circ$C/min) under dinitrogen atmosphere on a Shimadzu DTG-60H.

FTIR spectra were measured in the 4000-400 cm^{-1} range on a Perkin-Elmer Spectrum I spectrometer with samples prepared as KBr pellets.

UV-Vis spectra of the compounds in methanol (a typical concentration of 1 mM) were recorded in an Agilent Technologies Cary60 UV-Vis spectrophotometer using a cuvette of path length 10 mm.

Steady state emission spectra were obtained using a Perkin Elmer Fluorimeter (LS55) with a cuvette of 10 mm path length.

Optical rotations were recorded using Anton Paar Modular circular Polarimeter (MCP 300).

CD spectra were recorded out using a glass cell with 50 mm path length. CD spectra were recorded on a Chirascan spectropolarimeter (Applied Photo-physics, Leatherhead, Surrey, UK) using quartz cuvettes with a 2 mm path length.

Magnetic susceptibility measurements were carried out using the VSM option of an EC-II PPMS Quantum Design system to obtain χ versus temperature T in the temperature range 2 K to 380 K in an applied magnetic field H = 1 T, and the magnetization M versus magnetic field H at T = 2 K.

Raman spectra were recorded on a Renishaw InVia Raman microscope equipped with a 785 nm high-power near-infrared laser working at 300 mW power and a Renishaw CCD detector. Analysis of the Raman spectra were performed in reflection mode on powder samples placed on the sample stage and aligned in optical path by using a camera, with 0.1-0.5% laser power and by using 50X optics in the range of 400-2000 cm^{-1}.

Water adsorption measurements were recorded for pressures in the range 0–1.2 bar by the volumetric method using a BELSORP instrument. Each solid sample was transferred to pre-weighed analysis tubes, which were capped with transeals and evacuated by heating at a temperature between 110-150 °C (based on thermal profile obtained from TGA) under dynamic vacuum until an outgas rate of less than 2 mTorr min^{-1} (0.27 Pa min^{-1}) was achieved (ca. 12-24 hrs). The evacuated analysis tubes containing the degassed sample was then carefully transferred to an electronic balance and weighed again to determine the mass of sample. The tube was then placed back on the analysis port of the gas adsorption instrument. The outgas rate was again confirmed to be less than 2 mTorr min^{-1} (0.27 Pa min^{-1}). For all isotherms, warm and cold free-space (dead volume) correction measurements were performed using ultra-high-purity He gas (UHP grade 5.0, 99.999% purity). The change of the pressure was monitored and the degree of adsorption was determined by the decrease in pressure at the equilibrium state via computer controlled automatic operations that are set up at the start of each measurement. Oil-free vacuum pumps and oil-free pressure regulators were used for all measurements to prevent contamination of the samples during the evacuation process or of the feed gases during the isotherm measurements.

Powder X-ray data were recorded on a Rigaku Ultima IV diffractometer equipped with a 3 KW sealed tube Cu Kα X-ray radiation (generator power settings: 40 kV and 40 mA) and a DTex Ultra detector using parallel beam geometry (2.5° primary and secondary solar slits, 0.5° divergence slit with 10 mm height limit slit). Each sample grounded into a fine powder using a mortar and a pestle was placed on a glass sample holder that was placed on the sample rotation stage (120 rpm) attachment. The data were collected over an angle range 5° to 50° with a scanning speed of 1° per minute with 0.02° step with XRF reduction for the metals.

Single crystal X-ray analysis were performed by initial crystal evaluation and data collection were performed on a Kappa APEX II diffractometer equipped with a CCD detector (with the

crystal-to-detector distance fixed at 60 mm) and sealed-tube monochromated MoKα radiation using the program APEX2.[232] By using the program SAINT[232] for the integration of the data, reflection profiles were fitted, and values of F^2 and $\sigma(F^2)$ for each reflection were obtained. In some cases, a lot of efforts were invested to recollect data sets with new crystals a few times but no better data sets that are used here could be obtained. Data were also corrected for Lorentz and polarization effects. The subroutine XPREP[232] was used for the processing of data that included determination of space group, application of an absorption correction (SADABS)[232], merging of data, and generation of files necessary for solution and refinement. The crystal structures were solved and refined using SHELX 97.[233] In each case, the space group was chosen based on systematic absences and confirmed by the successful refinement of the structure. Furthermore, Flack parameters of all the structures confirmed the correct absolute configurations. Positions of most of the non-hydrogen atoms were obtained from a direct methods solution. Several full-matrix least-squares/difference Fourier cycles were performed, locating the remainder of the non-hydrogen atoms. In order to obtain reasonable thermal parameters compared to other atoms, the lowest residual factors and optimum goodness of fit with the convergence of refinement, occupancy factors of some of the atoms were adjusted accordingly. All hydrogen atoms were placed in ideal positions and refined as riding atoms with individual isotropic displacement parameters unless mention otherwise. The occupancy factors of some of the atoms were adjusted to obtain favorable thermal parameters. All hydrogen atoms were placed in ideal positions and refined as riding atoms with individual isotropic displacement parameters unless mentioned otherwise. All non-hydrogen atoms for all structures were refined with anisotropic displacement parameters except where mentioned. Crystallographic parameters and basic information pertaining to data collection and structure refinement for all compounds are summarized in Table A1-A5. All figures were drawn using Olex2[234] and MERCURY V 3.0[235] and hydrogen bonding parameters were generated using PLATON.[236]

2.3 Synthesis of Ligands

All amino acid based reduced Schiff base ligands are prepared using a common procedure which is constructed from the literature procedures[25-30] for few such ligands as most of the

ligands reported here are new. However, the conditions in each case vary depending on the amino acid and the aldehydes used and such variation of the conditions is described wherever applicable.

L-N-(benzyl)-Tyrosine (L-H_2Tyrbenz). To a solution of 500 mg of L-tyrosine (2.8 mmol) and 220 mg of NaOH (5.6 mmol) in 14 mL of a methanol:water mixture (v/v 1:1) was added 0.28 mL (2.8 mmol) of benzaldehyde. The resulting solution was refluxed for 1h. The yellow reaction mixture was brought to room temperature prior to the addition of 105 mg of $NaBH_4$ (4.8 mmol) at 0 °C. The solution was stirred until the yellow color disappeared. The pH of the solution was adjusted to 5 using (~2 mL) glacial acetic acid and stirred for half an hour. A white precipitate was filtered, washed with water and air dried. Yield: 350 mg (47%). HRMS (ESI-TOF): m/z calcd for $[(L\text{-}H_2Tyrbenzl)H]^+$, 272.1287; found, 272.1278. M.pt. 263 ^oC. ^1H NMR (D_2O): δ 2.62 (d, 2H), 3.17 (t, 1H), 3.41 (d, 1H), 3.60 (d, 1H), 6.43 (d, 2H), 6.83 (d, 2H), 7.16 – 7.28 (m, 5H). Selected FTIR peaks (KBr, cm^{-1}): 3174(s), 3011(w), 2827(w), 2747(w), 1603(w), 1580(br), 1516(s), 1437(m), 1396(s), 1253(s), 1106(s), 828(s), 743(s), 697(s). Specific rotation $[\alpha]_D^{20}$ = +12.50 (0.018%, H_2O).

L-N-(benzyl)-Serine (L-H_2Serbenz). It was prepared following the procedure described for L-H_2Tyrbenz except 500 mg (4.7 mmol) of L-serine was used instead of L-tyrosine. In this case, the resulting yellow Schiff base solution was refluxed for 8 h, prior to the addition of $NaBH_4$. A white precipitate was filtered, washed with water and air dried. Yield: 300 mg (32%). HRMS (ESI-TOF): m/z calcd for $[(L\text{-}H_2Serbenz)H]^+$, 196.0973; found, 196.0970. M.pt. 219 ^oC. ^1H NMR (D_2O): δ 2.51 (t, 2H), 3.00 (t, 1H), 3.42 (d, 1H), 3.58 (d, 1H), 6.30 (d, 2H), 6.69 (d, 2H), 7.20 (d, 2H), 7.91 (d, 2H). Selected FTIR peaks (KBr, cm^{-1}): 3245(br), 3197(s), 3063(s), 1625(s), 1596(s), 1534(s), 1471(s), 1455(w), 1276(s), 1201(s), 1080(s), 758(s), 648(w). Specific rotation $[\alpha]_D^{20}$ = +14.77 (0.018%, H_2O).

L-N-(methyl-2-thiophenyl)-Tyrosine (L-H_2Tyrthio). It was prepared following the procedure described for L-H_2Tyrbenz except 0.26 mL (2.8 mmol) of 2-thiophenecarboxyaldehyde was used instead of benzaldehyde. In this case, the resulting yellow Schiff base solution was refluxed for 3 h, prior to the addition of $NaBH_4$. A white precipitate was filtered, washed with water and air dried. Yield: 581 mg (76%). HRMS (ESI-

TOF): m/z calcd for [(L-H_2Tyrthio)H]$^+$, 278.1785; found, 278.0851. M.pt. 248 ^{o}C. ^{1}H NMR (D_2O): δ 2.59 (d, 2H), 3.16(t, 1H), 3.61 (d, 1H), 3.75 (d, 1H), 6.38 (d, 2H), 6.76-6.85 (m, 4H), 7.18 (d, 1H). Selected FTIR peaks (KBr, cm^{-1}): 3435(br), 3178(s), 3006(w), 2692(w), 2624(w), 1581(br), 1517(s), 1436(s), 1393(s), 1262(s), 1105(s), 821(s), 717(m), 533(s). Specific rotation $[\alpha]_D^{20}$ = -2.27 (0.018%, H_2O).

L-N-(methyl-4-pyridyl)-Tyrosine (L-H_2Tyr4-pyr). It was prepared following the procedure described for L-H_2Tyrbenz except 0.26 mL (2.8 mmol) of 4-pyridinecarboxyaldehyde was used instead of benzaldehyde. In this case, the resulting yellow Schiff base solution was stirred for 6 h, prior to the addition of $NaBH_4$. A white precipitate was filtered, washed with water and air dried. Yield: 670 mg (89%). HRMS (ESI-TOF): m/z calcd for [(L-H_2Tyr4-pyr)H]$^+$, 273.1239; found, 273.1245. M.pt. 250 ^{o}C. ^{1}H NMR (D_2O): δ 2.64 - 3.68 (m, 2H), 3.13 (t, 1H), 3.50 (d, 1H), 3.71 (d, 1H), 6.43 (d, 2H), 6.83 (d, 2H), 7.17 (d, 2H), 8.30 (d, 2H). Selected FTIR peaks (KBr, cm^{-1}): 3161(br), 2808(w), 2359(w), 1614(s), 1518(s), 1449(m), 1385(s), 1332(s), 1234(w), 1104(s), 872(s), 801(s), 573(m). Specific rotation $[\alpha]_D^{20}$ = +9.09 (0.018%, H_2O).

L-N-(methyl-2-thiophenyl)-Serine (L-H_2Serthio). It was prepared following the procedure described for L-H_2Tyrbenz except 500 mg (4.7 mmol) of L-serine and 0.278 mL (4.7 mmol) of thiophenecarboxyaldehyde was used instead of L-tyrosine and benzaldehyde, respectively. In this case, the resulting yellow Schiff base solution was stirred for 3 h at room temperature, prior to the addition of $NaBH_4$. A white precipitate was filtered, washed with water and air dried. Yield: 445 mg (42%). HRMS (ESI-TOF): m/z calcd for [(L-H_2Serthio)Na]$^+$, 224.1292; found, 224.0357. M.pt. 216.9 ^{o}C. ^{1}H NMR (D_2O): δ 3.05 (t, 1H), 3.56 (d, 2H), 3.75 (d, 1H), 3.87(d, 1H), 6.87-6.89 (m, 2H), 7.22-7.23 (dd, 2H). Selected FTIR peaks (KBr, cm^{-1}): 3251(br), 3079(w), 2989(w), 2424(w), 1622(s), 1567(s), 1479(s), 1443(m), 1368(s), 1328(s), 1214(s), 1160(s), 1086(s), 855(s), 722(s), 545(s). Specific rotation $[\alpha]_D^{20}$ = -22.73 (0.018%, H_2O).

L-N-(methyl-2-thiophenyl)-Phenylalanine (L-HPhethio). It was prepared following the procedure described for L-H_2Tyrbenz except 500 mg (3 mmol) of L-phenylalanine and 0.278 mL (3 mmol) of thiophenealdehyde was used instead of L-tyrosine and benzaldehyde,

respectively. In this case, the resulting yellow Schiff base solution was reflux for 24 h, prior to the addition of $NaBH_4$. A white precipitate was filtered, washed with water and air dried. Yield: 362 mg (46%). HRMS (ESI-TOF): m/z calcd for $[(L\text{-}HPhethio)Na]^+$, 284.1655; found, 284.0726. M.pt. 227 ^oC. ^1H NMR (D_2O): δ 2.69-2.76 (m, 2H), 3.20 (t, 1H), 3.63 (d, 1H), 3.79 (d, 1H), 6.81 (d, 1H), 6.83-6.86 (m, 1H), 7.06 (d, 2H), 7.12 (d, 1H), 7.18-7.20 (m, 3H). Selected FTIR peaks (KBr, cm^{-1}): 3418(br), 3179(s), 3010(w), 2806(w), 2689(w), 1603(w), 1586(br), 1515(s), 1438(m), 1397(s), 1346(s), 1252(s), 1106(s), 827(s), 746(m), 550(s). Specific rotation $[\alpha]_D^{20}$ = +30.40 (0.018%, H_2O).

L-N-(methyl-4-nitro)-Tyrosine (L-H_2Tyr-4-nitro). It was prepared following the procedure described for L-H_2Tyrbenz except 417 mg (2.8 mmol) of 4-nitrobenzaldehyde was used instead of benzaldehyde. In this case, the resulting yellow Schiff base solution was stirred for 3 h, prior to the addition of $NaBH_4$. An off-white precipitate was filtered, washed with water and air dried. Yield: 497 mg (57%). M.pt. 251 ^oC. ^1H NMR (D_2O): δ 2.62 (t, 2H, J = 6.2 Hz), 3.10 (d, 1H, J = 6.7 Hz), 3.51 (d, 1H, J = 13.6 Hz), 3.72 (d, 1H, J = 13.68 Hz), 6.31 (d, 2H, J = 2.2 Hz), 6.69 (d, 2H, J = 2 Hz), 7.20 (d, 2H, J = 8.8 Hz), 7.91 (d, 2H, J = 1.8 Hz). Selected FTIR peaks (KBr, cm^{-1}): 3418(br), 3179(s), 3010(w), 2806(w), 2689(w), 1603(w), 1586(br), 1515(s), 1438(m), 1397(s), 1346(s), 1252(s), 1106(s), 827(s), 746(m), 550(s). MS (ESI-TOF): m/z calcd for $[(H_2Tyr\text{-}4\text{-}NO_2)H]^+$, 317.1137; found, 317.1115.

L-N-(methyl-4-fluoro)-Tyrosine (L-H_2Tyr4-fluoro). It was prepared following the procedure described for L-H_2Tyrbenz except 350 mg of KOH (5.6 mmoles) and 0.35 mL (3.3 mmol) of KOH and para-fluorobenzaldehyde was used instead of NaOH and benzaldehyde, respectively. In this case, the resulting yellow Schiff base solution was stirred for 72 h at room temperature, prior to the addition of $NaBH_4$. A white precipitate was filtered, washed with water and air dried. Yield: 645 mg (81%). M.pt. 261 ^oC. ^1H NMR (D_2O): δ 2.60 (d, 2H, J = 6.6 Hz), 3.11 (t, 1H, J = 6.7 Hz), 3.62 (d, 1H, J = 12.6 Hz), 3.55 (m, 1H, J = 12.6 Hz), 6.40 (d, 2H, J = 1.84 Hz), 6.78 (d, 2H, J = 8.4 Hz), 6.94 (t, 2H, J = 6.8 Hz), 7.13 (t, 2H, J = 2.1 Hz). Selected FTIR peaks (KBr, cm^{-1}): 3164(w), 3089(s), 2731(w), 2553(w), 1631(s), 1615(w), 1589(s), 1518(s), 1443(s), 1396(s),

1330(s), 1227(s), 1100(s), 871(s), 821(s), 751(w), 529(s). HRMS (ESI-TOF): m/z calcd for $[(H_2Tyr\text{-}4\text{-}fluoro)H]^+$, 290.1192; found, 290.1183.

L-N-(methyl-4-methoxy)-Tyrosine (L-H_2Tyr4-methoxy). It was prepared following the procedure described above for H_2Tyrbenz except 0.34 mL (2.8 mmol) of para-methoxy benzaldehyde were used instead of benzaldehyde, respectively. In this case, the resulting yellow Schiff base solution was refluxed for 12 h, prior to the addition of $NaBH_4$. A white precipitate was filtered off using a G4 Crucible, washed with water and air dried. Yield: 730 mg (86%). M.pt. 217 ^oC. ^1H NMR (D_2O): δ 2.50 (t, 2H, J = 5.2 Hz), 3.00 (t, 1H, J = 5.4 Hz), 3.42 (d, 1H, J = 7.2 Hz), 3.58 (d, 1H, J = 12.2 Hz), 3.68 (d, 1H, J = 12.2 Hz), 6.30 (d, 2H, J = 1.9 Hz), 6.67 (d, 2H, J = 2.4 Hz), 7.22 (d, 2H, J = 6.7 Hz), 7.82 (d, 2H, J = 2.1 Hz). Selected FTIR peaks (KBr, cm^{-1}): 3380(br), 3238(s), 3025(w), 2923(w), 1627(s), 1495(s), 1455(s), 1435(m), 1371(s), 1344(s), 1241(w), 1079(s), 975(s), 747(s), 696(s). HRMS (ESI-TOF): m/z calcd for $[(H_2Tyr\text{-}4\text{-}methoxy)H]^+$, 302.3371; found, 302.3211.

L-N-(2-hydroxybenzyl)-Serine (L-H_3sersal). It was prepared following the procedure described above for H_2Tyrbenz except 500 mg of L-serine (4.8 mmol) and 0.5 mL (4.8 mmol) of salicylaldehyde were used instead of L-tyrosine and benzaldehyde, respectively. In this case, the resulting yellow Schiff base solution stirred for an hour at room temperature, prior to the addition of $NaBH_4$. A white precipitate was filtered off using a G4 Crucible, washed with methanol and air dried. Yield: 0.824 g (82%). ^1H NMR (D_2O): δ 3.21 (t, 1H), 3.69 - 3.72 (m, 2H), 3.80 (q, 2H), 6.56 – 6.60 (m, 2H), 7.00 – 7.06 (m, 2H). Selected FTIR peaks (KBr, cm-1): 3245(br), 3197(s), 3063(s), 1625(s), 1596(s), 1534(s), 1471(s), 1455(w), 1276(s), 1201(s), 1080(s), 758, 648. Specific rotation D[α]20 = -24.24 (0.033%, CH_3OH). Mpt. 205 °C. UV-Vis [λ, nm]: 205, 275.

L-N-(2-hydroxy-5-methoxybenzyl)-Serine (L-H_3ser-5-methoxy-sal). It was prepared following the procedure described above for H_2Tyrbenz except 500 mg of L-serine (4.8 mmol) and 0.594 mL (4.8 mmol) of 5-methoxysalicylaldehyde were used instead of L-tyrosine and benzaldehyde, respectively. In this case, the resulting yellow Schiff base solution stirred for 3 h at room temperature, prior to the addition of $NaBH_4$. A white precipitate was filtered off using a G4 Crucible, washed with methanol and air dried. Yield:

0.870 g (76%). M.pt. 211 ^{o}C. ^{1}H NMR (D_2O): δ 3.11 (t, 1H), 3.43 - 3.55 (q, 2H), 3.56 - 3.59 (m, 1H), 3.60 (s, 3H), 3.64 - 3.68(m, 1H), 6.42 (d, 1H) 6.58 -6.61 (q, 1H), 6.70 (d, 1H). Selected FTIR (KBr, cm^{-1}): 3245(br), 3180(w), 2833(s), 1631(s), 1598(w), 1568(w), 1516(s), 1455(w), 1362(w), 1322(m), 1267(s), 1230(s), 1077(s), 988(s), 809(s).

L-N-(2-hydroxy-5-nitrobenzyl)-Serine (L-H_3ser-5NO_2-sal). It was prepared following the procedure described above for H_2Tyrbenz except 500 mg of L-serine (4.8 mmol) and 795 mg (4.8 mmol) of 5-nitro salicylaldehyde were used instead of L-tyrosine and benzaldehyde, respectively. In this case, the resulting yellow Schiff base solution stirred for an hour at room temperature, prior to the addition of $NaBH_4$. A white precipitate was filtered off using a G4 Crucible, washed with methanol and air dried. Yield: 1g (82%). M.pt. 204 ^{o}C. ^{1}H NMR (D_2O): δ 3.09 (t, 1H), 3.39 - 3.53 (q, 2H), 3.54 - 3.65 (m, 2H), 6.34 (d, 1H) 7.83 - 7.86 (q, 1H), 7.92 (d, 1H). Selected FTIR (KBr, cm^{-1}): 3608(s), 3301(br), 1639(br), 1586(m), 1531(m), 1492(s), 1446(w), 1339(s), 1296(s), 1137(s), 1102(s), 1086(s), 837.

L-N-(2-hydroxy-5-chlorobenzyl)-Serine (L-H_3ser-5-Cl-sal). It was prepared following the procedure described above for H_2Tyrbenz except 500 mg of L-serine (4.8 mmol) and 745 mg (4.8 mmol) of 5-chlorosalicylaldehyde were used instead of L-tyrosine and benzaldehyde, respectively. In this case, the resulting yellow Schiff base solution stirred for 3 h at room temperature, prior to the addition of $NaBH_4$. A white precipitate was filtered off using a G4 Crucible, washed with methanol and air dried. Yield: 0.550 g (47%). M.pt. 214 ^{o}C. ^{1}H NMR (D_2O): δ 3.11 (t, 1H), 3.43 - 3.55 (q, 2H), 3.56 - 3.59 (m, 1H), 3.60 (s, 3H), 3.64 - 3.68 (m, 1H), 6.42 (d, 1H) 6.58 -6.61 (q, 1H), 6.70 (d, 1H). Selected FTIR peaks (KBr, cm^{-1}): 3257(br), 3196(s), 3063(s), 1629(s), 1592(s), 1535(s), 1477(m), 1446(m), 1362(s), 1272(s), 1199(s), 1078(s), 987(s), 824(s), 661(s).

L-N-(2-hydroxy-3-chlorobenzyl)-Serine (L-H_3ser-3Cl-sal). It was prepared following the procedure described above for H_2Tyrbenz except 500 mg of L-serine (4.8 mmol) and 745 mg (4.8 mmol) of 3-chlorosalicylaldehyde were used instead of L-tyrosine and benzaldehyde, respectively. In this case, the resulting yellow Schiff base solution stirred for 3 h at room temperature, prior to the addition of $NaBH_4$. A white precipitate was filtered off using a G4 Crucible, washed with methanol and air dried. Yield: 0.440 g (38%). M.pt. 203 ^{o}C. ^{1}H NMR

(D_2O): δ 3.11 (t, 1H), 3.46 (d, 1H), 3.55 - 3.59 (m, 2H), 3.64 - 3.68 (m, 1H), 6.33 (t, 1H), 6.92 (d, 1H), 7.07 (d, 1H). Selected FTIR (KBr, cm^{-1}): 3138(br), 3020(w), 2851(m), 1640(s), 1597(s), 1511(s), 1461(s), 1437(s), 1388(s), 1359(s), 1320(s), 1249(s), 1227(s), 1071(s), 938(s), 771(s).

L-N-(2-hydroxy-3methoxybenzyl)-Serine (L-H_3ser-o-van). It was prepared following the procedure described above for H_2Tyrbenz except 500 mg of L-serine (4.8 mmol) and 723 mg (4.8 mmol) of o-vanillin were used instead of L-tyrosine and benzaldehyde, respectively. In this case, the resulting yellow Schiff base solution stirred for 3 h at room temperature, prior to the addition of $NaBH_4$. A white precipitate was filtered off using a G4 Crucible, washed with methanol and air dried. Yield: 0.630 g (55%). M.pt. 215 ^oC. ^1H NMR (D_2O): δ 3.11 (t, 1H), 3.41 - 3.57 (m, 3H), 3.59 (s, 3H), 3.63 - 3.68 (m, 1H), 6.35 (t, 1H) 6.67 - 6.71 (m, 2H). Selected FTIR (KBr, cm^{-1}): 3151(br), 3047(w), 2839(s), 1636(s), 1596(s), 1493(m), 1462(s), 1438(s), 1386(s), 1366(w), 1273(s), 1185(s), 1093(s), 948(s), 735(s).

L-N,O-didansyl-tyrosine (L-HTyr-O,N-Didan). In a 10 mL round bottom flask, 100 mg (0.55 mmoles) of L-Tyrosine and 160 mg (4 mmoles) of NaOH were dissolved in 2 mL of water. To this, was added 300 mg (1.11 mmoles) of Dansyl chloride along with 2 mL of diethyl ether with stirring. The yellow solution was further stirred for 20 hours at room temperature. The aqueous phase was washed with diethyl ether, acidified with 0.05 N HCl (to obtain a pH of 5) and extracted with ethyl acetate. The organic phase was dried over $MgSO_4$ and the solvent was removed under vacuum to give a yellow solid. Yield: 226 mg (63%). ^1H NMR ($CDCl_3$): δ 2.75 (dd, 1H), 2.85-2.89 (m, 1H), 2.92 (s, 12H), 3.99-4.04 (m, 1H), 5.65 (br, 1H), 6.50 (d, 2H), 6.72 (d, 2H), 7.24 (d, 2H), 7.29 (d, 2H), 7.42-7.48 (m, 3H), 7.70 (t, 1H), 8.01 (d, 1H), 8.12 (d, 1H), 8.18 (d,1H), 8.50 (d, 1H), 8.56-8.62 (m, 2H).

L-N-dansyl-tyrosine (L-HTyr- N-dan). In a 10 mL round bottom flask, 75 mg (0.11 mmoles) of N,O-didansyl-1-tyrosine was suspended in a 1:1 mixture (4 mL) of 2N aq. solution of NaOH and methanol. The solution was refluxed for 2 hours. The yellow solution was acidified with 0.05 N HCl (to get a target pH~5) and extracted with ethyl acetate. The organic phase was dried over MgSO4 and the solvent was removed under vacuum to give a pale yellow solid. Yield: 46 mg (95%). ^1H NMR (CD_3OD): δ 2.65 (dd, 1H), 2.88 (m, 1H),

3.08 (s, 6H), 3.89 (dd, 1H), 6.33 (d, 2H), 6.72 (d, 2H), 7.23 (d, 1H), 7.44-7.51 (m, 2H), 7.99 (d, 1H), 8.22 (d, 1H), 8.49 (d, 1H).

2.4 Synthesis of Coordination Architectures

$\{[Cu(L\text{-}HTyrbenz)_2]\cdot CH_3OH\cdot 2H_2O\}_n$ (1). In a 10 mL round bottom flask, 25 mg (0.092 mmol) of L-H_2Tyrbenz and 5 mg (0.092 mmol) of KOH were dissolved in 3 mL methanol. To this was added 11.5 mg (0.046 mmol) of $CuSO_4\cdot 5H_2O$ with stirring. The reaction mixture turned blue and was stirred for 6 hours. After filtering off the K_2SO_4 precipitate, the blue filtrate was evaporated to dryness to obtain the product. Yield: 24 mg (77%). Anal. Calc. (%) for $C_{33}H_{40}N_2O_8Cu$ (MW 672.22): Calc. C, 58.96; H, 6.00; N, 4.17. Found: C, 59.13; H, 5.80; N, 4.29. Selected FTIR peaks (KBr, cm^{-1}): 3269(s), 3019(w), 2931(w), 1633(s), 1590(w), 1514(s), 1454(m), 1381(w), 1359(m), 1271(w), 1240(s), 1171(w), 806, 701. UV-Vis [λ_{max}, nm]: 204, 225, 278, 590. Specific rotation $[\alpha]_D^{20}$ = +56.0 (0.025%, CH_3OH).

$\{[Ni(L\text{-}HTyrbenz)_2(H_2O)]\cdot 8H_2O\}_n$ (2). In a 10 mL round bottom flask, 25 mg (0.092 mmol) of L-H_2Tyrbenz and 5 mg (0.092 mmol) of KOH were dissolved in 2 mL water. To this was added 12 mg (0.046 mmol) of $NiSO_4.6H_2O$ with stirring. The blue reaction mixture was stirred for 8 hours at room temperature. A bluish green precipitate was filtered off, washed with water and air dried. Yield: 16 mg (46%). Anal. Calc. (%) for $C_{32}H_{50}N_2O_{15}Ni$ (MW 761.44): Calc. C, 50.47; H, 6.62; N, 3.68. Found: C, 50.45; H, 5.90; N, 3.22. Selected FTIR peaks (KBr, cm^{-1}): 3370(br), 3275(w), 3220(w), 1628(w), 1590(m), 1515(s), 1453(m), 1398(m), 1334(w), 1246(s), 1174(w), 821(m), 750, 700. UV-Vis [λ_{max}, nm]: 250, 285, 390, 685. Specific rotation $[\alpha]_D^{20}$ = -24.0 (0.025%, DMSO: H_2O; 1:15).

$\{Zn(L\text{-}HTyrbenz)_2]\cdot 5H_2O\}_n$ (3). It was prepared following the procedure described for **2** except 13.5 mg (0.046 mmol) of $ZnSO_4.7H_2O$ was used instead of $NiSO_4\cdot 6H_2O$, respectively. After stirring for 8 hours at room temperature, a white precipitate was filtered off, washed with water and air dried. Yield: 27 mg (59%). Anal. Calc. (%) for $C_{32}H_{42}N_2O_{11}Zn$ (MW 696.06): Calc. C, 55.22; H, 6.08; N, 4.02. Found: C, 55.63; H, 5.22; N, 3.40. Selected FTIR peaks (KBr, cm^{-1}): 3421(br), 3283(w), 3220(w), 1625(w), 1604(w), 1590(m), 1517(s), 1441(m), 1397(m), 1337(w), 1243(s), 1171(w), 823(m), 737, 698.

{[Cd(L-HTyrbenz)$_2$(H$_2$O)]·4H$_2$O}$_n$ (4). It was prepared following the procedure described for **2** except 12.3 mg (0.046 mmol) of Cd(OAc)$_2$·2H$_2$O was used NiSO$_4$·6H$_2$O, respectively. After stirring for 12 hours at room temperature, a white precipitate was filtered off, washed with water and air dried. Yield: 24 mg (70.5%). Anal. Calc. (%) for $C_{32}H_{42}N_2O_{11}Cd$ (MW 743.09): Calc. C, 51.72; H, 5.70; N, 3.77. Found: C, 51.41; H, 5.10; N, 2.80. Selected FTIR peaks (KBr, cm^{-1}): 3371(br), 3270(w), 3169(w), 1611(w), 1582(s), 1515(s), 1443(m), 1392(m), 1335(w), 1237(s), 1090(s), 972(m), 811, 746, 697. Specific rotation $[\alpha]_D^{20}$ = -48.0 (0.025%, DMSO: H$_2$O; 1:15).

{[Cu(L-HSerbenz)$_2$]·3H$_2$O}$_n$ (5). In a 10 mL round bottom flask, 12 mg (0.065 mmol) of CuSO$_4$·5H$_2$O was dissolved in 1 mL water. To this was added a clear solution of L-KHSerbenz prepared by using 25 mg (0.13 mmol) of L-H$_2$Serbenz and 7 mg (0.13 mmol) of potassium hydroxide in 2 mL of water. The reaction mixture turned blue and was stirred for 3 hours at room temperature. A blue precipitate was filtered off, washed with water and air dried. Yield: 23 mg (71%). Anal. Calc. (%) for $C_{20}H_{30}N_2O_9Cu$ (MW 506.01): Calc. C, 47.47; H, 5.98; N, 5.54. Found: C, 46.71; H, 5.81; N, 5.37. Selected FTIR peaks (KBr, cm^{-1}): 3375(br), 3277(s), 1635(s), 1583(w), 1496(w), 1457(m), 1380(m), 1350(s), 1345(w), 1278(m), 1146(w), 1079(s), 972(m), 753(w), 694(s). UV-Vis [λ_{max}, nm]: 205, 254, 589. Specific rotation $[\alpha]_D^{20}$ = +51.0 (0.025%, CH$_3$OH).

{[Ni(L-HSerbenz)$_2$(H$_2$O)]·CH$_3$OH}$_n$ (6). It was prepared following the procedure described for **5** except 16.8 mg (0.065 mmoles) of NiSO$_4$.6H$_2$O was used instead of CuSO$_4$·5H$_2$O. After the reaction mixture was stirred for 12 hours, a bluish white precipitate was filtered off, washed with water and air dried. Yield: 24 mg (75%). Anal. Calc. (%) for $C_{21}H_{30}N_2O_8Ni$ (MW 497.16): Calc. C, 50.73; H, 6.08; N, 5.63. Found: C, 50.46; H, 6.02; N, 5.39. Selected FTIR peaks (KBr, cm^{-1}): 3384(br), 3262(w), 3063(w), 1606(br), 1590(w), 1493(m), 1454(m), 1396(s), 1352(m), 1209(s), 1095(s), 991(m), 802, 701. UV-Vis [λ_{max}, nm]: 250, 290, 360, 650. Specific rotation $[\alpha]_D^{20}$ = +46.0 (0.025%, DMSO: H$_2$O; 1:15).

{[Zn(L-HSerbenz)$_2$]·3H$_2$O}$_n$ (7). It was prepared following the procedure described for **5** except 18 mg (0.065 mmoles) of ZnSO$_4$.7H$_2$O was used instead of CuSO$_4$·5H$_2$O. After the reaction mixture was stirred for 10 hours, a white precipitate was filtered off, washed with

water and air dried. Yield: 22mg (67.5%). Anal. Calc. (%) for $C_{20}H_{30}N_2O_9Zn$ (MW 507.84): Calc. C, 47.30; H, 5.95; N, 5.52. Found: C, 47.49; H, 5.71; N, 5.37. Selected FTIR peaks (KBr, cm^{-1}): 3394(br), 3287(s), 3204(w), 1633(w), 1619(m), 1576(s), 1493(m), 1454(m), 1382(s), 1325(m), 1231(w), 1100(s), 897(w), 805, 751, 701. Specific rotation $[\alpha]_D^{20}$ = +50.0 (0.025%, DMSO: H_2O; 1:15).

$\{[Cd(L\text{-}HSerbenz)_2(H_2O)]\cdot CH_3OH\cdot H_2O\}_n$ (8). In a 10 mL round bottom flask, 25 mg (0.13 mmol) of L-H_2Serbenz and 7 mg (0.13 mmol) of potassium hydroxide were dissolved in 3 mL methanol. To this was added 17 mg (0.046 mmol) of $Cd(OAc)_2.2H_2O$ with stirring. The reaction mixture was stirred for 10 hours. After filtering off the K_2SO_4 precipitate, the colourless filtrate was evaporated to dryness to obtain the white product. Yield: 27 mg (74%). Anal. Calc. (%) for $C_{21}H_{32}N_2O_9Cd$ (MW 568.90): Calc. C, 44.34; H, 5.67; N, 4.92. Found: C, 44.57; H, 5.68; N, 4.26. Selected FTIR peaks (KBr, cm^{-1}): 3342(br), 3265(s), 3209(w), 1628(w), 1612(m), 1579(s), 1482(m), 1455(m), 1380(s), 1325(m), 1230(w), 1109(s), 890(w), 823, 731, 695. Specific rotation $[\alpha]_D^{20}$ = +46.0 (0.025%, CH_3OH).

$[Cu(L\text{-}Phebenz)_2(H_2O)]\cdot H_2O$ (9). In a 10 mL round bottom flask, 12 mg (0.045 mmol) of $CuSO_4\cdot 5H_2O$ was dissolved in 1 mL water. To this was added a clear solution of L-KPhebenz prepared by using 25 mg (0.09 mmol) of HPhebenz and 5 mg (0.09 mmol) of potassium hydroxide in 2 mL of water. The reaction mixture turned blue and was stirred for 10 hours at room temperature. A blue precipitate was filtered off, washed with water and air dried. Yield: 20 mg (69%). Anal. Calc. for For $C_{32}H_{36}N_2O_6Cu$ (MW 608.18): Calc. C, 63.20; H, 5.97; N, 4.61. Found: C, 63.60; H, 6.10; N, 4.72. Selected FTIR peaks (KBr, cm^{-1}): 3380(br), 3283(s), 1627(s), 1495(s), 1455(s), 1435(m), 1371(s), 1344(s), 1241(m), 1079(s), 975(s), 747(s), 696. UV-Vis [λmax, nm (ε, $L\cdot mol^{-1}\cdot cm^{-1}$)]: 576 (125) Specific rotation $[\alpha]_D^{20}$ = +26.0 (0.025%, CH_3OH).

$[Ni(L\text{-}Phebenz)_2(H_2O)_2]\cdot 4H_2O$ (10). It was prepared following the procedure described for **9** above except 13 mg (0.045 mmol) of $NiSO_4.6H_2O$ was used instead of $CuSO_4\cdot 5H_2O$. After stirring for 12 hours at room temperature, a blue precipitate was filtered off, washed with water and air dried. Yield: 30 mg (91%). Anal. Calc. (%) for $C_{32}H_{44}N_2O_{10}Ni$ (MW 674.39): Calc. C, 56.91; H, 6.57; N, 4.15. Found: C, 57.09; H, 6.00; N, 4.02. Selected FTIR peaks

(KBr, cm^{-1}): 3328(br), 3272(w), 3063(w), 1590(s), 1495(m), 1452(w), 1399(m), 1335(w), 1259(w), 1081(w), 906(w), 747, 698. UV-Vis [λ_{max}, nm]: 252, 310, 395, 650. Specific rotation $[\alpha]_D^{20}$ = -16.0 (0.025%, DMSO: H_2O; 1:15).

[Zn(L-Phebenz)$_2$(H_2O)]·3H_2O (11). It was prepared following the procedure described for **9** above except 14.5 mg (0.045 mmol) of $ZnSO_4.7H_2O$ was used instead of $CuSO_4·5H_2O$. After stirring for 10 hours at room temperature, a white precipitate was filtered off, washed with water and air dried. Yield: 31 mg (91.5%). Anal. Calc. (%) for $C_{28}H_{30}N_2O_7Zn$ (MW 646.05): Calc. C, 59.49; H, 6.24; N, 4.34. Found: C, 60.15; H, 5.71; N, 4.18. Selected FTIR peaks (KBr, cm^{-1}): 3424(br), 3274(w), 3063(w), 1617(w), 1454(w), 1438(m), 1386(m), 1079(w), 978(m), 750, 698. UV-Vis [λ_{max}, nm]: 229, 279, 585. Specific rotation $[\alpha]_D^{20}$ = -96.0 (0.025%, DMSO: H_2O; 1:15).

[Cd(L-Phebenz)$_2$(H_2O)$_2$]·H_2O (12). It was prepared following the procedure described for **9** above except 13 mg (0.045 mmol) of $Cd(OAc)_2·2H_2O$ was used instead of $CuSO_4·5H_2O$, respectively. After stirring for 12 hours at room temperature, a white precipitate was filtered off, washed with water and air dried. Yield: 31 mg (94%). Anal. Calc. (%) for $C_{32}H_{38}N_2O_7Cd$ (MW 675.06): Calc. C, 56.93; H, 5.67; N, 4.15. Found: C, 57.20; H, 5.25; N, 4.00. Selected FTIR peaks (KBr, cm^{-1}): 3406(br), 3284(w), 3027(w), 1596(w), 1579(m), 1495(m), 1453(w), 1392(s), 1327(w), 1243(w), 1080(w), 901(w), 746, 698. Specific rotation $[\alpha]_D^{20}$ = -24.0 (0.025%, DMSO: H_2O; 1:15).

{[Cu(L-HTyrthio)$_2$]·H_2O}$_n$ (13). In a 10 mL round bottom flask, 12 mg (0.045 mmol) of $CuSO_4·5H_2O$ was dissolved in 1 mL water. To this was added a clear solution of L-KHTyrthio, prepared by using 25 mg (0.09 mmol) of L-H_2Tyrthio and 5 mg (0.09 mmol) of potassium hydroxide in 2 mL of water. The reaction mixture turned blue and was stirred for 6 hours at room temperature. A purple precipitate was filtered off, washed with water and air dried. Yield: 24 mg (84%). Anal. Calc. (%) for $C_{28}H_{30}N_2O_7S_2Cu$ (MW 634.22): Calc. C, 53.03; H, 4.77; N, 4.42; S, 10.11. Found: C, 52.57; H, 4.68; N, 4.26; S, 9.75. Selected FTIR peaks (KBr, cm^{-1}): 3371(br), 3252(w), 3220(w), 1639(w), 1614(m), 1603(m), 1515(s), 1445(m), 1376(m), 1269(s), 1108(w), 881(m), 846, 714. UV-Vis [λ_{max}, nm]: 229, 279, 585. Specific rotation $[\alpha]_D^{20}$ = +46.0 (0.025%, CH_3OH).

{[Ni(L-HTyrthio)$_2$(H$_2$O)]·7H$_2$O}$_n$ (14). It was prepared following the procedure described for **13** except 11.5 mg (0.045 mmoles) of NiSO$_4$.6H$_2$O was used instead of CuSO$_4$·5H$_2$O. After stirring for 11 hours at room temperature, a green precipitate was filtered off, washed with water and air dried. Yield: 21 mg (62%). Anal. Calc. (%) for C$_{28}$H$_{44}$N$_2$O$_{14}$S$_2$Ni (MW 755.48): Calc. C, 44.51; H, 5.87; N, 3.71; S, 8.49. Found: C, 45.00; H, 6.65; N, 3.56; S, 9.45. Selected FTIR peaks (KBr, cm^{-1}): 3345(br), 3271(m), 2930(w), 1630(m), 1589(s), 1514(s), 1441(m), 1399(m), 1334(w), 1245(s), 1108(w), 831(m), 705. UV-Vis [λ_{max}, nm]: 252, 285, 670. Specific rotation $[\alpha]_D^{20}$ = +46.0 (0.025%, DMSO: H$_2$O; 1:15).

{[Zn(L-HTyrthio)$_2$(H$_2$O)]·3H$_2$O}$_n$ (15). It was prepared following the procedure described for **13** except 13 mg (0.045 mmoles) of ZnSO$_4$.7H$_2$O was used instead of CuSO$_4$·5H$_2$O. After stirring for 12 hours at room temperature, an off-white precipitate was filtered off, washed with water and air dried. Yield: 27 mg (87%). Anal. Calc. (%) for C$_{28}$H$_{36}$N$_2$O$_{10}$S$_2$Zn (MW 690.10): Calc. C, 48.73; H, 5.76; N, 4.06; S, 9.29. Found: C, 48.69; H, 4.94; N, 3.68; S, 9.70. Selected FTIR peaks (KBr, cm^{-1}): 3410(br), 3265(w), 3179(w), 1625(m), 1589(s), 1516(s), 1438(m), 1393(m), 1332(w), 1261(s), 1106(w), 827(m), 715.

{[Cd(L-HTyrthio)$_2$(H$_2$O)]·3H$_2$O}$_n$ (16). It was prepared following the procedure described for **13** except 12 mg (0.045 mmoles) of Cd(OAc)$_2$.2H$_2$O was used instead of CuSO$_4$·5H$_2$O, respectively. After stirring for 12 hours at room temperature, a white precipitate was filtered off, washed with water and air dried. Yield: 29 mg (87%). Anal. Calc. (%) for C$_{28}$H$_{36}$N$_2$O$_{10}$S$_2$Cd (MW 737.13): Calc. C, 45.62; H, 4.92; N, 3.80; S, 8.70. Found: C, 44.97; H, 3.44; N, 4.04; S, 9.21. Selected FTIR peaks (KBr, cm^{-1}): 3400(br), 3270(w), 3015(w), 1632(w), 1580(s), 1513(s), 1440(m), 1395(m), 1350(w), 1269(s), 1108(w), 881(m), 846, 714. Specific rotation $[\alpha]_D^{20}$ = +24.0 (0.025%, DMSO: H$_2$O; 1:15).

[Cu(L-HTyr4-pyr)$_2$(H$_2$O)]·3H$_2$O (17). In a 10 mL round bottom flask, 12 mg (0.045 mmol) of CuSO$_4$·5H$_2$O was dissolved in 1 mL water. To this was added a clear solution of L-KHTyr4-pyr, prepared by using 25 mg (0.092 mmol) of L-H$_2$Tyr4-pyr and 5 mg (0.09 mmol) of potassium hydroxide in 2 mL of water. The reaction mixture was stirred for 12 hours at room temperature. A green precipitate was filtered off, washed with water and air dried. Yield: 20 mg (641%). Anal. Calc. (%) for C$_{30}$H$_{38}$N$_4$O$_{10}$Cu (MW 678.19): Calc. C, 53.13; H,

5.65; N, 8.26. Found: C, 53.71; H, 5.46; N, 8.50. Despite our best effort, the CHN data could be fit with 2.5 water molecules. Selected FTIR peaks (KBr, cm^{-1}): 3434(br), 3237(s), 1644(s), 1612(s), 1517(s), 1453(s), 1379(s), 1264(s), 1088(s), 980(s), 798. UV-Vis [λ_{max}, nm] 224, 259, 282, 600. Specific rotation $[\alpha]_D^{20}$ = +96.0 (0.025%, CH_3OH).

[Ni(L-HTyr4-pyr)$_2$(H$_2$O)$_2$] (18). It was prepared following the procedure described for **17** except 12 mg (0.045 mmol) of $NiSO_4 \cdot 6H_2O$ was used instead of $CuSO_4 \cdot 5H_2O$. After stirring for 6 hours at room temperature, a green precipitate was filtered off, washed with water and air dried. Yield: 22 mg (82%). Anal. Calc. (%) for $C_{30}H_{34}N_4O_8Ni$ (MW 637.31): Calc. C, 56.54; H, 5.38; N, 8.79. Found: C, 56.37; H, 5.35; N, 8.63. Selected FTIR peaks (KBr, cm^{-1}): 3330(br), 3282s), 1601(s), 1514(s), 1497(m), 1392(s), 1351(w), 1259(s), 1087(s), 923(s), 824, 540. UV-Vis [λ_{max}, nm] 252, 290, 400, 650. Specific rotation $[\alpha]_D^{20}$ = +96.0 (0.025%, DMSO: H_2O; 1:15).

[Zn(L-HTyr4-pyr)$_2$(H$_2$O)$_2$]·3H$_2$O (19). It was prepared following the procedure described for **17** except 13.5 mg (0.045 mmol) of $ZnSO_4 \cdot 7H_2O$ was used instead of $CuSO_4 \cdot 5H_2O$. After stirring for 10 hours at room temperature, a white precipitate was filtered off, washed with water and air dried. Yield: 17 mg (48%). Anal. Calc. (%) for $C_{30}H_{40}N_4O_{11}Cu$ (MW 698.04): Calc. C, 51.62; H, 5.78; N, 8.03. Found: C, 51.14; H, 5.02; N, 7.99. Selected FTIR peaks (KBr, cm^{-1}): 3476(br), 3287(m), 3213(s), 1604(s), 1515(s), 1517(s), 1430(br), 1379(s), 1328(w), 1249(br), 1099(s), 992(s), 811.

[Cd(L-HTyr4-pyr)$_2$(H$_2$O)$_2$]·H$_2$O (20). It was prepared following the procedure described for **17** except 12.5 mg (0.045 mmol) of $Cd(OAc)_2 \cdot 2H_2O$ was used instead of $CuSO_4 \cdot 5H_2O$. After stirring for 12 hours at room temperature, a creamish precipitate was filtered off, washed with water and air dried. Yield: 29 mg (90.5%). Anal. Calc. (%) for $C_{30}H_{36}N_4O_9Cd$ (MW 709.04): Calc. C, 50.82; H, 5.12; N, 7.90. Found: C, 50.9; H, 5.15; N, 8.50. Selected FTIR peaks (KBr, cm^{-1}): 3424(br), 3279(s), 1609(s), 1598(s), 1515(s), 1457(w), 1380(s), 1349(m), 1320(w), 1256(s), 1222(m), 1068(m), 902(m), 824. Specific rotation $[\alpha]_D^{20}$ = +77.0 (0.025%, DMSO: H_2O; 1:15).

[Cu(L-HSerthio)$_2$(H$_2$O)] (21). In a 10 mL round bottom flask, 14 mg (0.057 mmol) of $CuSO_4 \cdot 5H_2O$ was dissolved in 1 mL water. To this was added a clear solution of KHSerthio,

prepared by using 25 mg (0.113 mmol) of L-H_2Serthio and 6.5 mg (0.113 mmol) of potassium hydroxide in 2 mL of water. The reaction mixture was stirred for 4 hours at room temperature. A blue precipitate was filtered off, washed with water and air dried. Yield: 18 mg (60%). Anal. Calc. (%) for $C_{16}H_{22}N_2O_7S_2Cu$ (MW 482.03): Calc. C, 39.87; H, 4.60; N, 5.81; S, 13.18. Found: C, 40.16; H, 4.42; N, 5.75; S, 13.00. Selected FTIR peaks (KBr, cm^{-1}): 3327(br), 3212(m), 1642(m), 1629(s), 1444(s), 1421(w), 1391(m), 1348(w), 1300(w), 1216(w), 1099(w), 1016(m), 716(s), 673(w). UV-Vis [λ_{max}, nm]: 235, 276, 586. Specific rotation $[\alpha]_D^{20}$ = +74.0 (0.025%, CH_3OH).

[Cu(L-Phethio)$_2$(H_2O)]·4H_2O (22). In a 10 mL round bottom flask, 12 mg (0.045 mmol) of $CuSO_4 \cdot 5H_2O$ was dissolved in 1 mL water. To this was added a clear solution of L-KPhethio, prepared by using 25 mg (0.09 mmol) of L-HPhethio and 5 mg (0.09 mmol) of potassium hydroxide. The reaction mixture was stirred for 10 hours at room temperature. A purple precipitate was filtered off, washed with water and air dried. Yield: 25 mg (77.5%). Anal. Calc. (%) for For $C_{28}H_{38}N_2O_9S_2Cu$ (MW 674.29): Calc. C, 49.87; H, 5.68; N, 4.15; S, 9.51. Found: C, 49.27; H, 5.50; N, 4.00; S, 9.67. Selected FTIR peaks (KBr, cm^{-1}): 3375(br), 3277(s), 1623(s), 1496(w), 1457(m), 1372(m), 1358(s), 1345(w), 1278(m), 1146(w), 1079(s), 972(m), 753(w), 694(s). UV-Vis [λ_{max}, nm]: 212, 235, 275, 582. Specific rotation $[\alpha]_D^{20}$ = +62.0 (0.025%, CH_3OH).

[Cu(L-HTyr4-nitro)$_2$(H_2O)]·2H_2O (23). In a 10 mL round bottom flask, 10 mg (0.04 mmol) of $CuSO_4 \cdot 5H_2O$ was dissolved in 1 mL water. To this was added a clear solution of L-KHTyrnitro was prepared by using 25 mg (0.08 mmol) of H_2Tyrnitro and 4.5 mg (0.08 mmol) of potassium hydroxide in 2 mL of water. The resulting blue reaction mixture was stirred for 48 h. A blue precipitate was filtered off using a G4 crucible, washed with water and air dried. Yield: 21 mg (71%). Anal. Calc. (%) for $C_{32}H_{36}N_4O_{13}Cu$ (MW 747.19): Calc. C, 51.37; H, 4.85; N, 7.49. Found: C, 51.09; H, 4.36; N, 7.28. Selected FTIR peaks (KBr, cm^{-1}): 3391(br), 3274(s), 1627(s), 1522(s), 1513(s), 1437(s), 1347(s), 1293(s), 1243(s), 1082(s), 704. UV-Vis in methanol [λ_{max}, nm (ε, $L \cdot mol^{-1} \cdot cm^{-1}$)]: 590 (213). Specific rotation $[\alpha]^D_{20}$ = +2.90 (conc. 0.02 %, CH_3OH).

[Ni(L-HTyr4-nitro)$_2$(H$_2$O)]·8H$_2$O (24). It was prepared following the procedure described for **23** except 10.5 mg (0.04 mmoles) of $NiSO_4 \cdot 6H_2O$ was used instead of $CuSO_4 \cdot 5H_2O$. The resulting reaction mixture was stirred for 6 h. A green precipitate was filtered off using a G4 crucible, washed with water and air dried. Yield: 27 mg (80%). Anal. Calc. (%) for $C_{32}H_{48}N_4O_{19}Ni$ (MW 851.43): Calc. C, 45.14; H, 5.68; N, 6.58. Found: C, 45.10; H, 5.97; N, 6.57. Selected FTIR peaks (KBr, cm^{-1}): 3389(br), 3280(w), 1600(s), 1582(m), 1516(s), 1445(s), 1400(s), 1348(s), 1246(s), 1107(s), 1071(s), 921, 701. UV-Vis in methanol [λ_{max}, nm (ε, $L \cdot mol^{-1} \cdot cm^{-1}$)]: 250, 280, 650. Specific rotation $[\alpha]^D_{20}$ = -16.0 (conc. 0.02 %, DMSO: H_2O; 1:15).

[Zn(L-HTyr4-nitro)$_2$(H$_2$O)]·4H$_2$O (25). It was prepared following the procedure described for **23** except 11 mg (0.04 mmoles) of $Zn(CH_3COO)_2.4H_2O$ was used instead of $CuSO_4 \cdot 5H_2O$. The reaction mixture was further stirred for 24 h. An off-white precipitate was filtered off, washed with water and air dried. Yield: 21 mg (76%). Same product is obtained while using $ZnSO_4 \cdot 7H_2O$ instead of $Zn(CH_3COO)_2 \cdot 4H_2O$, both in presence as well as in absence of a base. Anal. Calc. for $C_{32}H_{40}N_4O_{15}Zn$ (MW 786.06): Calc. C, 48.89; H, 5.13; N, 7.13. Found: C, 48.81; H, 4.66; N, 7.07. Selected FTIR peaks (KBr, cm^{-1}): 3431(br), 3261(m), 1611(s), 1519(s), 1443(m), 1390(s), 1347(s), 1255(s), 1123(w), 822. Specific rotation $[\alpha]_D^{20}$ = +32.0 (conc. 0.02 %, DMSO: MeOH 1:15).

[Cd(L-HTyr4-nitro)$_2$(H$_2$O)$_2$]·3H$_2$O (26). It was prepared following the procedure described for **23** except 10.5 mg (0.04 mmoles) of $Cd(OAc)_2 \cdot 2H_2O$ was used instead of $CuSO_4 \cdot 5H_2O$. The resulting reaction mixture was stirred for 10 h. An off-white precipitate was filtered off using a G4 crucible, washed with water and air dried. Yield: 21 mg (67.5%). Anal. Calc. (%) for $C_{32}H_{40}N_4O_{15}Cd$ (MW 833.09): Calc. C, 46.13; H, 4.84; N, 6.73. Found: C, 46.22; H, 4.41; N, 6.17. Selected FTIR peaks (KBr, cm^{-1}): 3423(br), 3245(m), 3178(s), 1603(s), 1577(s), 1519(s), 1443(m), 1397(m), 1347(s), 1255(s), 1105(m), 855, 744. Specific rotation $[\alpha]^D_{20}$ = -64.0 (conc. 0.02 %, DMSO: H_2O; 1:15).

[Cu(L-HTyr4-fluoro)$_2$(H$_2$O)]·2H$_2$O (27). In a 10 mL round bottom flask, 11 mg (0.044 mmol) of $CuSO_4 \cdot 5H_2O$ was dissolved in 1 mL water. To this was added a clear solution of L-KHTyrfluoro, prepared by using 25 mg (0.087 mmol) of L-H_2Tyrfluoro and 5 mg (0.087

mmol) of potassium hydroxide in 2 mL of water. The resulting blue reaction mixture was stirred for 15 h. A blue precipitate was filtered off using a G4 crucible, washed with water and air dried. Yield: 23 mg (77%). Anal. Calc. for $C_{32}H_{36}N_2O_9F_2Cu$ (MW 694.18): Calc. C, 55.37; H, 5.23; N, 4.04.. Found: C, 55.78; H, 4.87; N, 4.15. Selected FTIR peaks (KBr, cm^{-1}): 3309(br), 3276(s), 1643(s), 1614(s), 1512(s), 1444(s), 1370(s), 1229(s), 1100(s), 974(s), 836. UV-Vis [λ_{max}, nm (ε, $L \cdot mol^{-1} \cdot cm^{-1}$)]: 590 (183) Specific rotation $[\alpha]_D^{20}$ = -112 (conc. 0.025%, CH_3OH).

[Ni(L-HTyr4-fluoro)$_2$(H$_2$O)$_2$]·5H$_2$O (28). It was prepared following the procedure described for **27** except 11.5 mg (0.044 mmoles) of $NiSO_4 \cdot 6H_2O$ was used instead of $CuSO_4 \cdot 5H_2O$. The resulting blue reaction mixture was stirred for 5 hours at room temperature. A blue precipitate was filtered off using a G4 crucible, washed with water and air dried. Yield: 28 mg (85%). Anal. Calc. for $C_{32}H_{44}N_2O_{13}F_2Ni$ (MW 761.39): Calc. C, 50.48; H, 5.82; N, 3.68. Found: C, 50.77; H, 5.40; N, 3.16. Selected FTIR peaks (KBr, cm^{-1}): 3400(br), 3301(s), 1632(s), 1601(m), 1585(w), 1513(s), 1442(s), 1397(s), 1329(s), 1228(s), 1099(w), 969(w), 824.

[Zn(L-HTyr4-fluoro)$_2$(H$_2$O)]·4H$_2$O (29). It was prepared following the procedure described for **27** except 12.5 mg (0.044 mmoles) of $ZnSO_4 \cdot 6H_2O$ was used instead $CuSO_4 \cdot 5H_2O$, respectively. The resulting reaction mixture was stirred for 11 hours at room temperature. A white precipitate was filtered off using a G4 crucible, washed with water and air dried. Yield: 24 mg (75.8%). Anal. Calc. for $C_{32}H_{40}N_2O_{11}F_2Zn$ (MW 732.04): Calc. C, 52.5; H, 5.51; N, 3.83. Found: C, 52.31; H, 4.95; N, 3.46. Selected FTIR peaks (KBr, cm^{-1}): 3380(br), 3169(m), 3088(s), 1633(s), 1614(w), 1587(w), 1515(s), 1443(s), 1395(s), 1330(s), 1228(s), 1099(w), 969(m), 871, 528. Specific rotation $[\alpha]_D^{20}$ = +45.0 (conc. 0.025%, DMSO: H_2O; 1:15).

[Cd(L-HTyr4-fluoro)$_2$(H$_2$O)$_2$]·5H$_2$O (30). It was prepared following the procedure described for **27** except 11.5 mg (0.044 mmoles) of $Cd(OAc)_2 \cdot 2H_2O$ was used instead of $CuSO_4 \cdot 5H_2O$. The resulting reaction mixture was stirred for 15 hours at room temperature. A white precipitate was filtered off using a G4 crucible, washed with water and air dried. Yield: 28 mg (79.5%). Anal. Calc. for $C_{32}H_{36}N_2O_9F_2Cd$ (MW 815.11): Calc. C, 47.15; H, 5.44; N, 3.44. Found: C, 47.59; H, 5.38; N, 3.11. Selected FTIR peaks (KBr, cm^{-1}): 3422(br),

3274(m), 1640(m), 1600(s), 1512(s), 1443(s), 1395(s), 1331(s), 1229(s), 1101(s), 969(w), 827.

[Cu(L-HTyr4-methoxy)$_2$(H$_2$O)]·8H$_2$O (**31**)**.** In a 10 mL round bottom flask, 11 mg (0.044 mmol) of $CuSO_4 \cdot 5H_2O$ was dissolved in 1 mL water. To this was added a clear solution of L-KHTyr4-methoxy prepared by using 25 mg (0.086 mmol) of L-H_2Tyr4-methoxy and 5 mg (0.086 mmol) of potassium hydroxide in 2 mL of water. The resulting blue reaction mixture was stirred for 10 hours at room temperature. A blue precipitate was filtered off using a G4 crucible, washed with water and air dried. Yield: 26 mg (76%). Anal. Calc. for $C_{34}H_{54}N_2O_{17}Cu$ (MW 826.34): Calc. C, 49.42; H, 6.59; N, 3.39. Found: C, 49.03; H, 6.41; N, 3.46.Selected FTIR peaks (KBr, cm^{-1}): 3377(s), 3279(s), 1625(s), 1524(s), 1455(m), 1373(s), 1349(s), 1242(w), 1178(w), 975(s), 857. UV-Vis [λ_{max}, nm (ε, L·mol^{-1}·cm^{-1})]: 595 (133) Specific rotation $[\alpha]_D^{20}$ = +160.0 (conc. 0.020%, CH_3OH).

[Cu(L-HTyr4-nitro)(L-Tyrosine)]·2H$_2$O (32). In a 10 mL round bottom flask, 22 mg (0.086 mmol) of $CuSO_4.5H_2O$ was dissolved in 1 mL water. To this was added a clear solution of potassium L-H_2Tyr-4-nitro (L-KHtyrfluoro) and potassium L-tyrosine (L-Ktyr) [which was prepared by using 25 mg (0.086 mmol) of L-H_2Tyr-4-nitro, 16 mg (0.086 mmol) of L-tyrosine and 10 mg (0.172 mmol) of potassium hydroxide in 2 mL of water]. The reaction mixture turned blue and was stirred for 8 hours at room temperature. The blue precipitate was filtered off, washed with water and air dried. Yield: 34 mg (72.5%). Anal. Calc. for $C_{25}H_{29}N_3O_{10}Cu$ (MW 594.06): Calc. C, 50.46; H, 4.91; N, 7.06. Found: C, 50.48; H, 4.70; N, 7.20. Selected FTIR peaks (KBr, cm^{-1}): 3309(br), 3259(s), 2927(s), 1609(s), 1513(s), 1445(s), 1376(s), 1226(s), 1101(s), 824. UV-Vis [λ_{max}, nm (ε, L·mol^{-1}.cm^{-1})]: 570(230). Specific rotation $[\alpha]^D{}_{20}$ = +18.0 (0.025%, CH_3OH).

[Cu(L-HTyr4-fluoro)(L-Tyrosine)]·3H$_2$O (33). It was prepared following the procedure described for **32** except L-KHTyr-4-fluoro, prepared by using 25 mg (0.086 mmol) of L-H_2Tyr4-fluoro and 5 mg (0.086 mmol) of potassium hydroxide in 2 mL of water, was used instead of L-KHTyr-4-nitro. A blue precipitate was filtered using a G4 crucible, washed with water and air dried. Yield: 30 mg (59%). Anal. Calc. for $C_{25}H_{31}N_2O_9FCu$ (MW 586.07):

Calc. C, 51.23; H, 5.33; N, 4.78. Found: C, 51.42; H, 4.78; N, 4.88. Selected FTIR peaks (KBr, cm^{-1}): 3309(br), 3259(s), 2927(s), 1609(s), 1513(s), 1445(s), 1376(s), 1226(s), 1101(s), 824. UV-Vis [λ_{max}, nm (ε, $L \cdot mol^{-1}.cm^{-1}$)]: 575 (196). Specific rotation $[\alpha]^{D}_{20}$ = +9.80 (0.025%, CH_3OH).

{[Cu_2(L-Hsersal)$_2$(H_2O)]·2.5H_2O}$_n$ (34). In a 10 mL round bottom flask, 59 mg (0.24 mmol) of $CuSO_4.5H_2O$ was dissolved in 2 mL methanol. To this was added a clear solution of L-K_2Hsersal [which was prepared by using 50 mg (0.24 mmol) of L-H_3sersal and 26 mg (0.48 mmol) of potassium hydroxide in 2 mL of methanol]. The reaction mixture turned green and was stirred for 6 hrs at room temperature. The resulted green slurry was taken to dryness. Addition of 10 mL DMF to the solid followed by filtration provided a green filtrate which upon evaporation gave the desired product. The compound was recrystallized from methanol. Yield: 42 mg (65%). Anal. Calc. for $C_{20}H_{29}N_2O_{11.5}Cu_2$ (MW 608.54): Calc. C, 39.47; H, 4.80; N, 4.60. Found: C, 39.41; H, 4.61; N, 4.52. Selected FTIR peaks (KBr, cm^{-1}): 3400(br), 3233(s), 2937(s), 1613(s), 1581(s), 1486(s), 1449(s), 1253(s), 1116(w), 1043(s), 757. ESI-MS: [Cu_2(Hsersal)$_2$]H^+, (m/z, calc. 546.51; found 545.69). UV-Vis [λmax, nm (ε, $L \cdot mol^{-1} \cdot cm^{-1}$)]: 675 (123). Specific rotation $_D[\alpha]^{20}$ = +26.3 (0.023%, CH_3OH).

{[Ni_2(L-Hsersal)$_2$(H_2O)]·2H_2O}$_n$ (35). It was prepared following the procedure described for **34** above except 62 mg (0.24 mmoles) of $NiSO_4 \cdot 6H_2O$ was used instead of $CuSO_4 \cdot 5H_2O$. The reaction mixture turned bluish green and was stirred for 10 hrs at room temperature. The resulted slurry was taken to dryness. Addition of 10 mL DMF to the solid followed by filtration provided a greemish blue filtrate which upon evaporation gave the desired product. The compound was recrystallized from methanol. Yield: 48 mg (74.3%). Anal. Calc. for $C_{20}H_{28}N_2O_{11}Ni_2$ (MW 589.83): Calc. C, 40.73; H, 4.78; N, 4.75. Found: C, 40.93; H, 5.11; N, 4.33. Selected FTIR peaks (KBr, cm^{-1}): 3384(br), 3273(w), 2945(w), 1596(s), 1506(w), 1482(s), 1457(s), 1395(m), 1322(w), 1274(s), 1252(m), 1110(w), 1090(m), 1091(s), 875(s), 758(s). UV-Vis [λmax, nm (ε, $L \cdot mol^{-1} \cdot cm^{-1}$)]: 280, 350, 650. Specific rotation $_D[\alpha]^{20}$ = +34.92 (0.006%, CH_3OH).

{[Cu_2(L-Hser-5OMe-sal)$_2$(H_2O)]·DMF}$_n$ (36). In a 10 mL round bottom flask, 50 mg (0.20 mmol) of $CuSO_4.5H_2O$ was dissolved in 2 mL methanol. To this was added a clear solution

of L-K_2Hser-5OMe-sal [50 mg (0.20 mmol) of L-H_3ser-5OMe-sal and 24 mg (0.40 mmol) of potassium hydroxide in 2 mL of methanol]. The reaction mixture turned green and was stirred for 6 hrs at room temperature. The resulted green slurry was taken to dryness. Addition of 10 mL DMF to the solid followed by filtration provided a green filtrate which upon evaporation gave the desired product. The compound was recrystallized from methanol. Yield: 49 mg (68%). Anal. Calc. for $C_{25}H_{35}N_3O_{12}Cu_2$ (MW 696.65): Calc. C, 43.10; H, 5.06; N, 6.03. Found: C, 42.74; H, 4.99; N, 5.93. Selected FTIR peaks (KBr, cm^{-1}): 3400(br), 3239(w), 1633(s), 1603(s), 1492(s), 1456(w), 1390(s), 1350(m), 1268(s), 1222(s), 1156(s), 1090(m), 1042(s), 804(s), 718(s). UV-Vis [λmax, nm (ε, $L \cdot mol^{-1} \cdot cm^{-1}$)]: 680 (48). Specific rotation $_D[\alpha]^{20}$ = +34.92 (0.006%, CH_3OH).

{[Ni_2(L-Hser-5OMe-sal)$_2$(H_2O)]·2H_2O·CH_3OH}$_n$ (37). It was prepared following the procedure described for **36** above except 54.5 mg (0.20 mmoles) $NiSO_4 \cdot 6H_2O$ was used instead of $CuSO_4 \cdot 5H_2O$. The reaction was stirred for 10 hrs at room temperature. The resulted slurry was taken to dryness. Addition of 10 mL DMF to the solid followed by filtration provided a blue filtrate which upon evaporation gave the desired product. The compound was recrystallized from methanol. Yield: 58 mg (82%). Anal. Calc. for $C_{23}H_{36}N_2O_{14}Ni_2$ (MW 681.92): Calc. C, 40.51; H, 5.32; N, 4.11. Found: C, 40.74; H, 5.13; N, 3.78. Selected FTIR peaks (KBr, cm^{-1}): 3389(br), 3264(s), 2936(w), 1600(s), 1489(s), 1427(w), 1346(m), 1265(s), 1218(s), 1048(m), 1042(s), 790(m), 618(s). UV-Vis [λmax, nm (ε, $L \cdot mol^{-1} \cdot cm^{-1}$)]: 310, 390, 650. Specific rotation $_D[\alpha]^{20}$ = +67.09 (0.006%, CH_3OH).

{[Cu_2(L-Hser-5NO_2-sal)$_2$(H_2O)]·2H_2O}$_n$ (38). In a 10 mL round bottom flask, 50 mg (0.20 mmol) of $CuSO_4.5H_2O$ was dissolved in 2 mL methanol. To this was added a clear solution of L-K_2Hser-5NO_2-sal [50 mg (0.20 mmol) of L-H_3ser-5NO_2-sal and 22 mg (0.40 mmol) of potassium hydroxide in 2 mL of methanol]. The reaction mixture turned green and was stirred for 6 hrs at room temperature. The resulted green slurry was taken to dryness. Addition of 10 mL DMF to the solid followed by filtration provided a green filtrate which upon evaporation gave the desired product. The compound was recrystallized from methanol. Yield: 28 mg (42%). Anal. Calc. for $C_{20}H_{28}N_4O_{16}Cu_2$ (MW 689.53): Calc. C, 34.84; H, 3.80; N, 8.13. Found: C, 34.28; H, 3.42; N, 7.70. Selected FTIR peaks (KBr, cm^{-1}): 3430(br), 3225(s), 1627(s), 1601(s), 1481(s), 1340(s), 1303(s), 1188(s), 1100(s), 1025(s), 899(s),

658(s). UV-Vis [λmax, nm (ε, $L \cdot mol^{-1} \cdot cm^{-1}$)]: 684 (70). Specific rotation $_D[\alpha]^{20}$ = +8.0 (0.012%, CH_3OH).

{[Ni_2(L-Hser-5NO_2-sal)$_2$(H_2O)]·8H_2O}$_n$ (39). In a 10 mL round bottom flask, 52 mg (0.20 mmol) of $NiSO_4 \cdot 6H_2O$ was dissolved in 2 mL water. To this was added a clear solution of L-K_2Hser-5NO_2-sal [50 mg (0.20 mmol) of L-H_3ser-5NO_2-sal and 22 mg (0.40 mmol) of potassium hydroxide in 2 mL of water]. The reaction mixture was stirred for 10 hrs at room temperature. A yellowish green precipitate was filtered using a G4 crucible, washed with water and air dried. Yield: 50 mg (65%). Anal. Calc. for $C_{20}H_{38}N_4O_{21}Ni_2$ (MW 787.92): Calc. C, 30.49; H, 4.86; N, 7.11. Found: C, 30.73; H, 4.41; N, 6.66. Selected FTIR peaks (KBr, cm^{-1}): 3395(br), 3270(s), 2949(w), 1597(s), 1482(s), 1434(m), 1350(s), 1301(s), 1183(s), 1096(s), 1032(s), 834(m), 653(m). UV-Vis [λmax, nm (ε, $L \cdot mol^{-1} \cdot cm^{-1}$)]: 250, 340, 420, 650. Specific rotation $_D[\alpha]^{20}$ = +54.0 (0.012%, DMSO: H_2O; 1:15).

{[Cu_2(L-Hser-5Cl-sal)$_2$(H_2O)]·H_2O}$_n$ (40). In a 10 mL round bottom flask, 50 mg (0.20 mmol) of $CuSO_4.5H_2O$ was dissolved in 2 mL methanol. To this was added a clear solution of L-K_2Hser-5Cl-sal [50 mg (0.20 mmol) of L-H_3ser-5Cl-sal and 23 mg (0.40 mmol) of potassium hydroxide in 2 mL of methanol]. The reaction mixture turned green and was stirred for 10 hrs at room temperature. The resulted green slurry was taken to dryness. Addition of 10 mL DMF to the solid followed by filtration provided a green filtrate which upon evaporation gave the desired product. The compound was recrystallized from methanol. Yield: 28 mg (42%). Anal. Calc. for $C_{20}H_{24}N_2O_{10}Cu_2$ (MW 650.41): Calc. C, 36.93; H, 3.72; N, 4.31. Found: C, 36.22; H, 3.70; N, 4.10. Selected FTIR peaks (KBr, cm^{-1}): 3371(br), 3234(br), 1622(br), 1477(s), 1418(m), 1385(w), 1352(w), 1267(s),1191(s), 1125(s), 1092(m), 874(s), 667(s). UV-Vis [λmax, nm (ε, $L \cdot mol^{-1} \cdot cm^{-1}$)]: 663 (34). Specific rotation $_D[\alpha]^{20}$ = +32.97 (0.019%, CH_3OH).

{[Ni_2(L-Hser-5Cl-sal)$_2$(H_2O)]·H_2O·2CH_3OH}$_n$ (41). In a 10 mL round bottom flask, 52 mg (0.20 mmol) of $NiSO_4 \cdot 6H_2O$ was dissolved in 2 mL water. To this was added a clear solution of L-K_2Hser-5Cl-sal [50 mg (0.20 mmol) of L-H_3ser-5Cl-sal and 23 mg (0.40 mmol) of potassium hydroxide in 2 mL of water]. The reaction mixture was stirred for 10 hrs at room temperature. A green precipitate was filtered using a G4 crucible, washed with water and air

dried. Yield: 52 mg (70%). Anal. Calc. for $C_{21}H_{32}N_2Cl_2O_{12}Ni_2$ (MW 704.79): Calc. C, 37.49; H, 4.58; N, 3.97. Found: C, 37.54; H, 4.47; N, 3.31. Selected FTIR peaks (KBr, cm^{-1}): 3401(br), 3279(m), 2945(m), 1594(br), 1476(s), 1416(m), 1346(w), 1318(w), 1280(s),1184(s), 1093(m), 874(s), 673(s). UV-Vis [λmax, nm (ε, $L \cdot mol^{-1} \cdot cm^{-1}$)]: 250, 320, 400, 655. Specific rotation $_D[\alpha]^{20}$ = +45.8 (0.019%, DMSO: H_2O; 1:15).

{[Cu_2(L-Hser-3Cl-sal)$_2$(H_2O)]·3H_2O}$_n$ (42). In a 10 mL round bottom flask, 50 mg (0.20 mmol) of $CuSO_4.5H_2O$ was dissolved in 2 mL methanol. To this was added a clear solution of L-K_2Hser-3Cl-sal [50 mg (0.20 mmol) of L-H_3ser-3Cl-sal and 23 mg (0.40 mmol) of potassium hydroxide in 2 mL of methanol]. The reaction mixture turned green and was stirred for 11 hrs at room temperature. The resulted green slurry was taken to dryness. Addition of 10 mL DMF to the solid followed by filtration provided a green filtrate which upon evaporation gave the desired product. The compound was recrystallized from methanol. Yield: 43 mg (61.5%). Anal. Calc. for $C_{20}H_{28}N_2O_{12}Cu_2$ (MW 686.44): Calc. C, 34.98; H, 4.08; N, 4.08. Found: C, 34.98; H, 3.80; N, 4.02. Selected FTIR peaks (KBr, cm^{-1}): 3389(br), 3230(br), 1627(br), 1590(s), 1445(s), 1354(m), 1315(w), 1280(m), 1240(w), 1176(s), 1137(s), 1092(m), 846(s), 744(s). UV-Vis [λmax, nm (ε, $L \cdot mol^{-1} \cdot cm^{-1}$)]: 679 (64). Specific rotation $_D[\alpha]^{20}$ = -18.08 (0.019%, CH_3OH).

{[Ni_2(L-Hser-3Cl-sal)$_2$(H_2O)]·3H_2O}$_n$ (43). It was prepared following the procedure described for **42** above except 54 mg (0.20 mmoles) of $NiSO_4 \cdot 6H_2O$ was used instead $CuSO_4 \cdot 5H_2O$. The reaction mixture turned green and was stirred for 12 hrs at room temperature. The resulted green slurry was taken to dryness. Addition of 10 mL DMF to the solid followed by filtration provided a green filtrate which upon evaporation gave the desired product. The compound was recrystallized from methanol. Yield: 54mg (78%). Anal. Calc. for $C_{20}H_{28}N_2Cl_2O_{12}Ni_2$ (MW 676.74): Calc. C, 35.50; H, 4.17; N, 4.14. Found: C, 35.54; H, 4.47; N, 4.31. Selected FTIR peaks (KBr, cm^{-1}): 3423(br), 3261(br), 2923(s), 1590(s), 1444(s), 1352(w), 1321(m), 1281(m), 1134(s), 1039(m), 838(s), 626(s). UV-Vis [λmax, nm (ε, $L \cdot mol^{-1} \cdot cm^{-1}$)]: 250, 325, 397, 650.. Specific rotation $_D[\alpha]^{20}$ = -18.08 (0.019%, DMSO: H_2O; 1:15).

{[Cu_2(L-Hser-o-Van)$_2$(H_2O)]·3H_2O}$_n$ (44). In a 10 mL round bottom flask, 50 mg (0.20 mmol) of $CuSO_4.5H_2O$ was dissolved in 2 mL methanol. To this was added a clear solution

of L-K_2Hser-o-Van [50 mg (0.20 mmol) of L-H_3ser-o-Van and 24 mg (0.40 mmol) of potassium hydroxide in 2 mL of methanol]. The reaction mixture turned green and was stirred for 10 hrs at room temperature. The resulted green slurry was taken to dryness. Addition of 10 mL DMF to the solid followed by filtration provided a green filtrate which upon evaporation gave the desired product. The compound was recrystallized from methanol. Yield: 30 mg (48%). Anal. Calc. for $C_{22}H_{34}N_2O_{14}Cu_2$ (MW 677.5): Calc. C, 39.00; H, 5.06; N, 4.13. Found: C, 38.24; H, 4.46; N, 3.90. Selected FTIR peaks (KBr, cm^{-1}): Selected FTIR (KBr, cm^{-1}): 3401(br), 3226(w), 1633(br), 1478(s), 1384(w), 1354(m), 1267(m), 1237(s), 1186(w), 1079(s), 847(s), 740(s). UV-Vis [λmax, nm (ε, $L \cdot mol^{-1} \cdot cm^{-1}$)]: 672 (55). Specific rotation $_D[\alpha]^{20}$ = +17.6 (0.012%, CH_3OH).

{[Ni_2(L-Hser-o-Van)$_2$(H_2O)]·3H_2O}$_n$ (45). It was prepared following the procedure described for **44** above except 54.5 mg (0.20 mmol) of $NiSO_4 \cdot 6H_2O$ was used instead of $CuSO_4 \cdot 5H_2O$. The reaction mixture stirred for 9 hours at room temperature. The resulted slurry was taken to dryness. Addition of 10 mL DMF to the solid followed by filtration provided a bluish green filtrate which upon evaporation gave the desired product. The compound was recrystallized from methanol. Yield: 51 mg (74%). Anal. Calc. for $C_{22}H_{34}N_2O_{14}Ni_2$ (MW 667.90): Calc. C, 39.56; H, 5.13; N, 4.19. Found: C, 39.02; H, 5.07; N, 3.63. Selected FTIR peaks (KBr, cm^{-1}): Selected FTIR (KBr, cm^{-1}): 3389(br), 3266(w), 2940(w), 1598(s), 1476(s), 1404(w), 1350(m), 1287(m), 1232(s), 1110(w), 917(m), 849(s), 740(s), 618. UV-Vis [λmax, nm (ε, $L \cdot mol^{-1} \cdot cm^{-1}$)]: 290, 400, 650. Specific rotation $_D[\alpha]^{20}$ = +36.7 (0.012%, CH_3OH).

[Cu_2(4,4'-bpy)(L-Hsersal)$_2$]·2H_2O (46). In a 10 mL round bottom flask, 25 mg (0.04mmol) of **34** was dissolved in 3 mL methanol. To this was added 6 mg (0.04 mmol) of 4,4'-bipyridine and the mixture was stirred for 6 hours under reflux conditions. The green solution was evaporated completely to isolate **7**. Yield: 21 mg (69%). Anal. Calcd. For $C_{30}H_{34}N_4O_{10}Cu_2$ (MW737.70): Calc. C, 48.84; H,4.65; N, 7.59. Found: C, 49.07; H, 4.73; N, 8.05. Selected FTIR peaks (KBr, cm^{-1}): 3355(br), 3196(s), 2924(s), 1616(s), 1596(s), 1534(w), 1479(s), 1455(s), 1276(br), 1217(s), 1092(s), 758, 644. ESI-MS: [Cu_2(Hsersal)$_2$(4,4'bipyridine)]H^+, (m/z, calc. 702.69; found 702.82), [Cu_2(Hsersal)$_2$]H^+ (m/z,

calc. 546.51; found 545.04). UV-Vis [λmax, nm (ε, $L \cdot mol^{-1} \cdot cm^{-1}$)]: 655 (213). Specific rotation, $_D[\alpha]^{20}$ = +50.60 (0.02%, CH_3OH).

$[Cu_2(4,4'\text{-bpy})(L\text{-Hser-5-OMe-sal})_2]\cdot 6H_2O$ (47). It was prepared following the procedure described for **46** above except compound **36** was used instead of **34**. Yield: 28 mg (71%). Anal. Calc. for $C_{32}H_{46}N_4O_{16}Cu_2$ (MW 869.82): Calc. C, 44.18; H, 5.33; N, 6.44. Found: C, 43.70; H, 4.71; N, 5.87. Selected FTIR peaks (KBr, cm^{-1}): Selected FTIR (KBr, cm^{-1}): 3479(br), 3270(w), 3157 (m), 1657(m), 1606(s), 1495(s), 1424 (m), 1348(m), 1231(m), 1217(s), 1098(w), 1026(s), 802(s), 674(w). UV-Vis [λmax, nm (ε, $L \cdot mol^{-1} \cdot cm^{-1}$)]: 657 (40). Specific rotation $_D[\alpha]^{20}$ = +91.20 (0.012%, CH_3OH).

$[Cu_2(4,4'\text{-bpy})(L\text{-Hser-5-}NO_2\text{-sal})_2]\cdot H_2O$ (48). It was prepared following the procedure described for **46** above except compound **38** was used instead of **34**. Yield: 24 mg (60%). Anal. Calc. for $C_{30}H_{30}N_6O_{13}Cu_2$ (MW 809.68): Calc. C, 44.50; H, 3.73; N, 10.38. Found: C, 44.11; H, 3.14; N, 10.07. Selected FTIR peaks (KBr, cm^{-1}): Selected FTIR (KBr, cm^{-1}): 3401(br), 3229(m), 1642(s), 1597(s), 1477(s), 1439(w), 1394(w), 1353(m), 1290(br), 1217(s), 1185(m), 1079(s), 936(s), 645(s). UV-Vis [λmax, nm (ε, $L \cdot mol^{-1} \cdot cm^{-1}$)]: 680 (21). Specific rotation $_D[\alpha]^{20}$ = -16.0 (0.012%, CH_3OH).

$[Cu_2(4,4'\text{-bpy})(Hser\text{-5-Cl-sal})_2]\cdot 4H_2O.DMF$ (49). It was prepared following the procedure described for **46** above except compound **40** was used instead of **34**. Yield: 26 mg (67%). Anal. Calc. for $C_{33}H_{43}N_5O_{13}Cu_2$ (MW 915.72): Calc. C, 43.28; H, 4.73; N, 7.65. Found: C, 43.27; H, 4.69; N, 7.55. Selected FTIR peaks (KBr, cm^{-1}): Selected FTIR (KBr, cm^{-1}): 3382(br), 3235(w), 1634(s), 1614(s), 1473(s), 1417(s), 1389(w), 1350(m), 1287(s), 1219(s), 1123(w), 1070(s), 821(s), 644(s). UV-Vis [λmax, nm (ε, $L \cdot mol^{-1} \cdot cm^{-1}$)]: 673 (40). Specific rotation $_D[\alpha]^{20}$ = +27.2 (0.012%, CH_3OH).

$[Ni_2(Hhissal)_2(adi)(H_2O)_2]\cdot 8H_2O$ (50). In a 10 mL round bottom flask, 47 mg (0.18 mmol) of $NiSO_4.7H_2O$ was dissolved in 3 mL methanol. To this was added a clear mixture of monopotassium H_2hissal (KHhissal) [which was prepared by using 50 mg (0.18 mmol) of H_2hissal and 10 mg (0.18 mmol) of potassium hydroxide in 2.5 mL of methanol] and dipotassium adipate (K_2adi) [which was prepared by using 13 mg (0.09 mmol) of adipic acid and 10 mg (0.18 mmol) of potassium hydroxide in 2.5 mL of methanol]. The reaction

mixture that turned blue was stirred for 12 hrs. A blue solution was obtained via filtration and evaporated under reduced pressure to obtain a blue powder. Yield: 70 mg (76.5%). Anal. Calc. for $C_{32}H_{56}N_6O_{20}Ni_2$ (MW 962.20): Calc. C, 39.94; H, 5.87; N, 8.73. Found: C, 39.57; H, 5.92; N, 8.67. Selected FTIR peaks (KBr, cm^{-1}): 3390(br), 3274(br), 2919(w), 1592(w), 1567(s), 1480(s), 1452(s), 1408(s), 1289(s), 1192(w), 1082(s), 874, 761. Specific rotation $[\alpha]_D^{20}$ = -60 (0.02 %, CH_3OH).

$[Ni_2(Hhissal)_2(succ)(H_2O)_2]\cdot 4H_2O$ (51). It was prepared by the procedure described for **50** except 11 mg (0.09 mmol) of succinic acid was used instead of adipic acid. Yield: 45 mg (55%). Anal. Calc. for $C_{30}H_{46}N_6O_{16}Ni_2$ (MW 862.09): Calc. C, 41.80; H, 5.14; N, 9.75. Found: C, 41.94; H, 5.08; N, 9.89. Selected FTIR peaks (KBr, cm^{-1}): 3398(br), 3252(br), 2909(w), 1600(w), 1567(s), 1480(s), 1452(s), 1403(s), 1294(s), 1277(s), 1194(w), 1083(s), 878, 756. Specific rotation $[\alpha]_D^{20}$ = -20 (0.02 %, CH_3OH).

$[Ni_2(Hhissal)_2(mal)(H_2O)_2]\cdot 4H_2O$ (52). It was prepared by the procedure described for **50** except 11 mg (0.09 mmol) of maleic acid was used instead of adipic acid. Yield: 58 mg (71%). Anal. Calc. for $C_{30}H_{42}N_6O_{16}Ni_2$ (MW 860.07): Calc. C, 41.89; H, 4.92; N, 9.77. Found: C, 42.79; H, 4.79; N, 9.98. Selected FTIR peaks (KBr, cm^{-1}): 3384(br), 3250(br), 2892(w), 1598(w), 1574(s), 1480(s), 1452(s), 1401(s), 1294(s), 1277(s), 1194(w), 1083(s), 878, 756. Specific rotation $[\alpha]_D^{20}$ = +20 (0.02 %, CH_3OH).

$[Ni_2(Hhissal)_2(fum)(H_2O)_2]\cdot 6H_2O$ (53). It was prepared by the procedure described for **50** except 11 mg (0.09 mmol) of fumaric acid was used instead of adipic acid. Yield: 62 mg (73%). Anal. Calc. for $C_{30}H_{46}N_6O_{18}Ni_2$ (MW 896.10): Calc. C, 40.21; H, 5.17; N, 9.38. Found: C, 40.56; H, 4.96; N, 9.40. Selected FTIR peaks (KBr, cm^{-1}): 3384(br), 3250(br), 2892(w), 1598(w), 1574(s), 1480(s), 1452(s), 1401(s), 1294(s), 1277(s), 1194(w), 1083(s), 878, 756. Specific rotation $[\alpha]_D^{20}$ = +30 (0.02 %, CH_3OH).

With ligands having additional tagged fluorophore

$[Cu_2(HTyr\text{-}N\text{-}Dan)_4(H_2O)_2]\cdot 6H_2O$ (54). In a 10 mL round bottom flask, 38 mg (0.09 mmoles) of N-dansyl-1-tyrosine and 5 mg (0.09 mmoles) of KOH was dissolved in 1.5 mL of methanol. To this was added 11.5 mg (0.045 mmoles) of $CuSO_4.5H_2O$ along with

1.5 mL of methanol with stirring. The resultant green solution was further stirred for 6 hours at room temperature. The green filtrate was evaporated to dryness to get a green solid. Yield: 28 mg (63%). Anal. Calc. for $C_{84}H_{100}N_8O_{28}S_4Cu_2$ (MW 1925.08): calc. C, 52.41; H, 5.24; N, 5.82; S, 6.62. Found: C, 52.67; H, 4.81; N, 5.75; S, 6.45. Selected FTIR peaks (KBr, cm^{-1}): 3410 (br), 3271(br), 2931(m), 1614(m), 1589(s), 1574(s), 1515(s), 1452 (s), 1395 (s), 1232(s), 1140 (s), 1090(m), 788(s), 627(s), 586(s).

$[Zn_2(HTyr\text{-}N\text{-}Dan)_4(H_2O)_2]\cdot 6H_2O$ (55). It was prepared by the procedure described for **75** except 13 mg (0.09 mmol) of $ZnSO_4.7H_2O$ was used instead of $CuSO_4.5H_2O$. After stirring for 12 hours, resultant light yellow filterate was evaporated to dryness to obtain yellow solid. Yield: 30 mg (68%). Anal. Calc. for $C_{84}H_{100}N_8O_{28}S_4Zn_2$ (MW 1928.75): calc. C, 52.31; H, 5.23; N, 5.81; S, 6.65. Found: C, 52.55; H, 5.10; N, 5.84; S, 6.50. Selected FTIR peaks (KBr, cm^{-1}): 3405 (br), 3267(br), 2935(m), 1614(m), 1587(s), 1572(s), 1515(s), 1450 (s), 1390 (s), 1232(s), 1140 (s), 1090(m), 786(s), 627(s), 586(s).

$[Cu_2(HTyr\text{-}O,N\text{-}Didan)_4(H_2O)_2]\cdot 4H_2O$ (56). It was prepared by the procedure described for **75** except 44 mg (0.06 mmol) of HTyr-O,N-didan was used instead of H_2Tyr-N-Dan.The green filtrate was evaporated to dryness to get a green solid. Isolated yield: 36 mg (74%). Anal. Calc. for $C_{134}H_{140}N_{12}O_{34}S_8Cu_2$ (MW 2858.23): calc. C, 52.41; H, 5.20; N, 5.82; S, 8.97. Found: C, 52.79; H, 5.61; N, 5.87; S, 9.10. Selected FTIR peaks (KBr, cm^{-1}): 3434 (br), 3285(br), 2937(m), 1612(m), 1588(s), 1570(s), 1515(s), 1457(s), 1390(s), 1230(s), 1140 (s), 1092(m), 786(s), 626(s), 583(s).

$[Zn_2(HTyr\text{-}O,N\text{-}Didan)_4(H_2O)_2]\cdot 6H_2O$ (57). It was prepared by the procedure described for **75** except 44 mg (0.06 mmol) of HTyr-O,N-didan and 10 mg (0.03 mmol) of $ZnSO_4.7H_2O$ was used instead of H_2Tyr-N-Dan and $CuSO_4.5H_2O$, respectively. The yellow filtrate was evaporated to dryness to get a green solid. Isolated yield: 28 mg (58%). Anal. Calc. for $C_{132}H_{144}N_{12}O_{36}S_8Zn_2$ (MW 2861.89): calc. C, 55.40; H, 5.07; N, 5.87; S, 8.96. Found: C, 55.67; H, 4.81; N, 5.54; S, 9.34. Selected FTIR peaks (KBr, cm^{-1}): 3440(br), 3285(br), 2939(m), 1615(m), 1590(s), 1570(s), 1515(s), 1465(s), 1395(s), 1230(s), 1140 (s), 1089(m), 786(s), 626(s), 584(s).

2.4 For Sensing Experiments

For flip-flop halide sensor

Stock solutions of 0.6 mM of the sensor was prepared in methanol or DMSO whereas 0.1 mM solution of each anion was prepared in solvent ratio of 1:3; water: methanol or water: DMSO. For each measurement, 12.6μL of the analyte was added to 2 mL solution of the sensor.

For single receptor multi analyte sensing

Stock solutions of 3.5 mM NaHTyrthio, 2 mM of each metal salt/nitroaromatics/aniline, 0.1 M of each anion and 5 mM Na_4EDTA were prepared in methanol. For each measurement, 2 mL of NaHTyrthio was used for 300 μL of cationic or anionic analytes. For neutral small molecules, an aliquot of 100 μL of the analyte was introduced. For fluorescence titrimetry experiment, each time 10 μl of Cu^{2+} was added to the sensor. For lifetime measurements 0.72 mM solution of the sensor was used.

Chromogenic sensing

Stock solutions of 25 mM of the sensor was prepared in DMSO, 0.1 mM solution of each anionic analyte was prepared in water: DMSO (1: 3) solution. For each measurement, 0.45 mL of sensor and 0.1095 mL of anionic analytes were used.

Sensing using tagged fluorophore

Stock solutions of 2.5 mM of the ligand, 0.12 mM of the metal complex and 2 mM of each anionic analyte was prepared in methanol. For each measurement, 2 mL of sensor and 300 mL of the analytes were used.

Chapter III

Results and Discussion

There are two major sections in this chapter: (a) structural diversity in the self-assembled homochiral coordination architectures, and (b) selective chromogenic and/or fluorogenic sensing of cations, anions and neutral small molecules. The best way to bring structural and functional diversity is through judicious designing of the ligands. Further induction of chirality into these coordination architectures is best achieved by the self-assembly of optically pure chiral organic ligands with the metal ions. In making of chiral ligands, amino acids are preferred over other chiral analogues not only due to their low cost and easy availability but also due to their abilities to act both as hydrogen bond donors and acceptors and thus providing different binding modes with the metal centers through various functionalities present in these ligands, e.g., carboxylate, hydroxy, etc. These ligands are temporally engaged in the synthesis of around sixty neutral coordination architectures with unparallel properties which are detailed below. These coordination architectures are extensively characterized by various techniques like NMR spectroscopy, elemental analysis, UV-Vis, circular dichroism, magnetic studies, water vapor adsorption studies, isothermal titration calorimetry, IR and Raman spectroscopy, fluorescence spectroscopy, ESI mass spectrometry, single crystal and powder X-ray diffraction, polarimetry and thermogravimetric analysis. Thus the syntheses of these ligands are discussed first followed by the major sections.

3.1 SYNTHESIS OF LIGANDS

Two types of the amino acid based ligands (shown in Figure 1.7) are methodically synthesized and structurally characterized by a number of analytical techniques. First type is the amino acid based reduced Schiff bases and the second type is ligands with additional tagged fluorophores to the amino acids. For the first type of ligands, a general methodology was developed where the sodium salt of the respective L-amino acid and the appropriate aldehyde were stirred or refluxed depending upon the reactivity of the aldehyde. The formation of sodium salt of the amino acids prior to the addition of aldehyde not only helps in

solublizing the amino acid in the methanol-water mixture but also facilitates the availability of the $-NH_2$ group (only when pH > pKa) for the condensation reaction as an amino acid in its zwitter-ion form contains the NH_3^+ group. One can correlate the reaction conditions with respect to the substitution in the aldehyde; however, it was not the case for several of these and thus optimized conditions were obtained through design of experiments. The Schiff base was further reduced using sodium borohydride. The desired products were obtained by the addition of glacial acetic acid to the sodium salt of the reduced Schiff bases of the L-amino acids (as shown in Scheme 3.1).

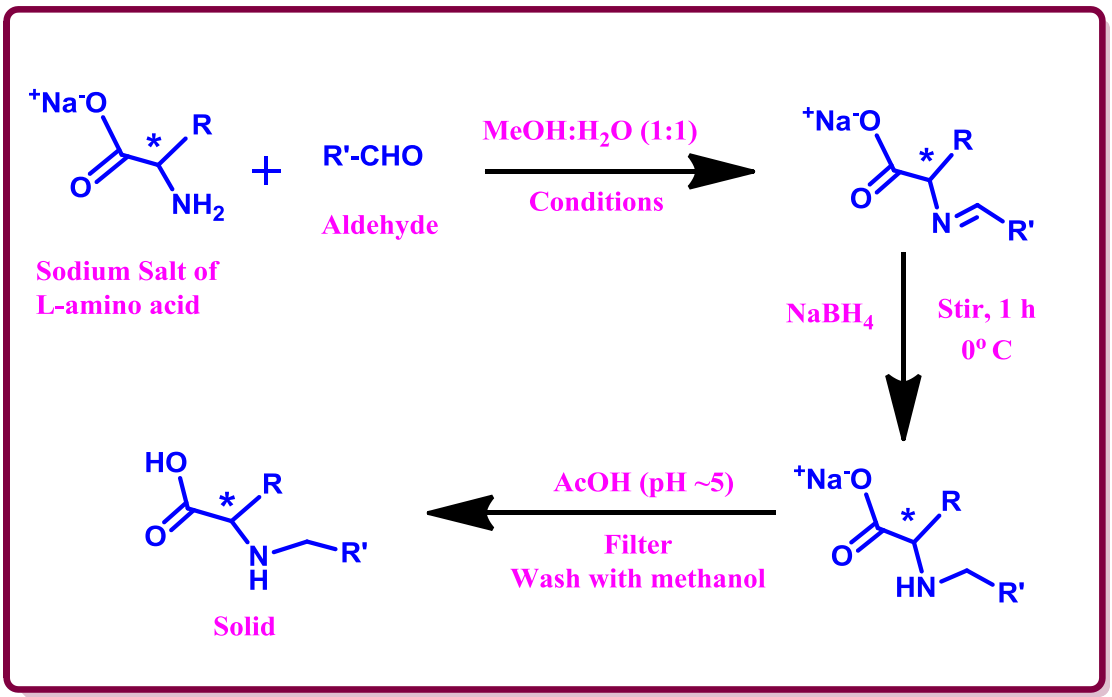

Scheme 3.1. General synthesis of amino acid based reduced Schiff base ligands.

For the second type of ligands, an additional fluorophore, like dansyl, is tagged to L-Tyrosine as shown in Scheme 3.2. In this case, the reaction between the disodium salt of L-Tyrosine and dansyl chloride via SN2 type substitution reaction leads to the formation of a didansylated tyrosine based ligand which on further reflux under basic condition ends up into a monodansylated product.

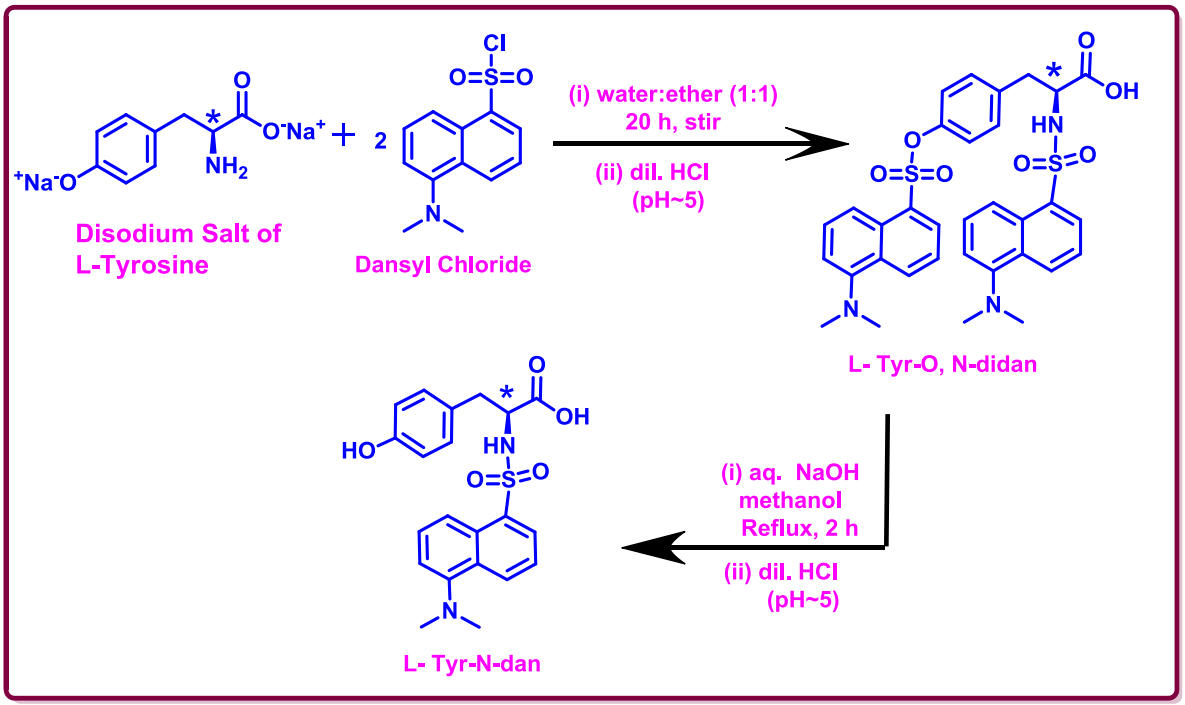

Scheme 3.2. General synthesis of ligands with additional tagged fluorophore.

3.2 STRUCTURAL DIVERSITY IN THE SELF-ASSEMBLED HOMOCHIRAL COORDINATION ARCHITECTURES

The coordination architectures were synthesized either via a two-component self-assembly reaction of divalent metal ions (Ni^{2+}, Cu^{2+}, Zn^{2+} and Cd^{2+}) and the respective mono or di potassium salt of the ligand in a 1:2 and 1:1 ratio or via a three component self-assembly reaction of a divalent metal ions (Ni^{2+} or Cu^{2+}), the respective mono- or dipotassium salt of the ligand and the linker in a 2:2:1 ratio. Unlike the bifunctional neutral linker, a dicarboxylate linker as the third component in the self-assembly reaction allows the ligand to be monoanionic instead of dianionic. This arises from the overall charge consideration of the coordination architectures as these are neutral in nature. The solvent for the reaction was chosen based on the solubility of the product and the by-product K_2SO_4/CH_3COOK.

3.2.1 Coordination architectures with amino acid based ligands

3.2.1.1 For a 1:2 metal to ligand ratio

3.2.1.1.1 *Coordination architectures containing homoligands*

Through the strategic design of monoanionic reduced Schiff base derivatives of amino acid based ligands, structural diversity in chiral coordination architectures under similar reaction conditions is demonstrated with the formation of either the CPs with a general formula $\{[MX_2]\cdot G\}_n$, where M^{2+} = Ni^{2+}, Cu^{2+}, Zn^{2+} and Cd^{2+}; X = L-HTyrbenz, L-HSerbenz or L-HTyrthio, or SCCs with a general formula $[MY_2(solvent)]\cdot G$, where Y = L-HTyr4-pyr, L-HSerthio, L-Phethio, L-HTyr4-NO_2, L-HTyr4-fluoro or HTyr4-methoxy, and solvent = water or methanol; in both the cases, G represents the lattice solvent molecules (water, methanol or DMSO). Clearly, the coordination of a water molecule to the metal center is controlled by the nature of substitution present in the ligand. Their formation is purely based on the coordination chemistry of a 1:2 metal to ligand complex.

Synthesis. The coordination architectures of the Cu^{2+} with various monoanionic ligands were synthesized via a two-component self-assembly reaction of $CuSO_4\cdot 5H_2O$ and the respective monopotassium salt of the ligand in a 1:2 ratio under ambient conditions. Except for **1**, all other compounds were obtained as precipitate on performing the reaction in water as unlike all other compounds, **1** was found to be moderately soluble in water. Hence, **1** was obtained from evaporating the filtrate where methanol serves as the solvent. The choice of the solvent depends on the differential solubility of the product and the by-product (K_2SO_4) in a particular solvent. Similar to the Cu^{2+}, other analogues of all these ten monoanionic ligands were synthesized via a two-component self-assembly reaction of respective metal salts ($NiSO_4\cdot 6H_2O$, $ZnSO_4\cdot 7H_2O$ or $Cd(OAc)_2\cdot 2H_2O$) along with the monopotassium salt of the ligand in a 1:2 ratio under ambient conditions (as shown in Schemes 3.3-3.5).

In most of the cases, water acts as a better reaction solvent whereas in few cases methanol serves as a better solvent depending on the solubility difference of the product and the by-product.

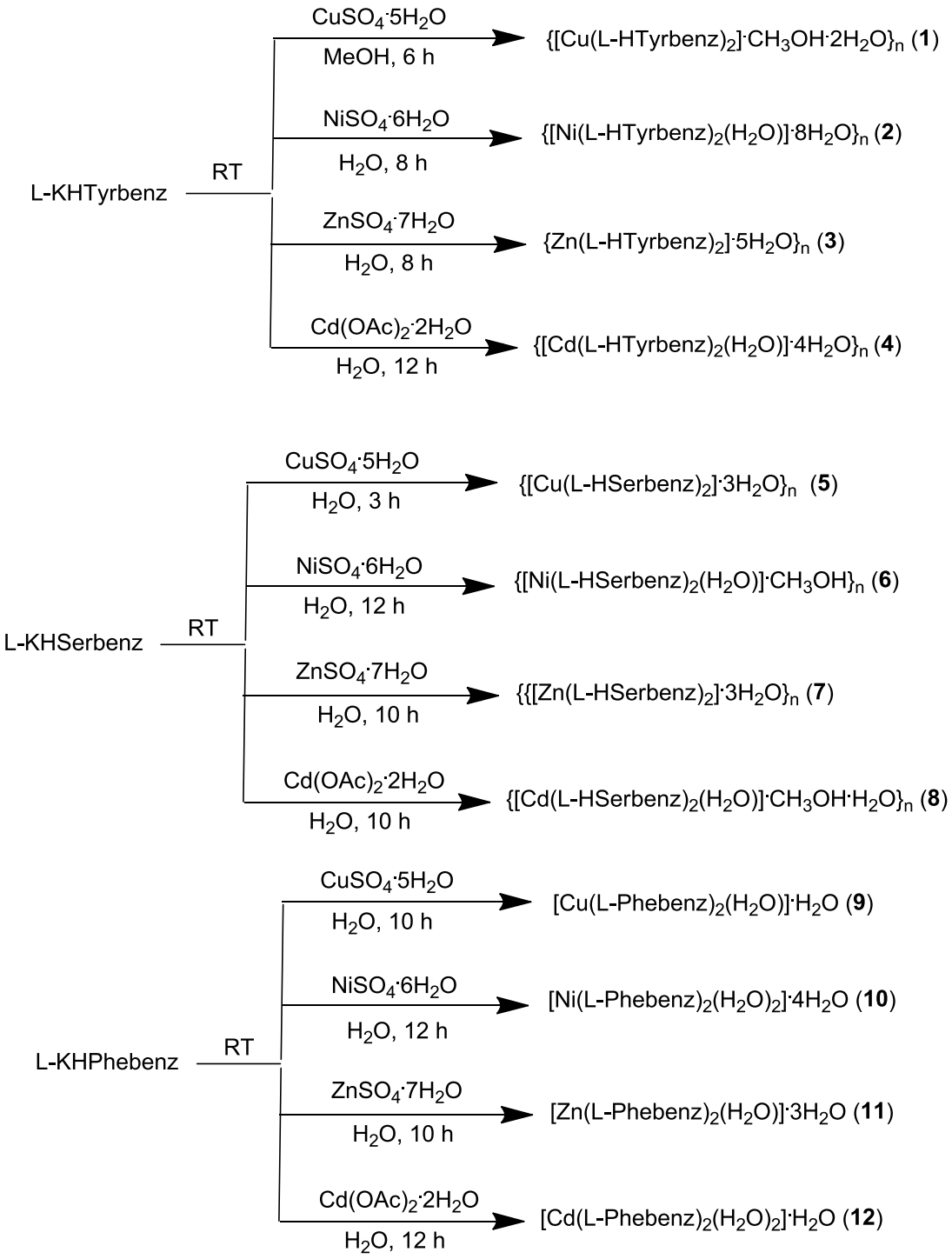

Scheme 3.3. Synthesis of **1-12**.

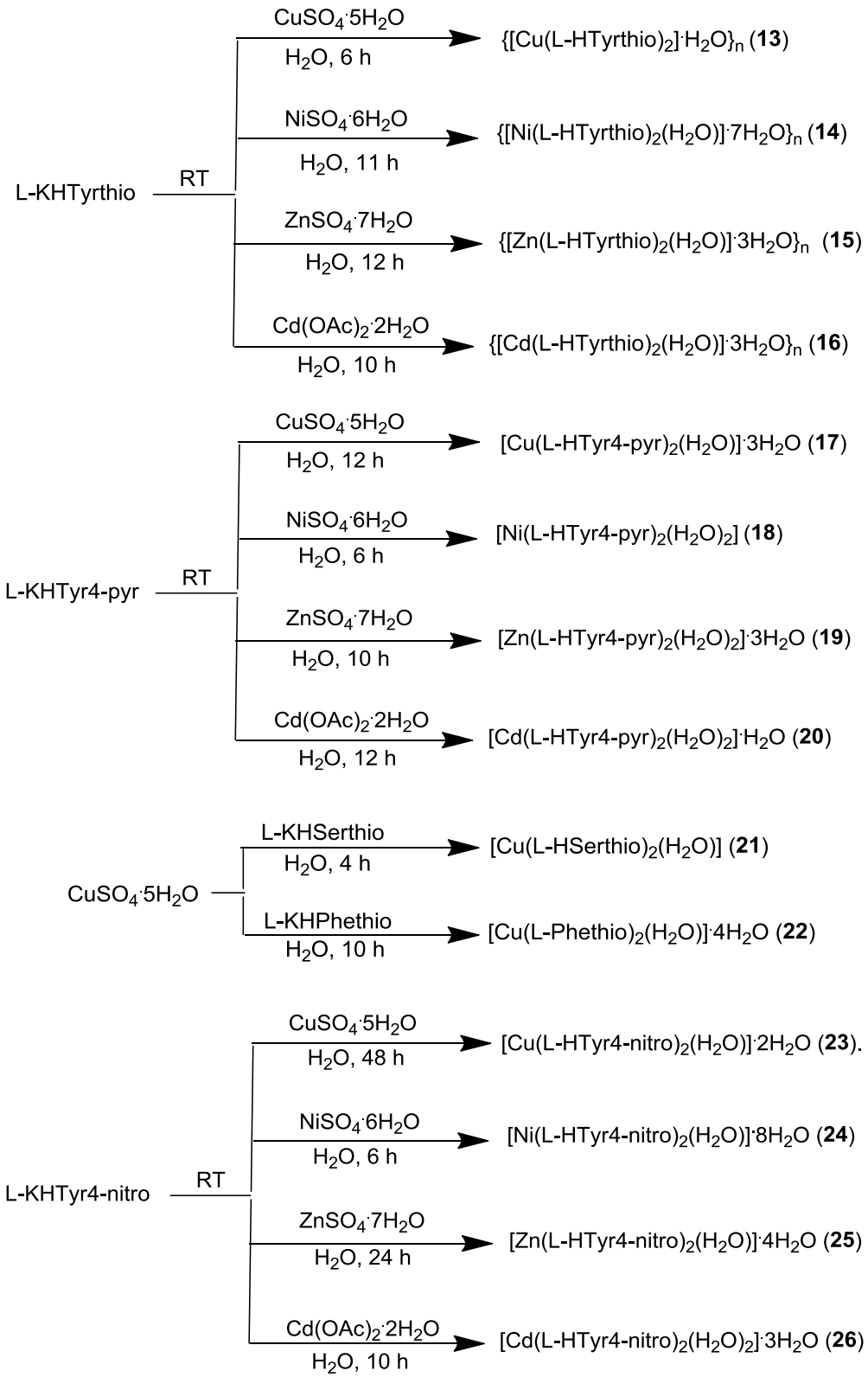

Scheme 3.4. Synthesis of **13-26**

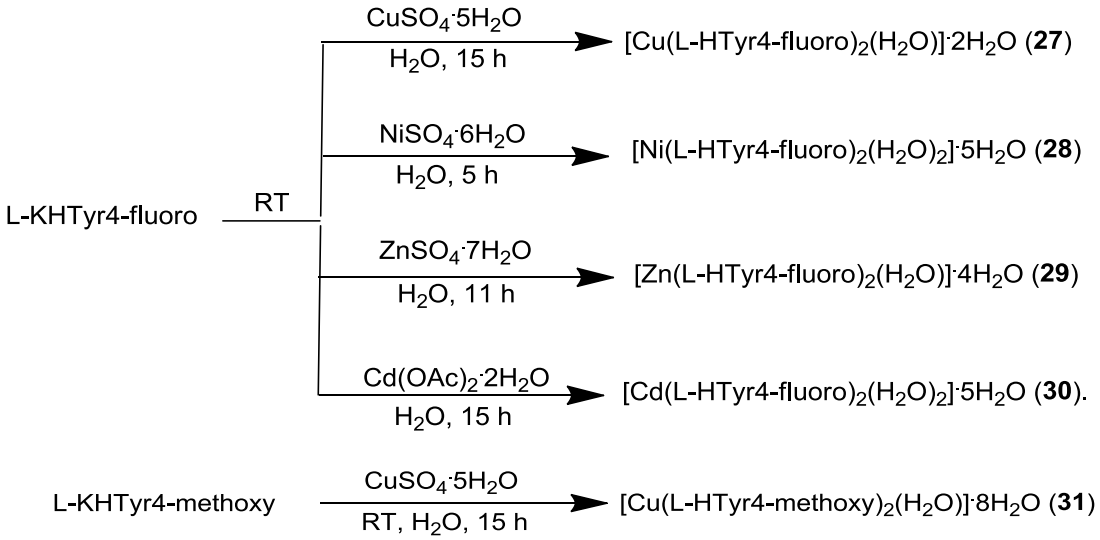

Scheme 3.5. Synthesis of **27-31**.

FT-IR spectroscopy. The IR spectra of these coordination architectures were recorded in solid state using KBr pellets. Various functional groups and their modes of binding to the divalent metal ions (Cu^{2+}, Ni^{2+}, Zn^{2+} and/or Cd^{2+}) in the coordination architectures can be well deduced from the FTIR stretching frequencies. In these coordination architectures, the binding mode of the carboxylates plays a very important role. The type of binding of carboxylates in the architectures can be well predicted from the $\Delta\nu$ value (difference between the asymmetric and symmetric stretching frequencies) of the carboxylates. The $\Delta\nu$ value above 250 cm^{-1} clearly indicates monodentate binding whereas a value of ~200 cm^{-1} suggests a bridging mode of carboxylate. A bridging carboxylate will serve the purpose of polymerization, hence forming a coordination polymer. This coordination polymer can also be achieved through the phenolic bridging by the phenolic side chain of L-Tyrosine. In that case the $\nu_{O\text{-}H}$ shows a lower value compared to that of the free ligand. However, if both these functionalities (carboxylate or phenolic -OH) are unable to achieve a bridging mode of binding then the coordination environment is satisfied by a coordinating water and thus giving rise to a supramolecular coordination complex (as shown in Scheme 3.6)

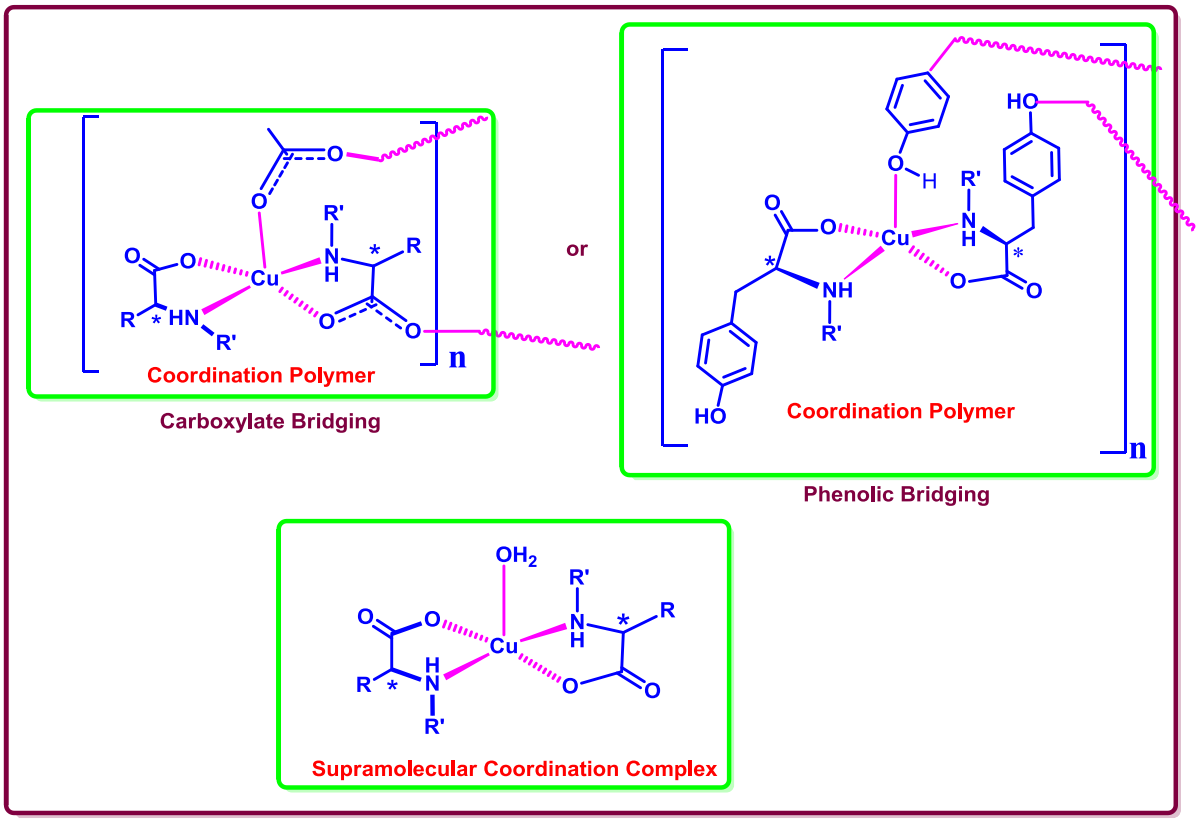

Scheme 3.6. Schematic reperesention of formation of coordination polymers and supramolecular coordination complexes of Cu^{2+} and monoanionc amino acid based reduced Schiff bases.

The bridging carboxylate (**1-8**) helps in generating a coordination polymer. In all other cases, the carboxylate stretching frequencies confirm a monodentate binding mode of carboxylate (as shown in Table 3.1). In the FT-IR spectra of **1-40**, the broad peak in the range of 3300-3400 cm^{-1} is due to the lattice water molecules. The peak at ~3250 cm^{-1} in tyrosine derived coordination architectures (**1-4**, **13-20** and **23-31**) are due to phenolic –OH of the respective ligands. The sharp peak observed at 3283-3300 cm^{-1} in various coordination architectures is due to the coordinated water molecule in the complex. The hydroxyl peak of the $–CH_2OH$ of serine based ligands in the coordination architecture (**5-8** and **21**) appears at 3100-3200 cm^{-1}. The peaks in the range of 2930-2950 cm^{-1} are for the N-H of amine part of the complexes.

Table 3.1. Carboxylate Stretching frequencies in FTIR spectra of **1**-**31**.

Compound	Carboxylate Peaks (cm^{-1})		$\Delta\upsilon_1$ (cm^{-1})	$\Delta\upsilon_2$ (cm^{-1})	Binding Mode
	asym	sym			
1	1633 1590	1359 1381	274	209	monodentate bridging
2	1628 1590	1334 1398	294	192	monodentate bridging
3	1625 1590	1337 1397	288	193	monodentate bridging
4	1611 1582	1335 1392	276	190	monodentate bridging
5	1635 1583	1350 1380	285	203	monodentate bridging
6	1606 1590	1352 1396	254	194	monodentate bridging
7	1633 1576	1325 1382	308	194	monodentate bridging
8	1628 1579	1325 1380	303	199	monodentate bridging
9	1627	1344	283	---	monodentate
10	1590	1335	255	---	monodentate
11	1617	1342	275	---	monodentate
12	1596	1327	269	---	monodentate
13	1639	1376	263	---	monodentate
14	1630	1334	296	---	monodentate
15	1625	1332	272	---	monodentate
16	1632	1350	274	---	monodentate
17	1644	1379	265	---	monodentate
18	1601	1351	251	---	monodentate
19	1604	1328	276	---	monodentate
20	1609	1320	289	---	monodentate
21	1629	1348	281	---	monodentate
22	1625	1358	267	---	monodentate
23	1627	1347	280	---	monodentate
24	1600	1348	252	---	monodentate
25	1611	1347	264	---	monodentate
26	1603	1347	256	---	monodentate
27	1643	1370	273	---	monodentate
28	1632	1329	303	---	monodentate
29	1633	1330	303	---	monodentate
30	1600	1331	269	---	monodentate
31	1625	1349	280	---	monodentate

The stretching frequency for the C-O is observed at 1250 cm^{-1}. The peaks at ~1200 cm^{-1} and ~700 cm^{-1} in the coordination architectures (**13-16** and 2**1-22**) are due to C=S and C-S present in the thiophene ring of the ligands (H_2Tyrthio, H_2Serthio and HPhethio).[237]

Thermogravimetric analyses. Thermal stabilities of these coordination architectures were studied as a function of temperature in the range of 25-500 ˚C (see Figures 3.1-3.8). The CPs show thermal stabilities up to 200 ˚C with an initial loss of the lattice solvent molecules at around 100 ˚C. Each of SCC shows loss of both lattice as well as coordinated solvent molecules at around 150 ˚C.

For **1**, it is a three-step weight loss profile. The first weight loss of 4.96% between 50-120 ˚C corresponds to loss of two lattice water molecule (ca. 5.2%). The second step showing weight loss of 15.4% between 120-220 ˚C indicates loss of three lattice water molecules along with loss of a CO_2 molecule from the ligand (ca. 14.9%). The third step showing weight loss of 50.1% between 220-400 ˚C indicates loss of the rest of the Cu-ligand complex (ca. 51.9%). Compared to **1**, the complexes **2**, **3** and **4** shows a two-step weight loss process (as shown in Figure 3.1).

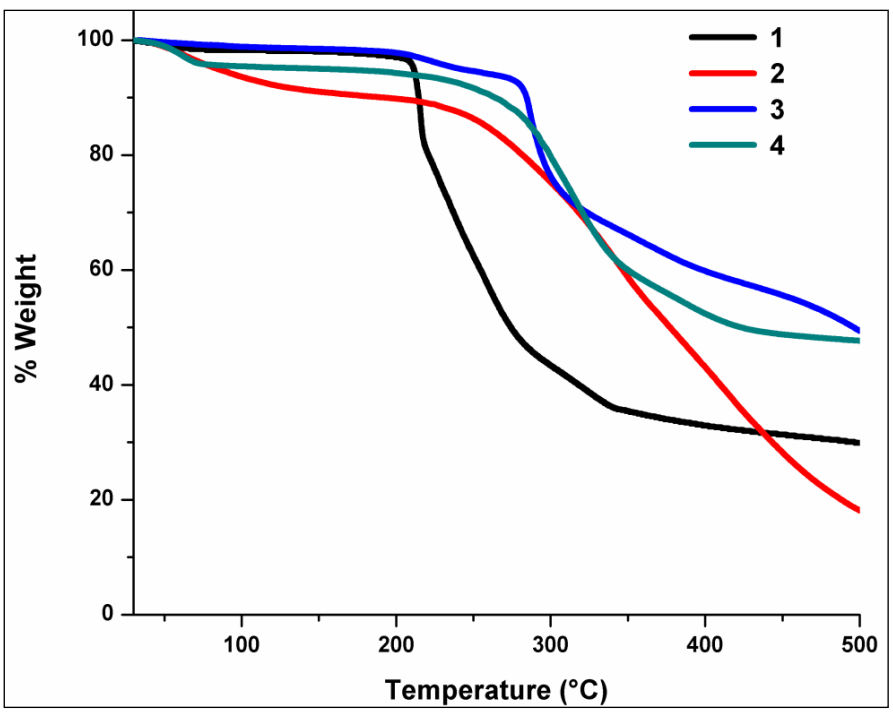

Figure 3.1. TGA scans for **1-4.**

For **1**, the loss of first two pair of uncoordinated water takes place before 150 ˚C, whereas for other analogues the first set of lattice solvents come out gradually upto 250 ˚C depicting higher thermal stabilities of these analogues over its Cu^{2+} analogue. The detailed TGA data for complexes **1-4** are summarized in Table 3.2.For **5**, it is a two-step weight loss profile. The first weight loss of 10.2% between 50-100 ˚C corresponds to loss of three lattice water molecule (ca. 10.7%). The second step showing weight loss of 64.7% between 200-400 ˚C indicates loss of the ligand (ca. 69.4%). The Ni, Zn and Cd analogues of H_2Serbenz ligand lose the first set of lattice solvent within 100 ˚C very similar to the **5**. The thermal profile of **5** and **8** are similar while after the loss of uncoordinated water molecules, **7** is stable upto 250 ˚C. Thus complex **7** is more stable than **5** and **8** while the coordination architecture of Ni^{2+} of H_2Serbenz shows a continuous loss of the components throughout (as shown in Figure 3.2). The detailed TGA data for complexes **5-8** are summarized in Table 3.2.

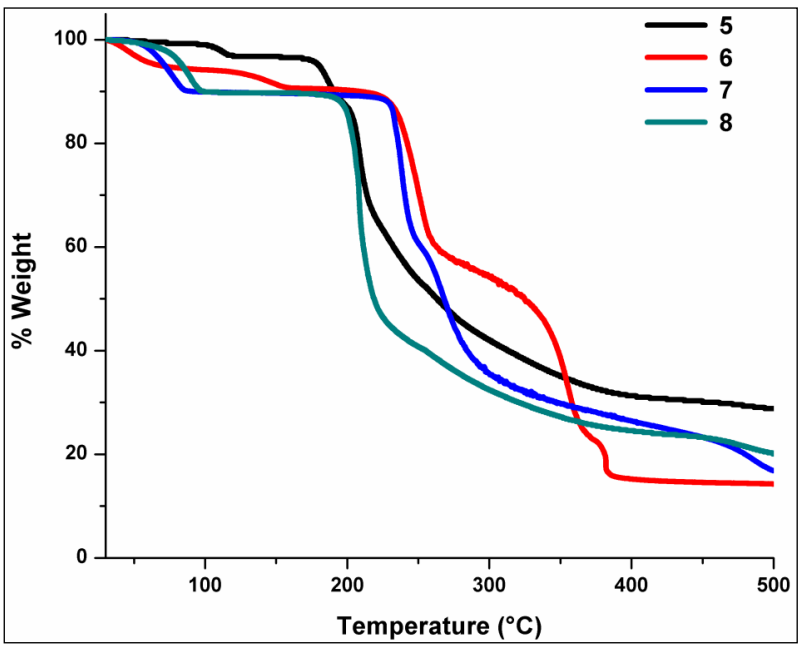

Figure 3.2. TGA scans for **5-8.**

For **9**, it is a two-step weight loss profile. The first weight loss of 3.1% between 50-140 ˚C corresponds to loss of one uncoordinated water molecule (ca. 2.97%). The second step showing weight loss of 63.04% between 200-400 ˚C indicates loss of one coordinated water, one ligand and the benzaldehyde moiety of the other ligand (ca. 62.9%). Complexes **10**, **11** and **12** shows higher stability than the complex **9**, after the intial loss of the lattice solvent at

Table 3.2. TGA data for **1-8**. u-uncoordinated, c-coordinated.

Comp	1st step loss			2nd Step loss			3rd Step loss		
	Obsd. %	Calcd. %	Loss	Obsd. %	Calcd. %	Loss	Obsd. %	Calcd. %	Loss
1	4.96	4.76	CH_3OH (u)	15.40	12.50	2 H_2O (u), CO_2	50.1	51.9	Metal-ligand complex
2	8.66	9.45	4 H_2O (u)	68.95	68.43	4 H_2O (u), H_2O (c), Metal-ligand comp.	-----	-----	------
3	2.02	2.31	H_2O (u)	47.01	48.37	4 H_2O (u), Metal-ligand complex	-----	-----	------
4	4.26	4.85	2 H_2O (u)	45.71	45.04	2 H_2O (u), H_2O (c), Metal-ligand comp.	-----	-----	------
5	10.20	10.67	3 H_2O (u)	64.7	69.4	Metal-ligand comp.	-----	-----	------
6	5.08	6.43	CH_3OH (u)	3.18	3.87	H_2O (c)	71.77	76.22	Metal-ligand complex
7	9.90	10.63	3 H_2O (u)	59.46	60.75	Metal-ligand comp.	-----	-----	------
8	8.23	8.79	CH_3OH (u), H_2O (u)	3.90	3.47	H_2O (c)	66.02	64.48	Metal-ligand complex

around 120 ˚C in each case. The loss of left over solvent and the coordination architecture takes place only ~300 ˚C while the same happens at ~200˚C for Cu^{2+} analogue of the HPhebenz ligand (as shown in Figure 3.3). For **13**, it is a three-step weight loss profile. The first weight loss of 4.22 % between 50-170 ˚C corresponds to loss of two lattice water molecules (ca. 4.2%). The second step showing weight loss of 12.9% between 160-230 ˚C indicates loss of a thiophene molecule (ca. 13.4%). The third step showing weight loss of 39.1% between 230-400 ˚C indicates loss of left over ligand (ca. 36.4%). The thermal profiles for other analogues of H_2Tyrthio show similar thermal behavior. In all these three cases there is a continuous loss of the lattice and coordinated solvents (as shown in Figure 3.4). Similar to above mentioned architectutres for different ligands the Cu^{2+} in this case also shows less stability compared to the other analogues of the same ligand. The detailed TGA data for complexes **9-16** are summarized in Table 3.3.For **17**, it is a three-step weight loss profile. The first weight loss of 8.03% between 50-110 ˚C corresponds to loss of three uncoordinated water molecules (ca. 7.98%). The second step showing weight loss of 3.45% between 110-200 ˚C indicates loss of one coordinated water molecule (ca. 2.88%). The third step showing weight loss of 46.2% between 200-330 ˚C indicates loss of one H_2Tyr4-pyr ligand and a copper atom (ca. 44.8%). Compared with the Cu, Ni and Zn analogue of H_2Tyr4-pyr, Cd complex (**20**) shows much more stability as shown in Figure 3.5. The detailed TGA data for complexes **17-20** are summarized in Table 3.4.

Apart from the role of various metal ions in the coordination architecture, the role of amino acid in thermal stability can be seen by comparing the Cu^{2+} complexes of thiophene derivative of various amino acids. Compound **21**, the Cu^{2+} complexes of H_2Serthio ligands shows one-step weight loss TGA profile confirming its high stability till 200˚C. The weight loss of 69.82% between 202-304 ˚C corresponds to loss of the coordinated water molecule and the ligand (ca. 67.1%). The comparison of **21** with the thermal stability of Cu^{2+} complex of HPhethio, **22** was also studied. For **22,** it is a three step weight loss profile. The first weight loss of 3.44% between 50-150 ˚C corresponds to loss of one lattice water molecule (ca. 2.87%). The second step showing weight loss of 6.97% between 150-190 ˚C indicates loss of two more lattice water molecules along with a coordinated water molecule (ca. 8.6%). The third step showing weight loss of 59.7% between 200-400 ˚C indicates further

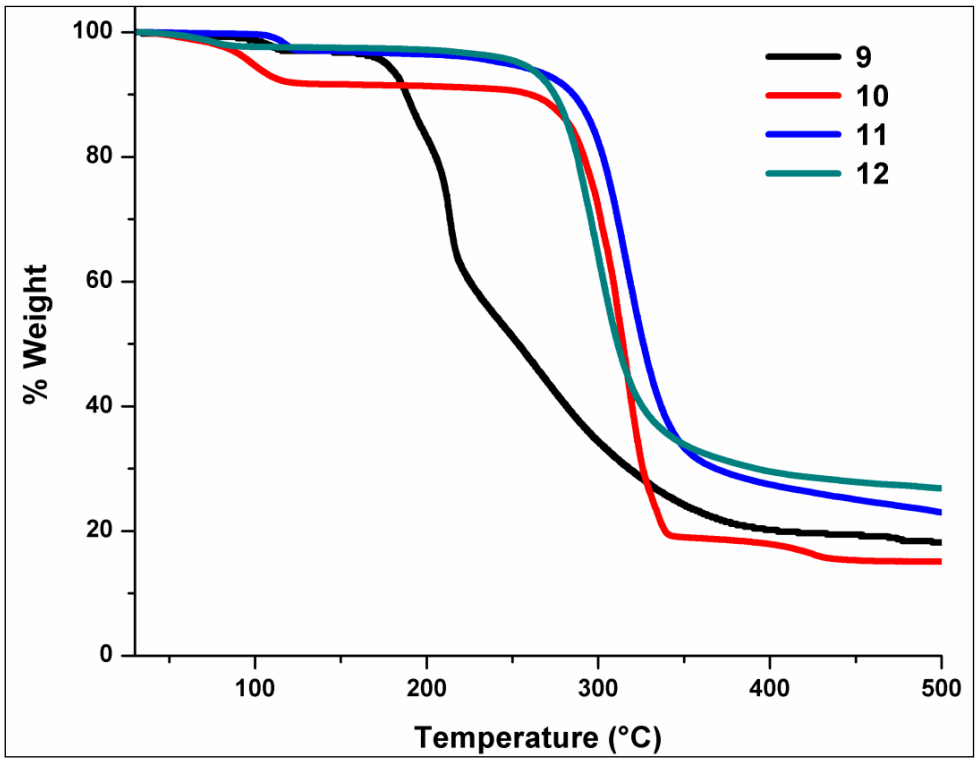

Figure 3.3. TGA spectra for **9-12.**

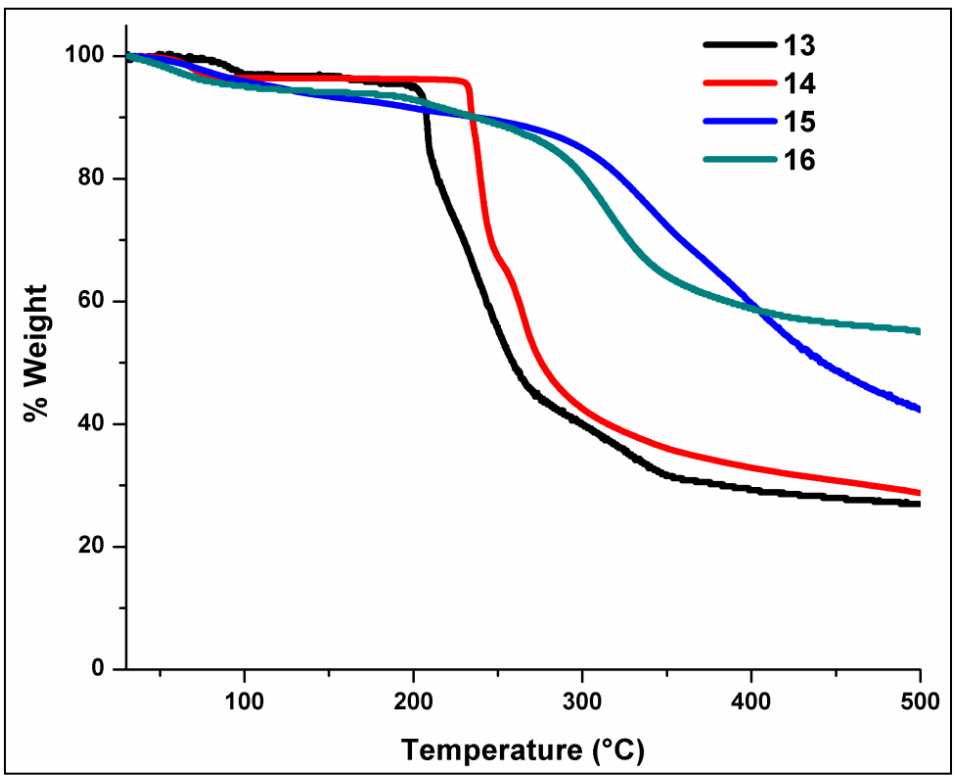

Figure 3.4. TGA scans for **13-16.**

degradation of the compound (ca. 60.20%). The complex **21** shows higher thermal stability than the **22** (as shown in Figure 3.6). In **13** and **22**, presence of the lattice solvent molecules accounts for the intial loss of the coordination architecture whereas the absence of any such lattice solvent in **21** further agrees with the fact of no intial loss of the architecture in the TGA profile of **21**. The detailed TGA data for **21-22** are summarized in Table 3.4.

Table 3.3. TGA data for **9-16**. u-uncoordinated, c-coordinated.

Compound	1st step loss			2nd Step loss			3rd Step loss		
	Obsd %	Calcd. %	Loss	Obsd. %	Calcd. %	Loss	Obsd. %	Calcd. %	Loss
9	3.1	2.96	H_2O (u)	63.04	62.90	H_2O (c), Metal-ligand complex	-----	-----	------
10	8.05	8.01	3 H_2O (u)	71.6	72.9	H_2O (u), 2 H_2O (c), Metal-ligand complex	-----	-----	------
11	2.62	2.79	H_2O (u)	70.17	71.77	2 H_2O (u), H_2O (c), Metal-ligand complex	-----	-----	------
12	2.07	2.67	H_2O (u)	68.63	69.90	2 H_2O (c), Metal-ligand complex	-----	-----	------
13	4.22	4.20	2 H_2O (u)	12.90	13.40	Thiophene molecule	39.10	39.40	Metal-ligand complex
14	12.01	11.90	5 H_2O (u)	8.75	8.11	2 H_2O (u), H_2O (c)	44.10	43.44	Metal ligand comp.
15	7.03	7.82	3 H_2O (u)	48.44	47.15	H_2O (c), Metal Ligand complex	-----	-----	------
16	7.12	7.32	3 H_2O (u)	3.28	2.63	H_2O (c),	49.10	48.78	Metal Ligand

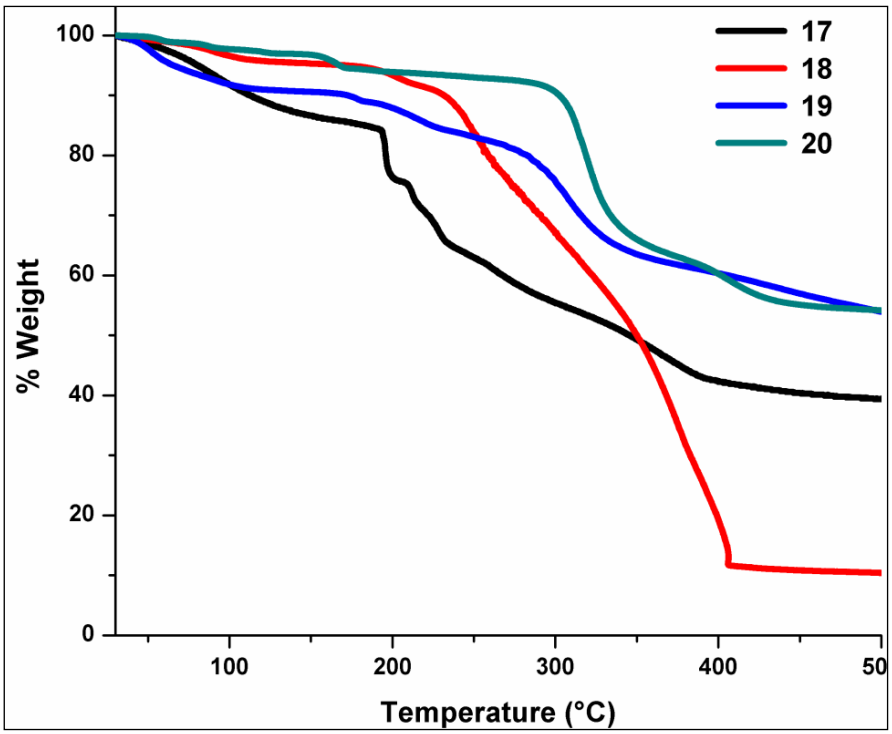

Figure 3.5. TGA scans for **17**-**20**.

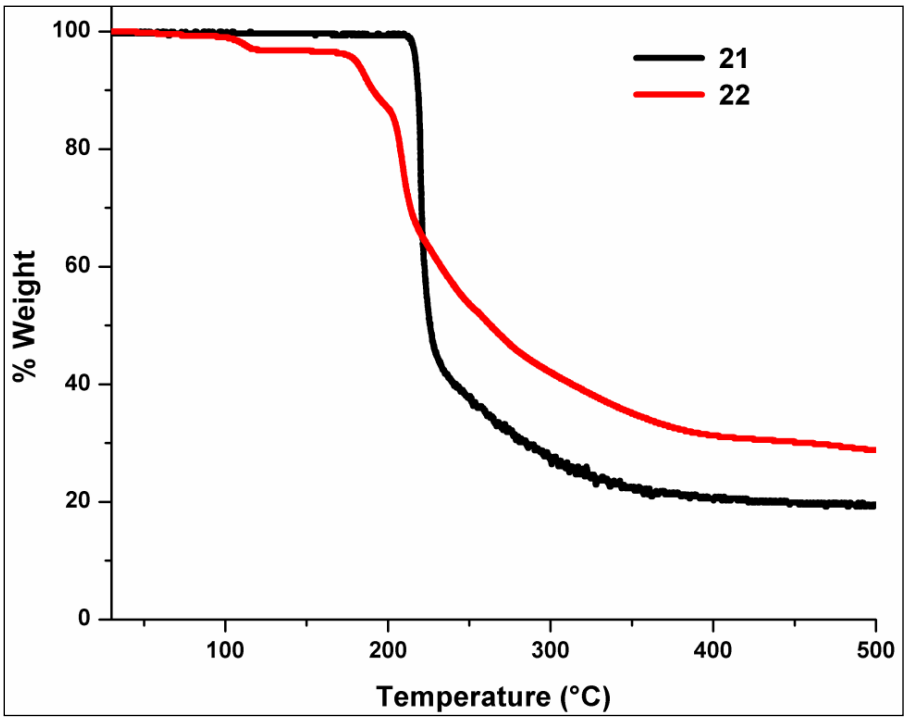

Figure 3.6. TGA scans for **21**-**22**.

Table 3.4. TGA data for **17-22**. u-uncoordinated, c-coordinated

Comp.	1st step loss			2nd Step loss			3rd Step loss		
	Obsd %	Calcd. %	Loss	Obsd %	Calcd. %	Loss	Obsd. %	Calcd. %	Loss
17	8.03	7.98	3 H_2O (u)	3.45	2.88	H_2O (c)	46.20	44.80	Metal-ligand complex
18	4.18	5.64	2 H_2O (c),	83.13	82.52	Metal-ligand complex	-----	------	------
19	8.60	7.74	3 H_2O (u)	6.80	5.59	2 H_2O (c)	23.7	21.74	Metal-ligand complex
20	3.04	2.53	H_2O (u)	5.67	5.21	2 H_2O (c)	37.80	35.86	Metal-ligand complex
21	69.82	67.10	H_2O (c) Metal-ligand complex	-----	------	------	-----	------	------
22	3.44	2.87	H_2O (u)	6.97	8.60	3 H_2O (u), H_2O (c)	59.70	60.20	Metal-ligand complex

To have a deeper introspect into the thermal stabilities of these coordination architectures, further substitutions of other functionalities on the benzene ring from the aldehyde part is also scrutinized. The Cu^{2+} complex of H_2Tyr4-nitro, **23** shows a three-step weight loss profile. The first weight loss of 2.5% between 50-130 ˚C corresponds to loss of an uncoordinated water molecule (ca. 2.40%). The second step showing weight loss of 2.9% between 130-180 ˚C indicates loss of another uncoordinated water molecule (ca. 2.46%). The third step showing weight loss of 31.8% between 180-400 ˚C indicates loss of the coordinated water molecule along with a nitro benzyl moiety and a copper atom (ca. 30.4%). The TGA profiles for the Ni and Cd analogues of H_2Tyr4-nitro (**24** and **26**) shows similar behavior while Ni

analogue, **25** shows different thermal pattern from **24** and **26**. Unlike **25**, **24** and **26** lose all the uncoordinated lattice solvents in very first step even before 150 °C (as shown Figure 3.7). The thermal profiles for complexes **23-26** are compiled in Table 3.5.

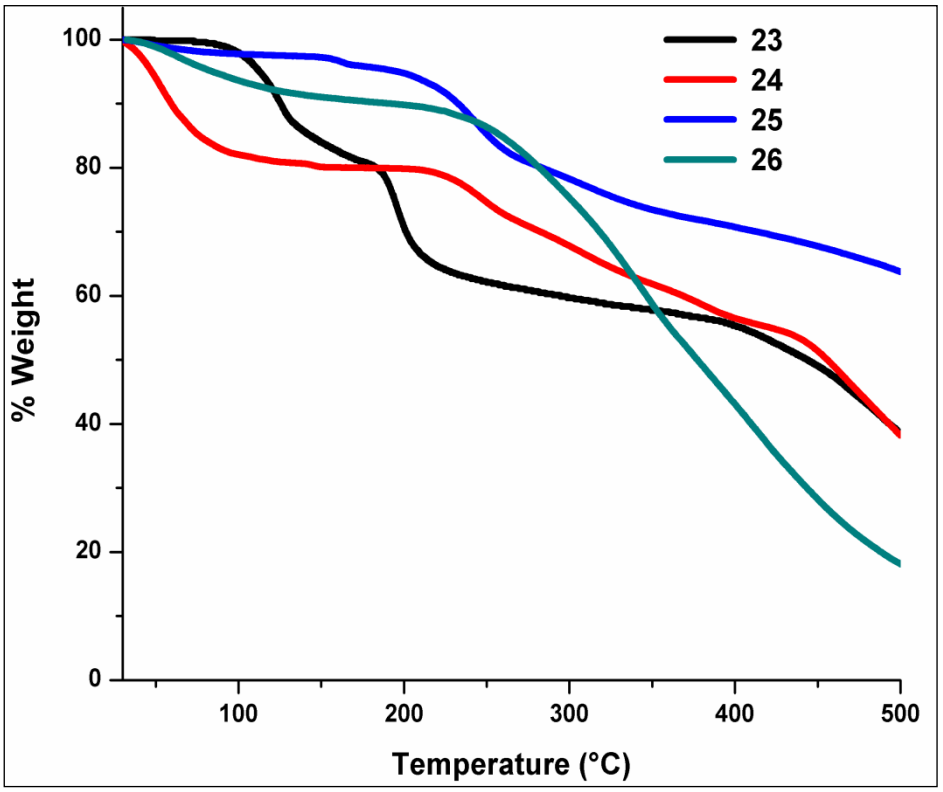

Figure 3.7. TGA scans for **23-26.**

Within the same context, various metal analogues of two other derivatised ligands (H_2Tyr4-fluoro and H_2tyr4-methoxy) are also studied for their thermo-chemical behavior. For Cu analogue of H_2Tyr4-fluoro, **27** it is a three-step weight loss profile. The first weight loss of 2.40% between 50-140 ˚C corresponds to loss of one uncoordinated water molecules (ca. 1.90%). The second step showing weight loss of 13.9% between 140-220 ˚C indicates loss of one uncoordinated water molecules, one coordinated water molecule, a carbon dioxide molecule and a dinitrogen molecule from the ligand (ca. 14.8%). The third step showing weight loss of 42.8% between 220-300 ˚C indicates loss of a left over tyrosine molecule, a fluorine molecule and a copper atom (ca. 46.0%). However for the Cu analogue of H_2Tyr4-methoxy **31** it is a three-step weight loss profile. First weight loss of 5.02% between 50-150 ˚C corresponds to loss of three molecules of uncoordinated water (ca. 6.53%). The second

step showing weight loss of 2.33% between 150-200 ˚C indicates loss of one uncoordinated water molecule (ca. 2.34%). The third step showing weight loss of 46.24% between 200-400 ˚C indicates loss of four uncoordinated and a coordinated water and some parts of metal-ligand complex (ca. 48.95%) (as shown in Figure 3.8). The detailed TGA data for complexes **27-31** are summarized in Table 3.5.

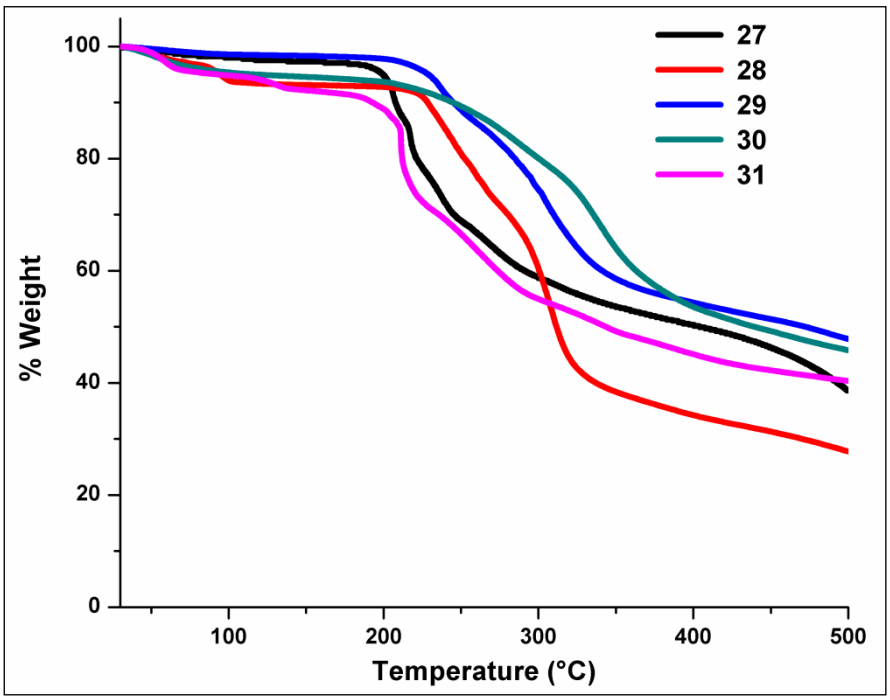

Figure 3.8. TGA scans for **27-31**.

Single Crystal Structure Analysis. To get a better insight into the coordination architecture at a molecular level, few of the metal analogues of these ligands esp. Cu^{2+} analogues are studied using single crystal diffraction studies. Crystals of {[Cu(L-HTyrbenz)$_2$]·CH_3OH·H_2O}$_n$ (**1**), {[Cu(L-HSerbenz)$_2$]·$3H_2O$}$_n$ (**5**), [Cu(Phebenz)$_2$(H_2O)]·$0.5H_2O$ (**9**), {[Cu(L-HTyrthio)$_2$]·H_2O}$_n$ (**13**), [Cu(L-HTyr4-pyr)$_2$(H_2O)]·$2H_2O$ (**17**) and [Cu(L-HSerthio)$_2$(H_2O)] (**21**) suitable for the single crystal X-ray study were grown from the slow evaporation of the respective methanolic solution: **1** in 10 days, **5** in 7 days, **9** in 10 days, **13** in 5 days, **17** in 7 days and **21** in 3 days. Despite numerous attempts, crystals of **22** suitable for data collection could not be obtained; however, a comparison of its spectroscopic data (UV-vis, CD and FTIR) with those of **13** and **21**

indicates their structural similarities (*vide infra*). Crystals of $[Cu(HTyr\text{-}4\text{-}nitro)_2(H_2O)]\cdot 2H_2O$ (**23**) were grown in both solvents (dimethylsulfoxide and methanol) to determine the single crystal structures of $[Cu(HTyr\text{-}4\text{-}nitro)_2(H_2O)]\cdot 2(CH_3)_2SO$ (**23a**) and $[Cu(HTyr\text{-}4\text{-}nitro)_2(H_2O)]\cdot 2CH_3OH$ (**23b**).

Table 3.5. TGA data for **23-31**. u-uncoordinated, c-coordinated.

Compound	1st step loss			2nd Step loss			3rd Step loss		
	Obs. %	Cal. %	Loss	Obs. %	Calc. %	Loss	Obs. %	Cal. %	Loss
23	2.90	2.50	H_2O (u)	2.90	2.46	H_2O (u)	31.80	30.40	H_2O (c), Metal-ligand complex
24	18.11	16.94	8 H_2O (u)	17.06	16.97	H_2O (c), N_2, CO_2	23.44	23.07	Metal-ligand complex
25	3.87	3.43	1.5 H_2O (u)	22.25	23.61	2.5H_2O (u), H_2O (c)	8.19	7.59	Metal-ligand complex
26	6.12	6.40	3 H_2O (u)	19.62	19.50	2 H_2O (c), 2 CO_2, N_2	24.72	23.44	Metal-ligand complex
27	2.40	1.90	H_2O (u)	13.9	14.80	H_2O (u), H_2O (c), CO_2, N_2	42.80	46.0	Metal-ligand complex
28	5.91	7.10	3 H_2O (u)	20.75	22.66	2 H_2O (u), H_2O (c), CO_2	32.86	32.33	Metal-ligand complex
29	1.23	1.22	0.5 H_2O (u)	43.59	45.56	3.5 H_2O (u), H_2O (u), Metal-ligand complex	-----	------	--------
30	4.54	5.17	2 H_2O (u)	43.94	42.79	H_2O (c), Metal-ligand Complex	-----	------	--------
31	5.02	6.53	3 H_2O (u)	2.33	2.34	H_2O (u)	46.24	48.95	4 H_2O (u), H_2O (c), Metal-ligand complex

Crystals suitable for single crystal X-ray study were grown from the slow evaporation of either its dimethylsulfoxide (DMSO) solution after 15 days (**23a**) or its methanolic solution within 7 days (**23b)**. Crystals of $[Cu(HTyrfluoro)_2(H_2O)]\cdot H_2O$ (**27**) and [Cu(HTyr4-methoxy)$_2$(CH_3OH)] (**31**) suitable for the single crystal X-ray study were grown from the slow evaporation of the respective methanolic solution: **27** in 12 days and **31** in 7 days.

Crystal structures of $\{[Cu(L\text{-}HTyrbenz)_2]\cdot CH_3OH\cdot H_2O\}_n$ (1) and $\{[Cu(L\text{-}HSerbenz)_2]\cdot 3H_2O\}_n$ (5). Compound **1** and **5** crystallize in the chiral monoclinic space group $P2_1$ and orthorhombic space group $P2_12_12_1$, respectively. The asymmetric unit of **1** and **5** consists of one Cu^{2+} center surrounded by two ligands (HTyrbenz and HSerbenz, respectively) and two lattice solvents (one methanol molecule and one water molecule) and three water molecules, respectively. Both are carboxylato-bridged 1D coordination polymers but the difference in geometry around the Cu^{2+} center arises from the substitution in the ligand. As shown in Figure 3.9a, the Cu^{2+} center in **1** has a distorted square pyramidal geometry with a coordination environment of O_3N_2 type - out of the four equatorial sites, two are occupied by the nitrogen atoms (N1 and N2) of the amine groups whereas the other two are occupied by the oxygen atoms (O3 and O5) of the carboxylates of two ligands, and the apical site is occupied by the oxygen atom (O4) of the carboxylate of the ligand bound to the adjacent metal center. The carboxylate group of one ligand binds in a monodentate fashion (with oxygen atom O3) while the carboxylate group of the second ligand (with oxygen atoms O4 and O5) bridges in a syn-anti fashion between two Cu^{2+} centers forming the 1D coordination polymer chain (see Figure 3.10 top). On the other hand, the Cu^{2+} center in **5** (see Figure 3.9b) has a distorted octahedral geometry having the sixth position occupied by the hydroxymethyl group of one of the ligands (Cu^{2+}-OH bond length: 2.723(1) Å).

Unlike **1**, the bridging carboxylate group of the ligand in **5** that forms the 1D coordination polymer chains (as shown in Figure 3.10 bottom) is in an anti-anti binding mode between two Cu^{2+} centers. This clearly indicates that the presence of a –OH group in side chain invokes the carboxylate to do the bridging. Examples of carboxylate bridging by tyrosine or tyrosine based ligands to form 1D CPs are limited in the literature: $\{Co(L\text{-tyrosine})\}_n$,[238] $\{Zn(L\text{-tyrosine})\}_n$,[238] $[Cu(tyrosine)_2]_n$,[239] $\{[Zn(tyrosine)_2(H_2O)](H_2O)\}_n$,[239] and

{[Cu_2(HTyrsal)$_2$(H_2O)](H_2O)}$_n$[167] (where H_2Tyrsal = N-(2-hydroxybenzyl)-tyrosine); unlike the first four complexes where the carboxylate group bridges between the Cu^{2+} or Zn^{2+} centers, respectively, the last one with the tyrosine based Schiff base ligand the carboxylate group bridges the bis(phenoxo)dicopper units in the polymeric structure. In **1**, the Cu-N_{amine} bond distances are 2.015(3) Å and 2.022(3) Å, comparable to 2.022(3) Å reported for [Cu(Ph-Tyr)(phen)(ClO_4)];[30] however, the Cu-$O_{(monodentate\ carboxylate)}$ distance in [Cu(Ph-Tyr)(phen)(ClO_4)], 1.958(3) Å, is comparable to one of the Cu-$O_{(bridged\ carboxylate)}$ distances of 1.957(3) Å in **1** but is slightly longer than the Cu-$O_{(monodentate\ carboxylate)}$ bond of 1.931(3) Å in **1**. For **1**, the bond angle $O_{(carboxylate)}$-Cu-$N_{(amine)}$ for each ligand is 82.68(14)˚ and 84.76(16)˚,

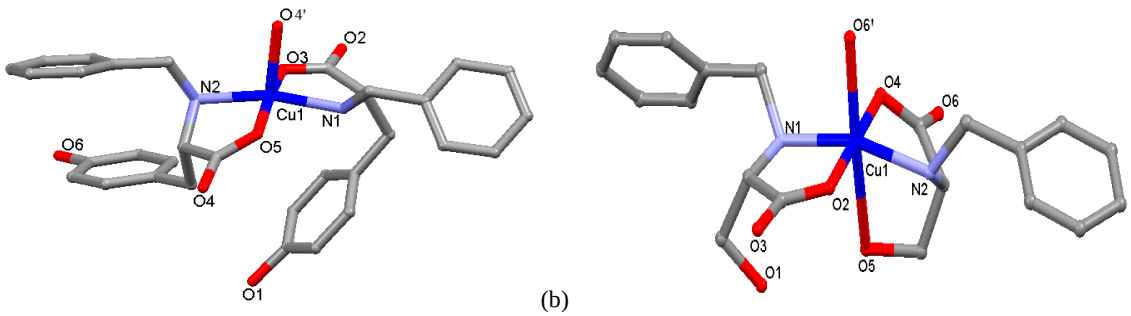

(a) (b)

Figure 3.9. Coordination environment around Cu^{2+} in (a) **1** and (b) **5**.

which are similar to that of 83.25(9)˚ in [Cu(Ph-Tyr)(phen)(ClO_4)]. The selected bond distances and bond angles for **1** and **5** are listed in Tables A6 and A9, respectively. Moreover the involvement of the phenolic group in the ligands for the hydrogen bonding network is very different in these complexes compared to **1**. The 1D CP chains in **1** are involved in extensive intermolecular hydrogen bonding with the lattice water and methanol molecules giving rise to a 2D supramolecular array. Out of the two phenolic groups (O1 and O6) of the HTyrbenz ligands in **1**, one (O6) is involved in connecting the 1D chains to generate the 2D network.

In this hydrogen bonding network, there are two sets: (a) between the oxygen atom (O7) of the lattice methanol molecule and –OH (O1) of the phenol group (O---O distance: 2.672(6) Å) and the uncoordinated oxygen atom (O2) of the monodentate carboxylate of the ligand (O--O distance: 2.667(8) Å) as shown in Figure 3.11, and (b) between the oxygen atom (O8) of the lattice water molecule and oxygen atom (O5) of the bridged carboxylate (O---O

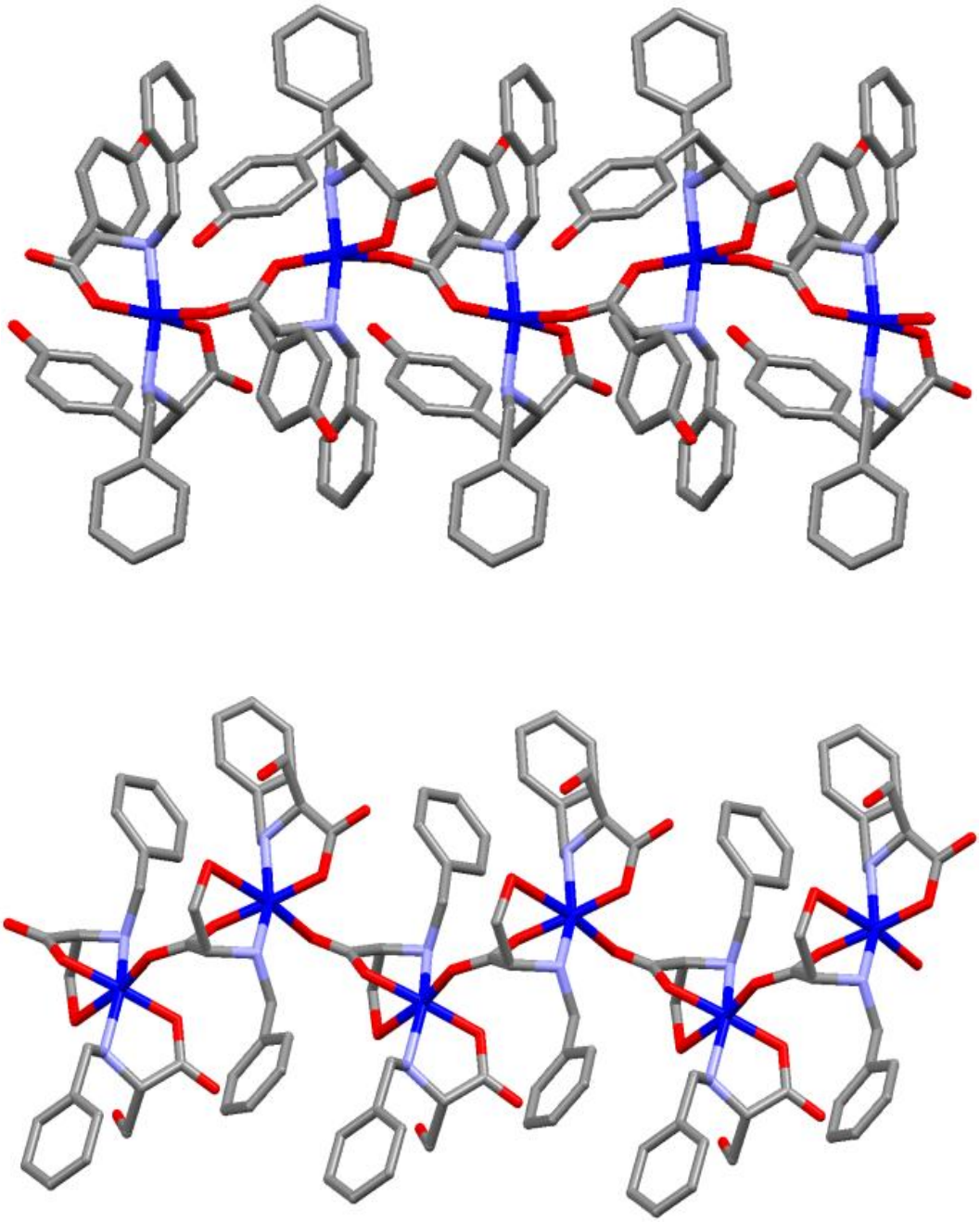

Figure 3.10. Comparison of the carboxylate bridging in the polymeric structures of **1** (top) and **5** (bottom).

distance: 2.985(8) Å) as well as the oxygen atom (O6) of the phenol part of the ligand (O---O distance:2.652(8) Å). O8 is also hydrogen bonded to the oxygen atom (O7) of the lattice methanol molecule (O---O distance: 3.049(7) Å).

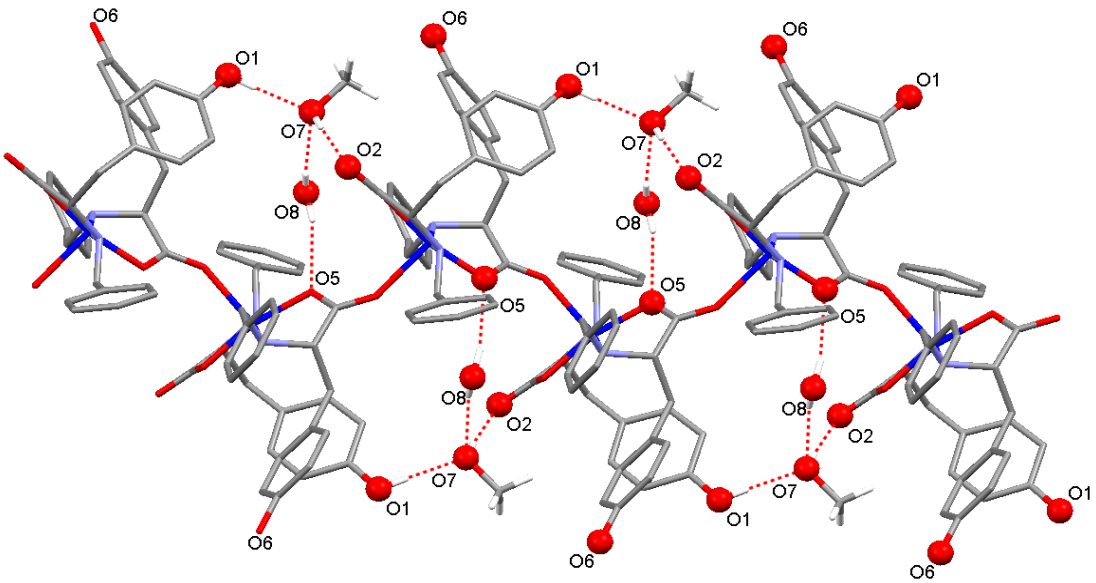

Figure 3.11. Hydrogen bonding network within the 1D chain in **1**.

Thus the O8 atom, which acts as a donor (bifurcated) as well as acceptor, connects the two 1D chains through O6 (see Figure 3.12) forming a $R_4^4(29)$ motif.[240] This 29-membered ring consists of four donor atoms (O6, O8, O6', O8'), four acceptor atoms (O5, O8, O5', O8') and some part of the ligand skeleton. In $\{Co(L\text{-tyrosine})\}_n$, and $\{Zn(L\text{-tyrosine})\}_n$, the phenolic –OH is deprotonated and thus the phenoxo group coordinates with another metal center.[238] In $[Cu(tyrosine)_2]_n$ and the phenolic -OH group is directly hydrogen bonded to the uncoordinated oxygen atom of the monodentate carboxylate group.[239]

In $\{[Cu_2(HTyrsal)_2(H_2O)]\cdot(H_2O)\}_n$, the phenolic -OH group is involved in both intrachain and interchain hydrogen bonding. It connects one of the oxygen atom of the bridging carboxylate groups to the lattice water molecule to form the 1D chain. For the interchain hydrogen bonding, the lattice water molecule and the phenolic -OH groups are involved.[241] In **1**, the $Cu^{2+}...Cu^{2+}$ distance is 5.833(6) Å, which is similar to that (5.763(6) Å) found in $\{[Cu_2(HTyrsal)_2(H_2O)](H_2O)\}_n$ though the Cu^{2+} centers in the latter are part of the bis(phenoxo) moities that alternates in the CP chain; this distance is much shorter (4.93(7) Å) in $[Cu(tyrosine)_2]_n$ due to the ant-anti bridging mode of the carboxylate group. On the other hand, the Cu...Cu distance in **5** is 5.495(3) Å.

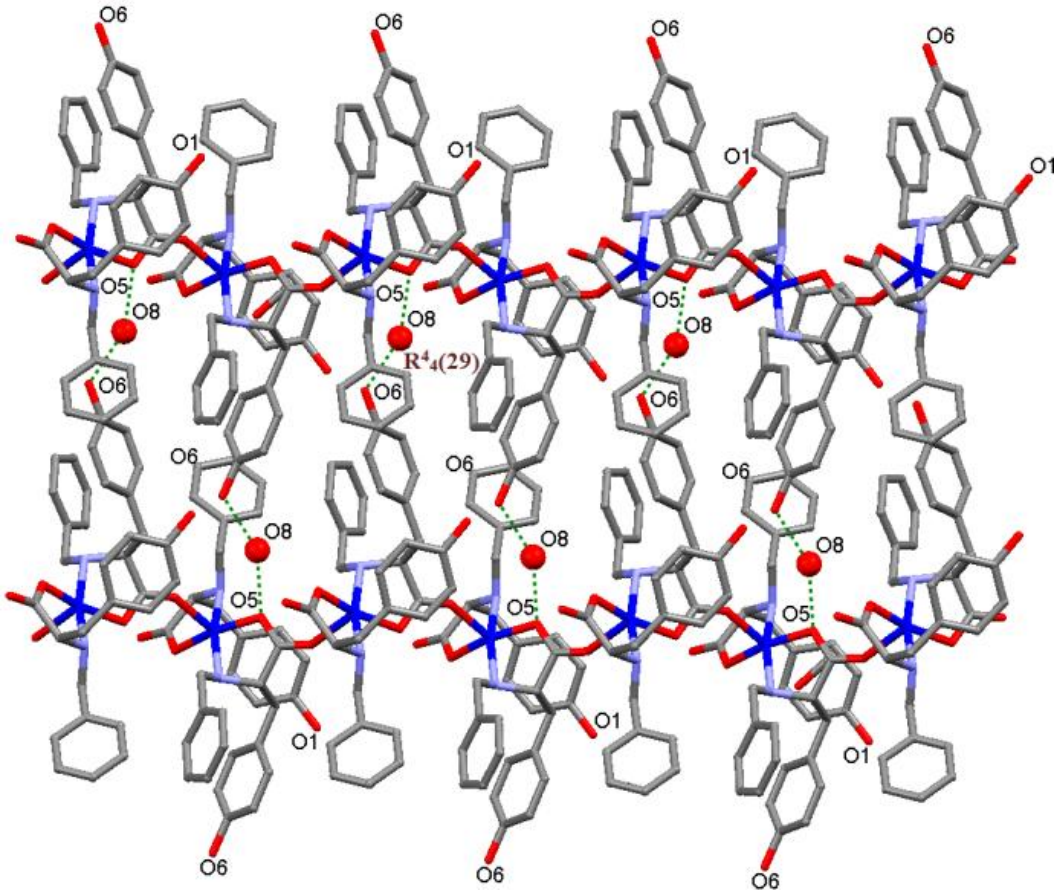

Figure 3.12. Two 1D chains connected via lattice water molecules in **1**.

In addition to hydrogen bonding, various C-H...O interactions like C26-H12A..O6 and C26-H12B..O4 with a donor-acceptor distances of 2.989(7) Å and 3.102(7) Å, respectively, further strengthens the association of the 1D CPs in **1**. The crystallographic parameters and basic information pertaining to data collection and structure refinement for **1** is summarized in Table A1. All hydrogen bonding parameters for **1** are listed in Table 3.6.

In **5**, all three lattice solvent molecules (water) forming a triad are involved in connecting these 1D chains through strong hydrogen bonding. However, each set of three lattice water molecules for each 1D chains are not connected to each other. For the hydrogen bonding within each 1D chain (see Figure 3.13) two out of the three lattice water molecules (O1S and O3S) are involved: O3S acts both as a hydrogen bond donor and a hydrogen bond acceptor. As a donor, O3S is hydrogen bonded to –OH (O5) of the $–CH_2OH$ (O---O distance: 2.915(4) Å) and the uncoordinated oxygen atom (O3) of the monodentate carboxylate of the ligand (O---O distance: 2.858(4) Å). As an acceptor, O3S is hydrogen bonded to the nitrogen (N1) of

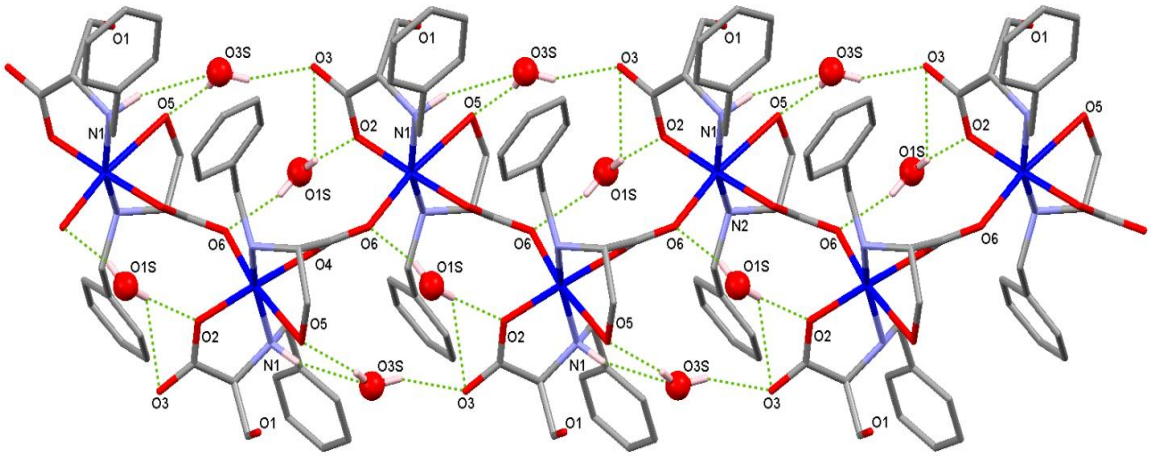

Figure 3.13. Hydrogen bonding network within the 1D chain in **5**.

the amine part of the ligand (N---O distance: 3.516(4) Å). Further reinforcement of the network is by the inter-chain hydrogen bonding between the two oxygen atoms (O1 and O5) of the -CH_2OH groups of the two ligands coordinated to each Cu^{2+} centers and oxygen atom of a lattice water molecule (O1S) (O1---O1S distance: 2.777(4) Å) and the uncoordinated oxygen atom (O3) of the monodentate carboxylate (O5---O3 distance: 2.972(4) Å) of the ligand, respectively. Thus both CH_2OH groups from two L-HSerbenz ligands are involved in connecting these 1D chains for the overall network in **5**. This is very different from the involvement of the phenolic groups of the L-HTyrbenz in **1**. All these hydrogen bondings in **5** lead to the formation of four different motifs: $R_3^4(11)$, $R_4^4(11)$, $R_5^4(14)$ and $R_2^2(10)$.[240] Both the eleven-membered motifs consist of four acceptor atoms (O1, N1, O2S and O2S'in $R_4^4(11)$ and O2S, O3S, O5 and N2 in $R_3^4(11)$; however, these vary in number of donor atoms (O1S, O3S, O3S' and O1S'in $R_4^4(11)$ and O3S, O3 and O2S in $R_3^4(11)$. The $R_5^4(14)$ motif comprises of four acceptor atoms (N1, O6, O3S, O1S) and five donor atoms (O3S, O1S, O3, O1S' and O2). The ten-membered ring in $R_2^2(10)$ has two donor atoms (O6 and O2) and two acceptor atoms (O1S and O1S'). In all these motifs, rest of the ring is made of some portion of the ligand skeleton. O1S shows a three center bifurcated hydrogen bonding with uncoordinated (O3) and coordinated (O2) oxygen atoms of the monodentate carboxylate (distances: O1S---O3, 3.577(4) Å; O1S---O2, 2.752(4) Å) and oxygen atom (O6) of the bridging carboxylate (O1S---O6 distance: 2.864(4) Å) of the ligand. The third lattice water molecule (O2S) plays a very significant role. Although it is not directly involved in the intra-

chain hydrogen bonding but as shown in Figure 3.14, it bridges between the two lattice water molecules O1S and O3S (O2S---O1S distance: 2.953(5) Å) (O2S---O3S distance: 2.865(6) Å) from different triads of different 1D chains to form the inter-chain hydrogen bonding, thus extending the dimensionality. The crystallographic parameters and basic information pertaining to data collection and structure refinement for **5** is summarized in Table A1. All hydrogen bonding parameters for **5** are listed in Table 3.6.

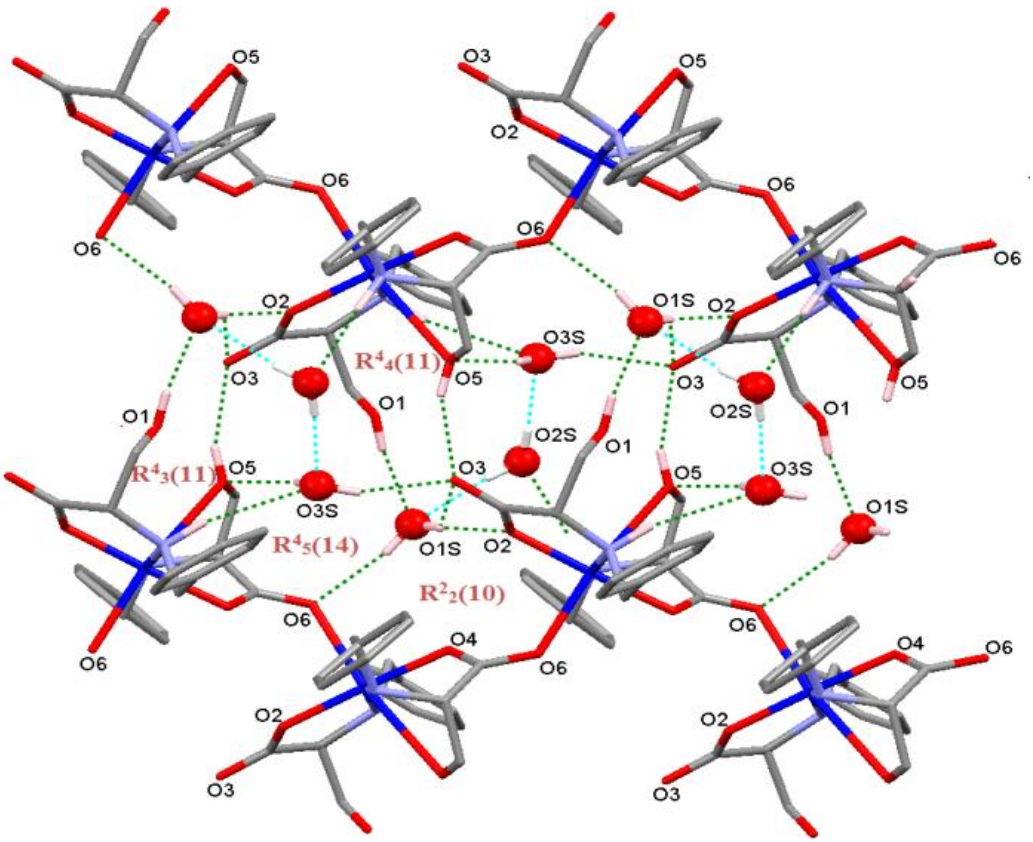

Figure 3.14. 3D supramolecular array in **5** involving 1D chains and lattice water molecules.

Crystal structure of $[Cu(Phebenz)_2(H_2O)]\cdot H_2O$ (9). Compound **9** crystallizes in triclinic chiral space group P1. X-ray crystallography studies indicated to have no lattice solvent molecule. The mononuclear metal complex in **9** consists of a pentacoordinating Cu^{2+} atom bound to two ligands (Phebenz) (as shown in Figure 3.15).

The pentaccordinating Cu^{2+} atom acquires a distorted square pyramidal geometry. The coordination environment around Cu^{2+} is O_3N_2 type; two equatorial sites are occupied by the nitrogen atoms of the amine group of the two bound ligands (HPhebenz) whereas the other

two equatorial sites are occupied by the oxygen atoms of the carboxylates of the two bound ligands, apical site is occupied by the oxygen atom of the bound water molecule.

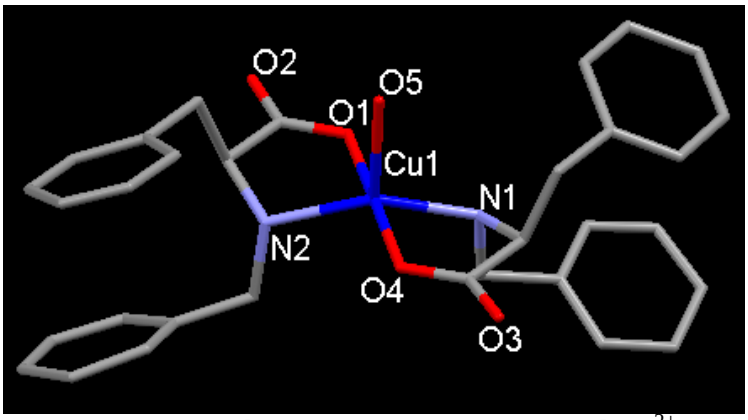

Figure 3.15. Coordination environment around Cu^{2+} in **9**.

Both the carboxylates bind to the metal center in a monodentate fashion. The unbound oxygen atom of the carboxylate and oxygen atom of the bound water are involved in hydrogen bonding thus giving rise to a 2D supramolecular assembly (as shown in Figure 3.16).

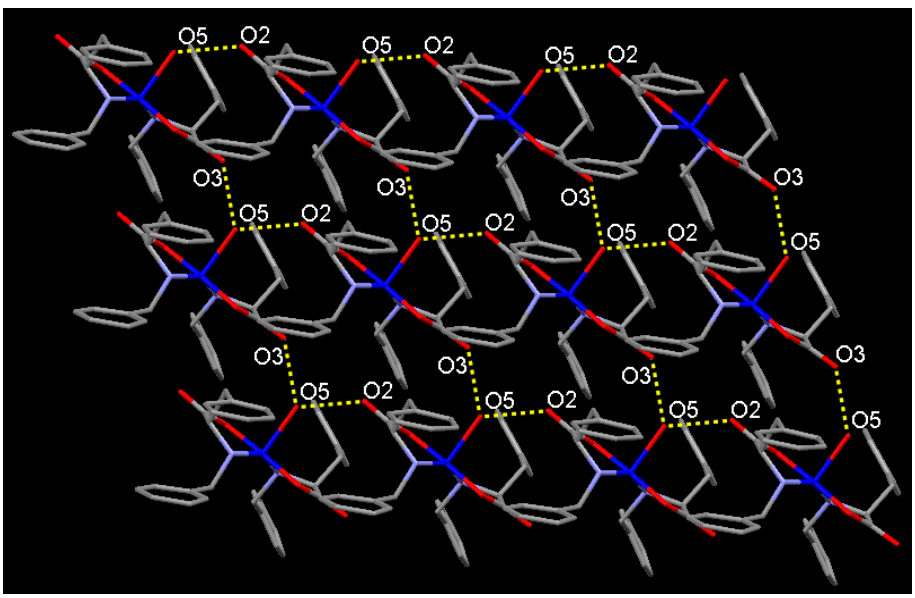

Figure 3.16. 2D supramolecular coordination network in **9**.

The oxygen atom of the bound water (O5) in the mononuclear unit is hydrogen bonded in a bifurcated fashion to two unbound oxygen atoms (O3 and O2) of the two carboxylates of two different mononuclear units (O---O distance: 2.717 and 2.733 Å) forming a SCC. The

presence of π–π interactions between two molecules (as shown in Figure 3.17) in the 2D network converts it to 3D supramolecular assembly. The crystallographic parameters and basic information pertaining to data collection and structure refinement for **9** is summarized in Table A1. The selected bond distances and bond angles for **9** are listed in Tables A6 and A10, respectively. All hydrogen bonding parameters for **9** are listed in Table 3.6.

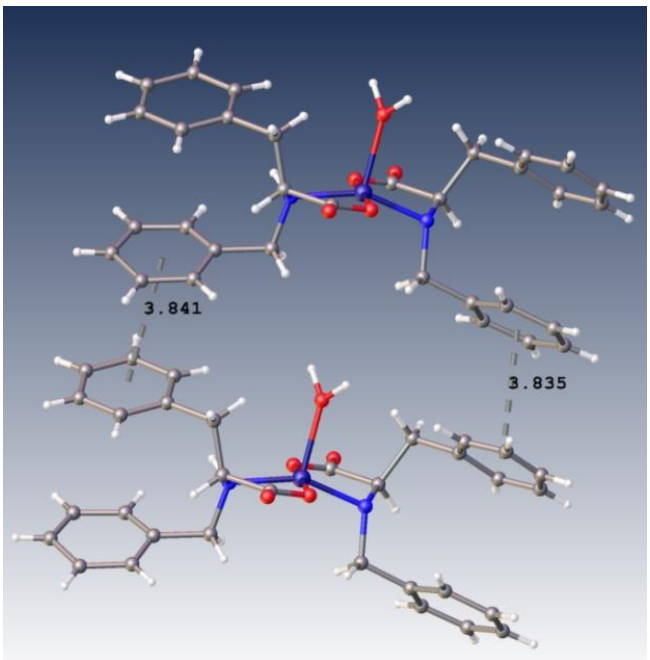

Figure 3.17. π–π interactions in **9**.

Crystal structure of {[Cu(L-HTyrthio)$_2$]·H$_2$O}$_n$ (13). Compound **13** crystallizes in the monoclinic chiral space group $P2_1$. The asymmetric unit of **13** comprises of a pentacoordinated Cu^{2+} center surrounded by two L-HTyrthio ligands and one lattice water molecule (as shown in Figure 3.18). The Cu^{2+} center has a distorted square pyramidal geometry with an O_3N_2 coordination environment. The four equatorial sites are occupied by the two nitrogen atoms (N1 and N2) of the amine group and two oxygen atoms (O2 and O4) of the carboxylates of the two ligands. Unlike **1** and **5**, both the carboxylates in **13** bind to the metal center in a monodentate fashion. The sulphur atoms in the two thiophene rings of the mononuclear unit point towards each other. The apical site is occupied by the phenolic oxygen (O3') of the ligand coordinating to the next metal center (Cu^{2+}-OH bond length: 2.704(5) Å) generating a spiral 1D coordination polymer (as shown in Figure 3.19). The selected bond distances and bond angles for **13** are listed in Tables S1 and S2 (appendix)

respectively. This kind of phenol-bridged coordination polymer is limited in the literature.[242-248]

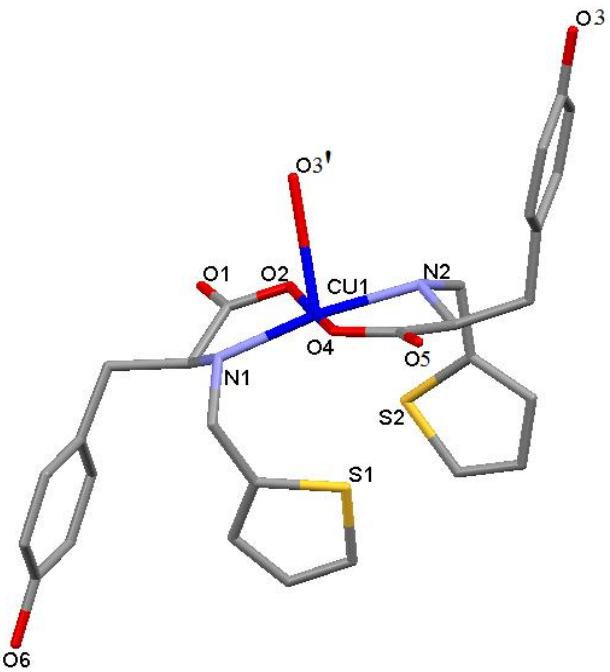

Figure 3.18. Coordination environment around Cu^{2+} in **13**.

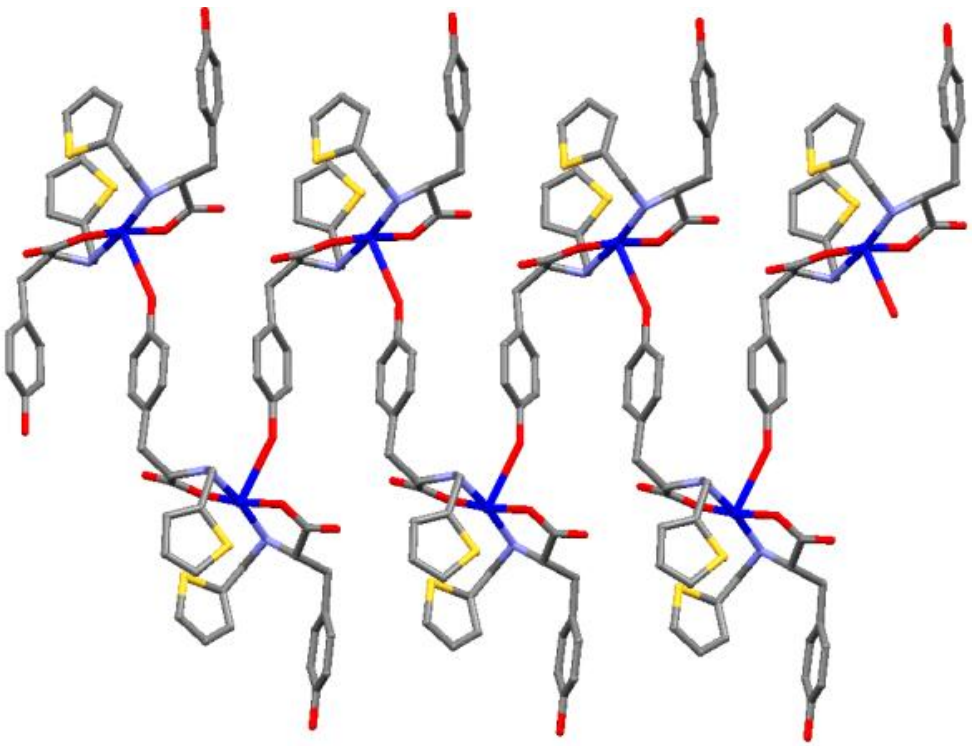

Figure 3.19. 1D helical structure of **13**.

The other phenolic groups (O6) of the second L-HTyrthio ligand shows a bifurcated hydrogen bonding with oxygen atoms (O4 and O5) of the monodentate carboxylate of the ligand (O6---O4 distance: 3.035(7) Å) (O6---O5 distance: 3.018(7) Å) coordinating to Cu^{2+} of the adjacent coordination polymer. The Cu...Cu distance between two adjacent Cu^{2+} centers in a spiral chain is 10.806(9) Å. Each 1D spiral chain is further extended by the intra-chain hydrogen bonding. The oxygen atom(O1S) of the lattice water molecule acts as a hydrogen bond acceptor showing bifurcated hydrogen bonding with the oxygen atom (O3) of the coordinated phenol (O---O distance: 2.672(7) Å) and nitrogen (N2) atom of the amine part of the ligand (O---N distance: 3.009(6) Å). This lattice water molecule (O1S) also acts as a hydrogen bond donor and shows hydrogen bonding with the oxygen atom (O1) of the carboxylate (O---O distance: 2.730(6) Å) of the ligand. This reinforcement of hydrogen bonding within each spiral chain forms two motifs labeled as $R_2^2(21)$ and $R_2^1(6)$ (see Figure 3.20).[240]

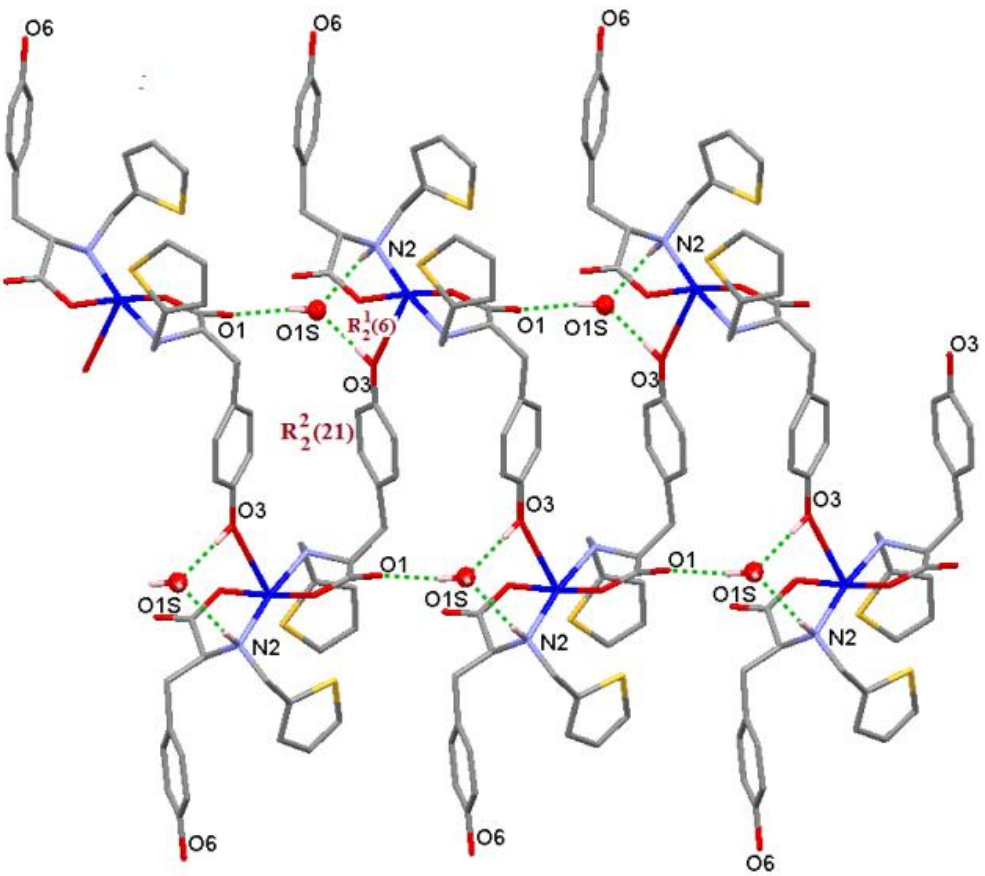

Figure 3.20. Hydrogen bonding within the spiral chain in **13**.

The 21-membered motif $R_2^2(21)$ consists of two donor atoms (O1S and O3) and two acceptor atoms (O5 and O1S). The six-membered motif $R_2^1(6)$ consists of O3 as acceptor and O1S and N2 as donor atoms. The remaining parts of both the motifs are made up of some part of the ligand. The lattice water O1S is also involved in inter-chain bifurcated hydrogen bonding with the oxygen atoms (O1 and O2) of the carboxylate of the ligands of the next chain (distances: O1S---O1, 3.195(7) Å; O1S---O2, 2.787(6) Å) (see Figure 3.21). The crystallographic parameters and basic information pertaining to data collection and structure refinement for **13** is summarized in Table A1. The selected bond distances and bond angles for **13** are listed in Tables A6 and A10, respectively. All hydrogen bonding parameters for **13** are listed in Table 3.6.

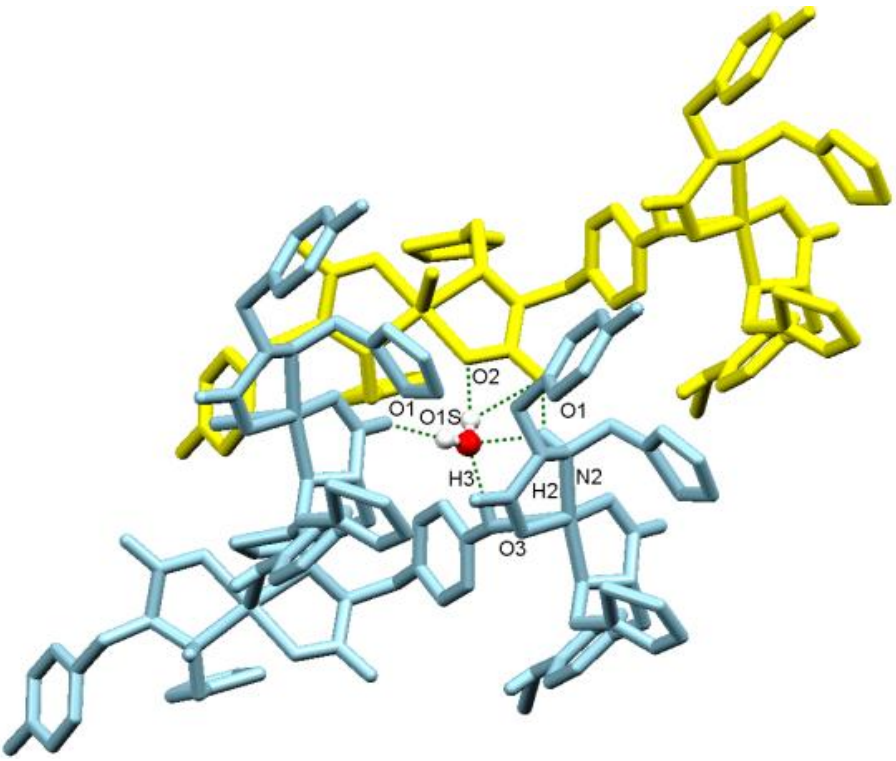

Figure 3.21. Inter-chain hydrogen bonding in **13** involving the lattice water molecule. (two chains are shown with different colors).

Crystal structure of $[Cu(L\text{-}HTyr4\text{-}pyr)_2(H_2O)]\cdot 2H_2O$ (17). Compound **17** crystallizes in the monoclinic chiral space group *C*2. A 2-fold axis that passes through the Cu^{2+} center and the coordinated water molecule generates the whole molecule from the asymmetric unit. There are two lattice water molecules per mononuclear unit. The Cu^{2+} center with an O_3N_2

coordination environment has a distorted square pyramidal geometry (see Figure 3.22) where two equatorial sites are occupied by the nitrogen atoms of the amine group and the other two equatorial sites are occupied by the oxygen atoms of the carboxylates of the two ligands. The apical site is occupied by a water molecule (O2). Both the carboxylates bind to the metal center in a mono- dentate fashion.

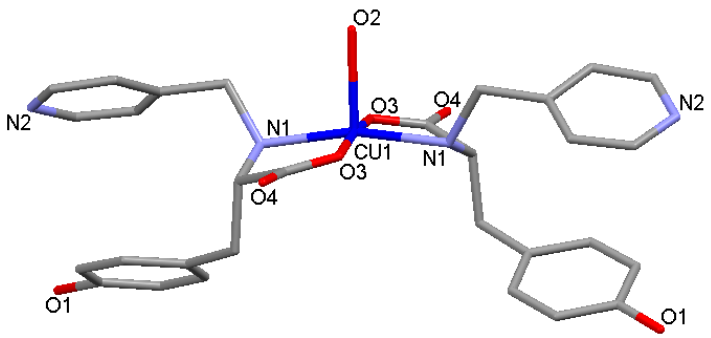

Figure 3.22. Coordination environment around Cu^{2+} in **17**.

The selected bond distances and bond angles for **17** are listed in Table S1 and S2 (appendix), respectively. The nitrogen atom (N2) of the pyridyl moiety is hydrogen bonded to the oxygen atom (O1) of the phenol moiety of the second ligand (N---O distance: 2.673(6) Å) and vice-versa, resulting in the formation of a network in the x direction (as shown in Figure 3.23, top). Few examples of this kind of hydrogen bonding between phenolic O-H and pyridyl N are also known.[249,250] In the system with co-crystals of 4,4′-bipyridine-N-monoxide (BPMO) and p-coumaric acid (PCA), the N---O distance is 2.689(3) Å.[249] In another co-crystal system of resorcinol and methyl ester of acrylic acid, two types of O-H..N bonding is observed (N---O distances: 2.787(4) Å and 2.800(4) Å).[250] The N--O distances in both the systems are comparable to the N--O distance in **5**. The oxygen atom (O2) of the coordinated water molecule is hydrogen bonded to the uncoordinated oxygen atom (O4) of the monodentate carboxylate of the ligand (O---O distance: 2.743(4) Å) to have the network propagated in the y direction, as shown in Figure 3.23, bottom. The 2D assembly in **17** has extensive hydrogen bonding thus forming a network with variable pore sizes. One of the lattice water molecules (O5) connects the phenolic oxygen atoms (O1) of the ligand via hydrogen bonding (O5---O1 distance: 2.934(6) Å). The other lattice water molecule (O6) is hydrogen bonded to the nitrogen (N1) of the amine (N---O distance: 3.182(7) Å) as well as to the coordinated oxygen

(O3) and uncoordinated oxygen atom (O4) of the monodentate carboxylate of the ligand (O6---O3 distance: 2.719(8) Å; O6---O4 distance: 3.146(8) Å). The selected bond distances and bond angles for **17** are listed in Tables A6 and A10, respectively.The C-H…O interactions C2-H2A…O5, C5-H5…O4 and C11-H11...O6 with donor-acceptor distances 3.410(5) Å, 3.371(6) Å and 3.358(8) Å, respectively, provide an additional strength to the network.

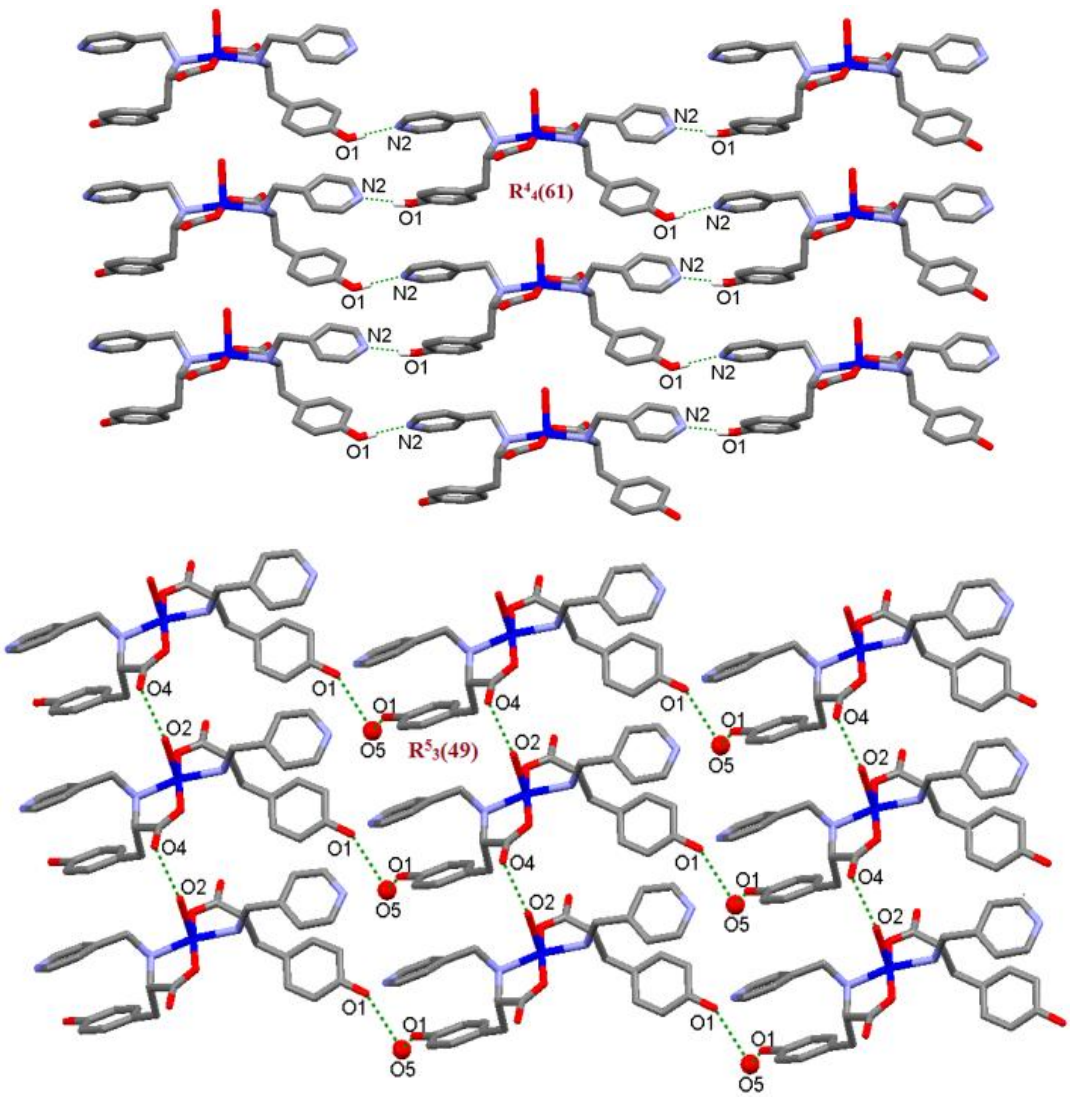

Figure 3.23. Hydrogen bondings in (a) x and (b) y directions for the formation of the 2D supramolecular network in **17**. Other lattice water molecule (O6) is omitted for clarity.

Various hydrogen bondings lead to two kinds of motif formation in **5**: $R_4^4(61)$ and $R_3^5(49)$.[240] The 61- membered motif $R_4^4(61)$ consists of four acceptor atoms (O1, O1', O1'', O1''') and four donor atoms (N2, N2', N2'', N2''') whereas 49-membered motif $R_3^5(49)$ consists of five acceptor atoms (O2, O5, O5', O5'', O5''') and three donor atoms(O4, O1 and O1'). Again,

in both the cases the motifs were completed by the ligand skeletons. The crystallographic parameters and basic information pertaining to data collection and structure refinement for **17** is summarized in Table A1. All hydrogen bonding parameters for **17** are listed in Table 3.6.

Crystal structure of [Cu(L-HSerthio)$_2$(H$_2$O)] (21). Compound **21** crystallizes in the monoclinic chiral space group $P2_1$. The asymmetric unit of **21** consists of two independent molecules (see Figure 3.24). Each mononuclear unit consists of a pentacoordinated Cu^{2+} center bound to two L-HSerthio ligands. The Cu^{2+} center has a distorted square pyramidal geometry with an O_3N_2 coordination environment; two equatorial sites are occupied by the nitrogen atoms of the amine group whereas the other two equatorial sites are occupied by the carboxylate oxygens of the ligands. The apical site is occupied by a water molecule. Both the carboxylates bind to the metal center in a monodentate fashion. The selected bond distances and bond angles for **21** are listed in Tables A6 and A10, respectively. The two independent molecules in the asymmetric unit not only differ in the arrangement of sulphur atoms in the two thiophene rings (in one molecule these point towards each other whereas in the other molecule these point away from each other), but also vary in their hydrogen bonding interactions.

Each molecule forms a unique 1D supramolecular chain via intermolecular hydrogen bonding as shown in Figure 3.25. In the first 1D chain, the two oxygen atoms (O6 and O7, respectively) of the –CH_2OH of one mononuclear unit shows an intermolecular hydrogen bonding with the uncoordinated oxygen atoms (O5 and O3, respectively) of the carboxylates of the next mononuclear units in an intermolecular fashion (O6---O5 distance: 2.686(12) Å; O7---O3 distance: 2.687(12) Å). The oxygen atom (O1) of the coordinated water molecule shows intermolecular hydrogen bonding with two coordinated oxygen atoms (O2 and O4) of the two carboxylates of two different molecules (O1---O2 distances: 2.868(11) Å and O1---O4 distance: 2.918(11) Å, respectively). The nitrogens (N2 and N1) of the amine part of the ligands of one mononuclear unit are hydrogen bonded to the oxygen atom (O1) of the coordinated water and oxygen atom (O6) of the –CH_2OH part of the ligand of the next unit respectively (distances: N2---O1, 3.240(12) Å; N1---O6, 3.014(13)Å). These hydrogen bondings lead to the formation of four motifs: $R_3^2(6)$, $R_2^2(8)$, $R_2^2(4)$ and $R_2^2(9)$.[240] All four motifs consist of two acceptor atoms (O1 and O1'in $R_3^2(6)$; O1 and O1' in $R_2^2(8)$; O1 and

O1'in $R_2^2(4)$ and N1 and N2 in $R_2^2(9)$ and two donor atoms (O2 and O7 in $R_2^2(8)$; O7 and O7' in $R_2^2(4)$ and O1 and O6 in $R_2^2(9)$ except the six-member $R_3^2(6)$ motif which consists of three donoratoms (O2, O3 and O3'). Like all the motifs, these also consist of some part of the ligands. In addition to the hydrogen bonding interactions observed in the first 1D chain, for the second 1D chain the coordinated water molecule (O8) shows hydrogen bonding with the oxygen atom (O12) of the $–CH_2OH$ of the ligand (O8---O12 distance: 2.962(12) Å). Similar to the first chain, the oxygen atoms (O14 and O11) of the $–CH_2OH$ of two ligands coordinated to same metal center are hydrogen bonded to the uncoordinated oxygen atoms (O10 and O13, respectively) of the carboxylate of the adjacent molecules in an intermolecular fashion (O14---O10 distance: 2.630(14) Å; O11---O13 distance: 2.725(13) Å). These hydrogen bondings give rise to three motifs within this chain: two $R_2^2(10)$ and one $R_2^2(12)$.[240] All motifs consist of two donor atoms (O17 and O18 in $R_2^2(10)$; O13 and O10 in $R_2^2(12)$) and two acceptor atoms (N3 and N4 in $R_2^2(10)$; O18 and O17 in $R_2^2(12)$) along with some parts of the ligands. The crystallographic parameters and basic information pertaining to data collection and structure refinement for **21** is summarized in Table A2. All hydrogen bonding parameters for **21** are listed in Table 3.6.

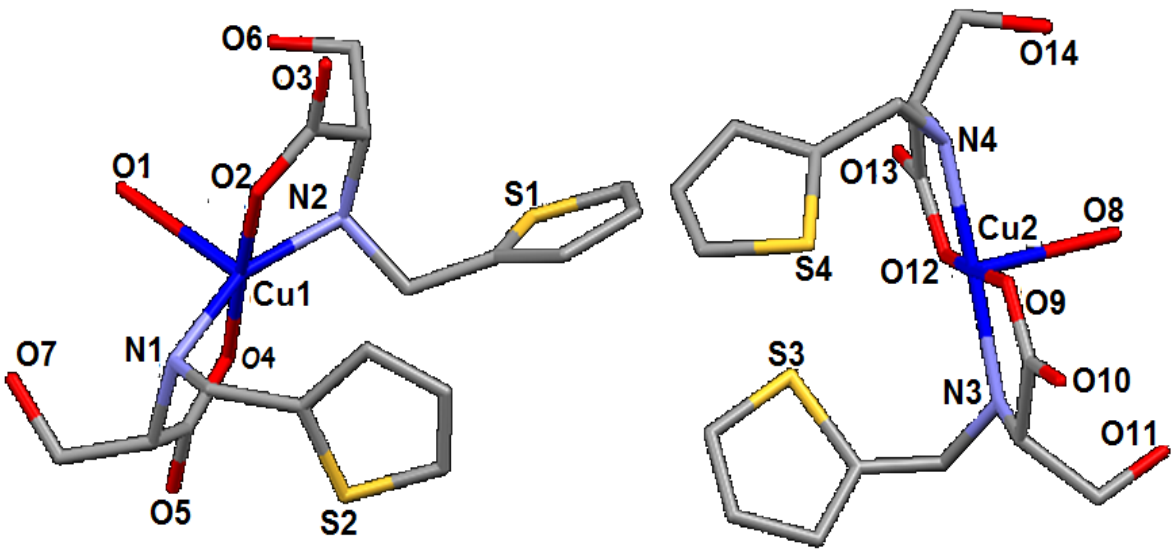

Figure 3.24. Coordination environment around Cu^{2+} in **21** for two independent molecules per asymmetric unit.

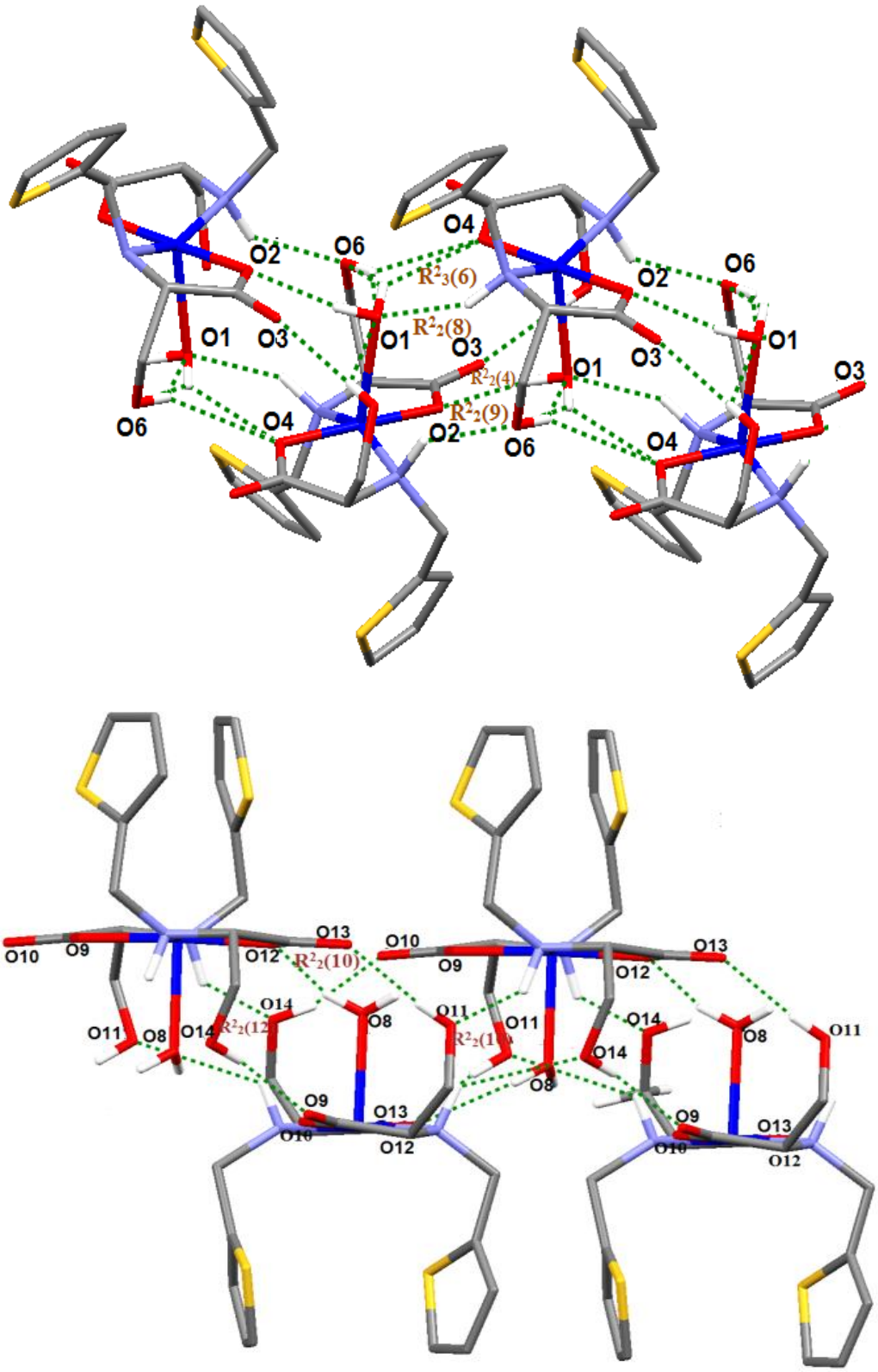

Figure 3.25. Two independent 1D supramolecular chains in **21**.

Table 3.6. Hydrogen bonding parameters for **1**, **5**, **13**, **17** and **21**.

D-H…A	r(D-H) (Å)	r(H…A) (Å)	r(D…A) (Å)	∠D-H…A (°)	Symmetry
1					
O1-H2..O7	0.82	1.86	2.672(6)	168	x,-1+y,z
O6-H5..O8	0.82	1.84	2.652(8)	171	1-x,-1/2+y,-z
O8-H12C..O7	0.75	2.31	3.049(7)	169	
O8-H12D..O5	0.87	2.17	2.985(8)	157	-x,1/2+y,-z
O7-H51..O2	0.82	1.86	2.667(8)	167	
C5-H20..O6	0.93	2.53	3.263(8)	136	1-x,-1/2+y,-z
C10-H26B..O5	0.97	2.43	3.317(6)	152	-x,1/2+y,-z
5					
O1-H1..O1S	0.82	1.96	2.777(4)	171	-x,-1/2+y,1/2-z
O1S-H1SB..O6	0.85	2.03	2.864(4)	167	-x,-1/2+y,1/2-z
N1-H1A..O3S	0.98	2.56	3.516(4)	165	-1+x,y,z
N2 -H2..O2S	0.98	2.10	3.078(5)	172	-1/2+x,1/2-y,-z
O1S-H1SA..O2	0.85	1.91	2.752(4)	171	1/2-x,1-y,1/2+z
O2S-H2SB..O1S	0.85	2.11	2.953(5)	173	1-x,-1/2+y,1/2-z
O2S-H2SA..O3S	0.86	2.01	2.865(6)	177	
O5-H5..O3	0.82	2.24	2.972(4)	149	-1/2+x,1/2-y,-z
O3S-H3SB..O3	0.85	2.05	2.858(4)	159	
O3S -H3SA..O5	0.85	2.10	2.915(4)	161	1+x,y,z
C13-H13B..O4	0.97	2.44	3.322(5)	151	1/2+x,3/2-y,-z
13					
O1S-H1SB..O1	0.85	1.90	2.730(6)	166	1-x,1/2+y,1-z
N2-H2..O1S	0.98	2.23	3.009(6)	135	1-x,1/2+y,1-z
O1S-H1SA..O1	0.86	2.57	3.195(7)	131	1+x,y,-1+z
O1S-H1SA..O2	0.86	1.95	2.787(6)	165	1+x,y,-1+z
O3-H3..O1S	0.82	1.87	2.672(7)	167	x,y,1+z
O6-H6..O4	0.84	2.24	3.035(7)	156	-1+x,y,z
O6-H6..O5	0.84	2.29	3.018(7)	145	-1+x,y,z
17					
N1-H1..O6	0.98	2.35	3.182(7)	142	-1/2+x,1/2+y,z
O1-H1A..N2	0.82	1.87	2.673(6)	164	1/2-x,-1/2+y,1-z
O2-H2..O4	0.84	1.91	2.743(4)	171	-1/2+x,1/2+y,z
O5-H5A..O1	0.87	2.07	2.934(6)	172	
O6-H6A..O4	0.84	2.33	3.146(8)	164	x,-1+y,z
O6-H6B..O3	0.84	1.94	2.719(8)	154	1/2-x,-1/2+y,-z
C2-H2A..O5	0.93	2.55	3.410(5)	154	1/2+x,1/2+y,z
C5-H5..O4	0.93	2.47	3.371(6)	162	-1/2+x,-1/2+y,z
C11-H11..O6	0.93	2.48	3.358(8)	157	x,1+y,z

21					
N1-H1..O6	0.98	2.18	3.014(13)	142	1-x,-1/2+y,1-z
O1-H1C..O4	0.85	2.11	2.918(11)	158	1-x,-1/2+y,1-z
O1-H1D..O2	0.85	2.03	2.868(11)	167	1-x,1/2+y,1-z
N2-H2..O1	0.98	2.40	3.240(12)	143	1-x,1/2+y,1-z
O6-H6..O5	0.82	1.87	2.687(12)	173	1-x,-1/2+y,1-z
O7-H7..O3	0.82	1.92	2.686(12)	154	1-x,1/2+y,1-z
O8-H8C..O12	0.85	2.28	2.962(12)	138	2-x,-1/2+y,-z
O14-H14A..O10	0.82	1.84	2.630(14)	160	2-x,1/2+y,-z
O11-H11..O13	0.82	1.92	2.725(13)	169	2-x,-1/2+y,-z
C1-H1F..O7	0.97	2.40	3.166(15)	136	1-x,1/2+y,1-z
C17-H17A..O10	0.97	2.57	3.335(15)	136	1-x,1/2+y,-z

Effect of the substitution on the ligands

In this study, a systematic change in the reduced Schiff base derivatives of amino acid ligands has been used to investigate the formation of products under similar reaction conditions. Clearly, the coordination of a water molecule to the Cu^{2+} center is controlled by the nature of substitution present in the ligand. This in turn forms either the CPs (**1**, **5** and **13**) with a general formula $\{[ML_2]\cdot Y\}_n$, or the supramolecular assemblies (**9**, **17**, **21** and **25**) with a general formula $[ML_2(H_2O)]\cdot Y$, where L is the ligand and Y represents the lattice solvent molecules. Their formation is purely based on the coordination chemistry of a 1:2 metal to ligand complex. After having four sites occupied by two ligands the fifth site around Cu^{2+} is occupied by the donor atom (either from the phenolic OH group or the carboxylate group) that is available in **1**, **5** and **13** while a water molecule occupies in **9**, **17, 21** and **22**. In $\{[Cu(HTyrbenz)_2]\cdot CH_3OH\cdot H_2O\}_n$ (**1**), the coordination polymer is formed via bridging carboxylate showing no role of the phenolic group in its formation. To further emphasize this point, L-tyrosine was replaced with L-serine to form another CP, $\{[Cu(HSerbenz)_2]\cdot 3H_2O\}_n$ (**5**). This confirms the role of –OH group in formation of a carboxylate coordination polymer. For proof of concept, on conversion from L-tyrosine to L-phenyalanine a SCC, $[Cu(Phebenz)_2(H_2O)]\cdot 0.5H_2O$ **(13)** was formed.

In changing from H_2Tyrbenz ligand to H_2Tyr4-pyr ligand (**1** vs **17**), the strong hydrogen bonding of the pyridyl nitrogen with the phenolic OH does not allow the latter to bind to Cu^{2+}. The structural assortment of compounds such as **17** can be accredited to the presence and position of the hetero atom in the ring. For example, as reported earlier the use of H_2tyr-

2pyr with Cu^{2+} results in the formation of a supramolecular assembly [Cu(Htyr2-pyr)$_2$].[251] But the environment around Cu^{2+} and the hydrogen bonding interactions present in the **5** is distinctly different from the supramolecular array in [Cu(Htyr2-pyr)$_2$]. In **17**, Cu^{2+} is pentacoordinated with an O_3N_2 environment, whereas in [Cu(Htyr2-pyr)$_2$], hexacoordinated Cu^{2+} is surrounded by an O_2N_4 environment. In both the cases, the nitrogen of the amine and oxygen of the carboxylate of the ligand bind to the metal center. In addition to that, the pyridyl nitrogens also coordinate to the Cu^{2+} in case of [Cu(Htyr2-pyr)$_2$] whereas in **17**, the fifth coordination of the Cu^{2+} center is completed by a water molecule. In [Cu(Htyr2-pyr)$_2$] the supramolecular assembly grows through the hydrogen bonding which involves the phenolic OH, oxygens of the carboxylates and the lattice solvent (water) molecules. In **17**, the above mentioned hydrogen bonding do exist along with another typical hydrogen bonding between the pyridyl nitrogen and the phenolic –OH of the ligand (vide supra). Thus the 2-pyr derivative forms a polymeric structure because no such pyr..HO(phenol) hydrogen bonding is possible.

Similarly, in changing from H_2Tyrthio to H_2Serthio (**13** vs **21**) the length of the –CH_2OH group in the latter is much less than the distance between the two Cu^{2+} centers to occupy the fifth site and thus a water molecule is coordinated. Thus the essence in the formation of {[Cu(HTyrthio)$_2$]·H_2O}$_n$ (**13**) lies in the growing of the spiral polymer via the unique phenolic bridging with a distance between two Cu^{2+} centers of 10.806 Å. This is further confirmed by reacting **21** with 2 eq of H_2Tyrthio in methanol to form **13** while the reverse was not possible. To further illustrate the significance of the phenolic part, the L-Tyrosine part in the ligand H_2tyrthio is supplanted with L-Phenylalanine and the resultant ligand HPhethio gives [Cu(Phethio)$_2$(H_2O)]·3H_2O (**22**). Although the crystal structure of **22** is not obtained even after several attempts, the values for the carboxylate stretching frequencies in its FTIR spectrum advocates the presence of monodentate carboxylate ($\Delta\upsilon = \upsilon_{asym} - \upsilon_{sym}$ = 267 cm^{-1}) and thus implicate no carboxylate-bridged CP formation.[239,252] The absence of the phenolic -OH group in L-Phethio further insinuate the formation of any phenolic bridged CP, thus confirming **22** to be a supramolecular assembly and not a CP.

Crystal Structures of [Cu(L-HTyr4-NO_2)$_2$(H_2O)]·2DMSO (23a) and [Cu(L-HTyr4-NO_2)$_2$(H_2O)]·2CH_3OH (23b). In order to display the solvent effect on the coordination

architectures, two solvates based on the L-HTyr4-NO_2 ligand [Cu(L-HTyr4-NO_2)$_2$(H_2O)]·2DMSO (**23a**) and [Cu(L-HTyr4-NO_2)$_2$(H_2O)]·2CH_3OH (**23b**) are reported. Both **23a** and **23b** crystallize in a chiral space group: **23a** in monoclinic *C2* whereas **23b** in monoclinic $P2_1$. In each case, one molecule of [Cu(HTyrnitro)$_2$(H_2O)] and two lattice solvent molecules (DMSO in **23a** and methanol in **23b**) are present in the asymmetric unit (see Figure 3.26a and 3.26b, respectively). In both the structures, the coordination environment around Cu(II) with a distorted square pyramidal geometry is O_3N_2 type; out of four equatorial sites, two are occupied by the nitrogen atoms of the amine group and the other two are occupied by the oxygen atoms of the monodentate carboxylates of the ligands. The apical site is occupied by the oxygen atom of the coordinated water molecule. Few mononuclear pentacoordinated complexes of tyrosine-based ligands, such as [Cu(S-fTyr)$_2$(pyrazine)], [Cu(S-fTyr)$_2$(pyridine)] and [Cu(S-fTyr)$_2$(H_2O)], were reported in the literature (where S-fTyr = ferrocenylmethyl-L-tyrosinate).[33] Similar to **23a** and **23b,** these three complexes show a distorted square pyramidal geometry with the pyrazine or pyridine or water molecule, respectively, occupying the apical position. In these three complexes, the Cu-O (monodentate carboxylate) bond distances are in the range of 1.921(12)-1.954(12) Å, which are comparable to those (1.919(3)-1.955(6) Å) in **23a** and **23b**.

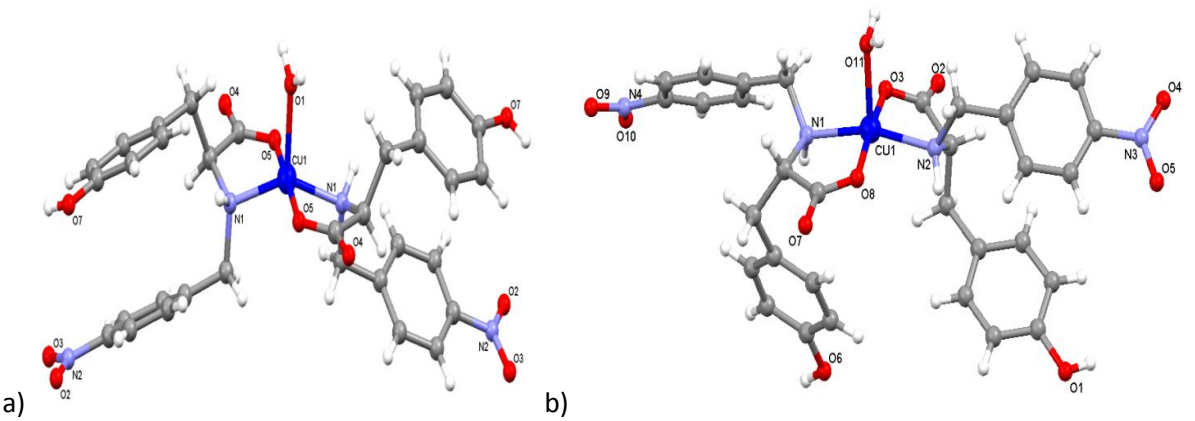

Figure 3.26. Asymmetric unit of **23a** and **23b** (solvent molecules are omitted for clarity).

Similarly, the Cu-N_{amine} bond distances in the ferrocenyltyrosynyl complexes are in the range of 2.0051(13)-2.044 (14) Å, which are similar to those (2.021(6)-2.034(6) Å) in **23a** and **23b**. The bond angles, O(carboxylate)-Cu-N(amine), in **23a** (94.68(13)˚) and **23b** (95.3(2)˚ and 92.8(2)˚) are similar to those of 94.43(8)˚ and 84.88(9)˚ in [Cu(S-fTyr)$_2$(pyrazine)], 94.27(6)˚ and 84.55(6)˚ in [Cu(S-fTyr)$_2$(Pyridine)] and 94.43˚ and 92.26(5)˚ in [Cu(S-fTyr)$_2$(H_2O)].

The Cu-O_{axial} in **23a** and **23b** is 2.183(6) and 2.197(5) Å, respectively, whereas it is much longer (2.453(2) Å) in [Cu(S-fTyr)$_2$(H_2O)]. The selected bond distances and bond angles for **23a** and **23b** are listed in Tables A6 and A11, respectively. Due to the variation of the lattice solvent (DMSO vs methanol) hydrogen bonding interactions in **23a** and **23b** are quite different and lead to a great deal of modulation in the conformation of the ligands around the metal center. Furthermore, **23a** has been found to be preferred over **23b** through (a) the conversion of **23b** to **23a** in dissolving the single crystals of **23b** in DMSO and (b) exclusive formation of **23a** from crystallizing **23** in a mixture of DMSO/methanol (1:1, v/v); in both cases, this is confirmed by unit cell measurements of the crystals.

In **23a**, the coordinated water molecule (O1) involved in an intermolecular bifurcated hydrogen bonding with the uncoordinated oxygen (O4) of the carboxylate group (O1---O4: 2.734 Å) of other two mononuclear subunits forming a 2D supramolecular assembly (Figure. 3.27a). Although the growth of this ensemble in the third direction seems prohibited by the hydrogen bonding interaction of the oxygen atom (O7) of the phenolic part of the ligand with the oxygen atom (O6) of the DMSO molecule (O6---O7 distance: 2.650 Å) (Figure 3.27b), the strong C-H…O interactions between methyl group of the DMSO molecule and oxygen atom of the nitro group enable the two aromatic rings of each ligand to arrange parallel to each other in **23a**, which is well evident from the presence of intramolecular π–π interactions as shown in Figure 3.28. This genre of intramolecular π–π interactions is not observed in **23b** as the planes consisting of the two aromatic rings are not parallel to each other (Figure 3.29). The intermolecular C-H…O interactions among DMSO molecules give rise to a ribbon-shaped structure. The hydrogen bonding interactions along with the strong C-H…O interactions encapsulate the DMSO clusters within the 2D array of **23a** (Figure 3.30). In **23b**, the adjacent mononuclear units with their coordinated waters pointing in the opposite directions are well interwoven with one another along with the lattice methanol molecules to form a dimeric synthon [R^3_3(13)]. These dimeric synthons are further connected to each other via strong intermolecular hydrogen bonding generating a 1D supramolecular chain (Figure 3.31), which further strengthened by the π–π interaction with **23b** (Figure 3.32).

Due to the variation of the lattice solvent (DMSO vs methanol), hydrogen bonding

interactions in these two SCCs are quite different and lead to a great deal of modulation in the conformation of the ligands around the metal center. It is observed that there is a solvent effect on their supramolecular network formation due to change in hydrogen bonding interactions and orientation of the ligands around the metal center. The alliance of these 1D chains to architect the formation of a 2D supramolecular array is quite evident from the Figure 3.33.

(a)

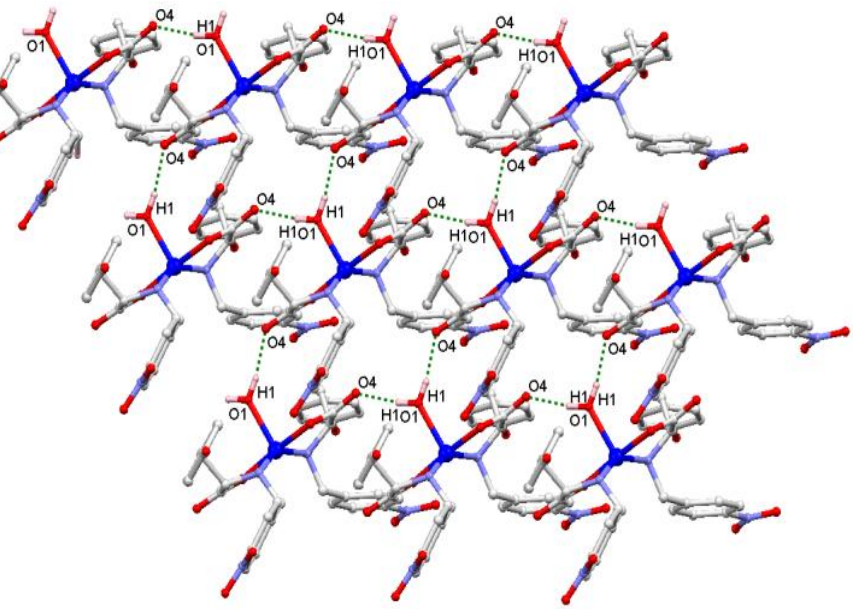

(b)

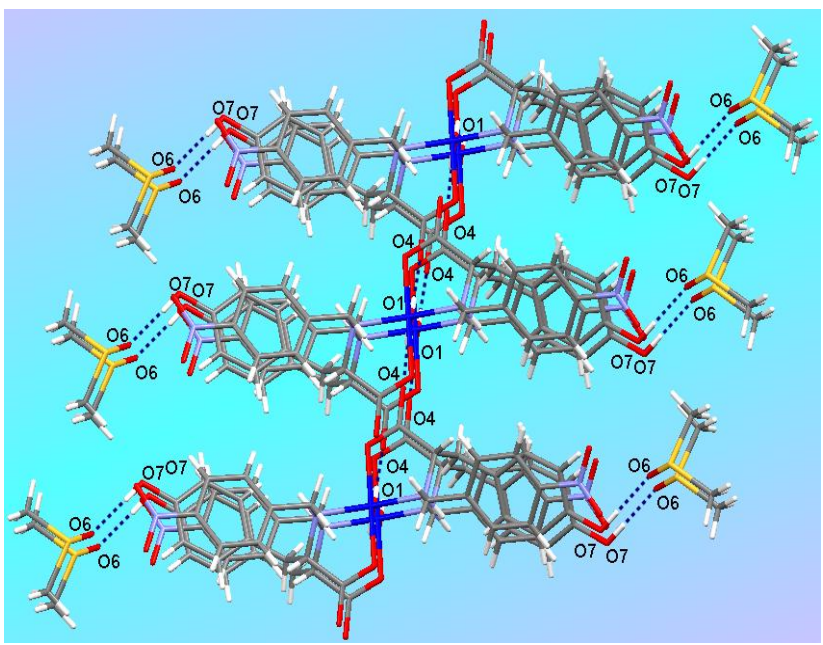

Figure 3.27. (a) 2D supramolecular ensemble in **23a**. (b) Interaction of the DMSO molecules with the supramolecular array in **23a**.

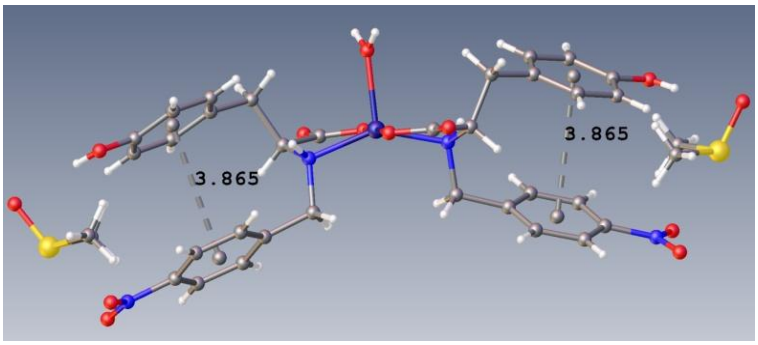

Figure 3.28. Intramolecular π–π interactions in **23a**.

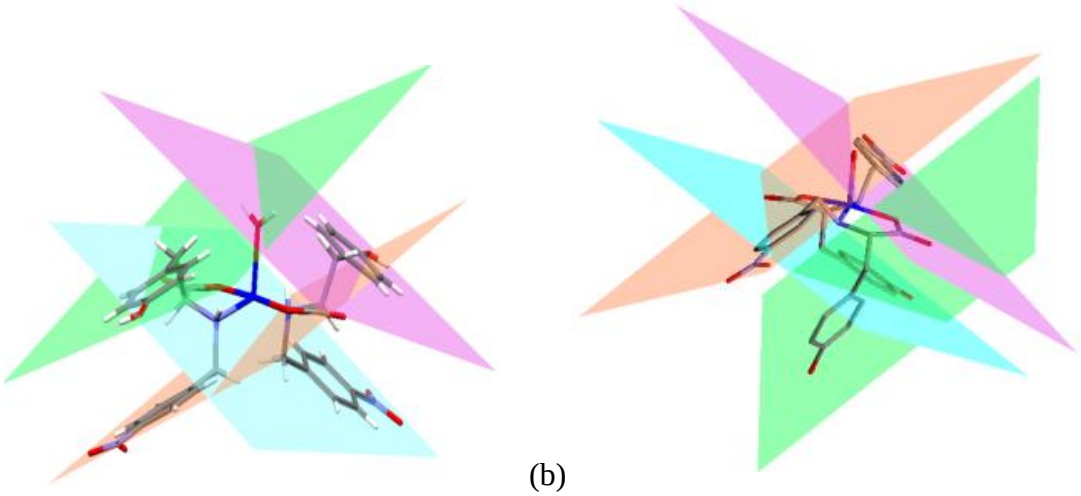

(a) (b)

Figure 3.29. (a) Parallel and (b) anti-parallel planes containing aromatic rings of the ligand in **23a** and **23b**, respectively.

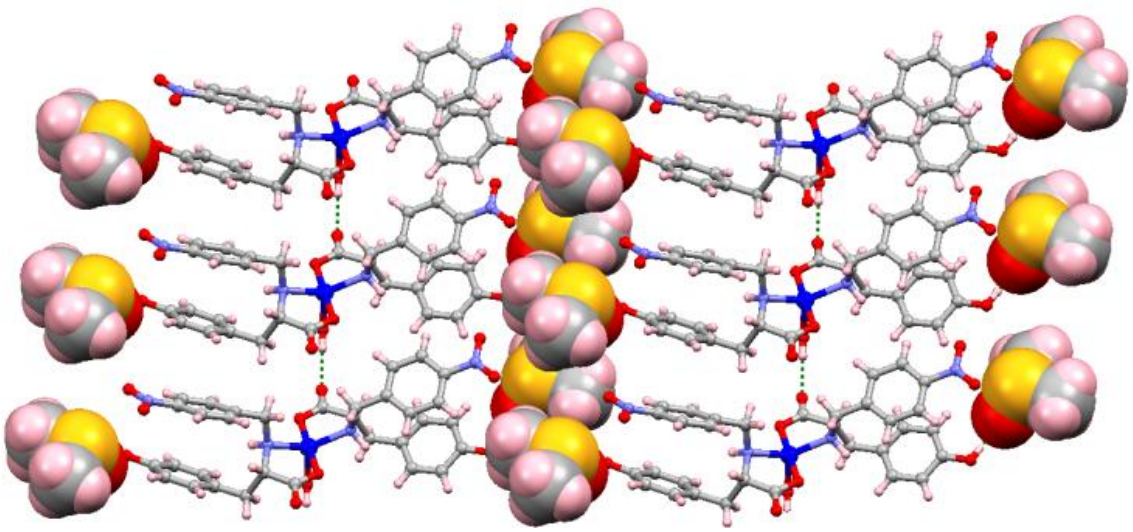

Figure 3.30. Encapsulation of the DMSO cluster within the supramolecular array in **23a**.

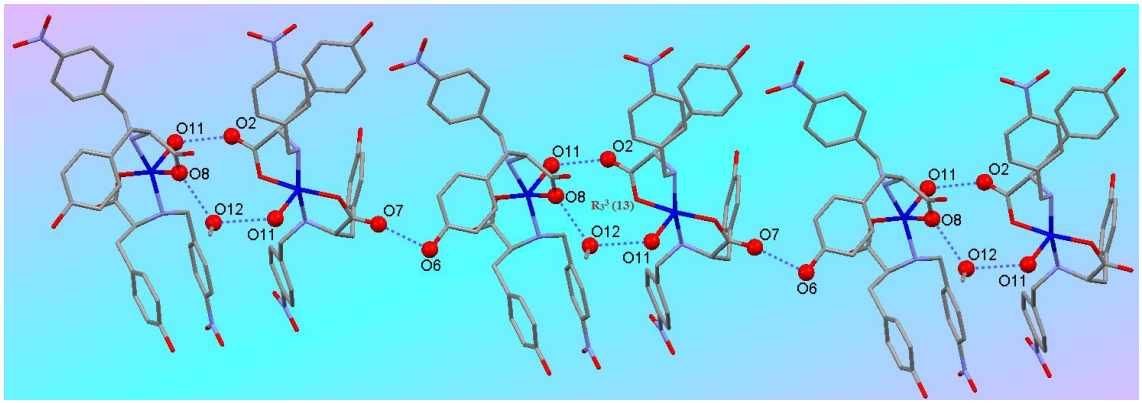

Figure 3.31. 1D supramolecular chain in **23b**.

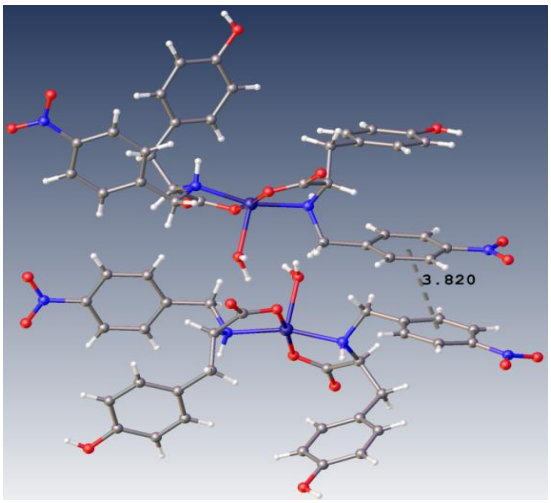

Figure 3.32. Intermolecular π–π interactions in **23b**.

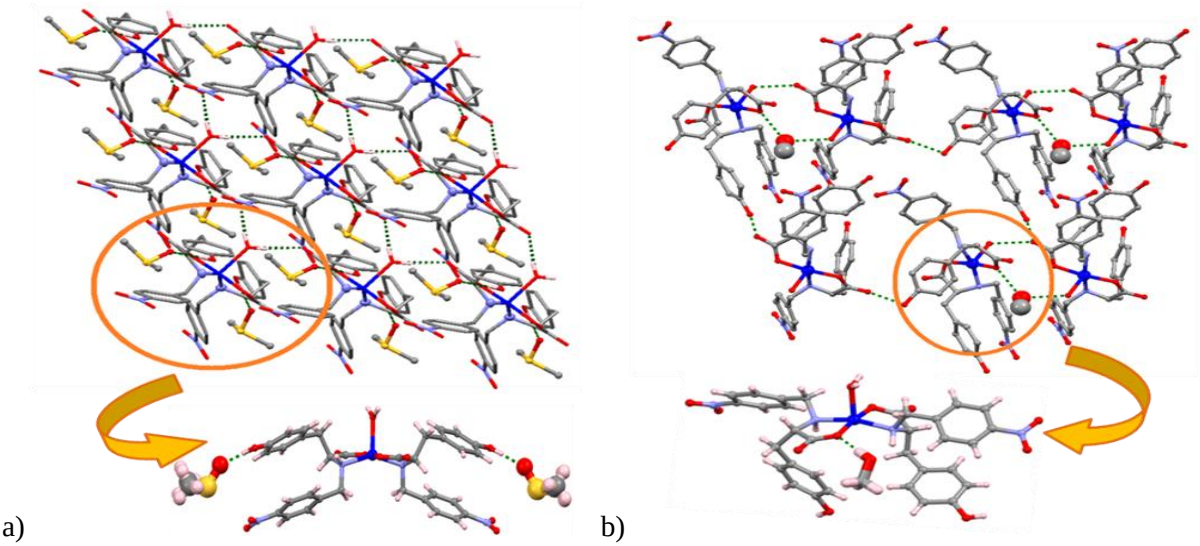

a) b)

Figure 3.33. 2D supramolecular assembly in (a) **23a** and (b) **23b**.

One of the phenolic oxygen atoms (O1) of the dimeric synthon in one of the 1D supramolecular chains is involved in an intermolecular hydrogen bonding interaction with the uncoordinated oxygen atom (O2) of the carboxylate group of the ligand in another 1D supramolecular chain (O1---O2 distance: 2.708 Å). Further strengthening of this 2D network is provided by the intermolecular π–π interaction between the π-nitrobenzyl rings of the ligands and several C-H…O interactions. Furthermore, the DMSO solvate has been found to be preferred over methanol solvate through (a) the conversion of the methanol solvate to the DMSO solvate in dissolving the single crystals of the former in DMSO and (b) exclusive formation of the DMSO solvate from crystallizing $[Cu(L\text{-}HTyr4\text{-}NO_2)_2(H_2O)]\cdot 2H_2O$ in a mixture of DMSO/methanol (1:1, v/v). The crystallographic parameters and basic information pertaining to data collection and structure refinement for **23a** and **23b** is summarized in Table A2. All hydrogen bonding parameters for **23a** and **23b** are listed in Table 3.7.

Table 3.7. Hydrogen bonding parameters for **23a** and **23b**.

D-H..A	r(D-H) (Å)	r(H..A) (Å)	r(D..A) (Å)	∠D-H..A (°)	Symmetry
23a					
O1-H1..O4	0.84	1.89	2.734(6)	171	1/2-x,1/2+y,1-z
O7-H7..O6	0.82	1.83	2.650(6)	176	1-x,y,-z
C7-H7B..O4	0.97	2.34	3.299(6)	168	1/2+x,-1/2+y,z
C18-H18B..O(6)	0.96	2.59	3.401(9)	143	1/2-x,-1/2+y,-z
23b					
O6-H6..O7	0.82	2.03	2.810(7)	158	2-x,1/2+y,1-z
O1-H1A..O2	0.82	1.90	2.708(8)	163	1-x,-1/2+y,-z
O11-H11B..O12	0.85	1.96	2.781(8)	164	1+x,y,-1+z
O11-H11A..O2	0.84	1.88	2.631(7)	147	2-x,-1/2+y,-z
O12-H12A..O8	0.82	2.23	2.749(7)	152	1-x,1/2+y,1-z
C18-H18..O7	0.93	2.57	3.270(9)	132	2-x,1/2+y,1-z
C8-H8..O1	0.98	2.55	3.296(9)	133	1-x,1/2+y,-z
C3-H3.. O7	0.93	2.51	3.431(10)	168	2-x,1/2+y,-z
C34-H34B..O5	0.96	2.48	3.420(14)	167	x,y,1+z

Crystal structure of [Zn(HTyrtnitro)$_2$(H$_2$O)]·2DMSO (25a). To explore the role of metal ions in the architecture of the complexes, Cu^{2+} in **23a** is replaced by Zn^{2+} giving rise to [Zn(HTyrtnitro)$_2$(H$_2$O)]·2DMSO (**25a**) crystallizing in the monoclinic chiral space group $P2_1$. The asymmetric units of **23a** and **25a** except for different metal ions (Cu^{2+} vs Zn^{2+}) are identical even with the orientation of the ligands (as shown in Figure 3.34). In **25a**, the coordination environment around Zn^{2+} with a distorted square pyramidal geometry is O_3N_2 type; out of four equatorial sites, two are occupied by the nitrogen atoms of the amine group and the other two are occupied by the oxygen atoms of the monodentate carboxylates of the ligands. The apical site is occupied by the oxygen atom of the coordinated water molecule (as shown in Figure 3.35). To explore the role of metal ions in the architecture of the complexes, **23a** and **25a** are ardently analyzed. Except the presence of a 2-fold axis passing through the metal ion center and the coordinated water molecule in **23a**, the supramolecular architecture of **23a** and **25a** are identical.

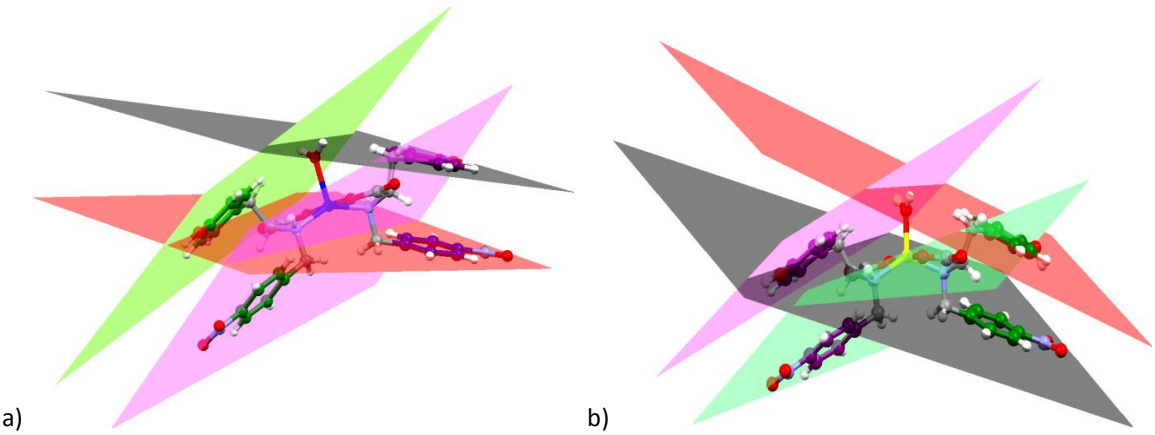

Figure 3.34. Comparative structural studies of the asymmetric units of (a) **23a** and (b) **25a**. One pair of parallel planes is shown in red and black and other in pink and green.

The strong intermolecular bifurcated hydrogen bonding between the oxygen atom of the coordinated water and uncoordinated oxygens of two different carboxylates of two different ligands (O1---O4 distance: 2.734 Å in **23a**; O1---O3 distance: 2.575 Å and O1---O5 distance: 2.575 Å in **25a**) generates a 2D supramolecular array (as shown in Figure 3.36). This 2D array is further strengthened by another pair of hydrogen bonding interactions between oxygen atom (O7 in **23a** and O8 in **25a**) of the phenol part of the ligand and the oxygen atom

(O6 in **23a** and O12 in **25a**) one of the lattice DMSO molecules (O6---O7 distance: 2.650 Å in **23a**; O8---O12 distance: 2.657 Å in **25a**) (as shown in Figure 3.37).

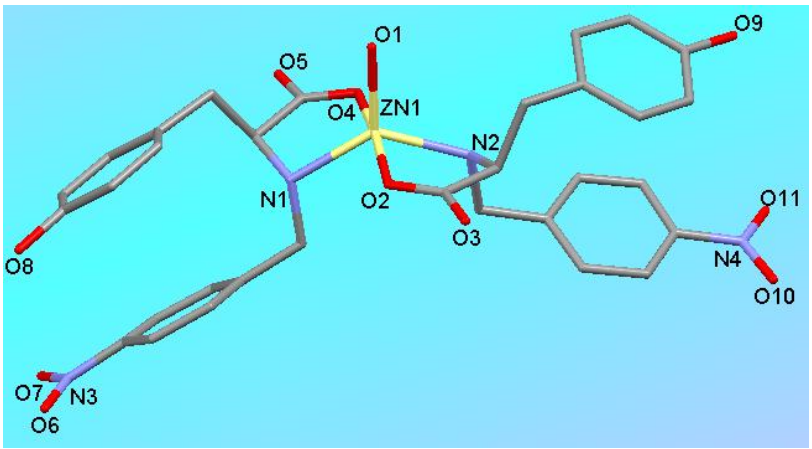

Figure 3.35. Asymmetric unit of **25a** (lattice DMSO molecules are omitted for clarity)

Along with these hydrogen bonding interactions, strong C-H…O interactions between methyl group of the DMSO molecule and oxygen atom of the nitro group (C18-H18C---O3 distance: 3.367 Å in **23a**; C33-H33c---O12 distance: 3.349 Å and C36-H36a---O13 distance: 3.371 Å in **25a**) enables the two aromatic rings (phenyl and nitrobenzyl ring) of each coordinated ligand to arranged parallel to each other which are well evident from the intramolecular π–π interactions present within **23a** and **25a**. Further increase in the dimentionality is obtained by the strong C-H..O interactions within the alternatively arranged DMSO molecules (C17-H17B---O6 distance: 3.417 Å, C18-H18B---O6 distance: 3.406 Å in **23a** and C34-H34b---O7 distance: 3.324 Å, C35-H35a---O13 distance: 3.383 Å in **25a**). The intermolecular C-H…O interactions within DMSO molecules forms a 1D chain (Figure 3.38). The hydrogen bonding interactions along with strong C-H..O interactions encapsulate this 1D DMSO chain within the 2D array of **25a** (Figure 3.39).

Thus a change in the center metal ion, neither change orientation of various ligands in the asymmetric unit nor does it affects the overall geometry of the supramolecular architecture**.** Although a small modulation is observed in the bond lengths and bond angles around Zn^{2+} in **25a** compared to Cu^{2+} in **23a**. In **23a** both Cu-O_{carb} distances are 1.919(3) Å whereas Zn-O_{carb} distances in 25a are 2.033(11) and 2.050(10) Å. Similarly, both Cu-N_{amine} distances in **23a**

are 2.022(4) Å whereas Zn-N_{amine} distances in **25a** are 2.083(11) and 2.089(12) Å. In both cases, as expected the distances around Zn^{2+} are a bit longer than that of Cu^{2+}; however, the Zn-$O_{coordinated\ water}$ (1.980(12) Å) distance is shorter as compared to Cu-Ocoordinated water

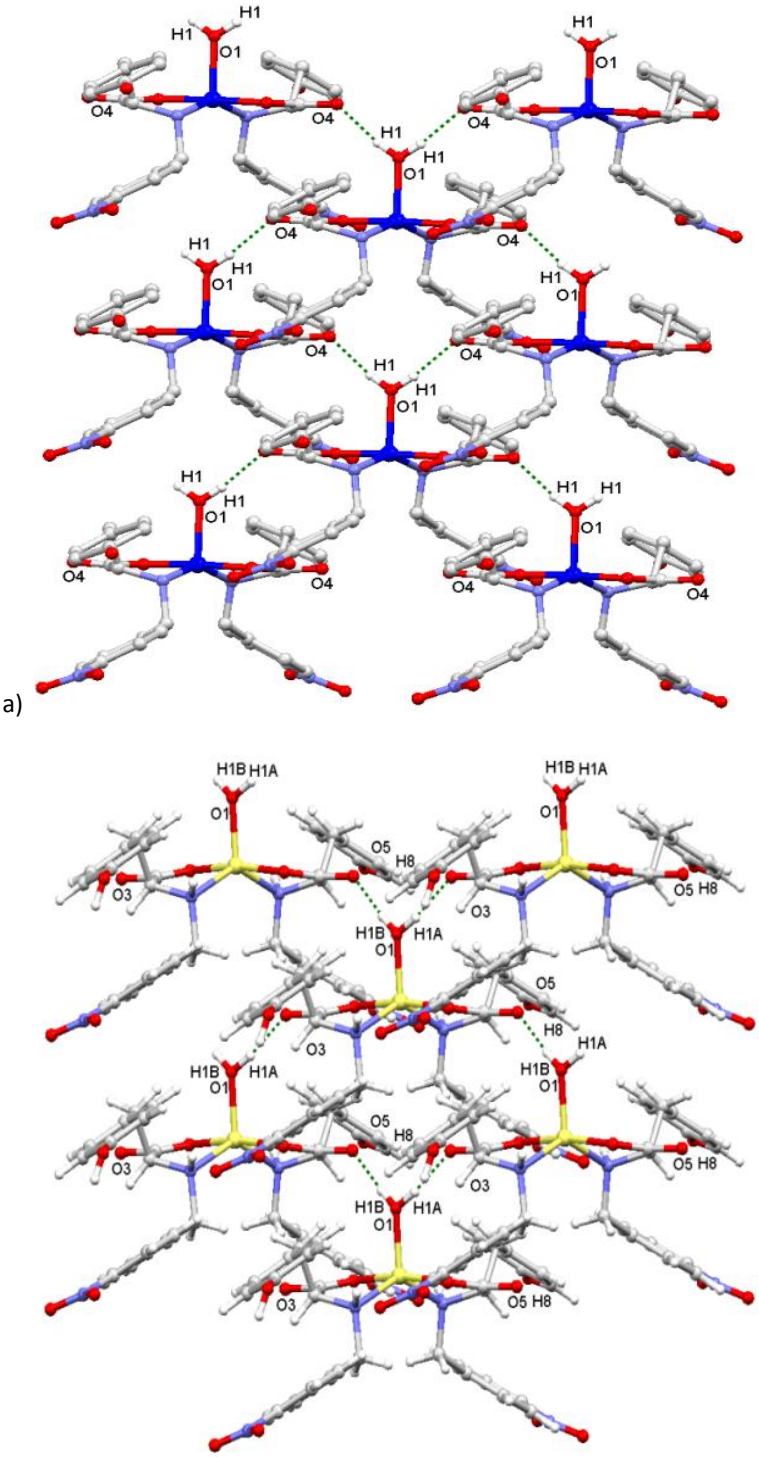

Figure 3.36. 2D sheet in (a) **23a** and (b) **25a**.

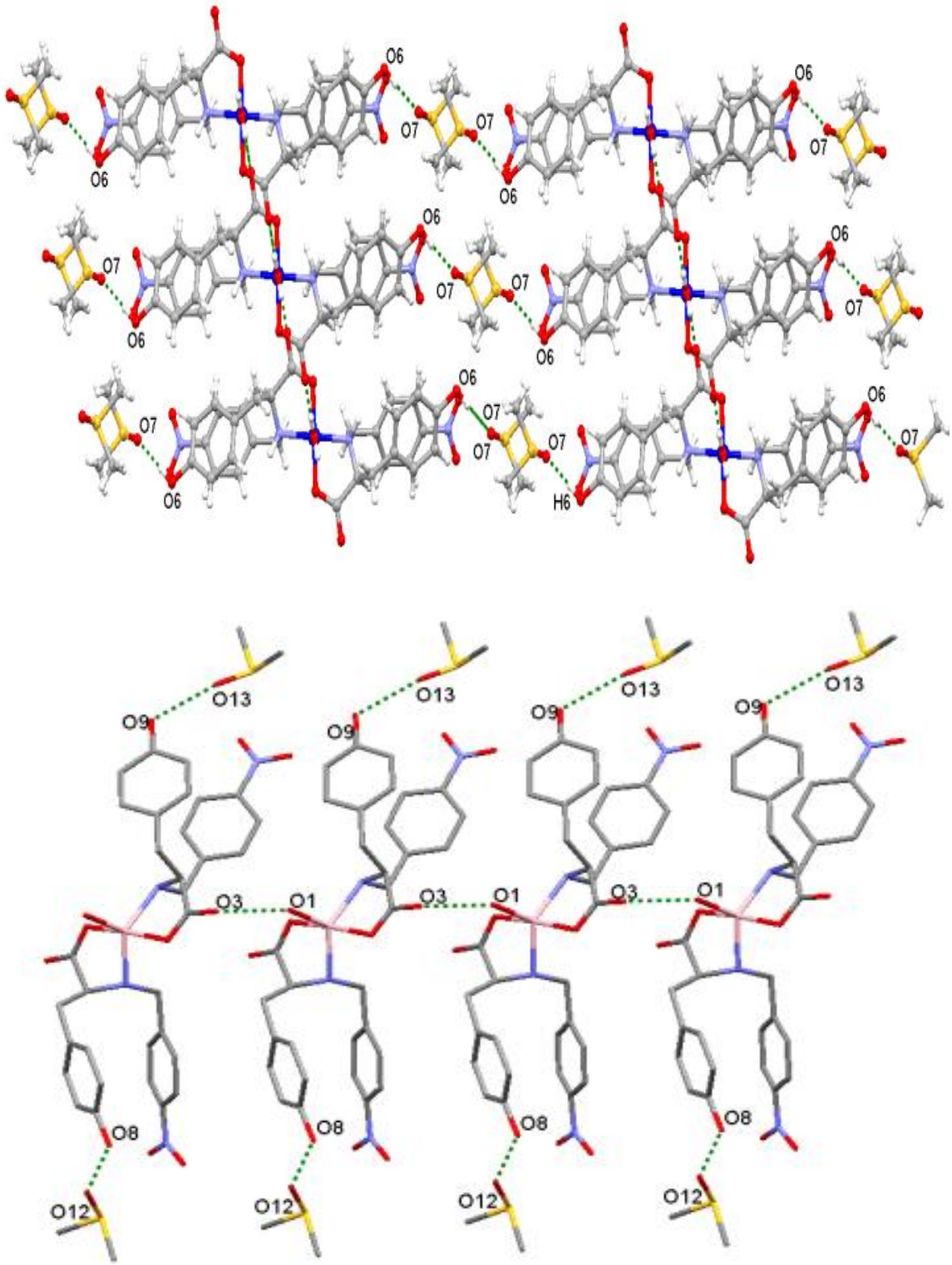

Figure 3.37. Interaction of the 2D sheet with DMSO molecule in **23a** (top) and **25a** (bottom).

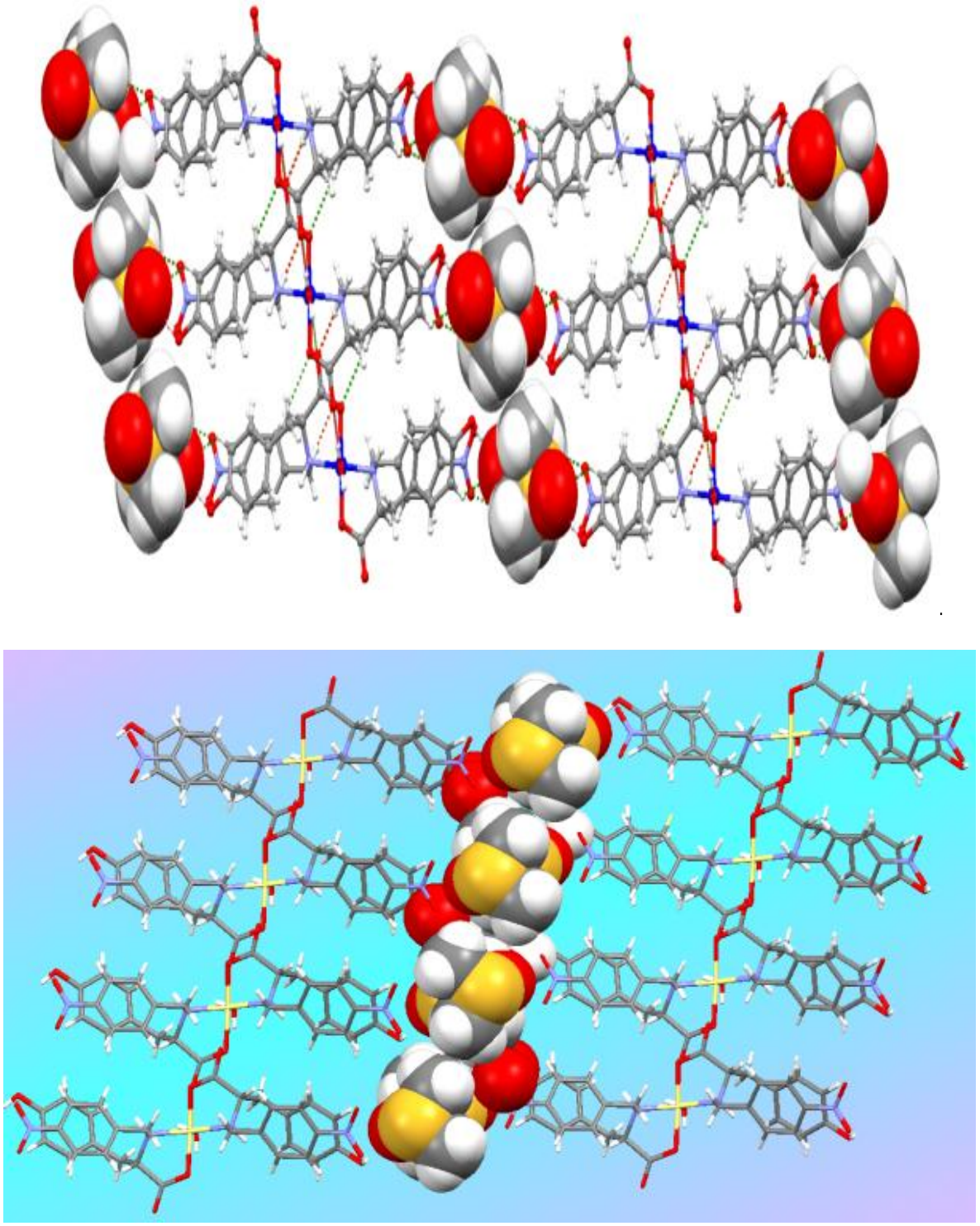

Figure 3.38. Encapsulation of the DMSO cluster within the 2D supramolecular array in **23a** and **25a.**

(2.183(6) Å) distance. The bond angles in **23a** are also slightly different from **25a.** In **23a**, all four bond angles almost ∠Ocarb-Cu-N_{amine} are 94.68(13)˚, 84.40(13)˚, 94.68(13)˚ and 84.40(13)˚, whereas the corresponding angles in **25a** (∠O_{carb}-Zn-N_{amine}), are 91.9(4)˚, 81.6(4)˚, 108.6(6)˚ and 82.2(4)˚, respectively. The two angles related to coordinated water (∠O_{carb}-metal ion-$O_{coordinated\ water}$) are 96.3(5)˚ and 93.2(5)˚ in **39a** but both are 91.61(15)˚ in **23a**. The selected bond lengths and bond angles for **25a** are tabulated in Table A7 and A11, respectively. The crystallographic parameters and basic information pertaining to data collection and structure refinement for **25a** is summarized in Table A3. All hydrogen bonding parameters for **25a** are listed in Table 3.4.

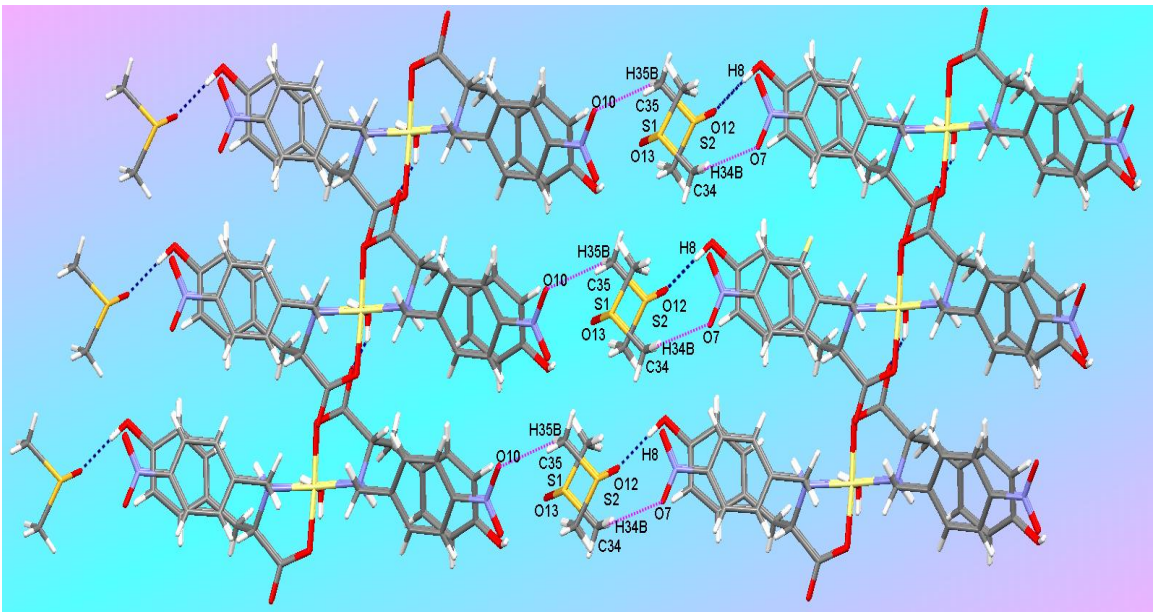

Figure 3.39. Hydrogen bonding and C-H..O interactions in **25a**.

Crystal structures of [Cu(HTyrfluoro)$_2$(H_2O)]·H_2O (27a) and [Cu(HTyr4-methoxy)$_2$(CH_3OH)] (31a). To demonstrate the role of various functional groups attached to the ligand on the formation of the framework, electron withdrawing nitro group in **23** is sequentially replaced by an electron withdrawing fluoro group and an electron donating methoxy group to form [Cu(HTyrfluoro)$_2$(H_2O)]·2H_2O (**27**) and [Cu(HTyr4-methoxy)$_2$(CH_3OH)]·3H_2O (**31**), respectively. Compounds **27** and **31** crystallize as [Cu(HTyrfluoro)$_2$(H_2O)]·H_2O (**27a**) and [Cu(HTyr4-methoxy)$_2$(CH_3OH)] (**31a**) in the chiral monoclinic space group *C*2 Even though crystals of **27a** and **31a** are grown from methanol

similar to **29b**, the asymmetric units of **27a** and **31a** are totally different from **23b** (as shown in Figure 3.40). The asymmetric unit of **27a** consists of two independent mononuclear entities along with a lattice water molecule (as shown in Figure 3.41). Unlike **23b** where none of the aromatic moieties shows π–π interaction, one of the mononuclear units in **27a** does show π–π interaction. One of the ligands in the mononuclear unit has the hydroxyl benzyl and nitrobenzyl moieties parallel to each other. The asymmetric unit in **31a** resembles more like **23a** (from DMSO) than **23b** (from methanol) with hydroxyl benzyl and nitrobenzyl rings of each ligand being parallel to each other. To have a deeper insight into the role of various substituent groups in the ligand on the architecture of these metal complexes, a thorough comparative study of **27a** and **31a** was carried along with **23b**. After crystallizing from the same solvent; the asymmetric unit of **27a** and **23b** are quite different. However, the overall supramolecular architecture of **27a** and **23b** are in resemblance with each other.

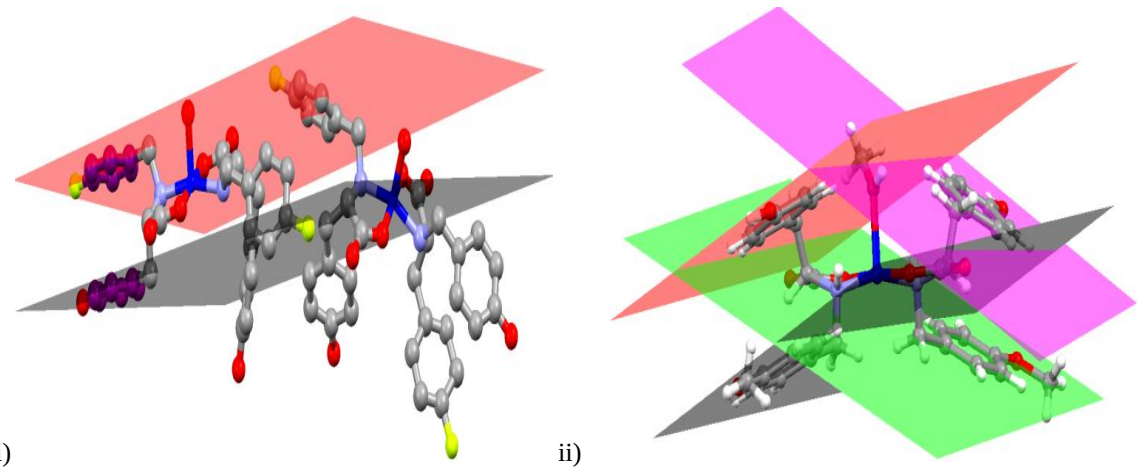

i) ii)

Figure 3.40. Comparative structural studies of the asymmetric units of (i) **27a** and (ii) **31a**. One pair of parallel planes showed in red and black and other pair in pink and green.

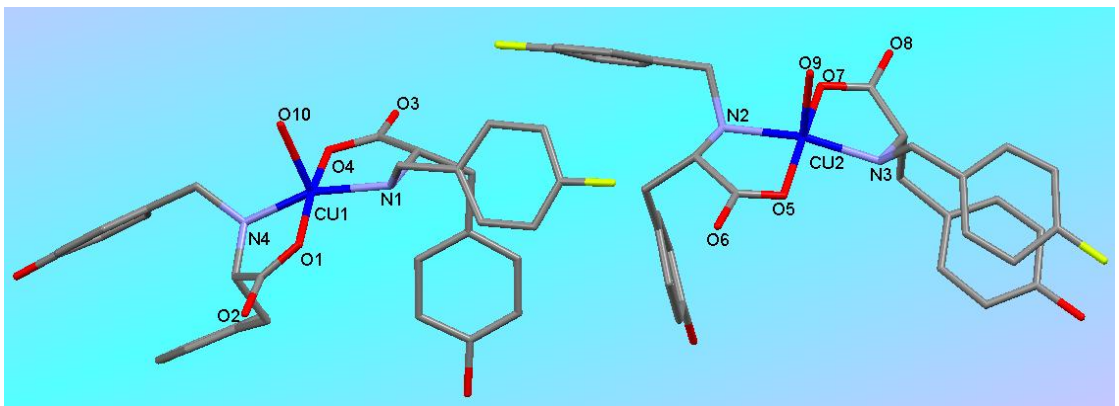

Figure 3.41. Asymmetric unit of **27a** (lattice solvent molecules are omitted for clarity).

In **23b**, the uncoordinated oxygen atoms (O2 and O7) of the two carboxylates in a mononuclear unit are hydrogen bonded to the oxygen atom (O11) of the coordinated water (O2---O11 distance: 2.636 Å) and the oxygen atom (O6) of phenol (O7---O6 distance: 2.089 Å) of two different mononuclear units respectively, giving rise to a 1D chain. This 1D chain is further hydrogen bonded in an intermolecular fashion to the lattice methanol molecule giving a porous structure within this chain. The oxygen atom (O12) of the lattice methanol shows a bifurcated hydrogen bonding with the uncoordinated oxygen atom (O8) of the carboxylate (O---O distance: 2.748 Å) of one mononuclear unit and the oxygen atom (O11) of the lattice water molecule (O---O distance: 2.786 Å). Similarly in **27a**, one of the independent mononuclear units in the asymmetric unit tends to form a supramolecular 1D chain via the participation of the lattice water molecules as well. The oxygen atom (O18) of lattice water molecule binds to coordinated oxygen atom (O4) of the carboxylate (O4---O18 distance: 2.726 Å) as well as to the oxygen atom of the (O10) coordinated water of another subunit (O10---O18 distance: 2.769 Å). The mononuclear subunits are further hydrogen bonded to each other through the uncoordinated oxygen atom (O2) of the carboxylate and the oxygen atom (O10) of the lattice water molecule (O2---O10 distance: 2.648 Å) (as shown in Figure 3.42).

The other mononuclear unit in **23a** also forms a similar 1D supramolecular chain; however in this case there is no involvement of the lattice solvent molecules. The oxygen atom (O8) of the uncoordinated carboxylate of the ligand is hydrogen bonded to the oxygen atom (O9) of the coordinated water (O---O distance: 2.731 Å) in an intermolecular fashion. Thus, in **27a** both the independent mononuclear moieties shows intermolecular hydrogen bonding with moieties of its own kind forming two classes of 1D supramolecular chains. In both kinds of chains in **27a** as well as 1D chain in **23b**, the adjacent mononuclear units have their bound water pointing towards each other (as shown in Figure 3.43)

The two classes of 1D supramolecular chain in **27a**, which differ in their assortment of the moieties, are interwoven with each other resulting in a 2D supramolecular network. A pair of interchain hydrogen bonding is well observed between the uncoordinated oxygen atom (O8 and O3) of the carboxylate and the phenolic oxygen atom (O11 and O12) of the ligands (O8--

-O11 distance: 2.626 Å and O3---O12 distance: 2.654 Å, respectively). This interchain hydrogen bonding in **27a** is similar to that observed in **23b**, where the phenolic oxygen atom (O1) in one of the 1D chain is hydrogen bonded to the uncoordinated oxygen atom (O2) of the carboxylate of the next 1D chain (O---O distance: 2.709 Å) to give rise to a 2D supramolecular network (as shown in Figure 3.44). The 2D supramolecular network in **27a** is further strengthening by intermolecular π–π interactions (as shown in 3.45).

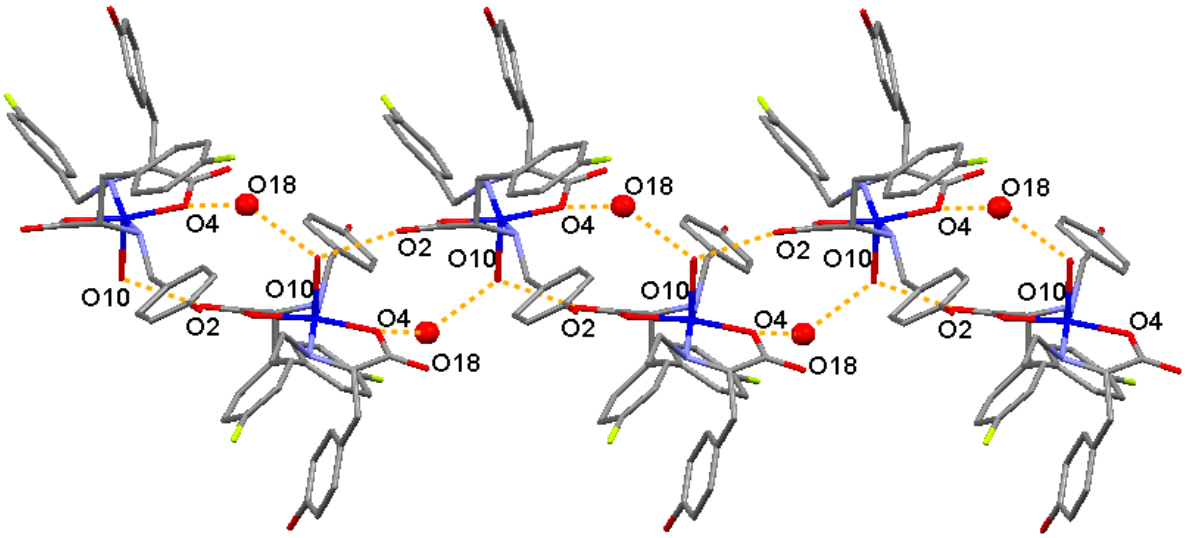

Figure 3.42. Hydrogen bonded mononuclear units in **27a** forming a 1D supramolecular chain.

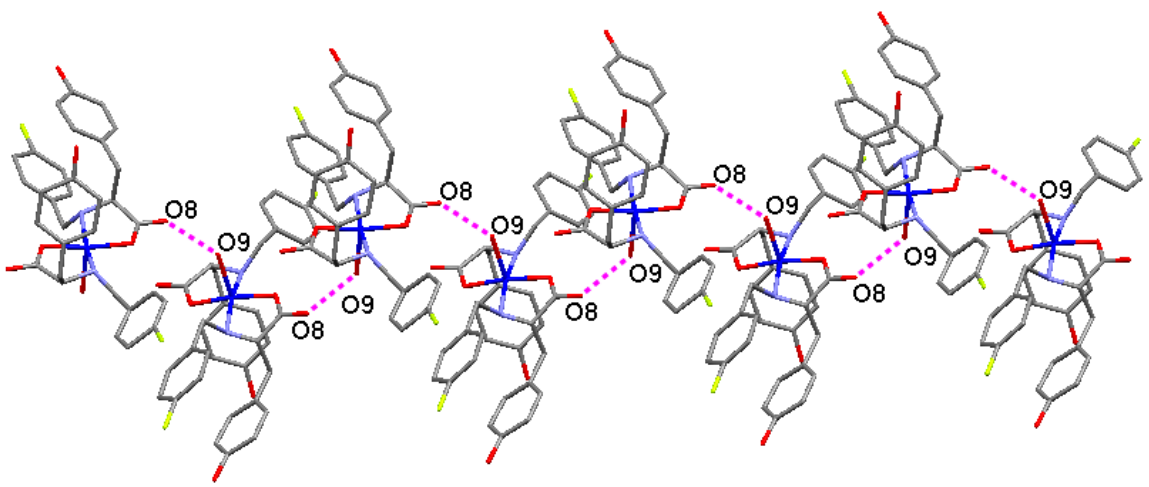

Figure 3.43. Another supramolecular 1D chain formed in **27a**.

In **27a**, an additional reinforcement to the supramolecular network is provided by an intra molecular π–π bonding along with O-H...F (O---F distance: 2.749 Å) and C-H...F (C---F

distance: 3.14 & 3.20 Å) interactions. Hence, going from para substitution of one electron withdrawing group (nitro) to another (fluoro) in the ligand does not affect the overall structural assortment of the 2D array of these metal complexes even though a remarkable change is observed in the asymmetric units of **23b** and **27a**. The crystallographic parameters and basic information pertaining to data collection and structure refinement for **27a** is summarized in Table A3. The selected bond distances and bond angles for **27a** are listed in Tables A7 and A11, respectively. All hydrogen bonding parameters for **27a** are listed in Table 3.8.

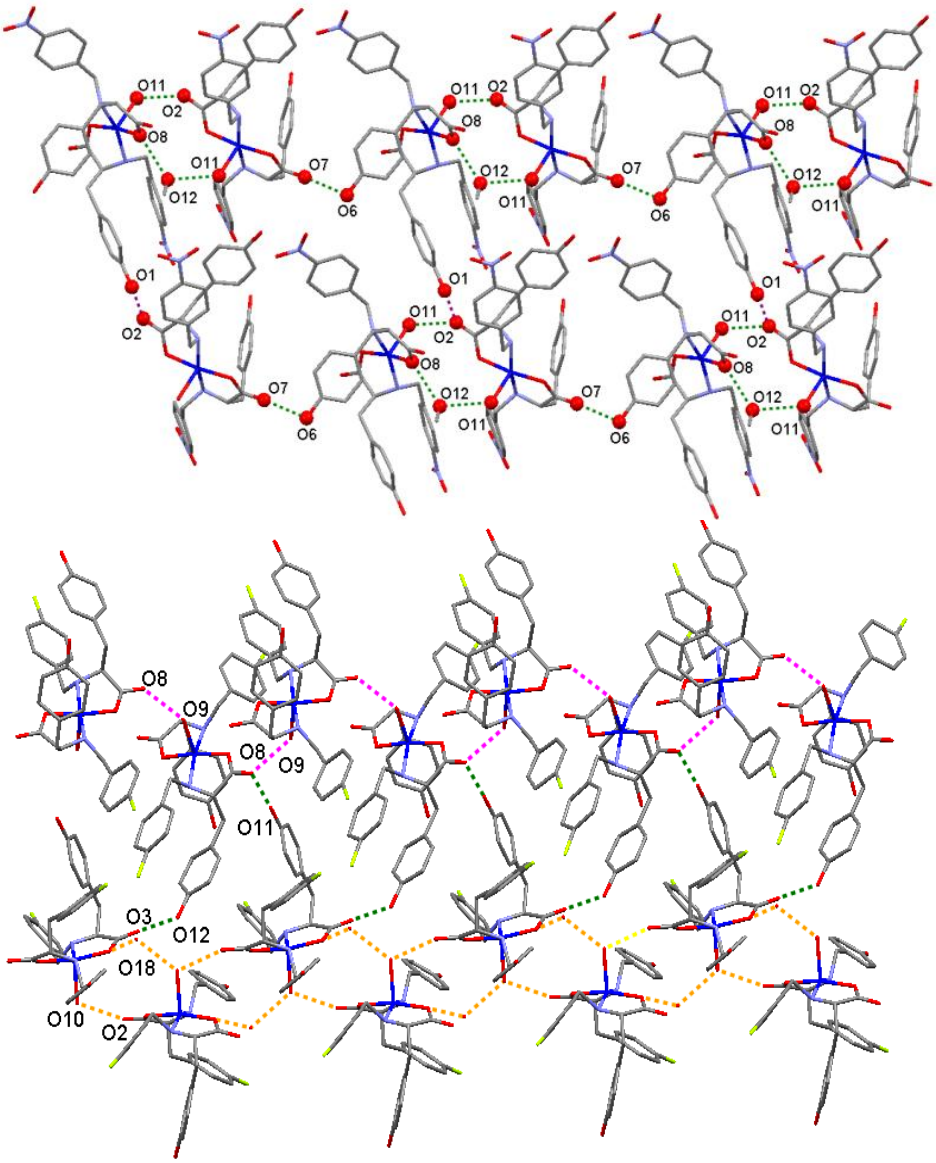

Figure 3.44. 2D supramolecular network in (a) **23b** and (b) **27a**.

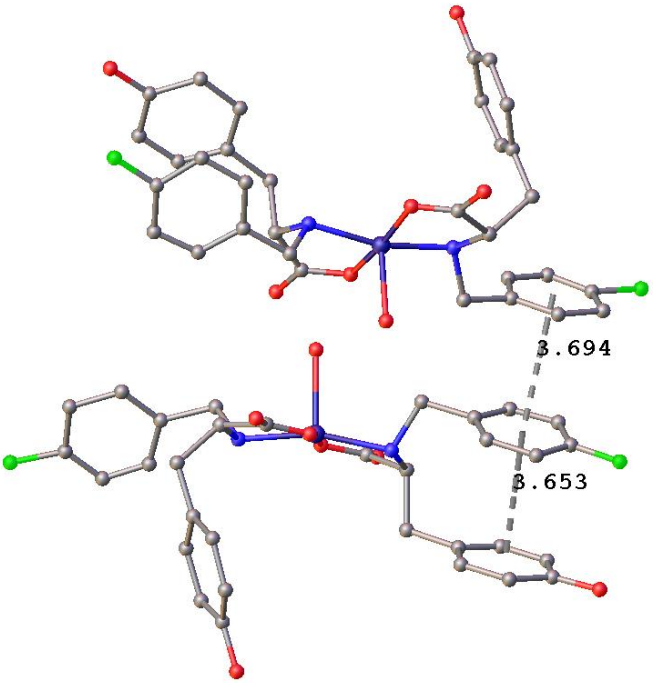

Figure 3.45. π–π interactions in **27a**.

However, a comparison between **23b** and **31a** clearly shows a remarkable difference in the asymmetric units as well as in the overall supramolecular arrays. The adjacent mononuclear units in **31a** have their bound water pointing in the same direction as contrast to that in **23b** where they point towards each other. Similar to **23b**, each mononuclear unit in **31a**, proliferates in both x and y directions by the intermolecular hydrogen bonding. The growth in x-direction proceed by the intermolecular hydrogen bonding between oxygen atom (O2) of the uncoordinated carboxylate of the ligand and the oxygen atom (O1) of the phenolic group of the ligand (O---O distance: 2.730 Å) whereas in y-direction proliferation takes place by the intermolecular hydrogen bonding between oxygen atom (O6) of the other uncoordinated carboxylate of the ligand and the oxygen atom (O9) of the coordinated methanol molecule (O---O distance: 2.714 Å)(as shown in Figure 3.46).

The interwining of these 1D supramolecular chains in **31a** to give rise to a 2D supramolecular array (as shown in Figure 3.47) is entirely different from the supramolecular array formed in **23a**.These interactions are further reinforced by intramolecular as well as intermolecular π–π interactions in 4a (as shown in Figure 3.48). The selected bond distances and bond angles for **31a** are listed in Tables A7 and A12, respectively.

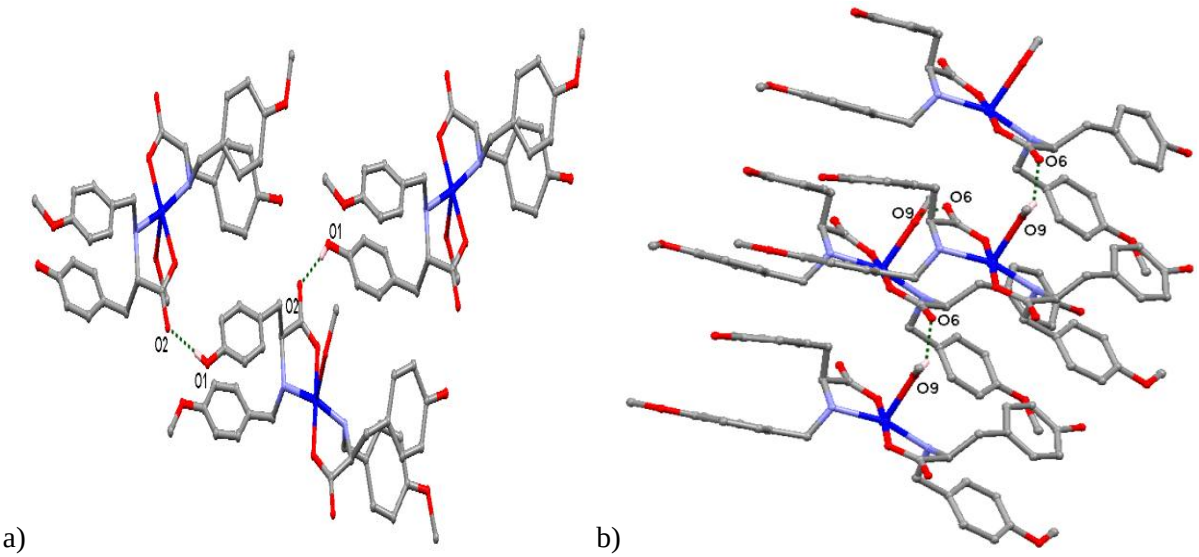

a) b)

Figure 3.46. Growth of supramolecular chains in (a) x-direction and (b) y-direction in **31a.**

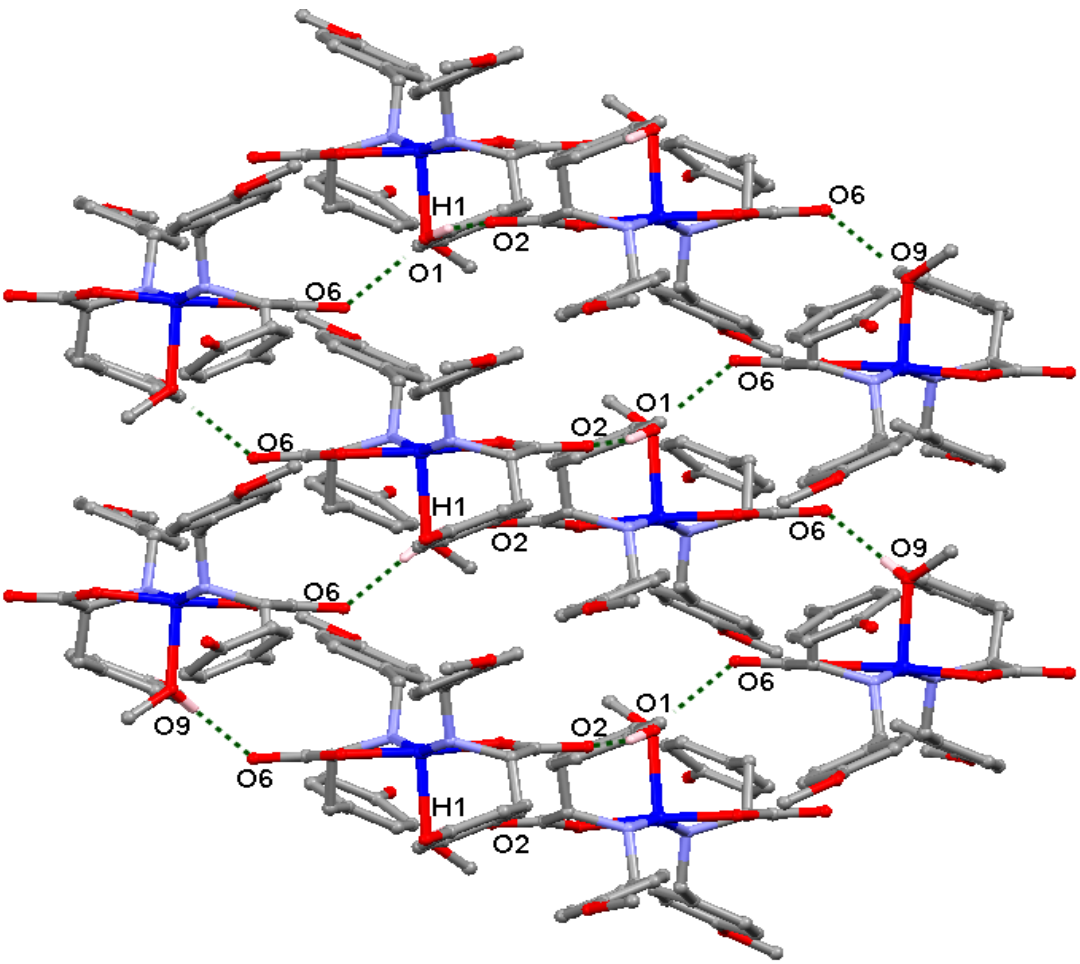

Figure 3.47. 2D supramolecular array in **31a**.

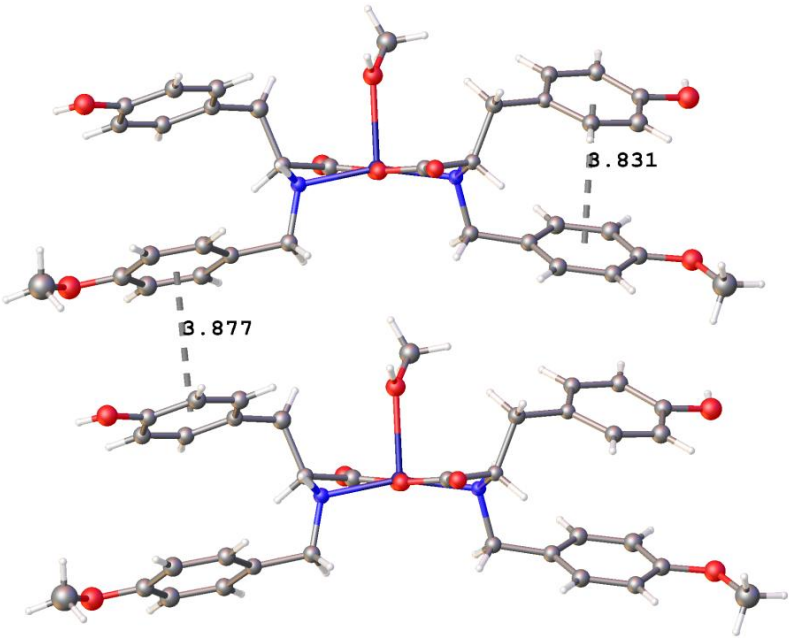

Figure 3.48. π−π interaction in **31a**.

In above cases (**23a**, **23b**, **27a** and **31a**), the metal center acquires a distorted square pyramidal geometry with O_3N_2 type coordination environment completed by one coordinated solvent molecule and two oxygen atoms of carboxylates and two nitrogen atoms of amines from two respective ligands (an oxygen and a nitrogen from each). Both the carboxylates coordinate to the metal center in a monodentate fashion. The lengths of Cu−N bonds and Cu-O are in the range of 1.998(14) - 2.022(4) Å and 1.919(3) - 2.183(6) Å, respectively (Table S2 of appendix). All hydrogen bonding parameters for **27a** and **31a** are listed in Table 3.8. All this orientation of the ligands around the metal ion is dictated by the various supramolecular interactions present in the compounds.Hence, replacement of an electron withdrawing (nitro) group in **23** with another electron withdrawing (fluoro) group does change the assortment of the asymmetric unit; however, the overall framework remains same with smaller alteration whereas the replacement of an electron withdrawing (nitro) group in **23** with a electron donating (methoxy) group not only changes the orientation of the ligands in the asymmetric unit but also the overall framework. This confirms that the orientation of the ligands around the metal ion in the asymmetric unit as well the overall architecture is dictated by the various substituents present in the ligand used in formation of the metal complexes. In addition to the detailed comparison of their spectroscopic data and TGA scans,

the crystallographic characterization of the Cu^{2+} analogs demonstrates such diversification due to change in ligands. The coordination architecture in each case is highly influenced by parameters like the substitution on the ligands, the solvent of crystallization, etc.

Table 3.8. Hydrogen bonding parameters for **25a, 27a** and **31a.**

D-H…A	r(D-H) (Å)	r(H…A) (Å)	r(D…A) (Å)	∠D-H…A (°)	Symmetry
25a					
O1S-H1SB..O1	0.85	1.90	2.730(6)	166	1-x,1/2+y,1-z
N2-H2..O1S	0.98	2.23	3.009(6)	135	1-x,1/2+y,1-z
O1S-H1SA..O1	0.86	2.57	3.195(7)	131	1+x,y,-1+z
O1S-H1SA..O2	0.86	1.95	2.787(6)	165	1+x,y,-1+z
O3-H3..O1S	0.82	1.87	2.672(7)	167	x,y,1+z
O6-H6..O4	0.84	2.24	3.035(7)	156	-1+x,y,z
O6-H6..O5	0.84	2.29	3.018(7)	145	-1+x,y,z
27a					
O1-H2..O7	0.82	1.86	2.672(6)	168	x,-1+y,z
O6-H5..O8	0.82	1.84	2.652(8)	171	1-x,-1/2+y,-z
O8-H12C..O7	0.75	2.31	3.049(7)	169	
O8-H12D..O5	0.87	2.17	2.985(8)	157	-x,1/2+y,-z
O7-H51..O2	0.82	1.86	2.667(8)	167	
C5-H20..O6	0.93	2.53	3.263(8)	136	1-x,-1/2+y,-z
C10-H26B..O5	0.97	2.43	3.317(6)	152	-x,1/2+y,-z
31a					
O1-H1..O1S	0.82	1.96	2.777(4)	171	-x,-1/2+y,1/2-z
O1S-H1SB..O6	0.85	2.03	2.864(4)	167	-x,-1/2+y,1/2-z
N1-H1A..O3S	0.98	2.56	3.516(4)	165	-1+x,y,z
N2 -H2..O2S	0.98	2.10	3.078(5)	172	-1/2+x,1/2-y,-z
O1S-H1SA..O2	0.85	1.91	2.752(4)	171	1/2-x,1-y,1/2+z
O2S-H2SB..O1S	0.85	2.11	2.953(5)	173	1-x,-1/2+y,1/2-z
O2S- H2SA..O3S	0.86	2.01	2.865(6)	177	
O5-H5..O3	0.82	2.24	2.972(4)	149	-1/2+x,1/2-y,-z
O3S-H3SB..O3	0.85	2.05	2.858(4)	159	
O3S -H3SA..O5	0.85	2.10	2.915(4)	161	1+x,y,z
C13-H13B..O4	0.97	2.44	3.322(5)	151	1/2+x,3/2-y,-z

With these monoanionic ligands, Cu^{2+} tend to form a pentacoordinated monomer where the two nitrogen (from amine group) and two oxygen (from the carboxylate group) from two homoligands fills the four equatorial positions forming two five membered stable moieties. The apical site if filled by a bridging carboxylate or a bridging side chain (like phenolic group in tyrosine), then the monomers grow into a coordination polymer. However, the

unavailablity of any of such bridging moieties would facilitates a water molecule to coordinate to the Cu^{2+}, which further can lead to hydrogen bonding with carboxylates of the next monomer thus forming a SCC.

Powder X-ray data analysis

To confirm whether the single crystal structure corresponds to the bulk material or not, powder X-ray diffraction patterns were recorded for those which show crystalline behaviour at room temperature. The experimental and simulated (from the single crystal data) patterns for **1**, **5**, **9**, **13, 17**, **27**, **29a, 29b, 33** and **37** were similar to each other (see Figure 3.49-3.54). The patterns obtained for all the Cu^{2+} coordination architectures confirm that the single crystal and bulk material are the same. It also confirms the phase purity of the bulk sample. Powder pattern of complexes without a crystal structure were recorded to check the crystalline nature of the compound. Even by comparing PXRD pattern of various complexes some structural aspects can be deduced even for the compounds without a crystal structure.

On comparing various metal analogues of H_2Tyrbenz (**1**, **3** and **4**), it is clear that the overall structural dimensions for the Zn and Cd complexes (**3** and **4**) are similar and that is quite distinct from the Cu analogue, **1** (as shown in Figure 3.49).

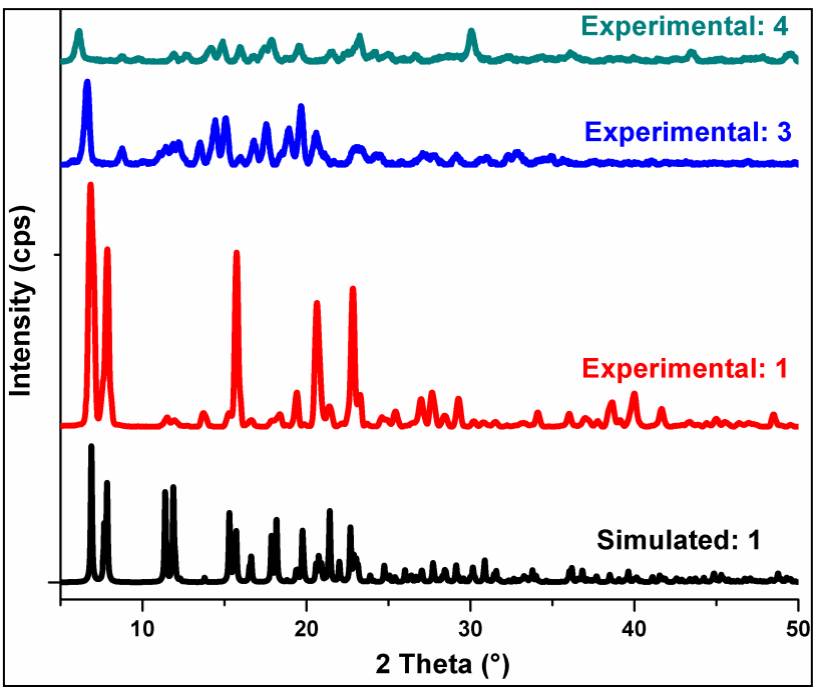

Figure 3.49. PXRD patterns of **1, 3** and **4**.

The crystal structure of **5** already shows a hexacoordinated Cu^{2+} and the similarity between the PXRD patterns of **5** and **7** suggests a probable hexacoordinated Zn^{2+} in **7**. On further comparing, **3** and **4** also show a striking similarity with **5**. This confirms that even with a change in the ligand system, the coordination environment around a metal ion and thus the overall coordination architecture decides the PXRD pattern of a complex. This fact is further proven by the variation of PXRD patterns of **1** and **5**. Even though both are carboxylate bridged CPs; however, the difference in the mode of bridging of the carboxylates (anti-anti vs anti-syn) and different coordination number of the central metal ion (Cu^{2+} in **1**: 5; Cu^{2+} in **5**: 6) (*vide infra*) brings out variation in the overall coordination architecture. For the serbenz ligand, however Ni^{2+} analogue (**6**) is quite distinct from **5** and **7** (as shown in Figure 3.50). The comparison of the PXRD patterns of other metal ion coordination architectures (**10**-**12**) with respect to their Cu^{2+} analogue (**9**) of HPhebenz ligand shows a similar structural pattern (as shown in Figure 3.51). This confirms that the all four architectures with HPhebenz ligand have same core structure irrespective of the metal ion. The small variations in the PXRD patterns are due to the change of the lattice solvent or the small modulation in the coordination atmosphere of the central metal ion. For **13**, not only the simulated and experimental patterns are in accordance with each other, even the conversion of **13** from **21** is confirmed by the PXRD (as shown in Figure 3.52). The PXRD pattern of **14** shows some similarity with the PXRD pattern of **13**.

The PXRD pattern for **17** is totally different from that of **18**, **19** and **20** suggesting a total different architecture of other analogues compared to the Cu analogue of the H_2tyr4-pyr ligand. Even though the similar PXRD pattern of **18** and **20** suggests a similar architecture of Ni and Cd analogue (as shown in Figure 3.53).

Comparing the Cu^{2+} complexes of thiophene derivative it is well seen that the PXRD pattern of **21** and **22** has some similarities, however due to the change of the aliphatic to aromatic side groups in amino acids (-CH_2OH in **21** and phenol in **22**) some variation also exists. In case of **22**, even though crystal structure is not available; PXRD pattern clearly suggests the crystalline nature of the architecture (as shown in Figure 3.54).

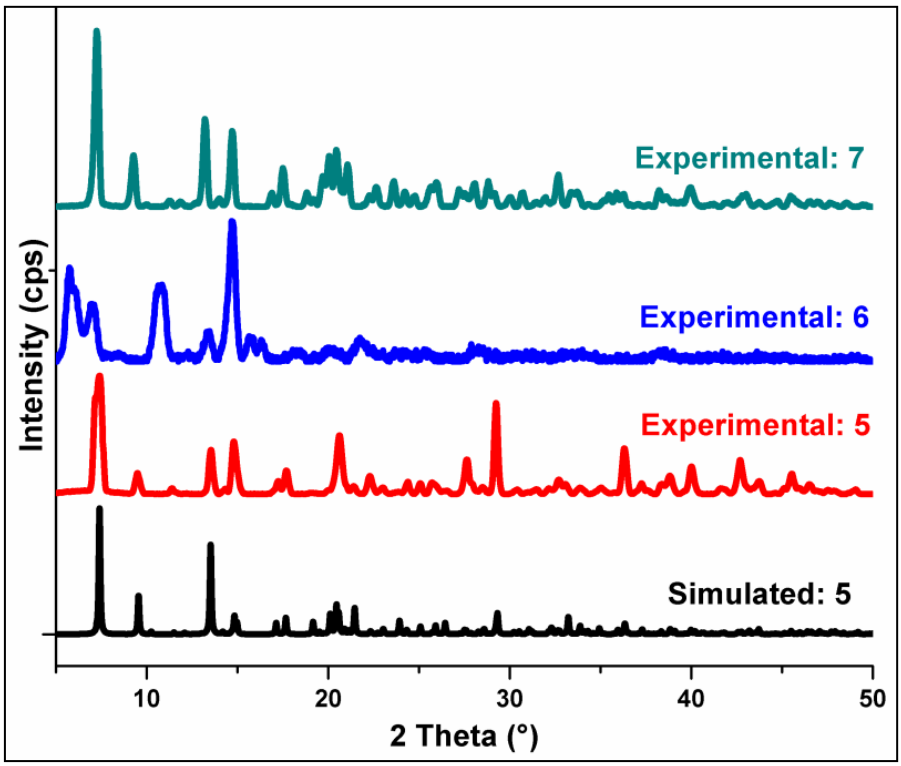

Figure 3.50. PXRD patterns of **5, 6** and **7**.

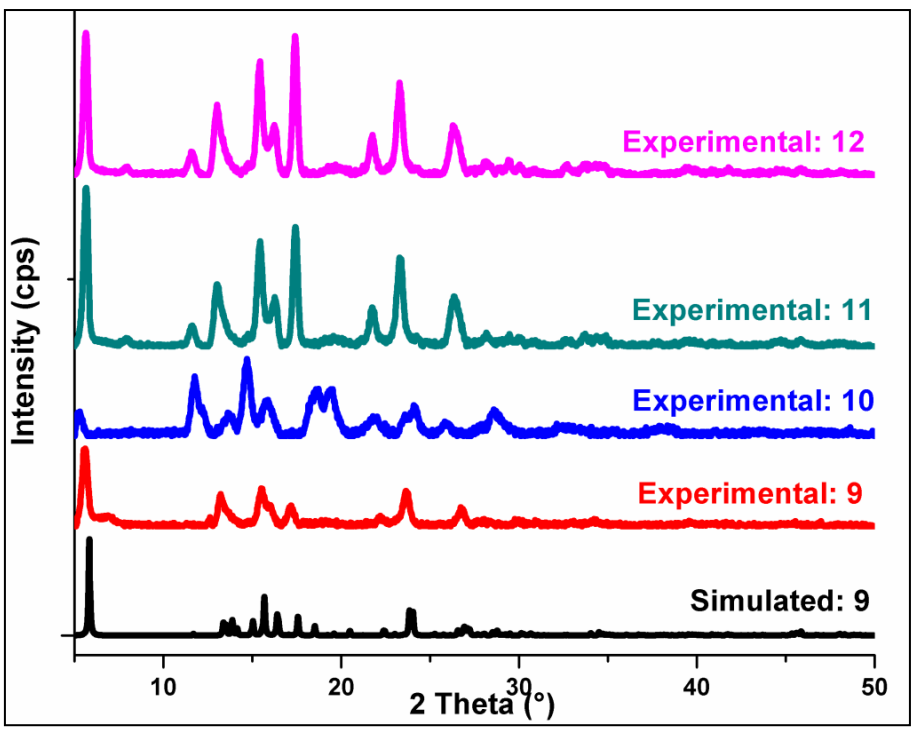

Figure 3.51. PXRD patterns of **9**, **10**, **11** and **12.**

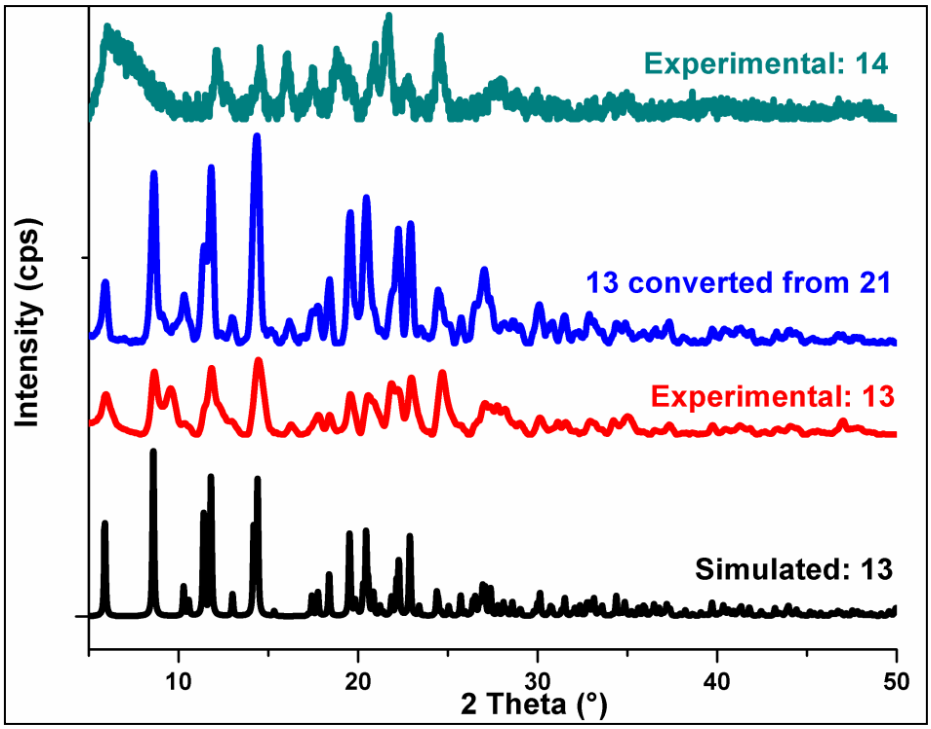

Figure 3.52. PXRD patterns of **13** and **14.**

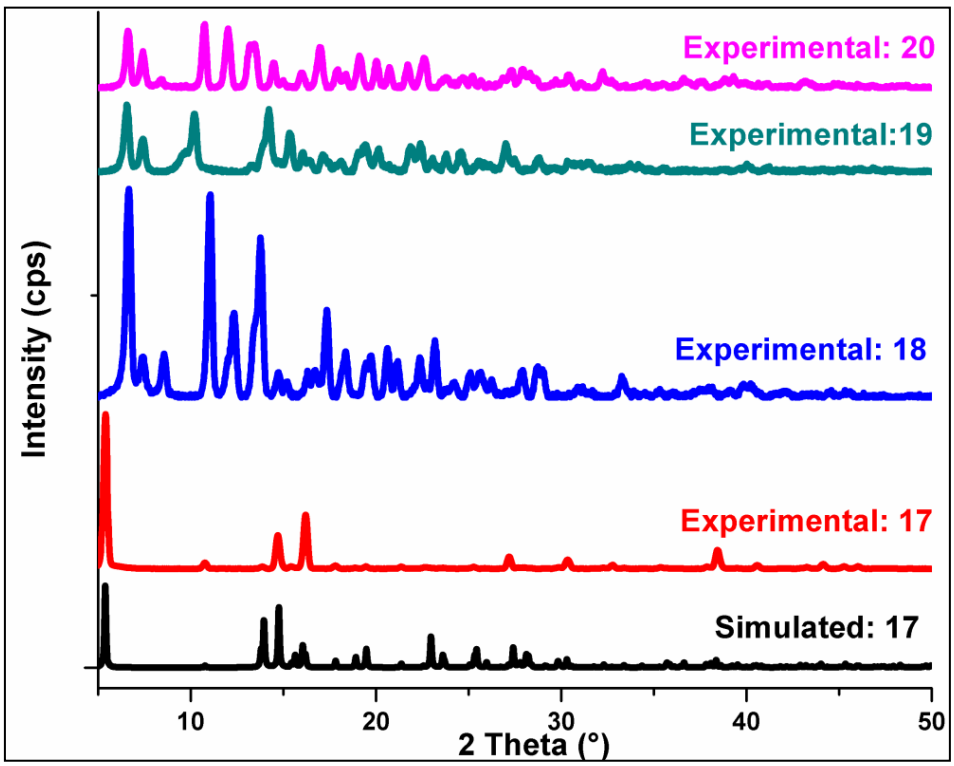

Figure 3.53. PXRD patterns of **17, 18, 19** and **20**.

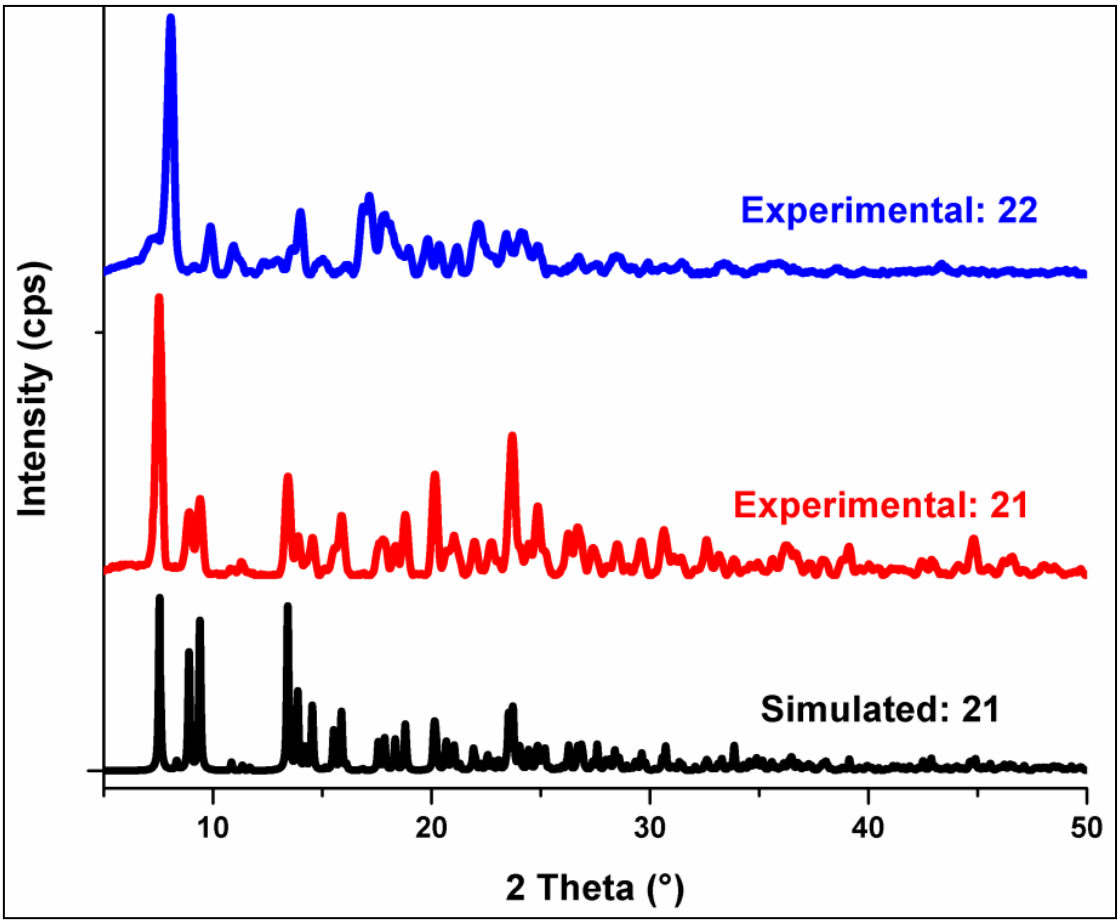

Figure 3.54. PXRD patterns of **21**and **22**.

A comparison of the PXRD patterns of coordination architectures with the ligands having different substituents (-NO_2, -F or -OCH_3) illustrates the influence of the ligands on generation of the overall network. In case of **23**, the solvate effect is well seen through the PXRD pattern of **23a** and **23b**. The similarity in the PXRD patterns of **23b** and **25** well corroborates with the similar crystal structure, whereas the similarity between **24** and **26** shows a similar architecture for Ni and Cd analogue (as shown in Figure 3.55). Again in case of coordination architectures with fluoro and methoxy substituents in the ligands, Cu analogues (**27** and **31**) show well accordance between their simulated and experimental PXRD patterns. Herein, the Ni and Zn analogues of H_2Tyrfluoro ligands (**28** and **29**), show similar PXRD patterns and thus a similar overall architecture (as shown in Figure 3.56).

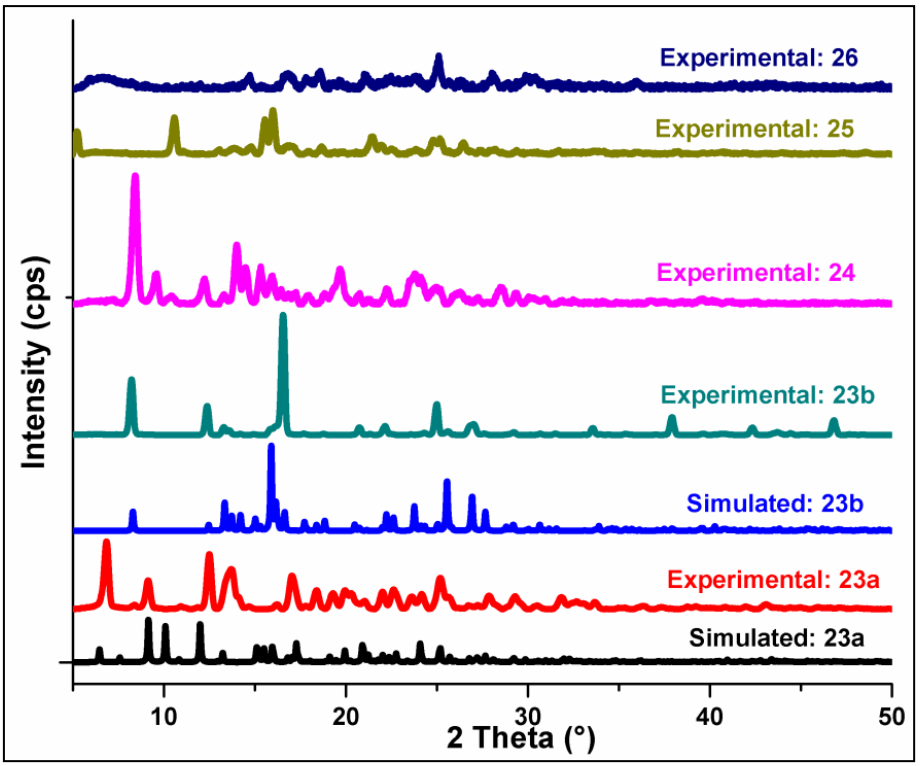

Figure 3.55. PXRD patterns of **23a, 23b, 24, 25** and **26.**

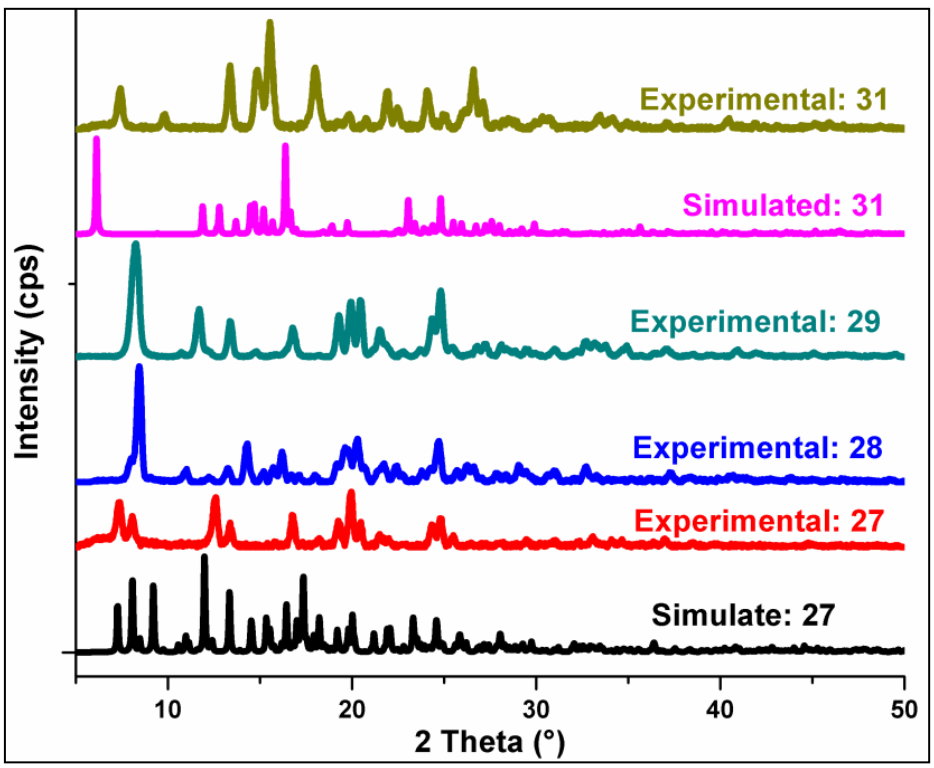

Figure 3.56. PXRD patterns of **27, 28, 29** and **31**.

UV-Vis and Circular Dichroism (CD) spectroscopy

UV-Visible and CD studies were carried using ~1 mM methanolic solution of Cu^{2+} and Ni^{2+} analogues of various coordination architectures**.** In the visible part of the spectra for Cu^{2+} compounds (**1**, **5**, **9**, **13**, **17**, **21**, **25**, **29**, **33** and **37**), major peaks are at 590 nm (ε = 159 $Lmol^{-1}cm^{-1}$), 589 nm (ε = 144 $Lmol^{-1}cm^{-1}$), 576 nm (ε = 125 L $mol^{-1}cm^{-1}$), 585 nm (ε = 200 $Lmol^{-1}cm^{-1}$), 600 nm (ε = 174 $Lmol^{-1}cm^{-1}$), 586 nm (ε = 152 $Lmol^{-1}cm^{-1}$) and 582 nm (ε = 153 $Lmol^{-1}cm^{-1}$), respectively (as shown in Figure 3.57a). These peaks are due to the d-d transition in Cu^{2+} (^2E_g to $^2T_{2g}$).[253] In the CD spectra (400-700 nm) for **1**, the positive Cotton effect is observed at 445 and 632 nm. The corresponding peaks for other complexes are as follows: **5**, 453 and 653 nm; **9**, 453 nm and 653 nm; **13**, 434 and 650 nm; **17**, 453 and 671 nm; **21**, 459 and 658 nm; **25**, 454 and 657 nm. For **1**, the negative Cotton effect is observed at 537 nm. The corresponding peaks for other complexes are as follows: **5**, 522 nm; **9**, 520 nm; **13**, 524 nm; **17**, 533 nm; **21**, 527 nm; **25**, 530 nm (as shown in Figure 3.57b). The peaks in the range of 520-540 nm are due to d-d transitions.[254]

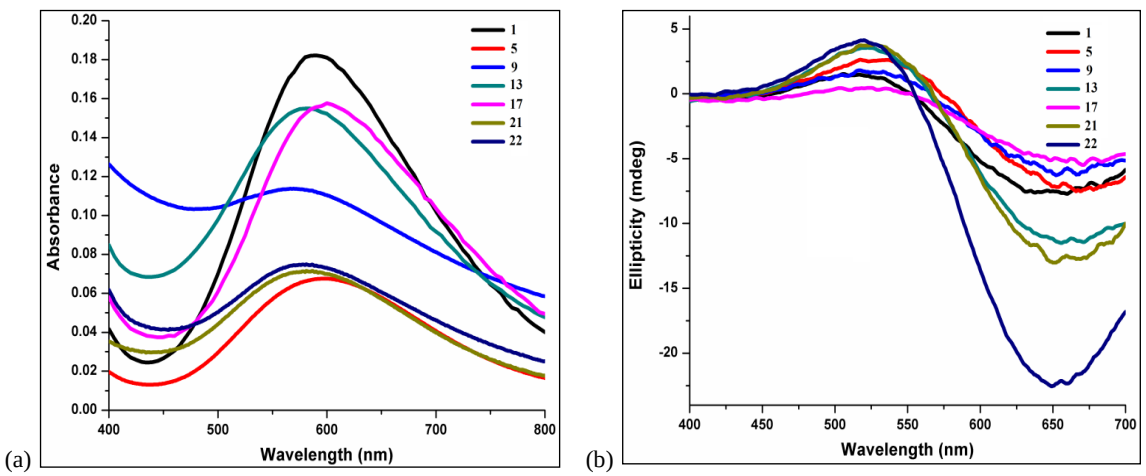

Figure 3.57. (a) UV-vis and (b) CD spectra for **1**, **5**, **9**, **13**, **17**, **21** and **22** in the wavelength range from 400 to 700 nm.

In the UV region of the spectra of these compounds (200 to 400 nm), the peaks at around 200 nm (π-π*) and 225 nm (n-π*) are due to the ligand. The peaks within the range of 250-275 nm in various spectra are due to the various substitutions in the aldehyde part of the ligands (as shown in Figure 3.58a). In the CD spectrum of **1** (200-400 nm), the positive Cotton effect is observed at 217, 240 and 273 nm. The corresponding peaks for other complexes are as

follows: **5**, 210 and 234 nm; **9**, 226 and 279 nm; **13**, 200 and 246 nm; **17**, 260 nm; **21**, 200 and 251 nm; **22**, 200 and 285 nm. For **1**, the negative Cotton effect is observed at 200 nm and 224 nm. The corresponding peaks for other complexes are as follows: **5**, 200 nm; **9**, 200 nm, 253 nm and 306 nm; **13**, 224 nm; **17**, 217 and 277 nm; **21**, 229 nm; **22**, 227 and 285 nm (as shown in Figure 3.58b).

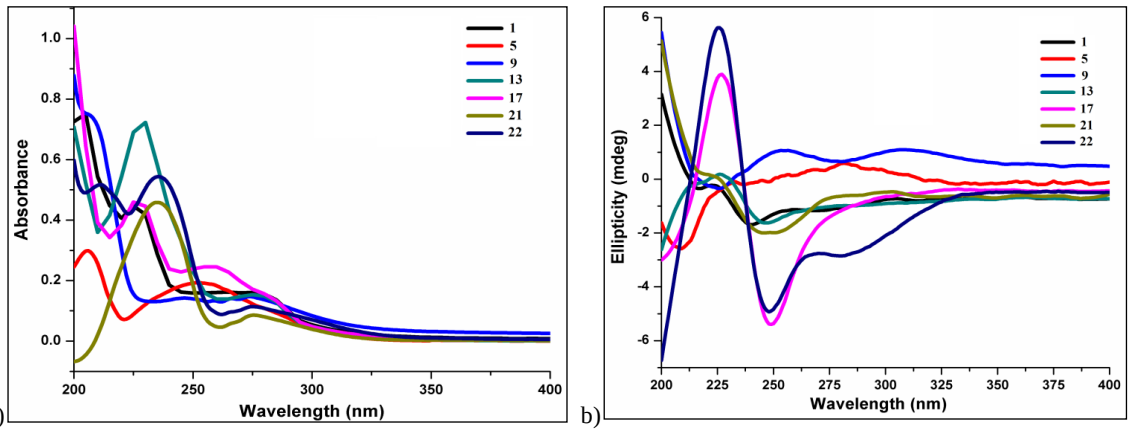

Figure 3.58. (a) UV-vis and (b) CD spectra for **1**, **5**, **9**, **13**, **17**, **21** and **22** in the wavelength range from 200 to 400 nm.

In the visible part of the spectra for Ni^{2+} compounds, major peaks are observed at ~350 nm and ~650 nm. The peaks at ~350 nm are due to LMCT whereas the peaks at ~ 650 nm are due to the d-d transition in Ni^{2+} (as shown in Figure 3.59). The peaks at ~650 nm are due to $^2A_{2g}$ to $^2T_{1g}$ (F) transition in Ni^{2+}whereas the peaks at ~350 nm are due $^2A_{2g}$ to $^2T_{1g}$ (P) transition.

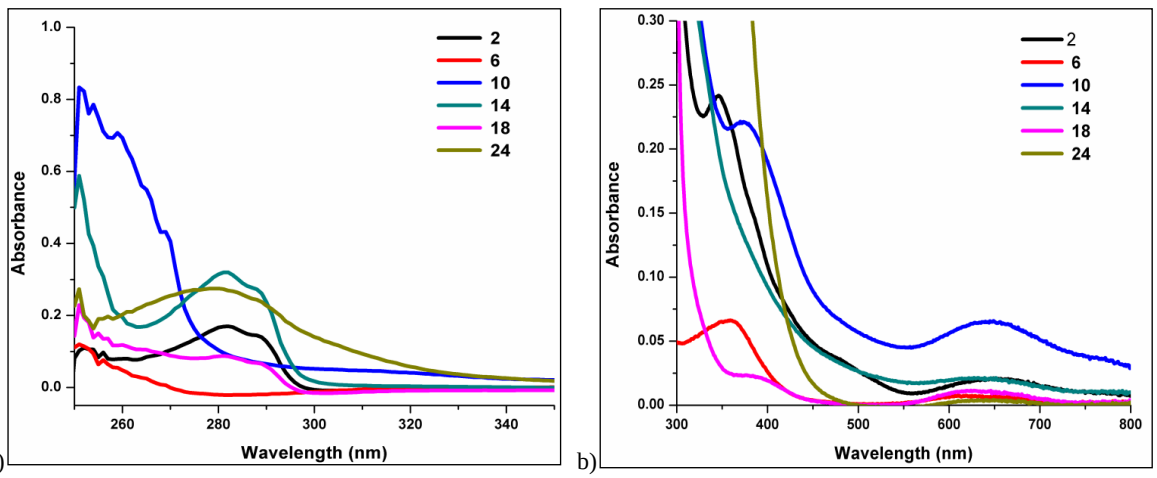

Figure 3.59. UV-Vis spectra of **2**, **6**, **10**, **14**, **18**, **22, 30** and **34** in wavelength range from (a) 250 to 350 nm and (b) 300 to 800 nm.

Photoluminescence properties

All L-Tyrosine and L-Phenylalanine based ligands show good fluorescence as tyrosine and phenylalanine itself are natural fluorophores. All the complexes were excited at 270 nm (as shown in Figure 3.60)

a)

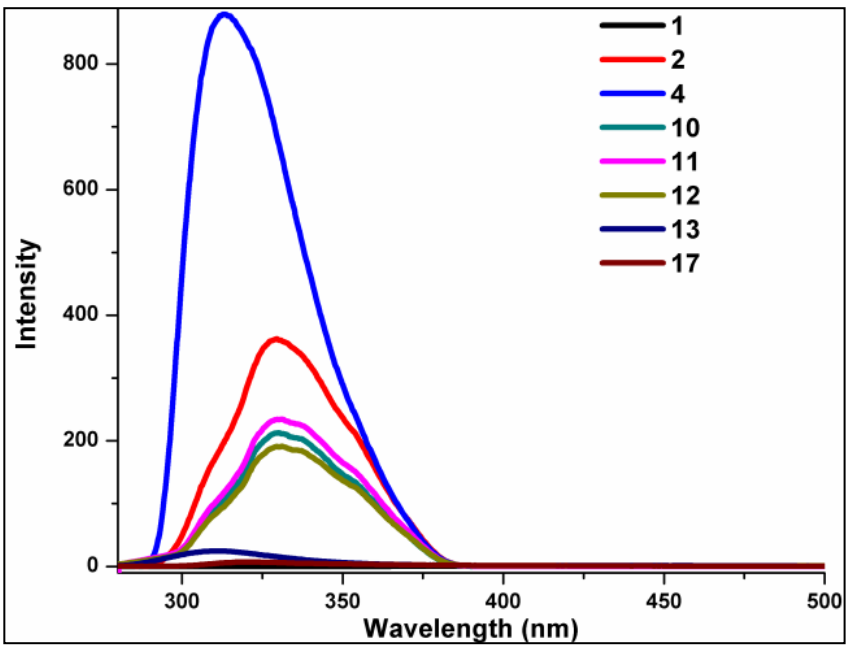

b)

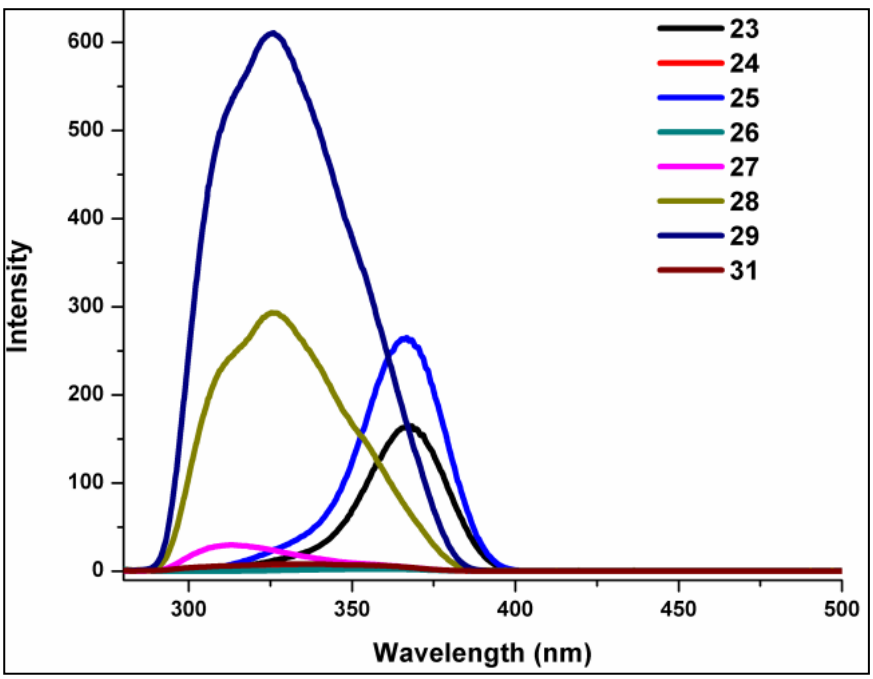

Figure 3.60. Emission spectra of (a) **1**, **2**, **4**, **10-13, 17**; (b) **23-31**.

Comparing the photoluminescence of all these coordination architectures, it is observed that in almost all the cases d^{10} metal analogue of every ligand esp. the Cd complex shows better photoluminescence then the other metal analogues of the same ligand. This fact can be explained by the property of d^{10} metals in providing more rigidity to the ligand systems than other metals and thus preventing the energy loss by non-radiative pathways.

3.2.1.1.2. *Coordination architectures containing heteroligands*

To analyse another aspect of the structural aesthetics, one of the homoligands in **23** and **27** is replaced by a hetero ligand: L-H_2Tyr4-NO_2 in **23** and L-H_2Tyr4-fluoro in **27** with L-tyrosine yielding [Cu(HTyr4-nitro)(Tyrosine)]·$4H_2O$ (**32**) and [Cu(HTyr4-fluoro)(Tyrosine)]·$3H_2O$ (**33**), respectively.

Synthesis. Two coordination architectures of the Cu^{2+} were synthesized via a three-component self-assembly reaction of $CuSO_4$·$5H_2O$, the respective monopotassium salt of the ligand and monopotassium salt of the L-Tyrosine in a 1:1:1 ratio under ambient conditions. Both the compounds were obtained as precipitates for the reaction in water (Scheme 3.7).

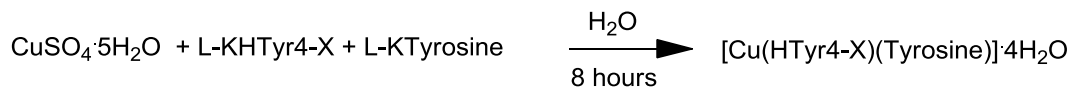

Scheme 3.7. Synthesis of **32** and **33**.

FTIR Spectroscopy. In the FT-IR spectra of **32**-**33**, the broad peak in the range of 3300-3400 cm^{-1} is due to the lattice water molecules. The absence of another peak in this region supports the fact that there is no coordinating water (see crystal structures below). The peak at ~3250 cm^{-1} in both complexes is due to the phenolic –OH of the ligands.

Thermogravimetric analyses. For **32** it is a one-step weight loss profile. The TGA profile of **32**, shows it to be highly stable till 180˚C thus confirming the presence of strong hydrogen bonding. The weight loss of 47.59% between 180-330 ˚C corresponds to loss of three uncoordinated water molecule along with Cu- tyrofloro- complex (ca. 50.2%). For **33** it is a three-step weight loss profile. First weight loss of 3.03% between 50-150 ˚C corresponds to

loss of uncoordinated water (ca. 2.21%). The second step showing weight loss of 10.75% between 150-200 ˚C indicates loss of one uncoordinated water molecule and a carbon dioxide molecule (ca. 14.25%). The third step showing weight loss of 17.92% between 200-400 ˚C indicates loss of some parts of metal-ligand complex (ca. 21.69%) as shown in Figure 3.61.

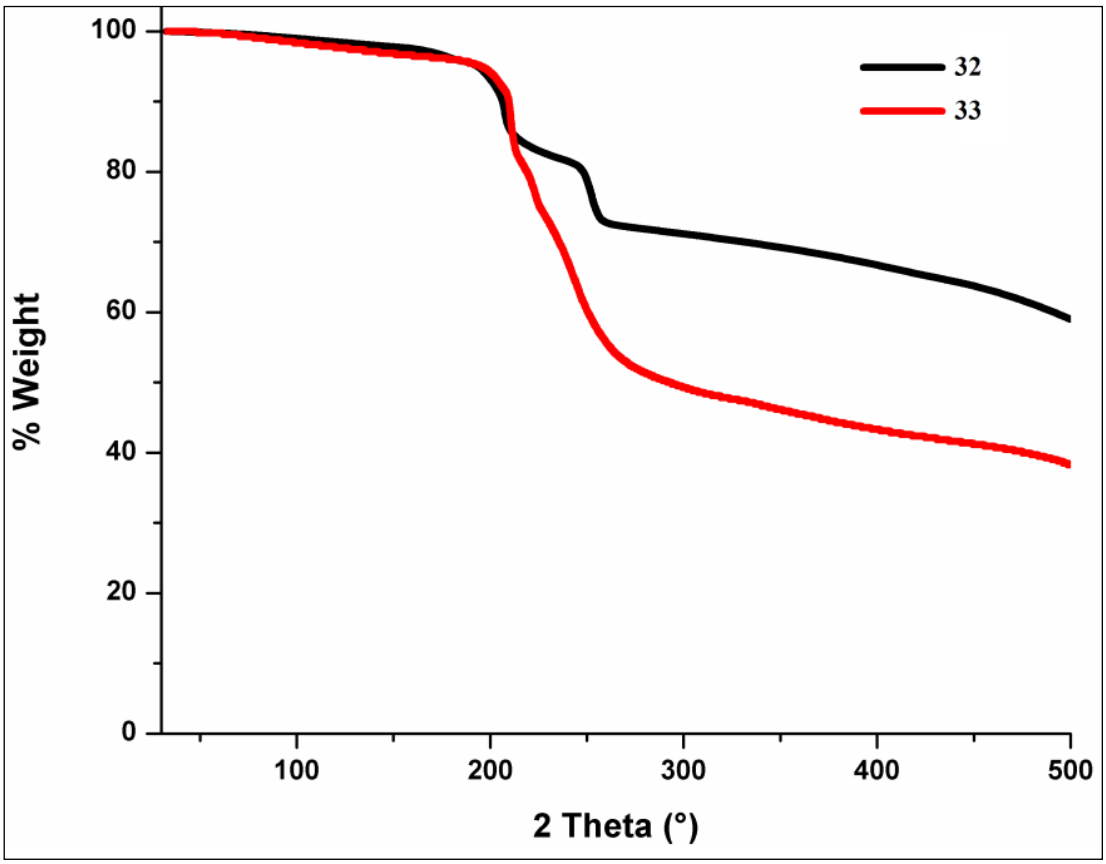

Figure 3.61. TGA scans for **32-33**.

Single Crystal Structure Analysis. Compound **33** crystallizes as [Cu(HTyr4-fluoro)(Tyrosine)]·2H_2O (**33a**) in triclinic chiral space group *P*1. The asymmetric unit of **33a** consists of a tetracoordinating Cu^{2+} bound to one HTyrfluoro ligand and one L-Tyrosine molecule (as shown in Figure 3.62). The Cu^{2+} ion acquires a distorted square planar geometry quite different from previous complexes where Cu^{2+} attains a distorted square pyramidal geometry due to the presence of coordinated solvent molecule which is absent in this case.

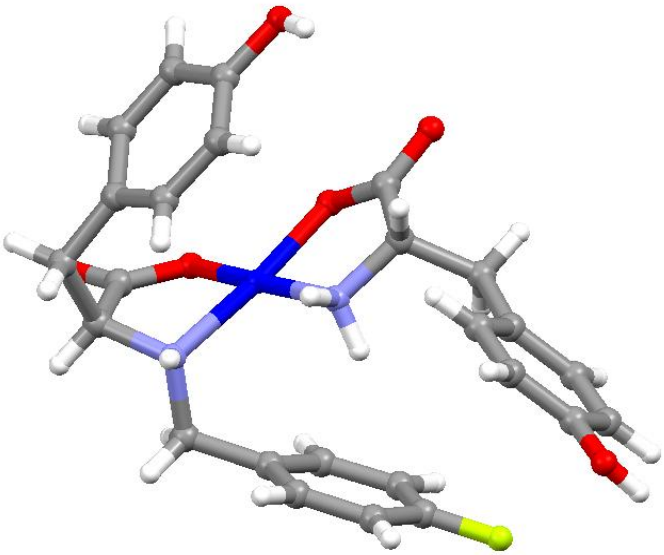

Figure 3.62. Asymmetric unit in **33a**.

The Cu-O and Cu-N distances in **33a** are in range of 1.918(4)-1.930(4) Å and 1.989(4)-1.996(4) Å, respectively which are in accordance with the Cu-O (1.900(3)-1.996(3) Å) and Cu-N (1.941(12)-2.036(3) Å) distances reported in the literature for tetrameric Cu^{2+} - amino acid complexes.[255-265] Same as **33a,** all these complexes has a distorted square-planar center Cu^{2+} ion with O and N donor atoms in trans position to each other. In the literature few cases of mixed ligands (amino acid derivatives) complexes of Cu(II) shows O and N donor atoms in cis position to each other.[266] However bond distances of Cu-O and Cu-N are similar to that of the previous ones. Other than the coordinated solvent molecule the coordination environment around Cu^{2+} is same as reported for previous compounds reported in this paper; both the carboxylates (one each from H_2Tyr-4 Fluoro and Tyrosine) binds to the metal center in a monodentate fashion. This mononuclear subunit is hydrogen bonded to next mononuclear subunit via the oxygen atoms of the carboxylates, oxygen atoms of phenoxo groups and lattice water molecules in an intermolecular fashion. The oxygen atom (O7) of one of the lattice water molecule is hydrogen bonded to the unbound oxygen atom (O1) of the monodentate carboxylate of the Htyr4-fluoro ligand (O---O distance: 2.8377 Å) as well as it also shows hydrogen bonding with the oxygen atom (O5) of the phenol moiety of the Htyr4-fluoro ligand (O---O distance: 2.6686 Å). The oxygen atom (O8) of another lattice water molecule is hydrogen bonded to the unbound oxygen atom (O4) of the monodentate carboxylate of the L-tyrosine ligand (O---O distance: 2.8567 Å). Even the oxygen atom (O5)

of the phenol moiety of the Htyr4-fluoro ligand is intermolecularly hydrogen bonded to the oxygen atom (O6) of the phenol moiety of the tyrosine ligand (O---O distance: 2.7602 Å). The two lattice water molecules are also intermolecularly hydrogen bonded to each other. This hydrogen bonded structure gives rise to a porous 2D framework (as shown in Figure 3.63). The selected bond distances and bond angles for **33a** are listed in Tables A7 and A11, respectively.

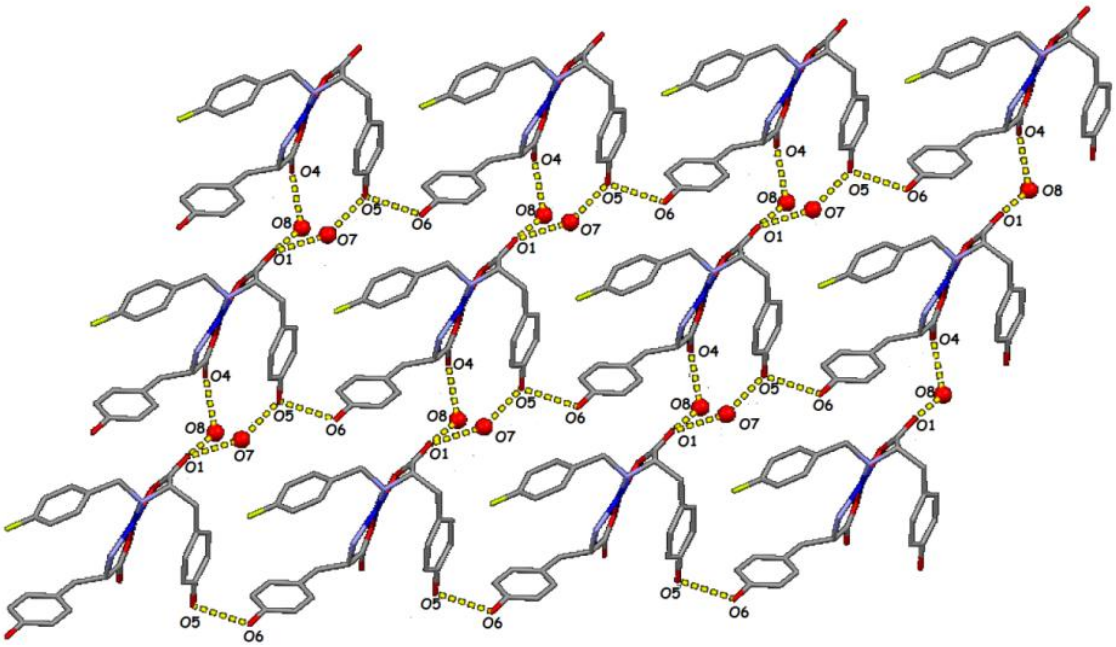

Figure 3.63. 2D network in **33a**.

However, in this case there are no π–π interactions to strengthen the framework. The supramolecular array formed in **33a** clearly shows that the strategy of employing hetero ligands can not only bring up a totally different coordination atmosphere around center metal ion but also influence the supramolecular interactions drastically. On proceeding from homoligands to hetero ligands not only the asymmetric unit but the final supramolecular structural network is also diversified. Thus, a fine tuning of the ligands with respect to the various substituents can lead to different structural motifs in the metal complexes, with desirable network arrangement and physico-chemical properties. The crystallographic parameters and basic information pertaining to data collection and structure refinement for **33a** is summarized in Table A3. All hydrogen bonding parameters for **33a** are listed in Table 3.9.

UV-Vis spectroscopy. UV-Visible spectroscopy was carried using ~1 mM methanolic solution of Cu^{2+} coordination architectures**.** In the UV part (200-400 nm range), peaks at 225nm and 275 nm are due to intraligand transitions (as shown in Figure 3.64a). In the visible part (400- 800 nm) of the spectra for Cu^{2+} compounds (**32** and **33**)**,** major peaks are at 607 nm (ε = 159 $L \cdot mol^{-1} \cdot cm^{-1}$), and 590 nm ($\varepsilon$ = 144 $L \cdot mol^{-1} \cdot cm^{-1}$) (as shown in Figure 3.64b). These peaks are due to the d-d transition in Cu^{II} (^2E_g to $^2T_{2g}$).[253]

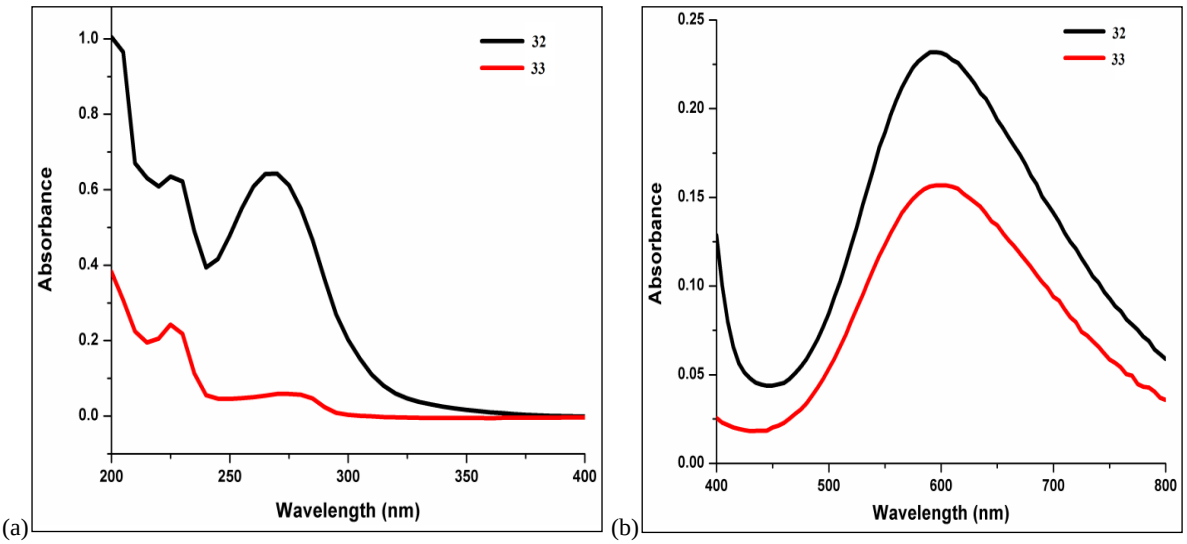

Figure 3.64. UV-Vis spectra for **32-33** in range of (a) 200-400 nm and (b) 400-800 nm.

Table 3.9. Hydrogen bonding parameters in **33a.**

D-H…A	r(D-H) (Å)	r(H…A) (Å)	r(D…A) (Å)	∠D-H…A (°)	Symmetry
33a					
N(1) --H(1) ..O(3)	0.98	2.07	3.0267	164	-1+x,y,z
O(7) --H(1SA) ..O(1)	0.92	2.00	2.8377	150	-1+x,y,z
O(8) --H(2SA) ..O(4)	0.86	2.09	2.8567	148	-1+x,y,z
O(5) --H(3) ..O(7)	0.82	1.89	2.6686	157	1+x,1+y,z
O(7) --H(1SB) ..O(8)	0.68	2.09	2.7602	175	-1+x,y,z
N(2) --H(10A) ..O(4)	0.97	1.98	2.9207	162	-1+x,y,z
O(6) --H(20) ..O(5)	0.82	1.98	2.7649	160	-1+x,y,1+z
C(16) --H(5) ..O(6)	0.93	2.5	3.3879	160	1+x,-1+y,z

3.2.1.2. For a 1:1 metal to ligand ratio

Synthesis. In this category, compounds were obtained by stirring a methanolic solution of divalent metal salts and the respective dipotassium salts of the ligands (in a 1:1 ratio) at room temperature. Compounds **34-45** were obtained by a two-component self-assembly reaction of metal salts and the respective ligand (in a 1:1 ratio) in methanolic solution at room temperature; the same products are obtained if the reactions are carried out under reflux conditions. This shows their stability towards heating in a solvent. The choice of the solvent (MeOH/Water) depends on the differential solubility of the product and the by-product (K_2SO_4/CH_3COOK) in a particular solvent (as shown in Scheme 3.8).

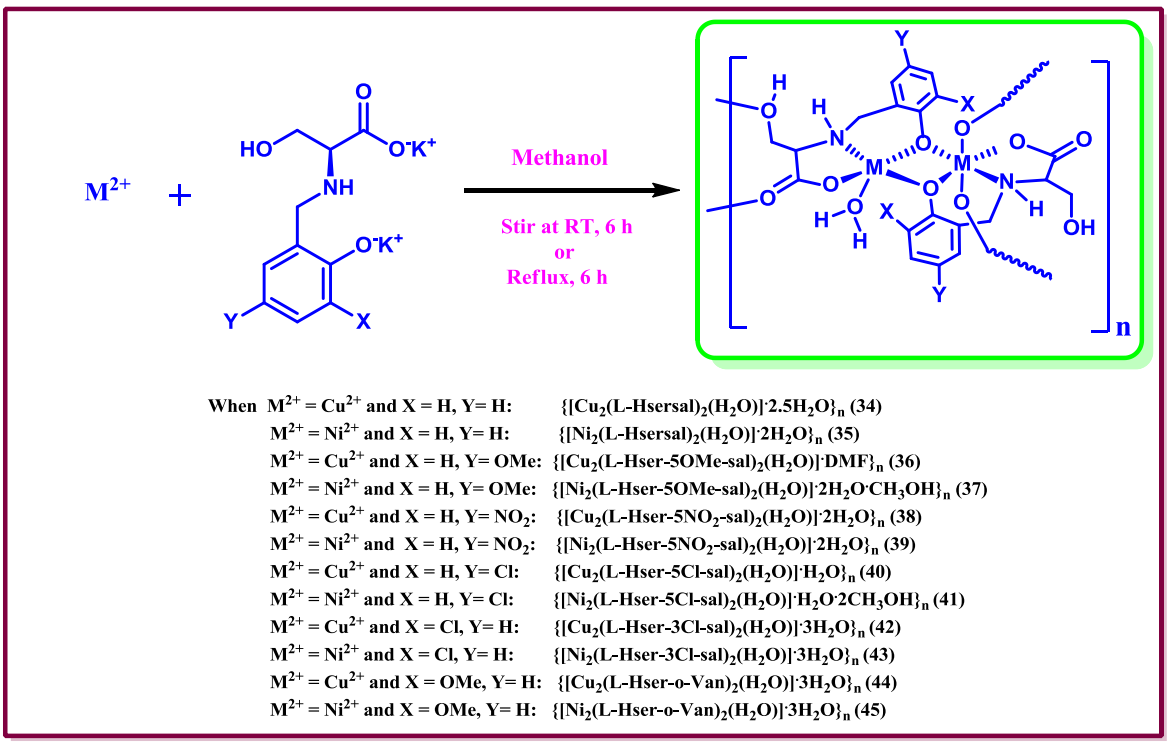

When $M^{2+} = Cu^{2+}$ and X = H, Y= H: $\{[Cu_2(L\text{-}Hsersal)_2(H_2O)]\cdot 2.5H_2O\}_n$ (34)
$M^{2+} = Ni^{2+}$ and X = H, Y= H: $\{[Ni_2(L\text{-}Hsersal)_2(H_2O)]\cdot 2H_2O\}_n$ (35)
$M^{2+} = Cu^{2+}$ and X = H, Y= OMe: $\{[Cu_2(L\text{-}Hser\text{-}5OMe\text{-}sal)_2(H_2O)]\cdot DMF\}_n$ (36)
$M^{2+} = Ni^{2+}$ and X = H, Y= OMe: $\{[Ni_2(L\text{-}Hser\text{-}5OMe\text{-}sal)_2(H_2O)]\cdot 2H_2O\cdot CH_3OH\}_n$ (37)
$M^{2+} = Cu^{2+}$ and X = H, Y= NO_2: $\{[Cu_2(L\text{-}Hser\text{-}5NO_2\text{-}sal)_2(H_2O)]\cdot 2H_2O\}_n$ (38)
$M^{2+} = Ni^{2+}$ and X = H, Y= NO_2: $\{[Ni_2(L\text{-}Hser\text{-}5NO_2\text{-}sal)_2(H_2O)]\cdot 2H_2O\}_n$ (39)
$M^{2+} = Cu^{2+}$ and X = H, Y= Cl: $\{[Cu_2(L\text{-}Hser\text{-}5Cl\text{-}sal)_2(H_2O)]\cdot H_2O\}_n$ (40)
$M^{2+} = Ni^{2+}$ and X = H, Y= Cl: $\{[Ni_2(L\text{-}Hser\text{-}5Cl\text{-}sal)_2(H_2O)]\cdot H_2O\cdot 2CH_3OH\}_n$ (41)
$M^{2+} = Cu^{2+}$ and X = Cl, Y= H: $\{[Cu_2(L\text{-}Hser\text{-}3Cl\text{-}sal)_2(H_2O)]\cdot 3H_2O\}_n$ (42)
$M^{2+} = Ni^{2+}$ and X = Cl, Y= H: $\{[Ni_2(L\text{-}Hser\text{-}3Cl\text{-}sal)_2(H_2O)]\cdot 3H_2O\}_n$ (43)
$M^{2+} = Cu^{2+}$ and X = OMe, Y= H: $\{[Cu_2(L\text{-}Hser\text{-}o\text{-}Van)_2(H_2O)]\cdot 3H_2O\}_n$ (44)
$M^{2+} = Ni^{2+}$ and X = OMe, Y= H: $\{[Ni_2(L\text{-}Hser\text{-}o\text{-}Van)_2(H_2O)]\cdot 3H_2O\}_n$ (45)

Scheme 3.8. General scheme for the synthesis of **34-45**.

FT-IR and Raman spectroscopy. The IR spectra of **34-45** recorded in the solid state as KBr pellets are similar but with slight shifts in some band positions. As an example, for **34** a broad band at 3400 cm^{-1} corresponds to the O-H stretching frequency of the $–CH_2OH$ of the ligand which is coordinated to the Cu^{2+} and the N-H stretching frequency appears at 3233 cm^{-1}. Two binding modes of the carboxylate group of the ligand (monodentate and bridged) observed in the crystal structure of **34** are in agreement with the presence of two types of asymmetric and

symmetric stretches for the -COO^- groups in **34**. These values are 1613 cm^{-1} and 1486 cm^{-1}, and 1581 cm^{-1} and 1363 cm^{-1}, respectively, corresponding to $\Delta\upsilon_1$ = 127 cm^{-1} (bridged) and $\Delta\upsilon_2$ = 218 cm^{-1} (monodentate) [where $\Delta\upsilon = \upsilon_{asym} - \upsilon_{sym}$]. The C-O stretching for the phenoxo part of the ligand, which is bridging between the two Cu^{2+} centers, appears at 1276 cm^{-1}. The corresponding values for **35-45** along with those for **34** are listed in Table 7. All these IR values for **35-45** are in well accordance with the similar dimeric compounds known in the literature.[237]

Table 3.10. Steching frequencies of various functional groups in FTIR spectra for **34-45**.

Compound	ν_{OH} (cm^{-1})	ν_{NH} (cm^{-1})	$\nu_{(COO^-, asymm)}$ (cm^{-1})	$\nu_{(COO^-, symm)}$ (cm^{-1})	$\nu_{(COphenoxo)}$ (cm^{-1})
34	3400	3233	1613	1486	1276
35	3384	3273	1596	1482	1274
36	3389	3242	1633	1492	1268
37	3389	3264	1600	1489	1265
38	3430	3225	1627	1481	1303
39	3395	3270	1597	1482	1301
40	3378	3234	1622	1476	1267
41	3401	3279	1594	1476	1280
42	3392	3230	1624	1445	1280
43	3423	3261	1590	1444	1281
44	3401	3235	1629	1478	1267
45	3389	3266	1598	1476	1287

In the Raman spectra of **34**, **36**, **38**, **40** and **42** the peak corresponding to the carboxylate stretching frequencies appears at 1638 cm^{-1}, 1615 cm^{-1}, 1603 cm^{-1}, 1599 cm^{-1} and 1592 cm^{-1}, respectively. The peak at 1282 cm^{-1} for **34**, 1310 cm^{-1} for **36**, 1297 cm^{-1} for **38**, 1283 cm^{-1} for **40** and 1278 cm^{-1} for **42** corresponds to the N-H bend of the ligand (see Figure 3.68).

Thermogravimetric analyses. The thermal stability of **34-45** was studied as a function of temperature in the range of 25-500 ˚C. In all CPs **34-45**, it is a two-step weight loss profile (see Figure 3.66-3.67). The first weight loss in all the cases at ~50-200 °C is due to loss of lattice solvents and in some loss of coordinated solvent took place as well. The next loss above 200 °C in all CPs is due to loss of the organic ligand and the remaining coordinating

solvent if any. The exact % loss values for **34-45** are reported in Table 3.11 and Table 3.12.

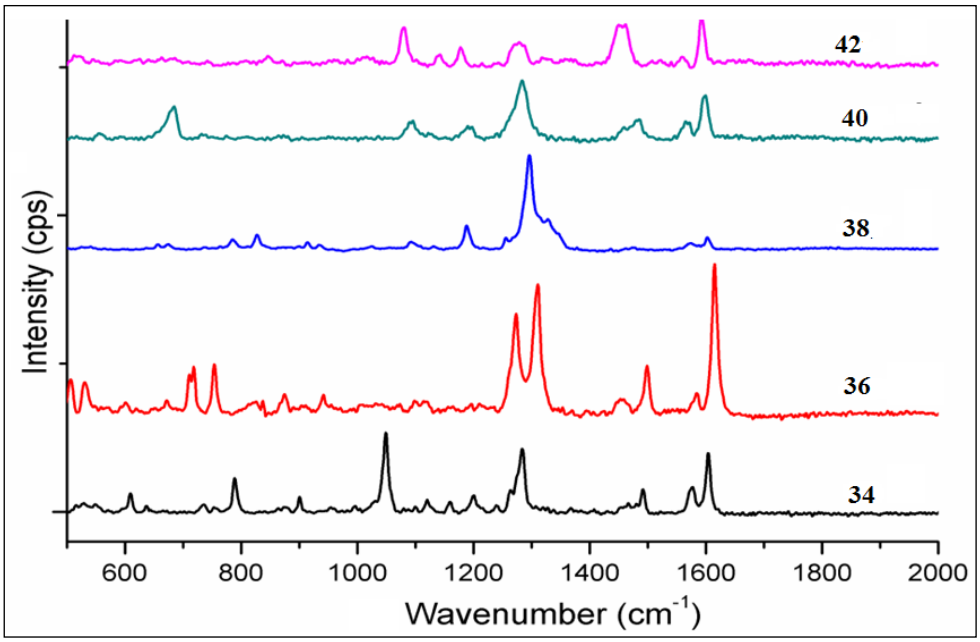

Figure 3.65. Raman spectra for **34**, **36**, **38, 40** and **42.**

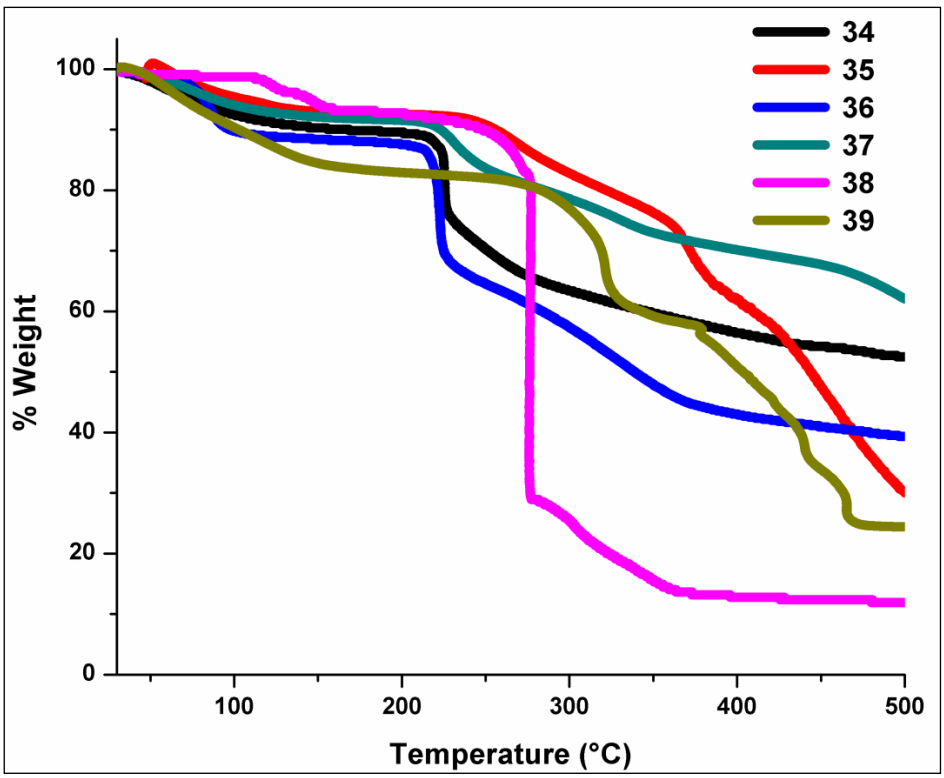

Figure 3.66. TGA scans for **34-39**.

Table 3.11. Thermogravimetric analysis for **34-39;** u – uncoordinated, c – coordinated.

Compound	1st step loss			2nd Step loss		
	Obsd. %	Calcd. %	Loss	Obsd. %	Calcd. %	Loss
34	9.30	10.30	2.5 H_2O (u), H_2O (c)	58.60	57.98	Ligands (H_3Sersal+serine)
35	6.22	6.11	2 H_2O (u)	58.17	56.0	H_2O (c), Metal-ligand complex
36	11.67	10.50	DMF (u)	45.67	48.49	H_2O (c), Metal-ligand complex
37	10.57	9.98	2H_2O (u), CH_3OH (u)	68.14	67.53	H_2O (c), Metal-ligand complex
38	6.33	5.22	2 H_2O (u)	79.53	76.52	H_2O (c), Ligand
39	16.19	16.21	7 H_2O (u)	56.25	55.92	H_2O (u), H_2O (c), Metal-ligand complex

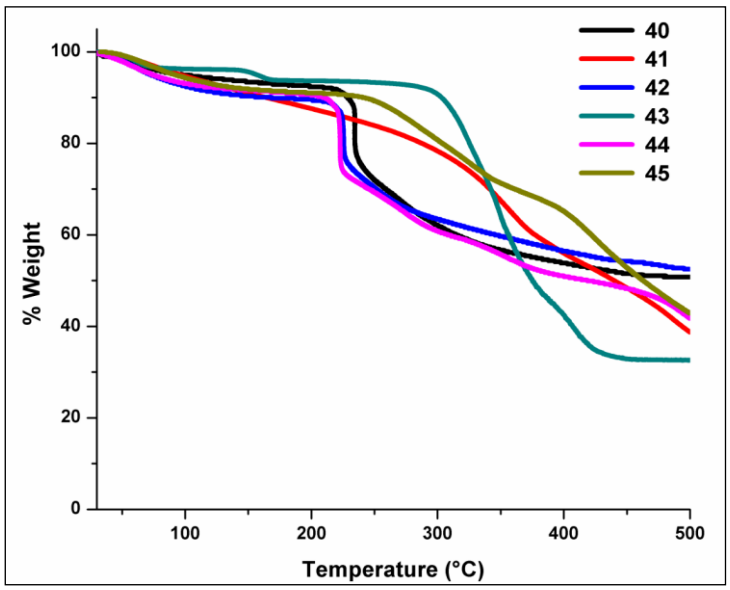

Figure 3.67. TGA scans for **40-45.**

Table 3.12. Thermogravimetric analysis for **40-45;** u – uncoordinated, c – coordinated.

Compound	1st step loss			2nd Step loss		
	Obsd. %	Calcd. %	Loss	Obsd. %	Calcd. %	Loss
40	6.87	5.53	H_2O (u), H_2O (c)	42.49	46.60	Metal-ligand complex
41	12.23	11.64	H_2O (u), 2CH_3OH (u)	50.14	50.16	H_2O (u), Metal-ligand complex
42	10.22	10.49	3 H_2O (u), H_2O (c)	37.08	38.20	Ligand
43	7.65	7.77	3 H_2O (u)	28.08	26.29	H_2O (c), metal-ligand complex
44	8.92	7.97	3 H_2O (u)	41.39	40.60	H_2O (c), Ligand
45	8.15	7.74	3 H_2O (u)	47.42	48.06	metal-ligand complex

Single crystal structure analyses. Crystals of $\{[Cu_2(Hsersal)_2(H_2O)]\cdot 2.5H_2O\}_n$ (**34**), and $\{[Cu_2(Hser\text{-}5Cl\text{-}sal)_2(H_2O)]\cdot 2H_2O\}_n$ (**40**) suitable for the single crystal X-ray study were grown from slow evaporation of the respective methanolic solution: **34** in 8-10 days and **40** in 15 days.

Crystal structures of $\{[Cu_2(Hsersal)_2(H_2O)]\cdot 2.5H_2O\}_n$ (34) and $\{[Cu_2(Hser\text{-}5Cl\text{-}sal)_2(H_2O)]\cdot 2H_2O\}_n$ (40). Compounds **34** and **40** are isostructural but **34** crystallize in the orthorhombic chiral space group $P2_12_12_1$ and **40** crystallizes in the monoclinic chiral space group $P2_1$. The dimeric subunit of both **34** and **40** (shown in Figure 3.68) consists of two Cu^{2+} centers and two ligands. The asymmetric unit of **34** contains one lattice water molecule while that of **40** contains one methanol molecule. The two Cu^{2+} centers in the subunit are not equivalent. In the dimeric unit, one hexacoordinated Cu^{2+} is in distorted octahedral geometry (Cu1) and the other five coordinated Cu^{2+} is in distorted square pyramidal geometry (Cu2). The coordination environment around Cu1 is O_5N type; two sites are occupied by two bridging phenoxo oxygen, the third site is occupied by an oxygen atom of the carboxylate of Hsersal ligand for **34** and Hser-5-Cl-sal ligand for **40** binding in a monodentate fashion, the fourth site is occupied by the N atom of ligand, the fifth site is occupied by oxygen of the bridging carboxylate of another ligand and the sixth site is occupied by the oxygen of hydroxyl group of the sidearm (CH_2OH) of another ligand. The coordination environment around Cu2 is O_4N type, where again as in Cu1 two sites are occupied by two bridging phenoxo oxygen, third site occupied by the oxygen of the monodentate carboxylate of the ligand, the fourth site is occupied by the nitrogen of the amine group of the ligand but the fifth site is occupied by the oxygen atom (O8 in **34** and O9 in **40**) of the coordinated water molecule. Thus Cu1 is coordinating to five oxygens from four different ligands whereas Cu2 is coordinating to four oxygen atoms, three of which are from two ligands and one from the coordinated water molecules.

The Cu...Cu distances in **34** and **40** are 3.002 Å and 2.997 Å, respectively, which fall in the range (2.950 Å - 3.023 Å) reported for compounds with the bis(phenoxo)dicopper core containing similar ligands.[17,31,51,241,267-270] Other bond distances ($Cu\text{-}O_{phenoxo}$, $Cu\text{-}O_{carboxy}$ and $Cu\text{-}N_{amine}$) in **34** and **40** are also found to be similar to those in these compounds.[31,241,268-270] The selected bond distances and bond angles for **34** are listed in Tables A7 and A12,

respectively. In both **34** and **40**, the carboxylate groups of the two ligands coordinating to the two copper centers show different binding modes: the carboxylate surrounding the Cu1 binds

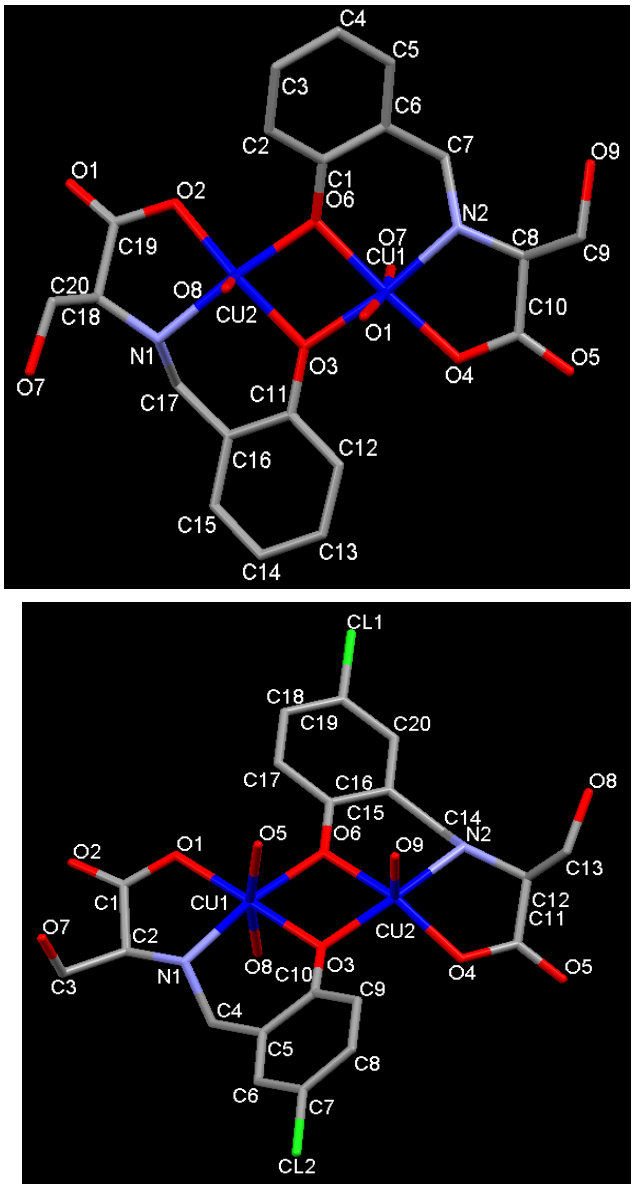

Figure 3.68. Dinuclear subunit in **34** (top) and **40** (bottom). Hydrogen atoms are omitted for clarity.

in a monodentate fashion with the uncoordinated oxygen atom O5 hydrogen bonded to the -CH_2OH group of another ligand but the carboxylate group coordinating to Cu2 is bridging between Cu2 of one asymmetric unit and Cu1 of next asymmetric unit. The two Cu--O_{carb} bond distances are similar (1.937(5) Å and 1.942(6) Å for **34** and 1.925 (5) Å and 1.939 (6) Å for **40**). This connectivity of the ligands in **34** and **40** generates the 2D network shown in

Figure 3.69 and Figure 3.71, respectively. The selected bond distances and bond angles for **40** are listed in Tables A7 and A13, respectively.

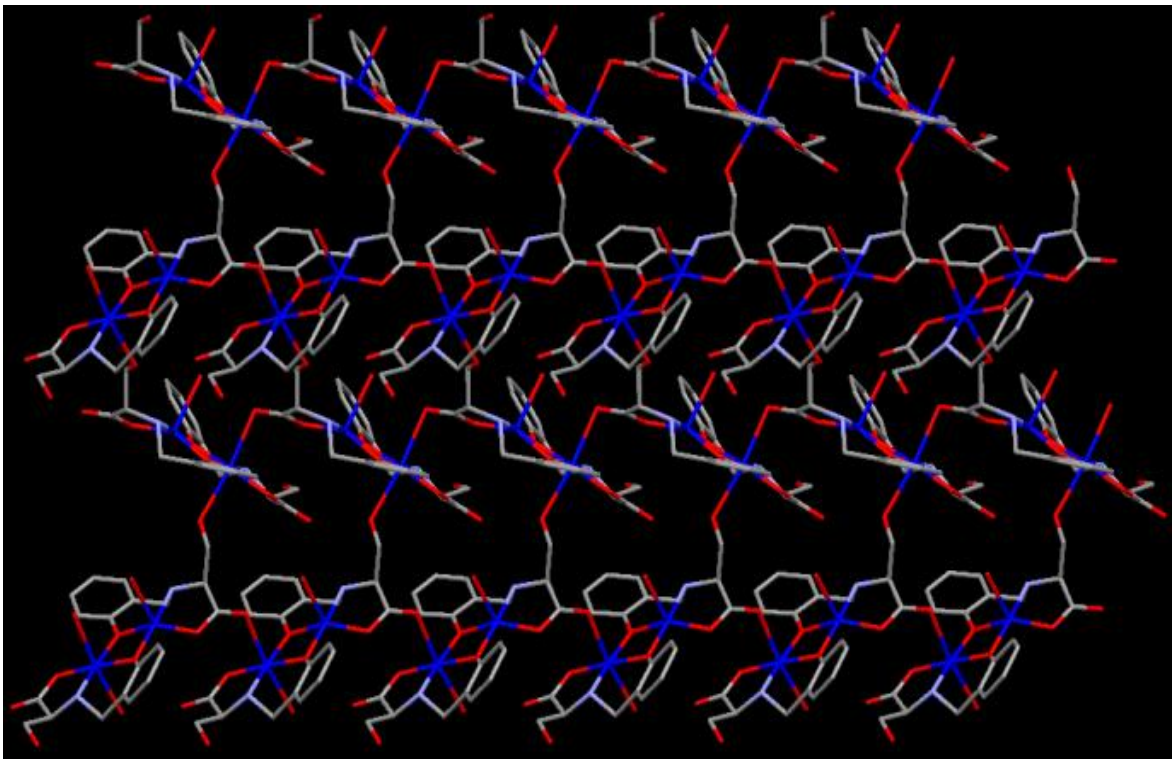

Figure 3.69. Perspective view of the 2D coordination network in **34**.

Within the 2D network in **34** and **40**, five copper centers (marked yellow in Figure 3.70 for **34** and Figure 3.72 for **40**) form a loop like structure that is repeated in both x and y directions. The dimension of the loop is 9.313 Å x 7.408 Å in **34** and 9.626 Å x 7.406 Å in **40**. This loop due to the diverse binding of the ligands is a unique structural feature in **34** and **40**. Compared to the structures of **34** and **40**, in the trinuclear compound, $\{[Cu_3(Hsersal)_3(H_2O)_2]\cdot 2H_2O\}_n$, mentioned earlier[31] the asymmetric unit contains two Cu^{2+} centers connected by a bis(μ-phenoxo) bridge and the third Cu^{2+} center without a phenoxo-bridge. However, in all three compounds **34**, **40** and the trinuclear compound, one of the two bis(μ-phenoxo) bridged Cu^{2+} is pentacoordinated while the other Cu^{2+} is hexacoordinated despite the fact that both carboxylates coordinating to Cu^{2+} in the trinuclear compound are bridging type compared to one monodendate carboxylate and one bridging carboxylate in both **34** and **40**.

This is due to the presence of two coordinated water molecules in the trinuclear compound

whereas in **34** and **40** the pentacoordinated Cu^{2+} is coordinated to one water molecule. Even when a solvent molecule (water) is coordinating to one of the metal centers in the CPs, a 2D coordination polymer is formed through the coordination of the oxygen atom of the side arm CH_2OH of the ligand; such binding of an alcoholic group to a metal center like Cu^{2+} is not so common.

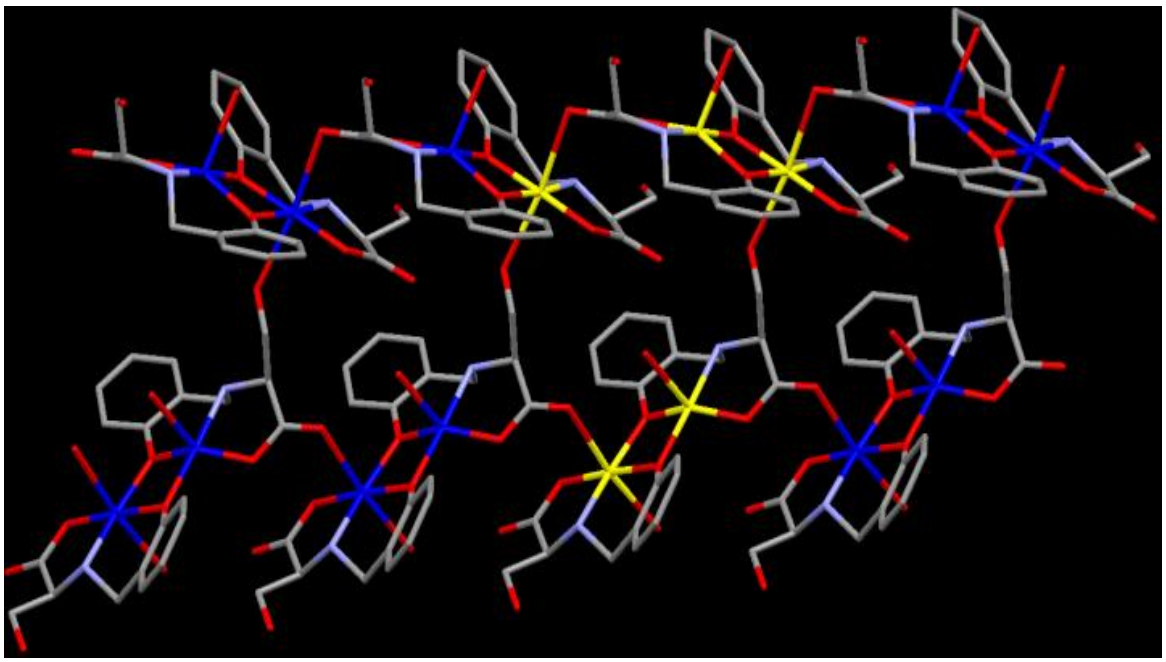

Figure 3.70. Perspective view of the five Cu^{2+} atoms (yellow colored) forming a loop in **34**.

In **34** the water molecule (O8) coordinated to the Cu^{2+} is intermolecularly hydrogen bonded to the coordinated oxygen atom of the bridged carboxylate (O1) of the ligand (O---O distance: 2.80 Å) and also to the uncoordinated oxygen atom of the monodentate carboxylate (O5) of the ligand (O---O distance: 2.85 Å). The uncoordinated oxygen atom of the monodendate carboxylate (O5) is strongly hydrogen bonded to the oxygen atom (O7) of the $–CH_2OH$ (O---O distance: 2.776 Å) of the ligand of the next asymmetric unit. The oxygen atom (O9) of the $–CH_2OH$ of the ligand is strongly hydrogen bonded to the oxygen atom (O10) of the lattice water molecule (O---O distance: 2.679 Å). One of the nitrogen atoms (N2) shows intermolecular hydrogen bonding with the oxygen atom (O2) of bridged carboxylate (N-H---O distance: 3.254 Å) whereas the other nitrogen atom (N1) is hydrogen bonded intermolecularly to the oxygen atom (O5) of the monodentate carboxylate of the

ligand (N-H---O distance: 3.087 Å). Similarly, in **40** the corresponding coordinated water molecule (O9) is intermolecularly hydrogen bonded to both the coordinated oxygen atom of the bridged carboxylate (O5) (O---O distance: 2.83 Å) and the uncoordinated oxygen atom of the monodentate carboxylate (O2) of the ligand (O---O distance: 2.86 Å). The uncoordinated oxygen atom of the monodendate carboxylate (O2) is hydrogen bonded to oxygen atom (O8) of the $–CH_2OH$ (O---O distance: 2.92 Å) of the ligand from the next asymmetric unit. The oxygen atom (O7) of the $–CH_2OH$ of the ligand is also hydrogen bonded to the oxygen atom (O10) of the lattice methanol molecule (O---O distance: 2.87 Å). One of the nitrogen atoms (N1) is intermolecularly hydrogen bonded with the oxygen atom (O10) of lattice methanol molecule (N-H---O distance: 2.88 Å) whereas the other nitrogen atom (N2) is hydrogen bonded in an intermolecular fashion to the oxygen atom (O2) of the monodentate carboxylate of the ligand (N-H---O distance: 2.91 Å). The crystallographic parameters and basic information pertaining to data collection and structure refinement for **34** and **40** is summarized in Table A4. The hydrogen bonding parameters for **34** and **40** are summarized in Table 3.13.

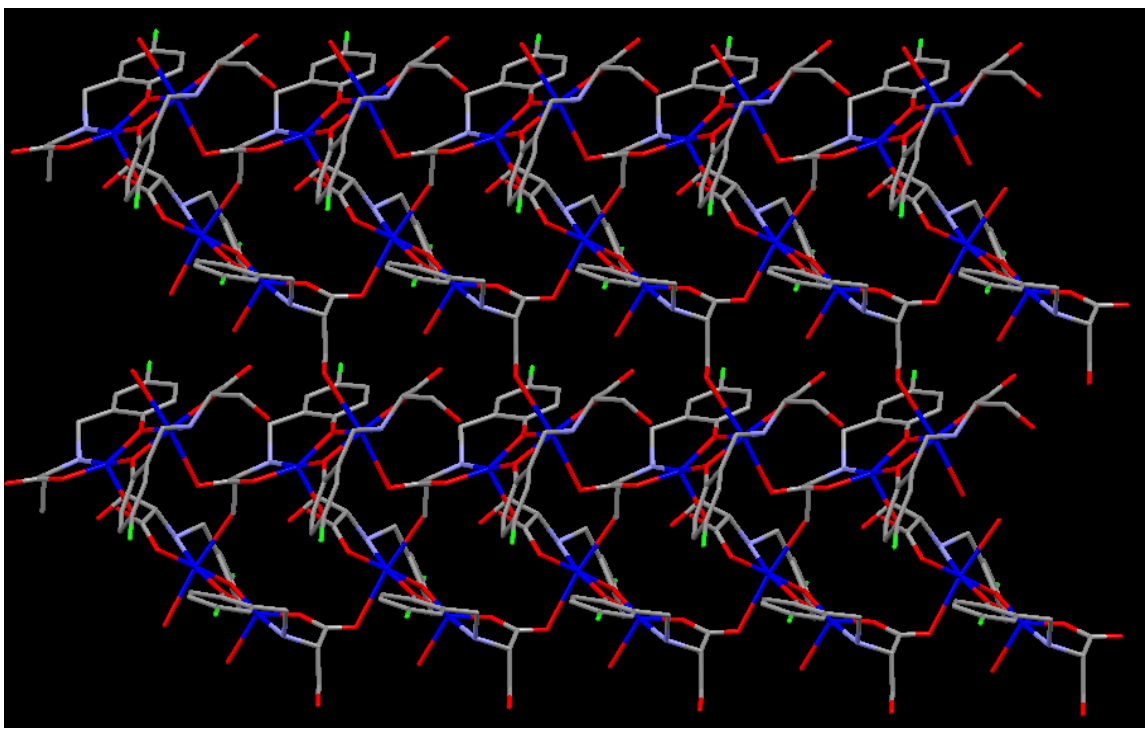

Figure 3.71. Perspective view of the 2D coordination network in **40**.

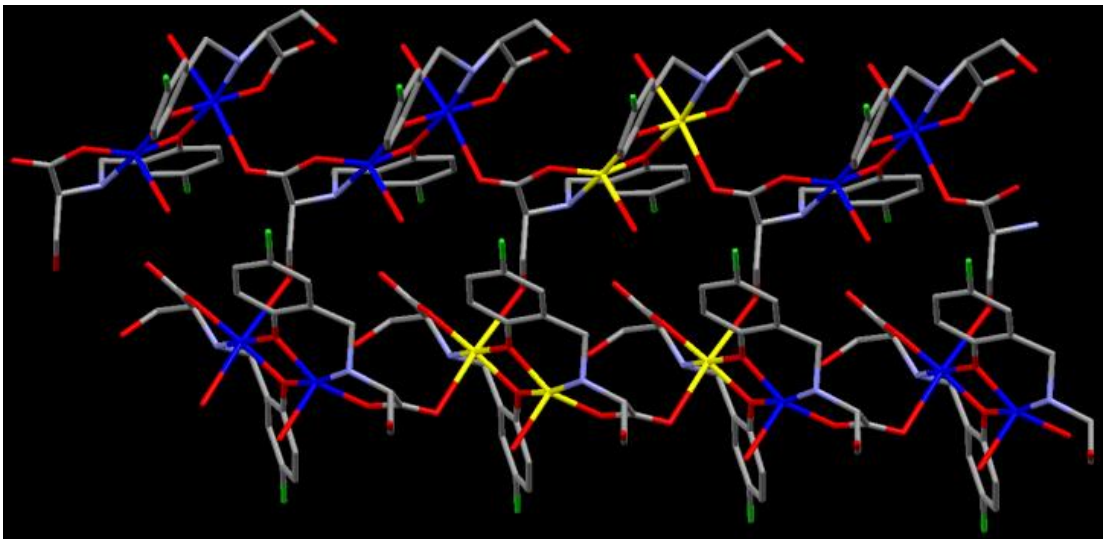

Figure 3.72. Perspective view of the five Cu^{2+} atoms (yellow colored) forming a loop in **40.**

Table 3.13. Hydrogen bonding parameters in **34** and **40**.

D–H…A	r (D-H) (Å)	r (H…A) (Å)	r (D…A) (Å)	∠D-H…A (deg)	Symmetry
34					
O7-H7...O5	0.868	1.98	2.776(6)	152	x-1, y, z
O8-H8B...O5	0.86	2.01	2.849(7)	166	-x+2, y+1/2, -z+1/2
O8-H8A...O1	0.86	2.02	2.800(7)	150	x+1, y, z
O9-H9...O10	0.82	1.88	2.679(13)	166	x+1/2, -y+3/2, -z
O10-H10A...O8	0.85	2.29	3.123(12)	164	
N1-H1…O5	0.98	2.13	3.087(8)	165	-x+2, y+1/2, -z+1/2
N2-H2...O2	0.98	2.64	3.254(7)	120	x+1, y, z
C2-H2A...O2	0.93	2.57	3.149(8)	121	
C7-H7A...O9	0.97	2.45	3.113(10)	125	
C12-H12...O4	0.93	2.37	3.159(9)	141	
C20-H20B...O4	0.97	2.6	3.281(8)	127	
40					
N(1) --H(1) ..O(10	1.00	1.88	2.8802	179	1+x,y,z
O(7) --H(11) ..O(10)	0.84	2.12	2.8752	150	1+x,y,z
N(2) --H(11A) ..O(2)	1.00	1.95	2.9103	161	2-x,1/2+y,1-z
O(9) --H(13A) ..O(1)	0.93	2.6	3.3229	135	2-x,1/2+y,1-z
O(9) --H(13A) ..O(2)	0.93	1.94	2.8563	169	2-x,1/2+y,1-z
O(9) --H(13B) ..O(5)	0.77	2.09	2.8344	160	1+x,y,z
O(8) --H(14) ..O(2)	0.84	2.2	2.9195	143	2-x,1/2+y,1-z
O(10) --H(15A) ..O(4)	0.84	1.91	2.7383	168	
C(4) --H(3B) ..O(8)	0.99	2.59	3.3357	132	1-x,-1/2+y,1-z
C(17) --H(12) ..O(1)	0.95	2.33	3.0902	137	

Powder X-ray data analysis. To confirm whether the single crystal structure corresponds to the bulk material or not, powder X-ray diffraction pattern was recorded for **34** and **40** at room temperature. The experimental and simulated (from the single crystal data) patterns were similar to each other (see Figure 3.73). The patterns obtained confirm that the single crystal and bulk material are the same. It also confirms the phase purity of the bulk sample. Additionally, powder patterns of **43** after drying at 100 °C for 15 minutes were recorded. There is no change in the powder pattern indicating the retention of structure and crystallinity due to this treatment. This also indicates that **43** does not go through any structural transformation due to heating in the solution or solid state. This also corroborates well with their thermal properties which is described below.

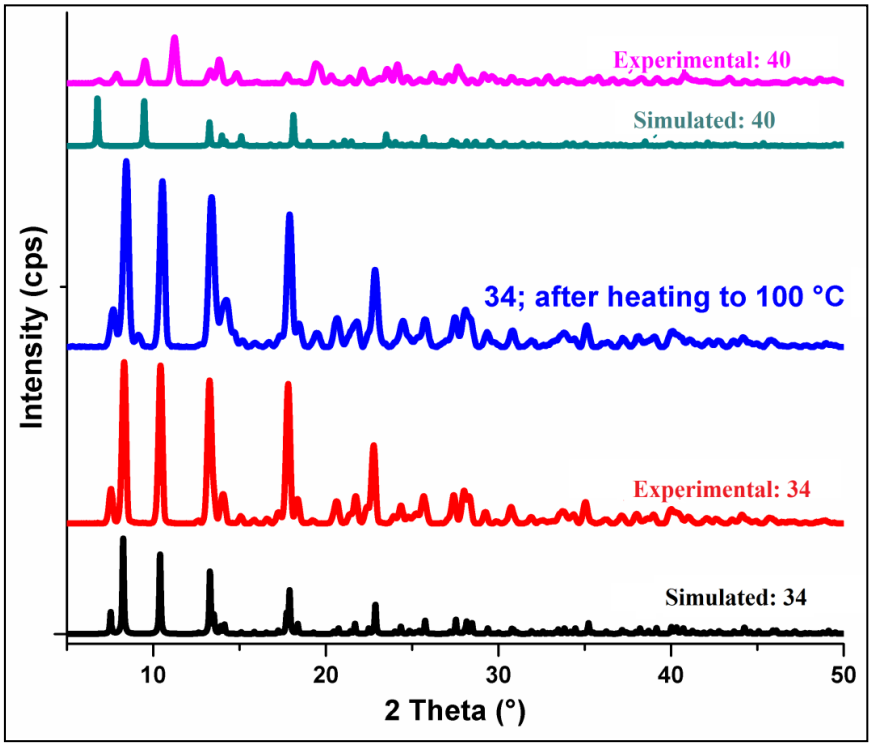

Figure 3.73. PXRD patterns of **34** and **40.**

UV-Vis and Circular Dichroism (CD) spectroscopy. UV-Visible and CD spectroscopic studies were carried using ~1 mM methanolic solution of **34**, **36**, **38**, **40**, **42** and **44** (see Figs. 3.74 and 3.75). The UV-vis spectral data for **34**, **36**, **38**, **40**, **42** and **44** are reported in Table 3.14. The peaks around 650-685 nm in these complexes are due to the d-d transition (^2E_g to $^2T_{2g}$) of copper(II) whereas the peaks around 370-420 nm are due to LMCT, i.e., from -C=O of carboxylate to the metal center.[253] These values for **34**, **36**, **38**, **40**, **42** and **44** are in well agreement with corresponding values for such phenoxo bridged Cu(II) compounds known in

the literature.[31,270] In the UV region of the spectrum (200 to 350 nm), the peak at around 200-210 nm (π-π*) is due to L-serine part of the ligand and 245-260 nm (n-π*) is due to the aldehyde part of the ligand.

The peaks in the CD spectra for **34**, **36**, **38**, **40**, **42** and **44** are reported in Table 3.15. The Cotton effects observed at around 400 are due to LMCT whereas the Cotton effects observed around 650 nm are due to d-d transitions.[254]

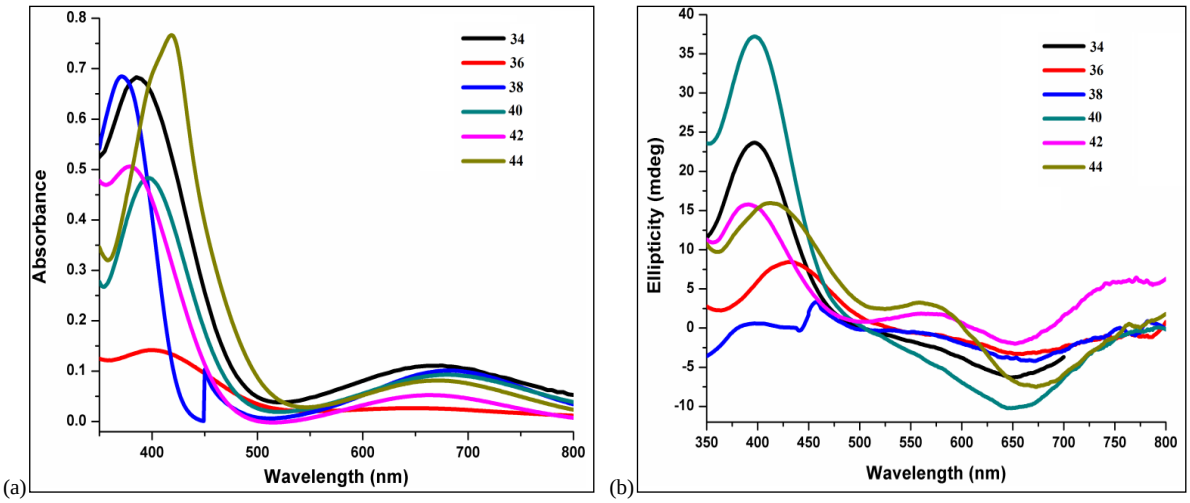

Figure 3.74. (a) UV-vis and (b) CD spectra for **34**, **36**, **38**, **40**, **42** and **44** in the wavelength range from 350 to 800 nm.

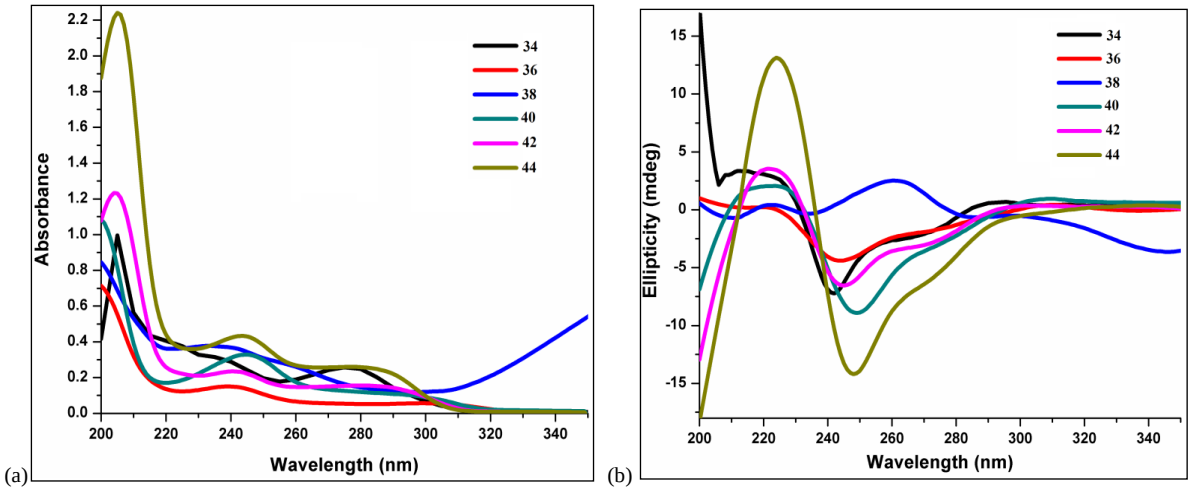

Figure 3.75. (a) UV-vis and (b) CD spectra for **34**, **36**, **38**, **40**, **42** and **44** in the wavelength range from 200 to 350 nm.

The absorbance spectra for the Ni analogues of these ligands are also recorded (as shown in Figure 3.76). In the visible part of the spectra for Ni^{2+} compounds, major peaks are observed at ~350 nm and ~650 nm. The peaks at ~350 nm are due to LMCT whereas the peaks at ~ 650 nm are due to the d-d transition in Ni^{2+} (as shown in Figure 3.76). The peaks at ~ 650 nm

are due to $^2A_{2g}$ to $^2T_{1g}$ (F) transition in Ni^{2+} whereas the peaks at ~ 360 nm are due $^2A_{2g}$ to $^2T_{1g}$ (P) transition.

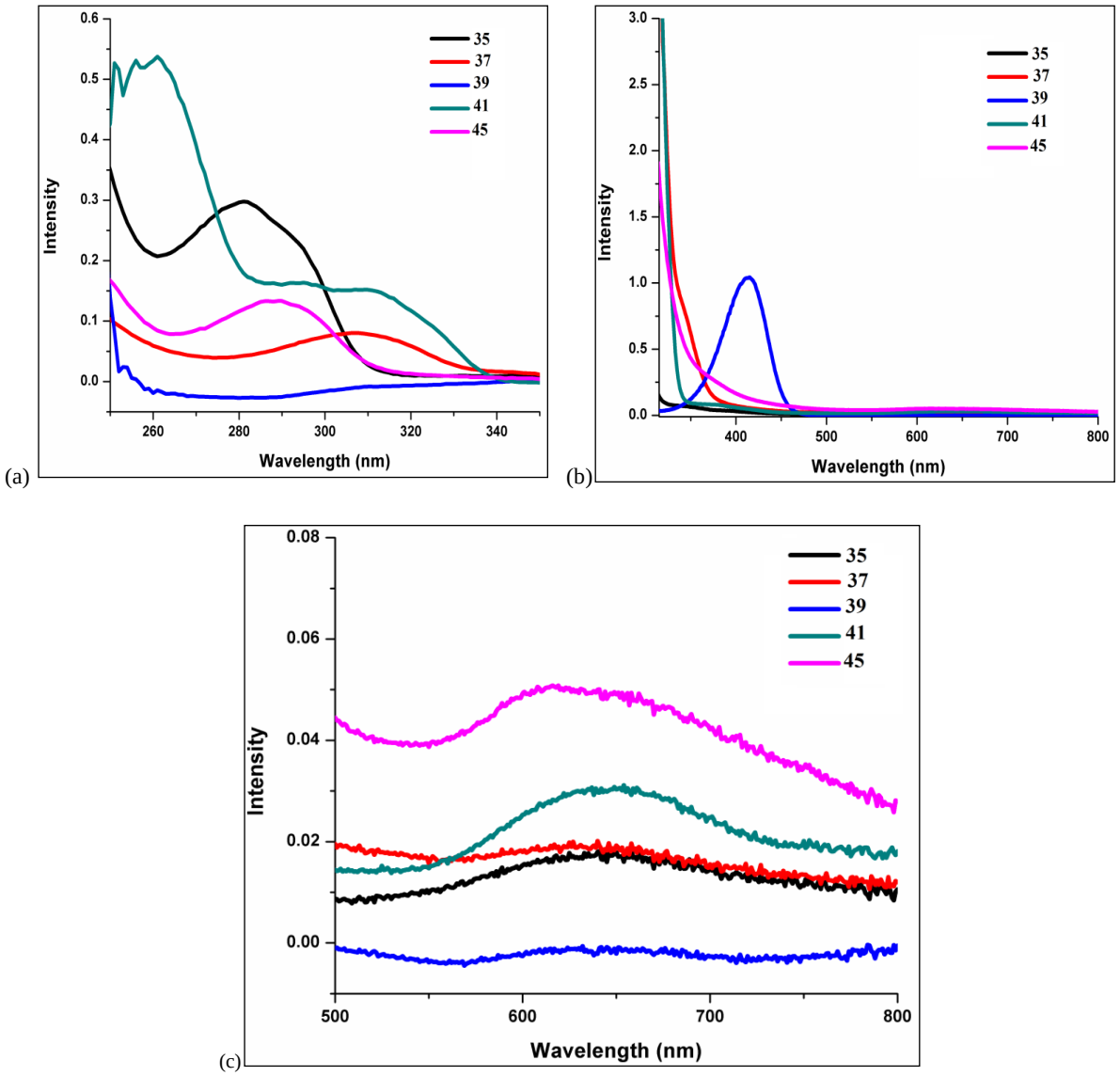

Figure 3.76. UV-vis spectra for **35**, **37**, **39**, **40**, **41** and **45** in the wavelength range from (a) 200 to 350 nm; (b) 350nm to 800 nm and (c) 500 to 800 nm.

Table 3.14. . Peaks in the absorption spectra for **34**, **36**, **38**, **40**, **42** and **44** (350 nm – 700 nm).

Compound	λ, nm (ε, $L \cdot mol^{-1} \cdot cm^{-1}$)	λ, nm (ε, $L \cdot mol^{-1} \cdot cm^{-1}$)
34	675 (123)	371 (883)
36	680 (48)	400 (296)
38	684 (70)	372 (2257)
40	663 (34)	379 (328)
42	679 (64)	376 (331)
44	672 (55)	418 (519)

Table 3.15. Peaks in CD spectra for **34**, **36**, **38**, **40**, **42** and **44** (350 nm – 700 nm).

Compound	Positive Cotton Effect (nm)	Negative Cotton Effect (nm)
34	650, 495,265, 245, 208	600, 400, 309, 225, 222
36	654, 265, 245	565, 435, 299, 262, 224
38	664, 345, 236, 212	403, 306, 221
40	644, 273, 273, 251	482, 401, 295, 221
42	651, 504, 271, 245	575, 394, 296, 223
44	664, 524, 267, 247	569, 416, 225

3.2.1.2a. For a 1:1 metal:ligand ratio and a neutral linker

Synthesis. Conversion of $\{[Cu_2(Hsersal)_2(H_2O)]\cdot 2.5H_2O\}_n$ (**34**) to $[Cu_2(4,4'\text{-bpy})(Hsersal)_2]\cdot 2H_2O$ (**46**),$\{[Cu_2(Hser\text{-}5OMe\text{-}sal)_2(H_2O)]\cdot DMF\}_n$ (**36**) to $[Cu_2(4,4'\text{-bpy})(Hser\text{-}5\text{-}OMe\text{-}sal)_2]\cdot 6H_2O$ (**47**), $\{[Cu_2(Hser\text{-}5NO_2\text{-}sal)_2(H_2O)]\}_n$ (**38**) to $[Cu_2(4,4'\text{-bpy})(Hser\text{-}5\text{-}NO_2\text{-}sal)_2]\cdot H_2O$ **(48)** and $\{[Cu_2(Hser\text{-}5Cl\text{-}sal)_2(H_2O)]\cdot 2H_2O\}_n$ (**40**) to $[Cu_2(4,4'\text{-bpy})(Hser\text{-}5\text{-}Cl\text{-}sal)_2]\cdot 4H_2O\cdot DMF$ (**49**) was achieved by refluxing a methanolic solution of **34** or **36** or **38** or **40** and 4,4'-bipyridine for 6 hrs, respectively (see Scheme 3.9). Compounds **46-49** can also be directly prepared by refluxing a methanolic solution of $CuSO_4\cdot 5H_2O$, the respective ligand and 4,4'-bipyridine (in a 1:1:0.5 ratio).

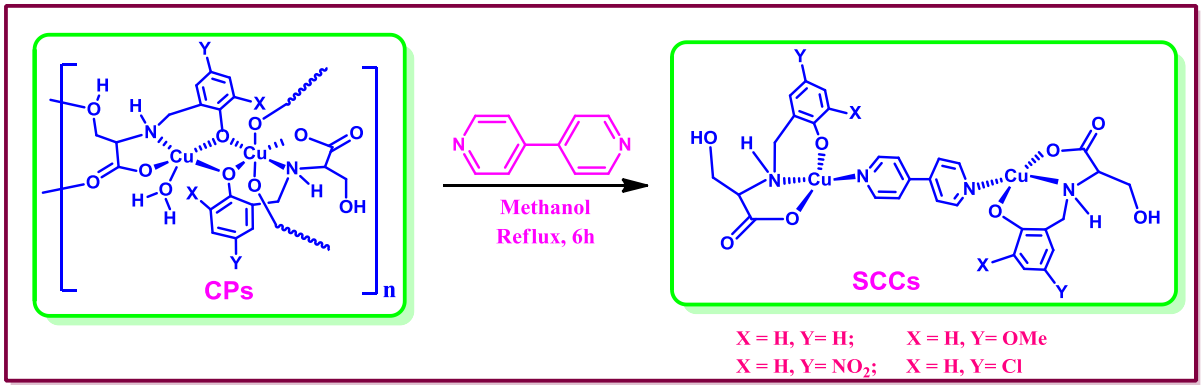

Scheme 3.9. General scheme for the synthesis of **46-49**.

FT-IR and Raman Spectroscopy. The IR spectra of **46-49** recorded in the solid state as KBr pellets are similar but with slight shifts in some band positions. As an example, for **46** the O-H stretching frequency of the $-CH_2OH$ of the ligand and the N-H stretching frequency appear at 3355 cm-1 and 3196 cm^{-1}, respectively. The peak at 1217 cm^{-1} in **46**, **47** and **48**, and 1219

cm^{-1} in **49** is from 4,4'-bipyridine.[31] The corresponding values for **47-49** along with those for **46** are listed in Table 3.16.

Table 3.16. Steching frequencies of various functional groups in FTIR spectra for **46-49**.

Compound	ν_{OH} (cm^{-1})	ν_{NH} (cm^{-1})	$\nu_{(COO^-, asymm)}$ (cm^{-1})	$\nu_{(COO^-, symm)}$ (cm^{-1})	$\nu_{(CO)}$ (cm^{-1})	From 4,4′-bipyridine (cm^{-1})
46	3355	3196	1616	1479	1276	1217
47	3479	3265	1657	1495	1272	1217
48	3410	3229	1642	1477	1290	1217
49	3382	3235	1634	1473	1287	1219

Thermogravimetric analyses. The thermal stability of **46-49** was studied as a function of temperature in the range of 25-500 ˚C. For **46-49**, it is a three-step weight loss profile (see Figure 3.77).

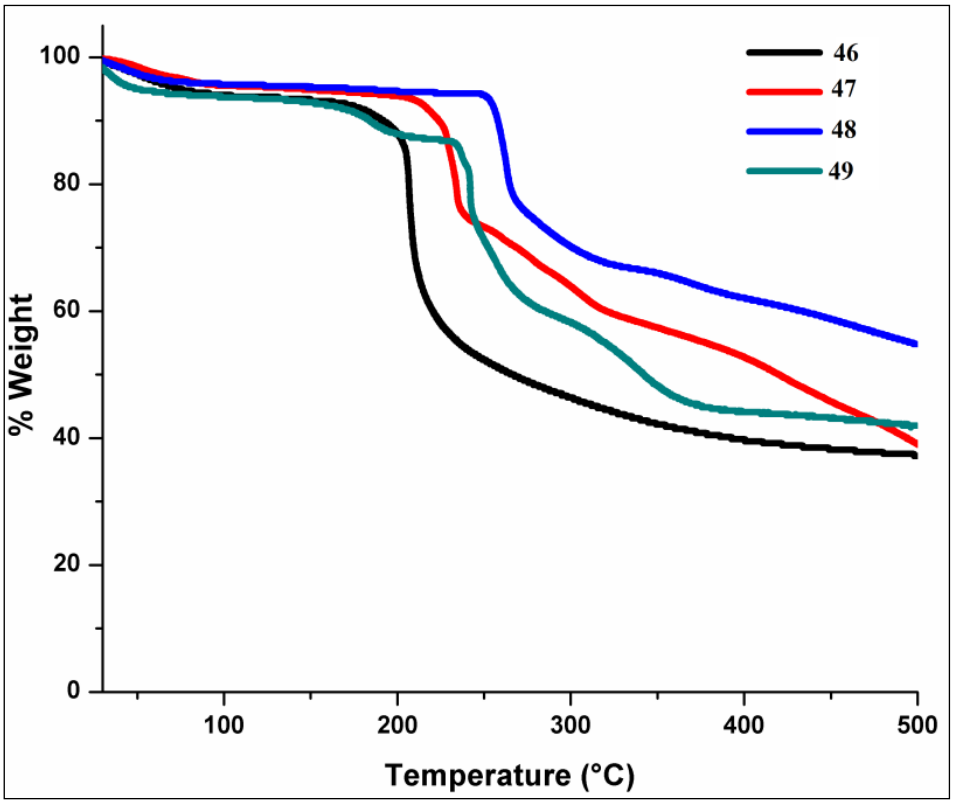

Figure 3.77. TGA Scans for **46-49**.

The first weight loss (~ 50-150 °C) in almost all cases is due to loss of uncoordinated solvent molecule, the second weight loss (~ 150-300 °C) is due to loss of remaining uncoordinated solvent and bipyridine molecule and the third weight loss (~ 300-500 °C) is due to loss of the remaining organic part of the complex. The exact % loss values for **46-49** are reported in

Table 3.17.

Table 3.17. Thermogravimetric analysis for **46-49;** u – uncoordinated, c – coordinated.

Compound	1st step loss			2nd Step loss			3rd Step loss		
	Obsd. %	Calcd. %	Loss	Obsd. %	Calcd. %	Loss	Obsd. %	Calcd. %	Loss
46	2.40	2.40	H_2O (u)	15.80	13.40	H_2O (u), 0.5 (4,4′– bpy)	37.30	38.90	0.5 (4,4′– bpy), ligand
47	4.83	4.14	2 H_2O (u)	21.06	18.00	4 H_2O (u), 0.5 (4,4′– bpy)	32.85	37.70	0.5 (4,4′– bpy), ligand
48	4.63	4.35	2 H_2O (u)	25.68	19.72	4,4′– bpy	13.74	13.27	ligand
49	5.15	5.90	3 H_2O (u)	23.90	19.62	H_2O (u), DMF (u), 0.5 (4,4′– bpy)	21.69	20.00	0.5 (4,4′– bpy), ligand

Single crystal structure analyses. Crystals of **46** and **47** suitable for the single crystal X-ray study were grown from slow evaporation of the respective methanolic solution: **46** in one day and **47** in 3-4 days. Crystals of **48** were grown from slow evaporation of DMSO: methanol (1:1) solution in 20 days.

Compounds **46** and **47** are isostructural and crystallize in the monoclinic chiral *C*2 space group. In each case, there are two equivalent tetracoordinated copper centers with slightly distorted square-planar geometry (as shown in Figure 3.78). The coordination environment around each copper center in **46** and **47** is N_2O_2 type. One of the oxygen binding to Cu^{2+} is from the phenoxy group of the respective ligands and other from the carboxylate of the ligand whereas one nitrogen coordinating to the Cu^{2+} comes from the NH group of the ligand and the other from the 4,4'-bipyridine. The Cu-$O_{phenoxo}$, Cu-$O_{carboxy}$ and Cu-N_{amine} bond distances in **46** and **47** are similar to those found in **34** and **40** and other complexes mentioned above. The selected bond distances and bond angles for **46** and **47** are listed in Tables A1 and A2 of appendix. The asymmetric unit in **46** has three lattice water molecules whereas in **47** there is only one lattice methanol molecule. In each case, the 4,4'-bipyridine acts as a bridge between the two copper centers forming a discrete dinuclear unit.

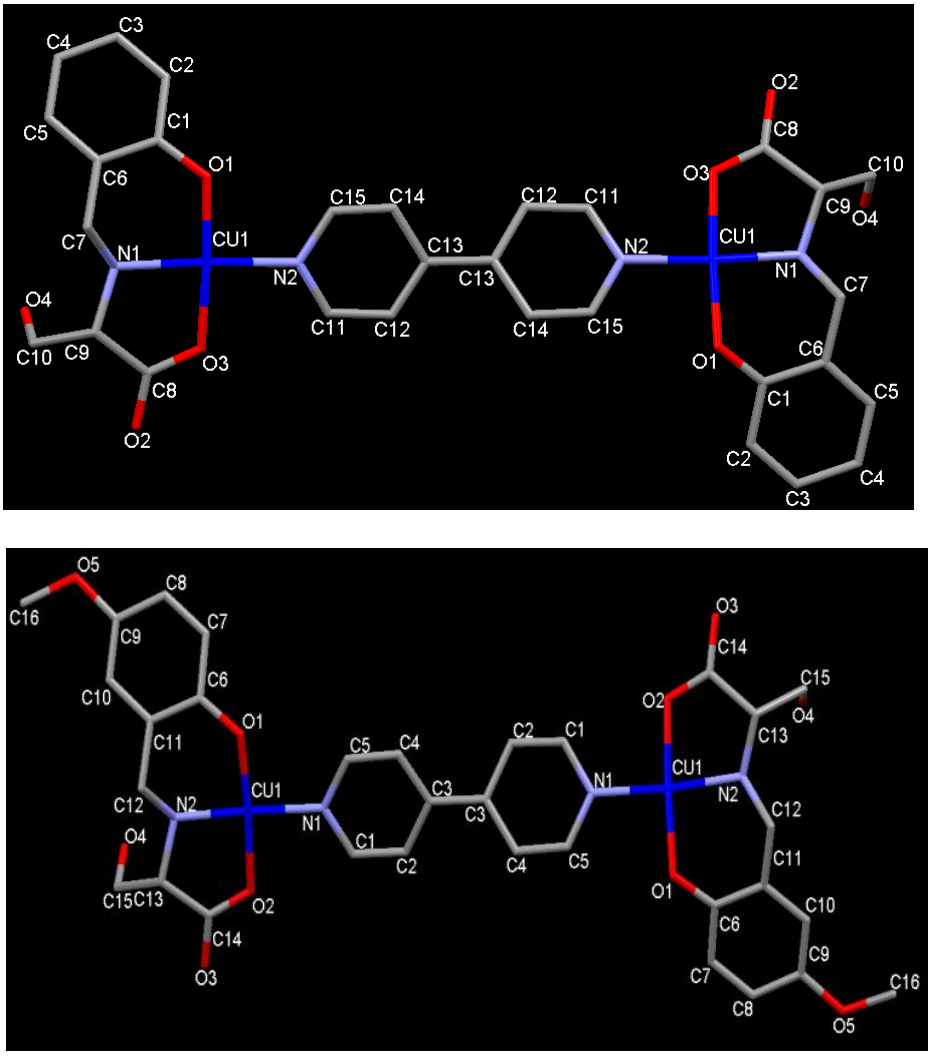

Figure 3.78. Dinuclear subunit in **46** (top) and **47** (bottom). Hydrogen atoms are omitted for clarity.

In **46**, the two phenyl rings of 4,4'-bipyridine are arranged with a twist of -21.5^{o} whereas in **47** these are arranged with a twist of -22.6^{o}. In the literature such a twist of two pyridyl rings of 4,4'-bipyridine is also observed in $[Cu_2(L\text{-tryptophanato})_2(4,4'\text{-bipyridine})(H_2O)_2](NO_3)_2$, where the dihedral angles are 10.6^{o} and 13.6^{o}.[271] These are different from the polymeric coordination compounds reported in the literature with the general formula $[Cu_2(L)_2(4,4'\text{-bpy})]_n$ where L can be any amino acid.[31,271-274] Furthermore, a compound with the formula [Cu(L')(4,4'-bpy)] is reported, where L' is the Schiff base form of the same ligand (H_3sersal) and 4,4'-bipyridine acts as a monodentate ligand.[275] Through intermolecular hydrogen bonding in **46**, the uncoordinated oxygen atom (O2) of the monodendate carboxylate connects oxygen atom (O4) of the CH_2OH (O---O distance: 2.68 Å) of the ligand of next asymmetric unit forming the supramolecular network of the $[Cu_2(4,4'\text{-bpy})(Hsersal)_2]\cdot 2H_2O$ (see Figure 3.79) with a pore size of 18.985 Å x 6.667 Å.

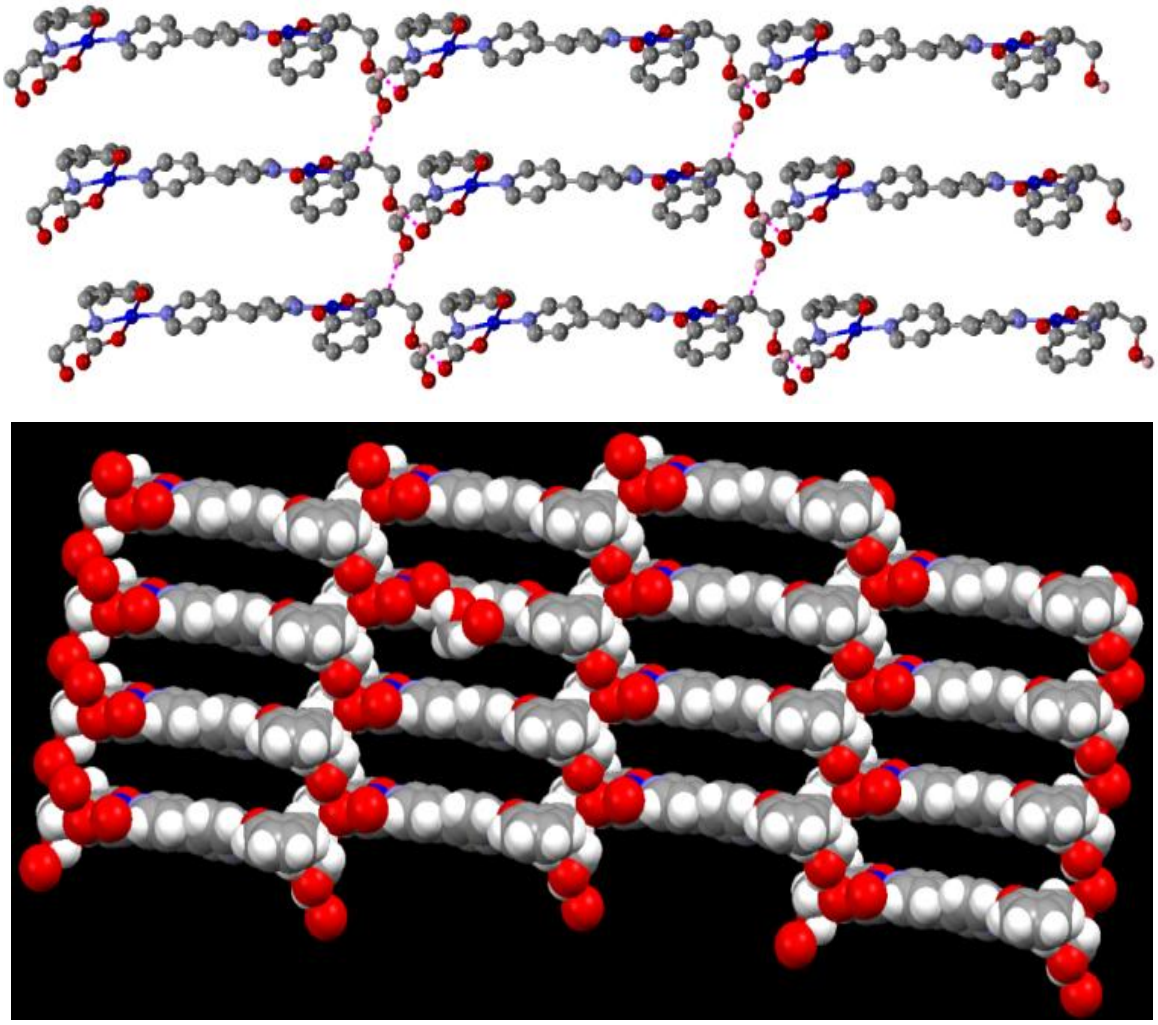

Figure 3.79. Perspective view of the 2D supramolecular assembly in **46** (top). Space-filling representation of the supramolecular assembly in **46** (bottom).

The next layer of the discrete unit is also forming a hydrogen bonded 2D supramolecular assembly. These two 2D supramolecular assemblies are further joined via the solvent molecules (see Figure 3.80). The lattice water molecules sit inside the pores and are hydrogen bonded to each other (O6---O7 distance: 2.893 Å) as well as to the uncoordinated oxygen atom of the carboxylate of the ligand (O6---O2 distance: 2.922 Å). The 1st layer of supramolecular assembly overlaps with the 3rd and the 2nd layer overlaps with the 4th layer (see Figure 3.81). Similarly in **47**, the strong intermolecular hydrogen bonding between the uncoordinated oxygen atom (O3) of the monodendate carboxylate and the oxygen atom (O6) of the CH_2OH (O---O distance: 2.70 Å) of the ligand of next asymmetric unit gives rise to a supramolecular network of $[Cu_2(4,4'\text{-bpy})(Hser\text{-}5\text{-}Cl\text{-}sal)_2]\cdot H_2O$ with pores (see Figure 3.82) having dimensions 19.095 Å x 6.805 Å. The selected bond distances and bond angles for **46** and **47** are listed in Tables A8 and A13, respectively.

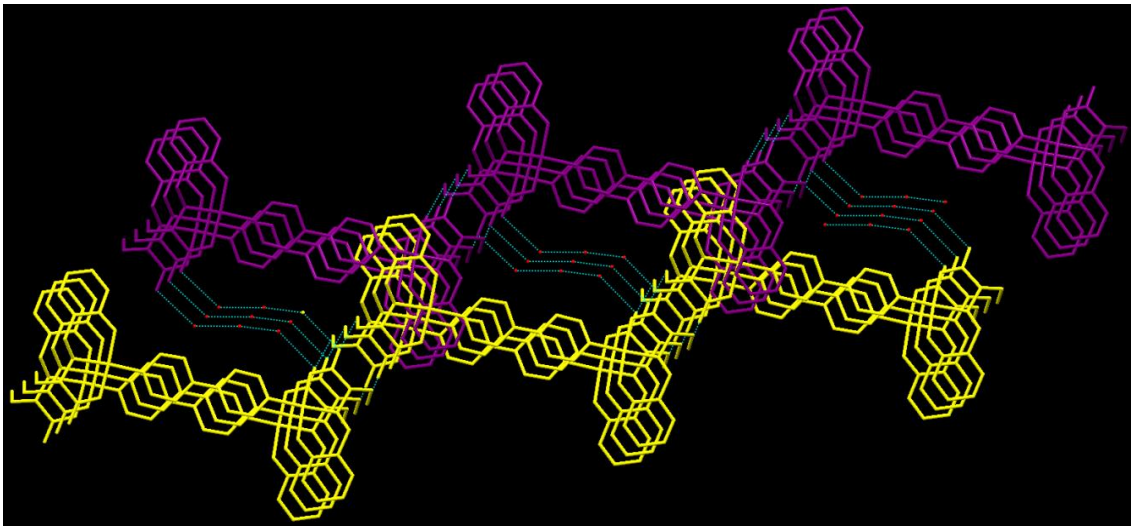

Figure 3.80. Two 2D supramolecular assemblies joined via solvent molecules in **46**. Hydrogen atoms are omitted for clarity.

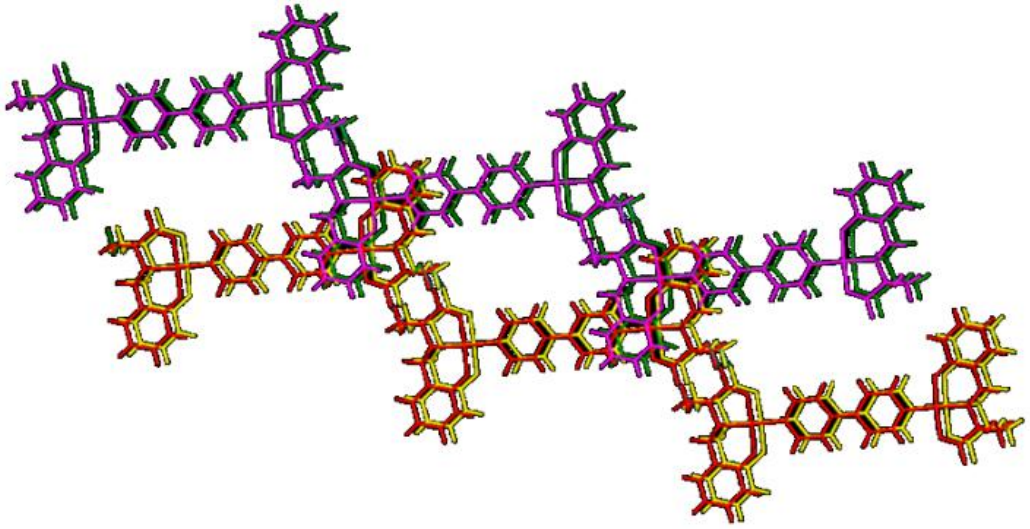

Figure 3.81. Overlap of 1st with 3rd and 2nd with 4th layers in 2D supramolecular layers in **46**.

Compound **48** crystallizes in the same chiral space group (C2) as **46** and **47**; its asymmetric unit (as shown in Figure 3.83) is also similar to those of **46** and **47** except **48** has three lattice DMSO molecules instead of lattice water molecules found in **46** and **47**. No supramolecular assembly is observed in **48** as the hydrogen bonding exists between the oxygen atom (O3) of the $-CH_2OH$ of the ligand and the oxygen atom (O7) of one of the lattice DMSO molecules (O---O distance: 2.671 Å) thus preventing O3 to do any further hydrogen bonding with the oxygen atom of the carboxylate of the next molecule. However, the supramolecular network in **48** is formed by the strong C–H···O interactions (see Figure 3.84). Each dinuclear unit is connected to the next one by the C10–H10···O6 (C···O distance 3.5 Å) interactions forming a

supramolecular chain. The DMSO molecules also show various C–H···O interactions among themselves, C16–H16C···O8 (C···O distance 3.270 Å) and C17–H17A···O8(C···O distance 3.279 Å), to form another chain in an alternate fashion with the dinuclear unit. Through other C– H···O interactions (C16–H16B···O2, C···O distance 3.592 Å; C17–H17B···O1, C···O distance 3.306 Å; and C2–H2A···O8, C···O distance 3.104 Å), the two hetero supramolecular chains add on to the dimentionality of the supramolecular network. Thus the encapsulation of the DMSO cluster within the supramolecular array of **48** is observed. The selected bond distances and bond angles for **48** are listed in Tables A8 and A14, respectively.The crystallographic parameters and basic information pertaining to data collection and structure refinement for **46, 47** and **48** is summarized in Table A4. Hydrogen bonding parameters for **46, 47** and **48** are summarized in Table 3.18.

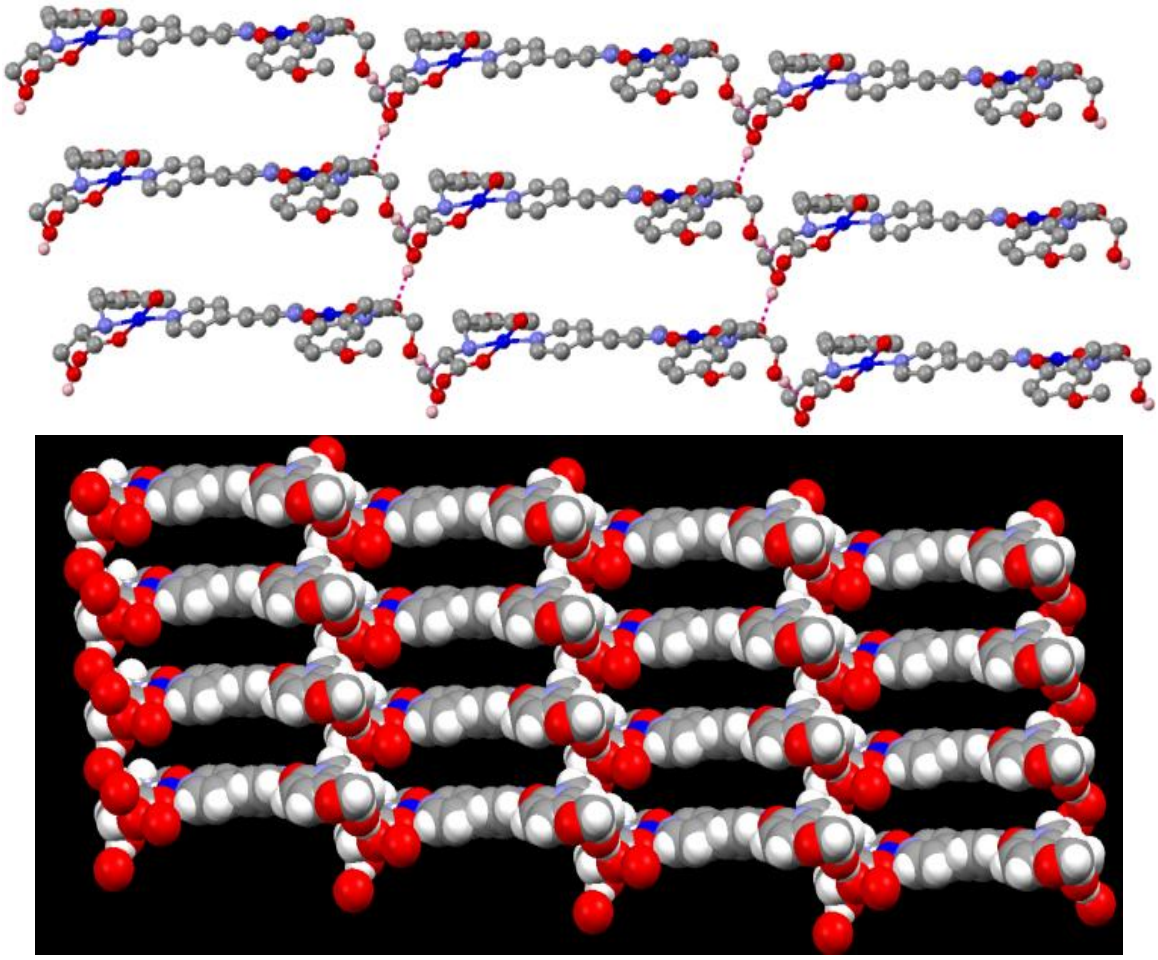

Figure 3.82. Perspective view of the 2D supramolecular assembly in **47** (top). Space-filling representation of the supramolecular assembly in **47** (bottom).

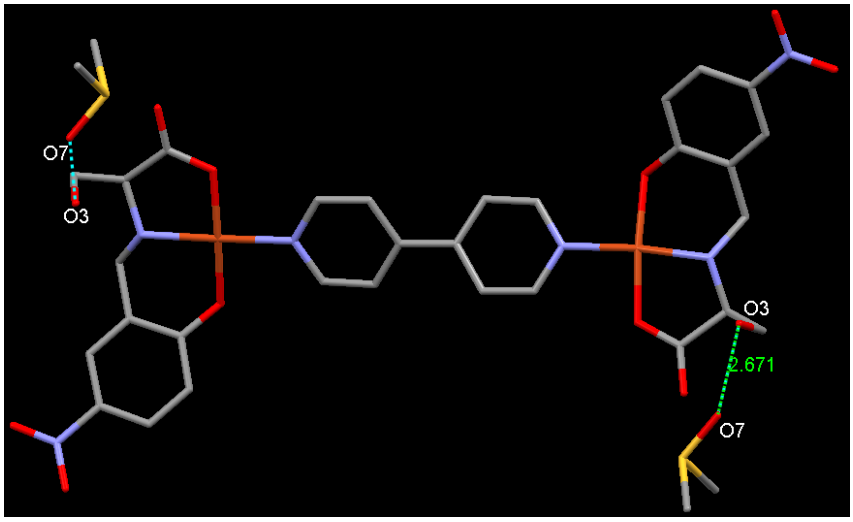

Figure 3.83. Dinuclear unit in **48**. Also shown hydrogen bonding with the lattice DMSO molecules. Hydrogen atoms are omitted for clarity

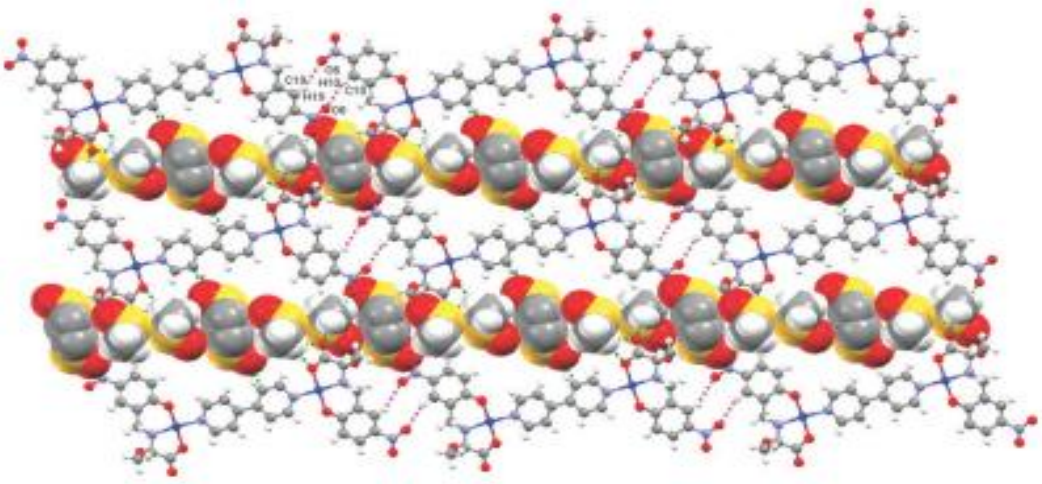

Figure 3.84. Perspective view of the supramolecular assembly in **48**. Encapsulated lattice DMSO molecules are shown in space-filling representation.

Conversion of CPs to SCCs.

Just considering the bonds broken in **34** and bonds formed in **46** (Scheme 6), it is very clear that it is not a *simple ligand exchange reaction*. First, the bis(phenoxo)dicopper core in **34** is very stable (Cu-O bonds are symmetrical) and thus inserting the neutral 4,4'-bpy ligand between the two Cu^{2+} centers to form **46** requires changing the bridging mode of the phenoxo groups to the monodendate mode. Secondly, during this transformation reaction the binding modes of both the $-CH_2OH$ and $-CO_2^-$ groups in the Sersal ligand are also affected showing a lot of changes around the copper centers in the polymeric structure of **34**. This can be understood by observing the change in the coordination numbers of the metal centers (Cu1: 6 to 4 and Cu2: 5 to 4) during this transformation. The strong hydrogen bonding between the dinuclear subunits in **46** that stabilized it over **34** should be considered. Even though a

coordination polymer (CP) is considered to be more stable than the networks of a dinuclear complex, different bindings of the functionalities of the same ligand as well as strong hydrogen bonding are responsible for such transformation. It should be noted that based on the PXRD data the bulk of **46** (in high yield) is same as its crystals used in structure determination removing any doubt that kinetic artefact of crystal growth could be the reason for its formation instead of thermodynamic end product. This is an unexpected finding and questions the strength of coordination bonds in polymeric structures. There is no prior example in the literature for such transformation. In fact, a *simple ligand exchange reaction* (substituting the water molecule on Cu2) to connect the 2D CP of **34** with the 4,4'-bpy ligand would have given an expected product.

Table 3.18. Hydrogen bonding parameters for **46, 47** and **48**.

D–H…A	r (D-H) (Å)	r (H…A) (Å)	r (D…A) (Å)	∠D-H…A (°)	Symmetry
46					
O(4) -H(19)..O(2)	0.84	1.84	2.680(15)	173	1/2-x,1/2+y,1-z
C(11)-H(11) ..O(4)	0.95	2.39	3.218(15)	146	1/2-x,1/2+y,1-z
C(14)-H(14) ..O(5)	0.95	2.56	3.50(2)	171	-x,y,1-z
47					
N(2) --H(4) ..O(1)	0.98	2.35	3.1447	137	1/2-x,-1/2+y,1-z
O(6) --H(6) ..O(3)	0.82	1.88	2.7	176	1/2-x,-1/2+y,2-z
C(5) --H(5) ..O(6)	0.93	2.43	3.2147	143	1/2-x,1/2+y,1-z
C(12) --H(12) ..O(3)	0.98	2.58	3.475	152	1/2-x,1/2+y,2-z
C(16) --H(16A) ..O(3)	0.96	1.8	2.7488	168	1/2-x,1/2+y,2-z
48					
O(3) --H(3) ..O(7)	0.82	1.94	2.6711	147	1/2-x,1/2+y,1-z
C(2) --H(2A) ..O(8)	0.93	2.28	3.104	147	
C(16) --H(16A) ..O(1)	0.96	2.31	3.1401	144	1/2-x,-1/2+y,1-z
C(17) --H(17A) ..O(8)	0.96	2.35	3.2791	163	
C(17) --H(17B) ..O(1)	0.96	2.57	3.3068	133	
C(17) --H(17C) ..O(1)	0.96	2.28	3.1928	159	1/2-x,1/2+y,1-z

Powder X-ray data analysis. To confirm whether the single crystal structure corresponds to the bulk material or not, powder X-ray diffraction patterns were recorded for **46**, **47**, **48** and **49** at room temperature. The experimental and simulated (from the single crystal data) patterns were similar to each other (see Figures 3.85). The patterns obtained confirm that the single crystal and bulk material are the same. It also confirms the phase purity of the bulk sample. Additionally, powder pattern **46** after drying at 100 °C for 15 minutes were recorded. No change in the powder pattern indicates the retention of structure and crystallinity due to this treatment.

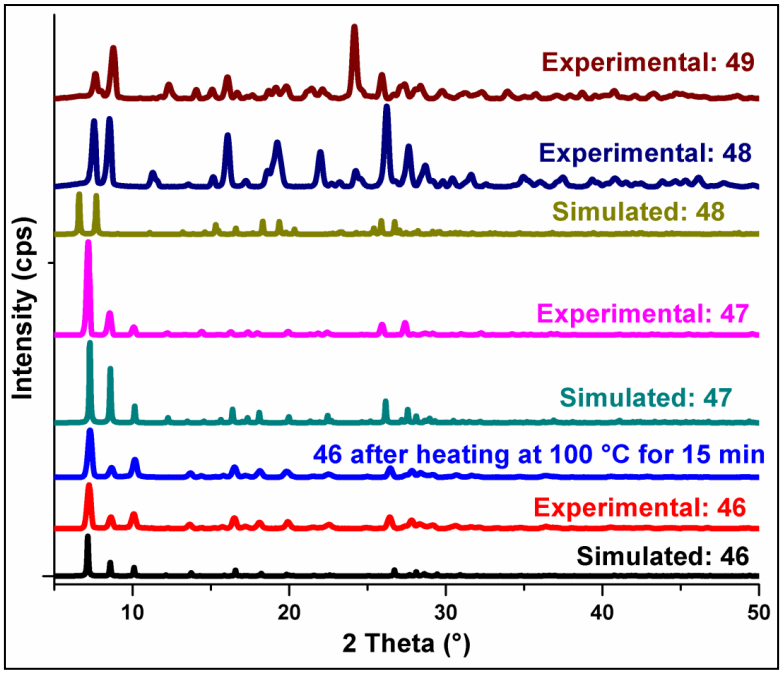

Figure 3.85. PXRD patterns for **46**, **47**, **48** and **49**.

UV-Vis and Circular Dichroism (CD) spectroscopy. UV-Visible and CD spectroscopic studies were carried using ~1 mM methanolic solution of **46-49** (see Figures 3.86 and 3.87). The UV-Vis spectral data for **46-49** are reported in Tables 3.19. The peaks around 650-685 nm in these complexes are due to the d-d transition (^2E_g to $^2T_{2g}$) of Cu^{2+} whereas the peaks around 370-420 nm are due to LMCT, i.e., from -C=O of carboxylate to the metal center.[253] In the UV region of the spectrum (200 to 350 nm), the peaks at around 200-210 nm (π-π*) is due to L-serine part of the ligand and 245-260 nm (n-π*) is due to aldehyde part of the ligand. In **46, 47, 48** and **49** a peak at around 235 nm for 4,4'-bipyridine (π-π*) is also observed.

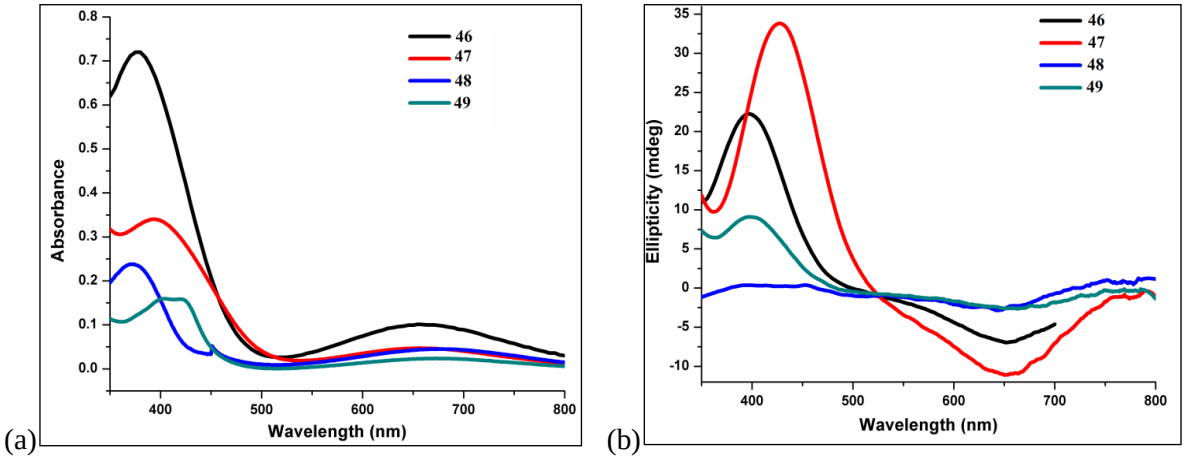

Figure 3.86. (a) UV-vis and (b) CD spectra for **46-49** in the wavelength range from 350 to 800 nm.

(a) 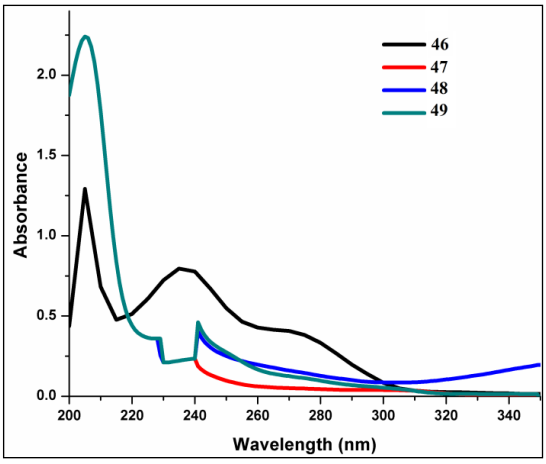

(b) 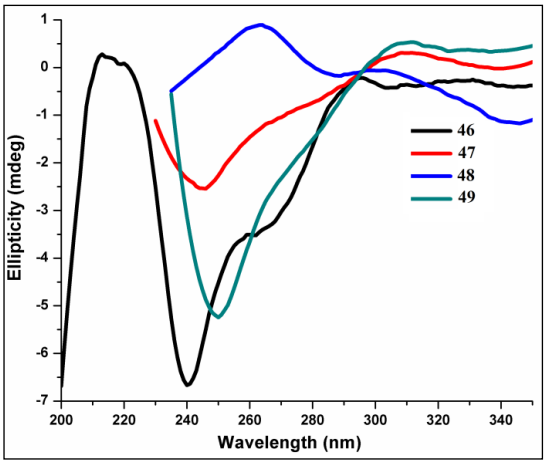

Figure 3.87. (a) UV-vis and (b) CD spectra for **46-49** in the wavelength range from 200 to 350 nm.

The peaks in the CD spectra for **46-49** are reported in Table 15. The Cotton effects observed at around 400 nm are due to LMCT whereas the Cotton effects observed around 650 nm are due to d-d transitions.[254] The peaks in the CD spectra for **46-49** are reported in Table 3.20.

Table 3.19. Peaks in the absorption spectra for **46-49**.

Compound	λ, nm (ε, $L \cdot mol^{-1} \cdot cm^{-1}$)	λ, nm (ε, $L \cdot mol^{-1} \cdot cm^{-1}$)
46	655 (213)	389 (736)
47	657 (40)	394 (289)
48	680 (40)	392 (4757)
49	673 (21)	403 (137)

Table 3.20. Peaks in CD spectra of **46-49**.

Compound	Positive Cotton Effect (nm)	Negative Cotton Effect (nm)
46	630, 260, 240, 200	500, 400, 309
47	648, 340, 271, 245	512, 430, 309
48	641, 343, 292	537, 399, 305, 264
49	658, 277, 251	487, 396, 308

Magnetic properties of $\{[Cu_2(Hsersal)_2(H_2O)]\cdot 2.5H_2O\}_n$ (34) and $[Cu_2(4,4'\text{-bpy})(Hsersal)_2]\cdot 2H_2O$ (46). For comparison, variable-temperature magnetic susceptibility measurements were performed on powdered samples of **34** and **46** in the temperature range 2-380 K. The plot of the observed magnetic susceptibility (χ_{obs}) versus temperature (T) including best fit theoretical line for **34** is shown in the inset of Fiure 3.92. The observed susceptibility (χ_{obs}) shows a broad maximum at around 200–250 K before decreasing at lower temperatures. Below about 20 K, χ_{obs} increases strongly. This lowest temperature behavior most likely arises from the presence of a small amount of paramagnetic impurities in the material.

The plot of χT versus T for 43 is shown in Figure 3.88. As expected, the value of χT is much lower than expected (0.375 cm^3/Cu mol) for free S = ½ moments with a g-factor of 2. This reduction is due to the fact that at 400 K the Cu^{2+} spins with S = ½ are already coupled antiferromagnetically. The χT continues to decrease with lowering T and goes to 0 as T tends to 0 as expected for a spin-singlet state of dimerized spins. The magnetic susceptibility of S = ½ dimers should have the following temperature dependence based on the modified Bleaney-Bowers equation[276]:

$$\chi_{dimer} = \frac{3C/T}{\left(3+\exp\left(\frac{\Delta}{T}\right)\right)}$$

where C is the Curie constant for S = ½ moments and Δ is the spin-gap produced by phenoxo-bridged dicopper units. Δ is also the strength of the magnetic interaction (Δ = -2J, where J is the antiferromagnetic exchange given by the nearest-neighbor Heisenberg Hamiltonian $H = -2JS_1.S_2$) between the S = ½ moments. The χ_{obs} therefore has two contributions - the intrinsic contributions from the strongly coupled dicopper units and the paramagnetic impurity contribution - as follows:

$$\chi_{imp} = \chi_0 + \frac{C_{imp}}{T-\theta}$$

where χ_0 is a temperature independent contribution, C_{imp} is the Curie constant of the impurity and θ is the Weiss temperature associated with interactions between these impurities. Thus, the χ_{obs} was fitted by the expression $\chi_{obs} = \chi_{imp} + \chi_{dimer}$. The main panel in Figure 3.89 shows the dimer susceptibility after the impurity part has been subtracted; the solid curve through the data is the theoretically expected χ_{dimer} for S = ½ dimers. An excellent fit was obtained as shown by the solid curve through the χ_{obs} data in the inset with the following values: C_{imp} = 0.009 cm^3/Cu mol K, θ = -4.7 K, C = 0.51 cm^3/Cu mol K, Δ = 400 K. In terms of the exchange interaction, -2J = 400 K = 278 cm^{-1}. This value is in the range observed for the bis(phenoxo) bridged square pyramidal Cu^{2+} dimers in CPs[241] or discrete compounds providing an excellent magneto-structural correlation (2J value versus Cu^{2+}-O-Cu^{2+} angle and Cu^{2+}...Cu^{2+} distance). [277-279]

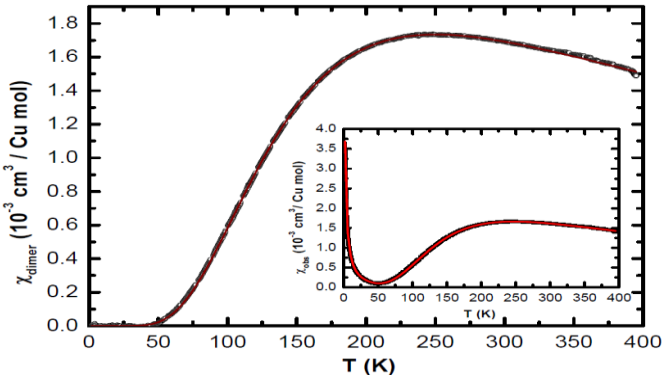

Figure 3.88. χ_{dimer} vs T plot for **43**; the solid line is the best fit to the experimental data. Inset: χ_{obs} vs T plot.

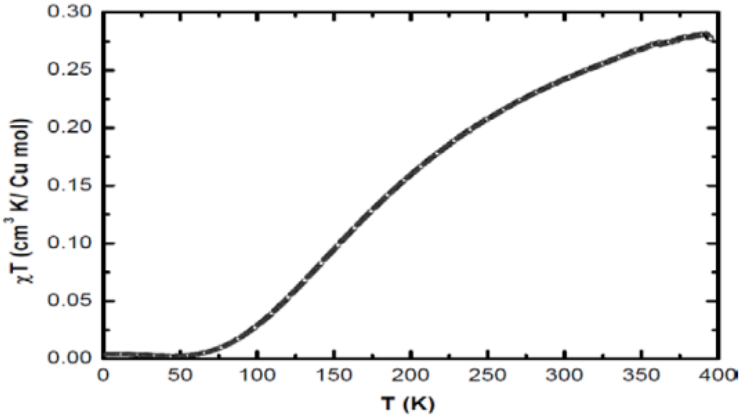

Figure 3.89. χT vs T plot for **34.**

In contrast, based on the structure of **46** for non-interacting Cu^{2+} ions (independent S = ½ moments) a Curie-Weiss like paramagnetic behavior is expected in the whole temperature range. This is exactly what is observed in magnetic measurements. Figure 3.90 shows the χT versus T data between 2-390 K. The value at 390 K is 0.375 cm^3/Cu molK, which is close to the value expected for S = ½ moments. The χT has weak T dependence down to the lowest temperatures and its value stays close to the expected free spin S = ½ value. The inset shows the inverse susceptibility 1/χ versus T data. The data could be fit using a Curie-Weiss expression:

$$\boldsymbol{\chi = \chi_0 + \frac{C}{T - \theta}}$$

The fit shown as the solid curve through the data gave the values χ_0 = -3.8 x 10^{-5} cm^3/Cu mol, C = 0.35 cm^3/Cu molK, and θ = 0 K. The obtained value of the Curie constant C is slightly lower than but close to the expected value 0.375 cm^3/Cu molK expected for S = ½ moments with a g-factor of 2. The θ = 0 indicates that the Cu^{2+} centers bridged by the 4,4'-bpy ligand do not interact at all.

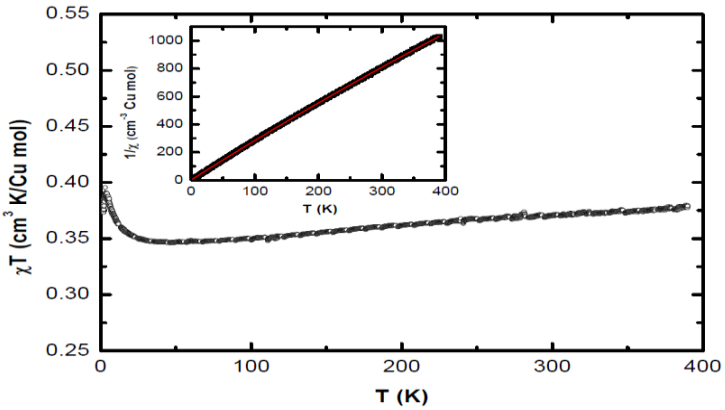

Figure 3.90. χT vs T plot for **46**; the solid line is the best fit to the experimental data. Inset: 1/χ vs T plot.

Water adsorption studies. In order to demonstrate the change in the porous nature of SCCs compared to non-porous CPs in the solid state structures (vide infra), water adsorption studies of **34** and **46** were carried out. Each sample of **34** and **46** was pretreated for 24 hours at 100 °C under vacuum followed by purging with nitrogen to use in this study. At $p/p_o = 1$ (where po is the vapor pressure at saturation), **34** adsorbed approx. 340 cm^3 water per g of sample with very little at low p/p_o value (see Figure 3.95). The least affinity towards water by **34** correlates well with its structure. On the other hand, **46** adsorbed approx. 220 cm^3 water per g of sample in a gradual uptake (see Figure 3.91). This value indicates strong adsorbate-adsorbate interactions via hydrogen bonding at higher p/p_o.

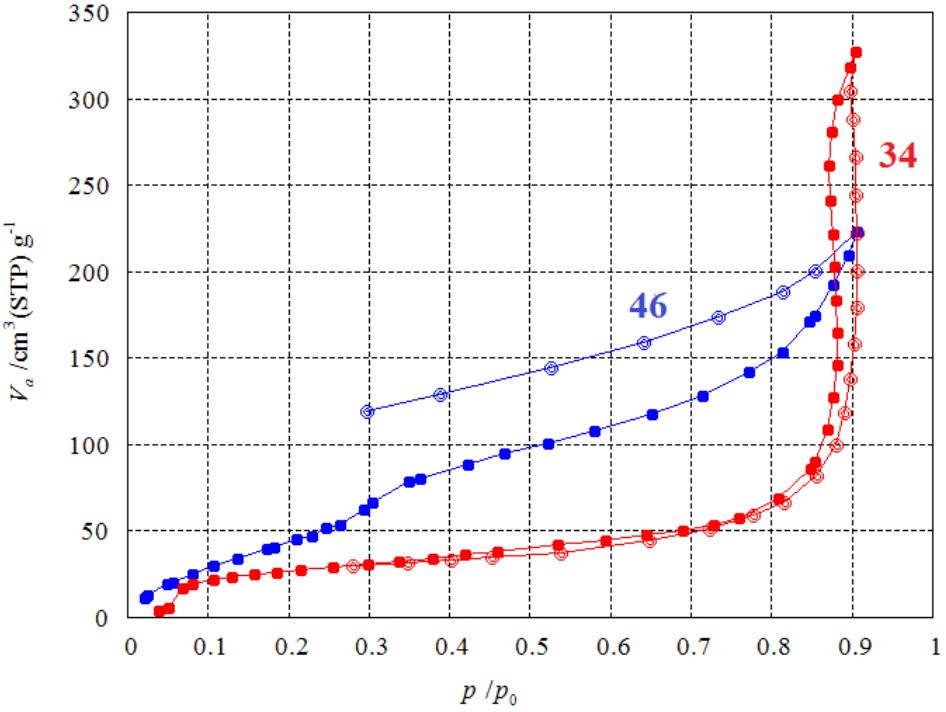

Figure 3.91. Water adsorption isotherms for **34** and **46** (Redlines: **34**, Bluelines: **46**; filled squares, adsorption and circles, desorption).

Its desorption curve does not follow the adsorption one generating a prominent hysteretic profile that is indicative of hydrophilic nature of the pore surfaces in it. On desorption it showed retention of water confirming the fact that at ambient conditions it retains two-third of the water upon rehydration. This study clearly indicates the conversion of a nonporous **34** into porous **46** (as shown in Figure 3.92).

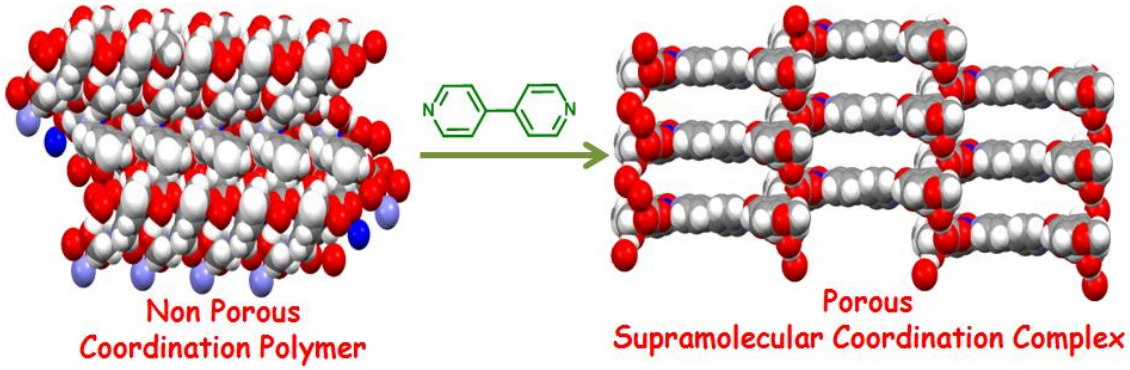

Figure 3.92. Conversion from nonporous **34** to porous **46.**

3.2.1.2b. For a 1:1 metal:ligand ratio with anionic linkers

Synthesis. In this category, the metal complex $[Ni_2(Hhissal)_2(adi)(H_2O)_2]\cdot 8H_2O$ (**50**) was obtained via a one pot synthesis by stirring a methanolic solution of $NiSO_4.7H_2O$, KHhissal and dipotassium salt of adipic acid (in a 1:1:0.5 ratio) for 12 hours at room temperature (as shown in Scheme 3.9). The desired product is obtained from evaporating the filtrate (the solid by-product K_2SO_4 insoluble in methanol is the precipitate) under reduced pressure. Following the same strategy synthesis of supramolecular assemblies using Ni^{2+} and KHhissal along with the use of other dicarboxylates:, $[Ni_2(Hhissal)_2(succ)(H_2O)_2]\cdot 4H_2O$ (**51**) and $[Ni_2(Hhissal)_2(mal)(H_2O)_2]\cdot 4H_2O$ (**52**) and $[Ni_2(Hhissal)_2(fum)(H_2O)_2]\cdot 6H_2O$ (**53**) are synthesized.

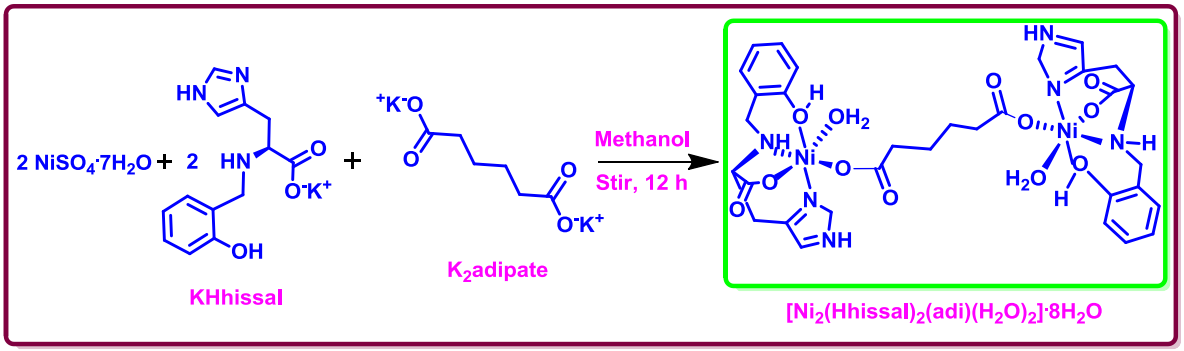

Scheme 3.10. Synthesis of **50**.

Generation of supramolecular assemblies due to hydrogen bonding interactions of the various water clusters with metal complexes and slight modifications in structures of these water clusters, opens the door towards their application in various fields, like host guest chemistry, sensing, molecular recognition, etc. The water octamer encapsulated within **50** is a zig-zag open chain. The higher stability of **50** can be attributed to the encapsulated octameric water ribbon within it which is extensively hydrogen bonded to this coordination architecture.

FT-IR Spectroscopy. The IR spectra of **50-53** recorded in the solid state as KBr pellets show two broad bands in the region of 3400-3200 cm^{-1}. For compound **50**, the broad peak at 3380 cm^{-1} is for H-bonded phenolic–OH. For **51**, **52** and **53** the corresponding peaks appear at 3375 cm^{-1}, 3384 cm^{-1} and 3380cm^{-1}, respectively. For N-H stretching, the peak for **50** appears at 3008 cm^{-1}, for **51** at 3017 cm^{-1}, for **52** at 3023 cm^{-1} and for **53** at 3025 cm^{-1}. The asymmetric stretch for the carboxylate of the ligand appears at around 1592 cm^{-1} for **50**, 1600 cm^{-1} for **51**, 1598 cm^{-1} for **52** and 1596 cm^{-1} for **53** while the symmetric stretch appears at 1480 cm^{-1} for **50**, 1481 cm^{-1} for **51**, 1480 cm^{-1} for **52** and 1480 cm^{-1} for **53**. The asymmetric stretch for the dicarboxylates appears at 1567 cm^{-1} for **50**, 1568 cm^{-1} for **51**, 1574 cm^{-1} for **52** and 1576 cm^{-1} for **53** while the symmetric stretch appears at 1406 cm^{-1} for **50**, 1397 cm^{-1} for **51**, 1401 cm^{-1} for **52** and 1404 cm^{-1} for **53**. In all four compounds C-O stretching for the phenoxo part of the ligand appears at around 1294 cm^{-1}. These comparative data indicate that all three compounds are isostructural.

Thermogravimetric Analyses. The thermal stability of compounds **50-53** (see Figures 3.93) was studied as a function of temperature in the range of 25-500 ˚C. For **50**, it is a three-step weight loss profile. The first weight loss of 7.63% between 50-160 ˚C corresponds to the loss of four uncoordinated water molecules (ca. 7.49%). The second step showing weight loss of 22.80% between 260-360 ˚C indicates loss of four uncoordinated water molecules, two coordinated water molecules and two carbon dioxide molecules (ca. 22.04%). The third weight loss of 31.59% between 370-470 ˚C indicates loss of ligand (ca. 37.0%). For **51**, it is a three-step weight loss profile. The first weight loss of 9.11% between 50-130 ˚C corresponds to the loss of four uncoordinated water molecules (ca. 8.35%). The second step showing weight loss of 18.7 % between 290-415 ˚C indicates loss of two uncoordinated water molecules, two coordinated water molecules and two carbon dioxide molecules (ca. 15.69%). The third weight loss of 26.3% between 420-500 ˚C indicates loss of ligand (ca. 22.4%). For **52**, it is also a three-step weight loss profile. The first weight loss of 10.3 % between 50-105

˚C corresponds to the loss of four uncoordinated water molecules (ca. 8.36%). The second step showing weight loss of 17.76% between 260-380 ˚C indicates loss of two coordinated water molecule and two carbon dioxide molecules (ca. 15.73%). The third weight loss of 25.69% between 400-500 ˚C indicates loss of histidine (ca. 22.61%). For **53**, it is also a three-step weight loss profile. The first weight loss of 11.3 % between 50-150 ˚C corresponds to the loss of six uncoordinated water molecules (ca. 12.05%). The second step showing weight loss of 16.89% between 230-350 ˚C indicates loss of two uncoordinated water molecules, two coordinated water molecules and two carbon dioxide molecules (ca. 15.73%). The third weight loss of 23.39% between 400-500 ˚C indicates loss of histidine (ca. 22.81%).

Single crystal Structure Analysis. Crystals of **50** suitable for the single crystal X-ray study were grown from the slow evaporation of its methanolic solution within a week. Compound **50** crystallizes in the chiral monoclinic space group *C*2. Each discrete dinuclear unit has two equivalent hexacoordinated nickel centers with slightly distorted octahedral geometry and linked together by one adipate molecule (as shown in Figure 3.94). A 2-fold axis generates the asymmetric unit.

The coordination environment around each nickel center is N_2O_4 type. The two oxygen atoms binding to Ni^{2+} are from the phenoxy group and the carboxylate of the Hhissal whereas the third oxygen binding to Ni^{2+} is from the carboxylate of the adipate and the fourth oxygen is from the coordinated water. One nitrogen coordinating to Ni^{2+} is from the NH of the amino group of the ligand whereas the other nitrogen is from the imidazole group of the ligand. The carboxylate of the ligand as well as the carboxylate of the adipate binds to Ni^{2+} in a monodentate fashion. Even after using two equivalent of base the phenolic oxygen of the ligand remains protonated. Selected bond distances and bond angles for **50** are listed in Table A8 and A14, respectively.

In the literature, the mononuclear complexes of the H_2hissal ligand $[Ni(Hhissal)_2].H_2O$[34,280] as well as $[Ni(hissal)].H_2O$[281] have been reported. Based on these two examples, it is inferred that whether phenolic –OH is protonated or not, depends on the intramolecular hydrogen bonding and does not depend on the amount of base used. Using some other neutral or monoanioic ligands like imidazole, SCN^- or benzoate supramolecular assemblies of $[Ni(hissal)(imidazole)_2]$, $[Ni(Hhissal)(SCN)(H_2O)]\cdot H_2O$ and $[Ni(Hhissal)(benzoate)(H_2O)]\cdot H_2O$ have been reported.[34,280] In case of $[Ni(Hhissal)_2]\cdot H_2O$, the ligand acts as a monoanion due to strong intermolecular hydrogen bonding between phenolic

OH group and the carboxylate group of the next molecule. On the other hand, in [Ni(Hhissal)(benzoate)(H_2O)]·H_2O the intramolecular hydrogen bonding between one of the oxygens of the benzoate and the OH group of the ligand is responsible for it to be a neutral species even when two equivalents of the base is used. In case of **50**, a similar strong hydrogen bonding is observed between oxygen of the carboxylate of the adipate and the phenolic –OH (O-O distance: 2.585 Å) hence, preventing deprotonation of the phenolic –OH despite the use of two equivalents of base (as shown in Figure 3.94).

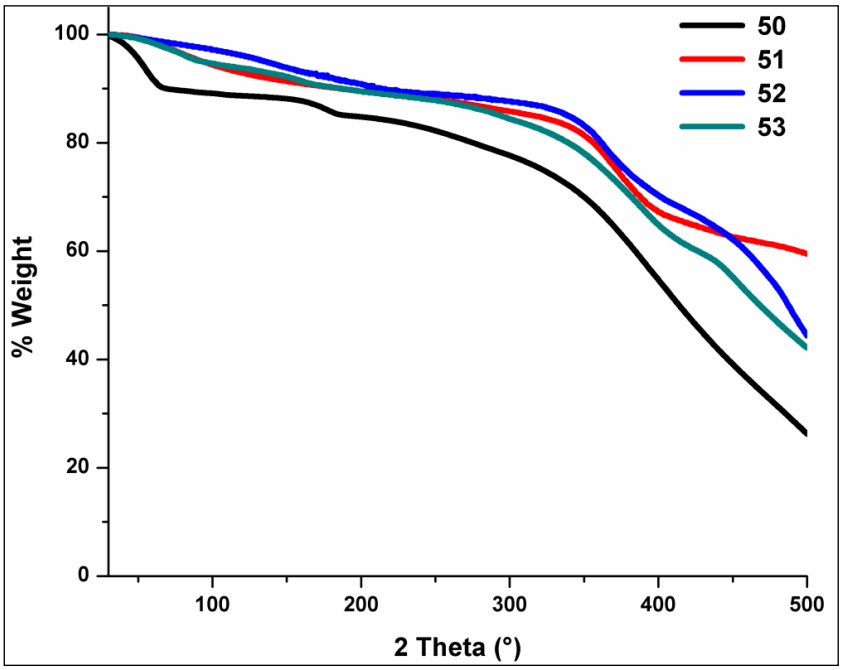

Figure 3.93. TGA scans for **50-53**.

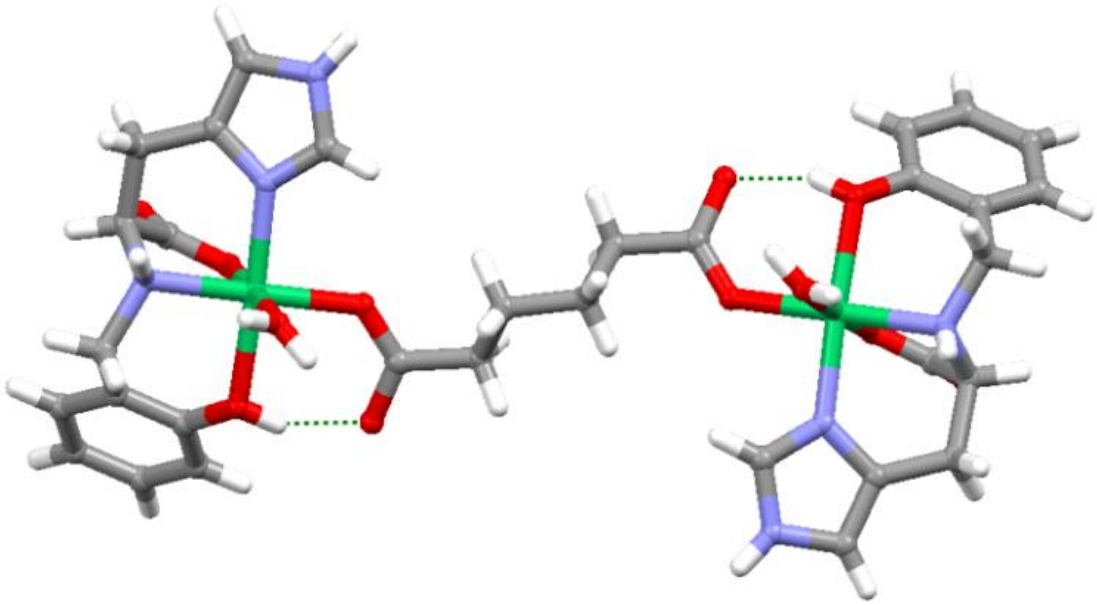

Figure 3.94. Dinuclear unit in **50**. Lattice water molecules are omitted for clarity.

The dimeric unit grows in one direction forming a 2D sheet-like structure via intermolecular hydrogen bonding. The nitrogen of the amine of the ligand and the oxygen atom of the coordinated water molecule of the dinuclear subunit is hydrogen bonded to the uncoordinated oxygen atom and the coordinated oxygen atom of the carboxylate of the ligand of the next subunit respectively forming a ladder like structure (as shown in figure 3.95). This 2D sheet is further hydrogen bonded to similar 2D sheet via hydrogen bonding giving a 3D network of intercalated ladder. The -NH of the imidazole ring of the ligand of first 2D sheet shows bifurcated hydrogen bonding with the oxygen atom (O6) of the coordinated water and the uncoordinated oxygen atom (O2) of the carboxylate forming this intercalated ladders (as shown in Fig 3.96). On each sides of the ladder the octameric chain of water was strongly hydrogen bonded to the dimeric unit (as shown in Fig 3.97).

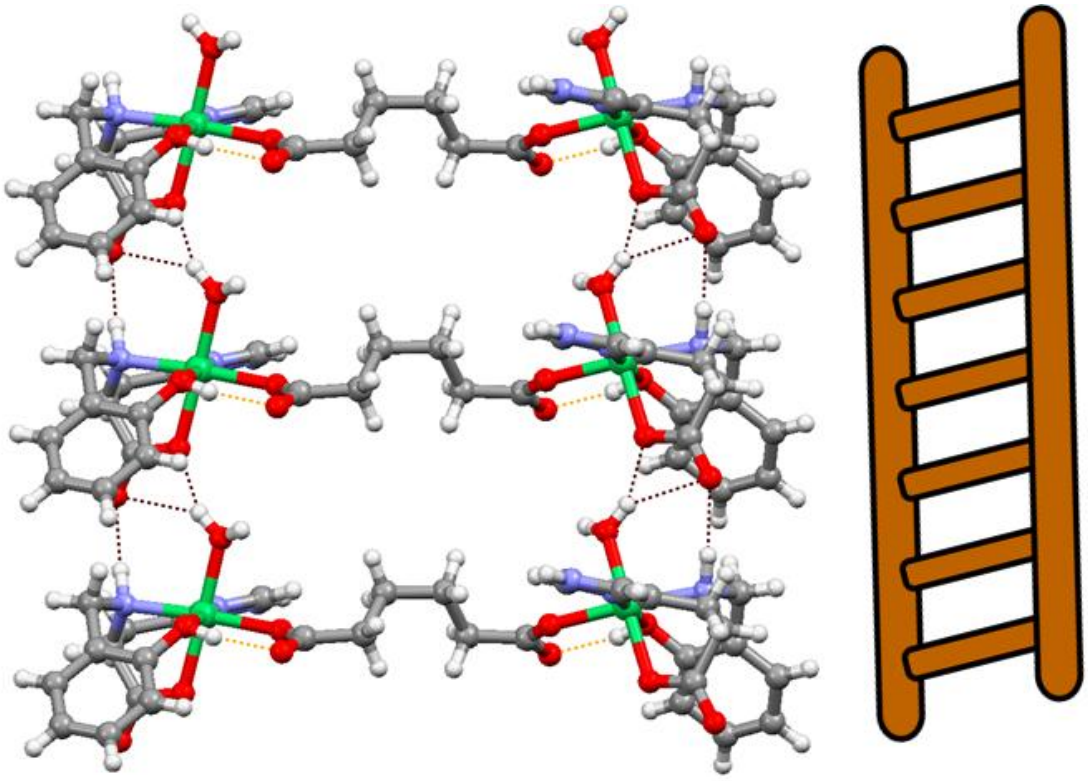

Figure 3.95. 2D sheet forming ladder structure in **50** via hydrogen bonding interactions (intramolecular hydrogen bonding shown in orange and intermolecular hydrogen bonding shown in violet).

While doing so, the lattice water octamer (O7, O7', O8, O8', O9, O9', O10 and O10') present in the molecule arranges itself in the form of a 1D zigzag chain via intermolecular hydrogen bonding. The six water molecules (two O8, two O9 and two O10) form the backbone of this

chain whereas two water molecules (two O7) are just attached to this backbone (as shown in 3.98).

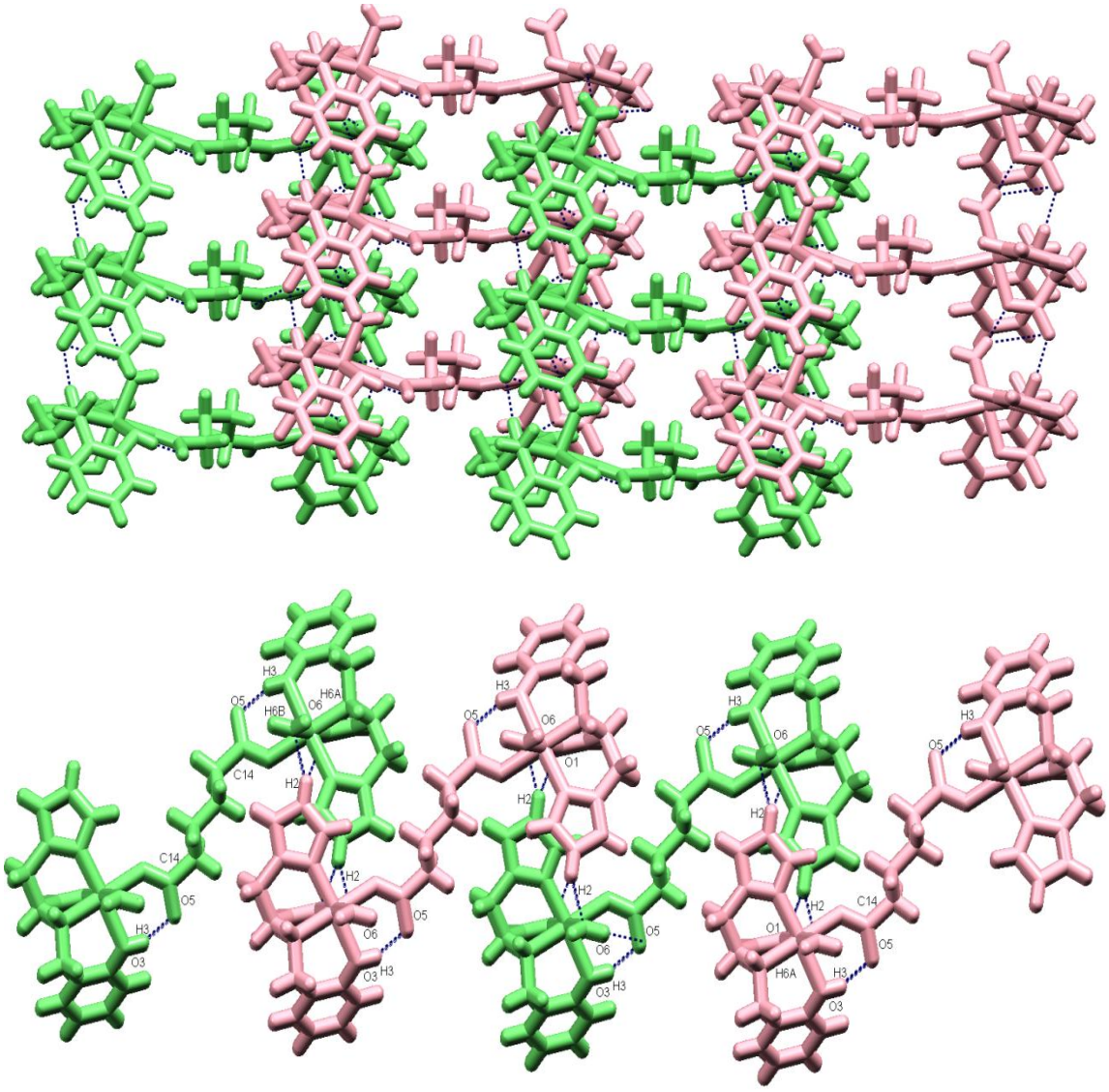

Figure 3.96. Intercalated 3D ladder structure in **50;(** a) along c-axis, (b) along with b-axis.

The octamer of water in **50** shows strong hydrogen bonding (the O-O distances range between 2.6620 Å to 2.7492 Å) and are found to be very close to the ice (2.783 Å) [282-284] The dinuclear units are strongly hydrogen bonded to octameric water chains on both the ends. So it is observed that the octameric chain of water is encapsulated between the hydrogen bonded 2D sheets of the dimeric units of **50** through strong hydrogen bonding (as shown in Figure 3.99). The crystallographic parameters and basic information pertaining to data collection and structure refinement for **50** is summarized in Table A5. The hydrogen bonding parameters found in **50** are summarized in Table 3.21.

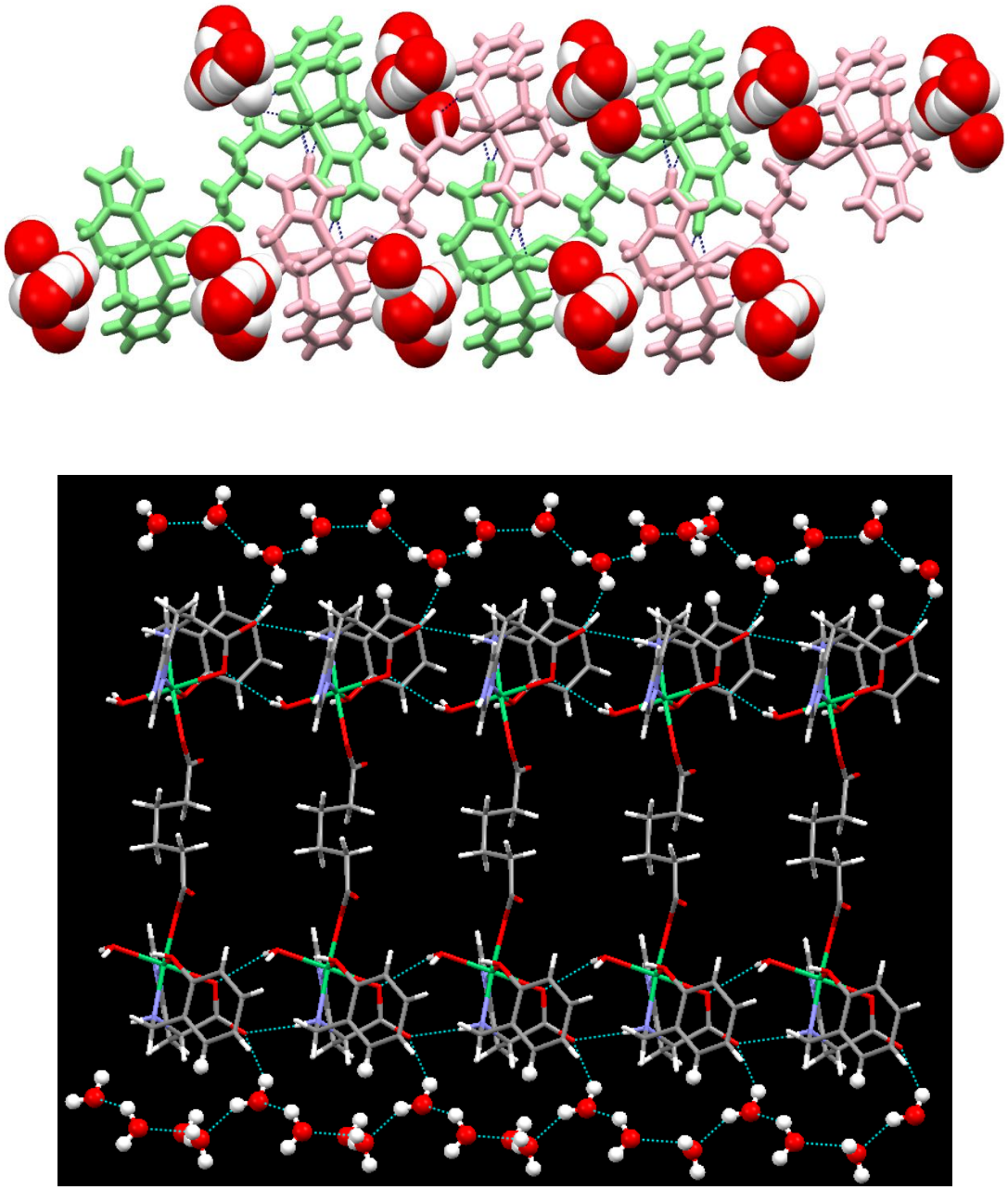

Figure 3.97. Octamers of water joining the dimeric units in **50** on both sides; along b axis (top) and along c-axis (bottom).

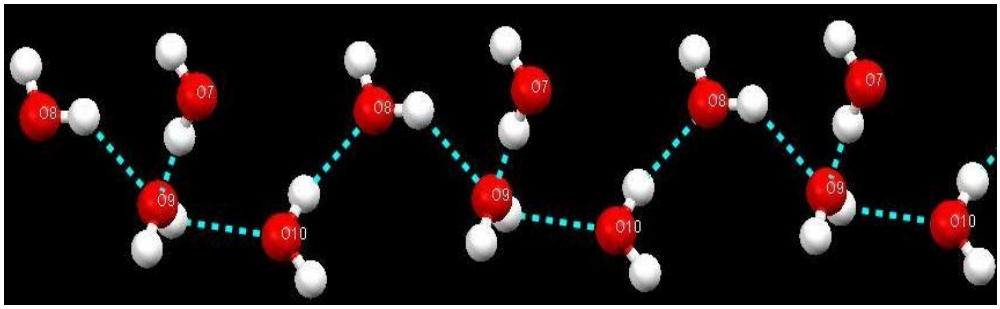

Figure 3.98. Zigzag octamer of lattice water chain in **50**.

Prior to our work, all reports describing the structure of water octamer have different arrangements. For example, theoretical studies suggested that water octamer of cube like arrangement with D_{2d} and S_4 symmetry would be most favourable;[285-287] while, the first crystallographic observation for water octamer was reported for $[A_2B](H_2O)_8$ where A = κ^4-[1,2-bis(2-oxy-2-methylpropanamido)4,5dimethoxybenzene]cobaltate(III) and B = bis-κ^3-(2,6-diacetamidopyridine)cobalt(II) where the water octamer forms a cube like structure with C_i symmetry.[288] In this structure, O...O...O bond angle varies from 79.9 to 92.1° whereas O...O bond length varies from 2.750 to 2.929 Å. Similarly in case of $[Y(dpdo)_2(H_2O)_4][Co(CN)_6]\cdot 4H_2O$, (where dpdo = 2,2´-dipyridine dioxide), the octameric water cluster has a book shaped hexamer with two dangling water molecules[289] where the O...O distance within the octamer varies from 2.677- 2.964 Å and O...O...O angle ranges from 79.4 - 105.7°. Another puckered water octamer is known in the literature[290] where the O-O bond distance is 2.745 Å and the O...O...O angle is 109.5 ° and 116 °. In $[V(phen)_2SO_4]_2O(H_2O)_4$ (phen = 1,10-phenanthroline), the water octamer shows a butterfly shaped [291] or open cube like where O…O distances within the octamer range from 2.76 to 2.91 Å. In **50**, a zigzag chain of water octamer is encapsulated within the 2D sheets with the O...O...O angle varied from 96.64 ° to 152.09 °. This arrangement enhances the stability of the water chain as evident from the thermal behavior of **50**.

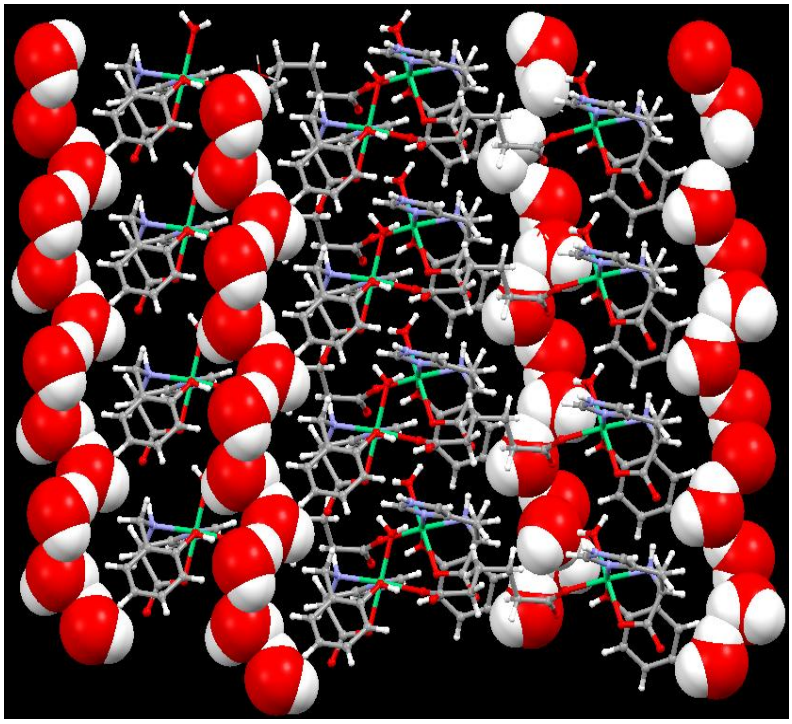

Figure 3.99. Encapsulated water octamer (shown in spacefilling model) within the hydrogen bonded 2D sheet of **50.**

Table 3.21. Hydrogen bonding parameters in **50.**

D---H…A (Å)	r(D-H) (Å)	r(H…A) (Å)	r(D…A) (Å)	∠D-H…A (deg)	Symmetry
N1 -H1…O2	0.91	2.14	3.0417	172	x,-1+y,z
N2 -H1…O1	0.86	2.16	2.9969	164	1/2-x,-1/2+y,-z
O6-H6B...O1	0.85	2.19	2.7556	123	x,-1+y,z
O6-H6B…N2	0.85	2.56	3.3463	153	1/2-x,-1/2+y,-z
O7-H7A…O9	0.86	1.84	2.6664	162	
O8-H8A…O9	0.86	1.98	2.662	135	1/2+x,-1/2+y,z
O8-H8B…O2	0.86	2.04	2.7333	137	
O9-H9B…O10	0.86	2.16	2.7492	125	
O10-H10D…O8	0.87	2.17	2.7391	123	-1/2+x,-1/2+y,z

Powder X-ray Data Analysis.

Powder X-ray diffraction pattern was recorded for **50-52** at room temperature (see Figures 3.100). In case of **50**, the experimental and simulated (from the single crystal data) patterns were similar to each other confirming that the single crystal and bulk material are the same. It also confirms the phase purity of bulk. The patterns for **51-53** show their crystalline nature. The PXRD patterns for **51-53** shows similar pattern as that of with slight variation in some peaks suggesting small variation in the crystal structure compared to **50**.

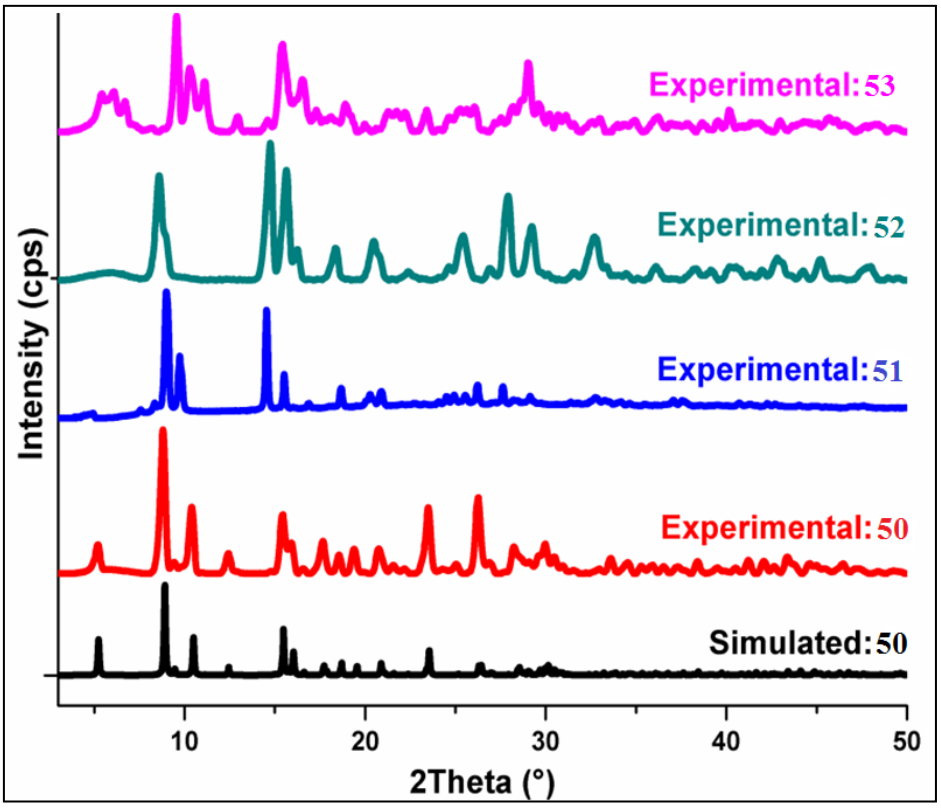

Figure 3.100. PXRD patterns for **50-53.**

UV-Vis and Circular Dichroism (CD) Spectroscopy

UV-Visible and CD studies were carried using 1.25 mM methanolic solution of **50-53**. In the visible region of the spectrum (325 to 700 nm), **50** shows a major peak at 590 nm (ε = 79 $L \cdot mol^{-1} \cdot cm^{-1}$) and a hump at 365 nm. For **51**, the major peak appears at around 599 nm (ε = 65 $L \cdot mol^{-1} \cdot cm^{-1}$) and a hump at 355; for **52**, the corresponding major peak appears at around 590 nm (ε = 73 $L \cdot mol^{-1} \cdot cm^{-1}$) and a hump at 350 nm and for **53**, the corresponding major peak appears at around 590 nm (ε = 80 $L \cdot mol^{-1} \cdot cm^{-1}$) and a hump at 350 nm (as shown in Figure 3.101a). These values are similar to the values reported in literature for similar compounds. All the above mentioned peaks are due to d-d transitions. The peaks around 600 nm are due to $^2A_{2g}$ to $^2T_{1g}$ (F) transition in Ni^{2+}whereas the humps around 360 nm are due $^2A_{2g}$ to $^2T_{1g}$ (P) transition. In the CD spectrum for **50**, the positive Cotton effect is observed at 389 nm (due to $^2A_{2g}$ to $^2T_{1g}$ (P) transitions) and 567 nm (due to $^2A_{2g}$ to $^2T_{1g}$ (F) transitions) and the negative Cotton effect is observed at 353 nm and 504 nm. For **51**, the positive Cotton effect is observed at 391 nm (due to $^2A_{2g}$ to $^2T_{1g}$ (P) transitions) and 576 (due to $^2A_{2g}$ to $^2T_{1g}$ (F) transitions) and the negative Cotton effect is observed at 343 nm and 509 nm. For **52**, the positive Cotton effect is observed at 389 nm (due to $^2A_{2g}$ to $^2T_{1g}$ (P) transitions) and 565 nm (due to $^2A_{2g}$ to $^2T_{1g}$ (F) transitions) and the negative Cotton effect is observed at 354 nm and 509 nm. For **53**, the positive Cotton effect is observed at 390 nm (due to $^2A_{2g}$ to $^2T_{1g}$ (P) transitions) and 567 nm (due to $^2A_{2g}$ to $^2T_{1g}$ (F) transitions) and the negative Cotton effect is observed at 352 nm and 512 nm (as shown in Figure 3.101b).

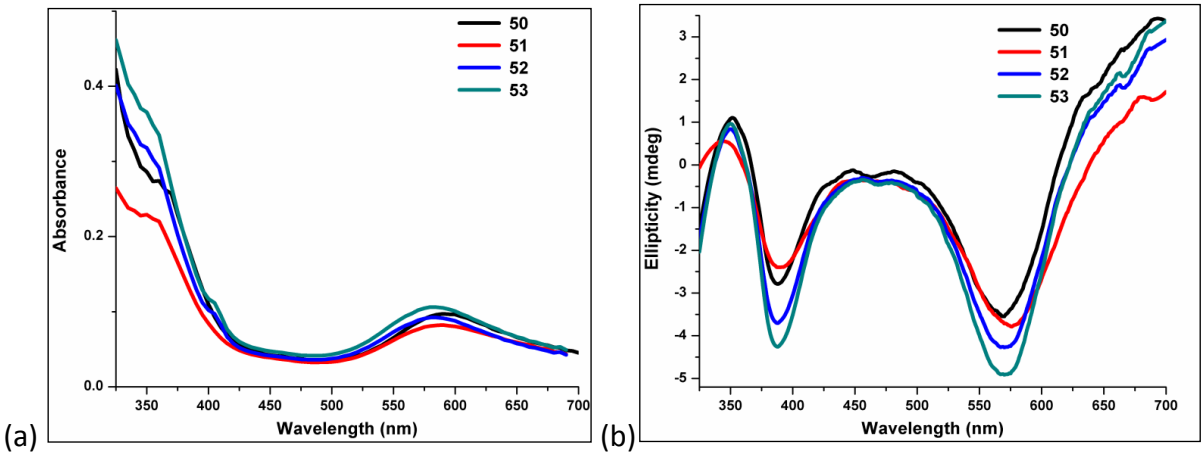

Figure 3.101. (a) UV-vis and (b) CD spectra for **50-53** in wavelength range from 325 to 700 nm.

In the UV region of the spectrum (200 to 325 nm), the peaks at 205 nm (π-π*) and a shoulder at around 245 nm is due to L-histidine part of the ligand and 290 nm (n-π*) is due to

salicylaldehyde part of the ligand (as shown in Figure 3.102a). In the CD spectrum for **50,** the positive Cotton effect is observed at 234 nm, 270 nm and negative Cotton effect at 210 nm, 258 nm, 289 nm. For **51**, the positive Cotton effect is observed at 234 nm, 271 nm and the negative Cotton effect at 208 nm, 258 nm, 289 nm. For **52**, the positive Cotton effect is observed at 233 nm, 270 nm and the negative Cotton effect at 211 nm, 258 nm, 289 nm. For **53**, the positive Cotton effect is observed at 230 nm, 272 nm and the negative Cotton effect at 210 nm, 258 nm, 290 nm (as shown in Figure 3.102b)

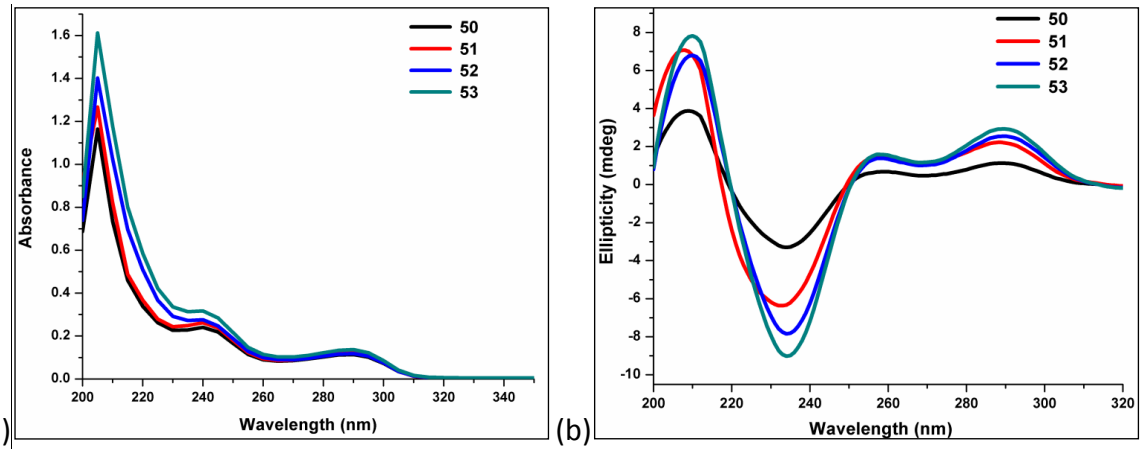

Figure 3.102. (a) UV-vis and (b) CD spectra for **50-53** in wavelength range from 200 to 325 nm.

Solid state diffuse reflectance and Fluorescence spectroscopy

The diffuse reflectance spectra of **50-53** (as shown in Figure 3.103a) are dominated by the d-d transitions of Ni(II). In all complexes, three absorption edges are observed: 271 nm, 370 nm and 575 nm (for **50**); 281 nm, 376 nm and 603 nm (for **51**); 296 nm, 374 nm and 603 nm (for **52**); 295nm, 372 nm and 593 nm (for **53**). The absorption edges at ~600 nm and ~370 nm can be assigned to the following transitions of Ni(II) in a distorted octahedral environment: $^2A_{2g}$ to $^2T_{1g}$ (F) and $^2A_{2g}$ to $^2T_{1g}$ (P), respectively.

The presence of an imidazole group in the ligand H_2hissal makes it a fluorophor. On being excited at 250 nm, for the ligand the emission maximum is obtained at 307 nm. However, in case of all the SCNs (**50-53**) synthesized using this ligand shows a quenching in the fluorescence (as shown in Figure 3.103b). This quenching can be due to the non-radiative decay of histidine based ligand due to the presence of Ni(II) by dexter type energy transfer between the orbitals of Ni(II) and the Hhissal ligand. Apart from this, another λ_{emi} peak at 284 is observed in case of the SCNs (**50-53**). In case of **51** two additional peaks at 343 nm and 358 nm are observed in emission spectrum indicating the variation in the structure of

succinate analogue from the other analogues and thus also confirming different non-radiative pathway in case of **51** compared to **50**, **52** and **53**.

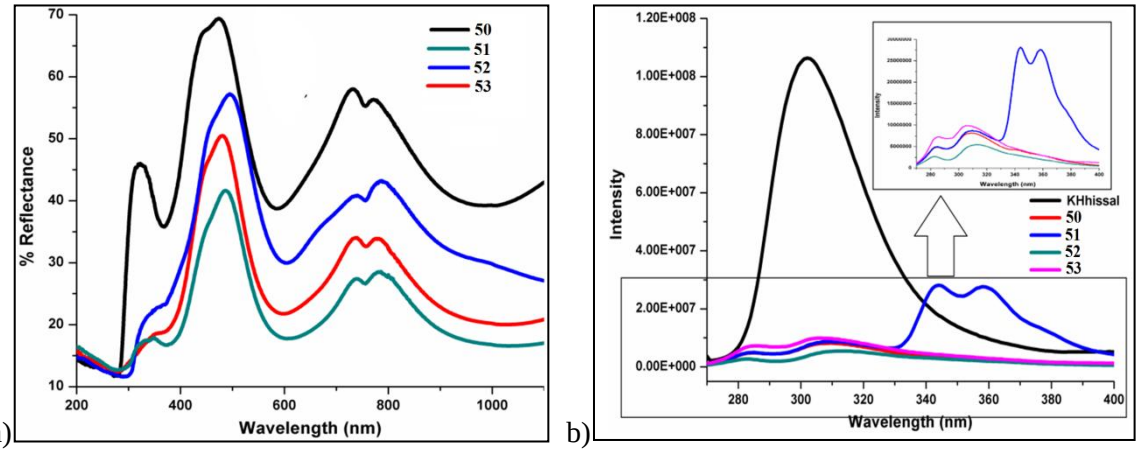

Figure 3.103. (a) Reflectance spectra for **50-53** in the wavelength range from 200 to 1100 nm and (b) Fluorescence spectra of KHhissal, **50-53** in methanol (λ_{exc} = 250 nm).

3.2.2. Coordination architectures with amino acid based ligands containing a tagged fluorophore

Tagging amino acids (L-Tyrosine) with some additional fluorophore like dansyl not only enhances their fluorescence properties but also brings diversification in their coordination architectures.

Synthesis. New homochiral luminescent compounds **54-57** were prepared by stirring a methanolic solution of dansylated amino acids and divalent metal salts (in a 2:1 ratio) under ambient conditions as shown in Scheme 3.10.

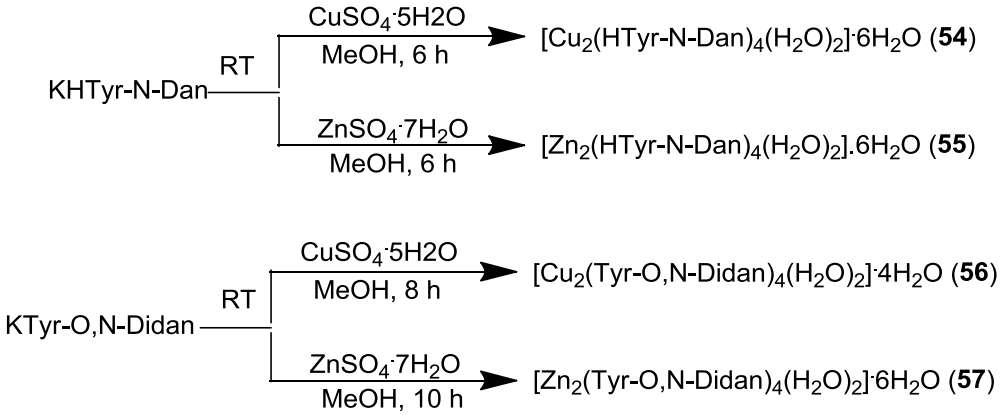

Scheme **3.11**. Synthesis of **54-57**.

FTIR Spectroscopy. The IR spectra of **54-57** recorded in the solid state as KBr pellets show a lot of similarities with each other. The FTIR spectrum of **54** shows broad peaks at ~ 3410 cm^{-1} and 3271 cm^{-1} corresponding to the lattice and coordinated water molecules,

respectively. The corresponding peaks for other complexes are 3405 cm^{-1} and 3267 cm^{-1} (**55**), 3434 cm^{-1} and 3285 cm^{-1} (**56**), and 3440 cm^{-1} and 3285 cm^{-1} (**57**). In **54** and **55**, the peak from phenolic –OH is masked in the broad peak at ~3270 cm^{-1}. The peak at ~2940 cm^{-1} in all the complexes corresponds to the NH of the ligand. The asymmetric and symmetric stretching frequencies for the carboxylate of the ligand appear at 1589 cm^{-1} and 1452 cm^{-1} for **54**, 1587 cm^{-1} and 1450 cm^{-1} for **55**, 1588 cm^{-1} and 1457 cm^{-1} for **56** and 1590 cm^{-1} and 1460 cm^{-1} for **57**, respectively. Hence, based on the difference ($\Delta\nu = \nu_{asymm} - \nu_{symm}$) of 137 cm^{-1} (**54**), 137 cm^{-1} (**55**), 131 cm^{-1} (**56**) and 130 cm^{-1} (**57**), a bridging type binding mode of the carboxylate is confirmed in all the four complexes. This not only cooroborates well with the bridinging mode in a paddle-wheel structure of **54** as determined by the single crystal structure determination (*vide infra*) but also their structural similarities. In all four complexes, the sharp peaks at ~1230 cm^{-1} and ~1140 cm^{-1} correspond to the C-O and SO_2, respectively.

Thermogravimetric Analyses. The thermal behaviour of **54-57** was studied as a function of temperature in the range of 25-500 ˚C (Figure 3.104). The TGA profile for each compound is a three-step weight loss profile; however, **57** is found to be the most stable (up to 240 ˚C) after the initial loss of water molecules. For **54**, the first weight loss of 5.16% between 50-150 ˚C corresponds to the loss of six lattice water molecules (ca. 5.61%). The second step showing weight loss of 12.1% between 150-220 ˚C indicates loss of two coordinated water molecules along with loss of four carbon dioxide molecules, each from one ligand (ca. 11.68%). The third step between 300-500 ˚C shows a gradual weight loss of 45.54% which is due to the degradation of the metal-ligand moiety. For **55**, the first weight loss of 2.34% between 50-110 ˚C corresponds to the loss of two uncoordinated water molecules (ca. 1.86%). The second step showing weight loss of 6.78% between 150-300 ˚C indicates loss of four uncoordinated water molecule and two coordinated water molecule (ca. 5.70%). The third weight loss of 18.3% between 320-500 ˚C indicates the loss of some part of the metal-ligand complex (ca. 19.8%). For **56**, the first weight loss of 3.01% between 50-100˚C corresponds to the loss of four uncoordinated water molecules (ca. 2.51%). The second step showing weight loss of 7.72% between 160-350 ˚C indicates loss of two coordinated water molecules and two carbon dioxide molecules (ca. 7.60%). The third weight loss of 28.9% between 400-500 ˚C indicates the degradation of metal-ligand complex (ca. 26.89%). For **57**, the first weight loss of 4.10% between 50-150 ˚C corresponds to the loss of six uncoordinated water molecules (ca. 3.77%). The second step showing weight loss of 16.89% between 250-

350 ˚C indicates loss of two coordinated water molecules, four carbon dioxide molecules and four SO_2 molecules (ca. 16.99%). The third weight loss of 33.44% between 400-500 ˚C indicates loss of metal-ligand complex (ca. 36.78%).

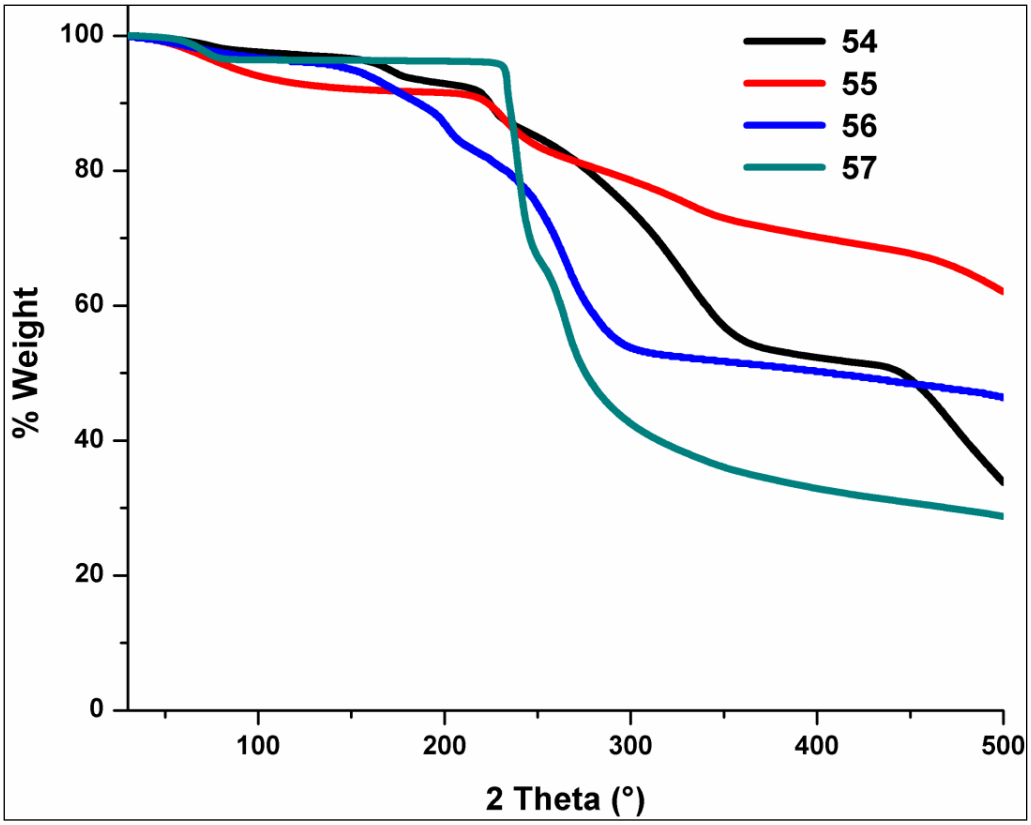

Figure 3.104. TGA scans for **54-57.**

Single Crystal Structure Analysis. Green block shaped crystals of $[Cu_2(HTyr\text{-}N\text{-}Dan)_4(H_2O)_2]$ (**54a**) are obtained from the evaporation of the methanolic solution of **54** within couple of weeks. Compound **54a** crystallizes in the tetragonal chiral space group *I4*. In the asymmetric unit of **54a**, a 4-fold axis that passes through the two Cu^{2+} ions of a dinuclear unit and the coordinated water molecule generates the whole molecule. Each Cu^{2+} ion of the dinuclear unit has four oxygens of the carboxylates from four different ligands in equatorial positions with the Cu...O distances in the range of 1.948 - 1.958 Å, and an oxygen from the water molecule at 2.148 Å at the axial position, completing the square pyramidal geometry around it. Thus, four carboxylates from four H_2Tyr-N-Dan ligands bridge between the two Cu(II) ions of a dinuclear unit to form a paddle-wheel structure with a Cu...Cu distance of 2.635 Å as shown in Fig. 3.105.

All bond distances and bond angles around Cu^{2+} ion are comparable to the paddle-wheel structures with the $Cu_2(\mu\text{-}O_2C)_4$ core.[292-299] However, the supramolecular array formed in the

tetra-μ-acetato-bisaquodicopper(II)[297,299] involves the axial water and the oxygen of the chelated acetate whereas in **54a** the axial water molecules do not participate in the formation of the supramolecular network.

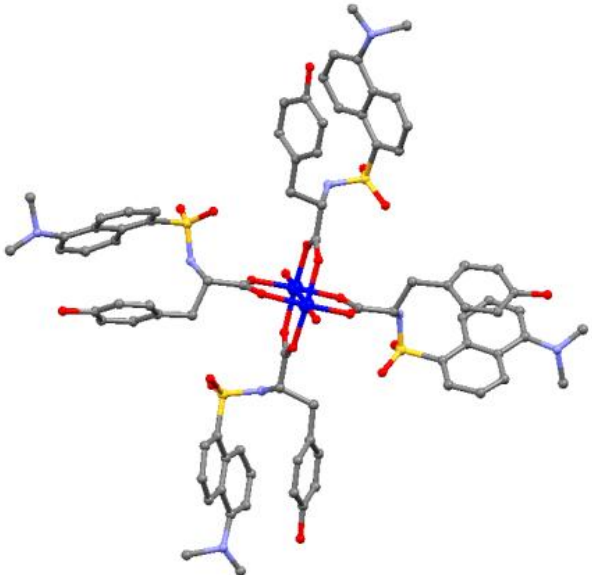

Figure 3.105. Paddle-wheel structure of **54a**.

Very few examples of paddle wheel complexes are reported in the literature where the axial water is not involved in any kind of hydrogen bonding.[297,300-302] In all these examples, the Cu-O(axial) distances lie in the range of 2.130-2.231 Å whereas in **54a**, this distance is 2.126 Å. The selected bond distances and bond angles for **54a** are listed in Tables A8 and A14, respectively. In **54a,** the phenolic oxygen (O5) of the ligand of one dinuclear unit is hydrogen bonded to the oxygen atom (O3) of the sulphato group in the ligand of the next dinuclear unit, giving rise to a supramolecular chain (O3...O5 distance: 2.8367 Å) as shown in Figure 3.106.

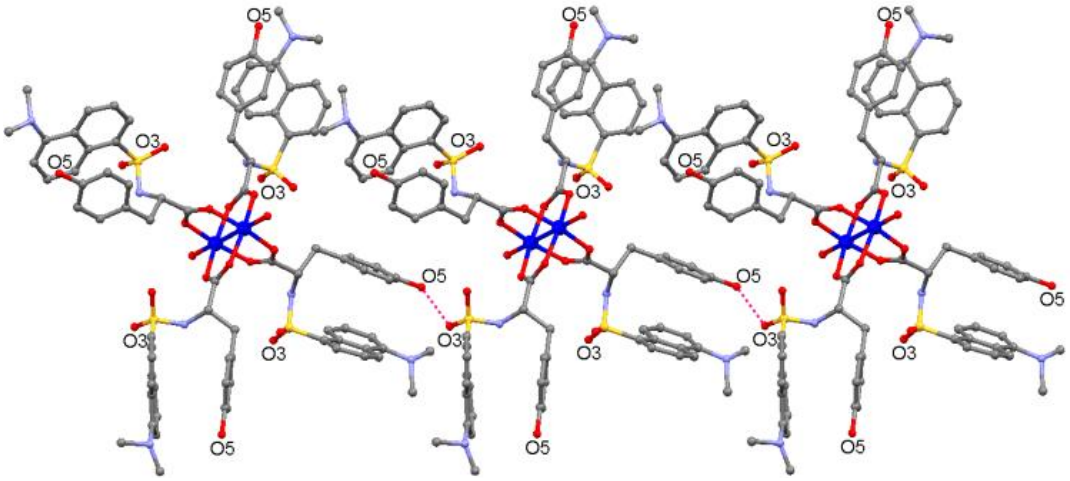

Figure 3.106. Supramolecular chain (growth shown in one direction only) in **54a**.

The four phenolic OH from four ligands coordinated to each dinuclear unit are intermolecularly hydrogen bonded to oxygen atom (O3) of the sulphato group of the ligand of four different dinuclear subunits (Figure 3.107a). Similarly, the oxygen atom (O3) of each sulphato group in a dinuclear unit is inter- molecularly hydrogen bonded to the phenolic OH (O5) of four other dinuclear subunits. Thus, each dinuclear subunit is hydrogen bonded to eight other dinuclear subunits (Figure 3.107b) forming an extended supramolecular network. The presence of a four-fold symmetry gives rise to a square synthon, where the Cu^{2+} ions of four dinuclear subunits surrounding a single dinuclear unit forms the nodes of the square synthon (see Figure 3.108a). Further growth of this synthon is due to the symmetry as well as due to the intermolecular hydrogen bonding (Figure 3.108b). The supramolecular network is further strengthened by the intra-ligand π–π interactions between the aromatic rings of the dansyl and that of the tyrosine moiety of the ligand (Figure 3.109). The crystallographic parameters and basic information pertaining to data collection and structure refinement for **54a** is summarized in Table A5. All hydrogen bonding parameters for **54a** are listed in Table 3.22.

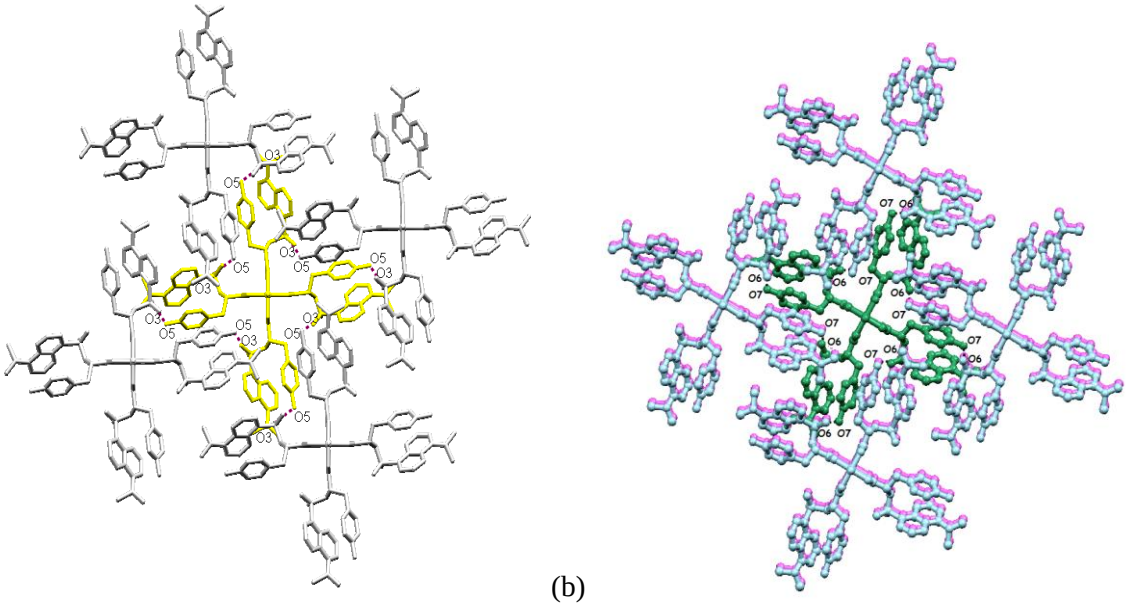

(a) (b)

Figure 3.107. (a) Dinuclear subunit surrounded by four other dinuclear subunits. (b) Hydrogen bonding of each dinuclear subunit with eight other dinuclear subunits in **54a**.

Table 3.22. Hydrogen bonding parameters for **54a**.

D---H…A	D-H (Å)	H…A (Å)	D…A (Å)	D-H…A (°)	Symmetry
O(5)--H(5)..O(3)	0.82	2.04	2.858(11)	173	1/2-y,1/2+x,-1/2+z
O(8)--H(8A)..O(1)	1.00	2.4(2)	3.112(19)	131	

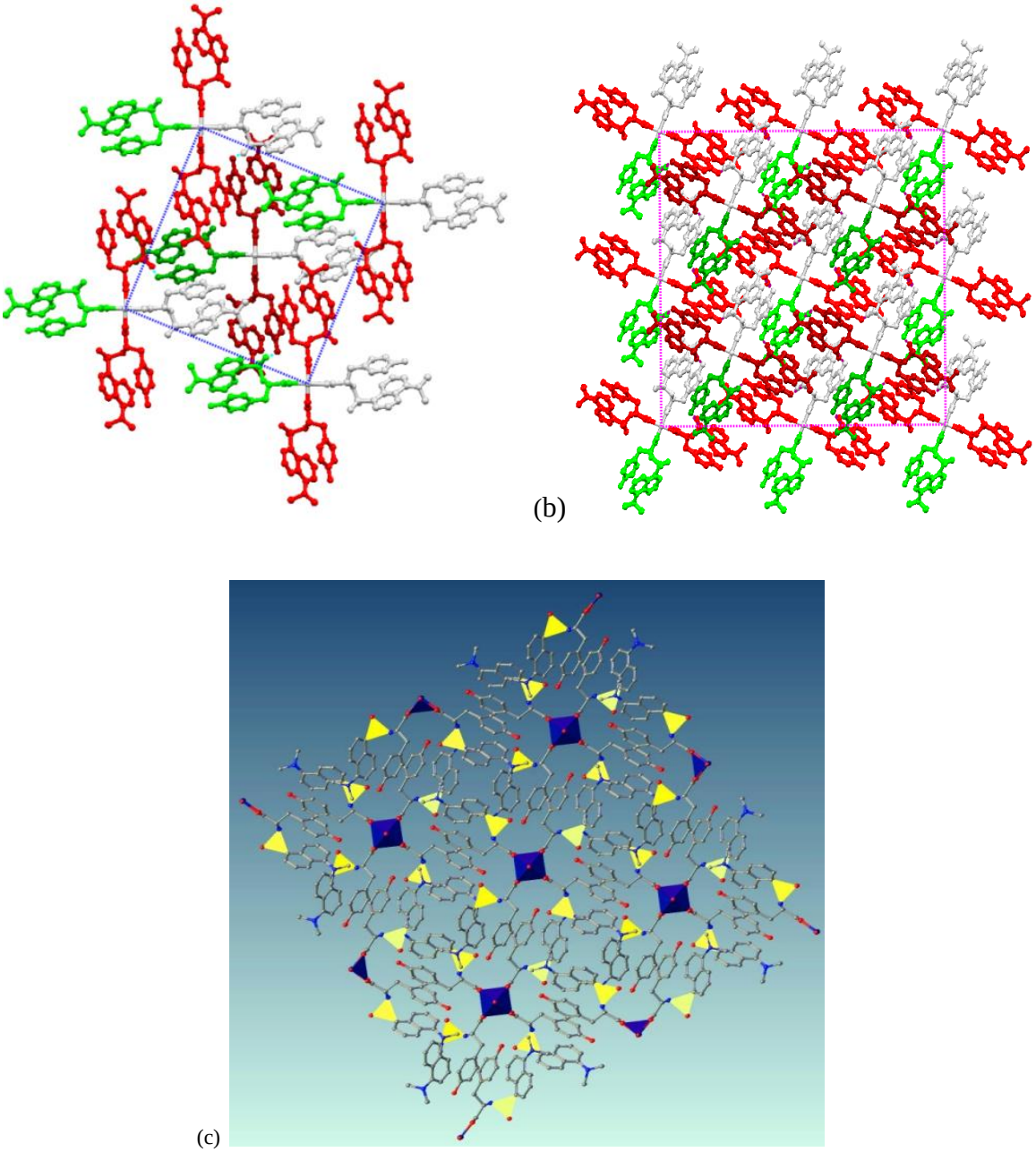

Figure 3.108. (a) Square synthon formed due to four fold symmetry in **54a** (different colors represent the symmetry operations); (b) Growth of the square synthon (different colors represent the symmetric operations); (c) Perspective view of the growth of the square synthon (blue polyhedral: metal dinuclear unit; yellow polyhedral; sulphato group of the ligand) in **54a**.

UV-vis Spectroscopy. Using ~1 mM methanolic solution of the ligand and **54**, UV-vis spectra were recorded Compared to the ligand, the spectrum of **54** shows an additional absorbance at λ_{max} = 738 nm due to the d-d transition (^2E_g to $^2T_{2g}$) of Cu^{2+} (Figure 3.110). In the UV part, the absorbances at 280 nm and 380 nm are due to the n–π* or π–π* transitions.

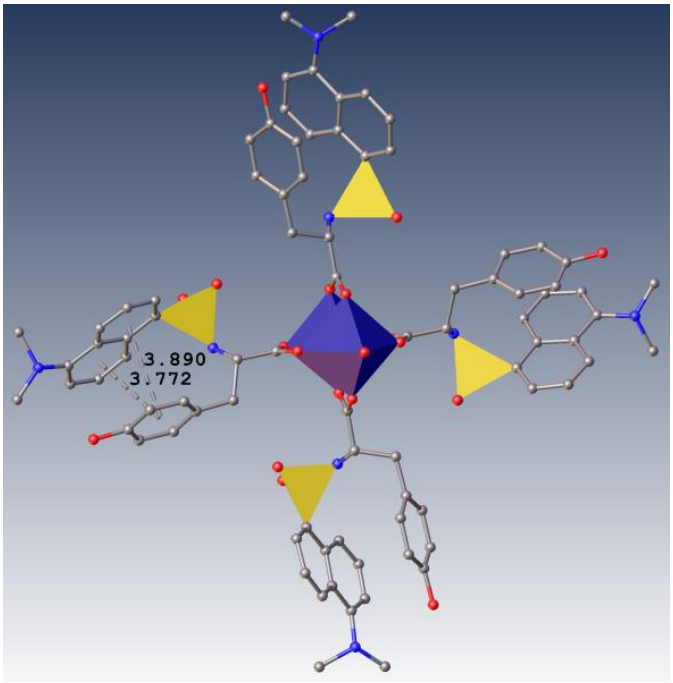

Figure 3.109. π–π interactions in **54a**.

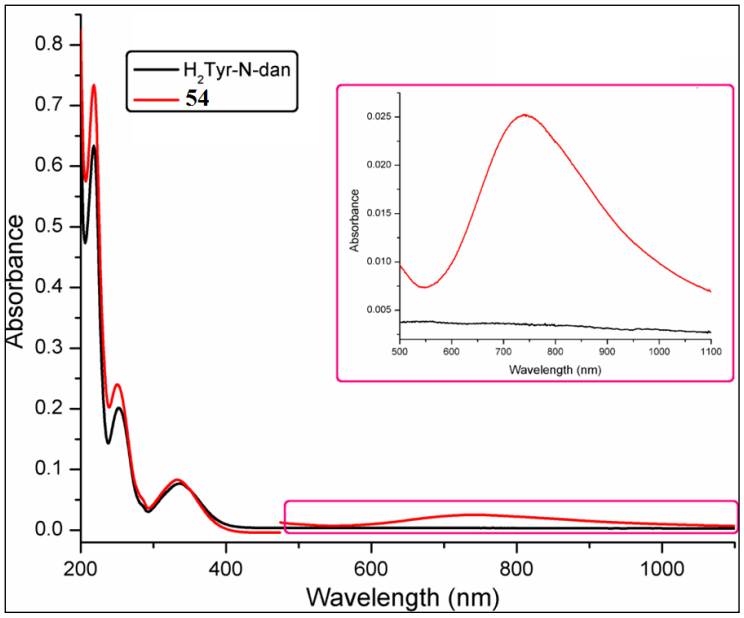

Figure 3.110. UV-Visible absorbance spectra of ligand and **54.** Inset: Absorbance in the visible region.

Photoluminiscence Properties. The presence of the dansyl moiety in the ligand makes the compound fluorescent. Thus, a comparative study of the photoluminescence behaviour of the two ligands and their Cu^{2+} complexes **54** and **56** was done. Both solutions of the ligand and metal complexes were excited at 370 nm and their photoluminescence spectra were recorded in the range of 385-700 nm. The λ_{emi} for both the ligands were observed at 530 nm. However, the ligand with didansylated tyrosine shows less fluorescence intensity compared to the

monodasylated tyrosine (as shown in Figure 3.111) indicating that in didansylated ligand the orientation of the dansyl groups is such that these assist the non-radiative pathways to come to the ground state faster than the monodansylated derivative.

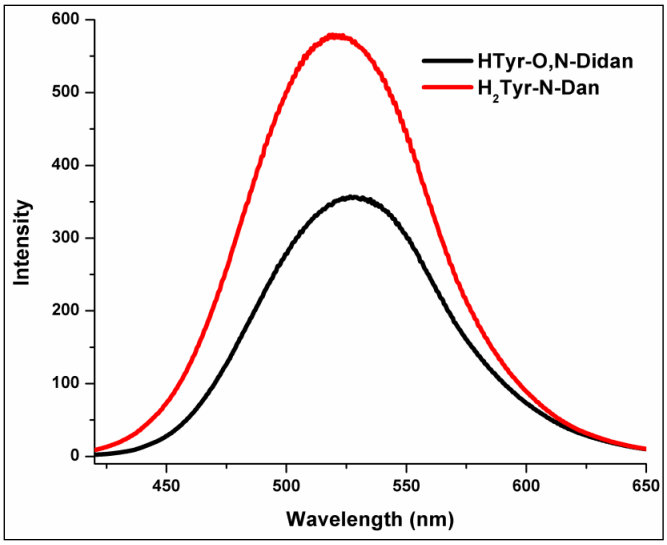

Figure 3.111. Photoluminiscence spectra for HTyr-O,N-Didan and H_2Tyr-N-Dan.

In case of the metal complexes (**54-57**), fluorescence quenching is observed compared to their respective ligands (Figure 3.112 and Figure 3.113). This quenching can be due to the non-radiative decay of dansyl fluorophore due to the presence of metal ions by dexter type energy transfer between the orbitals of M^{2+} (Cu^{2+} or Zn^{2+}) and the dansylated tyrosine.[303-309] On the other hand, for both ligands the quenching ability of Cu^{2+} is much more compared to Zn^{2+} which can be accredited to the better orbital overlap ability between Cu^{2+} and the dansylated tyrosine based ligands.

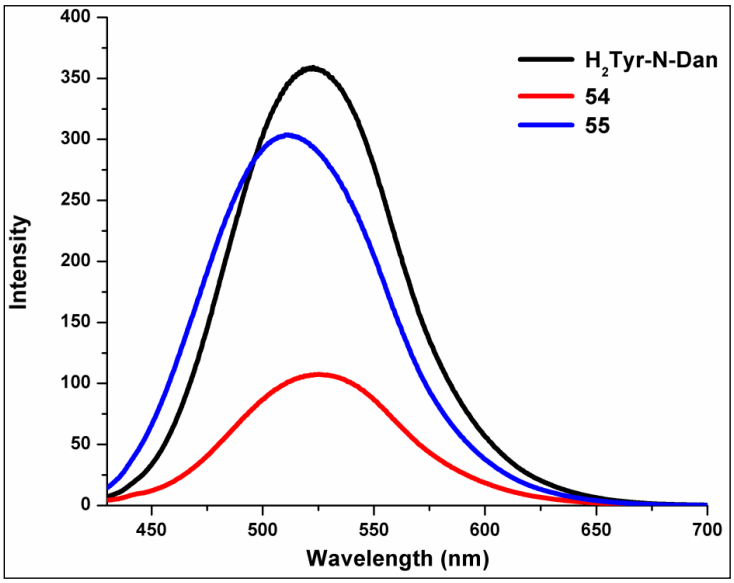

Figure 3.112. Photoluminiscence spectra for H_2Tyr-N-Dan, **54** and **55**.

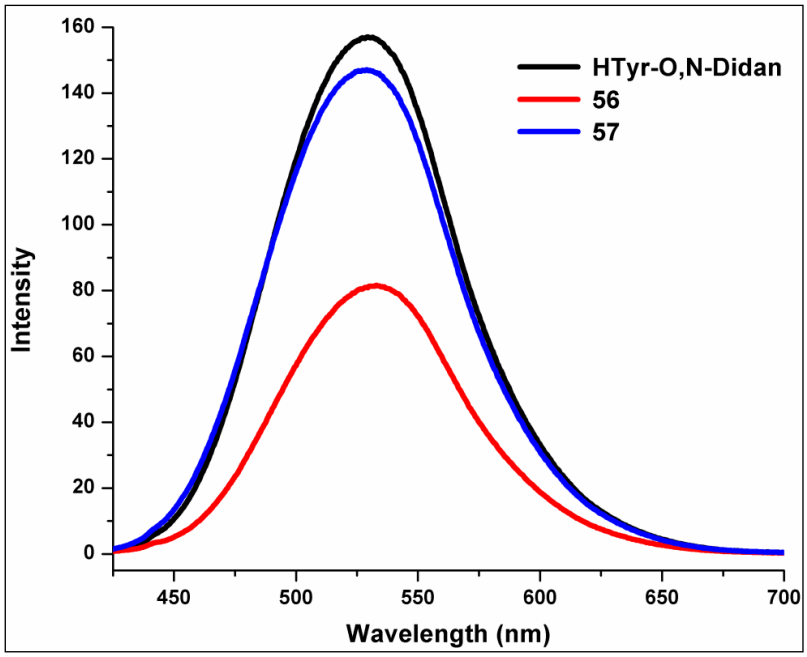

Figure 3.113. Photoluminiscence spectra for HTyr-O,N-Dan, **56** and **57**.

3.3. CHROMOGENIC AND/OR FLUOROGENIC SENSING OF CATIONS, ANIONS AND NEUTRAL SMALL MOLECULES

In this subsection, the role of various factors affecting the sensing abilities of the ligands and their selected coordination architectures are discussed intensively. Following the strategy used to enhance the anion sensing ability of the macrocycles with various electron withdrawing groups, which generates a positive quadruple over their aromatic part for the anion-π interactions, as an example a nitro group is attached at the para position of L-H_2Tyrbenz to obtain L-H_2Tyr4-NO_2. Amino acids like L-Tyrosine, L-Phenylalanine and L-Tryptophan act as fluorophores, and thus the ligands derived from these and their coordination architectures show good photoluminescence property that makes these flourogenic sensors. The mechanism involved for each sensor is also analysed based on the data obtained from various analytical techniques. These are grouped in four categories with details provided below:

3.3.1. A Triple Action Probe: Solvent mediated flip-flop fluoregenic sensors for halides (iodide/fluoride) and an optical pH indicator

The triplicate functionality of H_2Tyr-4-nitro (**L1)** based on a combination of two natural fluorophores, L-tyrosine and 4-nitrobenzaldehyde moieties, in acting as a solvent mediated differential halide sensor and a pH indicator was thoroughly explored.

As a sensor

Both the neutral ligand and its monosodium salt were examined but for comparison the latter being soluble in both solvents is discussed first and their comparison is mentioned later (*vide infra*). The monosodium salt of H_2Tyr-4-nitro (**L1a**) acts as an iodide sensor in methanol whereas the same probe in DMSO (**L1b**) acts as a fluoride sensor. Moreover, the switch in pH is determined simply by observing the color change of the receptor **L1** in DMSO on addition of H^+/OH^- (as shown in Figure 3.114).

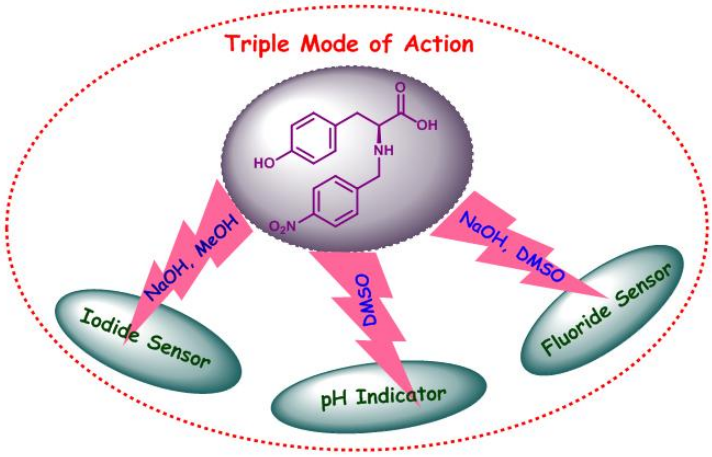

Figure 3.114. Triple mode of action of the H_2Tyr-4-nitro probe.

The photo-excitation of L1 in an aprotic solvent (DMSO) at 220 nm yields a fluorescence spectrum with an emission maximum at 365 nm. On addition of various anions, a significant change is observed in the fluorescence intensity (an enhancement) of the probe only for fluoride ion (Figure. 3.115). To analyse the role of a protic solvent in anion sensing, fluorescence spectrum of L1 in methanol was desired.

However, insolubility of **L1** in the protic solvents like methanol inhibited us to do so. On the other hand, utilization of the fact that the monosodium salt of **L1** is soluble in both DMSO and methanol solves this problem. On exciting at 220 nm, the fluorescence spectrum of monosodium salt of L1 in methanol (**L1a**) shows an emission maximum at 320 nm with a hump at 365 nm whereas in DMSO (**L1b**) shows an emission maximum at 365 nm. On addition of various anions, **L1a** shows selective quenching of fluorescence intensity by iodide ion whereas **L1b** shows selective enhancement of fluorescence intensity by fluoride anion (Figure 3.116). With subsequent addition of iodide to **L1a**, a sequential decrease in the main peak at 320 nm and an increase in the hump at 365 nm are well observed (Figure 3.117a and Figure 3.118a). On the other hand, an addition of fluoride ion to **L1b** gradually increases the

peak at 365 nm (Figure 3.117b and Figure 3.118b). The change in the fluorescence intensity for 1b is a two-step process (Figure 3.118b) indicating the involvement of two different interactions at different concentration (vide infra). Using the current probe, the detection limit for iodide ion is 3.15 ppm ($2.4x10^{-5}$ M) and for fluoride ion is 0.55 ppm ($2.4x10^{-5}$ M), which are comparable to those reported in the literature for each analyte.[ref] The homologous nature of the anion sensing abilities of **L1** and its anionic form **L1b** in DMSO nullifies the role of sodium ion and strengthens the part played by the solvent in sensing of various halides. This differential halide ion sensing by the same probe in different solvent can be accredited to the variation in orientation of the probe depending on the extent and type of interaction between

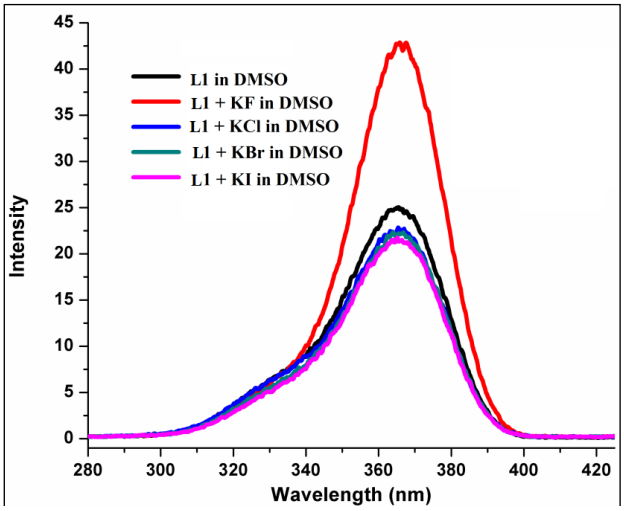

Figure 3.115. Fluorescence intensity of **L1** in DMSO and the effect of various anions on its fluorescence intensity.

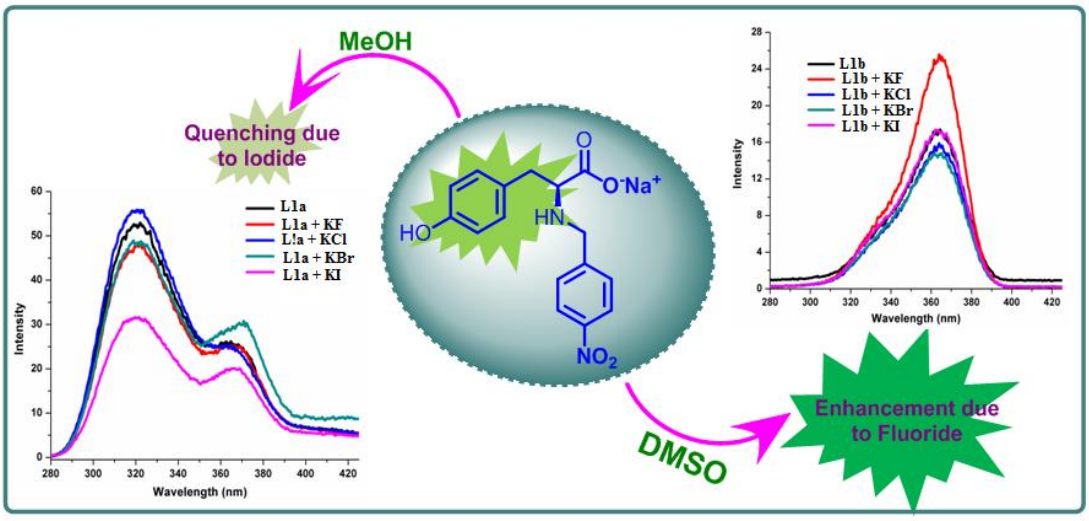

Figure 3.116. Fluorescence intensity of **L1a**, **L1b** and the effect of various anions on their fluorescence intensity.

both the probe and the halide ion with a particular solvent, which further depends on the protic nature of that solvent. With subsequent addition of iodide ion to **L1a**, a

sequential decrease in the main peak at 320 nm and an increase in the hump at 365 nm are well observed. However, on addition of fluoride ion to **L1b**, a gradual increase in the peak at 362 nm is seen (Figure 3.117). With addition of one equivalent of iodide to **L1a**, there is 72% decrease in the fluorescence intensity, whereas with the addition of one equivalent fluoride to **L1b**, there is 43% increase in the fluorescence intensity (Figure 3.118). One should note that the change in the fluorescence intensity for **L1b** is a two-step process indicating the involvement of two different interactions at different concentration (vide infra).

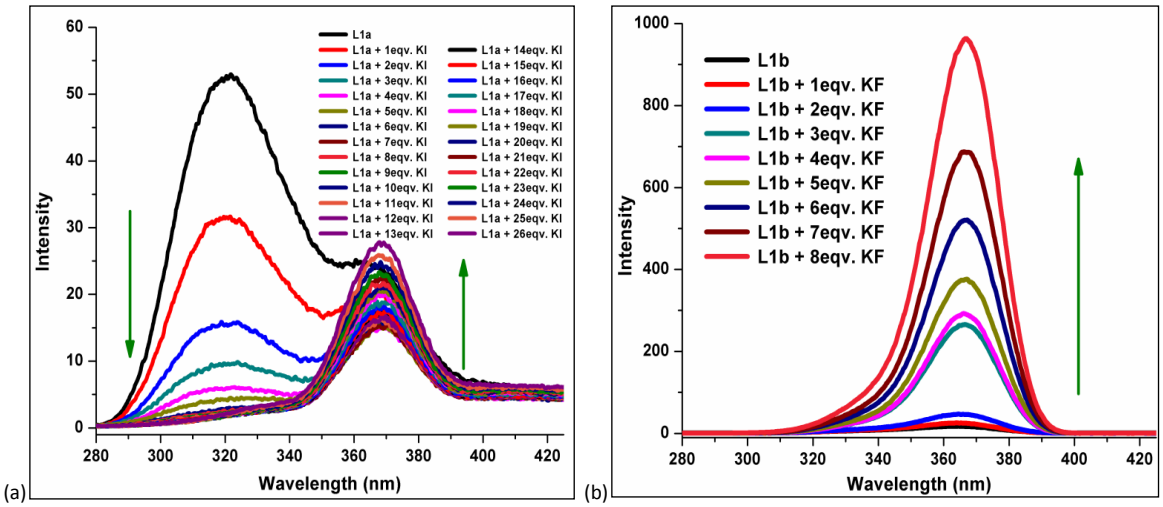

Figure 3.117. (a) Quenching of fluorescence in **L1a** upon addition of iodide ions and (b) enhancement of fluorescence in **L1b** upon addition of fluoride ion.

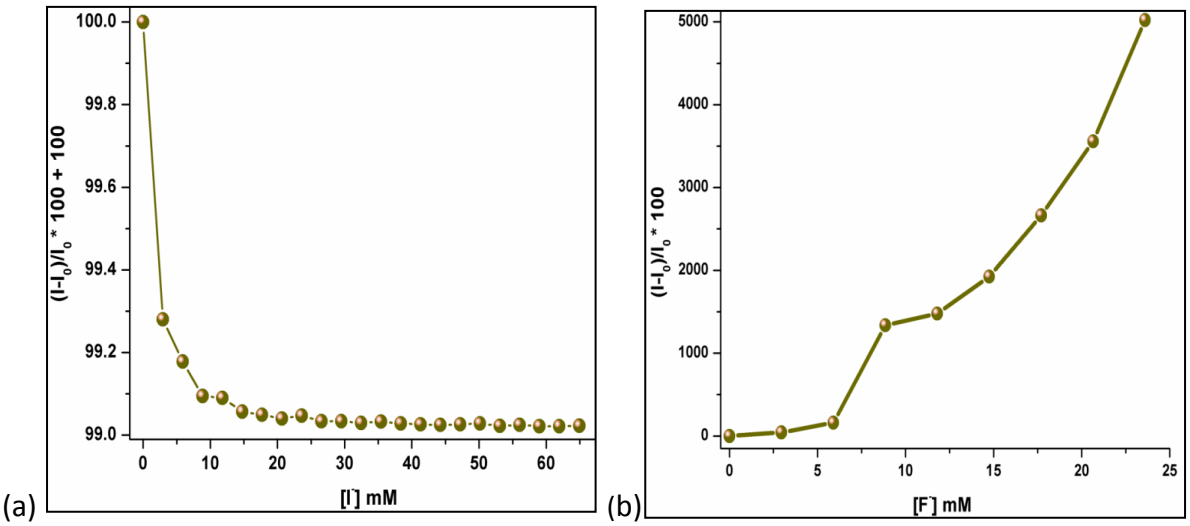

Figure 3.118. Percentage change in fluorescence intensity of (a) **L1a** upon addition of iodide ions (b) **L1b** upon addition of fluoride ions.

A comparative study of the detection limits for fluoride and iodide ions using the sensors **L1a** and **L1b**, respectively with respect to the best known sensors reported in the literature is summarized in Table 3.23a and Table 3.23b.

Table 3.23a. Comparative study for the detection limits of various F^- sensors.

Sr. No.	Complex used	Detection limit	References
1.	a fluoride ion nano colorimetric assay kit	0.1-0.5 ppm or 5.2×10^{-6} mol L^{-1} – 2.63×10^{-5} mol L^{-1}	310
2.	thiourea assisted self-assembly of citrate-capped gold nanoparticles	4 ppb or 1.1×10^{-8} mol L^{-1}	311
3.	N'-acetyl-2-(benzothiazol-2yl)-3-(3-chloro-5-methyl-4H-pyrazol-4-yl) acrylo hydrazide (ABPAH)	2.0×10^{-9} mol L^{-1}	312
4.	**L1a**	0.44 ppm or 2.4×10^{-5} mol L^{-1}	This work

Table 3.23b. Comparative study for the detection limits of various I^- sensors.

Sr. No.	Complex used	Detection limit	Reference
1.	Platinum-cationic porphyrin.	1×10^{-12} mol L^{-1}	313
2.	Z)-2-(4-[diethylamino]-2-hydroxybenzylideneamino) pyridine-3-carbaldehyde	0.24 μM or 2.4×10^{-7} mol L^{-1}	314
3.	bis(trans-cinnamaldehyde)-1,3propanediiminemercury(II) chloride ($Hg(BPPPB)Cl_2$)	8×10^{-7} mol L^{-1}	315
4.	Alkali-free lead phosphate glasses contg. silver oxide	0.05 μg cm^{-3} or 3.93×10^{-7} mol L^{-1}	316
5.	1,1,1-tris(1-oxophenalenyl-9-N-ethyl)amine	1.8×10^{-7} mol^{-1} L^{-1}	317
6.	**L1b**	3.15 ppm or 2.4×10^{-5} mol^{-1} L^{-1}	This work

For a deeper understanding of the mechanism of this differential sensing, a titration between the anions and the probe was followed by ^1H NMR spectroscopy. The ^1H

NMR titrimetry (see Figure 3.119) between iodide ion and NaHTyr-4-nitro in CD_3OD shows a downfield shift of all the aromatic protons (including protons of both nitrobenzyl and phenyl rings) whereas that between fluoride ion and NaHTyr-4-nitro in $(CD_3)_2SO$ shows an upfield shift of the protons of nitrobenzyl rings with slight change in the protons of the phenyl ring (peaks at 6.65). Hence, the fluoride sensing can be ascribed to the anion-π interaction[ref] between fluoride ion and the nitrobenzyl ring along with the hydrogen bonding between the NH group and fluoride ion. The presence of both these interactions is clearly seen in Figure. 3.118b where a two-step process is observed which suggests an increase in the electron density of the nitrobenzyl ring due to through-bond effects on addition of fluoride ion to **L1b** and thus supports an upfield shift of protons in Figure. 3.119 (bottom).

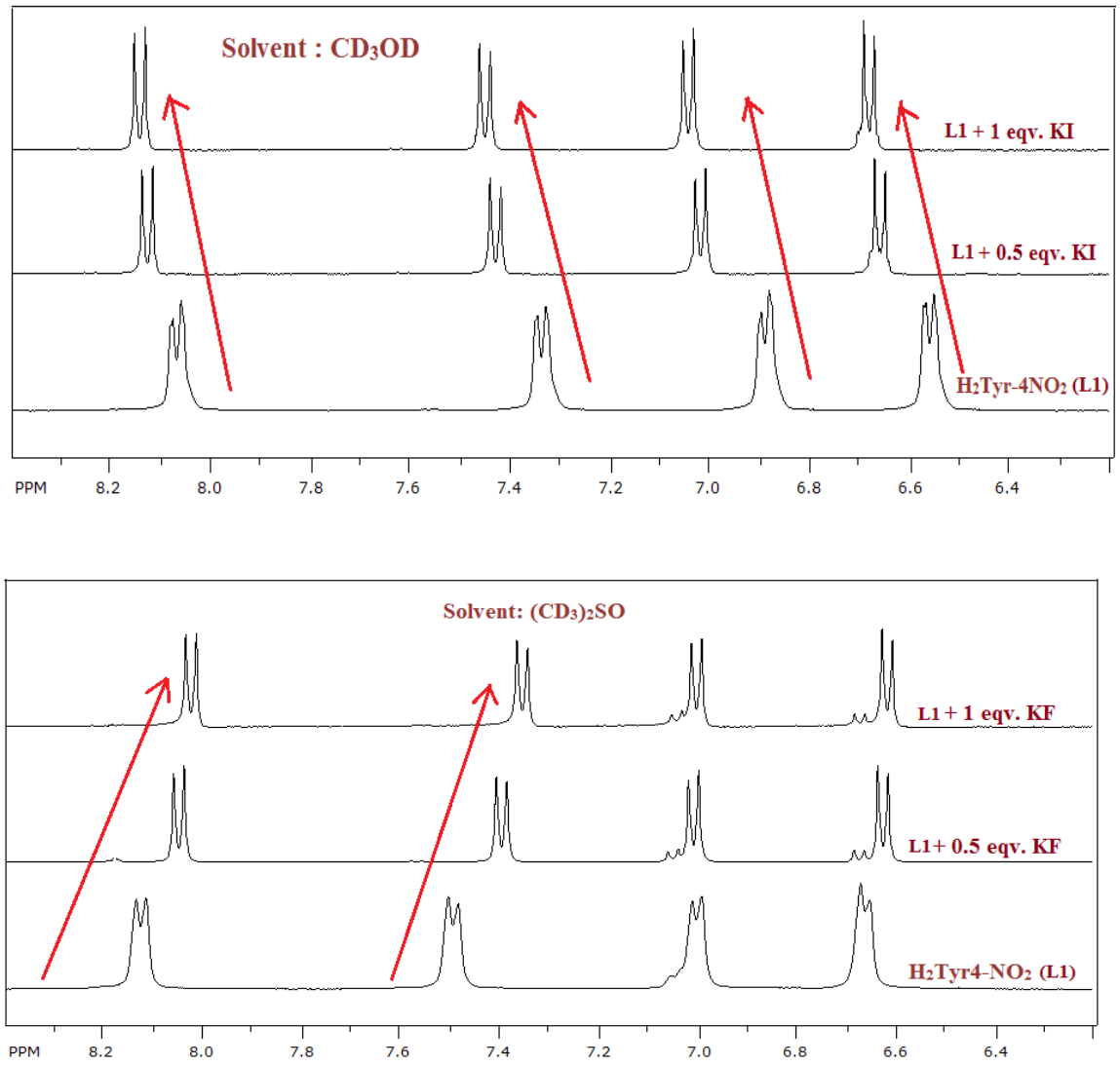

Figure 3.119. ^{1}H NMR titrimetry of NaHTyr-4-nitro (**L1**) with KI (top) and KF (bottom) as an analyte in CD_3OD and $(CD_3)_2SO$, respectively.

This shift seen in each case can be further enlightened by the structure obtained through MM2 calculation (3D ChemDraw) for energy minimization.As seen in Figure 3.119, in presence of methanol the hydrogen bonding is employed in such a way that the two probes come together forming a kind of cavity (which is well observed in the space-fill model). This cavity is suitable for the iodide to sit in, and thus decreases the electron density of the aromatic region causing a deshielding effect.

a) 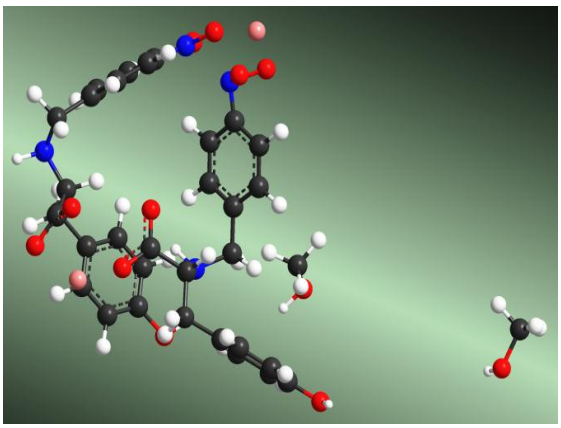 b) 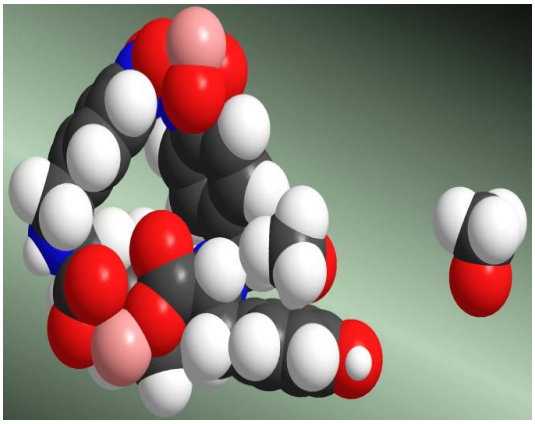

Figure 3.120. Energy minimized structure of NaHTyr-4-nitro in methanol using MM2 calculation (chem3D) (a) ball and stick model (b) space-filling model.

However, in case of DMSO no such cavity is observed in the structure of the probe (see Figure 3.120) and thus the fluoride ion shows an anion-π interaction due to an increase in electron density over the nitrobenzyl ring causing a shielding effect to yield an upfield shift of the protons.

a) 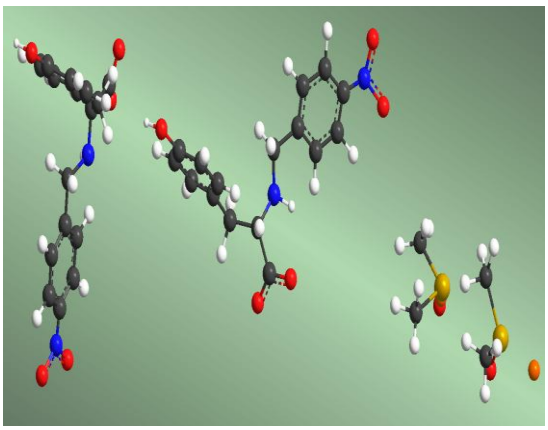 b) 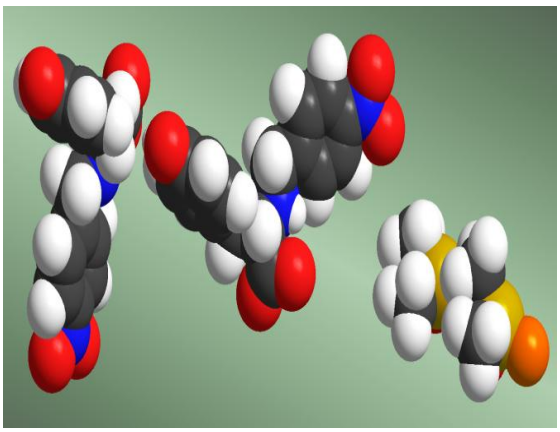

Figure 3.121. Energy minimized structure of NaHTyr-4-nitro in DMSO using MM2 calculation (chem3D) (a) ball and stick model (b) space-filling model.

The anion-π interaction is more prominent in aprotic solvents, like DMSO, as these do not interact with any halide and thus enhancing the anion–π interaction. However, in case of protic solvents, like methanol, the interaction between the solvent and the halide (esp. fluoride due to its small size and high electronegativity) diminishes the extent of anion-π interactions. The iodide ion being larger in size does not show much interaction with the solvent. The formation of a hydrophobic cavity by the probe in the methanolic solution (vide infra) helps in iodide sensing and also brings a downfield shifts of all the aromatic protons through-space effects, which polarize C-H bonds in proximity to hydrogen bond, creating the partial positive charge.

Thus, the mechanism of differential sensing of halides depending on the solvent can be summed up in Scheme 3.11. To comprehend the role of the protonated probe (H_2Tyr-4-nitro) vs. deprotonated probe (NaHTyr-4-nitro) on the halide ion sensing, H_2Tyr-4-nitro (**L1**) in DMSO was subjected to same sensing experiments as for **L1b**. The fluorescence spectra of **L1** (with/without halide ions) in DMSO (Figure 3.121) are very similar to the spectra obtained for **L1b** (with/without halide ions) (Figure 3.116b).

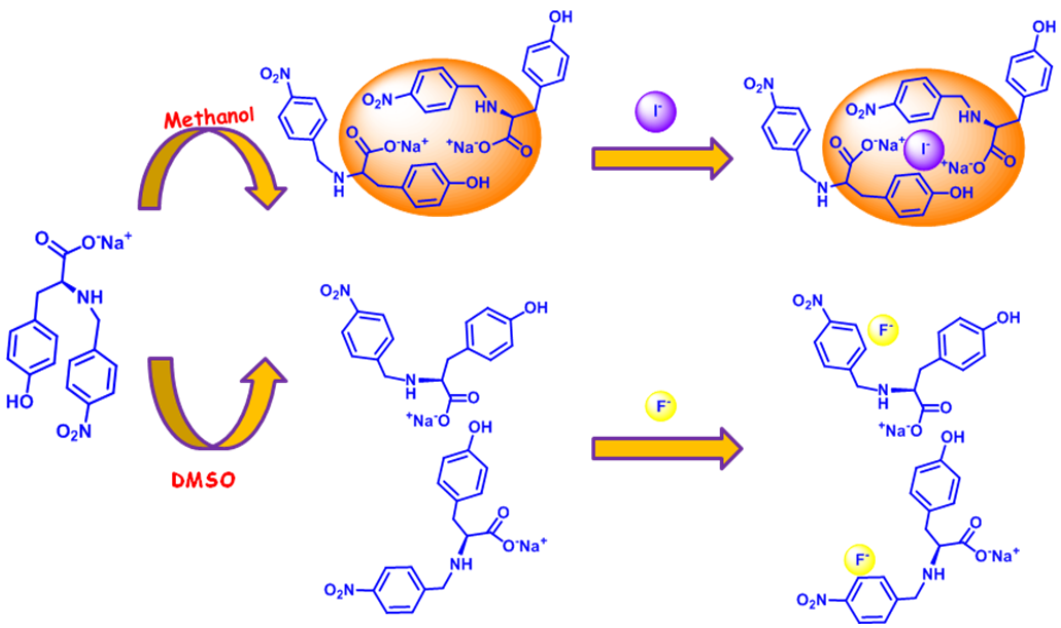

Scheme 3.12. Mechanism of flip flop solvent dependent differential halide sensing.

Comparison of protonated or deprotonated probe clearly suggests that both the probes acts in a similar way towards halide sensing. This nullifies the role of sodium salt and

strengthens the part played by the solvent in sensing of various halides. Similar to **L1b,** analyzing the role of the protonated counter part of **L1a** in sensing various halides was not been carried out due to the lack of solubility of **L1** in methanol.To consolidate the role of various groups in **L1** in sensing, its fine tuning through a chemical modification was carried out. The hydroxy group from **L1** is removed to obtain HPhe4-nitro (**L2**). Its anion sensing ability in DMSO indicates the same pattern as that for **L1** when excited at the same wavelength 220 nm (Figure 3.122a). Addition of fluoride ions to the DMSO solution of **2** shows an enhancement of the fluorescence intensity of the peak at 365 nm. Addition of one equivalent of fluoride ion enhances the fluorescence intensity by 1.6 folds thus confirming the importance of nitro group in sensing of fluoride ion. Subsequent addition of fluoride ions to the DMSO solution of **L2** shows a gradual increase in the intensity of the emission peak at 365 nm (Figure 3.122b). Thus, the halide sensing ability of the probes is attributed to the anion-π interaction between nitrobenzyl group and the halide ion.

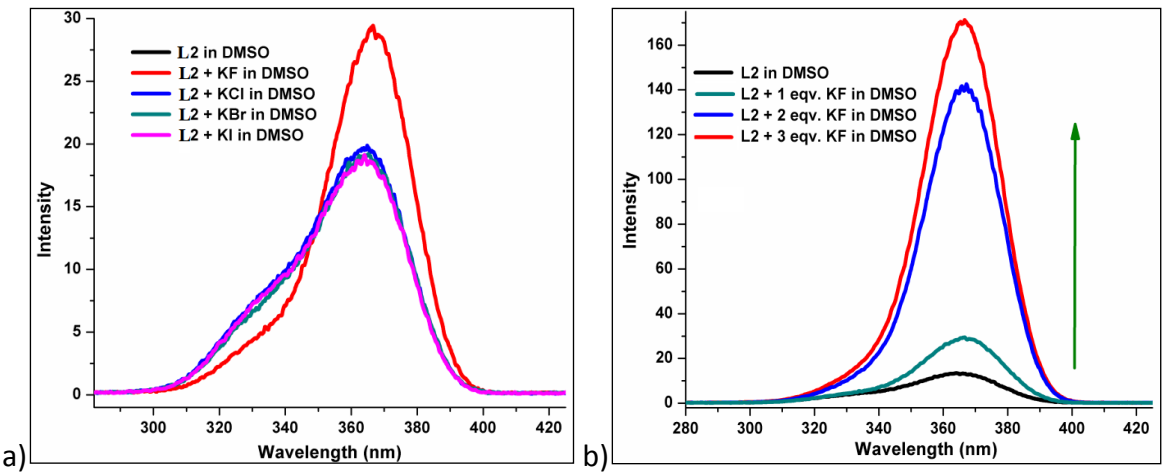

Figure 3.122. (a) Fluorescence intensity of **L2** in DMSO and the effect of various anions on its fluorescence intensity (b) Enhancement of the fluorescence intensity of **L2** on subsequent addition of fluoride ions.

As a pH indicator

The effect of pH on the absorption response of the probe **L1** in DMSO was analysed in the pH range of 2 to 14. The color of **L1** becomes yellow when the pH is acidic (~2) whereas it turns pink when the pH is alkaline (~9) (Figure 3.123).

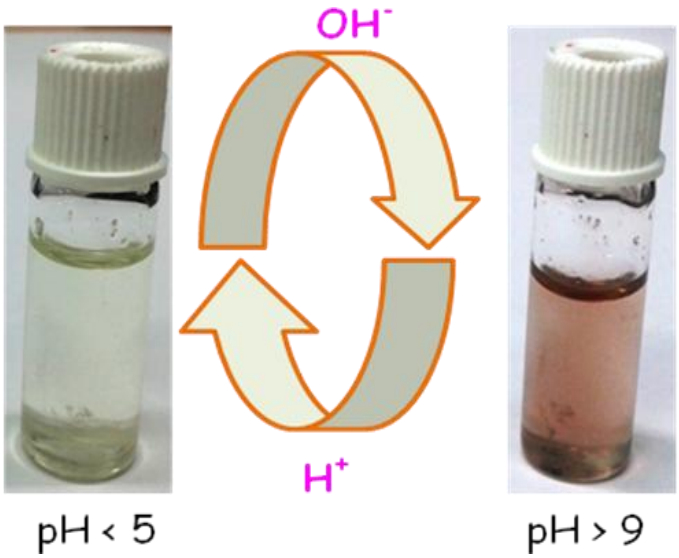

Figure 3.123. Visual of pH-dependent reversible behavior of H_2Tyr-4-nitro (in DMSO).

This pH dependent change in color (Figure 3.124) and the UV-Vis absorption (Fig. 3.125) are reversible even after several cycles of chronological alternative addition of HCl and NaOH. This suggests that **L1** in DMSO is a reversible optical pH indicator. A probable mechanism for the pH indicator behaviour of **L1** is summarised in Scheme 3.13. The pH of the creamish DMSO solution of H_2Tyr-4-nitro (**L1**) is ~5. On addition of base, first the deprotonation of the carboxylate (more acidic than phenol) of the sensor takes place (pH~9) giving rise to a colourless solution. On further addition of the base, pH rises above 9 and the solution turns pink due to the deprotonation of the phenolic group along with the deprotonation of the carboxylate of the sensor. On the other hand, on addition of acid, protonation of amine group of the sensor gives yellow color to the solution (pH<2)

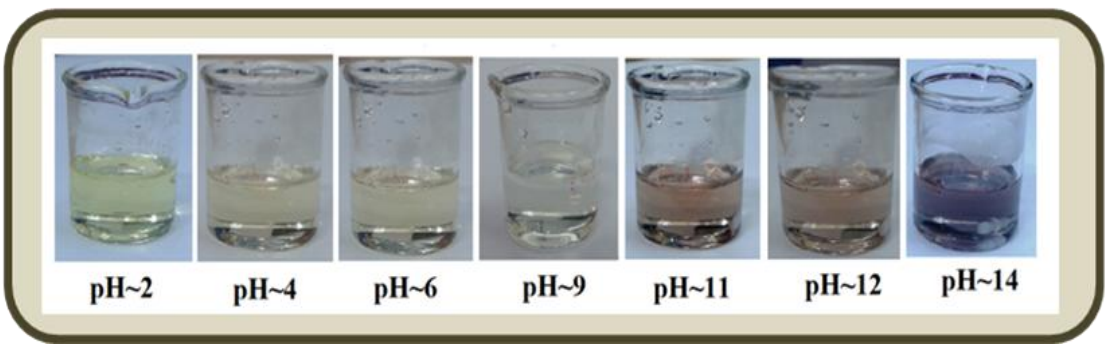

Figure 3.124. Change in color of the DMSO solution of H_2Tyr-4-nitro at different pH.

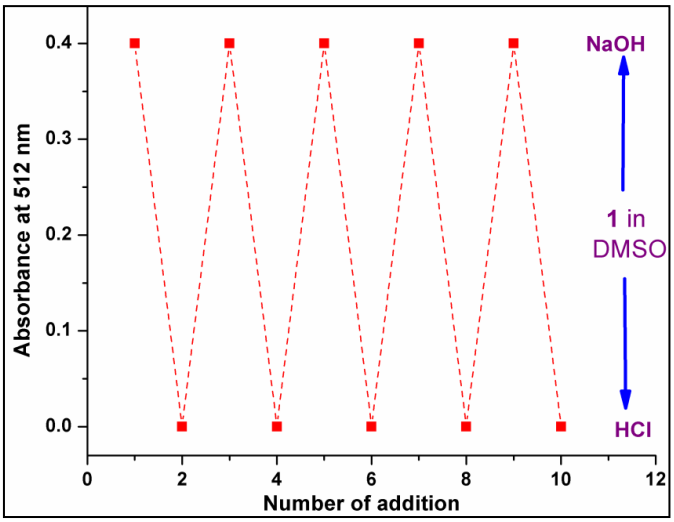

Figure 3.125. Reversible changes in absorbance of the probe **L1** at 512 nm after the sequential addition of HCl and NaOH to the DMSO solution of **L1**.

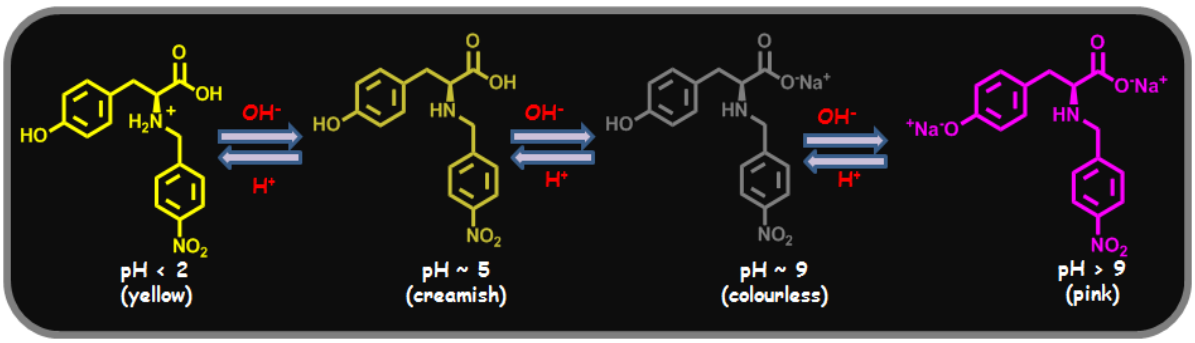

Scheme 3.13. Probable mechanism for the role played by H_2Tyr-4-nitro as a pH indicator.

3.3.2. Solvent assisted chromogenic and/or fluorogenic sensor for anions

For studying the receptor behaviour of $[Cu(HTyr\text{-}4\text{-}nitro)_2(H_2O)]\cdot 2H_2O$ (**23**) towards various anions, such as F^-, Cl^-, Br^-, I^-, OAc^-, in DMSO and methanol, respectively, the chromogenic responses were recorded. The naked eye colorimetric response for **23a** on addition of various analytes (in 1:3 solution of H_2O:DMSO mixture) is well evident from Figure 3.126, where F^- and OAc^- show quite distinct behaviour from the other analytes. Although **23a** is a neutral compound, its ability to sense various anions can be attributed to the anion-π interactions[318-328] along with hydrogen bonding. This is in contrast to the lysine based sensor $[Zn_2(slys)_2Cl_2]$ reported by Churchill et al.[329] that acts as a receptor for phosphate ions by substituting the coordinated chloride ions with the phosphate ions.

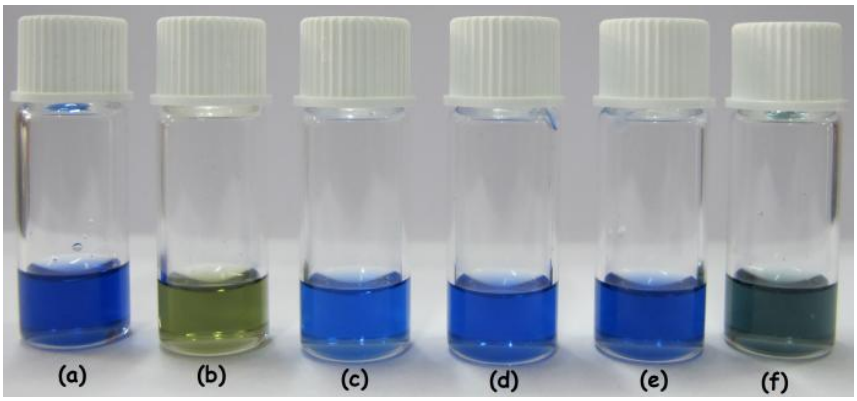

Figure 3.126. Chromogenic responses of solutions of **23a** in DMSO upon interaction with various anions: (a) Free host **23a** (3 mM); (b) **23a** + 1 eqv KF; (c) **23a** + 1 eqv KCl; (d) **23a** + 1 eqv KBr; (e) **23a** + 1 eqv KI; and (f) **23a** + 1 eqv NaOAc.

To analyse the anion–π interactions, absorbance spectra for **23a** (in DMSO) along with different analytes were also monitored. As can be seen from Figure 3.127, the λ_{max} values observed for various solutions are: 588 nm (a), 624 nm (b), 598 nm (c), 599 nm (d), 594 nm (e) and 636 nm (f). On addition of various analytes to **23a**, a shift of λ_{max} towards higher wavelength is observed indicating less energy required for the d-d transition in Cu(II) which is coordinated to two monoanionic HTyr-4-nitro ligands.

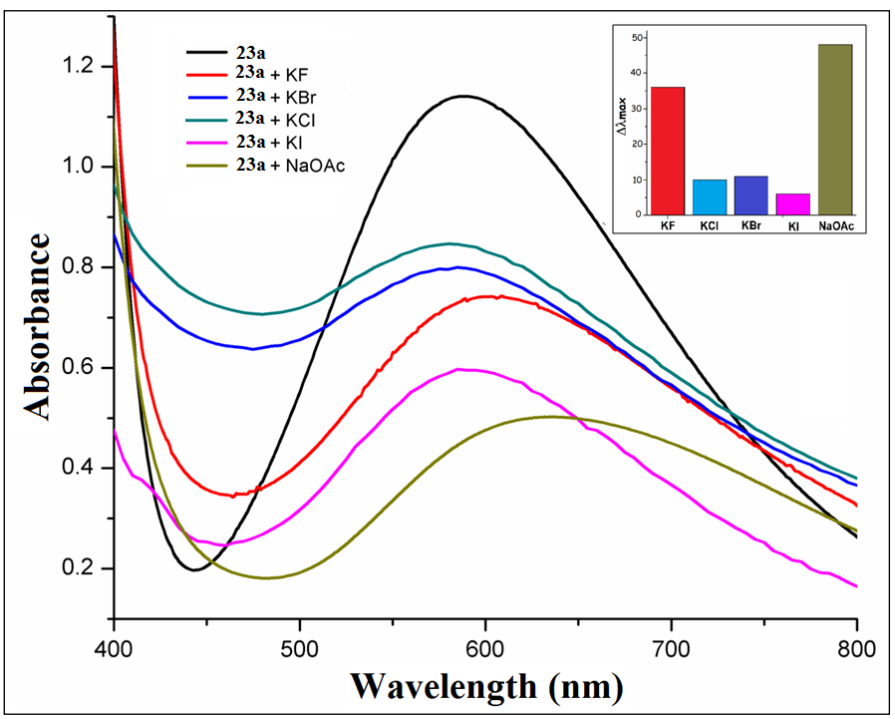

Figure 3.127. Effect of anions on the absorption spectra of **23a** in DMSO. Inset: selectivity plot of the various anions using **23a**.

This observation can be ascribed to the fact that the anion-π interactions between various anionic analytes and the aromatic part of the ligand can alter the energy states for the metal ion. On the other hand using UV-vis spectroscopy, the reversibility of the process is established through the decomplexation of **23a**·F^- with $Ca(NO_3)_2$, which leads to a color change from light green back to the original blue of **23a,** followed by addition of further KF to regain the light green color. The shifts observed for OAc^- and F^- corroborates well with the naked eye colorimetric responses. The above fact is further established by the Circular Dichroism (CD) spectra of **23a** along with different analytes (Figure 3.128). For **23a**, the positive and negative Cotton effects are observed at 507 nm and 636 nm, respectively. On addition of the analytes, a shift in the bisignate Cotton effect is observed. These shifts are most prominent in the case of NaOAc.

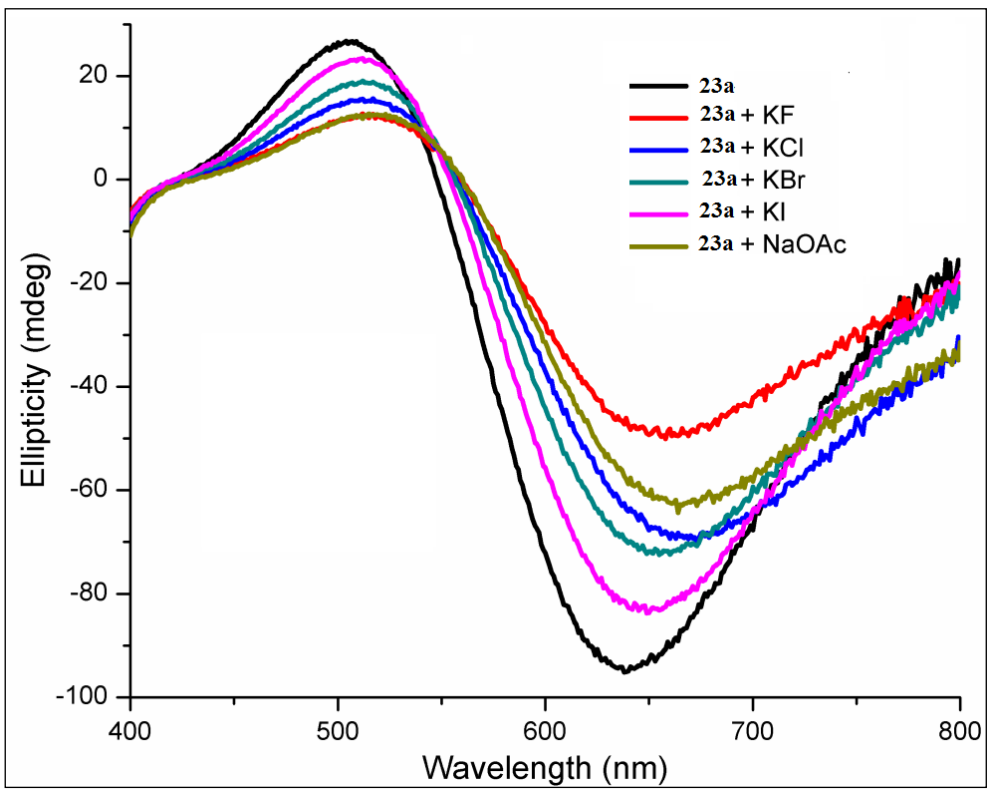

Figure 3.128. Effect of anions on the CD spectra of **23a** in DMSO.

A comparative study of the detection limits for acetate ion using the sensors **23a** and the other best known sensors reported in the literature is summarized in Table 3.24.

Table 3.24. Comparative study of the detection limits for the various acetate sensors.

Sr. No.	Complex used	Detection limit	Reference
1.	butane-2,3-dione,bis[(2,4-dinitrophenyl)hydrazone]	1.2×10^{-6} mol/L	330
2.	a rhodamine 6G phenylurea conjugate	1.8×10^{-7} mol/L	331
3.	**23a**	9.4×10^{-3} mol/L	This work

Since the maximum response was observed for NaOAc, the titrimetry of **23a** with it showed a concentration dependency on the λ_{max} value: with every consecutive addition of 0.1 eqv of NaOAc, the value shifts towards higher wavelength. This change is prominent till the addition of 0.5 eqv of the analyte, after which not much variation is noticeable (Figure 3.129).

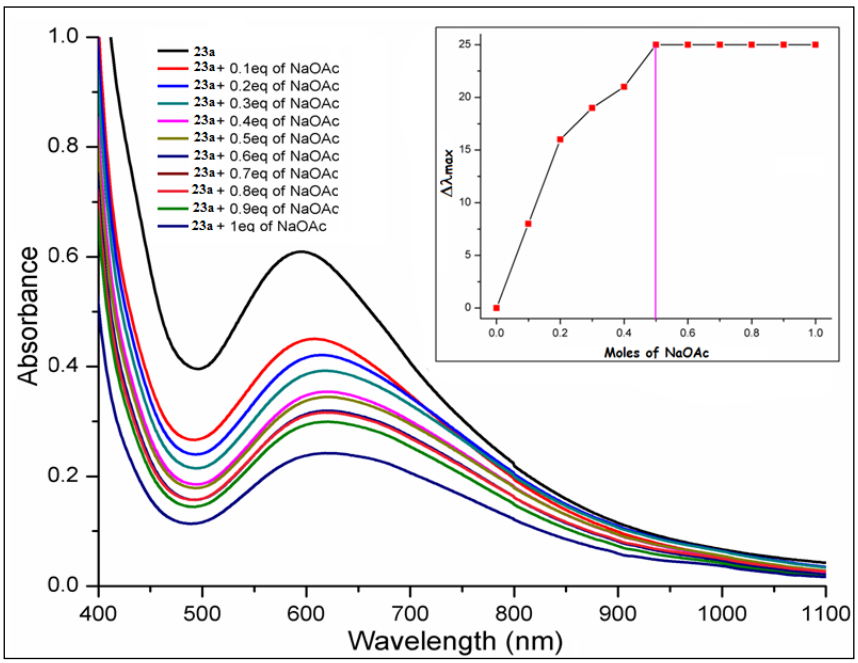

Figure 3.129. Titration of **23a** (in DMSO) against NaOAc solution. Inset: Change in λ_{max} value with addition of NaOAc to **23a** at different molar ratios.

This suggests that the sensor gets saturated with 0.5 eqv of the analyte, forming a 2:1 receptor to anion complex. Considering the dilution effect due to the addition of each aliquot of the analyte, the decrease in intensity of the peak is to some extent due to the perturbation of the electron density of the ligand, which is coordinated to the Cu(II) center, from its interaction

with the analyte. The titrimetry of **23a** with different concentrations of NaOAc is also followed by the Fluorescence spectroscopy using λ_{exc} at 220 nm for the 4-nitro-phenyl part of the ligand, which is away from the Cu^{2+} center. As can be seen from Figure 3.130, the intensity of the λ_{emi} at 376 nm is quenched maximally with 0.5 eqv of NaOAc; additional quantities of NaOAc do not have any further effect on it.This not only confirms the results of the UV-vis data indicating a 2:1 receptor to analyte ratio but more importantly, its interaction with the π electron density of the 4-nitro-phenyl moiety.

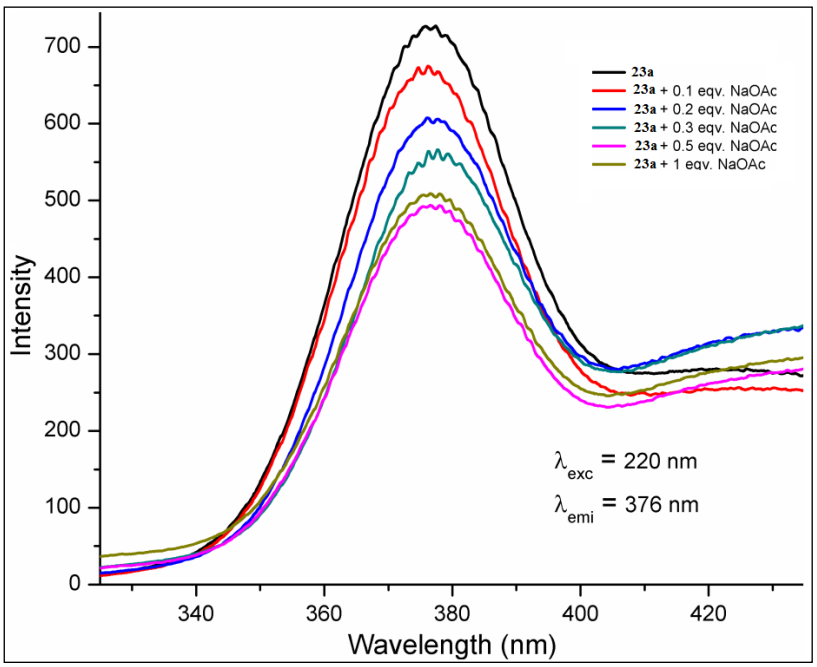

Figure 3.130. Fluorescence quenching of the 4-nitro-phenyl group of the ligand in **23a** upon addition of NaOAc at different molar ratios.

In order to clarify the receptor to anion ratio, negative mode electrospray ionization mass spectrometry (ESI-MS) was carried out for an acetonitrile solution ($0.2x10^{-4}$ M) of **23a** mixed with NaOAc at different molar ratios (0.125 to 2.0:1). For all ratios, it revealed that **23a** binds with acetate in a 2:1 stoichiometry (calc. for [(($\mathbf{23a}$)$_2$·OAc^-) + Na^+ + CH_3CN - H^+]: 1545.2945; found: 1545.2837 to 1545.2974). To further elaborate the interactions present between NaOAc and **23a**, a comparative study of the FTIR spectra (in the form of a mull using a drop of DMSO) of **23a**, 0.5 eqv. NaOAc in **23a** and only NaOAc were carried (Figure 3.131) A distinct change in the carboxylate region of **23a** is observed on addition of NaOAc: a peak at 1574 cm^{-1}, which is neither observed in **23a** nor in NaOAc, is present while the

peaks observed at 1694 cm^{-1} and 1562 cm^{-1} in the spectrum of NaOAc disappear. This suggests that NaOAc and **23a** are not present as two separate compounds in the mixture.

In order to show the distinct behaviour of **23** in methanol compared to DMSO that was described above, it was tested against one equivalent of NaOAc (1:3 solution of H_2O: methanol mixture). Its colour change on addition of NaOAc was not as prominent as that observed in DMSO. The absorbance spectrum of **23b** in methanol shows a smaller shift of λ_{max} from 590 nm to 605 nm (Figure 3.132a) due to the addition of NaOAc. The absorbance spectra and CD spectra of **23b** with other analytes were also monitored, and in both cases no significant changes were observed (Figure 3.132b). This can be for the fact that a protic solvent (methanol) interacts more with the anions (solvation of anions) compared to an aprotic solvent (DMSO) and thus decreases the extent of anion-π interactions.

As described earlier, the presence of interactions between DMSO molecules and the ligands make the parallel orientation of the ligands which forms a void within the four adjacent molecules. The presence of two DMSO molecules (one in front and one in back of this void) helps the anion to firmly sit inside the void and thus the anion-π and hydrogen bonding interactions are quite prominent for the anion sensing. To analyse the role of electron withdrawing group in anion sensing, compounds with other substituents are also employed. Since the anion sensing abilities of **23** in DMSO are much more prominent than in methanol, $\{[Cu(L\text{-}HTyrbenz)_2]\cdot CH_3OH\cdot H_2O\}_n$ (**1**), $[Cu(L\text{-}HTyr4\text{-}fluoro)_2(H_2O)].2H_2O$ (**27**) and $[Cu(L\text{-}HTyr4\text{-}methoxy)_2(H_2O)].3H_2O$ (**31**) are studied in DMSO.

Based on the chromogenic comparison **1**, **27** and **31** with **23**, it is clear that the addition of anions to a complex with electron withdrawing groups in the ligands brings a considerable change (Figure. 3.126 and 3.133(a)) as compared to one with an electron donating group (Figure 3.133(b)) as well as the one without any substitution on benzyl ring (Figure 3.133(c)). To further establish the fact, all four sensors **23**, **27**, **31** and **1** were monitored by absorption spectroscopy to see their role in anion sensing (Figure 3.134 and Figure 3.135). Naked eye colorimetric detection along with the absorption spectroscopy clearly suggests that **23** and **27** are better sensor for anions (especially OAc^-) as compared **31** and **1** (as shown in Figure 3.135). Addition of acetate to the DMSO solution of the receptor shows a large change in

λ_{max} (78 nm; red shift from 580 nm to 668 nm) in absorbance spectra of **27** compared to a red shift of 9 nm (595 nm to 604 nm) in case of **1** and that of 19 nm (red shift from 597 nm to 616 nm) in absorption spectrum of **31** (as shown in Figure 3.134 and Figure 3.135) emphasizing the obligatory roles of the electron withdrawing groups in anion sensing by anion–π interactions.[318-328]

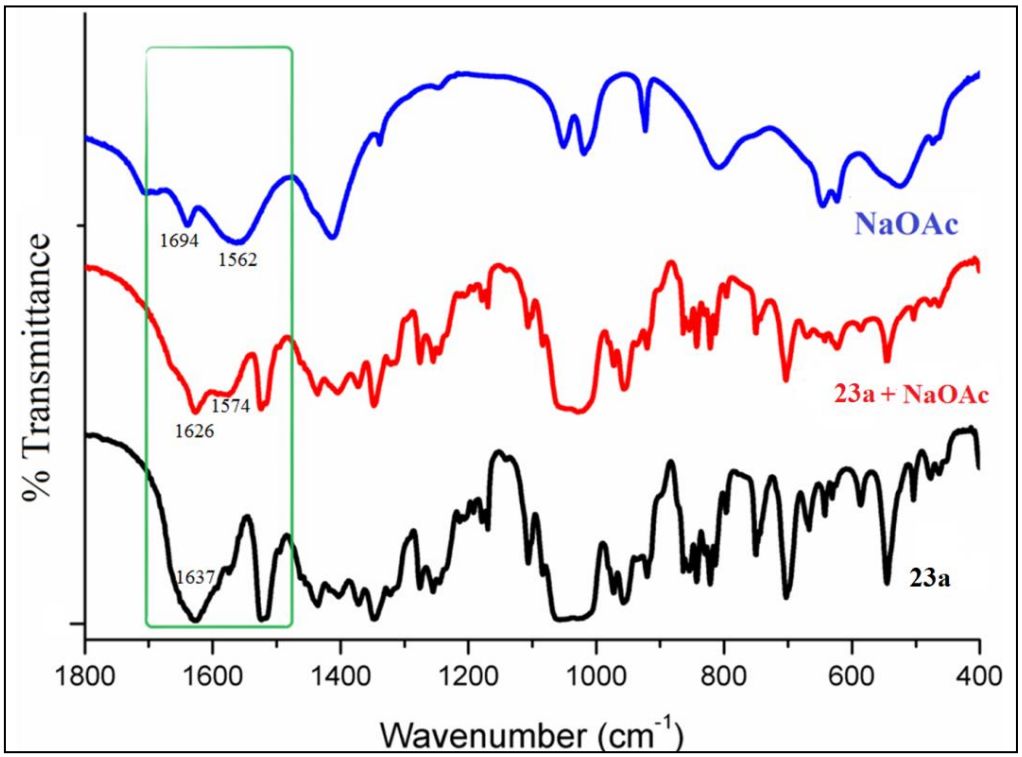

Figure 3.131. Comparison of carboxylatw frequencies in FTIR spectra of NaOAc, **23a**, and **23a** + 0.5 eqv. NaOAc.

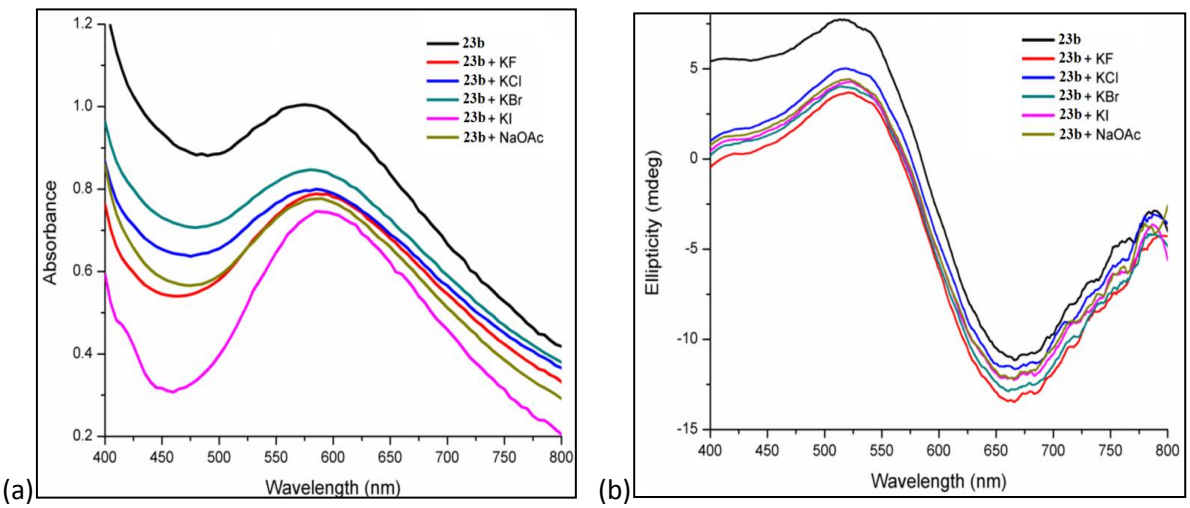

Figure 3.132. Effect of anions on the (a) absorption and (b) CD spectra of **23b** in methanol.

A comparison of all these four sensors (**23**, **27**, **31** and **1**) (Figure 3.136) further emphasizes the fact that electron withdrawing groups play a key role in anion-π interaction by generating a δ^+ (positive quadruple) environment over the aromatic ring thus making anion–π interactions going more favourable. However, the better sensitivity of sensor **31** towards anions as compared to **1**, even though sensor **31** consists of electron donating group can be accredited to the resonance effect of the methoxy group thus somehow balancing the δ^- (negative quadruple) produced by the electron donating ability of the this group.

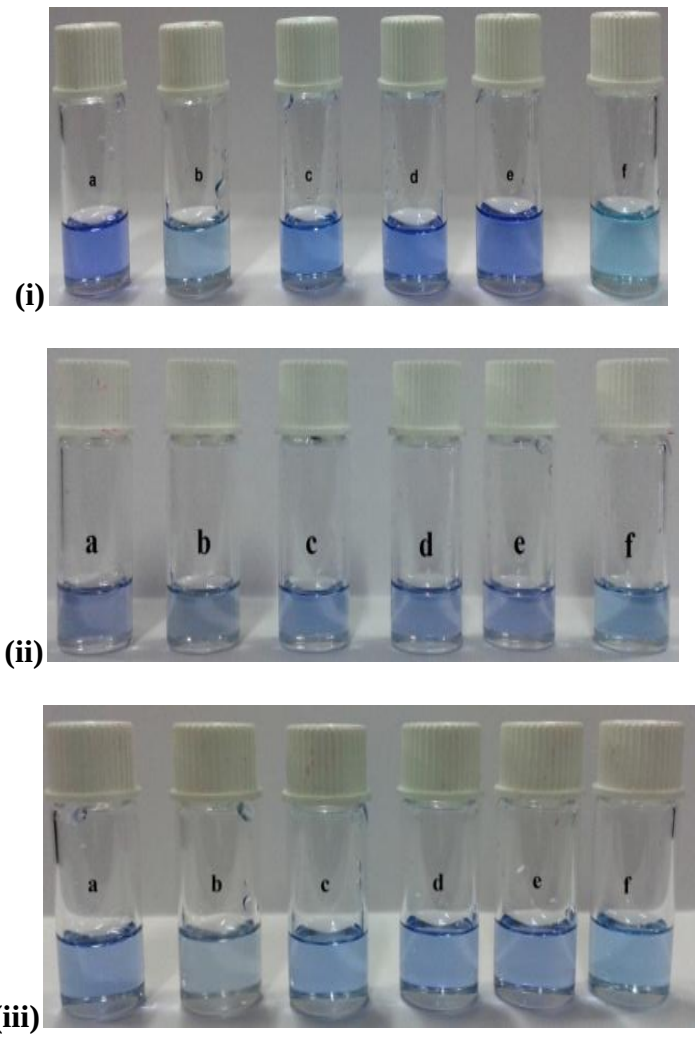

Figure 3.133. Chromogenic responses of solutions of (i) **27**, (ii) **31**and (iii) **1** in DMSO upon interaction with various anions. (a) Only sensor (3 mM); (b) Sensor + 1 eqv KF; (c) Sensor + 1 eqv KCl; (d) Sensor + 1 eqv KBr; (e) Sensor + 1 eqv KI; and (f) Sensor + 1 eqv NaOAc.

The role of electron withdrawing groups like nitro and fluoro in anion sensing is quite remarkable. Titrimetry of the sensor **27** with NaOAc shows the effect of the variation in

concentration of the analyte on the UV-vis spectrum of the sensor. With every consecutive addition of 0.1 equivalent of the analyte (NaOAc), the value of λ_{max} shifts towards higher wavelength. This change is prominent till the addition of 0.5 equivalent of the analyte, after which not much variation is noticed (see Figure 3.137). This suggests formation of 2:1, sensor: analyte complex for **27** similar to that for **23**.

To further accentuate the role of two same ligands (homoligands) with electron withdrawing groups on the anion sensing property of the sensors, one of the ligands in each case (**23** and **27**) was replaced with L-tyrosine to obtain [Cu(L-HTyr4-nitro)(L-Tyrosine)]·$2H_2O$ **(32)** and [Cu(L-HTyr4-fluoro)(L-Tyrosine)]·$3H_2O$ (**33)**, respectively.

The presence of one electron withdrawing group does not show any remarkable colorimetric or spectroscopic change on addition of anions to DMSO solution of **32** (Figure 3.138(i)). On addition of acetate, a red shift in λ_{max} was observed (610 nm to 634 nm) in case of **33**. This shift of 24 nm is much less as compared to the 78 nm change observed for **27**, on addition of acetate (Figure 3.139). For proof of concept, complex **33** with hetero ligands was also tested against various anions. It showed similar observation as seen for complex **32**. The addition of anions neither show any remarkable change in the λ_{max} of the absorption spectra nor does it show any distinct visual color change(as shown in Figure 3.138(ii)). On addition of acetate to the DMSO solution of compound **33** a red shift of 20 nm in λ_{max} was observed which is much less as compared to 48 nm observed in case of **23** (Figure 3.139).

The visual responses in both the above cases (32 and 33) comprehend for a poor anion sensing ability. The absorption spectroscopy further supports that an electron withdrawing group is a pre-requisite for anion-π interaction (Figure 3.140). In both the cases, an electron-withdrawing group is attached to one of the ligands coordinating to the Cu2+ center; however, they fail to produce the same effect as that of sensor 23 and 27, where both the ligands coordinating to the Cu2+ centre are having electron withdrawing groups attached to them. Comparing the crystal structures of 33a and 27a, it is seen that substitution of one HTyr4-fluoro ligand with L-tyrosine in 27a, not only changes the coordination geometry of Cu2+ (distorted square pyramidal in 27a as compared to square planar in 33a) but also the coordination environment as well as the orientation of the ligands. The effect of the variation

in the crystal structure of 33a consisting of hetero ligands as compared to the complexes with homo ligands (27a) can be seen influencing the anion sensing ability of 33. This example illustrates that along with the presence of an electron withdrawing group, a proper orientation

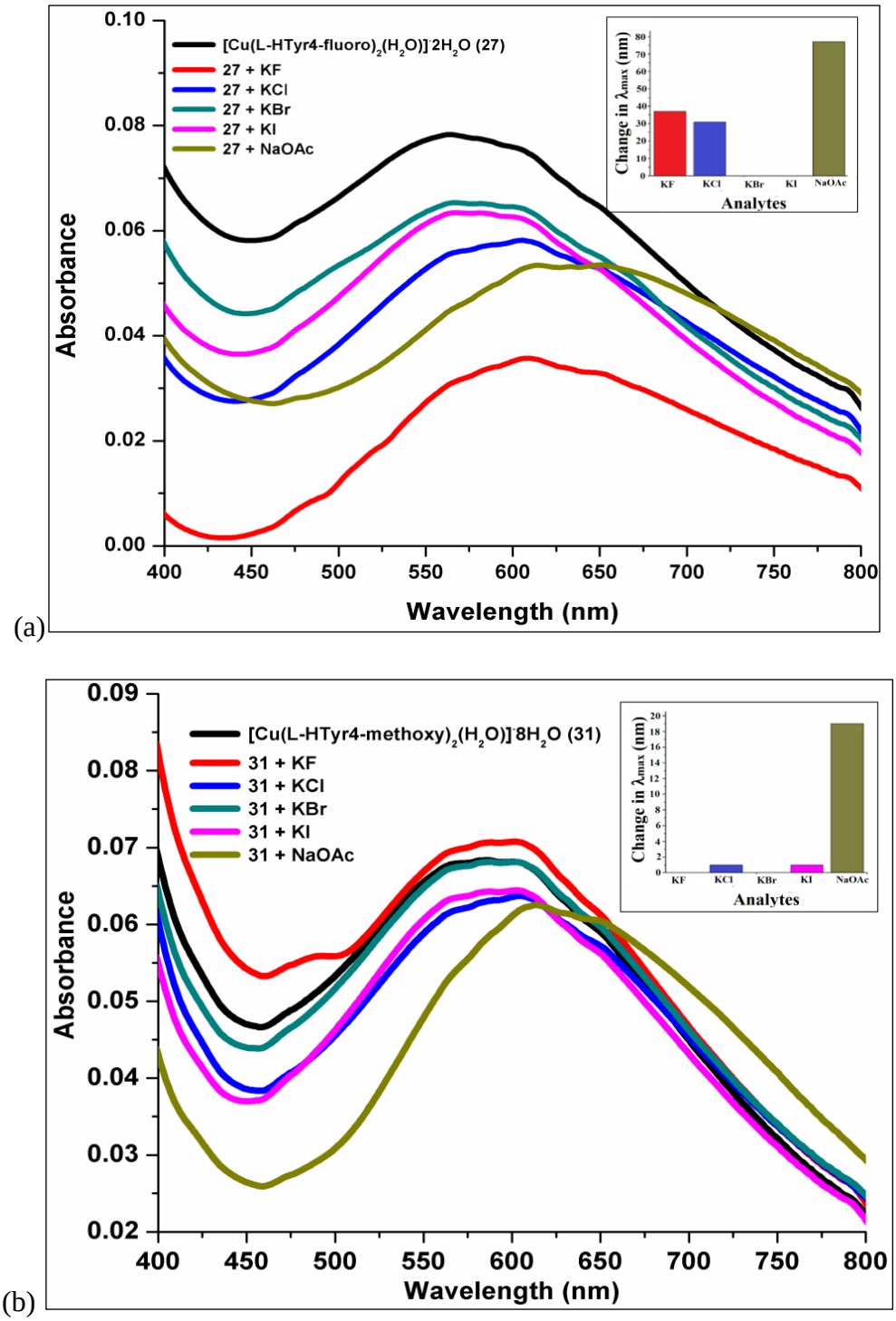

Figure 3.134. Effect of anions on the absorption spectra of (a) **27** and (b) **31** in DMSO. Inset: selectivity plot of the various anions using **27** and **31**.

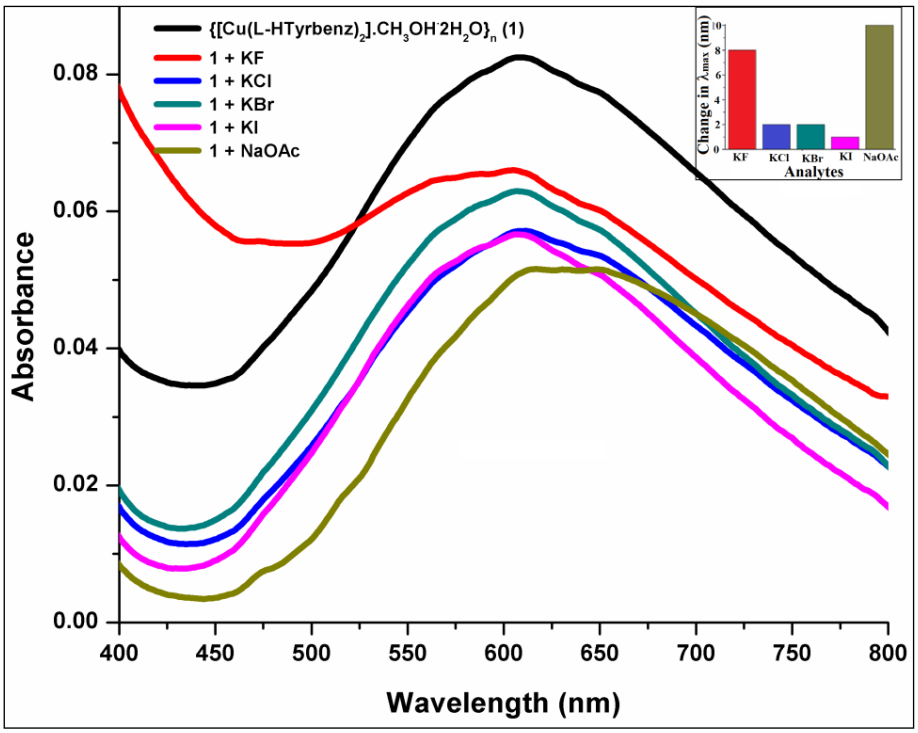

Figure 3.135. Effect of anions on the absorption spectra of **1** in DMSO. Inset: selectivity plot of the various anions using **1**.

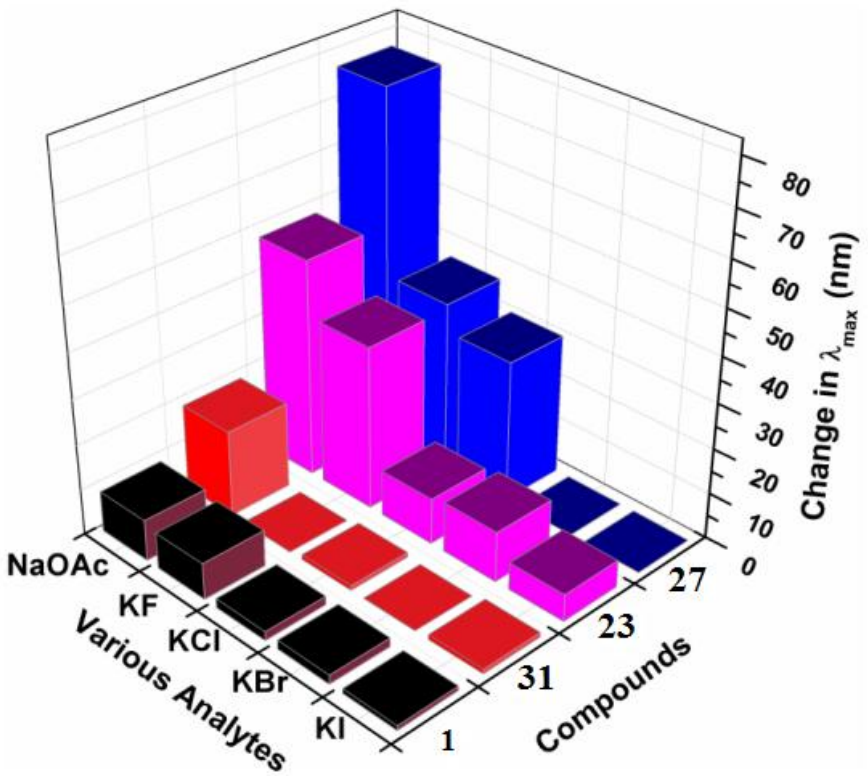

Figure 3.136. Change in λ_{max} on addition of various analytes in **1, 23, 27** and **31.**

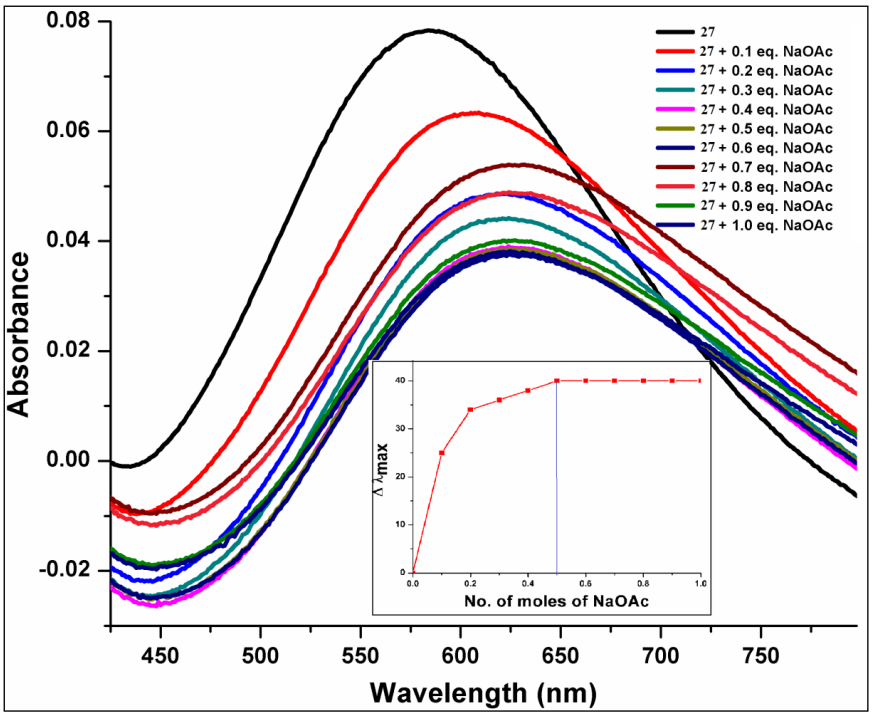

Figure 3.137. Titration of sensor **27** (in DMSO) against NaOAc solution. Inset: Change in λ_{max} with the addition of NaOAc to the DMSO solution of sensor.

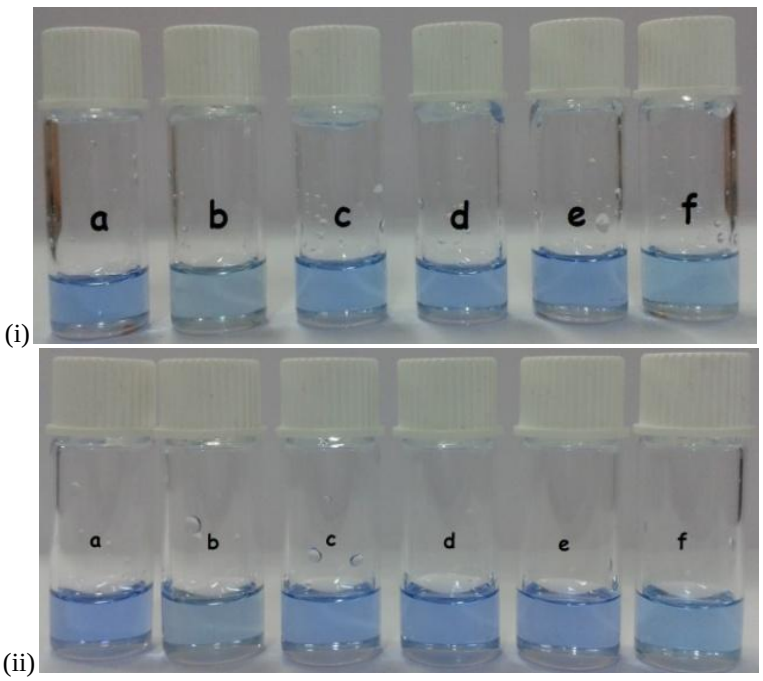

Figure 3.138. Chromogenic responses of solutions of (i) **32** and (ii) **33** in DMSO upon interaction with various anions. (a) Only sensor (3 mM); (b) Sensor + 1 eqv KF; (c) Sensor + 1 eqv KCl; (d) Sensor + 1 eqv KBr; (e) Sensor + 1 eqv KI; and (f) Sensor + 1 eqv NaOAc.

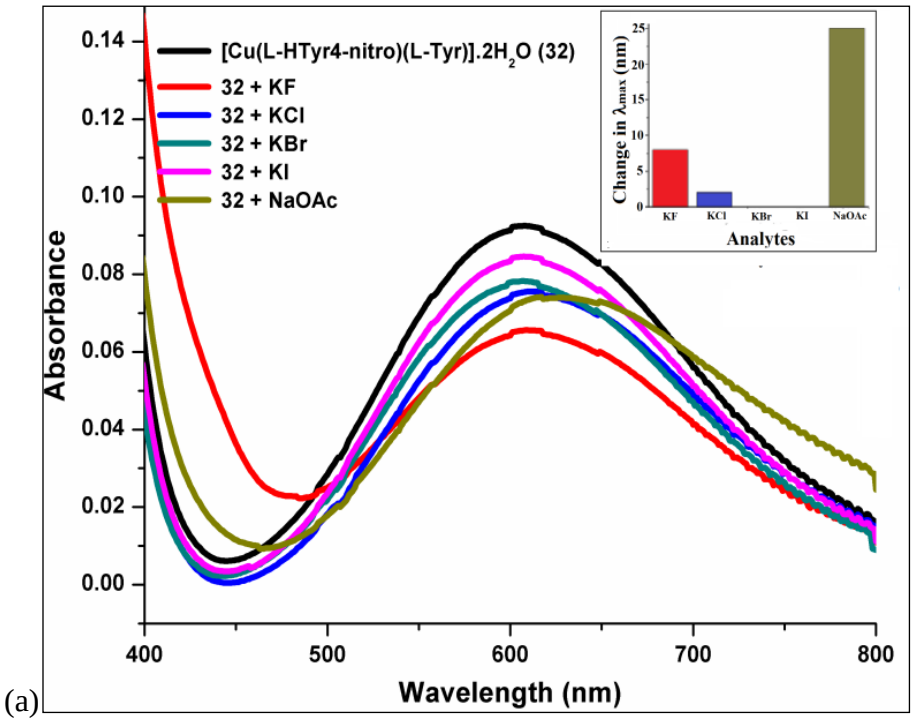

(a)

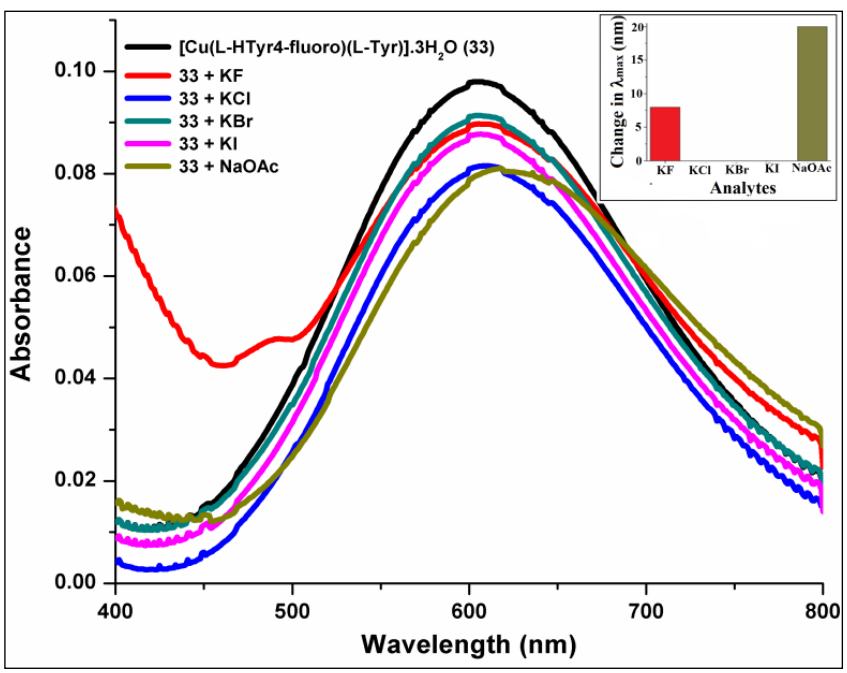

(b)

Figure 3.139. Effect of anions on the absorption spectra of (a) **32** and (b) **33** in DMSO. Inset: selectivity plot of the various anions using **32** and **33**.

is also necessary for anion-π interaction which is absent here as seen from the absence of any kind of π–π interactions in **33a**. This particular example also confirms the advanced role of

presence of two electron withdrawing groups attached to the ligands coordinating to the metal center in **23** and **27** as compared to the one present in **33** and **32**, in betterment of anion sensing ability.

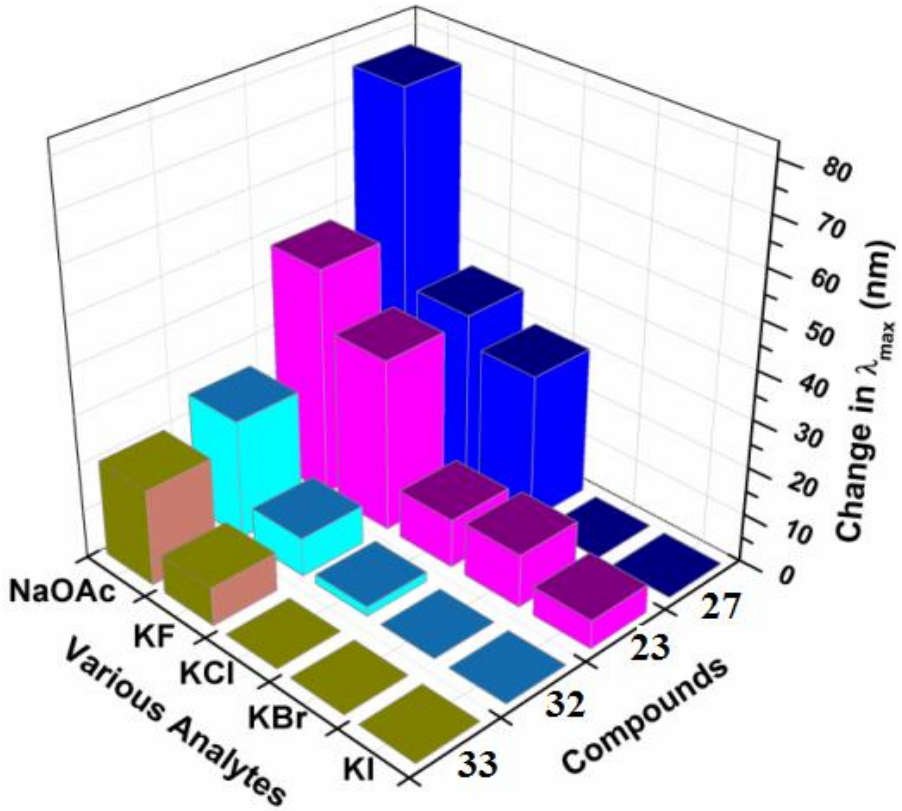

Figure 3.140. Change in λ_{max} on addition of various analytes in **23, 27, 32** and **33**.

After gaining full insight into the roles of various groups attached to ligands in anion sensing, the auxillary information on the function played by the metal center in anion sensing is also analysed. For this purpose complex $[Zn(L\text{-}HTyr4\text{-}nitro)_2(H_2O)]\cdot 4H_2O$ (**25**) is chosen as the model. However, in case of **25** due to presence of Zn, chromogenic detection of anions was not possible. To overcome this obstacle, fluorogenic property of the **25** was explored. To have a comparative study, fluorogenic property of **23** is also established. In both the cases the presence of two natural fluorophores (p-hydroxybenzyl group from tyrosine and nitrobenzaldehyde) makes the complexes fluorogenic in nature. The ligand itself is also fluorogenic but is not used in anion sensing because the use of metal complexes are preferred over their respective free ligands, as coordinating to a metal increases the π-acidity of the aromatic ligand thus increasing the anion-π interactions.[332,333]

H_2Tyrtnitro shows a good fluorescence when excited at 220 nm (due to nitobenzyl part) as well as at 270 nm (due to tyrosine part). Even **23** and **25** show enhanced fluorescence as compared to H_2Tyrtnitro when excited at 220 nm while when excited at 270 nm, **23** shows a decrease in fluorescence whereas **25** shows an enhancement in fluorescence (as shown in Figure 3.141).

On addition of various analytes to **23** as well as **25**, not much change is observed when excited at 270 nm but shows a remarkable change when excited at 220 nm (esp. for F^- and OAc^-) further proving the substantial role of electron withdrawing nitrogroup in anion-π interactions. On addition of one equivalent of analyte (F^- showing enhancement and OAc^- showing quenching) the change is quite distinct in case of **23** while it is not that distinct in case of **25**. However, on addition of five equivalent of analyte the same pattern was observed for **25** (Figure 3.142) as seen for **23** on addition of one equivalent of analyte to it. A comparative study clearly embarks that sensor **23** can fluorogenically sense anions (esp. F^-) better as compared to sensor **25** (sensing one equivalent of analyte by **23** as compared to five equivalents by **25**) (Figure 3.142(d)).

a) 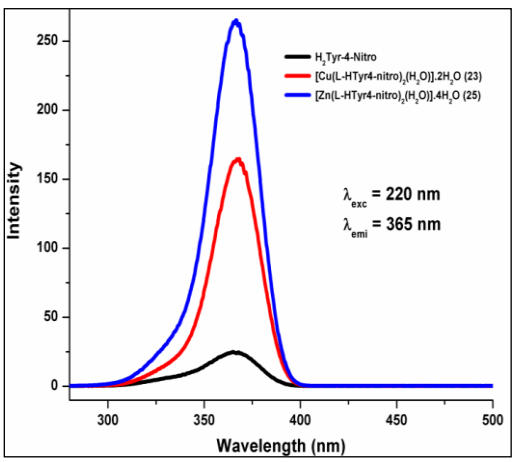

b) 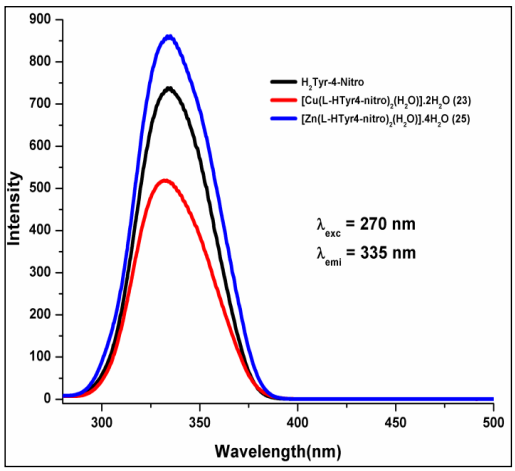

Figure 3.141. Fluorescence Spectra of H_2Tyr4-nitro, **23** and **25** on excitation at (a) 220 nm (b) 270 nm.

This disparity in anion sensing by complexes **23** and **25** can be explained on the basis of their crystal structures **23a** and **25a**, respectively. The coordination environment around Zn^{2+} in **25a** is same as that of Cu^{2+} in **23a** except the different distortion angles (variation in the bond lengths and bond angles around center metal ions due to the Jahn-Teller distortion in **25a**)

which can account for their difference in anion sensing properties. All these structural variations lead to the divergence in the anion sensing ability of the two compounds. Also, the extent of interaction of amine nitrogen with the metal center (Cu vs Zn) also dictates further hydrogen bonding ability of the hydrogen (on the amine nitrogen) with the various analytes.

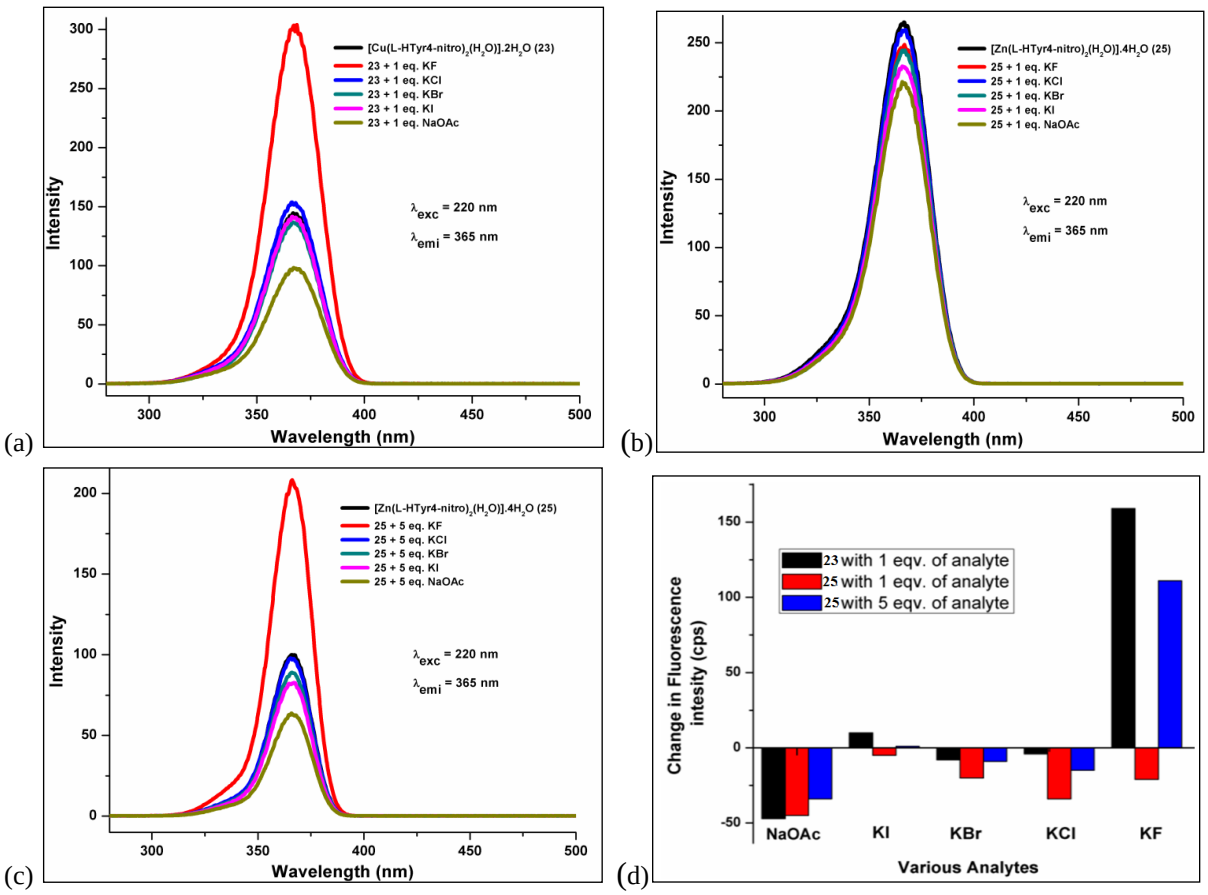

Figure 3.142. Fluorescence Spectra of (a) **23** on addition of one equivalent of various analytes; **25** on addition of (b) one equivalent (c) five equivalents of various analytes; (d) Comparative study of the effect of addition of various analytes in **23** and **25**.

3.3.3. One-for-three: a multi-responsive fluorogenic sensor for cations, anions and neutral molecules

In designing the NaHTyrthio (**L3**) sensor for the present work, the role of various functionalities in their photoluminescence abilities was first thoroughly analysed (see Figure 3.143). Based on a number of strategic modulations, the importance of phenol as well as thiophene moieties in its photoluminescence property was established. Attaching a benzyl group to tyrosine [forming H_2Tyrbenz = N-(benzyl)-tyrosine)] does not alter the fluorescence

intensity of tyrosine; however, a 4-methyl-pyridyl [forming H_2Tyr4-pyr = N-(methyl-4-pyridyltyrosine)] or a p-nitro-benzyl [forming H_2Tyr-4-NO_2-benz = N-(4-nitrobenzyl)-tyrosine)] substitution decreases the fluorescence intensity of tyrosine drastically whereas the placement of a thiophene group [forming H_2Tyrthio] enhances the intensity. To analyse any positional effect due to a phenol group in these sensors, the fluorescence spectra of an equimolar amount of NaHTyrbenz and NaPhe-4-OH (where HPhe4-OH = N-(4-hydoxybenzyl)-phenylalanine) were also scrutinized. The reversal of the position of the phenol and benzyl groups (NaHTyrbenz vs. NaPhe-4-OH) not only changes the intensity but also affects the spectral shape, thus further establishing the importance of the position of a phenol group from tyrosine in these tyrosine-based sensors. This could be due to the orientation of the molecule with respect to the chiral center (in solution) that decides the fate of its fluorescence ability. While a deeper introspection of the fluorescence spectrum of NaGly-4-OH (where HGly-4-OH = N-(4-hydoxybenzyl)-glycine) confirms the insignificant role of chirality in sensing ability of amino acid based ligands, all these derivatives are easily made from the cheap and readily available L-amino acids. Thus, NaHTyrthio is preferred due to its much better fluorescence ability compared to other analogues.

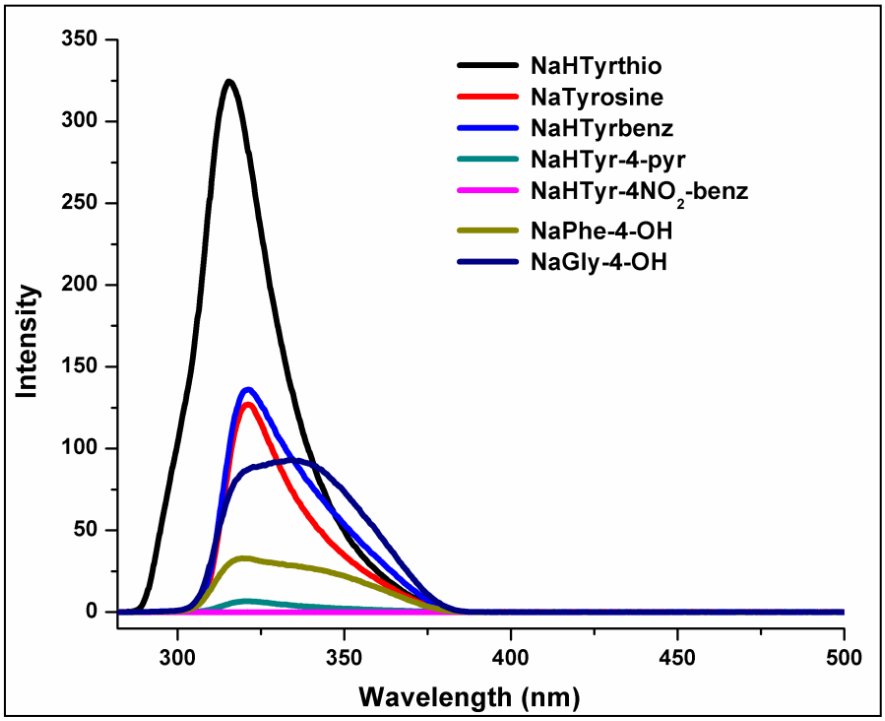

Figure 3.143. Comparison of photoluminescence ability of various amino acid based sensors using excitation wavelength = 270 nm.

A strategic fine tuning of the two fluorophores (phenol and thiophene groups) judiciously put together in a single compound is attributed to the sensing of multiple analytes by variable spectral responses. The sodium salt of N-(methyl-2-thiophenyl)-tyrosine (NaHTyrthio) is an unprecedented single-molecular multianalyte fluorogenic receptor, wherein it shows selective sensing of a cation (Cu^{2+}), neutral small molecules (nitrobenzene and aniline) and an anion (F^-) at the ppm or ppb level (Figure 3.144). The fluorescence quenching serves as a signal for sensing of Cu^{2+} and nitrobenzene (attributed to the phenol part) along with F^- (attributed to the thiophene part). On the other hand, the sensing of aniline is ascribed to the shift in emission wavelength of the phenol part of the receptor.

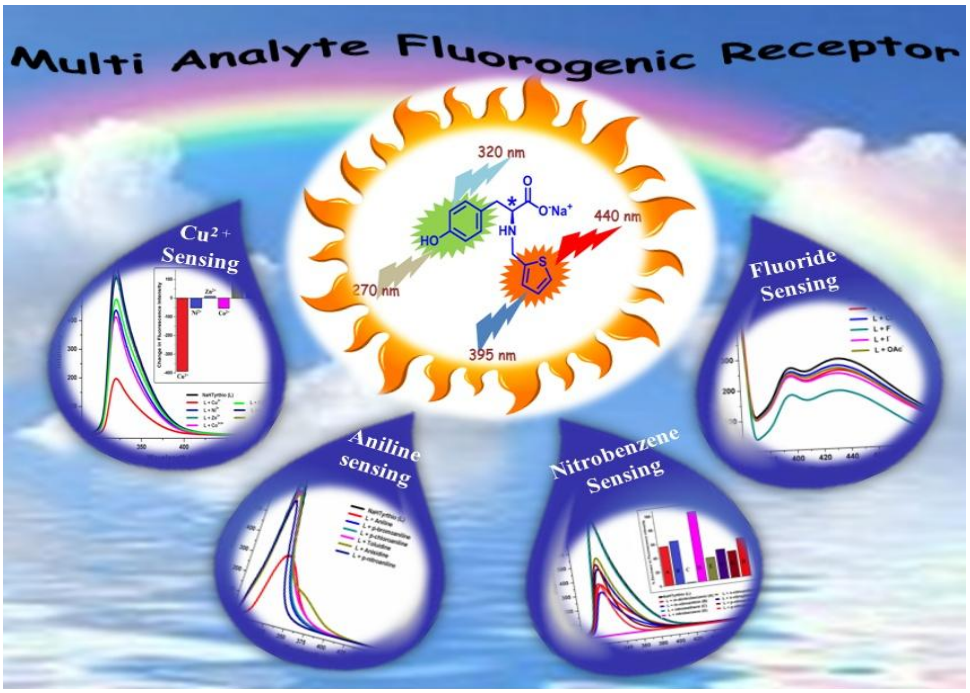

Figure. 3.144. A single receptor for the selective sensing of cations, neutral small molecules, and anions by variable spectral responses.

Sensing of cation: selectivity and sensitivity of Cu^{2+} over other metal ions

The fluorescence behaviour of NaHTyrthio towards various metal ions was explored in methanol. As shown in Figure 3.145, compared to K^+, Zn^{2+}, Ni^{2+}, Co^{2+}, Cd^{2+} and Cr^{3+}, the addition of Cu^{2+} to NaHTyrthio causes a substantial decrease in fluorescence intensity indicating much higher selectivity for Cu^{2+} over other metal ions. To explore the sensitivity of the sensor for Cu^{2+}, titration experiments were also performed using a ligand solution (3.6 mM, 2 mL) with a copper nitrate solution. Subsequent additions of Cu^{2+} to NaHtyrthio show

a gradual decrease in fluorescence intensity as shown in Figure 3.146. The fluorescence quenching of the phenol part of NaHTyrthio is observed while the thiophene part remains unaffected, which clearly suggests the binding of Cu^{2+} with the phenol group. This is further supported by the isolation and structural characterization of a 1D coordination polymer $\{[Cu(HTyrthio)_2]\cdot H_2O\}_n$ from the reaction of Cu(II) salt and NaHtyrthio (*vide infra*). Further analysis of the fluorescence quenching provides a detection limit of the sensor for Cu^{2+} to be 50 ppb (1% quenching); 30% and 99% quenching with 5 ppm and 150 ppm, respectively. This result clearly establishes an excellent selectivity and sensitivity of NaHTyrthio for Cu^{2+} ions over other divalent ions. A comparative study of the detection limits for Cu^{2+} using Natyrthio(**L3**) and various other sensors reported in the literature is summarized in Table 3.25.

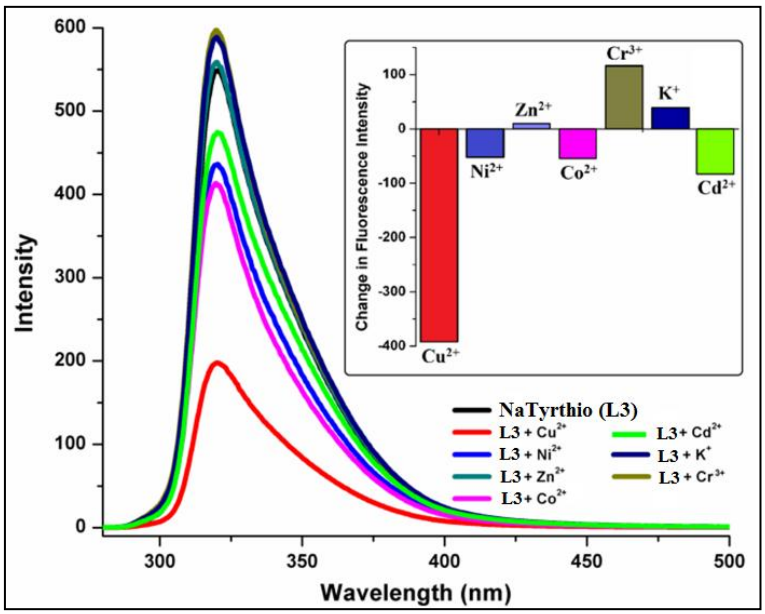

Figure 3.145. Emission spectra of NaHTyrthio upon the addition of various metal ions. Inset: Change in Fluorescence intensity of NaHTyrthio on the addition of different metal ions (λ_{exc} = 270 nm).

In order to understand the binding affinity of the analyte (Cu^{2+}) towards the sensor (NaHTyrthio), the powerful technique isothermal titration calorimetry (ITC) was employed. On the basis of the heat absorbed or evolved during the calorimetric titration three sequential binding modes, which corroborate well with its solid state structure (binding of Cu^{2+} with the amine, carboxylate and phenolic –OH groups), are formulated (see Figure 3.147) to obtain

the relevant thermodynamic parameters for these interactions which are summarized in Table 3.26. The control experiments in the absence of the sensor are performed to account for some of the unwanted heat effects like the heat of dilution and mixing.

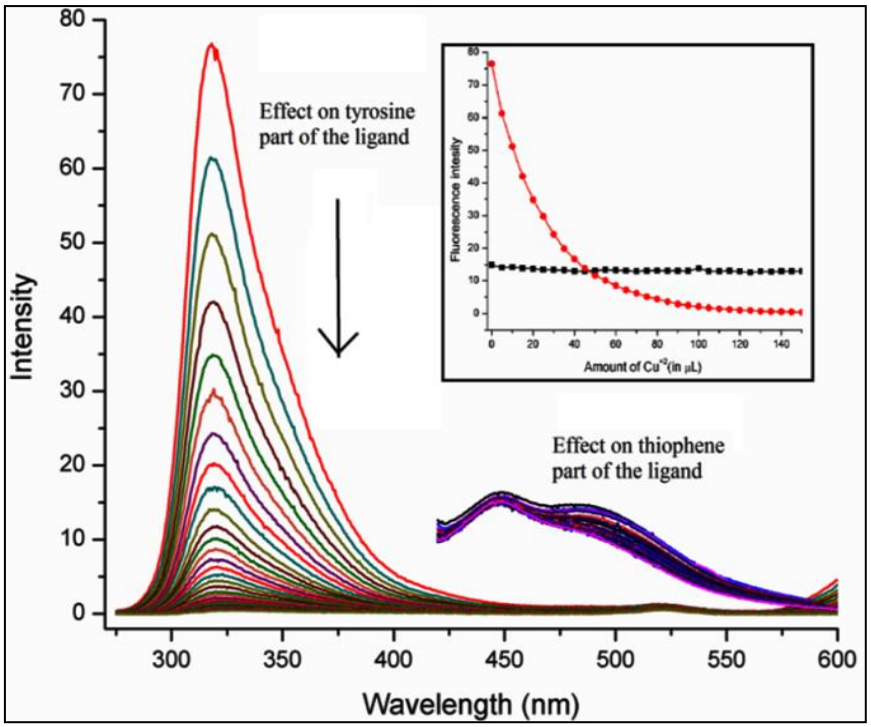

Figure 3.146. Quenching of fluorescence in the tyrosine part of NaHTyrthio upon addition of Cu^{2+} ions. Inset: Decrease in fluorescence intensity on the addition of Cu^{2+} to NaHTyrthio. Red circles: Tyrosine part of NaHTyrthio; Black squares: Thiophene part of NaHTyrthio.

Table 3.25. Comparative study of the detection limits for the various Cu^{2+} sensors.

Sr. No.	Complex used	Detection limit	Reference
1.	Magnetic nanocomposites surface (MNCS) with anionic surfactant	0.2 ng/ml or 3 x 10^{-9} mol L^{-1}	334
2.	4-methyl-2-((quinolinyl-8-amino)methyl) phenol (MQAMP)	1.1 × 10^{-7} mol L^{-1}	*335*
3.	Triangular silver nanoplates (TAg-NPs)	2.5 × 10^{-9} to 7.5 × 10^{-7} mol L^{-1}	336
4.	carbon nanodots (C dots) from o-phenylenediamine (OPD)	1.8 nM or 1.8 x 10^{-9} mol L^{-1}	337
5.	**L3**	50 ppb or 7.86 x 10^{-7} mol L^{-1}	This work

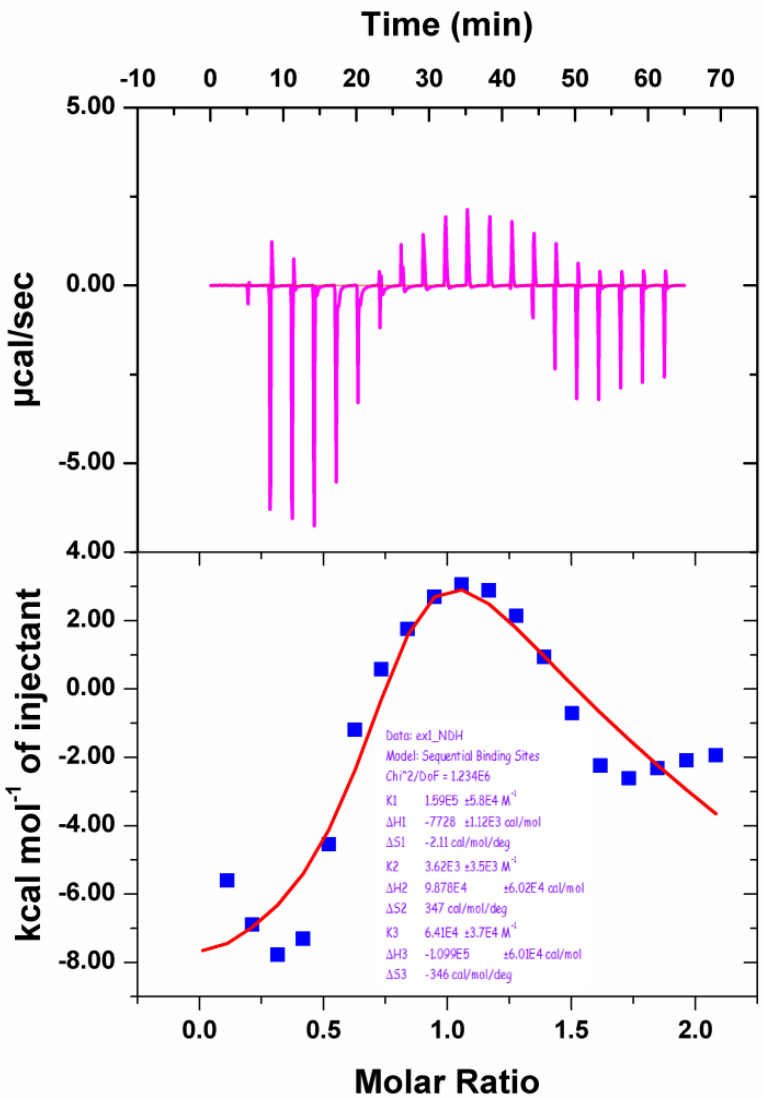

Figure 3.147. Binding isotherm corresponding to the ITC titration between Cu^{2+} and NaHTyrthio ([NaHTyrthio] = 5 mM in MeOH; [Cu^{2+}] = 0.5 mM at 25 °C).

For determining the quenching constant, the Stern–Volmer plot of relative fluorescence intensity (I_0/I) of NaHTyrthio against the concentration of Cu^{2+} ions in methanol (Figure 3.148) is considered. Based on its nonlinear fitting, the quenching constant is calculated to be 1.1 x 10^4 M^{-1}, which is moderate compared to the reported sensors for Cu^{2+} sensing.[98,338-343] This deviation in the Stern–Volmer plot from linearity indicates that the quenching is either static or a combination of static and dynamic. To ascertain the involvement of a dynamic mechanism in quenching, fluorescence lifetime of the sensor is measured with and without the quencher.

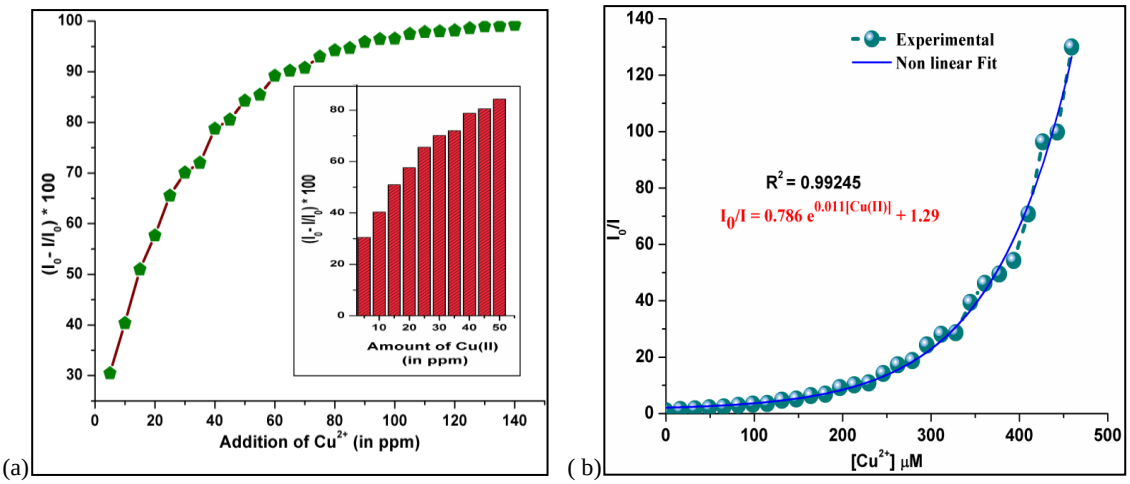

Figure 3.148. (a) Percentage decrease in the fluorescence intensity of NaHTyrthio on addition of Cu^{2+} in ppm level. (b) Stern–Volmer plot I_0/I versus $[Cu^{2+}]$ in methanol.

Table 3.26. Thermodynamic parameters for interactions between NaHTyrthio (5 mM) and Cu^{2+} (0.5 mM) in methanol at 25 ˚C.

Sequential binding Mode (binding Sites per molecule: 3)	**K (M^{-1})**	**ΔH (Kcal/mol)**	**ΔS (cal/mol/deg)**
1st site	1.59E5	-7.7	-2.11
2nd site	3.62E3	98.7	347
3rd site	6.41E4	-109.9	-346

As shown in Table 3.27 and Figure 3.149, the fluorescence lifetime of NaHTyrthio remains unchanged in the presence of Cu^{2+}, apparently suggesting that fluorescence quenching is via a static mechanism forming a non-fluorescent complex or 'dark state'.

For proof of concept, the role of NaHTyrthio as an ON-OFF sensor for Cu^{2+} ions was also studied. Since Na_4EDTA (where H_4EDTA = ethylenediaminetetraacetic acid) has more affinity for Cu^{2+} ions compared to NaHTyrthio, on addition of a Na_4EDTA solution [100 µL of 5 mM solution] to the quenched solution of NaHTyrthio, fortification of its fluorescence is observed. Further addition of Cu^{2+} ions to it again quenches its fluorescence. Thus, the alternative addition of Na_4EDTA solution and $Cu(NO_3)_2{\cdot}3H_2O$ solution shows the enhancement and quenching of the fluorescence of NaHTyrthio, respectively. This cycle was repeated several times as shown in Figure 3.150. A schematic representation of the recyclability of the sensor NaHTyrthio with respect to Cu(II) ion and EDTA is shown in Figure 3.151. Very few examples are reported in the literature where the sensor can be regained in original form to attain its activity.[344,345] Duan et al.[344] have reported a

naphthridine based sensor for Cu^{2+} (using absorbance spectroscopy) where activity of the sensor is made reversible by reacting the copper adduct with selected amino acids due to their higher binding affinities towards Cu^{2+}.

Table 3.27. Fluorescence decay parameters of the NaHTyrthio in methanol at 315 nm in the presence of different amounts of Cu(II).[a]

Sr. No.	$[Cu^{2+}] * 10^{-5}$ M	A_1 (%)	A_2 (%)	τ_1 (ns)	τ_2 (ns)	$<\tau>$ (ns)[b]
1	0	77	23	1.36	3.83	1.93
2	1.72	78	22	1.29	3.79	1.84
3	3.45	79	21	1.36	3.84	1.86
4	6.90	81	19	1.37	3.82	1.83
5	10.40	83	17	1.36	3.88	1.78
6	13.80	83	17	1.38	3.85	1.79
7	17.30	83	17	1.36	3.83	1.78

[a]Determined from $I = A_1 \exp(-t/\tau_1) + A_2 \exp(-t/\tau_2)$, where A and τ are the fractional amount and fluorescencence lifetime of the shorter (1)- and longer(2)-lived species, respectively; concentration of NaHTyrthio: 0.72 mM. [b]Weighted mean lifetime determined from $<\tau> = (A_1\tau_1 + A_2\tau_2)/(A_1 + A_2)$.

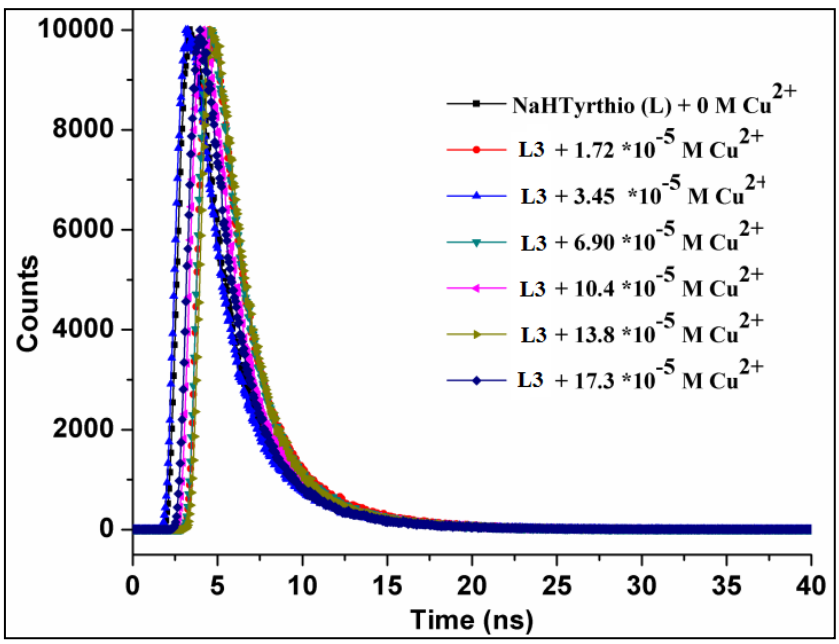

Figure 3.149. Lifetime decay profile of NaHTyrthio (3 mL, 0.72 mM/methanol) in presence of various concentrations of Cu^{2+} (λ_{exc} = 280 nm, monitored at 315 nm).

On the other hand, Shabani et al.[345] have reported a sensor for Cu^{+2} based on L-lysine functionalized gold cysteamine self-assembled monolayer using cyclic voltammetry and

impedance spectroscopy. In the present study, the activity of the sensor is recuperated by using the EDTA solution to ensure the use of amino acid based ligands as sensors for Cu^{+2} ions and EDTA to salvage the sensor back.

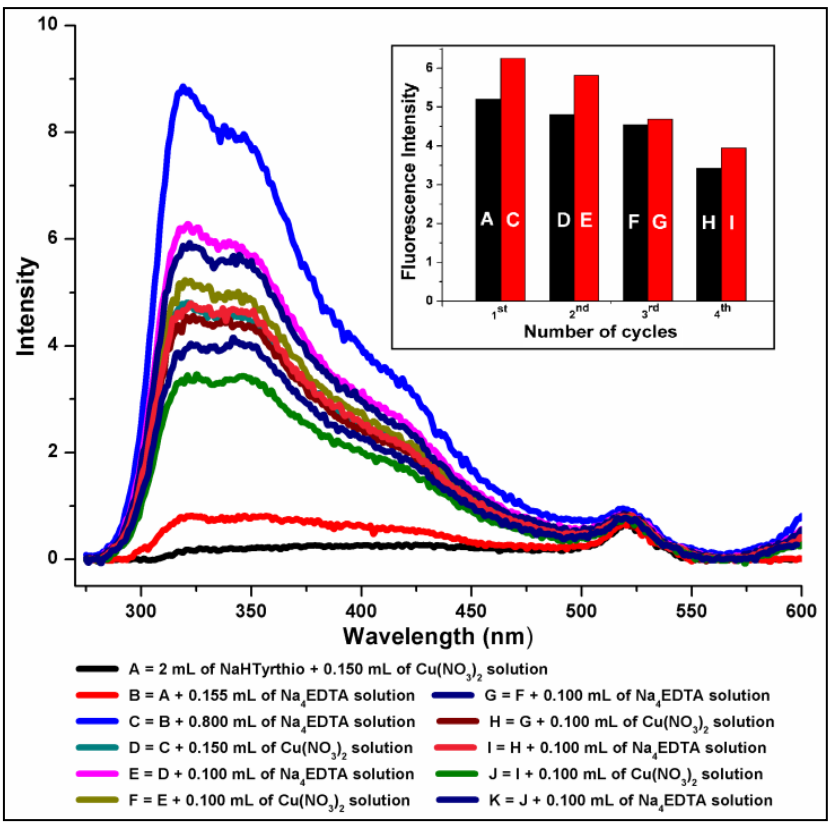

Figure 3.150. Emission spectra showing NaHTyrthio as an ON-OFF sensor for Cu^{2+}. Inset: Quenching of fluorescence by Cu^{2+} (black histogram) and redeeming the fluorescence by EDTA solution (red histogram) in subsequent cycles.

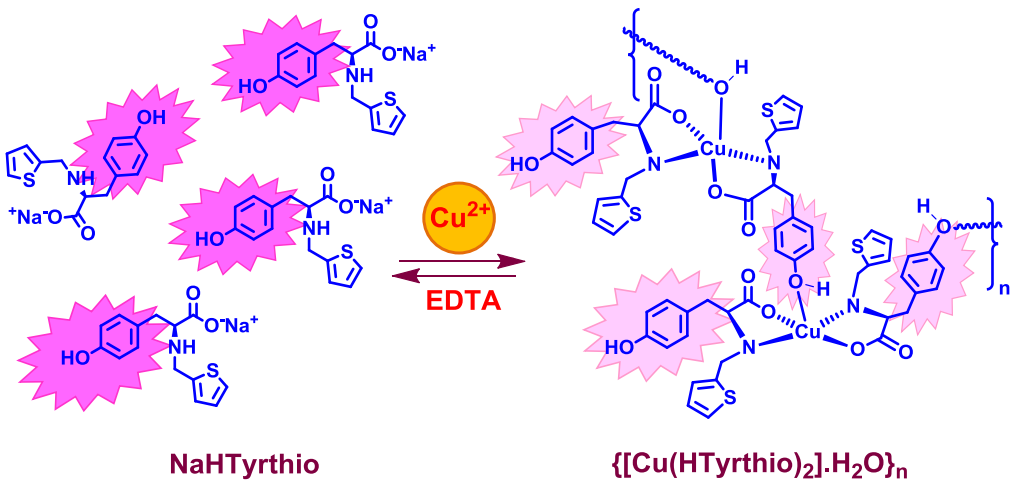

Figure 3.151. Recyclability of sensor NaHTyrthio with respect to Cu^{2+} ions.

Sensing of neutral small molecules: nitrobenzene and aniline sensed via dual module system

In the literature, nitroaromatics[169-174,346] or anilines[175-177] are generally sensed using π-electron rich conjugated cumbersome and bulky polymers. The simple and economical synthesis methodology for the receptor used in the present work make it a good candidate for sensing neutral small molecules. The variable responses of two different analytes (nitrobenzene and aniline) toward the same property (fluorescence) of the receptor provide an opportunity to use it for sensing two different neutral analytes. For the first time an amino acid based receptor is used to sense nitroaromatics as well as anilines. On addition of 100 μL of each nitroaromatic analyte (2 mM) to 2 mL methanolic solution of NaHTyrthio (3.6 mM), fluorescence quenching of the ligand is observed (Figure 3.152). Further introspection of the fluorescence quenching (see Figure 3.153a) provides a detection limit of the sensor for nitrobenzene to be 0.5 ppm (7% quenching); 15% and 90% quenching with 1 ppm and 30 ppm, respectively. Thus, NaHTyrthio shows a good selectivity and sensitivity towards nitrobenzene compared to a nitroaliphatic compound (such as nitromethane) and other nitroaromatics. A comparative study of the detection limits for nitrobenzene using the sensor **L3** and the other best known sensors reported in the literature is summarized in Table 3.28.

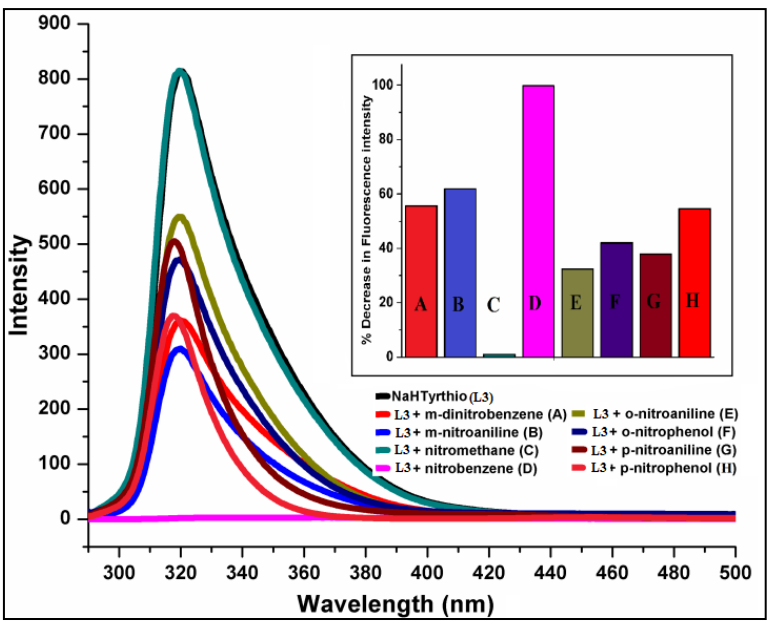

Figure 3.152. Fluorescence quenching of NaHTyrthio by various neutral analytes. Inset: Histograms showing fluorescence quenching (%) of NaHTyrthio by various analytes.

Table 3.28. Comparative study of the detection limits for the various nitrobenzene sensors.

Sr. No.	Complex used	Detection limit	Reference
1.	PDMS film-coated Au nanoparticle monolayer film	0.6 ppm or 4.6×10^{-6} mol L^{-1}	[347]
2.	Magnetic graphene nanocomposites	0.01 μg/L or 8.13×10^{-11} mol/L	[348]
3.	nonsilicon-cored 7,10-diphenylfluoranthene (DF) and silicon-cored bis(7,10-diphenylfluoranthen-8-yl)diphenylsilane (BDS)	50 ppm or 3.8×10^{-4} mol/L	[349]
4.	silver nanoparticles (Ag NPs) based sensor	1 μM or 1×10^{-6} mol/L	[350]
5.	gallium nitride (GaN) nanowires with titania (TiO_2) nanoclusters	100 ppb or 8.13×10^{-7} mol/L	[351]
6.	$[Zn_2(L)(4,4'\text{-bipy})(H_2O)_2]$ [1; H4L = p-[3,5-$(HO_2C)2C_6H_3NHCO]2C_6H_4$]	4×10^{-5} mol/L	[173]
7.	**L3**	0.5 ppm or 4.1×10^{-6} mol/L	This work

By fitting the non-linear Stern-Volmer plot (the relative fluorescence intensity (I_0/I) against concentration of nitrobenzene in methanol), a quenching constant 3.4 $x10^3$ M^{-1} is obtained (Figure 3.153b), which is remarkable compared to the reported sensors for nitrobenzene.[352-355] The nonlinearity in the Stern-Volmer plot can be attributed to either a self-absorption or a resonant energy transfer process. The probability of resonance energy transfer between the sensor and the analyte depends upon the extent of spectral overlap between the absorption band of the analyte and the emission band of the fluorophore. However, it is clear from the Figure 3.154 that the absorption band of nitrobenzene does not show any overlap with the emission band of the NaHTyrthio. This confirms that the fluorescence quenching in NaHTyrthio by nitrobenzene is entirely dependent on electron transfer with no role of resonant energy transfer between the sensor (NaHTyrthio) and analyte (nitrobenzene).

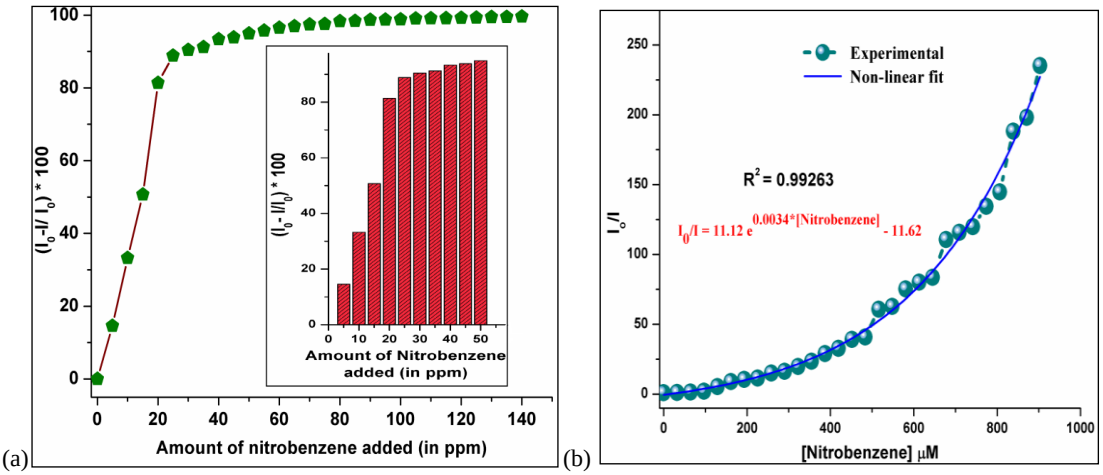

Figure 3.153. (a) Percentage decrease in the fluorescence intensity of NaHTyrthio on addition of nitrobenzene in ppm level; (b)Stern–Volmer plot I_0/I versus [Nitrobenzene] in methanol.

Similar to Cu^{2+}, the extent of quenching by nitrobenzene is also thoroughly analysed. In this case, the lifetime of the fluorophore is also not affected by the concentration of the quencher (nitrobenzene) molecule (Figure 3.155 and Table 3.29) which advocates for the fluorescence quenching via a static mechanism and formation of a dark ground state complex between NaHTyrthio and nitrobenzene. generates a positive quadruple and thus enhances the extent of π–π interaction between nitrobenzene and the phenol part of the sensor which accounts for the electron transfer.[173,356-359]

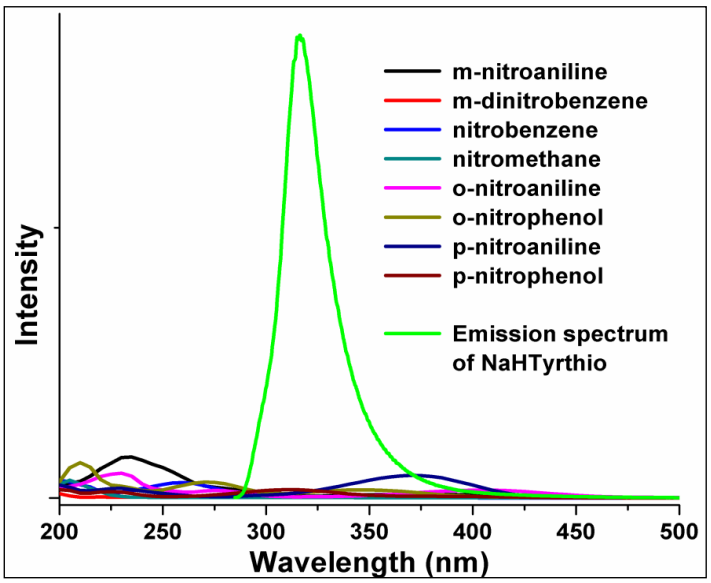

Figure 3.154. Overlap between the absorption spectra of various analytes and the emission spectrum of NaHTyrthio in methanol.

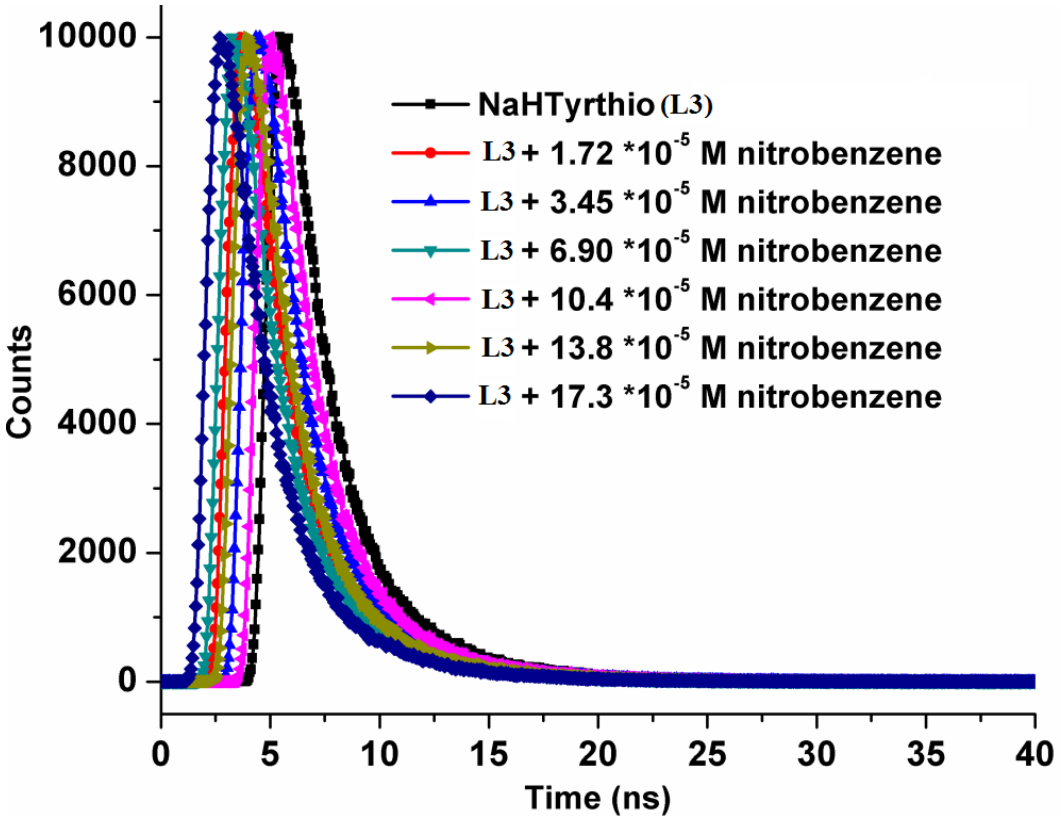

Figure 3.155. Lifetime decay profiles of NaHTyrthio (3 mL, 0.72 mM/methanol) in presence of various concentrations of nitrobenzene (λ_{exc} = 280 nm, monitored at 315 nm).

Table 3.29. Fluorescence decay parameters of the NaHTyrthio in methanol at 315 nm in the presence of different amounts of nitrobenzene[a]

Sr. No.	[NB] * 10^{-5} M	A_1 (%)	A_2 (%)	τ_1 (ns)	τ_2 (ns)	$<\tau>$ (ns)[b]
1	0	77	23	1.37	3.79	1.93
2	1.72	77	23	1.36	3.81	1.93
3	3.45	77	23	1.34	3.80	1.89
4	6.90	79	21	1.30	3.80	1.86
5	10.40	78	22	1.29	3.74	1.86
6	13.80	78	22	1.31	3.74	1.87
7	17.30	78	22	1.31	3.68	1.88

[a]Determined from $I = A_1 \exp(-t/\tau_1) + A_2 \exp(-t/\tau_2)$, where A and τ are the fractional amount and fluorescencence lifetime of the shorter (1)- and longer(2)-lived species, respectively; concentration of NaHTyrthio: 0.72 mM. [b]Weighted mean lifetime determined from $<\tau> = (A_1\tau_1 + A_2\tau_2)/(A_1 + A_2)$.

This interaction of nitrobenzene with NaHTyrthio (**L3**) is further analysed by an NMR titrimetry experiment (see Figure 3.156). A downfield shift of peaks in the aromatic region

i.e. four protons of the phenol part of the sensor on successive additions of the nitrobenzene is a clear indication of the interaction between the phenol part and nitrobenzene.

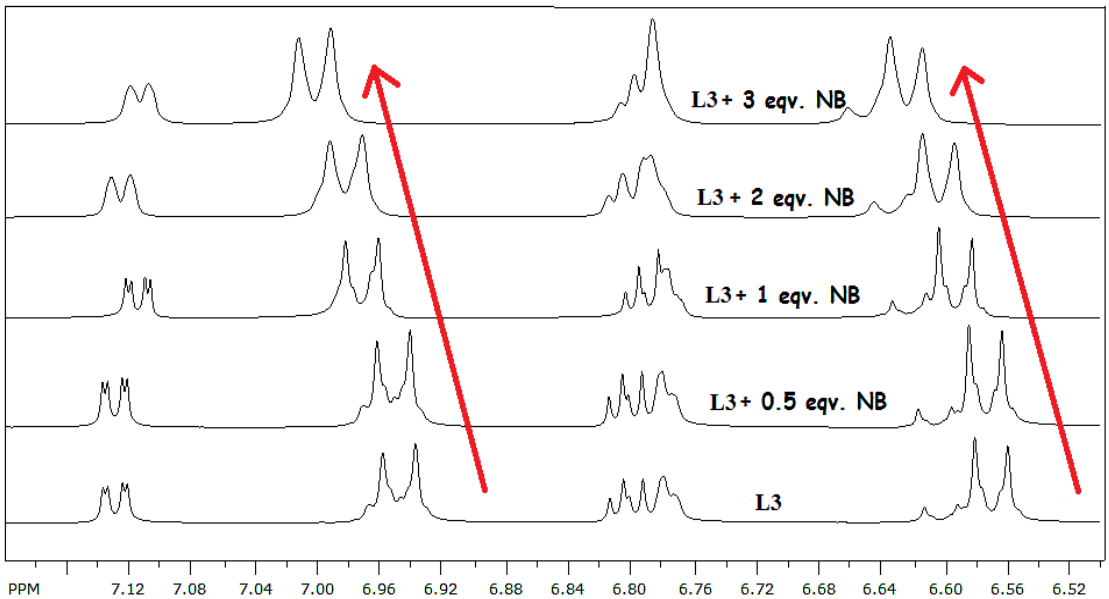

Figure 3.156. ^{1}H NMR titrimetry of NaHTyrthio (**L3**) with nitrobenzene (NB) as an analyte.

The differential responses for sensing similar type of analytes by a single sensor are further explored with aniline. However, in case of aniline its quenching is associated with a noticeable shift in λ_{emi} from 320 nm to 332 nm (Figure 3.157). The detection limit for aniline is 15 ppm based on the well observed shift of 2 nm in λ_{emi}. Thus, NaHTyrthio shows a good sensitivity towards aniline as well (Figure 3.158). To understand the interactions between aniline and NaHTyrthio, an NMR titrimetry experiment was carried out. The ^{1}H NMR spectrum obtained after addition of aniline to NaHTyrthio is not just the summation of the peaks for aniline and the sensor. Each spectrum on subsequent additions of aniline clearly shows the distortion in the peaks for sensor (protons of the phenol part) as well as for analyte, thus emphasizing the existence of the interaction between aniline and NaHTyrthio (Figure 3.159). These interactions can be accredited to the various possible hydrogen bonding patterns between aniline and NaHTyrthio (as shown in Figure 3.160) along with π–π interaction between these. A comparative study of the detection limits for aniline using the sensor **L3** and the other best known sensors reported in the literature is summarized in Table 3.30.

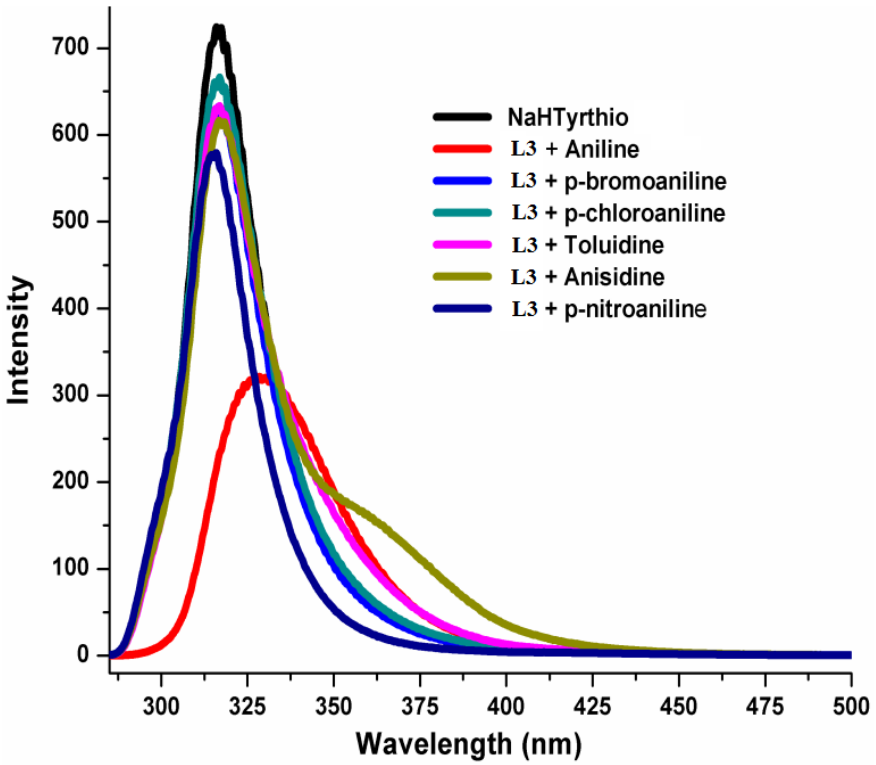

Figure 3.157. Change in λ_{emi} of NaHTyrthio on the addition of aniline compared to other aniline derivatives.

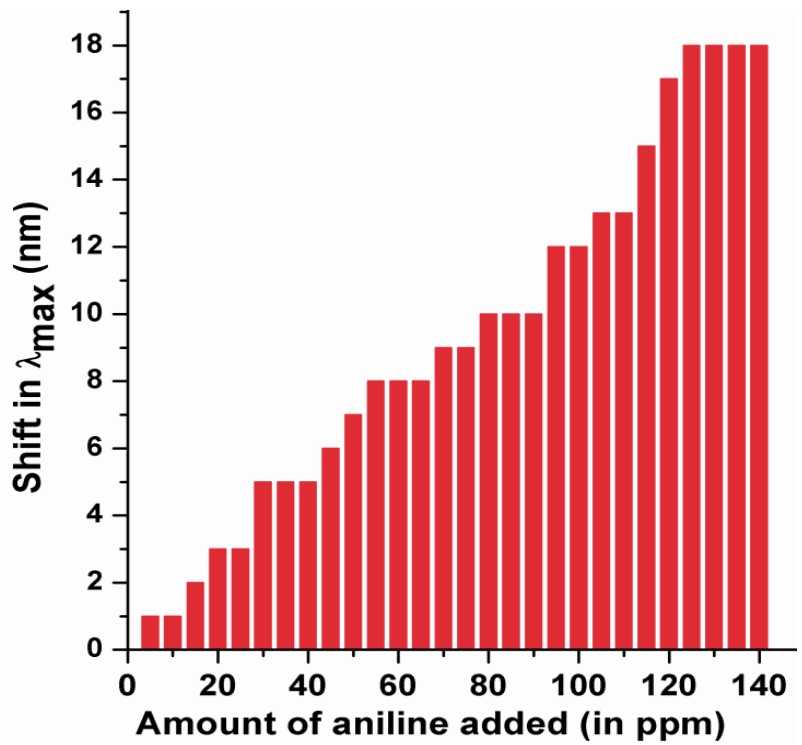

Figure 3.158. Shift in λ_{emi} of NaHTyrthio on addition of aniline in ppm level.

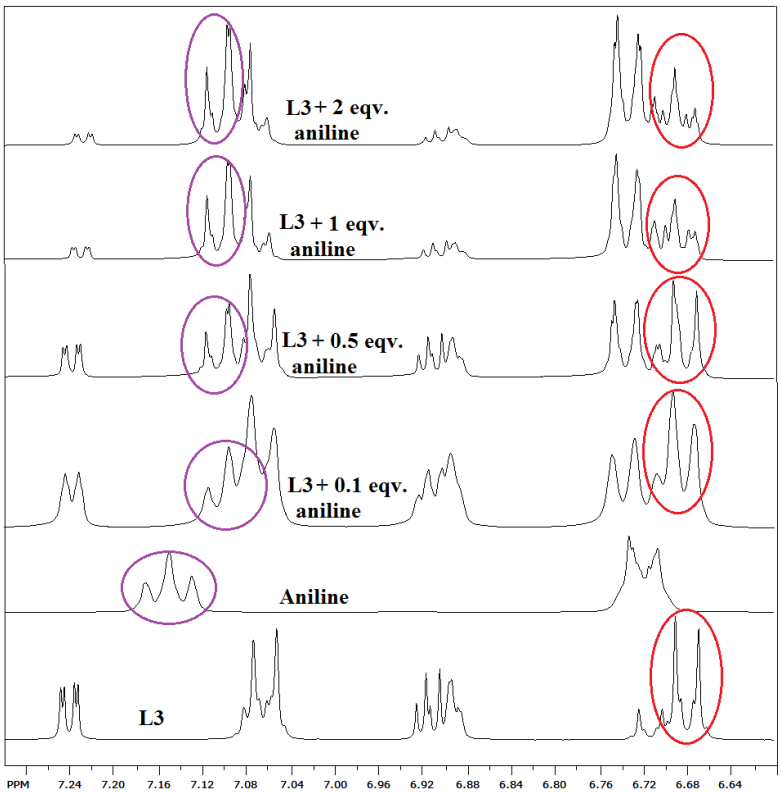

Figure 3.159. ^{1}H NMR titrimetry of NaHTyrthio (**L3**) with aniline as an analyte (distortion in peaks of sensor (red) and analyte (violet).

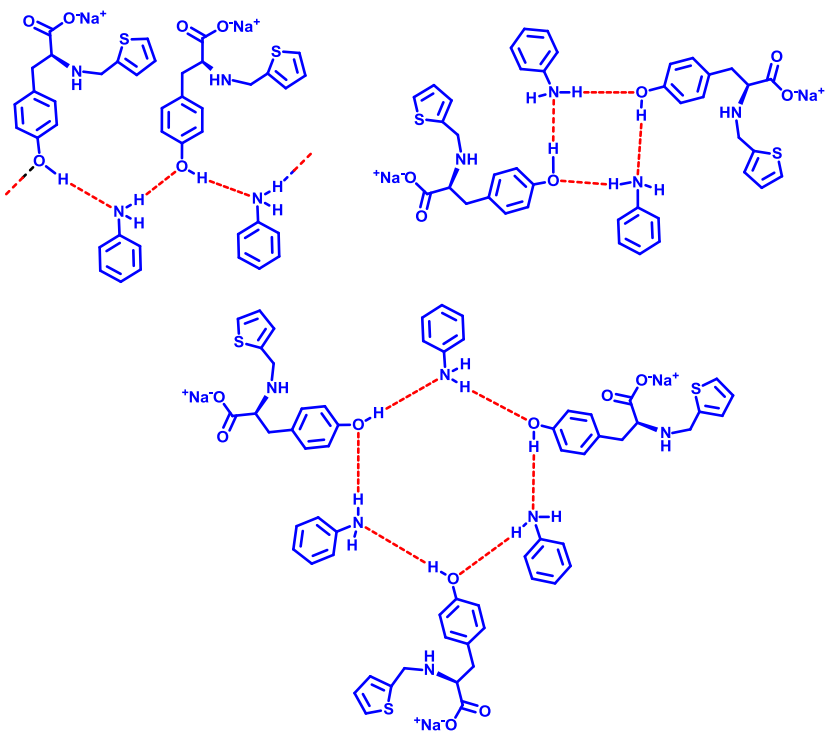

Figure. 3.160. Possible hydrogen bonding between aniline and NaHTyrthio.

Table 3.30. Comparative study of the detection limits for the various aniline sensors.

Sr. No.	Complex used	Detection limit	Reference
1.	gold nanoparticles (AuNPs) and Ruthenium (II) tris-(bipyridine) (Ru(bpy)2+3) doped nylon 6 (PA6) luminescent composite nanofibers (Ru-AuNPs-PA6)	5.0 nM or 5×10^{-9} mol/L	[360]
2.	ZnS/PTCDA (ZPNPs)	100 ppb or 8.13×10^{-7} mol/L	[361]
3.	**L3**	15 ppm or 5.37×10^{-4} mol/L	This Work

Sensing of anion: F^- over other anions

The thiophene part of the sensor is investigated for its role in anion sensing. The addition of various anions shows a quenching of fluorescence of the thiophene part of the receptor on excitation at 395 nm. However, quenching due to F^- is the most prominent compared to other anions (as shown in Figure 3.161). Based on the percentage decrease in fluorescence intensity upon sequential addition of F^- (see Figure 3.162a), its detection limit is 15.25 ppm ($2.62*10^{-4}$ M) with a 3% fluorescence quenching. The Stern-Volmer plot in this case is a bi-exponential with a non-linear fit (Figure 3.162b), which provides quenching constants 2.2 M^{-1} (up to 20 mM conc. of KF) and 1.12 $x10^2$ M^{-1} (above 20 mM conc. of KF).

Similar to Cu^{2+} and nitrobenzene, the effect of F^- on the lifetime of NaHTyrthio is measured (Table 3.31 and Figure 3.163). There is some alteration in the lifetime of NaHTyrthio with addition of different concentration of F^-, thus suggesting a blend of both dynamic and static quenching in fluorescence quenching of NaHTyrthio on addition of F^-. The time resolved emission spectroscopy further shows change in spectral property (fluorescence intensity) of the sensor in absence and presence of F^- (as shown in Figure 3.164)

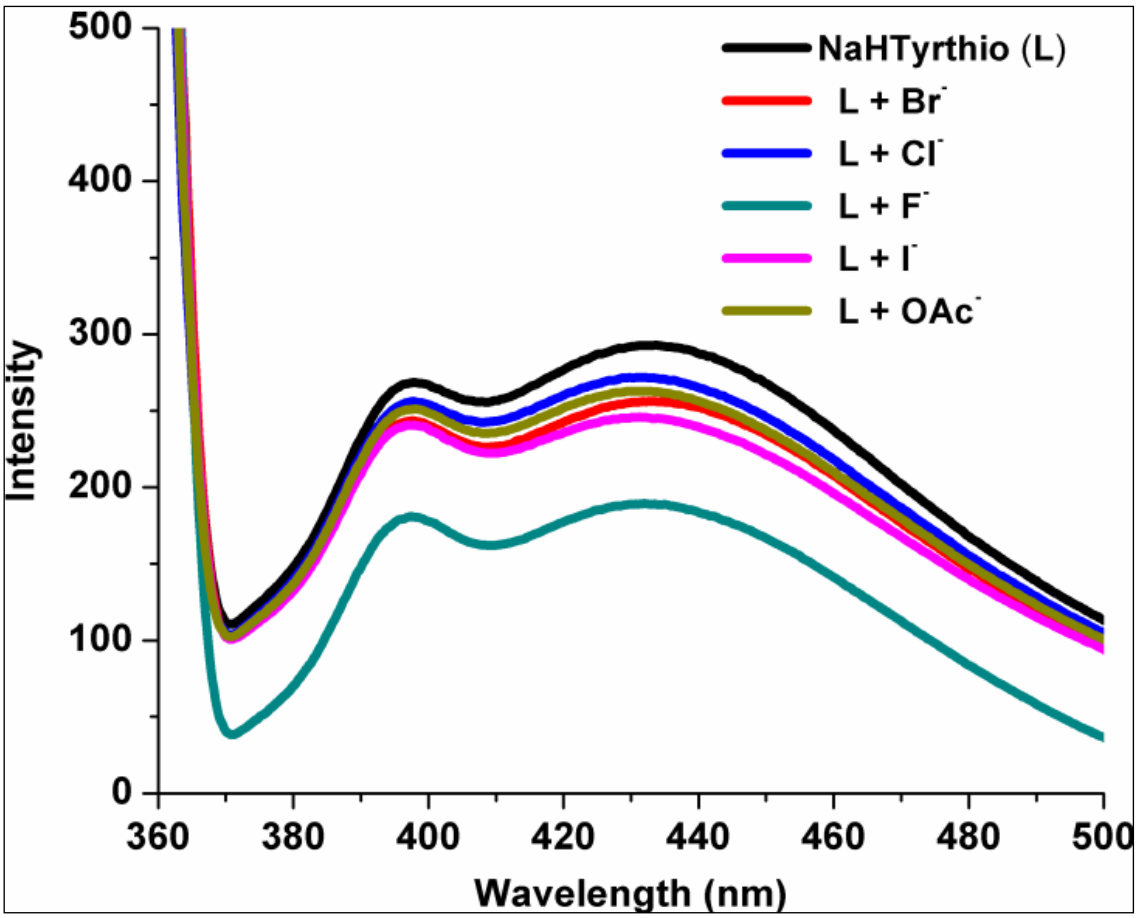

Figure 3.161. Fluorescence quenching of NaHTyrthio by various anions.

(a)

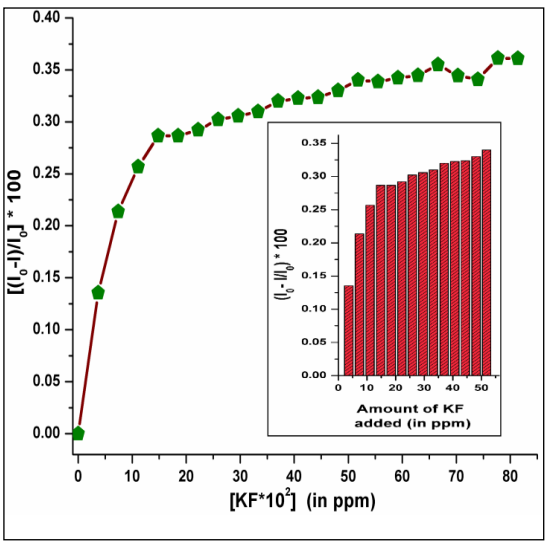

(b)

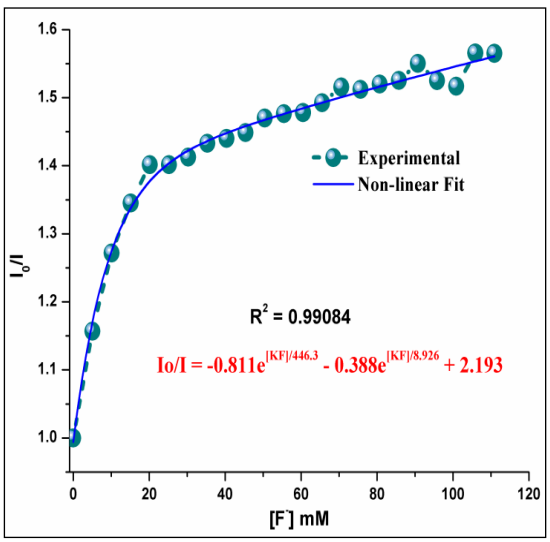

Figure 3.162 (a) Percentage decrease in the fluorescence intensity of NaHTyrthio on addition of KF in ppm level; (b) Stern–Volmer plot I_0/I versus [KF] in methanol.

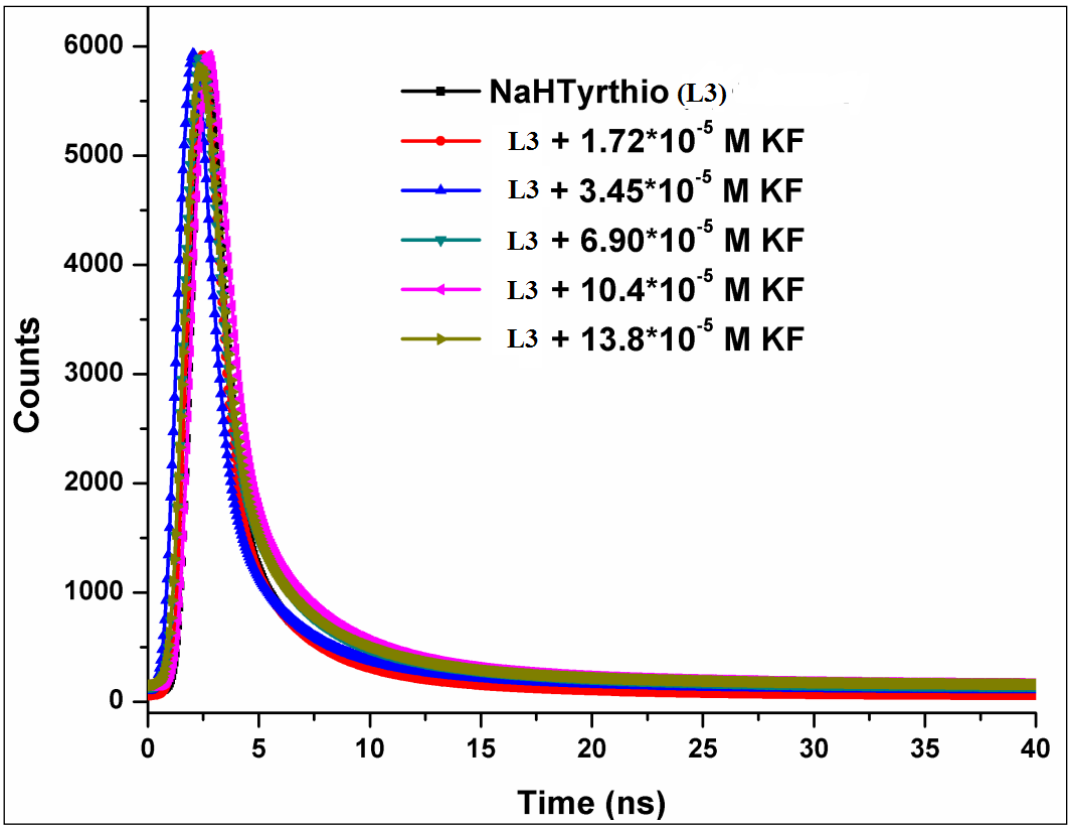

Figure 3.163. Lifetime decay profiles of NaHTyrthio (3 mL, 0.72 mM/methanol) in presence of various concentrations of F^- (λ_{exc} = 370 nm, monitored at 465 nm).

Table 3.31. Fluorescence decay parameters of the NaHTyrthio in methanol at 370 nm in the presence of different amounts of fluoride[a]

Sr. No.	$[F^-] * 10^{-5}$ M	A_1 (%)	A_2 (%)	A_3 (%)	τ_1 (ns)	τ_2 (ns)	τ_3(ns)	$<\tau>$ (ns)[b]
1	0	11	02	87	2.23	7.97	0.34	0.70
2	1.72	11	02	87	2.35	7.77	0.38	0.75
3	3.45	13	02	85	2.53	8.42	0.46	0.77
4	6.90	17	04	79	2.31	7.93	0.50	1.10
5	10.40	17	02	81	3.09	10.15	0.62	1.23
6	13.80	16	02	81	3.31	11.19	0.67	1.30

[a]Determined from $I = A_1 \exp(-t/\tau_1) + A_2 \exp(-t/\tau_2) + A_3 \exp(-t/\tau_3)$, where A and τ are the fractional amount and fluorescencence lifetime of the shorter (1)-, longer(2)-lived species and Very short lived (3) species respectively; concentration of NaHTyrthio: 0.72 mM. [b]Weighted mean lifetime determined from $<\tau> = (A_1\tau_1 + A_2\tau_2 + A_3\tau_3)/(A_1 + A_2 + A_3)$.

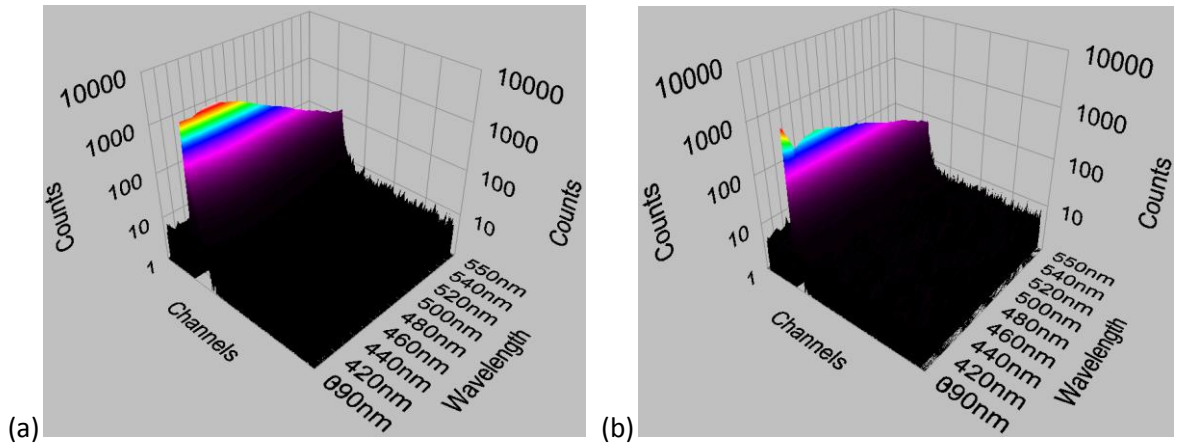

Figure 3.164. Time- resolved spectra of NaHTyrthio in (a) absence of F^- and (b) presence of F^- (λ_{exc} = 370 nm).

From the ^{1}H NMR titrimetry experiment, it is also clear that the protons attached to thiophene as well as diastereomeric methylene protons (next to –NH) show an upfield shift upon addition of KF to NaHTyrthio (Figure 3.165), which is observed until the saturation point for a 1:1 sensor to analyte ratio. This can be attributed to the anion-π interactions between the heterocyclic thiophene group and F^- (due to its small size and high electronegativity). Along with the anion–π interactions, the presence of hydrogen bonding between –NH and F^- is also quite evident from the upfield shift of the diastereomeric methylene protons just next to the –NH, even though the –NH protons are not seen in the spectra. This kind of hydrogen bonding between the –NH and F^- is well reported in the literature.[145,362-369]

3.3.4. Fluorogenic sensors with four-fold symmetry for nitroanilines

Nitroanilines are one of the important components of dye industries as well as it is used in explosives. Hence the detection of these nitroanilines becomes very important. For serving this purpose, the photoluminescence property of the ligand H_2Tyr-N-Dan and its Cu^{2+} and Zn^{2+} complexes were employed. A systematic analysis of various analytes gives a deeper insight into the role of various functional groups present in the analytes on the fluorescence quenching of the ligand (Figure 3.167). Comparing the quenching ability of nitromethane (19%), nitro benzene (43%) and aniline (11%), it is well understood that for quenching the presence of an electron withdrawing nitro group is a must and also aromatic moieties are better off for the π–π interaction between the sensor and the analytes. However, the presence

of two electron withdrawing nitro groups, meta to each other does not facilitate the quenching (22%) to a greater extent. On the other hand, the presence of an electron donating NH_2 or OH group along with an electron withdrawing NO_2 group on the aromatic ring makes them better analytes to be sensed by the dansylated tyrosine. Since the NH_2 group is a better electron donating group, a nitroaniline acts as a better analyte, while the p-nitroaniline is the best analyte which quenches the fluorescence of the ligand almost completely (99.5%).

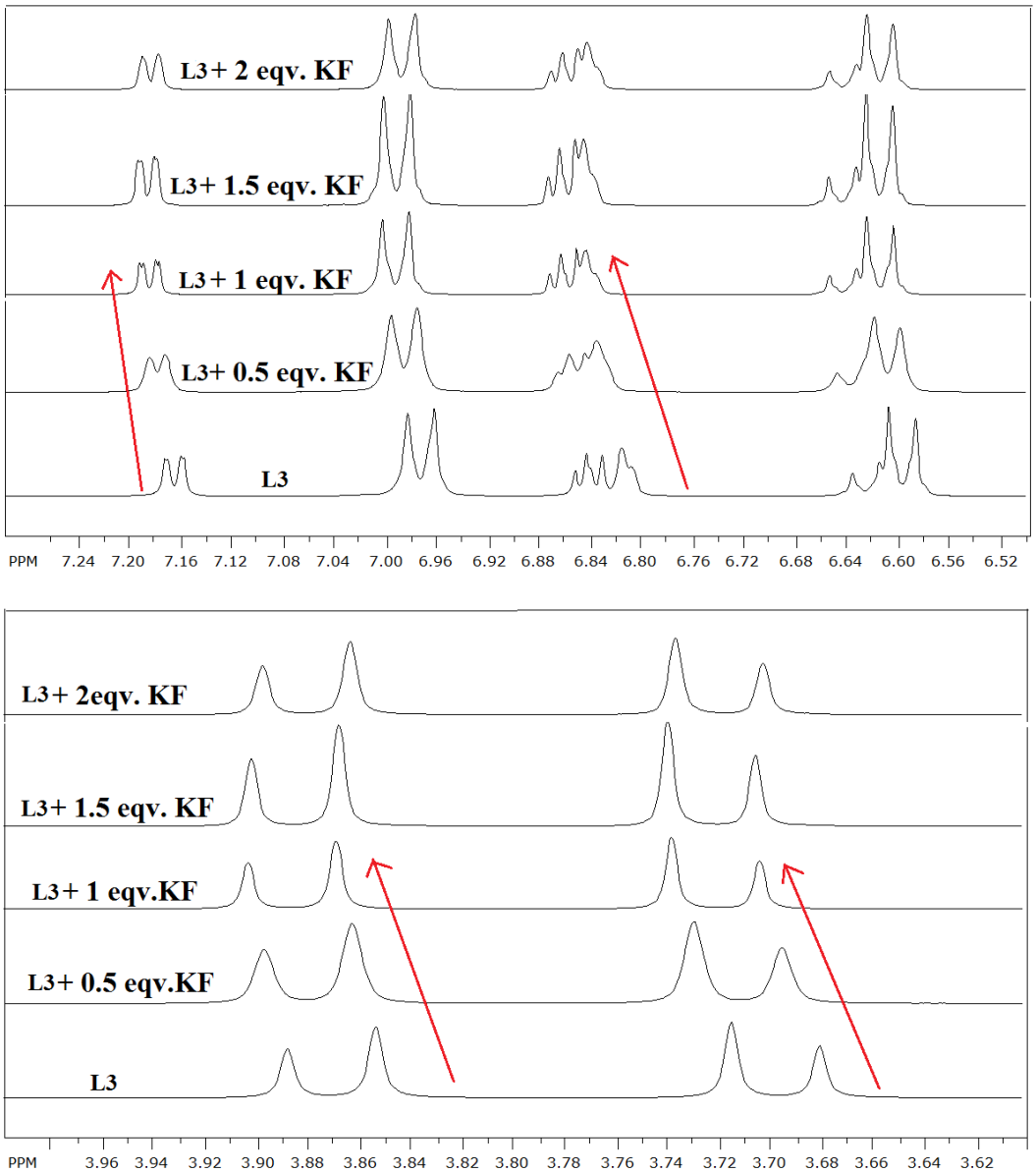

Figure 3.165. ^{1}H NMR titrimetry of NaHTyrthio (**L3**) with KF as an analyte: (a) effect on the thiophene protons (top) and (b) effect on the diastereomeric methylene protons (bottom).

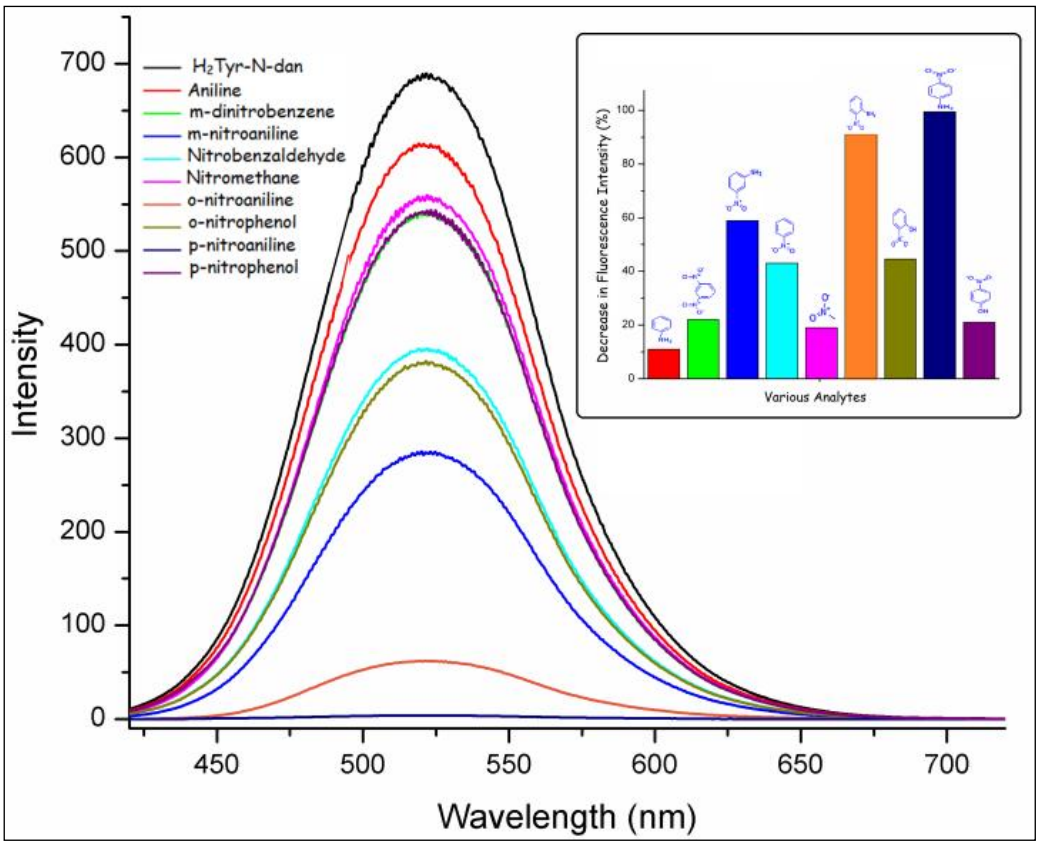

Figure 3.166. Fluorescence intensity changes for H_2Tyr-N-Dan in methanol upon addition of various analytes.

In the literature few sensors have been reported for sensing p-nitroaniline where the sensors are either based on macrocycles (generally calixarene) or cyclodextrin capped nanoparticles.[370,371] However, the cumbersome and costly synthetic procedures make the above reported sensors not so practically viable whereas the ligand reported herein is cost effective and easy to make. Since the aromatic moieties (dansyl part) of the analyte involve in π–π interactions between analyte and the sensor are far from the Cu^{2+} centers in $[Cu_2(HTyr\text{-}N\text{-}Dan)_4(H_2O)_2]\cdot 6H_2O$ **(54),** there is no marked difference observed in the quenching ability of various analytes towards **54** as compared to the ligand itself (Figure 3.168). The sensing ability of **55** is also analysed (Figure 3.169). Compound **55** shows sensing behavior very similar to **54**. A systematic study of various analytes has indicated selective behaviour of H_2Tyr-N-Dan, **54** and **55** as sensors for the nitroanilines (p-nitroaniline). The detection limit for p-nitroaniline for all three sensors is 0.5 ppm.

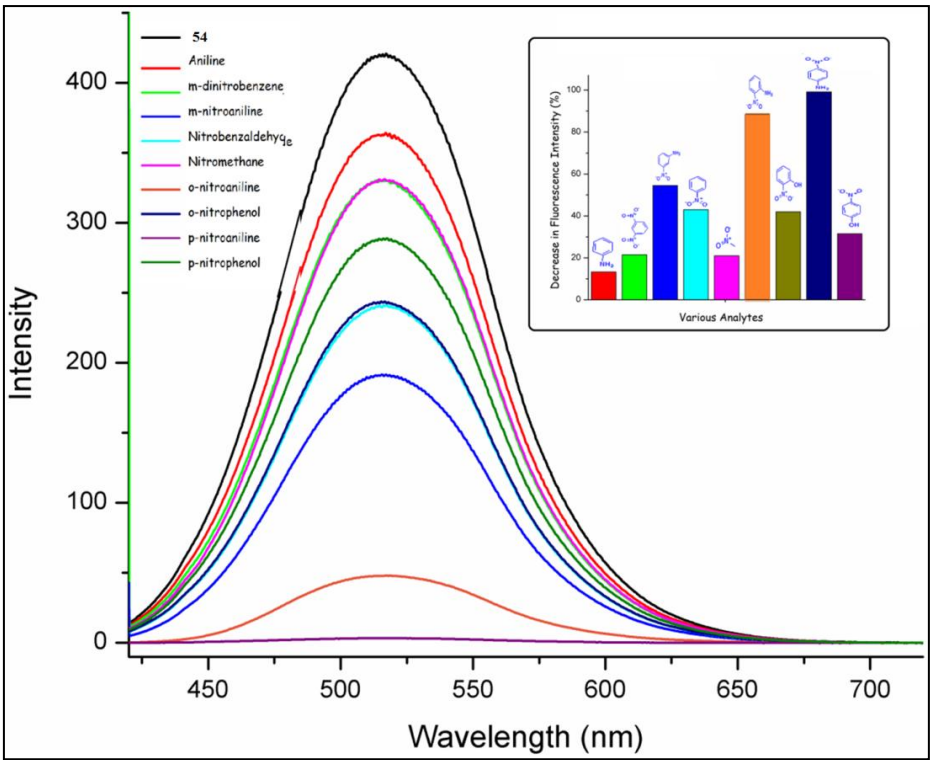

Figure 3.167. Fluorescence intensity changes for **54** in methanol upon addition of various analytes.

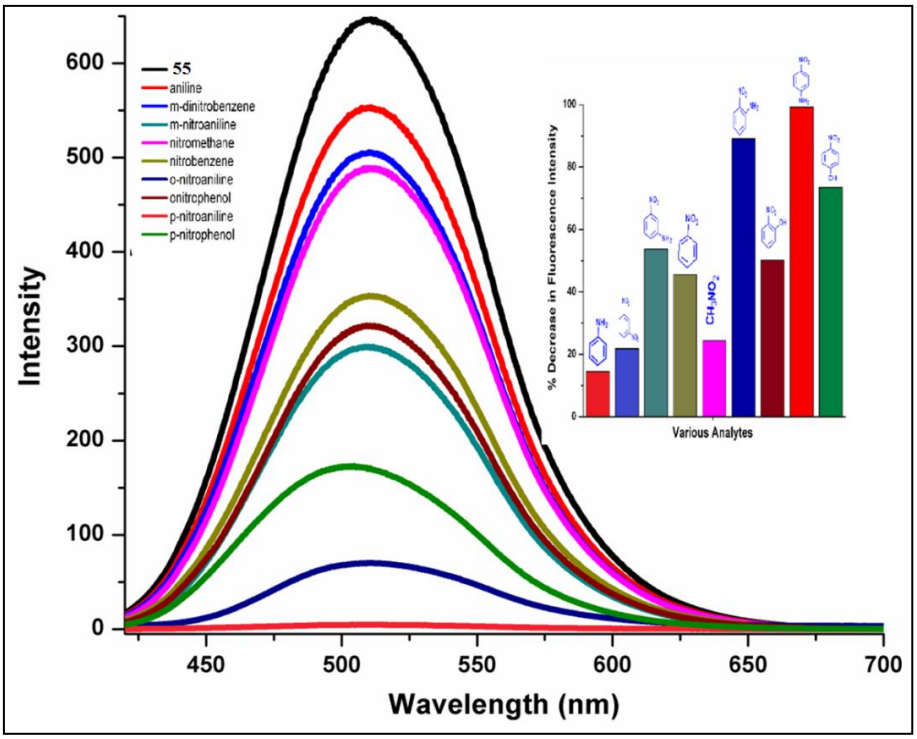

Figure 3.168. Fluorescence intensity changes for **55** in methanol upon addition of various analytes.

Chapter IV
Conclusions and Future Directions

Following conclusions can be drawn from the research work reported in this thesis:

(1) General protocols have been developed to synthesize two sets of amino acid based ligands in good yields and high purity. The first set is the amino acid based reduced Schiff bases and the second set is the ligands with additional tagged fluorophores to the amino acids. For the synthesis of any set of amino acid based ligands, the use of sodium salt of the respective amino acid is the key as the salt helps in enhancing the solubility of the amino acid in the solvent used (mostly water and/or methanol) as well as facilitates the availability of the $–NH_2$ group (present only when pH > pKa) for the condensation or substitution reactions. Optimized conditions for the synthesis of each ligand were obtained through a design of experiments. All the seventeen amino acid based ligands were thoroughly characterized by melting point measurements, NMR, FTIR and fluorescence spectroscopy (wherever applicable), ESI mass spectrometry and polarimetry.

(2) One pot synthesis of sixty homochiral coordination architectures using either a two-component or a three-component self-assembly reaction was carried out. In a two-component self assembly reaction, a divalent metal ion (Ni^{2+}, Cu^{2+}, Zn^{2+} or Cd^{2+}) and the respective mono or dipotassium salt of the amino acid based ligands were used in a 1:2 or 1:1 ratio. For a three-component self-assembly reaction, a divalent metal ion (Ni^{2+} or Cu^{2+}), the respective mono- or dipotassium salt of the amino acid based ligand and the linker were taken in a 2:2:1 ratio. Most of these coordination architectures were formed under ambient conditions, while a few of these were obtained under reflux conditions. Solvents were chosen for these reactions based on the differential solubility of the product and the by-product (K_2SO_4/ CH_3COOK). All these coordination architectures were reproduced several times at the optimized conditions. These coordination architectures were extensively characterized by various analytical techniques like elemental analysis, UV-Vis, FTIR, Raman, fluorescence and

circular dichroism spectroscopy, magnetic studies, water vapor adsorption studies, isothermal titration calorimetry, ESI mass spectrometry, single crystal and powder X-ray diffraction, polarimetry and thermogravimetric analysis.

(3) In the first section of this work, a systematic study to illustrate the role of various factros like ligands, metal salts, linkers and solvents in bringing structural diversification in the coordination architectures were thoroughly understood and can be categorized as:

(3a) The formation of diverse Cu^{2+} coordination architectures (CPs vs SCCs) with a 1:2 metal to ligand ratio was methodically controlled by strategic substitution on the reduced Schiff base ligands of the amino acids (L-Tyrosine, L-Serine and L-Phenylalanine). This is well established by the single crystal structures of these Cu^{2+} complexes. In doing so, it is observed that the presence or absence of bridging functionalities (carboxylate or phenolic -OH) is responsible for such outcome. The absence of any bridging moieties between two adjacent Cu^{2+} ions allows the coordinated water molecule to occupy the fifth site around the five-coordinated square-pyramidal (or six coordinated octahedral in one case) Cu^{2+}. The coordination architectures $[\{[Cu(L\text{-}HTyrbenz)_2]\cdot CH_3OH\cdot H_2O\}_n$ (**1**), $\{[Cu(L\text{-}HSerbenz)_2]\cdot 3H_2O\}_n$ (**5**) and $\{[Cu(L\text{-}HTyrthio)_2]\cdot H_2O\}_n$ (**13**)] which do not have any coordinated water molecule are 1D CPs but their formation is through different functionalities of the ligand (a syn-anti bridging carboxylate and hydroxy group of the L-tyrosine part of the ligand in **1** and **13**, respectively, and an anti-anti bridging carboxylate group of L-serine part of the ligand in (**5**). On the other hand, each of the seven complexes, $[Cu(L\text{-}Phebenz)_2(H_2O)]\cdot H_2O$ (**9**), $[Cu(L\text{-}HTyr4\text{-}pyr)_2(H_2O)]\cdot 2H_2O$ (**17**), $[Cu(L\text{-}HSerthio)_2(H_2O)]$ (**21**), $[Cu(L\text{-}Phethio)_2(H_2O)]\cdot 4H_2O$ (**22**), $[Cu(L\text{-}HTyr4\text{-}nitro)_2(H_2O)]\cdot 2DMSO$ (**23a**), $[Cu(L\text{-}HTyr4\text{-}nitro)_2(H_2O)]\cdot 2CH_3OH$ (**23b**), $[Cu(L\text{-}HTyr4\text{-}fluoro)_2(H_2O)]\cdot H_2O$ (**27a**) and $[Cu(L\text{-}HTyr4\text{-}methoxy)_2(CH_3OH)]$ (**31a**)) that contain a coordinated solvent molecule are supramolecular assemblies via extensive hydrogen bonding. Thus the involvement of the phenolic -OH group in the ligands derived from L-Tyrosine in a coordination bond is dictated by the substitution on the N atom of the ligand. For the methylthiophenyl containing ligands, the phenolic group in L-HTyrthio is long enough to bridge the two Cu^{2+} centers in **13** but the much shorter length of the $-CH_2OH$ group in L-HSerthio is responsible for the formation of **21**. Furthermore, the significance of the phenolic

part is observed when the L-Tyrosine part in the ligand L-H_2tyrthio is exchanged with L-Phenylalanine and the resultant ligand L-HPhethio gives **22**. In all these architectures the carboxylate stretching frequencies in FTIR spectra are in well accordance with the single crystal structures.

(3b) Extending the same strategy, other divalent metal ions (Ni^{2+}, Zn^{2+} or/and Cd^{2+}) are also used with the same set of ligands to generalize this method and generate more coordination architectures with a 1:2 metal to ligand ration. Even after several attempts crystals of most of these coordination architectures could not be obtained; however, using other analytical techniques like FTIR, elemental analysis and TGA, the structural and chemical constitutions of these architectures are well elucidated. Thus, FTIR frequencies (the position and broadness of –OH peaks confirms the presence of a coordinated or lattice solvent molecules and a comparison of the $\Delta\nu = \nu_{asymm} - \nu_{sym}$ values of the carboxylates for binding modes), elemental analysis (employing the empirical formula) and the TGA patterns (step-wise loss of solvent molecules explaining coordinated and lattice solvent molecules) help in confirming the presence of coordinated or/and uncoordinated solvent molecules and thus obtaining the formula of a complex correctly. From these analyses, it is clear that, even with a change in metal ion the commonalities in the architectures are well observed. Crystal structures of [Cu(L-HTyr4-nitro)$_2$(H_2O)]·2DMSO (**23a**) and [Zn(L-HTyr4-nitro)$_2$(H_2O)]·2DMSO (**25a**) clearly shows similar structural aesthetics with slight variations in the hydrogen bonding interactions.

(3c) The role of solvent for crystallization was well established through the formation of two different supramolecular assemblies of Cu^{2+}, ([Cu(L-HTyr4-NO_2)$_2$(H_2O)]·2DMSO (**23a**) and [Cu(L-HTyr4-NO_2)$_2$(H_2O)]·2CH_3OH (**23b**) in DMSO and methanol, respectively. The diversity in these two supramolecular networks is due to variation in the hydrogen bonding interactions and orientation of the ligands around the metal center depending on the polarity of the solvent of crystallisation.

(3d) Compared to the homoligands, the use of heteroleptic ligands yields a coordination

architecture with a 2:1 metal to ligand ratio [Cu(HTyr4-fluoro)(Tyrosine)]·3H_2O (**33**) where Cu^{2+} shows an unusual square planar geometry (rare in case of amino acid based ligands) and no coordinated water molecule is present. However, even with the absence of a coordinated water molecule, the mononuclear moiety grows in other dimensions via hydrogen bonding between the carboxylate of the ligand and the lattice water molecule, forming a 2D SCC.

(3e) Similarly, a series of 2D CPs with a 1:1 metal to ligand ratio is generated through the one-pot synthesis in high yields and purity: {[Cu_2(Hsersal)$_2$(H_2O)]·H_2O}$_n$ (**34**), {[Ni_2(Hsersal)$_2$(H_2O)$_2$]·H_2O}$_n$ (**35**), {[Cu_2(Hser-5OMe-sal)$_2$(H_2O)]·DMF}$_n$ (**36**), {[Ni_2(Hser-5OMe-sal)$_2$(H_2O)$_2$]·CH_3OH·H_2O}$_n$ (**37**), {[Cu_2(Hser-5NO_2-sal)$_2$(H_2O)]·2H_2O}$_n$ (**38**), {[Ni_2(Hser-5NO_2-sal)$_2$(H_2O)$_2$]·7H_2O}$_n$ (**39**), {[Cu_2(Hser-5Cl-sal)$_2$(H_2O)]·H_2O}ti$_n$ (**40**), {[Ni_2(Hser-5Cl-sal)$_2$(H_2O)$_2$]·CH_3OH}$_n$ (**41**), {[Cu_2(Hser-3Cl-sal)$_2$(H_2O)]·3H_2O}$_n$ (**42**) {[Ni_2(Hser-3Cl-sal)$_2$(H_2O)$_2$]·2H_2O}$_n$ (**43**), {[Cu_2(Hser-o-Van)$_2$(H_2O)]·3H_2O}$_n$ (**44**) and {[Ni_2(Hser-o-Van)$_2$(H_2O)$_2$]·2H_2O}$_n$ (**45**). Crystal structures of **34** and **40** suggest formation of a nonporous 2D coordination polymer. These polymers grow in one dimension through carboxylate bridging whereas in another direction, the growth is through –CH_2OH bridging.

(3f) An unprecedented conversion of a nonporous coordination polymer of Cu^{2+} to its porous supramolecular coordination complex by insertion of a neutral bifunctional linker provides the hierarchical importance of coordination bonds and hydrogen bonds as some of these CPs (**34**, **36**, **38** and **40**) are converted to SCCs, [Cu_2(4,4'-bpy)(Hsersal)$_2$]·2H_2O (**46**), [Cu_2(4,4'-bpy)(Hser-5-OMe-sal)$_2$]·6H_2O (**47**), [Cu_2(4,4'-bpy)(Hser-5-NO_2-sal)$_2$]·H_2O (**48**) and [Cu_2(4,4'-bpy)(Hser-5-Cl-sal)$_2$]·4H_2O·DMF (**49**). Based on the variable temperature magnetic susceptibility measurements between 2-380 K, strong antiferromagnetic coupling (2J = -278 cm^{-1}) for **34** and no interaction for **46** between the Cu^{2+} centers are observed. The dynamic behaviour and soft nature of **46** is well established through the water adsorption study. The presence of the hysteresis loop in water adsorption study of **46** clearly suggests the hydrophilic nature of the pores within SCC **46**.

(3g) Encapsulation of the first zig-zag water octamer within the supramolecular coordination complex of Ni^{2+}, [Ni_2(Hhissal)$_2$(adi)(H_2O)$_2$]·8H_2O (**50**) is well accomplished . This water

octamer shares striking similarity in hydrogen bonding with ice. The strong hydrogen bonding within water octamer as well as with the carboxylate groups of the ligand in the dinuclear unit provides greater stability to **50**. A comparison of these properties of **50** with those of $[Ni_2(Hhissal)_2(succ)(H_2O)_2]\cdot 4H_2O$ (**51**), $[Ni_2(Hhissal)_2(mal)(H_2O)_2]\cdot 4H_2O$ (**52**) and $[Ni_2(Hhissal)_2(fum)(H_2O)_2]\cdot 6H_2O$ (**53**) has indicated that these are isostructural. Further spectroscopic properties and thermal behaviour established for **50**-**53** provide required information for understanding such a system.

(3h) Coordination architectures of divalent metal ions and amino acid based ligands with tagged fluorophores in the ratio of 1:2 shows a highly luminescent behavior. Within this category, a new homochiral luminescent compound, $[Cu_2(HTyr\text{-}N\text{-}Dan)_4(H_2O)_2]\cdot 2H_2O$ (**54a**) with a four-fold symmetry has been synthesized and structurally characterized. In **54a,** each Cu^{2+} ion of the dinuclear unit has four oxygens of the carboxylates from four different ligands forming a paddle-wheel structure. Each dinuclear subunit is hydrogen bonded to eight other dinuclear subunits forming an extended SCC. This SCC is further strengthened by the intra-ligand π–π interactions between the aromatic rings of the dansyl and that of the tyrosine moiety of the ligand.

(3i) The CD spectra of these coordination architectures clearly suggest the translation of the chirality from the ligands to the coordination architectures. The CD spectra of these coordination architectures are concordant with the absorption spectra of these architectures. The photoluminescence properties of the coordination architectures with natural fluorophores (L-Tyrosine or L-phenylalanine derived) were fully explored to understand the role of various divalent metals especially the d^{10} metal ions in modulating the radiative pathways while coming back to the ground state.

(4) The functional aspect (sensing abilities) of these ligands and the coordination architectures are also thoroughly analysed in the second part of this work. The natural fluorescence property of the various amino acids (L-Tyrosine and L-phenylalanine) as well as of tagged fluorophores was well explored in the sensing applications. The role

played by the various functional groups and the solvents in sensing abilities of these sensors are methodically studied and can be concluded as:

(4a) Use of a triple action tyrosine based probe is demonstrated as a solvent dependent flip-flop halide (Iodide vs fluoride) sensor as well as an optical pH indicator. The monosodium salt of H_2Tyr-4-nitro in methanol (**L1a**) acts as iodide sensor whereas the same probe in DMSO (**L1b**) acts as fluoride sensor. Moreover, the switch in pH simply by observing the color change of receptor **L1** in DMSO on addition of H^+/OH^- is well observed. The change in the polarity of a solvent brings variation in the orientation of the sensor and thus the differential halide sensing.

(4b) Based on the anion-π and hydrogen bonding interactions, two supramolecular solvates of Cu^{2+} (DMSO and MeOH) show distinct chromogenic and fluorogenic receptor behaviour towards various anions (where F^- and OAc^- show the most colorimetric change) where a 2:1 receptor-anion formation is established through ESI-MS and CD data. The importance of the presence of an electron withdrawing group in anion-π interactions is well established by replacing the electron withdrawing group with electron donating groups and then studying these coordination architectures via naked eye detection as well as various spectroscopic techniques.

(4c) A methodical and judicious amalgamation of two fluorophores (phenol and thiophene groups) is attributed to the development of an unprecedented single-molecule multianalyte receptor, NaHTyrthio (**L3**), for the selective sensing of a cation (Cu^{2+}), neutral small molecules (nitrobenzene and aniline) and an anion (F^-) at the ppm or ppb level. Fluorescence quenching serves as a signal for sensing of Cu^{2+} and nitrobenzene (attributed to the phenol part) along with F^- (attributed to the thiophene part). On the other hand, the sensing of aniline is ascribed to the shift in emission wavelength of the phenol part of the receptor. Based on the lifetime measurements, sensing of Cu^{2+} and nitrobenzene is found to be a static quenching whereas sensing of F^- is a combination of static and dynamic quenching. In each case, the quenching constant calculated from the Stern-Volmer plot shows magnificent sensing ability towards each analyte. The role of electron transfer vs resonant energy transfer between sensor

(NaHTyrthio) and the analytes in fluorescence quenching is also thoroughly studied. In case of nitrobenzene, the quenching is via electron transfer based on the observation that there is no overlap between the absorption spectrum of nitrobenzene and fluorescence spectrum of NaHTyrthio. The role of NaHTyrthio as an ON-OFF sensor for Cu^{2+} is also demonstrated. The binding affinity of Cu^{2+} towards NaHTyrthio is thoroughly examined by the isothermal titration calorimetry (ITC) technique which is in concordance with the X-ray crystal structure of the resultant receptor-analyte complex $\{[Cu(HTyrthio)_2]\cdot H_2O\}_n$. For neutral small molecules and anions, the receptor-analyte interactions have been established by NMR titrimetry experiments.

(4d) A systematic study of various analytes has indicated that the dansylated ligand (H_2Tyr-N-Dan) and its coordination architectures (**54** and **55**) as potential chemosensors for the nitroanilines, particularly p-nitroaniline. The sensing of p-nitoaniline is via π–π interaction between the analyte and the dansyl moieties. The sensitivity of the ligand and the coordination architectures toward various analyte appears to be similar due to the distance between the dansyl moiety and the central metal ion.

Utilizing the knowledge reported in this thesis, further work can be done to explore other horizons in this field. Therefore, a few points are provided below for the future directions of this research:

(1) Other substitutions in the ligands, e.g., the thiophene ring can be replaced with an imidazole or the nitro group in the aromatic ring can be replaced by -CH_3, -Cl etc., may provide an opportunity to bring further diversification in this field.

(2) The coordination architectures especially the SCCs with coordinated water can be utilized in enantioselective catalysis. Using these chiral sensors enantiselective sensing can be achieved.

(3) In the category of hetero ligands, other amino acids like L-serine or L-tryptophan can be

used in place of L-Tyrosine.

(4) Other bifunctional linkers, such as 1,2-di(pyridin-4-yl)ethane, 1,2-di(pyridin-4-yl)ethene or 1,4-dicyano benzene, instead of 4,4'-bipyridine can be employed to generate more examples for understanding their effect on the structural and physicochemical properties of the coordination architectures.

(5) For the histidine based systems, more effort can be put with other metal centers and several different dicarboxylate ligands to illuminate the rich chemistry.

(6) Various other fluorophores, like anthracene or naphthalene, can be used to obtain other tagged amino acid based ligands to expand this section for different coordination architectures.

(7) Coordination architectures with L-Tryptophan or L-Phenylalanine can be explored for chemosensor studies.

(8) Utilising the stronger affinity of Cu^{2+} towards the CN^{-}, relay sensors for this important anion can be developed.

(9) Coordination architectures of lanthanides can provide both structural as well as functional analogues.

References

(1) Bauer, E. B. *Chem. Soc. Rev.* **2012**, *41*, 3153-3167.
(2) Allendorf, M. D.; Bauer, C. A.; Bhakta, R. K.; Houk, R. J. *Chem. Soc. Rev.* **2009**, *38*, 1330-1352.
(3) Wolff, J. J. *Angew. Chem., Int. Ed.* **1996**, *35*, 2195-2197.
(4) Steed, J. W.; Atwood, J. L. In *Supramolecular Chemistry*; CRC Press: Marcel Deckker, USA, 2009; Vol. 1.
(5) Rao, C. N.; Natarajan, S.; Vaidhyanathan, R. *Angew. Chem., Int. Ed.* **2004**, *43*, 1466-1496.
(6) Xuan, W.; Zhang, M.; Liu, Y.; Chen, Z.; Cui, Y. *J. Am. Chem. Soc.* **2012**, *134*, 6904-6907.
(7) Lehn, J. M. In *Supramolecular Chemistry: Concepts and Perspectives*; Wiley: New York, USA 1995.
(8) Rosi, N. L.; Kim, J.; Eddaoudi, M.; Chen, B.; O'Keeffe, M.; Yaghi, O. M. *J. Am. Chem. Soc.* **2005**, *127*, 1504-1518.
(9) Langner, A.; Tait, S. L.; Lin, N.; Rajadurai, C.; Ruben, M.; Kern, K. *Proc. Natl. Acad. Sci. USA* **2007**, *104*, 17927-17930.
(10) Subramanian, S.; Zaworotko, M. J. *Coord. Chem. Rev.* **1994**, *137*, 357-401.
(11) Burrows, A. D.; Chan, C.-W.; Chowdhry, M. M.; McGrady, J. E.; Mingos, D. M. P. *Chem. Soc. Rev.* **1995**, *24*, 329-339.
(12) Brammer, L. In *Perspective in Supramolecular Chemistry - Crystal Design: Structure and Function;* Wiley: New York, USA 2003; Vol. 7.
(13) Beatty, A. M. *CrystEngComm* **2001**, *3*, 243-255.
(14) Aakeröy, C. B.; Beatty, A. M. *Aust. J. Chem.* **2001**, *54*, 409-421.
(15) Desiraju, G. R. *J. Chem. Soc., Dalton Trans.* **2000**, 3745-3751.
(16) Khullar, S.; Gupta, V.; Mandal, S. K. *CrystEngComm* **2014**, *16*, 5705-5715.
(17) Khullar, S.; Mandal, S. K. *Cryst. Growth Des.* **2012**, *12*, 5329-5337.
(18) Khullar, S.; Mandal, S. K. *Cryst. Growth Des.* **2013**, *13*, 3116-3125.
(19) Khullar, S.; Mandal, S. K. *CrystEngComm* **2013**, *15*, 6652-6662.
(20) Khullar, S.; Mandal, S. K. *Cryst. Growth Des.* **2014**, *14*, 6433-6444.
(21) Wang, Q.; Chen, Y.; Ma, P.; Lu, J.; Zhang, X.; Jiang, J. *J. Mater. Chem.* **2011**, *21*, 8057-8065.
(22) Hang, T.; Zhang, W.; Ye, H.-Y.; Xiong, R.-G. *Chem. Soc. Rev.* **2011**, *40*, 3577-3598.
(23) Zhang, W.; Xiong, R. G. *Chem. Rev.* **2012**, *112*, 1163-1195.
(24) Zhang, W.; Chen, L. Z.; Xiong, R. G.; Nakamura, T.; Huang, S. D. *J. Am. Chem. Soc.* **2009**, *131*, 12544-12545.
(25) Verardo, G.; Geatti, P.; Pol, E.; Giumanini, A. G. *Can. J. Chem.* **2002**, *80*, 779-788.
(26) Quitt, P.; Hellerbach, J.; Vogler, K. *Helv. Chim. Acta* **1963**, *46*, 327-333.
(27) Biediger, R. J.; Dupre B., Hamaker, L. K.; Holland, G. W.; Kassir, J. M.; Li, W.; Market, R. V.; Nguyen, N.; Scott, I. L.; Wu, C.; Decker, E. R. Propanoic acid derivatives that inhibit the binding of integrins to their receptors. U. S. Patent Application 2003/0199692 Al. Oct 23, 2003.
(28) Biediger, R. J.; George, W.; Kassir, J. M.; Li, W.; Robert, V. ; Ian, L.; Dupre, B.; Hamaker, L. K.; Nguyen, N.; Decker E. R.; Wu, C. Propanoic acid derivatives that

inhibit the binding of integrins to their receptors. EP Application 1213288 A1. June 12, 2002.
(29) Biediger, R. J.; George, W.; Kassir, J. M.; Li, W.; Robert, V.; Ian, L. Propanoic acid derivatives that inhibit the binding of integrins to their receptors. PCT WO 00/68188. Nov 16, 2000.
(30) Goswami, T. K.; Gadadhar, S.; Karande, A. A.; Chakravarty, A. R. *Polyhedron* **2013**, *52*, 1287-1298.
(31) Nagarathinam, M.; Saravanan, K.; Leong, W. L.; Balaya, P.; Vittal, J. J. *Cryst. Growth Des.* **2009**, *9*, 4461-4470.
(32) Thio, Y.; Yang, X.; Vittal, J. J. *Dalton Trans.* **2014**, *43*, 3545-3556.
(33) Sahoo, S. C.; Ray, M. *Dalton Trans.* **2009**, 3230-3236.
(34) Sahoo, S. C.; Dubey, M.; Alam, M. A.; Ray, M. *Inorg. Chim. Acta* **2010**, *363*, 3055-3060.
(35) Alam, M. A.; Koner, R. R.; Das, A.; Nethaji, M.; Ray, M. *Cryst. Growth Des.* **2007**, *7*, 1818-1824.
(36) Alam, M. A.; Nethaji, M.; Ray, M. *Angew. Chem., Int. Ed.* **2003**, *42*, 1940-1942.
(37) Sahoo, S. C.; Kundu, T.; Banerjee, R. *J. Am. Chem. Soc.* **2011**, *133*, 17950-17958.
(38) Kundu, T.; Sahoo, S. C.; Banerjee, R. *CrystEngComm* **2013**, *15*, 9634-9640.
(39) Kundu, T.; Sahoo, S. C.; Saha, S.; Banerjee, R. *Chem. Commun.* **2013**, *49*, 5262-5264.
(40) Saha, S.; Bachl, J.; Kundu, T.; Díaz Díaz, D.; Banerjee, R. *Chem. Commun.* **2014**, *50*, 3004-3006.
(41) Kundu, T.; Sahoo, S. C.; Banerjee, R. *Cryst. Growth Des.* **2012**, *12*, 2572-2578.
(42) Carboni, S.; Pignataro, L.; Gennari, C.; Piarulli, U. *Tetrahedron: Asymmetry* **2009**, *20*, 1185-1190.
(43) Correia, I.; Marcão, S.; Koci, K.; Tomaz, I.; Adão, P.; Kiss, T.; Jakusch, T.; Avecilla, F.; Costa Pessoa, J. *Eur. J. Inorg. Chem.* **2011**, *2011*, 694-708.
(44) Ying, S.-M.; Huang, X.-H. *Transition Met. Chem.* **2013**, *38*, 413-418.
(45) Chandramohan, G.; Kiruthikajothi, K. *Int. J. Curr. Microbiol. App. Sci.*, **2013**, *2*, 24-28.
(46) Li, Z.-Z.; Du, L.; Zhang, X.-Z.; Li, Z.-L.; Li, L.; Yang, J.; Zhao, Q.-H. *Inorg. Chem. Commun.* **2014**, *45*, 20-24.
(47) Yang, X.-L.; Xie, M.-H.; Zou, C.; Wu, C.-D. *CrystEngComm* **2011**, *13*, 6422-6430.
(48) He, J.; Zhang, G.; Xiao, D.; Chen, H.; Yan, S.; Wang, X.; Yang, J.; Wang, E. *CrystEngComm* **2012**, *14*, 3609-3614.
(49) Li, Z.-Z.; Du, L.; Zhou, J.; Zhu, M.-R.; Qian, F.-H.; Liu, J.; Chen, P.; Zhao, Q.-H. *Dalton Trans.* **2012**, *41*, 14397-14403.
(50) Yang, X.-L.; Wu, C.-D. *CrystEngComm* **2014**, *16*, 4907-4918.
(51) Vittal, J. J. *Coord. Chem. Rev.* **2007**, *251*, 1781-1795.
(52) Koh, L. L.; Ranford, J. O.; Robinson, W. T.; Svensson, J. O.; Tan, A. L. C.; Wu, D. *Inorg. Chem.* **1996**, *35*, 6466-6472.
(53) Ito, M.; Gupta, L. P.; Masuda, H.; Kawahata, H. *Org. Geochem.* **2006**, *37*, 177-188.
(54) Callan, J. F.; de Silva, A. P.; Magri, D. C. *Tetrahedron* **2005**, *61*, 8551-8588.
(55) Martínez-Máñez, R.; Sancenón, F. *Coord. Chem. Rev.* **2006**, *250*, 3081-3093.
(56) Fabbrizzi, L.; Poggi, A. *Chem. Soc. Rev.* **1995**, *24*, 197-202.
(57) Beer, P. D. *Acc. Chem. Res.***1998**, *31*, 71-80.

(58) You, L.; Zha, D.; Anslyn, E. V. *Chem. Rev.* **2015**, DOI: 10.1021/cr5005524.
(59) Stang, P. J. *Chem. - Eur. J.* **1998**, *4*, 19-27.
(60) Cook, T. R.; Zheng, Y.-R.; Stang, P. J. *Chem. Rev.* **2013**, *113*, 734-777.
(61) Chakrabarty, R.; Mukherjee, P. S.; Stang, P. J. *Chem. Rev.* **2011**, *111*, 6810-6918.
(62) Fujita, M.; Tominaga, M.; Hori, A.; Therrien, B. *Acc. Chem. Res.* **2005**, *38*, 369-378.
(63) Hosseini, M. W. *Acc. Chem. Res.* **2005**, *38*, 313-323.
(64) Perry Iv, J. J.; Perman, J. A.; Zaworotko, M. J. *Chem. Soc. Rev.* **2009**, *38*, 1400-1417.
(65) Reboul, J.; Furukawa, S.; Horike, N.; Tsotsalas, M.; Hirai, K.; Uehara, H.; Kondo, M.; Louvain, N.; Sakata, O.; Kitagawa, S. *Nat. Mater.* **2012**, *11*, 717-723.
(66) Batten, S. R.; Champness, N. R.; Chen, X.-M.; Garcia-Martinez, J.; Kitagawa, S.; Öhrström, L.; O'Keeffe, M.; Suh, M. P.; Reedijk, J. *CrystEngComm* **2012**, *14*, 3001-3004.
(67) Chen, C.-T.; Suslick, K. S. *Coord. Chem. Rev.* **1993**, *128*, 293-322.
(68) Tripuramallu, B. K.; Das, S. K. *J. Solid State Chem.* **2013**, *197*, 499-507.
(69) Janiak, C. *Dalton Trans.* **2003**, 2781-2804.
(70) Du, M.; Li, C.-P.; Liu, C.-S.; Fang, S.-M. *Coord.Chem. Rev.* **2013**, *257*, 1282-1305.
(71) Ma, Z.; Moulton, B. *Coord. Chem. Rev.* **2011**, *255*, 1623-1641.
(72) Khullar, S.; Mandal, S. K. *RSC Adv.* **2014**, *4*, 39204-39213.
(73) Zhang, Z.; Ma, J.-F.; Liu, Y.-Y.; Kan, W.-Q.; Yang, J. *CrystEngComm* **2013**, *15*, 2009-2018.
(74) Liu, B. L. D., J.; Zhang, S. Q.; Wang , Q. L.; Tao, R. J. *Z. Naturforsch.***2010**, *B65*, 1240-1244.
(75) Oliveri, C. G.; Ulmann, P. A.; Wiester, M. J.; Mirkin, C. A. *Acc. Chem. Res.***2008**, *41*, 1618-1629.
(76) Shankar, B.; Elumalai, P.; Jackmil, P. J.; Kumar, P.; Singh, S.; Sathiyendiran, M. *J. Organomet. Chem.* **2013**, *743*, 109-113.
(77) Yan, X.; Li, S.; Pollock, J. B.; Cook, T. R.; Chen, J.; Zhang, Y.; Ji, X.; Yu, Y.; Huang, F.; Stang, P. J. *Proc. Natl. Acad. Sci. USA* **2013**, *110*, 15585-15590.
(78) Safin, D. A.; Babashkina, M. G.; Kubisiak, P.; Mitoraj, M. P.; Le Duff, C. S.; Robeyns, K.; Garcia, Y. *Eur. J. Inorg. Chem.* **2014**, *2014*, 5522-5529.
(79) Dinolfo, P. H.; Hupp, J. T. *Chem. Mater.* **2001**, *13*, 3113-3125.
(80) Stock, N.; Biswas, S. *Chem. Rev.* **2012**, *112*, 933-969.
(81) Cravillon, J.; Münzer, S.; Lohmeier, S.-J.; Feldhoff, A.; Huber, K.; Wiebcke, M. *Chem. Mater.* **2009**, *21*, 1410-1412.
(82) Huang, L. *Microporous Mesoporous Mater.* **2003**, *58*, 105-114.
(83) Tranchemontagne, D. J.; Hunt, J. R.; Yaghi, O. M. *Tetrahedron* **2008**, *64*, 8553-8557.
(84) Rabenau, A. *Angew. Chem., Int. Ed.* **1985**, *24*, 1026-1040.
(85) Ni, Z.; Masel, R. I. *J. Am. Chem. Soc.* **2006**, *128*, 12394-12395.
(86) Mueller, U.; Puetter, H.; Hesse, M.; Wessel, H.; Method for electrochemical production of a crystalline porous metal organic skeleton material. WO 2005/049892. 2005.
(87) Meek, S. T.; Greathouse, J. A.; Allendorf, M. D. *Adv. Mater.* **2011**, *23*, 249-267.
(88) Pichon, A.; Lazuen-Garay, A.; James, S. L. *CrystEngComm* **2006**, *8*, 211-214.
(89) Friščić, T.; Fábián, L. *CrystEngComm* **2009**, *11*, 743-745.
(90) de Silva, A. P.; Gunaratne, H. Q. N.; Gunnlaugsson, T.; Huxley, A. J. M.; McCoy, C. P.; Rademacher, J. T.; Rice, T. E. *Chem. Rev.* **1997**, *97*, 1515-1566.

(91) Martínez-Máñez, R.; Sancenón, F. *Chem. Rev.* **2003**, *103*, 4419-4476.
(92) Zheng, Y.; Orbulescu, J.; Ji, X.; Andreopoulos, F. M.; Pham, S. M.; Leblanc, R. M. *J. Am. Chem. Soc.* **2003**, *125*, 2680-2686.
(93) Gunnlaugsson, T.; Lee, T. C.; Parkesh, R. *Org. Lett.* **2003**, *5*, 4065-4068.
(94) Metivier, R.; Leray, I.; Valeur, B. *Chem.- Eur. J.***2004**, *10*, 4480-4490.
(95) Kwon, J. Y.; Jang, Y. J.; Lee, Y. J.; Kim, K. M.; Seo, M. S.; Nam, W.; Yoon, J. *J. Am.Chem. Soc.* **2005**, *127*, 10107-10111.
(96) Yoon, S.; Albers, A. E.; Wong, A. P.; Chang, C. J. *J. Am. Chem. Soc.***2005**, *127*, 16030-16031.
(97) Bricks, J. L.; Kovalchuk, A.; Trieflinger, C.; Nofz, M.; Büschel, M.; Tolmachev, A. I.; Daub, J.; Rurack, K. *J. Am. Chem. Soc.* **2005**, *127*, 13522-13529.
(98) Chan, Y.-H.; Chen, J.; Liu, Q.; Wark, S. E.; Son, D. H.; Batteas, J. D. *Anal. Chem.* **2010**, *82*, 3671-3678.
(99) Kim, B.-E.; Nevitt, T.; Thiele, D. J. *Nat. Chem. Biol.* **2008**, *4*, 176-185.
(100) Harris, E. D. *J. Nutr.* **1992**, *122*, 636-640.
(101) Plastino, J.; Green, E. L.; Sanders-Loehr, J.; Klinman, J. P. *Biochemistry* **1999**, *38*, 8204-8216.
(102) Schleper, B.; Stuerenburg, H. J. *J. Neurol.* **2001**, *248*, 705-706.
(103) Chen, P.; Solomon, E. I. *J. Am. Chem. Soc.* **2004**, *126*, 4991-5000.
(104) Radisky, D. C.; Levy, D. D.; Littlepage, L. E.; Liu, H.; Nelson, C. M.; Fata, J. E.; Leake, D.; Godden, E. L.; Albertson, D. G.; Angela Nieto, M.; Werb, Z.; Bissell, M. J. *Nature* **2005**, *436*, 123-127.
(105) Houstis, N.; Rosen, E. D.; Lander, E. S. *Nature* **2006**, *440*, 944-948.
(106) Trachootham, D.; Alexandre, J.; Huang, P. *Nat. Rev. Drug Discovery* **2009**, *8*, 579-591.
(107) Dickinson, B. C.; Chang, C. J. *Nat. Chem. Biol.***2011**, *7*, 504-511.
(108) G. Georgopoulos, A. R. M. J. Y. P. *J. Toxicol. Environ. Health, Part B* **2001**, *4*, 341-394.
(109) B. P. Zietz, H. H. D., M. Lakomek, H. Schneider, B. Kebler-Gaedtke and H. Dunkelberg *Sci.Total Environ.* **2003**, *302*, 127-144.
(110) Uauy, R.; Olivares, M.; Gonzalez, M. *Am. J. Clin. Nutr.* **1998**, *67*, 952S-959S.
(111) Mahapatra, A. K.; Hazra, G.; Das, N. K.; Goswami, S. *Sens. Actuators B* **2011**, *156*, 456-462.
(112) Barnham, K. J.; Masters, C. L.; Bush, A. I. *Nat. Rev. Drug Discovery* **2004**, *3*, 205-214.
(113) Song, Y.; Qu, K.; Xu, C.; Ren, J.; Qu, X. *Chem. Commun.* **2010**, *46*, 6572-6574.
(114) Gaggelli, E.; Kozlowski, H.; Valensin, D.; Valensin, G. *Chem. Rev.* **2006**, *106*, 1995-2044.
(115) Donnelly, P. S.; Xiao, Z.; Wedd, A. G. *Curr. Opin. Chem. Biol.* **2007**, *11*, 128-133.
(116) Tripathy, S. K.; Woo, J. Y.; Han, C.-S. *Nanotechnology* **2012**, *23*, 305502.
(117) Upadhyay, K. K.; Kumar, A. *Org. Biomol. Chem.* **2010**, *8*, 4892-4897.
(118) Karak, D.; Lohar, S.; Banerjee, A.; Sahana, A.; Hauli, I.; Mukhopadhyay, S. K.; Sanmartín Matalobos, J.; Das, D. *RSC Adv.* **2012**, *2*, 12447-12454.
(119) Lee, Y. J.; Seo, D.; Kwon, J. Y.; Son, G.; Park, M. S.; Choi, Y.-H.; Soh, J. H.; Lee, H. N.; Lee, K. D.; Yoon, J. *Tetrahedron* **2006**, *62*, 12340-12344.
(120) Kumar, M.; Kumar, N.; Bhalla, V. *Dalton Trans.* **2012**, *41*, 10189-10193.

(121) Kim, K. B.; You, D. M.; Jeon, J. H.; Yeon, Y. H.; Kim, J. H.; Kim, C. *Tetrahedron Lett.* **2014**, *55*, 1347-1352.
(122) Boiocchi, M.; Fabbrizzi, L.; Licchelli, M.; Sacchi, D.; Vazquez, M.; Zampa, C. *Chem. Commun.* **2003**, 1812-1813.
(123) Jung, H. S.; Kwon, P. S.; Lee, J. W.; Kim, J. I.; Hong, C. S.; Kim, J. W.; Yan, S.; Lee, J. Y.; Lee, J. H.; Joo, T.; Kim, J. S. *J. Am. Chem.Soc.***2009**, *131*, 2008-2012.
(124) Sirilaksanapong, S.; Sukwattanasinitt, M.; Rashatasakhon, P. *Chem. Commun.* **2012**, *48*, 293-295.
(125) Yao, J.; Zhang, K.; Zhu, H.; Ma, F.; Sun, M.; Yu, H.; Sun, J.; Wang, S. *Anal. Chem.***2013**, *85*, 6461-6468.
(126) Zhao, Y.; Zhang, X.-B.; Han, Z.-X.; Qiao, L.; Li, C.-Y.; Jian, L.-X.; Shen, G.-L.; Yu, R.-Q. *Anal.Chem.***2009**, *81*, 7022-7030.
(127) Liu, A.-C.; Chen, D.-C.; Lin, C.-C.; Chou, H.-H.; Chen, C.-h. *Anal. Chem.* **1999**, *71*, 1549-1552.
(128) Kumar, N.; Bhalla, V.; Kumar, M. *Analyst* **2014**, *139*, 543-558.
(129) Zhou, Y.; Zhang, J. F.; Yoon, J. *Chem. Rev.* **2014**, *114*, 5511-5571.
(130) Beer, P. D.; Gale, P. A. *Angew. Chem., Int. Ed.* **2001**, *40*, 486-516.
(131) Martínez-Máñez, R.; Sancenón, F. *J.Fluoresc.* **2005**, *15*, 267-285.
(132) Gale, P. A. *Coord. Chem. Rev.***2003**, *240*, 1.
(133) Bondy, C. R.; Loeb, S. J. *Coord. Chem. Rev.* **2003**, *240*, 77-99.
(134) Suksai, C.; Tuntulani, T. *Chem. Soc. Rev.* **2003**, *32*, 192-202.
(135) Horowitz, H. S. *J. Pub. Health Dent.* **2003**, *63*, 3-8.
(136) Jentsch, T. J. *Curr. Opin. Neurobiol.* **1996**, *6*, 303-310.
(137) Kleerekoper, M. *Endocrinol. Metab. Clin. North. Am.* **1998**, *27*, 441-452.
(138) Kirk, K. L. In *Biochemistry of the Halogens and Inorganic Halide*; Plenum Press:New York 1991.
(139) Riggs, B. L. In *Bone and Mineal Research Annual 2*; Elsevier: Amsterdam 1984.
(140) Wiseman, A. In *Handbook of Experimental Pharmacology XX/2 Part 2*; Springer-Verlag: Berlin, 1970.
(141) Weatherall, J. A. *Pharmacology of Fluorides in Handbook of Experimental PharmacologyXX/1 Part 1*; Springer-Verlag: Berlin, 1969.
(142) Dreisbuch, R. H. *Handbook of Poisoning*; Lange Medical Publishers: Los Altos, CA 1980.
(143) Cheng, T.-J.; Chen, T.-M.; Chen, C.-H.; Lai, Y.-K. *J. Cell. Biochem.* **1998**, *69*, 221-231.
(144) Chen, X.; Nam, S.-W.; Kim, G.-H.; Song, N.; Jeong, Y.; Shin, I.; Kim, S. K.; Kim, J.; Park, S.; Yoon, J. *Chem. Commun.* **2010**, *46*, 8953-8955.
(145) Kumar, S.; Luxami, V.; Kumar, A. *Org. Lett.* **2008**, *10*, 5549-5552.
(146) Bhalla, V.; Pramanik, S.; Kumar, M. *Chem. Commun.* **2013**, *49*, 895-897.
(147) Li, J.; Lin, H.; Cai, Z.; Lin, H. *Spectrochim. Acta Part A: Mol. Biomol. Spectrosc.* **2009**, *72*, 1062-1065.
(148) Hudnall, T. W.; Chiu, C.-W.; Gabbaï, F. o. P. *Acc. Chem. Res.* **2009**, *42*, 388-397.
(149) Lan, A.; Li, K.; Wu, H.; Olson, D. H.; Emge, T. J.; Ki, W.; Hong, M.; Li, J. *Angew. Chem., Int. Ed.* **2009**, *48*, 2334-2338.

(150) Pramanik, S.; Zheng, C.; Zhang, X.; Emge, T. J.; Li, J. *J. Am. Chem. Soc.* **2011**, *133*, 4153-4155.
(151) Pramanik, S.; Hu, Z.; Zhang, X.; Zheng, C.; Kelly, S.; Li, J. *Chem.- Eur. J.* **2013**, *19*, 15964-15971.
(152) Nagarkar, S. S.; Joarder, B.; Chaudhari, A. K.; Mukherjee, S.; Ghosh, S. K. *Angew. Chem., Int. Ed.* **2013**, *52*, 2881-2885.
(153) Chaudhari, A. K.; Nagarkar, S. S.; Joarder, B.; Ghosh, S. K. *Cryst. Growth Des.* **2013**, *13*, 3716-3721.
(154) Germain, M. E.; Knapp, M. J. *J. Am. Chem. Soc.* **2008**, *130*, 5422-5423.
(155) Li, L.; Zhang, S.; Xu, L.; Han, L.; Chen, Z.-N.; Luo, J. *Inorg. Chem.* **2013**, *52*, 12323-12325.
(156) Kim, T. K.; Lee, J. H.; Moon, D.; Moon, H. R. *Inorg.Chem.* **2013**, *52*, 589-595.
(157) Salinas, Y.; Martínez-Máñez, R.; Marcos, M. D.; Sancenón, F.; Costero, A. M.; Parra, M.; Gil, S. *Chem. Soc. Rev.* **2012**, *41*, 1261-1296.
(158) Germain, M. E.; Knapp, M. J. *Chem. Soc. Rev.* **2009**, *38*, 2543-2555.
(159) Boyd, S. A.; Sheng, G.; Teppen, B. J.; Johnston, C. T. *Environ. Sci. Technol.* **2001**, *35*, 4227-4234.
(160) Cronin, M. T.; Gregory, B. W.; Schultz, T. W. *Chem. Res. Toxicol.* **1998**, *11*, 902-908.
(161) Majumder, P. S.; Gupta, S. K. *Water Res.* **2003**, *37*, 4331-4336.
(162) Games, L. M.; Hites, R. A. *Anal. Chem.* **1977**, *49*, 1433-1440.
(163) Schultz, T. W.; Allison, T. C. *Bull. Environ. Contam. Toxicol.* **1979**, *23*, 814-819.
(164) Khan, M. F.; Kaphalia, B. S.; Boor, P. J.; Ansari, G. A. *Arch. Environ. Contam. Toxicol.* **1993**, *24*, 368-374.
(165) Bus, J. S.; Popp, J. A. *Food Chem. Toxicol.* **1987**, *25*, 619-626.
(166) Dalene, M.; Skarping, G. *J. Chromatogr. A* **1985**, *331*, 321-330.
(167) Yan, C. *Talanta* **2004**, *64*, 650-654.
(168) Laha, S.; Luthy, R. G. *Environ. Sci. Technol.* **1990**, *24*, 363-373.
(169) Qin, J.-S.; Bao, S.-J.; Li, P.; Xie, W.; Du, D.-Y.; Zhao, L.; Lan, Y.-Q.; Su, Z.-M. *Chem. Asian J.* **2014**, *9*, 749-753.
(170) Roy, S.; Katiyar, A. K.; Mondal, S. P.; Ray, S. K.; Biradha, K. *ACS Appl. Mater. Inter.* **2014**, *6*, 11493-11501.
(171) Liu, K.; Liu, T.; Chen, X.; Sun, X.; Fang, Y. *ACS Appl. Mater. Inter.* **2013**, *5*, 9830-9836.
(172) Zhang, Z.; Xiang, S.; Rao, X.; Zheng, Q.; Fronczek, F. R.; Qian, G.; Chen, B. *Chem. Commun.* **2010**, *46*, 7205-7207.
(173) Wang, G.-Y.; Yang, L.-L.; Li, Y.; Song, H.; Ruan, W.-J.; Chang, Z.; Bu, X.-H. *Dalton Trans.* **2013**, *42*, 12865-12868.
(174) Zhang, S.-R.; Du, D.-Y.; Qin, J.-S.; Li, S.-L.; He, W.-W.; Lan, Y.-Q.; Su, Z.-M. *Inorg. Chem.* **2014**, *53*, 8105-8113.
(175) Zhang, L.; Li, B. *Spectrochim. Acta Part A: Mol. Biomol. Spectrosc.* **2009**, *74*, 1060-1063.
(176) Prasad, R.; Kumar, R.; Prasad, S. *Anal. Chim. Acta* **2009**, *646*, 97-103.
(177) Kumar, M. S.; Tamilarasan, R.; Sreekanth, A. *Spectrochim. Acta Part A: Mol. Biomol. Spectrosc.* **2011**, *79*, 370-375.
(178) Lee, T. A.; Headley, L. M.; Hardy, J. K. *Anal. Chem.* **1991**, *63*, 357-360.

(179) Singh, N.; Kaur, N.; Ni Choitir, C.; Callan, J. F. *Tetrahedron Lett.* **2009**, *50*, 4201-4204.
(180) Manivannan, S.; Ramaraj, R. *Analyst* **2013**, *138*, 1733-1739.
(181) Guo, D.; Dong, Z.; Luo, C.; Zan, W.; Yan, S.; Yao, X. *RSC Adv.* **2014**, *4*, 5718-5725.
(182) Dong, Z.; Le, X.; Zhou, P.; Dong, C.; Ma, J. *New. J. Chem.* **2014**, *38*, 1802-1808.
(183) Kumar, M.; Kumar, N.; Bhalla, V. *Chem. Commun.* **2013**, *49*, 877-879.
(184) Nguyen, B. T.; Anslyn, E. V. *Coord. Chem. Rev.* **2006**, *250*, 3118-3127.
(185) Yang, H.; Song, H.; Zhu, Y.; Yang, S. *Tetrahedron Lett.* **2012**, *53*, 2026-2029.
(186) Jiménez, D.; Martínez-Máñez, R.; Sancenón, F.; Soto, J. *Tetrahedron Lett.* **2004**, *45*, 1257-1259.
(187) Goswami, S.; Das, S.; Aich, K.; Sarkar, D.; Mondal, T. K. *Tetrahedron Lett.* **2013**, *54*, 6892-6896.
(188) Lavigne, J. J.; Anslyn, E. V. *Angew. Chem., Int. Ed.***2001**, *40*, 3118-3130.
(189) Wiskur, S. L.; Floriano, P. N.; Anslyn, E. V.; McDevitt, J. T. *Angew. Chem., Int. Ed.***2003**, *42*, 2070-2072.
(190) Komatsu, H.; Citterio, D.; Fujiwara, Y.; Minamihashi, K.; Araki, Y.; Hagiwara, M.; Suzuki, K. *Org. Lett.* **2005**, *7*, 2857-2859.
(191) Komatsu, H.; Miki, T.; Citterio, D.; Kubota, T.; Shindo, Y.; Kitamura, Y.; Oka, K.; Suzuki, K. *J.Am. Chem. Soc.***2005**, *127*, 10798-10799.
(192) Raimundo, I. M.; Narayanaswamy, R. *Sens. Actuators B* **2003**, *90*, 189-197.
(193) Mikami, D.; Ohki, T.; Yamaji, K.; Ishihara, S.; Citterio, D.; Hagiwara, M.; Suzuki, K. *Anal.l Chem.* **2004**, *76*, 5726-5733.
(194) Kaur, N.; Kumar, S. *Chemical Communications* **2007**, 3069-3070.
(195) Kaur, N.; Kumar, S. *Tetrahedron Lett.* **2008**, *49*, 5067-5069.
(196) Schmittel, M.; Lin, H.-W. *Angew. Chem., Int. Ed.* **2007**, *46*, 893-896.
(197) Neupane, L. N.; Park, J.-Y.; Park, J. H.; Lee, K.-H. *Org. Let.* **2013**, *15*, 254-257.
(198) Yang, M.-H.; Thirupathi, P.; Lee, K.-H. *Organic Letters* **2011**, *13*, 5028-5031.
(199) Sener, G.; Uzun, L.; Denizli, A. *ACS Appl. Mater. Inter.* **2014**, *6*, 18395-18400.
(200) Ma, Z.; Cowart, D. M.; Ward, B. P.; Arnold, R. J.; DiMarchi, R. D.; Zhang, L.; George, G. N.; Scott, R. A.; Giedroc, D. P. *J. Am. Chem. Soc.***2009**, *131*, 18044-18045.
(201) Pandey, C. M.; Sumana, G.; Malhotra, B. D. *Biomacromolecules* **2011**, *12*, 2925-2932.
(202) Zhang, X.; Yin, J.; Yoon, J. *Chem. Rev.* **2014**, *114*, 4918-4959.
(203) Enkin, N.; Sharon, E.; Golub, E.; Willner, I. *Nano Lett.* **2014**, *14*, 4918-4922.
(204) Sinkeldam, R. W.; Greco, N. J.; Tor, Y. *Chem. Rev.* **2010**, *110*, 2579-2619.
(205) Deo, S.; Godwin, H. A. *J. Am. Chem. Soc.***2000**, *122*, 174-175.
(206) Kruppa, M.; König, B. *Chem. Rev.* **2006**, *106*, 3520-3560.
(207) Hanaoka, K.; Muramatsu, Y.; Urano, Y.; Terai, T.; Nagano, T. *Chem.-Eur. J.* **2010**, *16*, 568-572.
(208) Zhou, Y.; Li, Z.-X.; Zang, S.-Q.; Zhu, Y.-Y.; Zhang, H.-Y.; Hou, H.-W.; Mak, T. C. W. *Org. Lett.* **2012**, *14*, 1214-1217.
(209) Lee, H. G.; Lee, J. H.; Jang, S. P.; Park, H. M.; Kim, S.-J.; Kim, Y.; Kim, C.; Harrison, R. G. *Tetrahedron* **2011**, *67*, 8073-8078.

(210) Song, E. J.; Kang, J.; You, G. R.; Park, G. J.; Kim, Y.; Kim, S.-J.; Kim, C.; Harrison, R. G. *Dalton Trans.* **2013**, *42*, 15514.
(211) Lakowicz, J. R. In *Principles of Fluorescence Spectroscopy*; Springer: Singapore, 2006; Vol. 3rd edition.
(212) Passwater, R. A. In *Guide to fluorescence literature*; Plenum Press: New York 1969; Vol. II.
(213) Schmillen, A. In *Luminescence of organic substances*; Hellwege Verlag: Berlin, 1967.
(214) Konstantinova-Schlezinger, M. A. In *Fluoromestric analysis*; Davis Publishing Co.: New York, 1965.
(215) Berlman, L. In *Handbook of fluorescence spectra in aromatic molecules*; Academic Press: New York 1971; Vol. II.
(216) Guilbault, G. G. In *Fluorescence, theory, instrumentation and practice*; Marcel Dekker, Inc.: New York, 1967.
(217) While, C. E. In *Fluorescence analysis: a practical approach*; Marcel Dekker Inc: New York 1970.
(218) Gupta, V. K.; Singh, A. K.; Ganjali, M. R.; Norouzi, P.; Faridbod, F.; Mergu, N. *Sens. Actuators B* **2013**, *182*, 642-651.
(219) Wan, C.-F.; Lin, H.-Y.; Chien, C.; Wu, A.-T. *Luminescence* **2014**, *29*, 698-701.
(220) Chen, C.-H.; Liao, D.-J.; Wan, C.-F.; Wu, A.-T. *Analyst* **2013**, *138*, 2527-2530.
(221) Lee, S. A.; You, G. R.; Choi, Y. W.; Jo, H. Y.; Kim, A. R.; Noh, I.; Kim, S.-J.; Kim, Y.; Kim, C. *Dalton Trans.* **2014**, *43*, 6650-6559.
(222) Köse, M.; Ceyhan, G.; Tümer, M.; Demirtaş, İ.; Gönül, İ.; McKee, V. *Spectrochim. Acta Part A:Mol. Biomol. Spectrosc.* **2015**, *137*, 477-485.
(223) Saha, U. C.; Dhara, K.; Chattopadhyay, B.; Mandal, S. K.; Mondal, S.; Sen, S.; Mukherjee, M.;van Smaalen, S.; Chattopadhyay, P. *Org. Lett.* **2011**, *13*, 4510-4513.
(224) Rancan, M.; Dolmella, A.; Seraglia, R.; Orlandi, S.; Quici, S.; Armelao, L. *Chem. Commun.***2012**, *48*, 3115-3117.
(225) Rancan, M.; Tessarolo, J.; Casarin, M.; Zanonato, P. L.; Quici, S.; Armelao, L. *Inorg.Chem.* **2014**, *53*, 7276-7287.
(226) Rancan, M.; Tessarolo, J.; Quici, S.; Armelao, L. *Chem. Commun.* **2014**, *50*, 13761-13764.
(227) Rancan, M.; Tessarolo, J.; Zanonato, P. L.; Seraglia, R.; Quici, S.; Armelao, L. *Dalton Trans.* **2013**, *42*, 7534-7538.
(228) Cai, D.; Guo, H.; Wen, L.; Liu, C. *CrystEngComm* **2013**, *15*, 6702-6708.
(229) Zhang, X.; Wang, W.; Hu, Z.; Wang, G.; Uvdal, K. *Coord. Chem. Rev.* **2015**, *284*, 206-235.
(230) O'Neil, E. J.; Smith, B. D. *Coord. Chem. Rev.* **2006**, *250*, 3068-3080.
(231) Mishra, A.; Ravikumar, S.; Song, Y. H.; Prabhu, N. S.; Kim, H.; Hong, S. H.; Cheon, S.; Noh, J.; Chi, K.-W. *Dalton Trans.* **2014**, *43*, 6032-6040.
(232) Bruker AXS Inc: Madison, WI, USA 2008.
(233) Sheldrick, G. M. *Acta Crystallogr. A* **2007**, *64*, 112-122.
(234) Dolomanov, O. V.; Bourhis, L. J.; Gildea, R. J.; Howard, J. A. K.; Puschmann, H. *J. Appl.Crystallogr.* **2009**, *42*, 339-341.
(235) Macrae, C. F.; Bruno, I. J.; Chisholm, J. A.; Edgington, P. R.; McCabe, P.; Pidcock, E.; Rodriguez-Monge, L.; Taylor, R.; van de Streek, J.; Wood, P. A. *J. Appl.*

Crystallogr. **2008**, *41*, 466-470.
(236) Spek, A. L.; Version 1.62 ed.; University of Utrecht 1999.
(237) Nakamoto, K. In *Infrared Spectra of Inorganic and Coordination Compounds Part B.*; 6th ed.; John Wiley & Sons: New York, , 2009.
(238) Zhou, B.; Silva, N. J. O.; Shi, F.-N.; Palacio, F.; Mafra, L.; Rocha, J. *Eur. J.Inorg. Chem.* **2012**, *2012*, 5259-5268.
(239) Wojciechowska, A.; Daszkiewicz, M.; Bieńko, A. *Polyhedron* **2009**, *28*, 1481-1489.
(240) Bernstein, J.; Davis, R. E.; Shimoni, L.; Chang, N.-L. *Angew. Chem., Int. Ed.* **1995**, *34*, 1555-1573.
(241) Yang, C.-T.; Vetrichelvan, M.; Yang, X.; Moubaraki, B.; Murray, K. S.; Vittal, J. J. *Dalton Trans.* **2004**, 113-121.
(242) Jia, L.; Tang, N.; Vittal, J. J. *Inorg. Chim. Acta* **2009**, *362*, 2525-2528.
(243) Sreenivasulu, B.; Vittal, J. J. *Inorg. Chim. Acta* **2009**, *362*, 2735-2743.
(244) Sreenivasulu, B.; Vittal, J. J. *Angew. Chem., Int. Ed.* **2004**, *43*, 5769-5772.
(245) Yang, L.-J.; Lei, T.; Liu, W.; Chen, W.-Q.; Lin, M.-S.; Li, L.; Li, W.; Li, Y. *Inorg. Chem. Commun.* **2012**, *21*, 12-15.
(246) Feng, L.; Chen, Z.; Zeller, M.; Luck, R. L. *Inorg. Chim. Acta* **2013**, *394*, 729-740.
(247) Lü, Z.; Zhang, D.; Gao, S.; Zhu, D. *Inorg. Chem. Commun.* **2005**, *8*, 746-750.
(248) Fang, X.-Q.; Deng, Z.-P.; Huo, L.-H.; Wan, W.; Zhu, Z.-B.; Zhao, H.; Gao, S. *Inorg. Chem.* **2011**, *50*, 12562-12574.
(249) Saraswatula, V. G.; Bhat, M. A.; Gurunathan, P. K.; Saha, B. K. *CrystEngComm* **2014**, *16*, 4715-4721.
(250) Elacqua, E.; Kaushik, P.; Groeneman, R. H.; Sumrak, J. C.; Bučar, D.-K.; MacGillivray, L. R. *Angew. Chem., Int. Ed.* **2012**, *51*, 1037-1041.
(251) Xinfa, L; Rong, C. *Chinese J. Struct. Chem.* **2009**, *28*, 1439.
(252) Wojciechowska, A.; Daszkiewicz, M.; Staszak, Z.; Trusz-Zdybek, A.; Bieńko, A.; Ozarowski, A. *Inorg. Chem.* **2011**, *50*, 11532-11542.
(253) Dunn, T. M. In *The visible and ultraviolet spectra of complex compounds in modern coordination chemistry*; Interscience: New York 1960.
(254) K. Nakanishi, Berova, N; Woody, R. W. In *Circular Dichroism: Principles and Applications*; VCH: New York 1994.
(255) Kaitner, B.; Kamenar, B.; Pauliç, N.; Raos, N.; Simeon, V. L. *J. Coord. Chem.* **1987**, *15*, 373-381.
(256) Kaitner, B.; Paulić, N.; Pavlović, G.; Sabolović, J. *Polyhedron* **1999**, *18*, 2301-2311.
(257) Kaitner, B.; Paulic, N.; Raos, N. *J. Coord. Chem.* **1992**, *25*, 335-335.
(258) Kaitner, B.; Paulić, N.; Raos, N. *J. Coord. Chem.* **1991**, *24*, 291-304.
(259) Kaitner, B.; Paulić, N.; Raos, N. *J. Coord. Chem.* **1992**, *25*, 337-347.
(260) Kaitner, B.; Pavlović, G.; Paulić, N.; Raos, N. *J. Coord. Chem.* **1995**, *36*, 327-338.
(261) Ohata, N.; Masuda, H.; Yamauchi, O. *Inorg. Chim. Acta* **1999**, *286*, 37-45.
(262) Ohata, N.; Masuda, H.; Yamauchi, O. *Inorg. Chim. Acta* **2000**, *300-302*, 749-761.
(263) Nash, C. P.; Schaefer, W. P. *J. Am. Chem. Soc.***1969**, *91*, 1319-1324.
(264) Fawcett, T. G.; Ushay, M.; Rose, J. P.; Lalancette, R. A.; Potenza, J. A.; Schugar, H. J. *Inorg. Chem.* **1979**, *18*, 327-332.
(265) Comba, P.; Hambley, T. W.; Lawrance, G. A.; Martin, L. L.; Renold, P.; Varnagy, K. *J. Chem. Soc., Dalton Trans.* **1991**, 277-283.
(266) Macías, B.; Villa, M. V.; Sánchez-Mesonero, L.; Sanz, F.; Borrás, J.; González-

Álvarez, M. *Z. Anorg. Allg. Chem.* **2007**, *633*, 1937-1944.
(267) Ganguly, R.; Sreenivasulu, B.; Vittal, J. J. *Coord. Chem.Rev.***2008**, *252*, 1027-1050.
(268) Ranford, J. D.; Vittal, J. J.; Wu, D.; Yang, X. *Angew. Chem., Int. Ed.* **1999**, *38*, 3498-3501.
(269) Yang, X.; Wu, D.; Ranford, J. D.; Vittal, J. J. *Cryst. Growth Des.***2005**, *5*, 41-43.
(270) Yang, X.; Ranford, J. D.; Vittal, J. J. *Cryst. Growth Des.* **2004**, *4*, 781-788.
(271) Wisser, B.; Lu, Y.; Janiak, C. *Z. Anorg. Allg. Chem.* **2007**, *633*, 1189-1192.
(272) Biradha, K. *CrystEngComm* **2003**, *5*, 374-384.
(273) Guo, W.-T.; Miao, Z.-M.; Wang, Y.-L. *Z. Naturforsch. B* **2012**, *67*, 774-782.
(274) Lou, B.-Y.; Hong, M.-C. *Acta Crystallogr. E Struct. Rep. Online* **2008**, *64*, m405-m405.
(275) Karmakar, R.; Choudhury, C. R.; Mitra, S.; Dahlenburg, L. *Struct. Chem.* **2005**, *16*, 611-616.
(276) Bleaney, B; Bowers, K. D. *Proc. R. Soc. London, Ser. A* **1952**, *214*, 451-465.
(277) Gupta, R.; Mukherjee, S.; Mukherjee, R. *J. Chem. Soc., Dalton Trans.* **1999**, 4025-4030.
(278) Mandal, S. K.; Thompson, L. K.; Newlands, M. J.; Gabe, E. J.; Nag, K. *Inorg. Chem.* **1990**, *29*, 1324-1327.
(279) Saimiya, H.; Sunatsuki, Y.; Kojima, M.; Kashino, S.; Kambe, T.; Hirotsu, M.; Akashi, H.; Nakajima, K.; Tokii, T. *J. Chem. Soc., Dalton Trans.* **2002**, 3737-3742.
(280) Sahoo, S. C.; Ray, M. *Chem.-Eur. J.* **2010**, *16*, 5004-5007.
(281) Bandyopadhyay, S.; Mukherjee, G. N.; Drew, M. G. B. *Inorg. Chim. Acta* **2006**, *359*, 3243-3251.
(282) Liu, K.; Cruzan, J. D.; Saykally, R. J. *Science* **1996**, *271*, 929-933.
(283) Ludwig, R. *Angew. Chem., Int. Ed.***2001**, *40*, 1808-1827.
(284) Ghosh, S. K.; Bharadwaj, P. K. *Angew. Chem., Int. Ed.* **2004**, *43*, 3577-3580.
(285) Gruenloh, C. J. *Science* **1997**, *276*, 1678-1681.
(286) Tsai, C. J.; Jordan, K. D. *J. Chem.Phys.* **1991**, *95*, 3850-3853.
(287) Buck, U.; Ettischer, I.; Melzer, M.; Buch, V.; Sadlej, J. *Phys. Rev. Lett.* **1998**, *80*, 2578-2581.
(288) Blanton, W. B.; Gordon-Wylie, S. W.; Clark, G. R.; Jordan, K. D.; Wood, J. T.; Geiser, U.; Collins, T. J. *J. Am. Chem. Soc.***1999**, *121*, 3551-3552.
(289) Ma, B.-Q.; Sun, H.-L.; Gao, S. *Chem. Commun.***2005**, 2336-2338.
(290) Atwood, J. L.; Barbour, L. J.; Ness, T. J.; Raston, C. L.; Raston, P. L. *J. Am. Chem. Soc.***2001**, *123*, 7192-7193.
(291) Doedens, R. J.; Yohannes, E.; Khan, M. I. *Chem. Commun.* **2002**, 62-63.
(292) Ferguson, G.; Glidewell, C. *Acta Crystallogr. E Struct. Rep. Online* **2003**, *59*, m710-m712.
(293) Psomas, G.; Raptopoulou, C. P.; Iordanidis, L.; Dendrinou-Samara, C.; Tangoulis, V.; Kessissoglou, D. P. *Inorg. Chem.* **2000**, *39*, 3042-3048.
(294) Brown, G. M.; Chidambaram, R. *Acta Crystallogr. B Struct. Crystallogr. Cryst. Chem.* **1973**, *29*, 2393-2403.
(295) Mehrortara, R. C; Bohra, R. In *Metal Carboxylates*; Academic Press: London 1983.
(296) B. Kozlevčar, I. K., Z. Jagličić, A. Pevec, N. Kitanovski, P. Strauch, P. Šegedin, *Croat. Chem Acta* **2009**, *82*, 463-467.
(297) van Niekerk, J. N.; Schoening, F. R. L. *Acta Crystallogr.* **1953**, *6*, 227-232.

(298) Smith, T. D.; Pilbrow, J. R. *Coord. Chem. Rev.* **1974**, *13*, 173-278.
(299) de Meester, P.; Fletcher, S. R.; Skapski, A. C. *J. Chem. Soc., Dalton Trans.* **1973**, 2575-2578.
(300) Kim, T. K.; Suh, M. P. *Chem. Commun.* **2011**, *47*, 4258-4260.
(301) Ma, L.; Lin, W. *J. Am. Chem. Soc.* **2008**, *130*, 13834-13835.
(302) H.K. Lee, D. M., B.-Y. Cho, S. W. Lee *Bull. Kor. Chem. Soc.* **2004**, *25*, 1955-1958.
(303) Lohani, C. R.; Kim, J. M.; Lee, K.-H. *Tetrahedron* **2011**, *67*, 4130-4136.
(304) Lohani, C. R.; Neupane, L. N.; Kim, J.-m.; Lee, K.-H. *Sens. Actuators B* **2012**, *161*, 1088-1096.
(305) Ma, L.-J.; Cao, W.; Liu, J.; Zhang, M.; Yang, L. *Sens. ActuatorsB* **2013**, *181*, 782-786.
(306) Zhao, M.; Ma, L.; Zhang, M.; Cao, W.; Yang, L.; Ma, L.-J. *Spectrochim. Acta A: Mol. Biomol.Spectrosc.* **2013**, *116*, 460-465.
(307) Fu, L.; Mei, J.; Zhang, J.-T.; Liu, Y.; Jiang, F.-L. *Luminescence* **2013**, *28*, 602-606.
(308) Neupane, L. N.; Kim, J. M.; Lohani, C. R.; Lee, K.-H. *J.Mater. Chem.* **2012**, *22*, 4003-4008.
(309) Hatai, J.; Pal, S.; Jose, G. P.; Bandyopadhyay, S. *Inorg. Chem.***2012**, *51*, 10129-10135.
(310) Bhattacharya, A. B.; Bakuli, S.; Chattopadhyay, P.; Das, S.; Bera, S.; Dolui, T.; Maiti, S. *Adv. Sci., Eng. Med.* **2014**, *6*, 985-990.
(311) Nooredeen Abbas, M.; Radwan, A.-L. A.; Nawwar, G. A.; Zine, N.; Errachid, A. *Anal. Meth.* **2015**, *7*, 930-942.
(312) Li, L.; Ji, Y.; Tang, X. *Anal. Chem.* **2014**, *86*, 10006-10009.
(313) Masih, D.; Aly, S. M.; Alarousu, E.; Mohammed, O. F. *J. Mater. Chem. A* **2015**, *3*, 6733-6738.
(314) Patil, R.; Tayade, K.; Sahoo, S. K.; Singh, J.; Singh, N.; Hundiwale, D.; Kuwar, A. *J. Mol. Recog.* **2014**, *27*, 683-688.
(315) Karimipour, G.; Gharaghani, S.; Ahmadpour, R. *E-J. Chem.***2012**, *9*, 2565-2574.
(316) Nomura, T.; Hikichi, Y.; Nakagawa, G. *Bull. Chem. Soc. Jap.***1988**, *61*, 2993-2995.
(317) Wu, Y.-S.; Li, C.-Y.; Li, Y.-F.; Tang, J.-L.; Liu, D. *Sens. Act.. B: Chem.***2014**, *203*, 712-718.
(318) Quiñonero, D.; Frontera, A.; Deyà, P. M. *ChemPhysChem* **2008**, *9*, 397-399.
(319) Gural'skiy, I. y. A.; Escudero, D.; Frontera, A.; Solntsev, P. V.; Rusanov, E. B.; Chernega, A. N.; Krautscheid, H.; Domasevitch, K. V. *Dalton Transactions* **2009**, 2856-2864.
(320) Gamez, P.; Mooibroek, T. J.; Teat, S. J.; Reedijk, J. *Acc. Chem. Res.***2007**, *40*, 435-444.
(321) Frański, R.; Gierczyk, B.; Schroeder, G. *J. Amer.Soc. Mass. Spectrom.* **2009**, *20*, 257-262.
(322) Chakravarty, S.; Sheng, Z.-Z.; Iverson, B.; Moore, B. *FEBS Letters* **2012**, *586*, 4180-4185.
(323) Garau, C.; Frontera, A.; Quiñonero, D.; Ballester, P.; Costa, A.; Deyà, P. M. *ChemPhysChem* **2003**, *4*, 1344-1348.
(324) Gil-Ramírez, G.; Escudero-Adán, E. C.; Benet-Buchholz, J.; Ballester, P. *Angew.Chem., Int. Ed.* **2008**, *47*, 4114-4118.
(325) de Hoog, P.; Gamez, P.; Mutikainen, I.; Turpeinen, U.; Reedijk, J. *Angew. Chem.*

2004, *116*, 5939-5941.
(326) Rosokha, Y. S.; Lindeman, S. V.; Rosokha, S. V.; Kochi, J. K. *Angew. Chem., Int. Ed.***2004**, *43*, 4650-4652.
(327) Chifotides, H. T.; Dunbar, K. R. *Acct. Chem. Res.***2013**, *46*, 894-906.
(328) Wang, D.-X.; Wang, M.-X. *J. Am.Chem. Soc.* **2013**, *135*, 892-897.
(329) Khatua, S.; Choi, S. H.; Lee, J.; Kim, K.; Do, Y.; Churchill, D. G. *Inorg. Chem.***2009**, *48*, 2993-2999.
(330) Gupta, V.; Goyal, R.; Sharma, R. *Talanta* **2008**, *76*, 859-864.
(331) Hu, Z.-Q.; Wang, X.-M.; Feng, Y.-C.; Ding, L.; Li, M.; Lin, C.-S. *Chem. Commun.* **2011**, *47*, 1622-1624.
(332) White, N. G.; Lovett, H. G.; Beer, P. D. *RSC Adv.***2014**, *4*, 12133.
(333) Caballero, A.; White, N. G.; Beer, P. D. *CrystEngComm* **2014**, *16*, 3694-3698.
(334) Mirabi, A.; Shokuhi Rad, A.; Khodadad, H. *J.Magn. Magn. Mater.* **2015**, *389*, 130-135.
(335) Cui, M.-h.; Liu, Q.; Fei, Q.; Fei, Y.-q.; Liu, Y.-m.; Shan, H.-y.; Feng, G.-d.; Huan, Y.-F. *Anal. Methods* **2015**, *7*, 4252-4256.
(336) Hou, X. Y.; Chen, S.; Tang, J.; Long, Y. F.; Zhu, L. *Anal. Methods* **2015**, *7*, 2542-2546.
(337) Vedamalai, M.; Periasamy, A. P.; Wang, C.-W.; Tseng, Y.-T.; Ho, L.-C.; Shih, C.-C.; Chang, H.-T. *Nanoscale* **2014**, *6*, 13119-13125.
(338) Cao, Y.; Ding, L.; Wang, S.; Liu, Y.; Fan, J.; Hu, W.; Liu, P.; Fang, Y. *ACS Appl. Mater. Inter.* **2014**, *6*, 49-56.
(339) Anbu, S.; Ravishankaran, R.; Guedes da Silva, M. F. C.; Karande, A. A.; Pombeiro, A. J. L. *Inorg. Chem.* **2014**, *53*, 6655-6664.
(340) Wang, H.; Sun, L.; Li, Y.; Fei, X.; Sun, M.; Zhang, C.; Li, Y.; Yang, Q. *Langmuir* **2011**, *27*, 11609-11615.
(341) Li, Z. a.; Lou, X.; Yu, H.; Li, Z.; Qin, J. *Macromolecules* **2008**, *41*, 7433-7439.
(342) Yuan, Z.; Cai, N.; Du, Y.; He, Y.; Yeung, E. S. *Anal. Chem.* **2014**, *86*, 419-426.
(343) Strambini, G. B.; Gabellieri, E. *J.Phys. Chem.* **1991**, *95*, 4347-4352.
(344) Duan, Y. L.; Shi, Y. G.; Chen, J. H.; Wu, X. H.; Wang, G. K.; Zhou, Y.; Zhang, J. F. *Tetrahedron Lett.* **2012**, *53*, 6544-6547.
(345) Shabani, R; Mozafferi, S. A.; Husain, S. W.; Tehrani, M. S. *Iran. J. Sci. Technol., Trans. A*, **2009**, *33*, 335-347.
(346) Wang, X.-L.; Luan, J.; Lin, H.-Y.; Le, M.; Liu, G.-C. *Dalton Transactions* **2014**, *43*, 8072-8082.
(347) Qian, C.; Guo, Q.; Xu, M.; Yuan, Y.; Yao, J. *RSC Adv.* **2015**, *5*, 53306-53312.
(348) Chen, K.; Xu, M.; Ren, Y.; Song, G.; Hu, Y.; Cheng, H.; Shang, C. *Chromatogr.***2014**, *78*, 131-137.
(349) Xie, H.; Wang, H.; Xu, Z.; Qiao, R.; Wang, X.; Wang, X.; Wu, L.; Lu, H.; Feng, S. *J. Mater. Chem. C* **2014**, *2*, 9425-9430.
(350) Rameshkumar, P.; Viswanathan, P.; Ramaraj, R. *Sens. Act. B: Chem.***2014**, *202*, 1070-1077.
(351) Aluri, G. S.; Motayed, A.; Davydov, A. V.; Oleshko, V. P.; Bertness, K. A.; Rao, M. V. *IEEE Sens. J.***2013**, *13*, 1883-1888.
(352) Meaney, M. S.; McGuffin, V. L. *Anal.Chim. Acta* **2008**, *610*, 57-67.
(353) Goodpaster, J. V.; McGuffin, V. L. *Anal. Chem.* **2001**, *73*, 2004-2011.

(354) Nakamura, T.; Thomas, J. K. *Langmuir* **1985**, *1*, 568-573.
(355) Seely, G. R. *J. Phys.Chem.***1969**, *73*, 125-129.
(356) Gole, B.; Bar, A. K.; Mukherjee, P. S. *Chem. Commun.* **2011**, *47*, 12137-12139.
(357) Gole, B.; Shanmugaraju, S.; Bar, A. K.; Mukherjee, P. S. *Chem.Commun.* **2011**, *47*, 10046-10048.
(358) He, Y.-C.; Zhang, H.-M.; Liu, Y.-Y.; Zhai, Q.-Y.; Shen, Q.-T.; Song, S.-Y.; Ma, J.-F. *Cryst. Growth Des.***2014**, *14*, 3174-3178.
(359) Del Re, J.; Moore, M. H.; Ratna, B. R.; Szuchmacher Blum, A. *Phys. Chem. Chem. Phys.* **2013**, *15*, 8318.
(360) Wang, X.; Yang, Y.; Gao, H. *J. Lumin.* **2014**, *156*, 229-234.
(361) Wang, K.; Yang, H.; Qian, X.; Xue, Z.; Li, Y.; Liu, H.; Li, Y. *Dalton Trans.* **2014**, *43*, 11542-11547.
(362) Batista, R. M. F.; Oliveira, E.; Costa, S. P. G.; Lodeiro, C.; Raposo, M. M. M. *Org. Lett.***2007**, *9*, 3201-3204.
(363) Aydogan, A.; Koca, A.; Şener, M. K.; Sessler, J. L. *Org. Lett.***2014**, *16*, 3764-3767.
(364) Thiampanya, P.; Muangsin, N.; Pulpoka, B. *Org. Lett.***2012**, *14*, 4050-4053.
(365) Mahanta, S. P.; Kumar, B. S.; Baskaran, S.; Sivasankar, C.; Panda, P. K. *Org. Lett.* **2012**, *14*, 548-551.
(366) Chandra, B.; Mahanta, S. P.; Pati, N. N.; Baskaran, S.; Kanaparthi, R. K.; Sivasankar, C.; Panda, P. K. *Org. Lett.* **2013**, *15*, 306-309.
(367) Kumari, N.; Jha, S.; Bhattacharya, S. *J. Org. Chem.* **2011**, *76*, 8215-8222.
(368) Boyle, E. M.; Comby, S.; Molloy, J. K.; Gunnlaugsson, T. *J. Org. Chem.* **2013**, *78*, 8312-8319.
(369) Jo, Y.; Chidalla, N.; Cho, D.-G. *J. Org.Chem.* **2014**, *79*, 9418-9422.
(370) Teixeira, C. M.; Costa, A. I.; Prata, J. V. *Tetrahedron Lett.* **2013**, *54*, 6602-6606.
(371) Zhan, J.; Zhu, X.; Fang, F.; Miao, F.; Tian, D.; Li, H. *Tetrahedron* **2012**, *68*, 5579-5582.

APPENDIX

Table A1. Crystal Structure Data and Refinement Parameters for **1**, **5**, and **9**.

Compound	**1**	**5**	**9**
Chemical Formula	$C_{33}H_{38}CuN_2O_8$	$C_{20}H_{30}CuN_2O_9$	$C_{32}H_{37}CuN_2O_4$
Formula Weight	654.19	506.00	577.18
Temperature (K)	260(2)	296(2)	200(2)
Wavelength (Å)	0.71073	0.71073	0.71073
Crystal System	Monoclinic	Orthorhombic	Triclinic
Space Group	$P2_1$	$P2_12_12_1$	$P1$
a (Å)	12.7195(19)	9.2543(6)	7.1532(9)
b (Å)	9.7533(14)	10.0380(8)	7.1678(11)
c (Å)	14.170(2)	23.8749(19)	15.319(2)
a (°)	90	90	91.476(10)
β (°)	115.087(9)	90	97.637(10)
γ (°)	90	90	112.158(9)
Z	2	4	1
V (Å^3)	1592.1(4)	2217.9(3)	718.52(17)
Density (mg/cm^3)	1.365	1.515	1.334
μ (mm^{-1})	0.739	1.039	0.799
F (000)	686	1060	304
Theta (°) Range for Data Coll.	1.59 to 25.26	1.71 to 25.14	3.08 to 23.61
Reflections Collected	15183	13150	2087
Independent Reflections	5589	3868	1592
Reflections with I > 2σ(I))	4668	3282	1358
R_{int}	0.0435	0.0506	0.0296
No. of parameters refined	407	309	367
GOF on F^2	0.936	0.916	0.846
Final R_1[a]/wR_2[b] (I > 2σ(I))	0.0378/0.0762	0.0341/0.0616	0.0591/ 0.1418
R_1/wR_2 (all data)	0.0507/0.0831	0.0480/0.0675	0.0685/ 0.1483
Flack Parameter	0.027(9)	0.014(10)	0.4(0)
Largest diff. peak and hole (eÅ^{-3})	0.249 and -0.245	0.284 and -0.315	0.921 and -0.682

[a] $R_1 = \Sigma||F_o| - |F_c||/\Sigma|F_o|$. [b] $wR_2 = [\Sigma w(F_o^2 - F_c^2)^2/\Sigma w(F_o^2)^2]^{1/2}$, where $w = 1/[\sigma^2(F_o^2) + (aP)^2 + bP]$, $P = (F_o^2 + 2F_c^2)/3$

Table A2. Crystal Structure Data and Refinement Parameters for **13** and **17**.

Compound	**13**	**17**
Chemical Formula	$C_{28}H_{30}CuN_2O_7S_2$	$C_{30}H_{36}CuN_4O_9$
Formula Weight	634.2	660.17
Temperature (K)	296(2)	260(2)
Wavelength (Å)	0.71073	0.71073
Crystal System	Monoclinic	Monoclinic
Space Group	$P2_1$	$C2$
a (Å)	10.2891(10)	12.0163(8)
b (Å)	9.0692(9)	7.7380(5)
c (Å)	14.9871(17)	17.1859(14)
a (°)	90	90
β (°)	91.668(7)	107.324(3)
γ (°)	90	90
Z	2	2
V (Å^3)	1397.9(3)	1525.49(19)
Density (mg/cm^3)	1.507	1.437
μ (mm^{-1})	0.980	0.776
F (000)	658	690
Theta (°) Range for Data Coll.	1.98 to 25.14	2.48 to 25.04
Reflections Collected	8182	5711
Independent Reflections	4273	2469
Reflections with I > 2σ(I))	3435	2291
R_{int}	0.0435	0.0322
No. of Parameters refined	371	218
GOF on F^2	0.941	0.936
Final R_1[a]/wR_2[b] (I > 2σ(I))	0.0411/0.0776	0.0336/0.0691
R_1/wR_2 (all data)	0.0582/0.0858	0.0378/0.0711
Flack Parameter	0.011(13)	0.022(11)
Largest diff. peak and hole (eÅ^{-3})	0.283 and -0.309	0.182 and -0.196

[a] $R_1 = \Sigma||F_o| - |F_c||/\Sigma|F_o|$. [b] $wR_2 = [\Sigma w(F_o^2 - F_c^2)^2/\Sigma w(F_o^2)^2]^{1/2}$, where $w = 1/[\sigma^2(F_o^2) + (aP)^2 + bP]$, $P = (F_o^2 + 2F_c^2)/3$

Table A3. Crystal Structure Data and Refinement Parameters for **21**, **23a**, and **23b**.

Compound	**21**	**23a**	**23b**
Chemical Formula	$C_{16}H_{22}CuN_2O_7S_2$	$C_{36}H_{44}CuN_4O_{13}S_2$	$C_{20}H_{30}CuN_2O_9$
Formula Weight	482.01	868.41	506.00
Temperature (K)	296(2)	100(2)	296(2)
Wavelength (Å)	0.71073	0.71073	0.71073
Crystal System	Monoclinic	Monoclinic	Orthorhombic
Space Group	$P2_1$	$C2$	$P2_12_12_1$
a (Å)	10.6279(19)	11.9587(7)	9.2543(6)
b (Å)	7.9827(14)	7.9940(5)	10.0380(8)
c (Å)	23.447(4)	21.4277(11)	23.8749(19)
a (°)	90	90	90
β (°)	94.130(3)	96.212(3)	90
γ (°)	90	90	90
Z	4	2	4
V (Å^3)	1988.6(6)	2036.4(2)	2217.9(3)
Density (mg/cm^3)	1.610	1.416	1.515
μ (mm^{-1})	1.349	0.706	1.039
F (000)	996	906	1060
Theta (°) Range for Data Coll.	1.92 to 24.96	0.96 to 25.08	1.71 to 25.14
Reflections Collected	17388	7085	13150
Independent Reflections	6862	3073	3868
Reflections with I > 2σ(I))	4195	2713	3282
R_{int}	0.0768	0.0226	0.0506
No. of Parameters refined	514	260	309
GOF on F^2	1.002	1.010	0.916
Final R_1[a]/wR_2[b] (I > 2σ(I))	0.0590/ 0.1251	0.0322/ 0.0720	0.0341/0.0616
R_1/wR_2 (all data)	0.1118/ 0.1490	0.0402/ 0.0917	0.0480/0.0675
Flack Parameter	-0.001(13)	0.0(0)	0.014(10)
Largest diff. peak and hole (eÅ^{-3})	0.578 and -0.729	0.209 and -0.281	0.284 and -0.315

[a] $R_1 = \Sigma||F_o| - |F_c||/\Sigma|F_o|$. [b] $wR_2 = [\Sigma w(F_o^2 - F_c^2)^2/\Sigma w(F_o^2)^2]^{1/2}$, where $w = 1/[\sigma^2(F_o^2) + (aP)^2 + bP]$, $P = (F_o^2 + 2F_c^2)/3$

Table A4. Crystal Structure Data and Refinement Parameters for **25a** and **27a**.

Compound	**25a**	**27a**
Chemical Formula	$C_{36}H_{44}N_4O_{13}S_2Zn$	$C_{28}H_{30}CuN_2O_7S_2$
Formula Weight	870.24	634.2
Temperature (K)	296(2)	296(2)
Wavelength (Å)	0.71073	0.71073
Crystal System	Triclinic	Monoclinic
Space Group	*P*1	$P2_1$
a (Å)	7.1137(18)	10.2891(10)
b (Å)	7.1898(17)	9.0692(9)
c (Å)	21.127(5) Å	14.9871(17)
a (°)	86.028(17)°	90
β (°)	86.778(15)°	91.668(7)
γ (°)	67.351(16)°	90
Z	1	2
V ($Å^3$)	994.3(4)	1397.9(3)
Density (mg/cm^3)	1.453	1.507
μ (mm^{-1})	0.791	0.980
F (000)	454	658
Theta (°) Range for Data Coll.	1.93 to 25.14°	1.98 to 25.14
Reflections Collected	6682	8182
Independent Reflections	4859	4273
Reflections with I > 2σ(I))	3181	3435
R_{int}	0.0600	0.0435
No. of Parameters refined	517	371
GOF on F^2	1.033	0.941
Final $R_1{}^a/wR_2{}^b$ (I > 2σ(I))	0.0754/ 0.1632	0.0411/0.0776
R_1/wR_2 (all data)	0.1217/ 0.1887	0.0582/0.0858
Flack Parameter	0.100(13)	0.011(13)
Largest diff. peak and hole ($eÅ^{-3}$)	0.768 and -1.013	0.283 and -0.309

$^aR_1 = \Sigma||F_o| - |F_c||/\Sigma|F_o|$. $^bwR_2 = [\Sigma w(F_o^2 - F_c^2)^2/\Sigma w(F_o^2)^2]^{1/2}$, where $w = 1/[\sigma^2(F_o^2) + (aP)^2 + bP]$, $P = (F_o^2 + 2F_c^2)/3$

Table A5. Crystal Structure Data and Refinement Parameters for **31a** and **33a**.

Compound	**31a**	**33a**
Chemical Formula	$C_{30}H_{36}CuN_4O_9$	$C_{25}H_{29}CuFN_2O_8$
Formula Weight	660.17	568.06
Temperature (K)	260(2)	296(2)
Wavelength (Å)	0.71073	0.71073
Crystal System	Monoclinic	Triclinic
Space Group	*C*2	P1
a (Å)	12.0163(8)	5.9033(3)
b (Å)	7.7380(5)	10.3514(7)
c (Å)	17.1859(14)	11.7221(8)
a (°)	90	64.447(4)
β (°)	107.324(3)	81.231(4)
γ (°)	90	81.410(4)
Z	2	1
V (Å^3)	1525.49(19)	635.88(7)
Density (mg/cm^3)	1.437	1.489
μ (mm^{-1})	0.776	0.918
F (000)	690	297
Theta (°) Range for Data Coll.	2.48 to 25.04	1.94 to 24.99
Reflections Collected	5711	5569
Independent Reflections	2469	3705
Reflections with I > 2σ(I))	2291	3124
R_{int}	0.0322	0.0291
No. of Parameters refined	218	336
GOF on F^2	0.936	0.932
Final R_1[a]/wR_2[b] (I > 2σ(I))	0.0336/0.0691	0.0440/0.0775
R_1/wR_2 (all data)	0.0378/0.0711	0.0569/0.0832
Flack Parameter	0.022(11)	0.0(0)
Largest diff. peak and hole (eÅ^{-3})	0.182 and -0.196	0.358 and -0.309

[a] $R_1 = \Sigma||F_o| - |F_c||/\Sigma|F_o|$. [b] $wR_2 = [\Sigma w(F_o^2 - F_c^2)^2/\Sigma w(F_o^2)^2]^{1/2}$, where $w = 1/[\sigma^2(F_o^2) + (aP)^2 + bP]$, $P = (F_o^2 + 2F_c^2)/3$

Table A6. Crystal Structure Data and Refinement Parameters for **34**, **40** and **46**.

Compound	**34**	**40**	**46**
Chemical Formula	$C_{20}H_{26}Cu_2N_2O_{10}$	$C_{24}H_{27}Cl_2Cu_2N_4O_6$	$C_{21}H_{26}Cu_2N_2O_{10}Cl_2$
Formula Weight	581.51	665.47	664.44
Temperature (K)	150(2)	180(2)	150(2)
Wavelength (Å)	0.71073	0.71073	0.71073
Crystal System	Orthorhombic	Monoclinic	Monoclinic
Space Group	$P2_12_12_1$	$P2_1$	$C2$
a (Å)	7.4080(10)	7.4056(15)	25.187(5)
b (Å)	14.011(2)	13.343(3)	6.6672(13)
c (Å)	21.402(4)	13.433(3)	10.488(2)
a (°)	90	90	90
β (°)	90	103.786(3)	100.653(11)
g (°)	90	90	90
Z	4	2	2
V ($Å^3$)	2221.4(6)	1289.1(5)	1730.9(6)
Density (mg/cm^3)	1.709	1.714	1.415
μ(mm^{-1})	1.971	1.906	1.286
F(000)	1160	678	760
Theta (°) Range for Data Coll.	1.74° to 25.04°	2.18° to 24.99°	1.98° to 25.04°
Reflections Collected	14127	9580	5622
Independent Reflections	3915	4231	3007
Reflections with I > 2σ(I))	3314	4086	2804
R_{int}	0.0567	0.0186	0.0168
No. of Parameters refined	305	344	208
GOF on F^2	0.967	1.177	1.091
Final R_1[a]/wR_2[b] (I > 2σ(I))	0.0415/0.0882	0.0195/ 0.0421	0.0524/0.1632
R_1/wR_2 (all data)	0.0561/0.0954	0.0205/0.0423	0.0558/0.1657
Flack Parameter	0.0(0)	0.0(0)	0.0(0)
Largest diff. peak and hole ($eÅ^{-3}$)	1.002 and -0.592	0.235 and -0.231	1.311 and -0.479

[a] $R_1 = \Sigma||F_o| - |F_c||/\Sigma|F_o|$. [b] $wR_2 = [\Sigma w(F_o^2 - F_c^2)^2/\Sigma w(F_o^2)^2]^{1/2}$, where $w = 1/[\sigma^2(F_o^2) + (aP)^2 + bP]$, $P = (F_o^2 + 2F_c^2)/3$

Table A7. Crystal Structure Data and Refinement Parameters for **47** and **48**.

Compound	**47**	**48**
Chemical Formula	$C_{33}H_{38}Cu_2N_4O_{11}$	$C_{36}H_{46}Cu_2N_6O_{15}S_3$
Formula Weight	793.75	1026
Temperature (K)	180(2)	180(2)
Wavelength (Å)	0.71073	0.71073
Crystal System	Monoclinic	Monoclinic
Space Group	*C*2	*C*2
a (Å)	24.808(6)	23.4909(19)
b (Å)	6.1829(13)	6.8770(5)
c (Å)	10.517(3)	13.6838(12)
a (°)	90	90
β (°)	100.984(4)	101.667(5)
g (°)	90	90
Z	2	2
V ($Å^3$)	1745.0(7)	2164.9(3)
Density (mg/cm^3)	0.986	1.781
μ(mm^{-1})	0.656	2.104
F(000)	542	1140
Theta (°) Range for Data Coll.	1.67° to 25.16°	1.77° to 25.06°
Reflections Collected	8112	7839
Independent Reflections	2287	3380
Reflections with I > 2σ(I))	2115	2723
R_{int}	0.0268	0.0431
No. of Parameters refined	228	281
GOF on F^2	1.098	0.935
Final R_1[a]/wR_2[b] (I > 2σ(I))	0.0490/0.1434	0.0494/0.1315
R_1/wR_2 (all data)	0.0534/.1518	0.0654/0.1451
Flack Parameter	0.0(0)	0.0(0)
Largest diff. peak and hole ($eÅ^{-3}$)	1.169 and -0.391	1.099 and -0.405

[a] $R_1 = \Sigma||F_o| - |F_c||/\Sigma|F_o|$. [b] $wR_2 = [\Sigma w(F_o^2 - F_c^2)^2/\Sigma w(F_o^2)^2]^{1/2}$, where $w = 1/[\sigma^2(F_o^2) + (aP)^2 + bP]$, $P = (F_o^2 + 2F_c^2)/3$

Table A8. Crystal Structure Data and Refinement Parameters for **50** and **54a**.

Compound	**50**	**54a**
Chemical Formula	$C_{20}H_{26}Cu_2N_2O_{10}$	$C_{84}H_{92}Cu_2N_8O_{24}S_4$
Formula Weight	581.51	1852.97
Temperature (K)	150(2)	296(2)
Wavelength (Å)	0.71073	0.71073
Crystal System	Orthorhombic	Tetragonal
Space Group	$P2_12_12_1$	$I4$
a (Å)	7.4080(10)	20.3483(8)
b (Å)	14.011(2)	20.3483(8)
c (Å)	21.402(4)	11.0831(5)
a (°)	90	90
β (°)	90	90
g (°)	90	90
Z	4	2
V ($Å^3$)	2221.4(6)	4589.0(4)
Density (mg/cm^3)	1.709	1.341
μ(mm^{-1})	1.971	0.630
F(000)	1160	1932
Theta (°) Range for Data Coll.	1.74° to 25.04°	1.42 to 25.02°
Reflections Collected	14127	15737
Independent Reflections	3915	4021
Reflections with I > 2σ(I))	3314	3050
R_{int}	0.0567	0.0423
No. of Parameters refined	305	282
GOF on F^2	0.967	1.061
Final $R_1{}^a/wR_2{}^b$ (I > 2σ(I))	0.0415/0.0882	0.0533/ 0.1411
R_1/wR_2 (all data)	0.0561/0.0954	0.0764/0.1623
Flack Parameter	0.0(0)	0.0(0)
Largest diff. peak and hole ($eÅ^{-3}$)	1.002 and -0.592	0.506 and -0.296

$^aR_1 = \Sigma||F_o| - |F_c||/\Sigma|F_o|$. $^bwR_2 = [\Sigma w(F_o^2 - F_c^2)^2/\Sigma w(F_o^2)^2]^{1/2}$, where $w = 1/[\sigma^2(F_o^2) + (aP)^2 + bP]$, $P = (F_o^2 + 2F_c^2)/3$

Table A9. Selected Bond lengths (Å) for **1**, **5**, **9**, **13**, **17**, **21**, **23a** and **23b**.

1			
Cu1-O3	1.931(3)	Cu1-O5	1.957(3)
Cu1-N2	2.015(3)	Cu1-N1	2.022(3)
Cu1-O4	2.211(4)		
5			
Cu1-O2	1.939(3)	Cu1-O4	1.970(3)
Cu1-N1	2.009(4)	Cu1-N2	2.015(3)
Cu1-O6	2.313(3)	Cu1-O5	2.723(1)
9			
Cu1-O4	1.939(13)	Cu1-O1	1.962(13)
Cu1-N2	1.976(13)	Cu1-N1	1.978(12)
Cu1-O5	2.219(11)		
13			
Cu1-O2	1.901(5)	Cu1-O4	1.929(5)
Cu1-N1	1.997(5)	Cu1-N2	2.030(5)
Cu1-O3’	2.704 (5)		
17			
Cu1-O3	1.927(2)	Cu1-O3	1.927(2)
Cu1-N1	2.047(3)	Cu1-N1	2.047(3)
Cu1-O2	2.217(5)		
21			
Cu1-O2	1.918(8)	Cu1-O4	1.922(8)
Cu1-N1	1.980(9)	Cu1-N2	2.003(9)
Cu1-O1	2.328(9)	Cu2-O9	1.906(8)
Cu2-O12	1.931(8)	Cu2-N4	1.993(10)
Cu2-N3	1.996(9)	Cu2-O8	2.38(9)
23a			
Cu1-O5	1.919(3)	Cu1-O5	1.919(3)
Cu1-N1	2.022(4)	Cu1-N1	2.022(4)
Cu1-O1	2.183(6)		
23b			
Cu1-O8	1.933(5)	Cu1-O3	1.955(6)
Cu1-N1	2.021(6)	Cu1-N2	2.034(6)
Cu1-O11	2.197(5)		

Table A10. Selected Bond lengths (Å) for **25a**, **27a**, **31a**, **33a**, **34** and **40**,

25a			
Zn1-O1	1.980(12)	Zn1-O2	2.033(11)
Zn1-O4	2.050(10)	Zn1-N1	2.083(11)
Zn1-N2	2.089(12)		
27a			
Cu1-O4	1.944(12)	Cu1-O1	1.947(10)
Cu1-N1	2.008(12)	Cu1-N4	2.011(12)
Cu1-O10	2.158(10)	Cu2-O7	1.945(11)
Cu2-O5	1.951(12)	Cu2-N2	1.998(14)
Cu2-N3	2.018(13)	Cu2-O9	2.214(11)
31a			
Cu1-O5	1.924(4)	Cu1-O3	1.948(4)
Cu1-N1	1.998(5)	Cu1-N2	2.008(5)
Cu1-O9	2.324(5)		
33a			
Cu1-O3	1.918(4)	Cu1-O2	1.930(4)
Cu1-N2	1.989(4)	Cu1-N1	1.996(4)
34			
Cu2-O6	1.920(5)	Cu2-O2	1.950(4)
Cu2-O3	1.973(5)	Cu2-N1	1.982(6)
Cu2-O8	2.360(5)	Cu1-O4	1.950(5)
Cu1-O6	1.958(5)	Cu1-N2	1.983(6)
Cu1-O3	1.989(5)	Cu1-O7	2.389(5)
40			
Cu1-O3	1.925(2)	Cu1-O1	1.925(2)
Cu1-N1	1.966(3)	Cu1-O6	1.971(2)
Cu2-O9	2.257(3)	Cu2-O3	1.931(2)
Cu2-O4	1.939(2)	Cu2-O6	1.964(2)
Cu2-N2	1.984(3)		

Table A11. Selected Bond lengths (Å) for **46**, **47**, **48**, **50** and **54a**.

46			
Cu1-O1	1.909(6)	Cu1-O3	1.933(6)
Cu1-N1	1.984(7)	Cu1-N2	1.997(7)
47			
Cu1-O1	1.898(4)	Cu1-O2	1.952(5)
Cu1-N2	1.979(6)	Cu1-N1	1.997(5)
48			
Cu1-O2	1.906(6)	Cu1-O4	1.930(6)
Cu1-N2	1.981(8)	Cu1-N1	1.991(7)
50			
Ni1-N3	2.039(4)	Ni1-O6	2.052(4)
Ni1-O4	2.053(3)	Ni1-N1	2.057(4)
Ni1-O1	2.090(3)	Ni1-O3	2.128(3)
54a			
Cu1-O6	1.947(5)	Cu1-O6	1.947(5)
Cu1-O6	1.947(5)	Cu1-O6	1.947(5)
Cu1-O1	2.131(14)	Cu1-Cu2	2.638(19)
Cu2-O7	1.968(5)	Cu2-O7	1.968(5)
Cu2-O7	1.968(5)	Cu2-O7	1.968(5)
Cu2-O2	2.160(15)		

Table A12. Selected Bond angles (°) for **1** and **5**.

1			
O3-Cu1-O5	167.04(15)	O3-Cu1-N2	95.74(14)
O5-Cu1-N2	82.68(14)	O3-Cu1-N1	84.76(16)
O5-Cu1-N1	93.32(15)	N2-Cu1-N1	164.36(17)
O3-Cu1-O4	94.17(15)	O5-Cu1-O4	98.75(14)
N2-Cu1-O4	101.18(14)	N1-Cu1-O4	94.36(15)
5			
O2-Cu1-O4	177.84(12)	O2-Cu1-N1	85.00(14)
O4-Cu1-N1	94.02(13)	O2-Cu1-N2	97.71(14)
O4-Cu1-N2	82.48(13)	N1-Cu1-N2	157.76(15)
O2-Cu1-O6	89.97(11)	O4-Cu1-O6	92.03(11)
N1-Cu1-O6	94.78(13)	N2-Cu1-O6	107.25(13)

Table A13. Selected Bond angles (°) for **9**, **13**, **17** and **21**.

9			
O4-Cu1-O1	176.9(7)	O4-Cu1-N2	96.9(6)
O1-Cu1-N2	82.9(6)	O4-Cu1-N1	84.2(5)
O1-Cu1-N1	94.5(5)	N2-Cu1-N1	152.5(5)
O4-Cu1-O5	91.3(5)	O1-Cu1-O5	91.8(5)
N2-Cu1-O5	102.4(6)	N1-Cu1-O5	105.0(6)
Cu1-O5-H5B	125.(3)	C2-N1-Cu1	107.3(10)
C9-N1-Cu1	109.9(10)	C33-O1-Cu1	115.3(15)
C1-O4-Cu1	116.2(13)	Cu1-N1-H1	109.7
Cu1-O5-H5A	127.(3)	C16-N2-Cu1	108.4(12)
C24-N2-Cu1	109.3(8)	Cu1-N2-H2	108.8
13			
O2-Cu1-O4	171.0(2)	O2-Cu1-N1	84.9(2)
O4-Cu1-N1	93.8(2)	O2-Cu1-N2	99.6(2)
O4-Cu1-N2	82.7(2)	N1-Cu1-N2	172.1(2)
17			
O3-Cu1-O3	172.2(3)	O3-Cu1-N1	84.79(11)
O3-Cu1-N1	94.20(11)	O3-Cu1-N1	94.20(11)
O3-Cu1-N1	84.84(11)	N1-Cu1-N1	165.2(2)
O3-Cu1-O2	93.90(13)	O3-Cu1-O2	93.90(13)
N1-Cu1-O2	97.40(11)	N1-Cu1-O2	97.40(11)
21			
O2-Cu1-O4	177.7(4)	O2-Cu1-N1	95.9(3)
O4-Cu1-N1	85.3(3)	O2-Cu1-N2	85.1(3)
O4-Cu1-N2	93.1(3)	N1-Cu1-N2	157.7(3)
O2-Cu1-O1	86.6(3)	O4-Cu1-O1	95.4(3)
N1-Cu1-O1	91.6(3)	N2-Cu1-O1	110.7(3)
O9-Cu2-O12	176.2(4)	O9-Cu2-N4	94.1(4)
O12-Cu2-N4	85.1(4)	O9-Cu2-N3	86.1(4)
O12-Cu2-N3	94.9(4)	N4-Cu2-N3	177.7(4)
O9-Cu2-O8	88.3(4)	O12-Cu2-O8	88.0(3)
N4-Cu2-O8	92.1(4)	N3-Cu2-O8	90.2(3)

Table A14. Selected Bond angles (°) for **23a**, **23b**, **25a** and **27a**.

23a			
O5-Cu1-O5	176.8(3)	O5-Cu1-N1	84.40(13)
O5-Cu1-N1	94.68(13)	O5-Cu1-N1	94.68(13)
O5-Cu1-N1	84.40(13)	N1-Cu1-N1	147.2(2)
O5-Cu1-O1	91.61(15)	O5-Cu1-O1	91.61(15)
N1-Cu1-O1	106.39(11)	N1-Cu1-O1	106.39(11)
23b			
O8-Cu1-O3	171.8(2)	O8-Cu1-N1	84.7(2)
O3-Cu1-N1	95.3(2)	O8-Cu1-N2	92.8(2)
O3-Cu1-N2	84.6(2)	N1-Cu1-N2	161.4(2)
O8-Cu1-O11	99.4(3)	O3-Cu1-O11	88.7(3)
N1-Cu1-O11	95.8(2)	N2-Cu1-O11	102.8(2)
25a			
O1-Zn1-O2	96.3(5)	O1-Zn1-O4	93.2(5)
O2-Zn1-O4	170.3(5)	O1-Zn1-N1	119.8(6)
O2-Zn1-N1	91.9(4)	O4-Zn1-N1	81.6(4)
O1-Zn1-N2	108.6(6)	O2-Zn1-N2	82.2(4)
O4-Zn1-N2	96.7(4)	N1-Zn1-N2	131.6(5)
Zn1-O1-H1A	124.(4)	C1-N1-Zn1	113.3(9)
C8-N1-Zn1	105.6(7)	Zn1-N2-H2	108.6
Zn1-O1-H1B	123.(4)	Zn1-N1-H1	108.4
C17-N2-Zn1	113.6(8)	C24-N2-Zn1	106.6(8)
C9-O4-Zn1	115.6(9)	C32-O2-Zn1	113.2(9)
27a			
O4-Cu1-O1	169.7(5)	O4-Cu1-N1	85.2(5)
O1-Cu1-N1	93.1(5)	O4-Cu1-N4	92.5(5)
O1-Cu1-N4	85.4(5)	N1-Cu1-N4	158.4(5)
O4-Cu1-O10	96.7(5)	O1-Cu1-O10	93.6(5)
N1-Cu1-O10	98.7(5)	N4-Cu1-O10	103.0(4)
O7-Cu2-O5	171.5(6)	O7-Cu2-N2	94.8(6)
O5-Cu2-N2	84.1(6)	O7-Cu2-N3	83.8(5)
O5-Cu2-N3	95.2(5)	N2-Cu2-N3	165.6(6)
O7-Cu2-O9	92.7(5)	O5-Cu2-O9	95.8(5)
N2-Cu2-O9	94.1(5)	N3-Cu2-O9	100.3(5)

Table A15. Selected Bond angles (°) for **31a, 33a** and **34**.

31a			
O5-Cu1-O3	175.50(19)	O5-Cu1-N1	85.33(19)
O3-Cu1-N1	93.5(2)	O5-Cu1-N2	96.5(2)
O3-Cu1-N2	83.2(2)	N1-Cu1-N2	161.5(2)
O5-Cu1-O9	91.99(18)	O3-Cu1-O9	92.48(17)
N1-Cu1-O9	98.7(2)	N2-Cu1-O9	99.6(2)
C35-O5-Cu1	115.6(4)	C26-N1-Cu1	109.8(4)
C25-N1-Cu1	107.4(4)	Cu1-N1-H1A	109
C34-O9-Cu1	126.0(4)	C8-N2-Cu1	107.4(4)
Cu1-O9-H9	120.(5)	Cu1-N2-H2A	108.7
C10-N2-Cu1	110.8(4)	C9-O3-Cu1	113.7(4)
33a			
O3-Cu1-O2	91.17(15)	O3-Cu1-N2	84.16(17)
O2-Cu1-N2	172.9(2)	O3-Cu1-N1	174.25(19)
O2-Cu1-N1	83.93(17)	N2-Cu1-N1	100.99(17)
C17-O3-Cu1	116.8(3)	C10-N1-Cu1	113.1(3)
C8-N1-Cu1	104.3(3)	C10-N1-H1	109.6
C9-O2-Cu1	113.1(3)	Cu1-N1-H1	109.6
C18-N2-Cu1	111.4(3)	Cu1-N2-H10B	109.4
Cu1-N2-H10A	109.4		
34			
O6-Cu2-O2	98.2(2)	O6-Cu2-O3	80.1(2)
O2-Cu2-O3	151.5(2)	O6-Cu2-N1	174.1(2)
O2-Cu2-N1	86.0(2)	O3-Cu2-N1	94.3(2)
O6-Cu2-O8	90.8(2)	O2-Cu2-O8	109.5(2)
O3-Cu2-O8	99.06(19)	N1-Cu2-O8	91.8(2)
O4-Cu1-O6	176.7(2)	O4-Cu1-N2	84.3(2)
O6-Cu1-N2	93.4(2)	O4-Cu1-O3	103.5(2)
O6-Cu1-O3	78.8(2)	N2-Cu1-O3	172.1(2)
O4-Cu1-O7	91.52(18)	O6-Cu1-O7	86.31(19)
N2-Cu1-O7	96.4(2)	O3-Cu1-O7	84.21(19)
Cu2-O8-H8A	110.1	Cu2-O8-H8B	109.5
C18-N1-Cu2	108.5(4)	C17-N1-Cu2	107.6(4)
C11-O3-Cu2	124.1(4)	C11-O3-Cu1	135.3(4)
Cu2-O3-Cu1	98.6(2)	C10-O4-Cu1	115.4(4)
C1-O6-Cu2	128.1(4)	C1-O6-Cu1	124.4(4)
Cu2-O6-Cu1	101.5(2)	C20-O7-Cu1	115.6(4)
Cu2-N1-H1	108.9	Cu1-O7-H7	125.(2)
C19-O2-Cu2	114.4(4)	Cu1-N2-H2	107.5

Table A16. Selected Bond angles (°) for **40, 46** and **47**.

40

O3-Cu1-O1	177.01(11)	O3-Cu1-N1	93.95(10)
O1-Cu1-N1	84.64(10)	O3-Cu1-O6	79.19(9)
O1-Cu1-O6	102.57(10)	N1-Cu1-O6	169.42(10)
O3-Cu1-Cu2	39.07(7)	O1-Cu1-Cu2	142.43(7)
N1-Cu1-Cu2	132.93(8)	O6-Cu1-Cu2	40.30(7)
O3-Cu2-O4	97.39(10)	O3-Cu2-O6	79.21(10)
O4-Cu2-O6	154.69(11)	O3-Cu2-N2	169.36(11)
O4-Cu2-N2	85.70(10)	O6-Cu2-N2	93.62(10)
O3-Cu2-O9	91.35(10)	O4-Cu2-O9	104.62(10)
O6-Cu2-O9	100.54(10)	N2-Cu2-O9	97.73(11)
O3-Cu2-Cu1	38.91(7)	O4-Cu2-Cu1	133.05(7)
O6-Cu2-Cu1	40.48(7)	N2-Cu2-Cu1	134.02(8)
O9-Cu2-Cu1	94.70(7)	C1-O1-Cu1	114.7(2)
C10-O3-Cu1	123.5(2)	C10-O3-Cu2	132.1(2)
Cu1-O3-Cu2	102.02(11)	C11-O4-Cu2	115.4(2)
Cu2-O6-Cu1	99.22(11)	C2-N1-Cu1	107.7(2)
C4-N1-Cu1	111.0(2)	Cu2-N2-H11A	108.5
C12-N2-Cu2	109.0(2)	Cu1-N1-H1	108
C16-O6-Cu2	126.3(2)	C16-O6-Cu1	134.4(2)

46

O1-Cu1-O3	176.2(3)	O1-Cu1-N1	92.7(3)
O3-Cu1-N1	83.7(3)	O1-Cu1-N2	92.0(3)
O3-Cu1-N2	91.7(3)	N1-Cu1-N2	172.4(4)
C8-O3-Cu1	117.7(6)	C1-O1-Cu1	124.9(5)
C15-N2-Cu1	120.9(6)	C7-N1-Cu1	112.9(5)
C9-N1-Cu1	109.6(5)	C11-N2-Cu1	122.4(6)
Cu1-N1-H1	107.2		

47

O1-Cu1-O2	176.3(2)	O1-Cu1-N2	93.7(2)
O2-Cu1-N2	83.1(2)	O1-Cu1-N1	91.44(19)
O2-Cu1-N1	91.9(2)	N2-Cu1-N1	173.2(4)
Cu1-N2-H4	106.3	C1-N1-Cu1	121.4(4)
C5-N1-Cu1	121.5(4)	C13-O2-Cu1	116.2(5)
C12-N2-Cu1	110.3(4)	C11-N2-Cu1	113.0(5)
C6-O1-Cu1	123.2(4)		

Table A17. Selected Bond angles (°) for **48, 50** and **54a**.

48			
O2-Cu1-O4	172.6(3)	O2-Cu1-N2	83.8(3)
O4-Cu1-N2	93.9(3)	O2-Cu1-N1	91.1(3)
O4-Cu1-N1	92.1(3)	N2-Cu1-N1	170.2(4)
Cu1-N2-H2	106.5	C5-N1-Cu1	122.2(6)
C1-N1-Cu1	120.9(6)	C13-N2-Cu1	109.6(5)
C12-N2-Cu1	113.1(6)	C6-O4-Cu1	122.0(5)
C14-O2-Cu1	116.9(6)		
50			
N3-Ni1-O6	94.64(16)	N3-Ni1-O4	91.84(14)
O6-Ni1-O4	86.20(15)	N3-Ni1-N1	88.38(15)
O6-Ni1-N1	97.49(15)	O4-Ni1-N1	176.28(15)
N3-Ni1-O1	87.41(14)	O6-Ni1-O1	177.66(15)
O4-Ni1-O1	94.87(13)	N1-Ni1-O1	81.42(13)
N3-Ni1-O3	176.23(15)	O6-Ni1-O3	88.85(15)
O4-Ni1-O3	89.80(13)	N1-Ni1-O3	89.77(14)
O1-Ni1-O3	89.07(13)	C1-O1-Ni1	112.7(3)
C9-O3-Ni1	117.2(3)	C9-O3-H3	104.5(19)
Ni1-O3-H3	114.(4)	C14-O4-Ni1	130.5(3)
Ni1-O6-H6A	122.(2)	Ni1-O6-H6B	121.(2)
C13-N3-Ni1	127.1(3)	Ni1-N1-H1	107.6
C11-N3-Ni1	126.4(3)	C3-N1-Ni1	114.5(3)
54a			
O6-Cu1-O6	169.0(4)	O6-Cu1-O6	89.47(4)
O6-Cu1-O6	89.47(4)	O6-Cu1-O6	89.47(4)
O6-Cu1-O6	89.47(4)	O6-Cu1-O6	169.0(4)
O6-Cu1-O1	95.5(2)	O6-Cu1-O1	95.5(2)
O6-Cu1-O1	95.5(2)	O6-Cu1-O1	95.5(2)
O6-Cu1-Cu2	84.5(2)	O6-Cu1-Cu2	84.5(2)
O6-Cu1-Cu2	84.5(2)	O6-Cu1-Cu2	84.5(2)
O1-Cu1-Cu2	180	O7-Cu2-O7	167.5(4)
O7-Cu2-O7	89.33(4)	O7-Cu2-O7	89.33(4)
O7-Cu2-O7	89.32(4)	O7-Cu2-O7	89.33(4)
O7-Cu2-O7	167.5(4)	O7-Cu2-O2	96.23(18)
O7-Cu2-O2	96.23(18)	O7-Cu2-O2	96.23(18)
O7-Cu2-O2	96.23(18)	O7-Cu2-Cu1	83.77(18)

List of Publications

1. 'Hierarchical importance of coordination andhydrogen bonds in the formation of homochiral 2D coordination polymers and 2D supramolecular assemblies' Kumar, N.; Khullar, S.; Singh, Y.; Mandal, S. K. *CrystEngComm*, **2014**, *16*, 6730.
2. 'A homochiral luminescent metal organic coordination network with a four-fold symmetry' Kumar, N.; Khullar, S.; Mandal, S. K. *RSC Adv.*, **2014**, *4*, 47249.
3. 'Solvent effect on the neutral chiral supramolecular assemblies and their distinct receptor behaviour towards anions' Kumar, N.; Khullar, S.; Mandal, S. K. *Dalton Trans.*, **2015**, *44*, 1520.
4. 'Controlling the self-assembly of homochiral coordination architectures of Cu^{II} by the substitution in amino acid based ligands: synthesis, crystal structures and physicochemical properties' Kumar, N.; Khullar, S.; Mandal, S. K. *Dalton Trans.*, **2015**, *44*, 5672.
5. 'Encapsulation of water octamer by the chiral dimetal subunits comprised of Ni(II) centers and dicarboxylate linkers' Kumar, N.; Khullar, S.; Mandal, S. K., manuscript submitted.
6. 'Demonstration of structural diversity in tyrosine based chiral coordination architectures of Cu(II) and their chromogenic/fluorogenic selective anion sensing abilities' Kumar, N.; Khullar, S.; Kumar, N.; Mandal, S. K., manuscript to be submitted.
7. 'One-for-Three: a chiral fluorogenic receptor for selective sensing of cations, neutral small molecules, and anions' Kumar, N.; Mandal, S. K., manuscript to be submitted.
8. 'Triple action of a tyrosine derived probe: a solvent mediated flip-flop halide (iodide/fluoride) sensor and a pH indicator' Kumar, N.; Mandal, S. K., manuscript submitted.

Vita

The author, Navnita Kumar, was born on July 7, 1985 in Kasauli, H.P., India. She did her B.Sc in Chemistry (Hons.) and M.Sc. in Chemistry (Hons.) from Panjab University, Chandigarh in 2008 and 2010, respectively. She joined Indian Institute of Science Education and Research, Mohali, with a fellowship from MHRD, Government of India, to pursue her Ph.D. in Chemistry under the supervision of Professor Sanjay K. Mandal in August 2010.